Loong

ICANS

twelve

Volume 2

New Sources
Accelerator Workshop
Target Station Workshop

Rutherford Appleton Laboratory Report Number 94 — 025

Proceedings of the Twelfth Meeting of the

International Collaboration on Advanced Neutron Sources ICANS - XII

24 28 May 1993

held at the Cosener's House, Abingdon, Oxfordshire, U.K.

Volume 2

New Sources
Accelerator Workshop
Target Station Workshop

Editors:
Uschi Steigenberger
Tim Broome
Grahame Rees
A Soper

Science and Engineering Research Council, Rutherford Appleton Laboratory

Preface

The twelfth meeting of the International Collaboration on Advanced Neutron Sources - ICANS-XII- was held at the Cosener's House, Abingdon, UK, during the week of May 24 - 28, 1993, hosted by the Rutherford Appleton Laboratory.

The development of accelerator-based neutron sources is at an interesting and possibly critical point. The operational sources KEK, IPNS, LANSCE and ISIS continue to produce excellent science, fully justifying the original faith in these techniques and impressing supporters and critics alike. One new source, SINQ, is at an advanced stage of construction and is due to become operational in 1995, and advanced high power sources are under active consideration in Japan, Europe and America.

Technical experience from these sources and from the pulsed reactor IBR-2 are shared at ICANS meetings and common problems aired, often in a very frank and open way. This has contributed in no small measure to their successful developments, and will continue to be vital as next generation sources with beam powers in excess of 1 MW are planned.

The success of the Meeting resulted from the collective effort of many people. The Meeting would not have succeeded without the dedicated effort of the ISIS Organisation Committee and the suggestions of the ICANS contacts, but particular thanks must go to the participants themselves who made it such a stimulating week.

The ICANS collaboration is now over twenty years old: I look forward to a further twenty years of scientific interchange and international friendship.

Andrew Taylor
Head, ISIS Facility

Contents

Volume 1

Instrument Workshop

New Science from Pulsed Sources
J L Finney — I - 1

New Instrument Ideas - Old Instrument Problems

Reference Instrument Complement for IPNS Upgrade
R K Crawford — I - 24

A European Network for Neutron Instrumentation
M W Johnson — I - 32

The Use of Chopper Spectrometers for Cold-to-Epithermal Neutron Scattering at IPNS
C-K Loong, L I Donley, G E Ostrowski, R Kleb, J P Hammonds, L Soderholm, S Takahashi — I - 36

A New Chopper Spectrometer for Neutron Brillouin Scattering and Low-Angle Neutron Inelastic Scattering: PHAROS (Phase I)
R A Robinson, M Nutter, R L Ricketts, E Larson, J P Sandoval, P Lysaght, B J Olivier — I - 44

First Results from PHAROS, the New Chopper Spectrometer at LANSCE
B J Olivier, J P Sandoval, P Lysaght, M Nutter, R A Robinson — I - 52

MAPS: A Chopper Spectrometer to Measure High Energy Magnetic Excitations in Single Crystals
T G Perring, A D Taylor, R Osborn, D McK Paul, A T Boothroyd, G Aeppli — I - 60

Cold Neutrons on Pulsed Sources for High Resolution Spectroscopy and Long d-spacing Diffraction
C J Carlile, M A Adams, J B Forsyth, P S R Krishna — I - 73

Multicrystal Inverted Geometry Spectrometer NERA-PR at the IBR-2 Pulsed Reactor
I Natkaniec, S I Bragin, J Brankowski, J Mayer — I - 89

Performance of ROTAX
H Tietze-Jaensch, W Schmidt, R Geick — I - 97

Less Background, Better Contrast by Cooling Analyser Crystals
C J Carlile, M A Adams, P S R Krishna, M Prager, K Shibata, P Westerhuijs — I - 106

A new Beamline for Cold Neutron Storage Experiments on ISIS
E Jericha, H Rauch, M Schuster, C J Carlile — I - 118

The New Fourier Diffractometer at the IBR-2 Reactor: Design and First Results
V L Aksenov, A M Balagurov, V G Simkin, Yu V Taran, V A Trounov, V A Kudrjashev, A P Bulkin, V G Muratov, P Hiismaki, A Tiita, O Antson I - 124

SXD: Novel Single Crystal Studies using the Time-of-Flight Laue Technique
C C Wilson I - 132

Performance of the Amorphous Materials Diffractometer GLAD at IPNS
A J G Ellison, K J Volin, D L Price, R K Crawford I - 144

SPIDA - A Special Intense Diffractometer for Amorphous Materials
A C Hannon, A K Soper, R J Newport, W S Howells I - 152

ENGIN - An Engineering Strain Scanner at the ISIS Facility
M W Johnson , L Edwards, H G Priesmeyer, F Rustichelli, P J Withers, J S Wright I - 158

Small/Medium- Angle Diffractometer WINK
M Furusaka , K Suzuya, N Watanabe, M Osawa, I Fujikawa, S Satoh I - 166

A Very-Low-Q Diffractometer for an Advanced Spallation Source
P A Seeger, R P Hjelm I - 172

Detectors and Data Acquisition

ISIS Neutron Detectors
N J Rhodes, A J Boram, M W Johnson, E M Mott, A G Wardle I - 185

The Scintillation PSD JULIOS and its use in TOF-Diffractometry at ISIS
W Schäfer, E Jansen, A Szepesvary, R Skowronek, G Will, R Reinartz, K D Müller I - 200

Linearity and Calibration of Charge-Division and Rise-Time Encoded Gas PSDs
R K Crawford, P Thiyagarajan, J Chen I - 208

The ISIS Second Generation Data Acquisition Electronics System
J Norris, S Quinton, D Allen I - 216

Measuring Techniques and Special Sample Environment

Measurements of Strain in Individual Phases of Composites Before, During and After Mechanical Loading
J A Goldstone, M A M Bourke, D Davis, N Shi, A C Lawson, J E Allison I - 224

Time Resolved Studies on a Millisecond Time Scale: Transient Properties of the Ferroelectric Phase Transition in Rb_2ZnCl_4
U Steigenberger, G Eckold, M Hagen I - 232

The Effect of Inelastic Scattering upon Small Angle Diffraction Measurements
R K Heenan, A R Rennie I - 241

A Measurement of the Proton Wavefunction in Molecular Hydrogen by Neutron Compton Scattering
J Mayers I - 248

Development and Use of Pulsed Magnetic Fields for Neutron Diffraction Experiments
M Motokawa, M Arai, M Mino, K Ubukata, T Bokui, M Fujita I - 260

Neutron Diffraction to 10 GPa and Beyond: The State of the Art of the Paris-Edinburgh Cell
S Klotz, J M Besson, G Hamel, R J Nelmes, J S Loveday, R M Wilson, S Hull I - 268

Data Analysis

Rietveld Refinement of Magnetic Structures from Pulsed Neutron Source Powder Diffraction Data
R A Robinson, A C Lawson, A C Larson, R B von Dreele, J A Goldstone I - 273

A Dynamical Labelling Method for Extracting Partial Structure Factors
M Arai, A C Hannon, T Otomo I - 283

Applications of Bayesian Model Selection in Neutron Scattering
D Sivia I - 291

New Scans and Data Visualisation on ROTAX
W Schmidt , H Tietze-Jaensch, R Geick I - 292

Better Visualisation of Neutron Scattering Data using UNIRAS at ISIS
K Crennell I - 301

Using Databases for Improved Instrument Operations and Administration at ISIS
K Crennell I - 308

A Resolution Function Model for a Multi-Analyser Spectrometer
M Hagen, U Steigenberger I - 314

A Parametric Formulation of the Resolution Function of a Pulsed-Source Chopper Spectrometer
C-K Loong, J M Carpenter, S Ikeda I - 320

The Resolution Function of the Chopper Spectrometer HET at ISIS
T G Perring I - 328

Polarized Beams and Beamline Devices

^{3}He Nuclear Polarization and Neutron Spin Analysis
Y Masuda, K Asahi, M Doi, K Sakai, H Sato, Z Z Jian I - 338

Recent Progress in Supermirrors at PSI
P Böni, I S Anderson, P A Buffat, O Elsenhans, H P Friedli, H K Grimmer, R Hauert, K Leifer, J Penfold, J Söchtig I - 347

Polarized Neutron Reflection at LANSCE
M R Fitzsimmons, G S Smith, R Pynn, M A Nastasi I - 355

New Aspect in Employing Magnetic Anisotropic FeCo Thin Films as Neutron Polarizers
D A Korneev I - 363

User Dedicated Neutron Guide System at SINQ
W Wagner, J Duppich I - 368

Comparison of Neutron Efficiency of Reactor and Pulsed Source Instruments
F Mezei I - 377

Contents

Volume 2

Proposals for new Spallation Neutron Sources

Study of a European Spallation Source
H Lengeler — P - 1

Plans for a New Pulsed Spallation Source at Los Alamos
R Pynn — P - 7

IPNS Upgrade - A 1 MW Spallation Neutron Source
B S Brown, J M Carpenter, Y Cho, R K Crawford, A E Knox — P - 13

An Intense Pulsed Spallation Neutron Source using a High-Power Proton Linac for Nuclear Transmutation
N Watanabe — P - 21

AUSTRON - a Spallation Neutron Source for Central and Eastern Europe
H Schönauer, H Aiginger, W H Breunlich, P J Bryant, K Hübner, W Pirkl, M Regler, G H Rees, K Schindl, A Wrulich — P - 26

Advanced Neutron Source for Physical Research
Yu Ya Stavissky, Yu V Senichev — P - 36

Accelerator Workshop

Summary of the Accelerator Sessions
M K Craddock — A - 1

Reaching 200 μA on ISIS
C W Planner — A - 4

Study of Dual Harmonic Acceleration in ISIS
C R Prior — A - 11

Preliminary Report on the BNL Spallation Neutron Source Design Study
L N Blumberg — A - 20

Machine Studies at the Los Alamos Proton Storage Ring
R J Macek — A - 25

Overview of the NCNR Accelerator Studies
A J Jason — A - 33

Ion Source Development in the Culham Laboratory of AEA Technology
A J T Holmes — A - 41

Funneling Experience at Los Alamos: Experiments and Design
A J Jason, K F Johnson and S Nath A - 49

Conceptual Design for 1 MW Spallation Neutron Source at Argonne
Y Cho, J Bailey, B Brown, F Brumwell, J Carpenter, K Crawford, D Horan, D Jerng, R Kleb, A Knox, R Kustom, E Lessner, D McGhee, F Mills, H Moe, R Nielsen, C Potts, A Rauchas and K Thompson A - 57

IPNS - Upgrade RF System Design
R Kustom and D Horan A - 64

Study of 1 MW Neutron Source Synchrotron Dual Frequency Power Circuit for the Main Ring Magnets
D G McGhee A - 73

Basis for the Power Supply Reliability of the 1 MW Neutron Source
D G McGhee and M Fathizadeh A - 80

Performance of the 70 MeV Injector to the ISIS Synchrotron
N D West A - 85

Replacing a Popular Accelerator Control System
R P Mannix A - 93

Low Intensity and Injection Studies on the ISIS Synchrotron
C M Warsop A - 101

The ISIS Synchrotron RF System at High Intensity
P J S Barratt A - 109

Matching Problems between Linac and Compressor Ring
K Bongardt A - 115

Accelerator Studies at the KEK-PS Booster, Problems related with High Intensity Beam
I Yamane A - 124

Very Low Output Impedance RF System for High Intensity Accelerators
Y Irie A - 131

Operation of the RF System at the KEK PS
S Ninomiya A - 137

Room Temperature Vs Superconducting Linacs
H Heinrichs A - 144

FFAG Studies for a 5 MW Source
S A Martin, P F Meads, G Wustefeld, E Zaplatin and K Ziegler A - 153

A 2-Stage 5 MW FFAG
R Kustom A - 159

Compressor Ring Studies for a 5 MW Spallation Neutron Source
G H Rees A - 168

Choice of Proton Energy for New Sources
I S K Gardner A - 176

Target Station Workshop

Experience with IPNS targets
J M Carpenter and A G Hins T - 1

Measurement of Cooling Characteristics of the ISIS Tantalum Target
G M Allen, T A Broome, M A Clarke-Gayther and C W Planner T - 12

Operational Consequences of Induced Activity on the ISIS Target Station
T A Broome T - 20

LAHET Code System/CINDER'90 Validation Calculations and Comparison with Experimental Data
T O Brun, C A Beard, L L Daemen, E J Pitcher, G J Russell, W B Wilson T - 26

Inclusion of Preequilibrium Calculation into High Energy Transport Code
K Ishibashi, H Takeda, Y Yoshizawa, N Matsufuji, T Nakamoto, Y Wakuta and Y Nakahara T - 44

Pulsed Neutron Source of Moscow Meson Factory
M I Grachev, L V Kravchuk, A V Kuzin, S G Lebedev, V M Lobashev, V G Miroshnichenko, V A Mateev, O V Ponomarev, V N Sazanov, Yu V Senichev, S F Sidorkin, N M Sobolevsky, and Yu Ya Stavissky T - 53

Target-Moderator-Reflector Assembly for a High Power Pulsed Spallation Source
H Conrad T - 61

Pulsed Neutron Source of the Moscow Meson Factory on the base of Uranium Targets
A D Dementyev, V G Miroshnichenko, I Y Mosievskaya, S F Sidorkin, N M Sobolevsky, Y Y Stavissky, I I Konovalov, A A Maslov, I T Tretyakov, V I Trushkin T - 71

Spallation Neutron Measurement at Incident Proton Energies of 0 8 to 3 GeV
T Nakamoto, K Ishibashi, N Matsufuji, K Maehata, Y Wakuta, N Numajiri, H Takeda, S Meigo, S Chiba, Y Watanabe, T Nakamura and M Arai T - 80

Comparison of the Slow Neutron Intensity -0 8 GeV vs 3 GeV Protons
Y Kiyanagi, N Watanabe and M Arai T - 90

Conceptual Design of the Target Stations of the IPNS Upgrade
J M Carpenter, R K Crawford, R Kleb and A E Knox T - 95

Heat Generation and Neutron Beam Characteristics in a High Power Pulsed Neutron Source
D W Jerng and J M Carpenter T - 105

Target Station Design for a 1 MW Pulsed Spallation Neutron Source
G J Russell, G D Baker, R J Brewton, A Bridge, T O Brun, M Cappiello, C E Cummings, L L Daemen, D Davis, D Grisham, R P Hjelm, J S Elson, A Kernodle, M A Merrigan, E J Pitcher, H Robinson, L Walker and R Woods T - 115

The Choice of Optimum Proton Energy for a High Power Spallation Source - Issues for the Target Station
T A Broome T - 128

D_2 Cold Moderator System at SNQ
H Spitzer, K Geissmann, W Wagner and G S Bauer T - 132

First Experience of Cold Moderator Operation and Solid Methane Irradiation at the IBR-2 Pulsed Reactor
A A Beljakov, V G Ermilov, V L Lomidze, V V Melichov, and E P Shabalin T - 144

The ISIS Methane Moderator
T A Broome, J R Hogston, M Holding and W S Howells T - 156

Tailoring Intensities and Pulse shapes in Coupled Moderator-Reflector systems
J M Carpenter, Y Kiyanagi, N Watanabe H Iwasa and M Nakajima T - 164

Some Optimisation Studies on Flux-Trap Moderators for Increasing the Slow-Neutron Beam Intensity
Y Kiyanagi, N Watanabe and M Nakajima T - 172

Moderator Materials and Neutronic Performance
L L Daemen, G J Russell and E J Pitcher T - 181

Premoderator Studies for a Coupled Liquid-Hydrogen Moderator
Y Kiyanagi, N Watanabe, H Iwasa and Y Nakayama T - 196

A Hybrid Be/D_2O Reflector for ISIS
L L Daemen, E J Pitcher, G J Russell, T A Broome and M Holding T - 202

Studies of Decoupled Composite Moderators of Liquid Hydrogen and Zirconium Hydride
Y Kiyanagi, J M Carpenter, N Watanabe H Iwasa and M Nakajima T - 206

STUDY OF A EUROPEAN SPALLATION SOURCE

H Lengeler

Abstract

A brief account is given of a study proposed for a European Pulsed Spallation Neutron Source.

1. Introduction

Following a 1990 report on "Large Facilities" to the Commission of the European Community, (CEC), on how to secure neutron scattering in Europe beyond the year 2000, a series of meetings on Accelerators, Target Technologies and Neutron Scattering Instrumentation were held in 1991 and 1992 under a joint initiative of KFA, Jülich and RAL, Didcot, and which was supported by the CEC.

The conclusion of these meetings was that a two year, site independent feasibility study was needed for an Accelerator Driven, Pulsed Spallation Neutron Source (ESS), of the following specification:

5 MW average proton beam power at spallation targets, giving average thermal neutral fluxes comparable to that of the ILL Research Reactor;
Proton pulse durations of less than 3 μs; and
Pulse repetition rates of ≤ 50 Hz and 10 Hz at separate target stations.

The aims of the feasibility study were:

Produce a design with definite options;
Produce a realistic capital and operating cost estimate, to within ± 20%;
Relate the source performance to costs;
Identify future research and development, including prototypes; and
Evaluate safety aspects and availability of the proposed source.

An ESS Council has been constituted, and the Council has agreed on the 2 year, site independent ESS study and on the management structure shown on the appended table.

European Spallation Source

Proposed Management Structure

for the

ESS Study Project

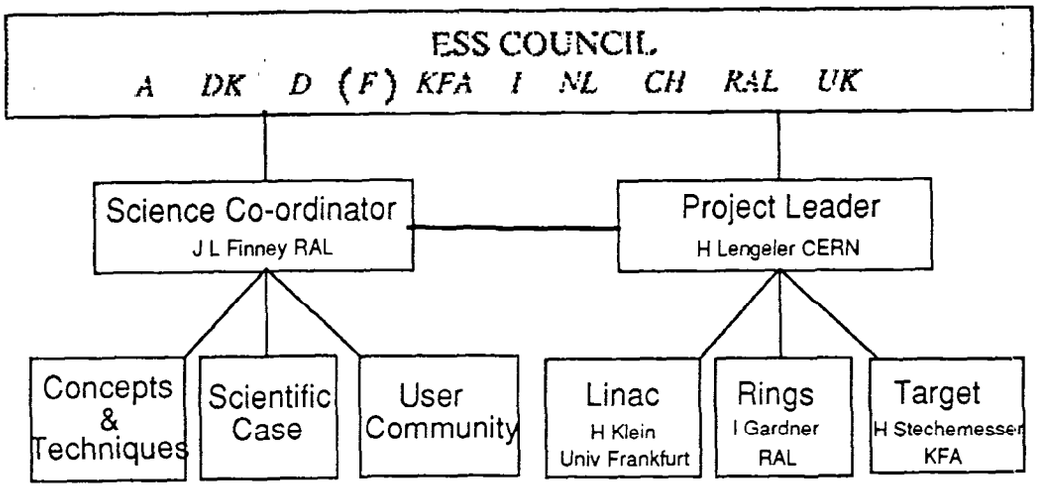

2. Accelerator Options

The main accelerator options are shown on a schematic diagram of the 5 MW source. The ring of the schematic represents one of the following:

a 0.46 - 3 (or 1.6) GeV Fixed Field Alternating Gradient Accelerator, FFAG;
a 0.8 to 3 GeV Rapid Cycling Synchrotron, RCS;
a single 2.4 GeV Accumulator Ring;
two 1.2 GeV Accumulators; or
three 0.8 GeV Accumulators.

For all these options, the H^- linear accelerator injector operates at 50 Hz, with the output energy as indicated. Two further options include a 1 GeV linear induction accelerator and a 30 GeV KAON Factory type accelerator. The linac consists of a radio frequency quadrupole unit (RFQ), fed from a H^- ion source, and followed by a drift tube and coupled cavity linac. A further option is the use of superconducting low-β cavities in place of the drift tube linac, and superconducting high-β cavities in place of the coupled cavity linac. The important design issues for the linacs include:

The requirement of low beam losses for hands-on-maintenance;
The further development of H^- ion sources;
The need (or not) of low energy linac funneling; and
The question of optimum beam chopper design.

Large circulating currents are needed in the rings, 2 10^{14} protons for the FFAG and RCS, and 2.6 10^{14} for the Accumulators. By comparison, the ISIS RCS has stored 4 10^{13} at 70 MeV and accelerated 2.5 10^{13} to 800 MeV. The important ring design issues are:

Choices of options;
Very low injection losses (problem of H° excited states);
Very low losses at all stages of storage, acceleration and extraction;
Use of complex, space charge, beam dynamic codes;
Specialised beam diagnostics and beam loss monitoring; and
High efficiency, localised beam loss collection.

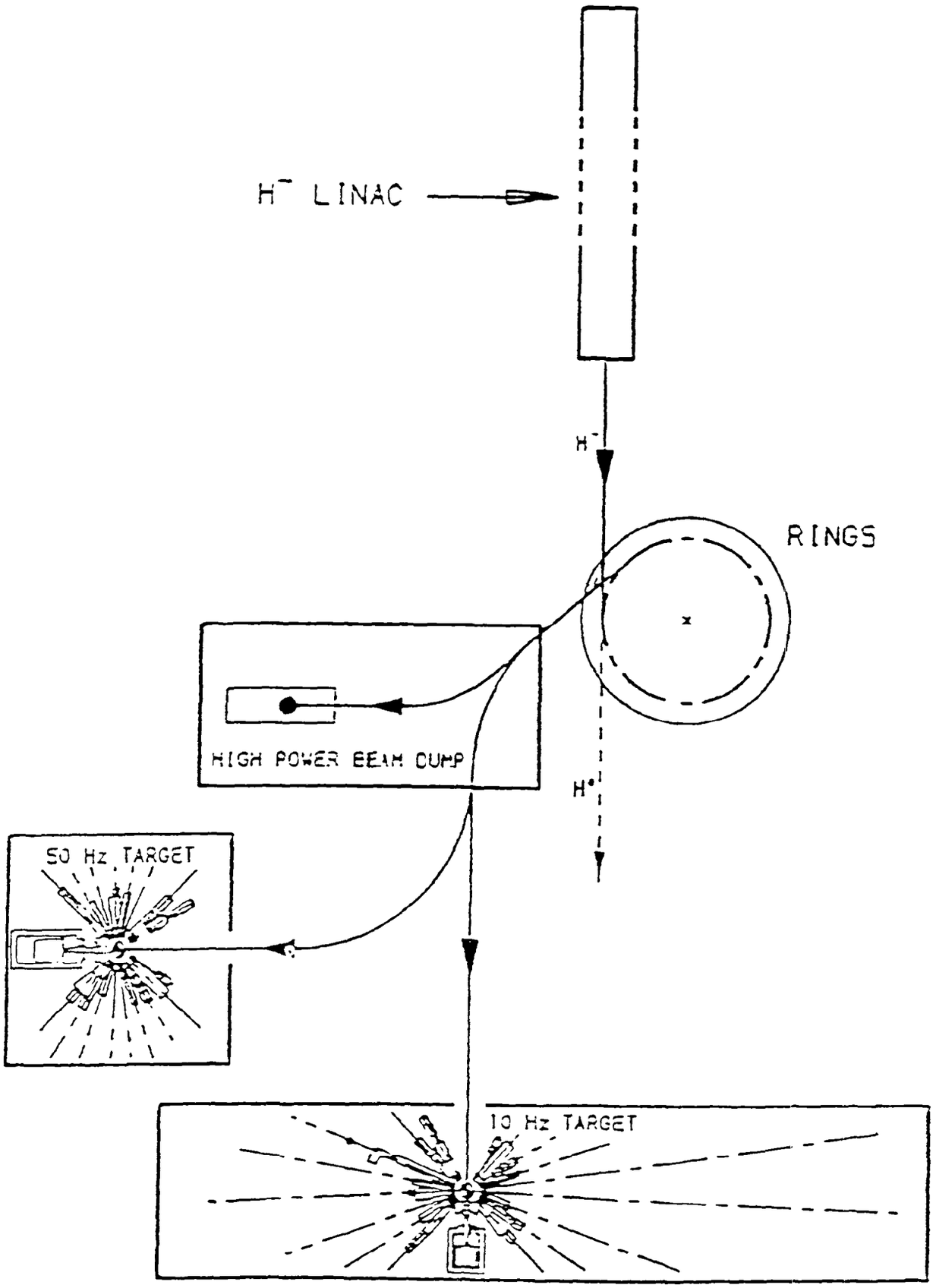

SCHEMATIC OF 5 MW SOURCE

3. Target and Material Research

Beam powers envisaged at the targets are 1 MW at 10 Hz and up to 5 MW at the 50 Hz station. Possible options for the 5 MW target, which has a power density of 2 MW/litre (2½xISIS), include:

A fixed, solid target;
A rotating, solid target; and
A liquid target.

The important design issues are:

Material problems due to radiation damage;
Optimum target, moderator and reflector configurations; and
Technology of liquid targets.

Innovative engineering solutions appear necessary.

4. Manpower and Possible Study Programme for ESS

The manpower estimate for the two year study is 45 man years. Various laboratories and universities will provide some resources for an interim phase, and this will grow to 25 man years in the CEC funded phase. In addition, a CEC contribution of 20 man years has been requested. A possible time scale for the ESS study is shown.

5. Final Remarks

Three study areas are emphasised:

a. New ideas and technologies may open up new options;
b. Reliable costing requires detailed collaboration with industry; and
c. Very high availability and reliability of the source is demanded to meet the stringent demands of ~ 2000 users, undertaking ~ 900 experiments per year.

Possible programme for ESS

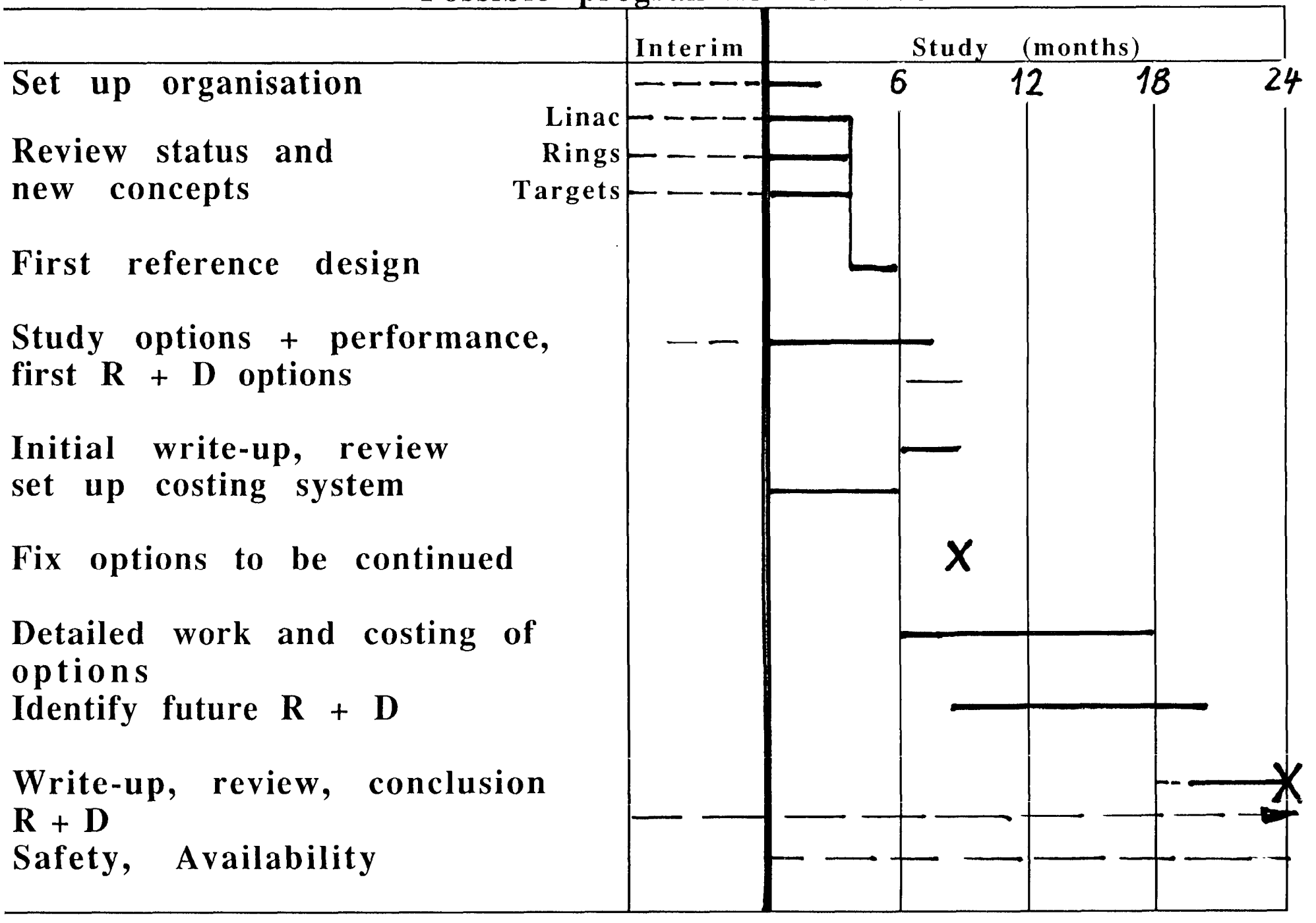

Plans for a New Pulsed Spallation Source at Los Alamos

Roger Pynn
Manuel Lujan Jr. Neutron Scattering Center, Los Alamos National Laboratory,
Los Alamos, NM 87545, USA

ABSTRACT

Los Alamos National Laboratory has proposed to change the emphasis of research at its Meson Physics Facility (LAMPF) by building a new pulsed spallation source for neutron scattering research. The new source would have a beam power of about one megawatt shared between two neutron production targets, one operating at 20 Hz and the other at 40 Hz. It would make use of much of the existing proton linac and would be designed to accommodate a later upgrade to a beam power of 5 MW or so. A study of technical feasibility is underway and will be published later this year.

Introduction

The US, which took a leading role in establishing the field of neutron scattering, has fallen seriously behind Europe in the provision of modern facilities for this type of research. At a time when there is increasing recognition of the important contributions that neutrons can and will make to national initiatives in materials science and engineering as well as biotechnology, correction of this problem is increasingly urgent. A recent panel, convened by the US Department of Energy and chaired by Professor Walter Kohn concluded that "the nation has a critical need for a complementary pair of sources: a new reactor, the Advanced Neutron Source (ANS)...; and a 1-MW pulsed spallation source (PSS)" to meet this challenge. In response to the Kohn panel, Los Alamos National Laboratory has proposed that a high-power spallation source be constructed, using much of the existing infrastructure of the Los Alamos Meson Physics Facility (LAMPF).

Specifications for the New Source

The design parameters of the proposed new facility are summarised below:

- 800 MeV linac plus compressor ring
- 1.25 mA average current (1 mA demonstrated*)
- Ion Source — 40 mA peak
- Linac — 20 mA peak (17 mA demonstrated*)
- Macropulse length — 1.8 msec
- Duty Factor — 10.8% (10% demonstrated*)
- Chopping — 400 nsec on, 200 nsec off
- 60 Hz operation — two targets @ 20 Hz and 40 Hz
- Nine months operation per year
- Greater than 90% availability
- 24 hours maintenance period every two weeks

---

* refers to production mode for the present H^+ operation

As planned, the new facility will make use of a number of existing LAMPF assets that would be expensive to reproduce elsewhere and are very appropriate as part of a modern accelerator complex. The 800-metre long, shielded tunnel that contains the present linac will remain as will buildings, cooling towers, 30 MW of site electrical power, and the 600-metre existing coupled-cavity linac (cf Figure 1). The cost saving that would result from the use of LAMPF as an injector for a new spallation source is at least $100M. Our current (rather rough) estimate of the cost of the new facility—which includes $100M for new neutron spectrometers and $100M in contingency—is $575M.

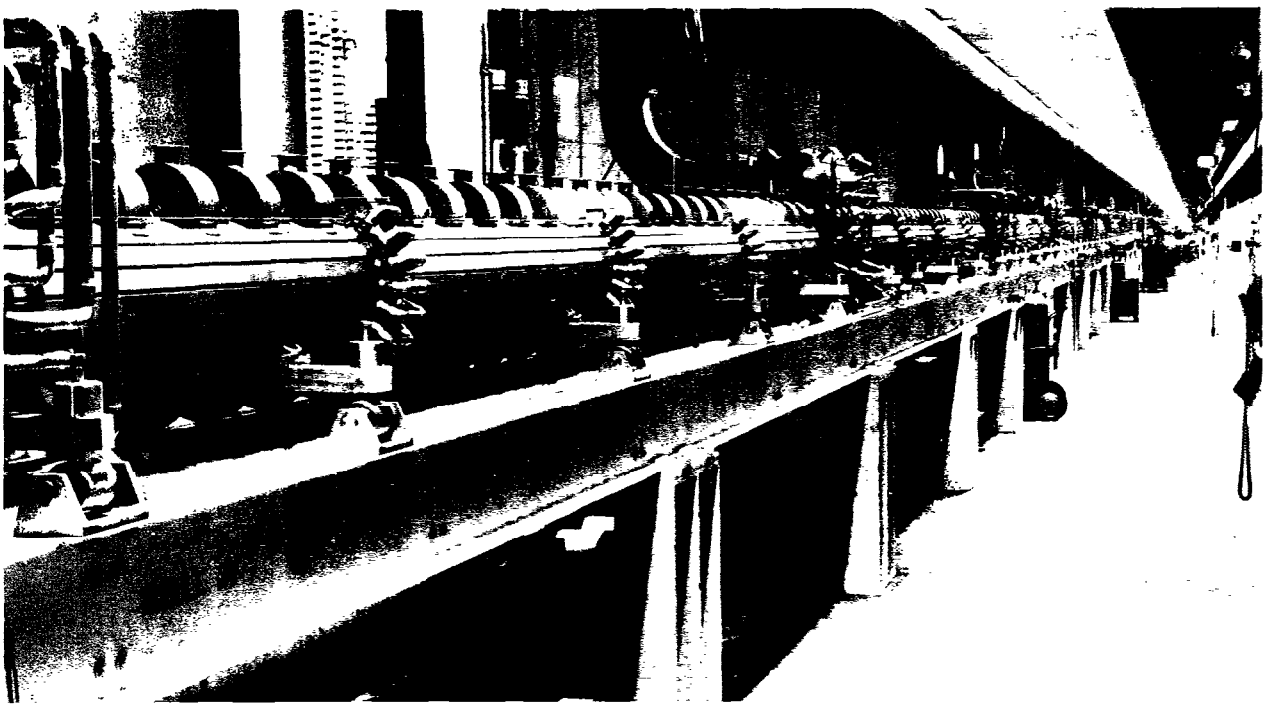

Figure 1: The 600-m-long coupled-cavity linac of the existing LAMPF accelerator will be retained for the new pulsed spallation source

Those parts of the linac that have given trouble in the past—the 201 MHz section, for example—or which could be improved by the application of modern methods will be replaced, taking full advantage of accelerator technology that Los Alamos and other laboratories have developed as part of the strategic defense initiative (SDI). There will be a new H^- ion source, a front end based on a radio-frequency quadrupole (cf Figure 2), a modern RF power system using klystrons instead of vacuum tubes, a new bridge-coupled linac, and a sophisticated RF control system. Our present reference design calls for injection of 800 MeV protons from the upgraded LAMPF linac into a compressor ring (cf Figure 3) that is similar in concept to the existing Proton Storage Ring. However, we are studying an option that would increase the proton energy and, perhaps, permit an easier upgrade to higher beam power in the future.

The new accelerator complex will produce 60 proton pulses per second, each of about 0.5 μsec duration, and distribute them between two neutron production targets operating at 40 Hz and 20 Hz. Power dissipation will be in the same ratio, with a total beam power of about 1 MW. Our reference design calls for vertical injection of the proton beam from below each target, a geometry that offers some neutronic advantages as well as the obvious 360° access for flight paths. There are disadvantages of this scheme, of course—cost and difficulty of maintaining underground proton transport lines, for example—which may eventually drive the design towards horizontal injection.

For both technical and environmental reasons, clad tungsten or a tantalum-tungsten alloy will be used as target material. Cooling and stress calculations have been carried out for several target designs and it appears that either a micro-channel target or a rod bundle with 15% to 20% coolant water fraction would work. A more serious issue may be the effect of spallation products on the mechanical properties of the target material as well as the propensity for such foreign atoms to migrate to the target surface and into the cooling water. Evidently, R&D will be needed to qualify materials for the target of a high-power source.

Figure 2: The radio-frequency quadrupole linac, designed and fabricated by Los Alamos National Laboratory for the Superconducting Supercollider, has now been commissioned.

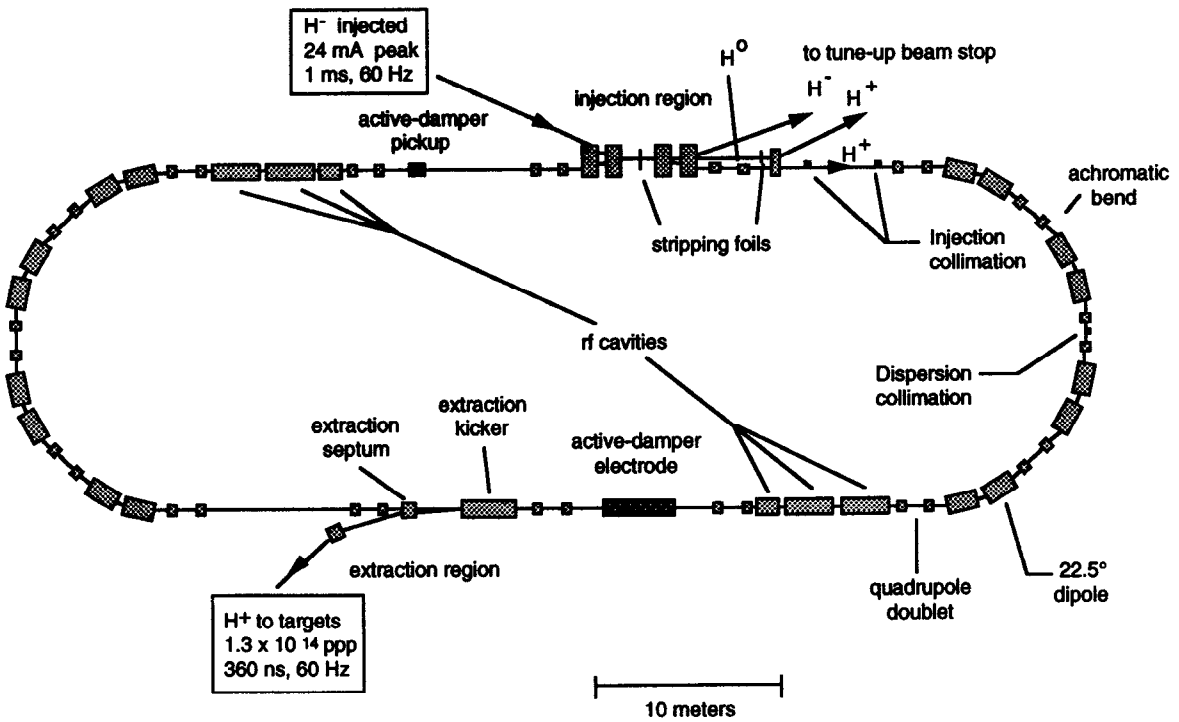

Figure 3: The new proton compressor ring draws on lessons learned from the existing PSR as well as computer-aided engineering tools developed at Los Alamos.

Flux trap moderators (first used at LANSCE), several of which will be in backscattering geometry, will provide the maximum possible flux of useful neutrons, and minimise those high-energy neutrons that contribute to background in scattering experiments. Gary Russell and his colleagues are working hard to design an optimised target/moderator system and have presented some of their thoughts in other sessions of this meeting. We expect the 40 Hz target to provide four to five times the average neutron flux generated by ISIS. Coupled cold moderators at the 20 Hz target will give twenty five times the flux of the present LANSCE. There will be room for 16 beam lines around each target. An arrangement for a possible instrument suite has been generated, principally to determine the number and nature of moderators as well as the dimensions of the single experimental hall that will house both targets.

A key design parameter for this source, which has to be considered in detail during the design stage, is reliability. In addition to engineering components so that breakdowns are minimised, Los Alamos designers have been giving serious thought to ease of maintenance and the time needed to recover from various failures. In the increasingly stringent regulatory environment in which a new source would be built, it is also important to think carefully about remote handling and the required safety systems. There is now widespread acceptance that most mitigation of radiation accidents should be based primarily on passive shielding rather than on active devices that shut down the accelerator when beam spill is detected. Since dose limits and other regulatory boundaries are likely to be a moving target during the coming decade, facility designers must adopt a conservative, proactive philosophy.

Capability of a "1 MW" Pulsed Spallation Source

At a recent workshop, held under the auspices of the Kohn panel, an international group of experts in neutron scattering instrumentation concluded that a pulsed spallation source with a beam power of about 1 MW could duplicate the capabilities of the ILL *and* provide facilities that exceed the ILL for some experiments. In other words, a 1 MW source would give the US the same capability as the ILL *plus* the obvious advantages over ISIS. An interesting concept that was introduced at the instrument workshop is that of a "matched pair" of complementary reactor and pulsed spallation sources. In such a pair, each source is used for what it does best, although there is a large area of overlap—science that can be done equally well at either source. The idea is that the ILL and ISIS form a matched pair, as would a 1 MW pulsed spallation source and the proposed Advanced Neutron Source (ANS) at Oak Ridge. A complementary pair of sources involving a 1 MW pulsed source and the ANS would clearly provide the best of all worlds for the US scientific community. However, if both sources could not be built, a 5 MW source would be required to duplicate and extend the neutron-scattering capabilities of the ANS.

Although the notion of complementarity of the ANS and a 1 MW PSS sounds intuitively appealing, it is a little difficult to quantify. The first thing one is tempted to examine is the region of Q-E space that can be probed at the two sources. As Figure 4 shows, this is largely governed by neutron kinematics so that there is no great difference between the sources in this respect. It is perhaps easier to achieve high resolution with neutron spin echo at the ANS (to achieve neV resolution would likely require a 10 Hz PSS) while the PSS has greater access to high energy transfers.. But broadly speaking the two sources access the same region of Q and E, both for elastic and inelastic scattering.

The two sources do not perform equivalently, however, even in the broad Q-E range which both can access. As Phil Seeger has demonstrated elsewhere at this meeting, some areas, such as very small Q diffraction, that were once considered impractical for a PSS can, in

fact, be addressed. At a wavevector of 0.0005 $Å^{-1}$, however, an experiment at a 1 MW pulsed source would likely take thirty times as long as the same experiment at the ANS. On the other hand, measurements made on the same sample at ILL and LANSCE indicate that the PSS would be thirty times faster for many Reitveld analyses. Short of writing a long and detailed treatise, the best I have been able to do to express the complementarity of the two sources is contained in the following table. And one can easily find exceptions to most of the points listed.

Strengths of the ANS	Strength of a "1 MW" PSS
• Ability to make detailed measurements in a small Q-E window	• Large dynamic range, including an ability to make *in situ* measurements of elastic and inelastic scattering
• High integrated cold flux	• Copious hot neutrons
• Large signal strengths, especially for relaxed resolutions	• Intrinsically good signal-to-noise
• Ability to relax resolution and focus in Q-E space	• Intrinsically good resolution
• Polarisation analysis can be implemented on almost any spectrometer	• Very high pressures, pulsed high fields & single-pulse experiments are facilitated
• Flexibility of spectrometer hardware	• Flexibility to change experimental conditions in software during analysis
• UCN beams	• Bottled UCN

The natural competition between the two types of sources is likely to make their relative strengths a "movable feast", conditioned by the neutron technology of the day. In the final analysis, this competition may even be the best reason for building a balanced pair of sources because it will stimulate our field to progress towards overcoming the real problems of neutron scattering—that it is signal-limited at any source.

Next Steps

Within the next few months we expect to publish the results of our technical studies of a high-power spallation source, including a much better cost estimate for the proposed facility. An external committee has been established to advise the Laboratory Director on the needs of the scientific communities which could benefit from a new pulsed spallation source. We are hopeful that a site-independent study of the various technical options will be carried out in the near future by a team based at Lawrence Berkeley Laboratory. This study will provide ample opportunity for potential users of the new source to influence the design, particularly of the neutron spectrometers. To make proper use of a new facility of this type—or of the ANS for that matter—will require a dedicated program of R&D to

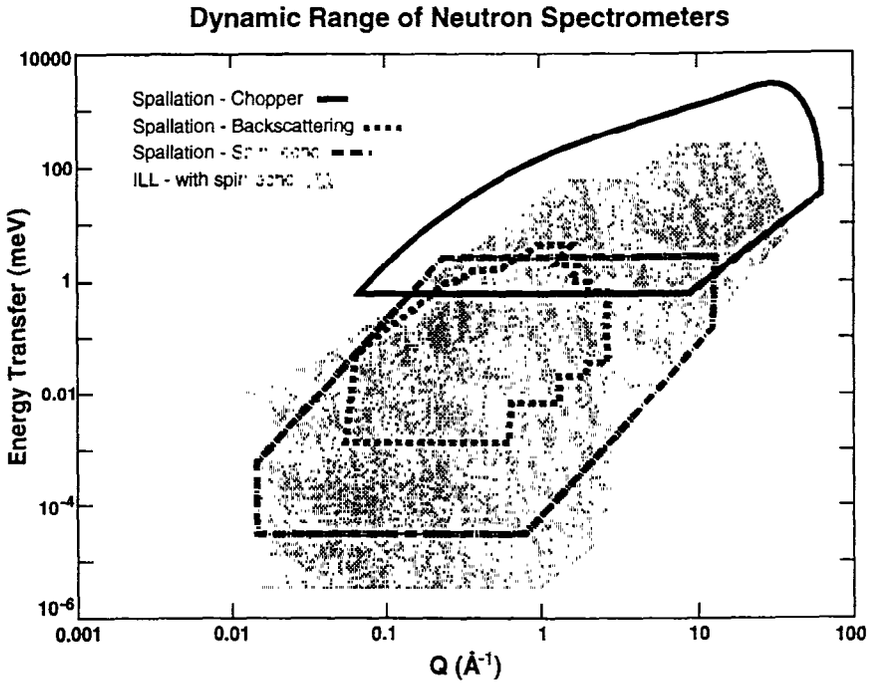

Figure 4: The Q-E space accessible to spectrometers at the ILL and at a "1 MW" PSS

develop better neutron detectors, better schemes for data visualisation and treatment, as well as improved neutron optical elements. We will work to obtain funds for this work, which should also lead to improvements at existing sources.

IPNS UPGRADE-A 1 MW SPALLATION NEUTRON SOURCE

B. S. Brown, J. M. Carpenter, Y. Cho, R. K. Crawford, A. E. Knox
Argonne National Laboratory, Argonne, IL 60439, USA

A feasibility study of a new 1 MW pulsed neutron source, the Intense Pulsed Neutron Source (IPNS) Upgrade, has recently been completed. The source will consist of a 400 MeV Linac injecting 500 microamps of protons into a Rapid Cycling Synchrotron, which accelerates to a final energy of 2.2 GeV. The beam will be delivered to two target stations at 10 and 30 Hz. Six moderators (water, liquid hydrogen or liquid methane) provide 18 beamlines from each target. Radiation effects facilities and neutron activation capabilities will be available. The use of existing buildings will result in a savings of more than $100M. The preliminary results of this study are discussed in this paper, and covered in further detail in 6 other papers at this ICANS meeting.

Introduction

Accelerator based pulsed neutron sources have been performing neutron scattering research for over ten years. During this time, beam intensities have increased by a factor of 100 and there are now more than 50 spectrometers operating world-wide. The pulsed neutron sources have proven to be highly effective and are complementary to reactor based sources in that there are important scientific areas for which each type of source has unique capabilities. The need for more intense neutron sources has been the subject of many meetings and reports. Major workshops took place at Shelter Island, NY, in October, 1984; Abingdon, UK, in February 1992; Oak Brook, IL, in September, 1992; and Argonne National Laboratory in May, 1993. The conclusion of the workshops is that the case for a new higher flux neutron source is extremely strong and such a facility will lead to qualitatively new advances in condensed matter science. It was also concluded that there are unique scientific opportunities at both the next generation reactor and next generation spallation neutron sources as well as a broad middle ground where both are able to make significant contributions. A conceptual design for the Advanced Neutron Source (ANS) has recently been completed which will result in the most powerful steady state neutron source in the world. The complementary nature of pulsed and steady state neutron sources argues strongly for also developing advanced pulsed source capabilities. This was one of the major recommendations of the BESAC Panel on Neutron Sources (1992) chaired by W. Kohn.

The potential for significant increases in the near future in neutron scattering capabilities at accelerator-based spallation neutron sources is great. The IPNS Upgrade would represent a factor of 6 gain over the present level of ISIS (UK), the world's most powerful spallation neutron source, which has operated since 1985. A source with an increase by another factor of 5 is being proposed for the European Spallation Source (ESS). In addition, there is significant potential for future enhancements in advanced spallation sources since there are no fundamental limitations for even further improvements in the technology.

Argonne is proposing that the capabilities of pulsed neutron sources be further pursued by means of an advanced spallation source that will produce 500 μA at 2.2 GeV (a nominal beam power of 1 MW). Some of the present IPNS system and facilities will be incorporated in the design. The new neutron source, named the IPNS Upgrade, will be the most powerful pulsed source in the world and also act as a test bed for concepts for more intense sources in the future. This facility (shown in figure 1) represents the next advance in spallation neutron sources and can be accomplished soon with modest extensions of existing technology.

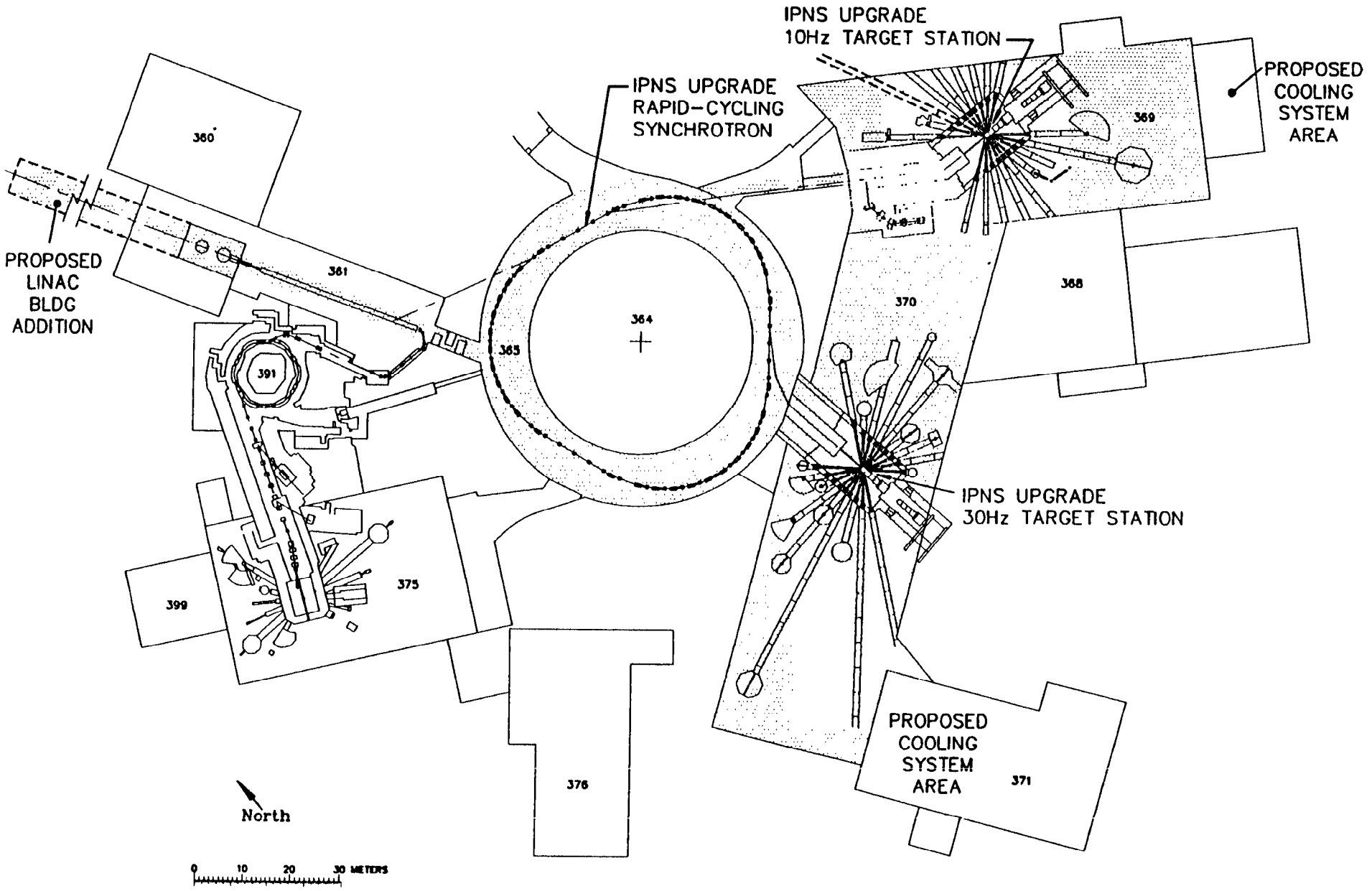
IPNS UPGRADE
10Hz TARGET STATION
PROPOSED
COOLING
SYSTEM
AREA
IPNS UPGRADE
RAPID-CYCLING
SYNCHROTRON
PROPOSED
LINAC
BLDG
ADDITION
360
361
364
365
369
370
368
391
375
399
376
371
IPNS UPGRADE
30Hz TARGET STATION
PROPOSED
COOLING
SYSTEM
AREA
North
0 10 20 30 METERS

The IPNS Upgrade would require approximately 4 years from the design decision to completion and would be site specific and use existing Argonne infrastructure (buildings, water and electrical systems, shielding, etc.) which will result in a cost savings of more than $100M. The total project cost is estimated to be less than $500M assuming that the project is initiated in FY 1996. Capabilities are included for 36 neutron scattering beam ports, radiation effects facilities in both targets, rabbit tube irradiation and activation facilities; and other capabilities are being considered. As part of the design process, joint workshops were held with Los Alamos on Accelerators for Future Spallation Neutron Sources in Santa Fe on Feb. 16-20 and on Scientific Opportunities at Future Spallation Neutron Sources at Argonne on May 13-16, 1993.

Feasibility studies have begun on the various components of the IPNS Upgrade. These studies, including cost estimates, are directed by:

Accelerator systems-Y. Cho
Targets and moderators-J. Carpenter, A. Knox
Instrumentation-K. Crawford

Table 1 summarizes the design specifications for the IPNS Upgrade. The major subsystems are discussed briefly in the following sections. Additional details of the IPNS Upgrade are given in papers presented at this ICANS meeting on:

- **Neutronic Studies for a High Power Pulsed Spallation Neutron Source**
- **Conceptual Design of the Target Station the IPNS Upgrade**
- **Proposed Instrument Complement for the IPNS Upgrade**
- **Conceptual Design of the Accelerator System for a 1 MW Spallation Source at ANL**
- **RF System for the IPNS Upgrade Rapid Cycling Synchrotron**
- **Study of 1 MW Neutron Source Synchrotron Dual Frequency Power Circuit for the Main Ring Magnets**

Neutron Scattering Instrumentation

The decision on the repetition frequency of the accelerator was based on the optimal frequency for the neutron scattering instruments. A survey of opportunities and an evaluation of preliminary designs for neutron scattering instruments for a 1 MW pulsed source led to a table of the various requirements that they place on the neutron source, which have fundamentally affected the definition of the project. A repetition frequency of 30 Hz was found to be clearly preferable to 60 Hz.

Two roughly equally populated categories of instruments emerged from the study of scattering instruments, those for which 30-Hz pulsing (but not much higher) is satisfactory, and those which require lower frequency of pulsing and for which 10 Hz is satisfactory. Serving these two categories of instruments led to the requirement of two separate targets. The total number of instruments and correspondingly the number of neutron beams and, in addition, the number of differently optimized moderators needed exceed the number that can be arranged around a single shielded target station; and this also spells the need for two target stations to provide for the required number of moderators and beams. Therefore the accelerator delivers one out of three pulses to a low frequency station at 10 Hz, the high frequency station normally receiving the remainder of the 30-Hz pulse train in iambic pattern.

Table 1 --IPNS Upgrade Parameters

Accelerator

Linac Energy	**400 MeV**
Synchrotron Energy	**2.2 GeV**
Pulsing Frequency	**30 Hz**
Current	**500 μA**
Extraction	**Single turn extraction, 300 nanosec pulses**

Target Stations

Operating frequency	**One at 10 Hz** **One at 30 Hz (with every third pulse missing)**
Target Material	**Tantalum**
Target Cooling	**Water**
Moderators	**6 at each target** **Liquid water, methane and hydrogen** **plus water premoderators**

Instrumentation

Beam ports	**18 on each target station, 36 total**
Neutron scattering instruments	**Initial complement of 27**
Other capabilities	**Radiation effects** **Neutron activation**
Capabilities under consideration	**Muon spin rotation** **Neutrino studies** **Isotope production**

The IPNS Upgrade will provide 36 beam ports for neutron scattering instruments, 18 each at the 30-Hz and 10-Hz target stations. Neutron beams for more than one instrument will be extracted from a single beam port in some cases, so more than 36 neutron scattering instruments can be supported at this facility. There will be a total of 12 moderators, one for every three beam ports, so the moderator characteristics can be optimized to the requirements of the individual instruments. A representative set of 27 instruments that would occupy 24 of the beam ports and would provide a well-balanced initial instrumentation complement is given in the accompanying ICANS paper, **Proposed Instrument Complement for the IPNS Upgrade**. The remaining 12 uninstrumented beam ports will be available for later development and installation of new state-of-the-art instruments, as well as for the installation of specialized instruments developed by Participating Research Teams (PRT's). This representative set of instruments has been used in selection of the target station parameters, in laying out the locations of the target stations within the experimental halls, and

in providing the cost estimates. This is certainly not the exact set of instruments that will be built, and considerably more input from the user community will be solicited before deciding on the actual instrument complement to be included as part of the project. It is anticipated that up to 10 instruments that are currently operating at IPNS would be refurbished and transferred to the IPNS Upgrade as part of this initial instrument complement. This will provide a core of proven instruments ready for operation on day one. The neutron scattering instruments will be located in existing experimental halls, which can provide internal space for beamlines up to 50 m long (see figure 2). Beamlines can easily be extended outside the buildings if necessary, since much of the external space is parking lots.

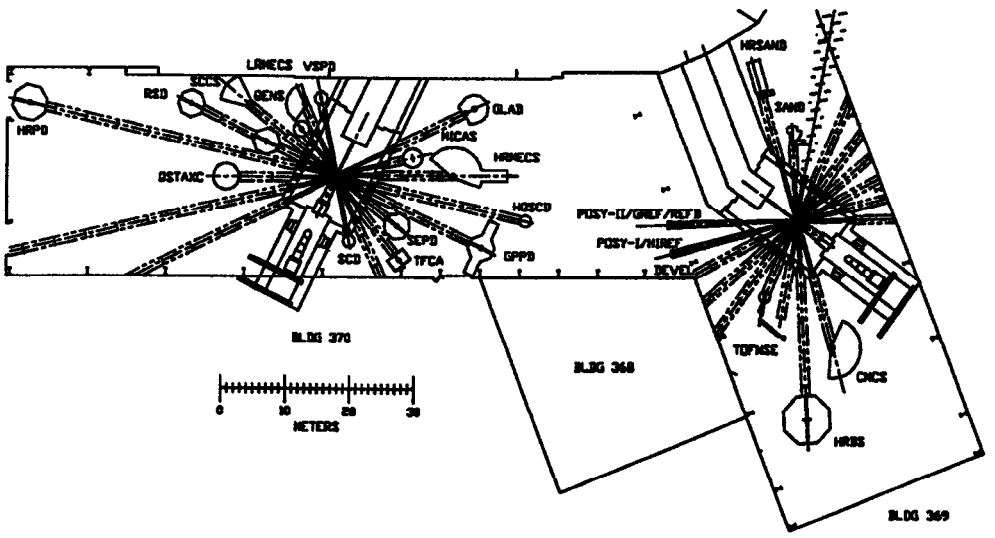

Figure 2. Location of the reference set of instruments on the neutron beamlines.

Most of the neutron scattering instruments will use the neutron time-of-flight (TOF) principle for determination of neutron wavelengths. Of these, the majority require good wavelength resolution, and for such instruments the IPNS Upgrade target stations will provide roughly 50 times the intensity available at IPNS. However, for those instruments which do not require good wavelength resolution, for example small-angle-scattering instruments, the moderators can be optimized to provide roughly 200 times the intensity available at IPNS.

However, the IPNS Upgrade will be sufficiently intense that it will no longer be necessary that all instruments be based on TOF techniques. With moderators optimized for total neutron output rather than for sharp neutron pulse structure, time-averaged thermal or cold neutron fluxes will be equivalent to those at a medium flux reactor. (A cold neutron flux of 5×10^{13} n/cm^2/s has been calculated for one of the liquid hydrogen moderators at the IPNS Upgrade.) Thus, any instrument that would work at a medium-flux reactor can be made to work at least as well at the IPNS Upgrade. Furthermore, even a moderator optimized for high time-averaged flux will have a pulse width of less than one millisecond, and so will have a duty factor of 1:30 or less. This time structure can be used to significant advantage even on nominally steady-state instruments to reduce background, eliminate unwanted orders from crystal monochromators, etc. A cold-neutron triple-axis spectrometer operating in this "quasi-steady-state" (QSS) mode is proposed as one of the initial complement of the IPNS Upgrade instruments, and several other types of QSS instruments are under consideration which might have unique advantages for particular types of experiments.

Although the primary function of the IPNS Upgrade is neutron scattering, the facility can provide many other types of capabilities as well. Some of these, such as neutron

radiography, could utilize one or more of the neutron beam ports. Although no such use is included among the instrumentation for the first 24 beam ports, the feasibility study will discuss several potential uses of this type.

The IPNS Upgrade is well suited to the performance of neutron irradiations for radiation damage studies, isotope production, and neutron activation analysis. Facilities for these purposes are included as part of the IPNS Upgrade project. Space is available for other experimental facilities not included in the scope of the project, such as pulsed muon spin rotation, nuclear physics, neutrino physics and medical isotope production.

Accelerator

In September 1991, there was a gathering of accelerator builders, neutron generating target builders and neutron source users-near Jülich, Germany organized by KFA-Jülich and Rutherford-Appleton Laboratory, UK to discuss the next generation European neutron source. Concepts for the 5-MW European Spallation Source (ESS) were formulated in this meeting. Within several months of the initial meeting, there were three accelerator meetings, a target workshop and a meeting on scientific utilization of the proposed ESS.

In parallel to these activities in Europe, IPNS and Advanced Photon Source (APS) personnel at Argonne have been reviewing design studies that had been developed during the 1980's relating to accelerator based sources along with other state-of-the-art accelerator and target capabilities. Specific items reviewed by this study group were:

1. What is the optimum beam power of the accelerator system?

A design goal of 1 MW was chosen for a detailed study. The most powerful spallation source available today is ISIS at Rutherford-Appleton Laboratory, UK, operating at 800 MeV and 0.2 mA, giving 160 kW of beam power. The design goal of 1 MW is about 6 times the power of ISIS, and 5 MW is 30 times. Extending accelerator capability by a factor of 6 is a reasonable approach with minimal risk in attaining the performance goals.

2. What is the best machine energy to provide 1 MW of beam power? Should the machine configuration consist of a high energy linac and a pulse compressor or should it consist of a lower energy linac and a circular accelerator which raises the beam energy and at the same time compresses the pulse length?

The decision was made to inject into a circular machine at the lowest possible energy and to accelerate to the highest possible energy. The considerations were based on future operational ease and the possible impact of beam loss during the capture, acceleration and extraction of the protons from a circular machine. It is generally accepted that the most significant beam losses occur during the injection and capture processes, and there is very little loss during the acceleration and extraction processes. Beam loss can cause not only radiation around the facility but also can produce residual radioactivities along the machine. If beam loss is unavoidable, then the preference would be losses at lower energy than higher energy because remedial action at lower energy loss is easier than that at high energy.

3. Could the former Argonne Zero Gradient Synchrotron (ZGS, a machine used for high energy physics operating at 12 GeV) infrastructure be used to save construction costs? If so, what would be the energy of the machine comfortably fitting into the structure?

The ZGS was decommissioned in 1980 and the complex has some 500 thousand square feet of building space, with a replacement value of more than $100M. The ZGS tunnel can house a 1 MW, 2.2 GeV rapid-cycling synchrotron comfortably. In order to achieve the required 1

MW of beam power, the machine has to deliver a time-averaged current of 0.5 mA. Space charge limits in a circular machine dictate that the injection energy of the machine should be about 400 MeV. The result of these considerations is that the accelerator system consists of a 400 MeV linac operating at 30 Hz and providing a pulse current of 33 mA and pulse width of 0.5 msec and a 30 Hz rapid-cycling synchrotron.

It is important to note that the $100M savings could also be realized utilizing the high energy linac-storage ring concept. The former ZGS buildings can accommodate either design, and the present choice for a lower energy linac-synchrotron is based on technical considerations, and not the necessity to build around an existing accelerator. All of the accelerator components in the IPNS Upgrade will be new and state-of-the-art.

Various concepts developed so far will be optimized further to meet the proposed performance goals with emphasis on reliable operations. The accelerator system consists of:

- Negative Hydrogen Ion Source
- A 2-MeV radio-frequency Quadrupole
- Beam Chopper
- 70 MeV Drift Tube Linac
- Matching Section
- Coupled Cavity Linac (70 MeV-400 MeV)
- Low Energy Transfer Line
- 30 Hz Synchrotron (400 MeV to 2.2 GeV)
- Single turn extraction with 300 nanosec pulses
- High Energy Transfer Lines.

Studies will include both theoretical analyses as well as some prototyping of the hardware. The following is a list of studies being proposed:

- Lattice Optimization
- Injection and Capture
- H^- ion source
- Acceleration
- Beam Stability
- Physics Design of Magnets
- Ring Magnet Power Supplies
- Radio-frequency Acceleration System
- Vacuum System
- Injector Linac

For further information, see the accompanying ICANS papers:
- **Conceptual Design of the Accelerator System for a 1 MW Spallation Source at ANL**
- **RF System for the IPNS Upgrade Rapid Cycling Synchrotron**
- **Study of 1 MW Neutron Source Synchrotron Dual Frequency Power Circuit for the Main Ring Magnets**

Target Stations

Shielded proton beam transport lines carry two extracted proton beams to the two target stations, where the protons are injected horizontally into the targets. Each station contains a neutron-producing target consisting of water-cooled tantalum plates in two sections. The proton beam power of 1 MW incident on the IPNS Upgrade target will be 6 times that presently incident on the ISIS target. Although it is determined in the feasibility study that no radically new target concepts are necessary, such as rotating or liquid targets, significant

R&D will be necessary. Areas include neutronics, metallurgical studies and tests, thermohydraulics, safety, shielding and target monitoring.

Six differently-optimized moderators positioned close to each target slow down neutrons from the primary source energies (about 1 MeV) to useful energies (less than about 10 eV). Moderators, all flowing systems, will be of normal water, liquid methane and liquid hydrogen. Reflectors of beryllium metal surround the moderators to enhance the intensities of the neutron beams. Decouplers and heterogeneous poisons within the moderator-reflector system tailor the spectra and pulse characteristics to the neutron beams. Each moderator provides three slow neutron beams, for a total of 18 beams for each target station. Massive steel and concrete shields surround the targets and moderators and provide multiple levels of confinement of radioactive materials within. Beam holes equipped with movable gates lead the neutrons to the instruments. R&D areas are neutronics, hydrocarbon production, cryogenic systems and control, safety, and changing of moderator components.

Targets and moderators will have finite service lifetimes in the proposed facility. Furthermore, it can be expected that it will be necessary to change the moderator-poisoning-decoupling-reflector arrangements from time to time as changing instrument requirements demand. To enable changes to be made with minimal impact on operations and minimal radiation exposure to personnel, each target station has a shielded hot cell with high density windows, manipulators and associated remote handling equipment.
For further information, see the accompanying ICANS papers:

- **Neutronic Studies for a High Power Pulsed Spallation Neutron Source**
- **Conceptual Design of the Target Station the IPNS Upgrade**

Conventional Facilities, Cost and Schedule

A newly constructed extension of the existing linac enclosure will house the new linac. The synchrotron will be in the existing shield formerly used to house the 12-GeV ZGS accelerator. The targets and instruments are located in existing large buildings that formerly housed high energy experiments at ZGS, a use very similar to the new use. System control rooms, maintenance facilities, and laboratory and office space for resident personnel and for visitors will be provided in existing buildings. Water systems, cooling towers, main power and transformer systems, roads, sewers, and general infrastructure items already exist, which the new project will employ. Thus there will little need for new construction of conventional facilities, and this will result in a savings in construction time and cost of more than $100M. The project contains an allowance for the cost of refurbishing these existing facilities.

Construction of the new components and refurbishment of the existing parts will not interfere with IPNS operation until the very end. Then, an interval about one year's duration will be required for installing the new linear accelerator and for reworking the scattering instruments that are to be transferred and installing them in their new locations. A commissioning period of about six months for the accelerator systems would then lead to the commissioning and use of the instruments.

Acknowledgments

The operation of IPNS is funded by the U.S. Department of Energy, BES-Materials Science, under contract W-31-109-ENG-38, and the National Science Foundation (DMR-91-20000) through the Science and Technology Center for Superconductivity.

An Intense Pulsed Spallation Neutron Source using a High-Power Proton Linac for Nuclear Transmutation

N. Watanabe

National Laboratory for High Energy Physics, 1-1 Oho, Tsukuba-shi, Ibaraki, 305, Japan

Abstract

The construction of a high-power proton linac is being planned by the Japan Atomic Energy Research Institute for the nuclear transmutation of rare actinides in nuclear wastes (Omega Program, Science and Technology Agency, Japan/OECD NEA). The accelerator can also be utilized in basic science. An intense spallation neutron source for condensed-matter science is a typical application. This will provide an opportunity to realize a MW-class pulsed spallation neutron-source. We would propose this as a next-next-generation (post JHP/KENS-II) pulsed spallation neutron source in Japan. We discuss here the possibility of realizing this idea.

1. Introduction

The construction of an intense proton linac, called ETA (Engineering Test Accelerator), has been proposed by the Japan Atomic Energy Research Institute (JAERI) as a part of R&D plans for an accelerator-based rare actinide transmutation system.(1) The specifications of ETA are given in Table I.

Table I. Basic Specification of ETA

Proton-beam energy	1.5 GeV
Time averaged proton beam current	10 mA
Pulse length	1 msec
Repetition rate	100 Hz
Duty cycle	10 %
Proton beam power	15 MW

Such a high-power proton linac is of great importance not only for nuclear transmutation, but also for various fields of basic-science. An intense neutron source, especially for neutron scattering (condensed matter research) and other neutron-beam experiments, would be among the most important and promising fields of utilization. It is important to consider one can take full advantage of such a high-power proton linac with a high repletion rate (100 Hz) and long pulse length (1 msec) for an intense neutron source. The present paper presents various possible applications.

2. Possible Neutron Sources

The various possible types of neutron sources using the proposed proton linac are listed in Table II. The first option is of the SINQ type, in which the pulse structure of the proton beam is completely ignored. From simple scaling one can expect a maximum time-averaged thermal neutron flux of

the order of 3×10^{15} n/cm^2-sec, provided that a compact high-power target comprising of low neutron-absorbing heavy metal(s) can be developed.

Table II. Possible Neutron Source using ETA

Option	Type	Performer	Remarks
Full p-beam			non full-time
1	SINQ-Type	$\bar{\phi}_{th} \sim 3\times10^{15} n/cm^2 \cdot s$	
2	SNQ-Type	$\sim 3 * \phi_{th}^{SNQ}$	
3	μCF	$\bar{\phi}_{th} \sim 3\times10^{15} n/cm^2 \cdot s$	
H^-beam/Compressor ring			full-time
4	Pulsed Spallation N. S.	1-3MW	

The second option is of the SNQ type, in which the pulse structure of the proton beam can be utilized to some extent. However, the longer pulse length (1 msec) may decrease the merits of a time-modurated neutron source, as considered with SNQ. Further R&D studies concerning the target engineering will be necessary in order to utilize a higher beam power (15 MW).

The third option is a neutron source based on muon-catalyzed fusion (μCF); this type, however, is more or less in a state of art. The energy cost to produce one muon (about 10 GeV) and a cycle rate of about 100 (one muon can catalyze the D-T fusion reaction 100 times) has already been confirmed.(2) Although the energy cost is larger than that in the case of a spallation neutron source, the heat generated in a muon production target can be removed separately from a μCF target. We assumed a spherical μCF target having a radius of 20 cm in a large D_2O tank as SINQ. The absorption of slow neutrons in the target is the most serious neutronic problem regarding this type of neutron source. In the case of μCF, a target with a small absorption cross section can be considered. Although the neutron energy is higher (14 MeV) than in the case of spallation, it can be shown by a simple calculation that this neutron source can provide a maximum time-average thermal neutron flux of about 2×10^{15} n/cm^2-sec, as estimated in Table III.

Table III. Possible μCF Neutron Source using ETA

Energy cost (MeV/n)	$E_\mu/X_c \sim 100$
Neutron yield (10^{17} n/s-MW)	0.62
Average neutron energy (MeV)	14
Neutron leakage rate	1
Thermal neutron conversion efficiency (ϕ_{th}/Q)	2.24×10^{-3} (assuming R_c = 20 cm)
ϕ_{th}/P (10^{13} n/cm^2·s·MW proton beam)	14
ϕ_{th} (P = 15 MW)	2×10^{15}

The three options mentioned above require full-time and full-beam from the linac, if we are to aim at realizing one of the best intense neutron sources. It is, however, not realistic since the first priority of this linac is nuclear transmutation. We must therefore find a compromise in the beam intensity and/or the beam time. Such a compromise would make the new source less attractive.

The forth option is a pure pulsed spallation neutron source. In this case H^--beam acceleration and a compressor ring become indispensable. Generally, the simultaneous acceleration of H^- beam along with protons is feasible. One of the most important specifications is the beam current which can be obtained from an H^- ion source within the required beam emittance. Some important parameters which determine the beam power are listed in Table IV (parameters for JHP were given by Yamazaki[3]). In the linac considered for the Japan Hadron Project (JHP), rather modest, but more realistic, parameters are assumed, as listed in the first calumn of JHP. A time-average beam power of about 0.2 MW can be obtained under these assumptions. For a 1 MW beam, the typical specifications listed in the second column of JHP become necessary. At present, no H^--ion source is available which can satisfy such specifications.

Table IV. Important Parameters Determining the Beam Power

	JHP		ETA
Energy	1 GeV	1 GeV	1.5 GeV
Peak H^- current	20 mA	62 mA	20 mA
Emittance (90%, normalized)	1 πmm mrad	1 πmm mrad	1 πmm mrad
Beam pulse length	400 μs	500 μs	1000μs
Chopping factor	0.5	0.65	0.65
Repetition rate	50 Hz	50 Hz	100 Hz
Average beam power	0.2 MW	1 MW	2 MW

Although the detailed design for ETA has not yet been completed, we can compare here the parameters for ETA with those for JHP. One advantage of ETA is a longer pulse length (1 msec), which produces a higher beam power with a given peak current of the H^- beam. With the modest peak current assumed in JHP, we predict that a time-average beam current of 1.3 mA is possible. Since ETA will have FR power supplies with a higher powder than those for JHP, acceleration of H^- beams at this intensity will be easy. The maximum beam current acceptable in a compressor ring is determined by the space-charge limit. The present current is below this limit. If we can expect a higher peak current of the H^- beam (as listed in the second column of JHP), the average beam power can be increased up to 6 MW. In this case two identical compressor rings would be necessary.

3. Utilization of the Proposed Neutron Source

A higher proton beam energy (1.5 GeV) is quite acceptable. We studied by computer simulation the slow-neutron intensities as a function of the proton energy in the 0.8 - 3 GeV range, thus confirming that 1.5-GeV protons are as useful as those of 1.1 GeV (the minimum energy cost).[4]

How to use a high-power pulsed spallation neutron-source with a high repetition rate (100 Hz) is the next important problem. A high repetition rate (100 Hz) is usually thought to be too high for a pulsed neutron source for condensed-matter research. For simplicity, let's compare two cases: one is one 2-MW pulsed neutron source of 50 Hz; the other is two 1-MW sources, also operated at 50 Hz. There generally exists a finite idling time of the source due to target or moderator repair work, as well as of the instruments for sample-changing, temperature changing, etc (especially in the case

of elastic scattering). When we take into account such idling losses, the total time-integrated net beam intensity from two half-power (1MW) sources is larger than that from the one full-power (2 MW) source. Although there should be some experiments or instruments which require the highest intensity, rather than the total time-integrated intensity, two half-power sources would be, at least, as useful as one source on the average, except for the disadvantage in the higher construction costs for the extra target station, additional instruments and another experimental hall. However, it must be mentioned that the accelerator is the most expensive component in spallation neutron facilities. There would exist various engineering merits for adopting multi target stations which share the full beam power. The life for the half-power target will be about 2-times longer than that for the full-power one, and further neutronic optimization would be possible in the case of multi-target stations. Although the optimal number of target stations and the optimal beam delivery scheme for each target station are other questions to be discussed, the choice is very flexible. In concluding, a high-power beam of 100 Hz can be usefully utilized with multi target stations.

4. Direct Use of Proton Pulses from the Linac

In neutron-scattering experiments using cold neutrons, the time-integrated-intensity of cold neutrons is sometimes more important than the pulse width.(5) Small-angle scattering (SANS), as well as CRISP-type, TOP-type experiments are of this category. The pulse length of protons directly obtained from the linac (1 msec) is sufficiently narrow for such experiments. For example, let's consider a SANS experiment using neutrons having a wavelength range of 4 - 10 Å with a total flight path length between the source and the detector of 10 m, which would be the shortest. The wavelength resolution in this experiment is about $\Delta\lambda/\lambda = 0.1 \sim 0.04$, which is quite acceptable. The wavelength resolution should usually be much better than the above values, since the total flight path length is longer than 10 m. If we take 10 direct proton pulses out of 100 pulses per second from the proton linac, the beam power becomes 1.5 MW, which means that this source can be the most intense pulsed cold neutron source operated at 10 Hz.

We developed a high-efficiency pulsed cold-neutron moderator, a liquid-hydrogen moderator with premoderator coupled to a reflector.(6) The combination of this moderator with the 1.5-MW pulsed spallation neutron source operated at 10 Hz should provide the cold-neutron flux given in Table V.

Table V. Intense Pulsed Cold Neutron Source using 10 pulses of Proton Beam from ETA

Fast neutrons per pulse	1.9×10^{16}
Fast neutrons per sec.	1.9×10^{17}
Cold neutron conversion efficiency (4π-equivalent cold Maxwellian neutron* flux on the moderator per fast neutron emitted from the target)	$\sim 0.96 \times 10^{-3}$
Time-averaged cold neutron flux (n/cm^2·s)	$\sim 1.8 \times 10^{14}$
Time-averaged neutron flux at Maxwellian peak (at ~2 meV) (n/cm^2·s·eV)	$\sim 1.4 \times 10^{16}$
Pulse width of cold neutrons in FWHM (ms)	~ 1 ms
Pulse peak flux at Maxwellian peak (n/cm^2·s·eV)	1.4×10^{18}

* Integrated flux over Maxwellian spectrum, ie. $\int_{Maxwell} \phi(E)dE$, not $\int_0^{0.005eV} \phi(E)dE$

Although the time-averaged cold-neutron flux is by about a factor 2 ~ 3 lower than that of ILL, the peak flux is about 20-times higher than that of ILL.

5. Concluding Remarks

We are keen to realize KENS-II (a part of JHP) as soon as possible. However, it has unfortunately not yet been financed. We are proposing a phased program for KENS-II while aiming at an earlier realization. Although the present proposal is independent of KENS-II, various possibilities for a future intense spallation neutron source should always be considered. In conclusion, if ETA is realized for the R&D of the nuclear transmutation techniques, we can consider one of the best pulsed neutron sources early in the next century.

References

(1) M. Mizumoto, K. Hasegawa, H. Yokobori, H. Mino, H. Murata, K. Sakogawa, H. Oguri, Y. Okumura, H. Takada, T. Nishida and T. Takizuka; "High Intensity Proton Accelerator for Nuclear Waste Transmutation", Proc. Linear Accelerator Conf. (Ottawa, Ontario, 24-28, 1992), AECL-10728, Vol. 1 (1992) p. 749.

(2) Yu. V. Petrov: Muon Catalyzed Fusion 1 (1987) 351.

(3) Y. Yamazaki: to be published in Proc. Workshop on Research and Developments for JHP and Related Topics (Institute for Nucl. Study, Univ. of Tokyo, Mar. 5, 1993).

(4) Y. Kiyanagi, N. Watanabe and M. Arai: "Comparison of Target-Moderator Neutronic Performance for 0.8 GeV and 3 GeV Protons": in this Proc.

(5) N. Watanabe: Physica B 180 & 181 (1992) 893.

(6) Y. Kiyanagi, N. Watanabe and H. Iwasa: Nucl. Instrum. Methods A 312 (1992) 561.

AUSTRON - a Spallation Neutron Source for Central and Eastern Europe

Presented by
H. Schönauer, CERN, CH-1211 Geneva 23

With contributions from
H. Aiginger, W.H. Breunlich, P.J. Bryant, K. Hübner,
W. Pirkl, M. Regler, G.H. Rees, K. Schindl, A.Wrulich

Introduction

A medium-sized spallation neutron source was initially promoted by the "Central European Initiative" (CEI) as a promising venture for the central and eastern part of Europe. At a workshop held at CERN in fall 1991 potential users and accelerator specialists evaluated a machine configuration matching both the user requirements as formulated there and budget constraints. This machine, which could be located in the eastern part of Austria, has tentatively been dubbed the "AUSTRON". Amongst half a dozen scenarios compared, the combination of a 70 Mev H^- Linac with a 1.6 GeV synchrotron yielding 100 kW average beam power in "stage 1" emerged as the most cost-effective solution. It delivers 4 kJ per pulse of <1 μs length of 1.6 GeV protons at 25 Hz repetition frequency. "Stage 2" foresees the addition of a second ring; this would be used either to double the beam power, or, operating as a storage ring, to double the energy per pulse at half the repetition rate or to modify the time structure of the proton beam.

A fairly modest additional investment will enable the AUSTRON to accelerate light ions (up to Ne) to some hundreds of MeV/nucleon for medical research. The proposed configuration and the options for stage 2 are presented, as well as the most recent evolution of the project after a meeting on AUSTRON held in Vienna in May 1993.

Recently, the Austrian Government has agreed to assure one third of the estimated construction cost (January 1992 prices) of ATS 3 Billions ($ 265 M) of the AUSTRON, if the remaining two thirds will be contributed by other European countries.

User Requirements

Prior to the meeting at CERN a working group "Scientific Case" chaired by Prof. P. Povinec (Bratislava) had prepared the following priorities, which were reviewed and confirmed :

1. A pulsed spallation neutron source featuring

   - 100 - 200 kW average beam power on target
   - 25 Hz repetition rate
   - <1 μs pulse length

   The short pulse length combined with low repetition rate favours time-of-flight measurements, in addition the latter increases the peak neutron flux.

2. Neutrons in the few 100 keV range with a time structure of

   - a few 100 Hz pulse repetition rate
   - a r.m.s. pulse length ~2.5 ns .

3. Independently of the working group, a number of medical institutions expressed strong interest in a parasitic production of light ions with the requirements:

- light ions up to neon
- energy up to 400 Mev/nucleon
- 10^9 ions/s .

There was general agreement on the principle that the machine design should be conservative to favour a short construction time. This automatically excludes major R & D on novel accelerator concepts, as interesting as they might be, leaving R & D to the instrument designers. The users were well aware of the initiatives in the EC to build a neutron source in the 5 MW range, but it was felt that the rather long planning and construction time of this machine (estimated not to be operating before 2010) ruled out all arguments about competing projects.

The Machine Configurations Considered

A total of six scenarios was evaluated, which are compiled with their characteristic features in Fig.1. The majority of them are scaled versions of existing machines or projects. So configuration #1 is derived from ISIS by halving the cycle frequency and doubling the energy, configuration #2 is the LAMPF + PSR concept, the FFAG (#5) has been studied at Jülich, Argonne and recently at the Hahn-Meitner Institute. Scenarios #3 and #4 are crossbreeds with elements from ISIS and TRIUMF KAON; the technique of #4 to store four pulses from the 50 Hz synchrotron stems from the CERN PS in its LHC injector role. Scenario #6 is derived from an original idea of C. Rubbia in the context of drivers for inertial fusion.

To tag a price to the different configurations, a rather coarse scaling from the costs of the "parent" machines and projects had to be done. Even so, since the results are quite divergent, some scenarios are ruled out by their cost. This is particularly true for scenario #2, which is the only one thas has an upgrading potential up into the MW beam power zone envisaged by the next machine generation.

As there is no existing FFAG machine, it was felt difficult to produce a cost estimate and to predict the duration of design and commissioning periods. This applies even more to the double-helix machine #6. For this reason both concepts have been excluded from the final choice.

The 5 GeV scenario #3, although competitive in cost, was finally discarded in favour of #1, which features more flexible upgrading options and which would not prohibit acceleration of light ions (as would do the coupled-cavity linac section in stage 2 of #3).

Configuration #4 would be a very desirable machine; unfortunately the price tag and the absence of a straightforward staging approach weigh against it.

The Proposed Accelerator Complex

Consequently, the final choice was configuration #1, the 1.6 GeV, 25 Hz rapid cycling synchrotron with a circumference of about 200 m and a 70 MeV drift tube linac as injector. It produces a beam pulse consisting of two bunches of 50 ns length each at a distance of 350 ns, i.e. a total pulse length of about 420 ns. It is shown together with the light-ion add-on's in Fig. 2; note however, that the final ion energy should read 400 MeV/nucleon instead of the 250 MeV/nucleon initially proposed. A tentative set of machine parameters is compiled in the Table "AUSTRON Stage 1 Parameter List". The column "First Upgrade" refers to the recommendations of a recent meeting on AUSTRON of which the conclusions are appended to this article.

Upgrading Options

Fig. 2 also shows three options proposed for a future Stage 2. They are

- **Option 1 :** A second, identical RCS (rapid cycling cyclotron). It would pulse and eject in synchronism with the first. Both mean and peak power are doubled with respect to Stage 1 to 200 kW and 8 kJ/pulse, respectively. The pulse frequency of 25 Hz remains unchanged.
- **Option 2 :** Adding a 1.6 GeV, same circumference storage ring (SR). It could be operated in two ways :
  (i) Every other pulse of the RCS is stored in the SR and ejected together with the following pulse from the RCS. This halves the repetition frequency to 12.5 Hz and doubles the proton energy per pulse. The mean beam power remains unchanged.
  (ii) Every pulse is stored in the SR, debunched and rebunched at a higher harmonic number (h=12 instead of h=2). After shortening the bunches to ~10 ns length, they would be extracted one by one at a rate of 300 Hz. (this operation requires a fixed-frequency RF system of about 17 MHz and a few hundred kV). In this way the time structure required for fast neutron physics can be realized.
- **Option 3 :** Adding a larger machine of 5 GeV, say, slowly cycling at 12.5 Hz and accelerating ~5 μA protons. This option does not improve the neutron spallation yield. However, the secondary beams generatied by 5 GeV protons may represent an attractive regional facility for nuclear physics and related research.

These options are by no means exhaustive. The basic configuration appears flexible and allows many extensions and upgrades. In the light of the recent improvements of ISIS, now producing 160 kW mean beam power in operation, one may even envisage to boost the Stage 1 performance from the beginning.

Light Ions for Medical Research

The rather unusual option for a spallation neutron source to produce light ions would lead to a considerable enlargement of the users community. This may well balance the loss of the order of five percent of beam time for neutron physics (a typical operational mode would be 1-2 minutes of ion beam production every 30 minutes). The proposed ion species, up to $_{20}Ne^{10+}$, all feature a ratio of q/m = 1/2; the energy required is around 400 MeV/nucleon, corresponding to a penetration of O^{8+} ions in water of ca. 20 cm.

The major items to be added to the bare proton accelerator would be (cf. also Fig.2) :

1. A second pre-injector in form of an Electron Cyclotron Resonance (ECR) source and an ion Radio-Frequency Quadrupole (RFQ). Note that the ion travelling speed in the drift tube linac in the "2 $\beta\lambda$" - mode is half of the one of the protons.
2. Upgrading the RF acceleration system of the RCS to a larger frequency swing (cf. Parameter List)
3. Switching magnets and a beam transport line to the medical facility of variable magnetic rigidity, possibly tracking the field cycle of the main accelerator magnets; this applies equally to the extraction kicker and septum.

The extra cost of <100 MATS (<9 M$) (accelerator only) estimated for the ion option is less than that of a dedicated facility; the real savings, however, occurs in operation costs, as they are a fraction (comparable to beam time share) of the operation costs of the neutron source.

Acknowledgement

The continuous encouragement and support by Prof. M. Regler was of great help and a driving force of the project.

AUSTRON PARAMETER LIST (Stage 1)

Synchrotron			**First Upgrade**
Output energy	1.6	GeV	
average current	63	μA	126 μA
repetition rate	25	Hz	
beam power	100	kW	200 kW
number of p per pulse	$1.6\ 10^{13}$		$3.2\ 10^{13}$ p/p
transverse emittance (invariant, 86%)	150	π μm	205 π μm
pulse length (2 bunches of 50 ns each, 350 ns spacing)	420	ns	
circumference	200	m	
injection energy	70	MeV	
RF frequency	1.1 - 2.8	MHz	1.43 - 2.8 MHz
peak RF voltage	170	kV	
harmonic number	2		
bunch area	0.5	eVs	

Injector (H^- source, R.F. Quadrupole, Drift Tube Linac)

Linac output energy	70	MeV	130 MeV
repetition rate	25	Hz	
pulse length	~100	μs	~130 μs
beam current during pulse	30	mA	~40 mA
numb. of turns injected into RCS	~60	turns	~90 turns

Light Ions (up to $_{20}Ne^{10+}$)

Electron Cyclotron Resonance Source	~ 2	keV/n	
Radio-Frequency Quadrupole	250	keV/n	
Linac output energy	16.5	MeV/n	
pulse length	~100	μs	
beam current during pulse	>10	μAe	
Synchrotron RF frequency range	1.1 - 4.3	MHz	1.43 - 4.3 MHz
harmonic number	4		
output energy	400	MeV/n	

	Estimated Cost [M$]		+	-
1)	120	70 MeV, 25 Hz → 63 microamps, 100 kW, 25 Hz	**Fits cost limit** No R&D (reminiscent of ISIS) Broad upgrading potential Light ion acceleration feasible	Only 100 kW in Stage 1
2)	210	120 MeV, CCL, 800 MeV, 10 Hz → 250 microamps, 200 kW, 10 Hz; SR 800 MeV	Low repetition rate 200 kW beam power No R&D required (reminiscent of LAMPF-PSR)	*Too expensive* No light ions
3)	125 (205)	120 MeV, CCL, 25 Hz → 20 (40) microamps, 100 (200) kW, 25 Hz	Stage 1 **fits cost limit** Upgrading to 200 kW by adding a 400 MeV CCL	Only 100 kW in Stage 1 No light ions in Stage 2
4)	175	160 MeV, 50 Hz → 167 microamps, 200 kW, 10 Hz; storing 4 RCS pulses	Low repetition rate 200 kW beam power No R&D	*Too expensive* No light ions
5)	?	100 MeV, 50 Hz → 125 microamps, 200 kW, 10 Hz; FFAG 1.6 GeV; storing 5 Linac pulses	Low repetition rate 200 kW beam power	Major R&D effort needed (No reference machine) *Cost not known*
6)	??	100 MeV, 8.33 Hz → 200 microamps, 200 kW, 8.33 Hz; Double Helix 1 GeV 8.33 Hz	Very low repetition rate 200 kW beam power light ions (probably) feasible	Considerable R&D *Cost uncertain*

FIG. 1 AUSTRON: Accelerator configurations considered

Acronyms used: **DTL** = Drift Tube Linac (Alvarez type)
CCL = Coupled Cavity Linac
RCS = Rapid Cycling Synchrotron
SR = Storage Ring (or Compressor Ring)
FFAG = Fixed Field Alternating Gradient Cyclotron/Synchrotron

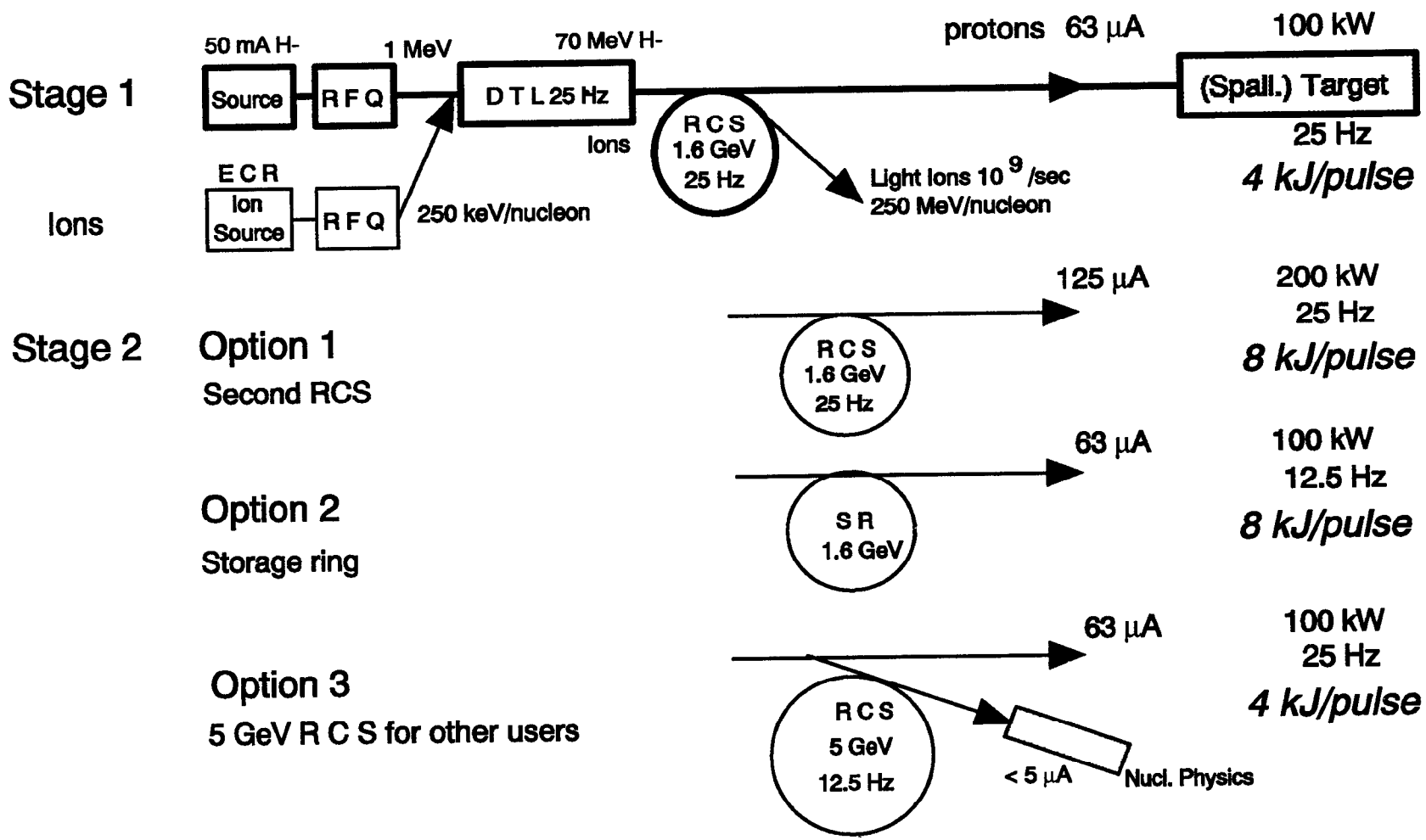

Fig 2: AUSTRON, preferred Stage 1 accelerator complex, with options for Stage 2

Recent Evolution

(Summary of a Meeting on AUSTRON held in Vienna on May 3-4, 1993)

P.J. Bryant
CERN, CH-1211 Geneva 23

The AUSTRON was conceived primarily as an advanced neutron spallation source with a performance comparable to that of the ISIS machine at the Rutherford Appleton Laboratory. It was also planned that it should devote a small fraction of its time to producing light ions for medical research. The consensus of opinion at the meeting endorsed this basic concept with the following points that strengthen the justification for a spallation source:

- The competitive atmosphere in the ISIS user community indicates a strong demand.
- Industrial exploitation is still at an early stage of development.
- The progressive closure of nuclear reactors will restrict access to neutrons.

The meeting also showed great interest in the medical research that could be carried out with light-ions. This was seen as an essential step in the comparison of the different radiation therapies and their applications to various types of cancer. Only after such research, would it possible to plan dedicated facilities with full confidence that the best choices were being made.

While the basic concept and design parameters of the AUSTRON were well received, there was also a strong interest in the upgrade potential of the facility. The basic indicator for performance is the power delivered by the accelerator complex to the target, since this determines the neutron production. There are three ways of increasing this power:

- Increasing the beam energy (e.g. 1.6 to 3.2 GeV).
- Increasing the beam current (e.g. 63 to 126 μA).
- Increasing the repetition rate (e.g. 25 to 50 Hz).

The discussions during the meeting were of fundamental importance for arriving at a balanced judgement of the advantages and disadvantages of each method for increasing the delivered power and it was in this domain that the meeting had most influence on the accelerator design. The choice between increasing beam energy or intensity falls mainly on accelerator considerations, while the repetition rate is also influenced by physics requirements.

Increasing the beam energy is the surest way, from an accelerator point of view, of increasing the delivered power. Doubling the energy, rather than doubling the intensity, also eases the thermal problems in the target. Against these positive features, it was shown that raising the energy had a more detrimental effect on the installation and running costs. There is also more induced activity from a beam loss at 3.2 GeV than at 1.6 GeV. Thus machine access may be restricted. A higher beam energy implies a longer target, which has a negative implication for physics. Finally, it was mentioned that detailed target designs and moderator layouts did not exist at higher energies. The feelings were that there was no gain to be made above 5 GeV and in the range of 2-3 GeV it could not be guaranteed that doubling the energy would double the neutron yield.

As a corollary to the above, upgrading the beam current has the advantages of being cheaper both for the installation and running costs. It is also what could be described as the 'higher technology' method. It implies a better theoretical understanding of beam dynamics, higher precision in all aspects of operation, possible need of feedback systems, design of a low -impedance environment for the beam and so on. Space-charge limitations make it necessary to increase the injection energy from 70 MeV to about 130 MeV before the beam current can be doubled Since most of the beam losses occur during RF trapping, the increased injection energy will make loss management a little more difficult and will increase the induced activity per particle lost. However, the consensus from the meeting was that 150 MeV was a 'soft'

threshold for this problem. It is also a problem that can be reduced by techniques such as chopping the beam and improving RF trapping and collimation techniques.

Since the basic design already foresees an increase in energy on the target from the 800 MeV of ISIS to 1.6 GeV and the above statements do not favour any further increase, it was felt that the upgrade programme should concentrate on doubling the beam current

With regard to the repetition rate, the time structure of the proton beam determines that of the neutron beam and thus the physics requirements play an important role in the choices to be made. Physics requirements for the neutrons fall into three broad categories:

- Sub-eV pulsed at about ten Hz with a pulse length (rms) < 1 μs.
- A few eV, pulsed at several tens of Hz with a pulse length (rms) ≤ 1 μs
- A few hundred keV, pulsed at several hundred Hz with a pulse length (rms) ≤ 2.5 ns.

Frequencies up to tens of Hz can be achieved by the whole accelerator complex, but the last user group requires several hundred Hz. This can only be satisfied by using a different radio-frequency system in a second ring and is therefore regarded as a 'far-future' upgrade because of its substantial cost. The second user group are more concerned with average power than the exact value of the repetition rate and would be satisfied by the ISIS value of 50 Hz. The first user group see a definite need for a low rate of the order of 10 Hz.. Thus, the 25 Hz chosen for the basic design can be understood as a solution that biased the repetition rate to a lower value in favour of the first group while using the cost advantage of the slower machine to help pay for a higher energy, so that the second group would not be disadvantaged by the reduced average power. Since it is better to use a sub-harmonic of the power distribution system, this optimisation fell on 25 Hz. While the second group of users is not disadvantaged, the first group is only partially satisfied. The beam current upgrade would automatically improve this situation by enabling operation at 12.5 Hz with the same neutron yield as the basic design without the need for any major installation (stretcher ring).

The maximum ion production rate of 10^9 ion/s (4×10^7 ion/pulse) was maintained. The basic design allows for a 'pulse per pixel' mode of treatment of a tumour that would irradiate 1500 pixels in a one-minute treatment. The energy will be controllable so that the tumour can be treated in slices of constant depth. The more sophisticated continuous scanning will only be possible with a slow spill from a storage ring and is therefore regarded as a 'far-future' upgrade. It became clear from early discussions that the original energy of 250 MeV/nucleon was not sufficient to support a full medical research programme. Fortunately, modifications with a very modest cost were possible to achieve 400 MeV/nucleon that corresponds to a penetration in water of 20 cm for oxygen ions.

The principle stages in the building of the AUSTRON accelerator complex with the estimated prices are tabulated below. Figures 1 and 2 shows the main parameters and schematic layouts.

The above conclusions imply that the target should be designed for 250 kW average power at 1.6 GeV with a 25 Hz repetition rate. This would take into account the first upgrade, which is likely to be implemented almost directly, and possible operational improvements over the first decade of operation. In the longer term, it is likely that an additional ring and a second target would be preferred to an upgrade of the first target station.

BASIC DESIGN	MATS	MATS
Protons: power on target 100 kW (1.6 GeV, 63 μA, 25 Hz) Ions: Up to neon, operation in 1-2 min. periods, 10^9 ion/s (max), 1 pulse per pixel operation with controlled energy and intensity	1450.	1450.
Immediate improvement of ion operation from 250 MeV/nucleon to 400 MeV/nucleon	5.	
Preparation for First Upgrade (must be included in basic design)	47.	
	52.	1502.
FIRST UPGRADE TO DOUBLE CURRENT		
Protons: injection energy increased from 70 to 130 MeV, power on target 200 kW (1.6 GeV, 126 μA, 25 Hz)	190.	
	190.	1692.
FURTHER UPGRADES		
Storage/stretcher ring for 12.5 Hz/300 Hz and/or slow spill Second target station etc. These are major investments.for the far future.	--.	--.

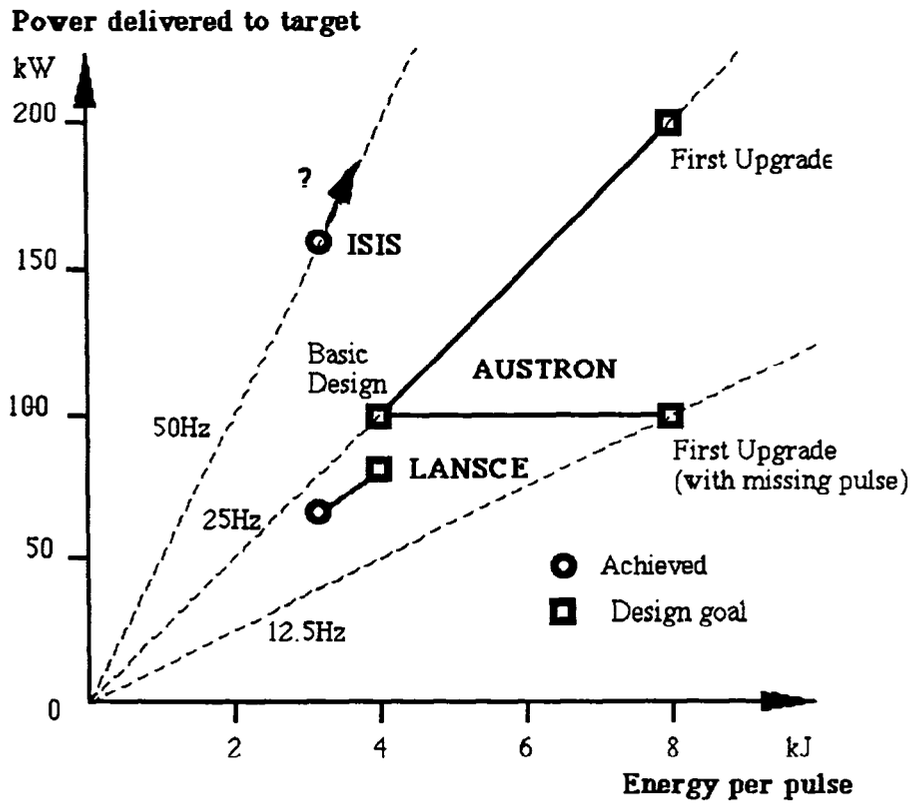

Figure 1 The AUSTRON and comparable neutron sources

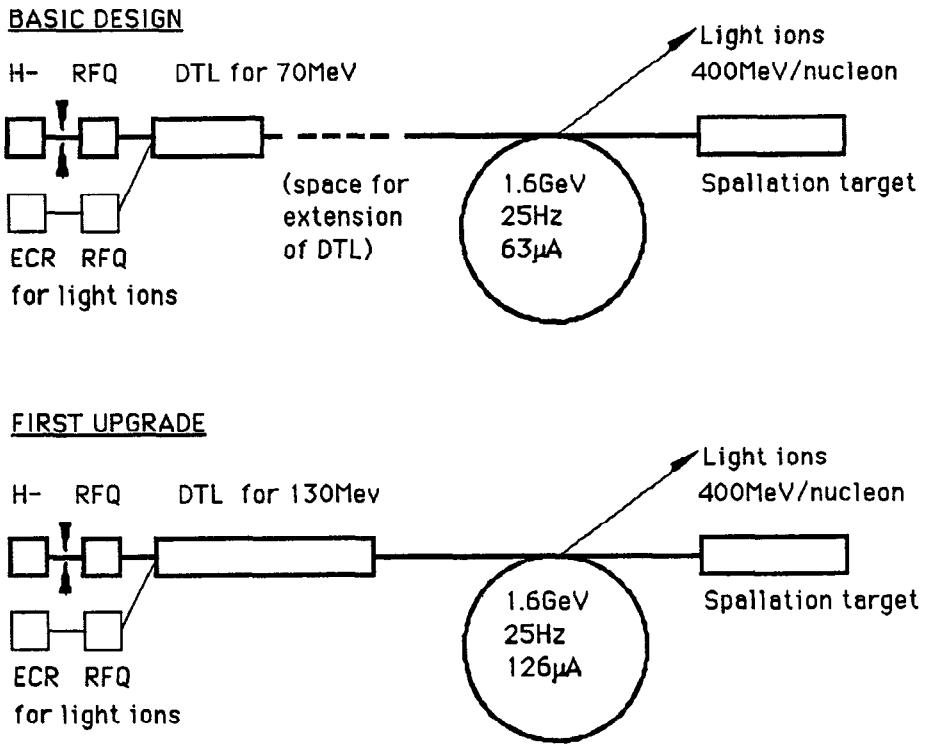

Figure 2 Schematic layout of Basic Design and First Upgrade

(H^- = negative ion hydrogen source, DTL = Drift tube linac, ECR = Electron cyclotron resonance source, RFQ = Radio-frequency quadrupole)

* * *

ADVANCED NEUTRON SOURCE FOR PHYSICAL RESEARCH

Yu. Ya. Stavissky, Yu. V. Senichev
Institute for Nuclear Research Russian Academy of
Science, Moscow

The possibility to create the super-intensive pulsed neutron source for solid state neutron research based on fast-cycling proton synchrotron, liquid-metal Pb-Bi, PuO_2-Na multiplying targets is discussed. The thermal neutron peak flux as high as ~ 10^{18} n/cm^{2}s is expected to be achieved using this scheme.

Slow neutrons (resonant, thermal and cold) are quite effective means for investigation of fundamental properties of matter. The unique features of neutrons (strong interactions with nuclear matter, absence of electric charge and corresponding limitations, connected with ionization losses in matter as well as Coulomb barriers in nuclei) reveals themselves most completely at low neutron energies. These features of neutron, high intensities, accessible in nuclear reactors (flux densities up to (2-3) 10^{15} neut/cm^{2}s) give wide possibilities for development of neutron research in regions of particle physics, nuclear physics and, in particular, condensed matter research (up to 85% program of research on nuclear reactors). The future of these investigations depend on the possibility to increase intensity of neutron sources. However, neutron flux in research nuclear reactors is limited by heat release density in fuel and safety problems. Respectively, already in the middle of sixties the possibility to obtain the thermal neutron flux up to 10^{16} neut/cm^{2}sec by spallation process at energy 1 GeV was considered. However, having the gain in flux about 5, the facility was overcomplicated and too expensive (ING, "Canadian project").

At present, in our opinion, the only way to increase significantly (tens and hundreds times) the effiency of neutron experiments is using a pulsed neutron spallation source. The pulsed slow neutron source allows to develop practically the same research program as the steady-state one if their thermal neutron flux densities (but pulsed) are comparable.

Now, we see a number facilities, being in operation or under construction or development, that are based on proton synchrotrons or storage rings with charge-exchange injection from linear proton accelerators and one-turn extraction of proton bursts onto neutron targets. Those in operation are KENS (KEK), IPNS (Argonne Lab), LANSCE (LANL), ISIS (Rutherford Lab); the construction of the Moscow meson factory's pulse neutron source IN-06 /2/ is at the final stage. All this facilities are driven with proton beams with energy of 0,5-1 GeV and average proton currents up to 200 mA.

The next generation of spallation pulsed neutron sources with tens times higher intensity is being developed - 1 MW Spallation Source in USA, European Spallation Sources (ESS).

The first priority for this sources, intended for wide physical research program (tens of simultaneously running experiments), is their reliability. As a consequence, in our opinion, we should use elaborated accelerator and nuclear facility technologies and look for optimal complex ways to create such a facility.

1. The radiation damages of the first wall of the target due to primary protons are of special importance for reliability. Among other factors the energy of primary protons plays, maybe, the decisive role. The optimal proton energy for neutron production in extent targets lies in the region of 1.5 to 2 GeV. This value is determined by competition between nuclear interaction and ionization losses. At low proton energies (below 1 GeV) the direct proton ionization losses prevail, while at energies above 1 GeV the ionization of electron-photon showers, initiated by π^0-meson decay, becomes more important. The results of computations, that were carried out by V. Miroshnichenko, N. Sobolevsky, A. Kuzin and S. Lebedev which are consistent with the experiments on neutron yield measurements in region up to 70 Gev, (/4/, /5/), are presented on Figs. 1 and 2. While the proton energy increases above 1.5 -2 GeV, the specific neutron yield (per unit of thermal neutron flux density on surface of water moderator and unit of proton energy) decreases slowly (Fig. 1), but the specific first wall radiation damage rate decreases significantly (Fig. 2).

2. The second significant factor is the limitations due to the space charge and collective effects in proton beams. These effects are approximately inversely proportional to the proton energy for a constant neutron yield.

3. After all, the high energy of protons and, as a consequence, relatively small proton current provide more possibilities to create the radiation pure accelerator system localising radioactive wastes within the easy-serviceable target system. Therefore, apparently, the most realistic scheme of an advanced pulsed neutron source (ANS) may be based on a fast-cycling proton synchrotron for about 10 GeV, 50 pps, with average current 500 mA or more, with injection from 1 GeV linac and one-turn extraction onto the neutron target system. To enlarge the experimental possibilities of the source it is expedient to use two independent neutron targets with vertical (from bottom up) beam injection.

The first target - liquid-metal Pb-Bi /6/ or water cooled tungsten /2/ with thick beryllium reflector and water moderators inside is intended for high pulse repetition rate (40 pps), moderate average pulsed neutron flux densities and small neutron background between pulses (below 10^{-5}).

For experiments with high pulsed neutron fluxes of thermal and cold neutrons it is expedient to use a multiplying target with moderate gain factor (~ 15) /7/. So, the fast breeder prototype, based on plutonium or uranium oxide core with sodium cooling, inner tungsten proton-to-neutron converter, thick Ni reflector with air cooling, water and liquid hydrogen moderators inside the reflector may be considered as the most suitable concept. There is many-years experience of successful operation (since the end of fifties) of plutonium-oxide fast reactors with compact core, sodium cooling - BR-5, BR-10 (Physical - Energetical Institute, Russia, /8/), pulsed reactor IBR-2 (JINR, Dubna) /9/, experimental fast reactors EBR-2 (USA), Phoenix (France).

The peak thermal neutron flux density at repetition rate 10 pps and pulse width ~30 ms will be about ~10^{18} neut/cm^{2}sec. This value by approximately two orders of magnitude exceeds the flux density in the most powerful research pulsed or steady-state reactors. The background power between pulses will be 4-5% in system without movable mechanical reflector elements.

Since the main requirements for high intensity proton accelerator complex are the reliability and the radioactive purity, which are the same as for Meson and Kaon factories,

many technical and scientific decisions are given from Moscow Kaon project ("The proposal of the accelerator complex of the Moscow Kaon Factory", Yu. Senichev et al., San Francisco, IEEE, PAC /10/).

The accelerator complex consists of proton linac and fast cycling synchrotron (FCS) with average beam intensity 500 mA and energy 10 GeV.

The injector includes 100 KeV H-source and RFQ with final energy 2 MeV and resonant frequency 198.2 MHz.

The Linac consists of two parts DTL and DW structures with transition at 100 MeV. The Linac accelerates the beam with a pulse length 1 ms and amplitude 10 mA up to 1 GeV with repetition frequency 50 Hz.

Then each pulse is transferred in FCS and is injected during 1 ms on flat-bottom magnetic field. During 16 ms particles are accelerated and then magnetic field fall up to initial magnitude. Resonant frequency is changed from 33 MHz up to 37.6 MHz. For optimization of RF cavity number the magnet waveform is complicated and consists of three parts - harmonic, linear and harmonic.

Since FCS is of high-intensity synchrotron with large transverse beam size, deep beam loading and significant collective instability, we have focussed on the following features of structure :

- the transition energy has to be high enough to satisfy conditions of collective instability
- the dynamic aperture in presence of chromaticity-correcting sextupoles has to be more than three emittance of beam which satisfy to not crossing of integer and half-integer resonances with space charge
- long dispersion-free straight sections are required for RF cavity, extraction and injection system
- eddy current problem has to be solved in RF tuner and vacuum chamber of dipole.

From the general consideration the lattice with both modulation of quadrupoles strength and distribution of bend magnets is most suitable for FCS /10/. The synchrotron has a racetrack shape with two 180 degree arc and two dispersion-free straight sections. The arcs have 8 superperiods. Each superperiod contains 4 FODO cells, two central half-cells do not have dipoles ("missing magnet"). The horizontal tune of are equals to 3, that gives zero dispersion in 5-cells FODO straight sections. The phase advance of the straight section in vertical plane equals to 2.66/2 and in horizontal plane is 1.66/2. Each arc is a second order achromt. A high energy transition energy is reached by "missing" scheme and equals to 17 GeV. In order to reduce the tune spread, 32 sextupoles are placed in arcs for chromaticity correction.

In FCS RF cavity has to be very fast retuned so the usual variant with ferrite tuner looks not very reliable due to ferrite heating. Idea to use reactive properties of electron cloud in magnetron type diode for tuning of accelerating cavity in fast cycling synchrotrons was proposed under development Moscow Kaon project. In 1990 first tests of "varactor" in

scheme of capacitor divider have shown possibility to change capacity in range 100-160 pf with applied voltage 20 kV /11/.

The very important question in FCS is the ceramic vacuum chamber. The first stage of our investigations in this field was successfully completed in 1991. We have now a technology for producing a ceramic segments with lengths 250-500 mm and wall thickness 4 mm.

The basic parameters of accelerators and targets complex ANS is given in Table 1.

TABLE 1

1 GeV - Linac	
av. current	0.5 ma (50 pps, 1 msec)
RFQ	2 MeV
DTL - (Alvarez) structure	100 MeV
DW - (Andreev) structure	1 GeV
10 GeV - FCS	
total circumference	573 m
revolution time	2 msec
max horizontal size	75 mm
max vertical size	60 mm
Pb -Bi target system	
power	2 MW
Dimensions	
target	15 cm
Be-reflector	75 cm
H_2O-moderator	15 x 5 cm^2
av. proton current	.4 mA
pulse repetition rate	40 pps
av. density of thermal neutron flux	$3:1\text{-}12:10^{13}$neutr/cm^2sec
peak density of thermal neutron flux (30 mcs)	$2.6\text{-}10.10^{16}$neutr/cm^2sec
first wall radiation damage rate	14 dpa/year
PuO_2- Na target system	
power	15 MW
background power	4.5 %
core	23 x 30 cm
W-convertor	5 x 30 cm
Ni-reflector	83 cm
H_2O-moderator	12 x 5 cm
av.proton current	100 mA
multiplication factor	15
life-time of prompt neutron	130 nsec
pulse repetition rate	10 pps
av.demsity of thermal neutrons	$2.2\cdot10^{14}$neutr/cm^2sec
peak density of thermal neutrons (27 mcs)	$8.4\cdot10^{17}$neutr/cm^2sec
first wall radiation damage rate	60 dpa/year

Comparative parameters of intensive neutron sources for research in solid state physics region placed in TABLE 2.

TABLE 2

Facility	Type	av.current on target	T neut/cm^2	T sec	K =	dpa/year
IBR-2 (~ILL)	pulsed reactor,4MWt	PuO_2+Na	10^{13} (120	10^{16} mcs)	1*	12
ISIS	PS,70 MeV- -0.8 GeV	0.2mA U238	$2.1 \cdot 10^{12}$	$1.4 \cdot 10^{15}$	3.3*	6.3
MMF IN-06	stor.ring 0.6 GeV	0.5 mA U238	$4 \cdot 10^{12}$	$1.3 \cdot 10^{15}$	6.4**	14
		0.15 mA U233	$1.8 \cdot 10^{13}$	$2. \cdot 10^{16}$	30**	14.5
ESS	stor.ring 1 GeV	6.3 ma Pb-Bi	$6.3 \cdot 10^{13}$	$4.2 \cdot 10^{16}$	100**	125
ANS	PS, 1 GeV- 10 GeV	0.4 mA Pb-Bi	$3.1 \cdot 10^{13}$	$2.6 \cdot 10^{16}$	50**	14
		0.1 mA PuO_2-Na	$2.2 \cdot 10^{14}$	$8.4 \cdot 10^{17}$	350***	60

* - design parameters (now K~1.6)
** - real geometry of 1 stage IN-06 (thin Be-reflector)
*** - thick reflector

The experimental possibilities of the high-power pulsed reactor IBR-2 with design parameters (pulse width 100 ms, average power ~4 MW) are close to those of a high-flux steady-state research reactor (ILL, Grenoble). These parameters are still not achieved - (170 ms, 2 MW power now). The comparison of pulse systems are made using the figure-of-merit factor Φ_T / θ_T^2 . Here Φ_T - average thermal neutron flux density on the water moderator surface, θ_T - thermal neutron pulse width.

In conclusion we would like to express our best acknowledgements to S. K. Esin, N. A. Khryastov, N. V. Kolmichkov, V. A. Kuzmin, V. D. Laptev, V. A. Matveev, V. G. Miroshnichenko, I. Yu. Mosievskaya, S. F. Sidorkin, N. M. Sobolevsky, S. G. Lebedev, A. V. Kuzin, M. T. Voronzov for useful discussion and collaboration.

References

1. Bartolomew G. A., Milton Y.C.D., Vogt E.W., Rep AECL 2059, 1964

2. Stavissky Yu. Ya., Proc. of the 11 ICANS meeting, KEK, TSUKUBA, 1990 v.1, p. 87.

3. Bauer G. et al., Proc. of Juelich conf., IAEA, 1985, IAEA-CN 46/79.

4. Vasilkov R. G. et al., Proc. of the 11 ICANS meeting, KEK, TSUKUBA, 1990 v.1, p. 340

5. Akopyan A. G. et al., ibid, p. 579

6. Bauer G. Proc. of INES, Moscow, 1989, v.1, p.43

7. Stavissky Yu. Ya. Preprint N-389, PEI, Obninsk, 1973

8. Leipunsky A. I. et al., Proc. of Conf. on research reactor, Vienna, IAEA, 1961, rep SM-18.22, p. 315

9. Ananiev V. D. et al., At. Energia, 57, 227 (1984)

10. Senichev Yu. V. et al., Proc. IEEE PAC, S Francisco, 1991, p. 2823

11. Iliev A. I. et al., ibid

12. Kuznetsov M. et al., Proc. EPAC 92, Berlin. 1992, v. 2, p. 1242.

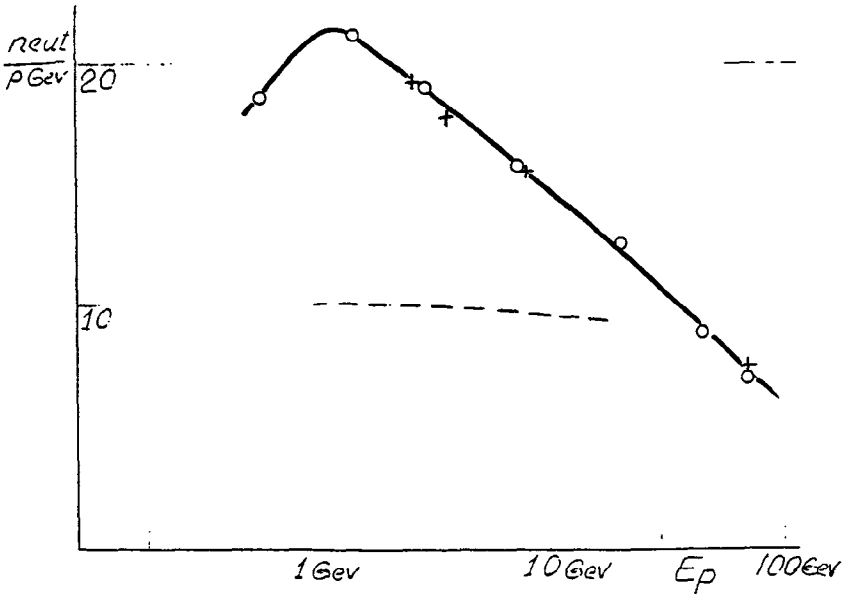

Fig.1.
Specific yield of spallation neutrons (per 1 GeV proton energy, Pb); - - - - - - thermal neutron flux density on surface water moderator per one source neutron (arbitrary units); O - calculation, + experiment

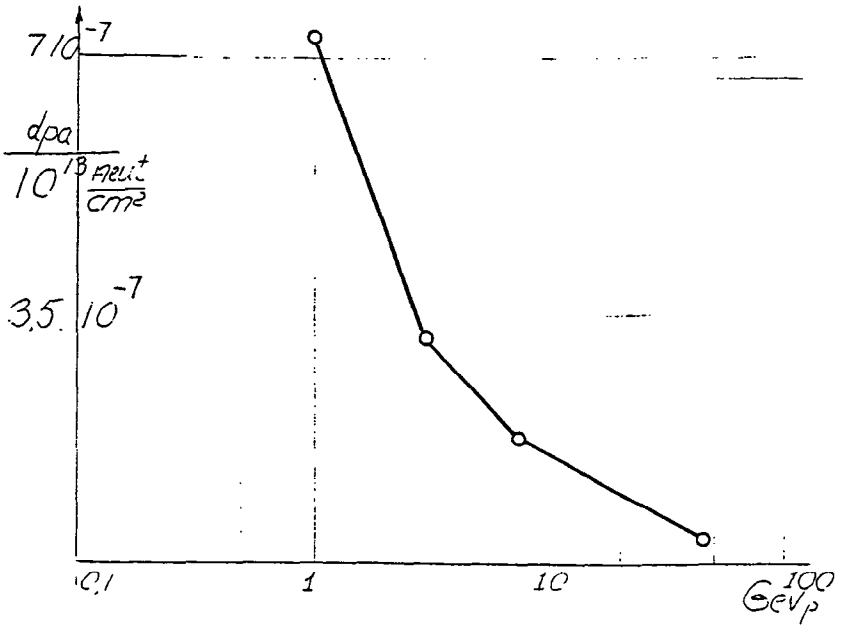

Fig.2.
Radiation damage first wall (iron) for 10^{13} neutrons/cm^2 on water moderator surface for protons (beam cross-section 20cm^2)

SUMMARY OF THE ACCELERATOR SESSIONS

M.K. Craddock
Physics Department, University of British Columbia
and TRIUMF, 4004 Wesbrook Mall, Vancouver, B.C. Canada V6T 2A3

The nine accelerator sessions were attended by about 30 delegates, who heard 26 papers covering both development of the existing sources and design considerations for future ones. Unfortunately, only the highlights can be mentioned in this brief summary; for full details the reader is referred to the individual papers.

From the existing sources (Table 1) some remarkable progress was reported since the last ICANS meeting. At ISIS the beam current has been doubled to over 200 μA, and the machine availability has also been increased. The extra intensity is the result of a number of improvements, in particular doubling the number of rf power tubes, incorporating feedforward compensation, and rapid programming of the betatron tunes and closed orbit. Plans are now being laid to raise the current towards 300 μA with the help of higher harmonic cavities. LANSCE has also made major strides, the beam current being raised to 80 μA. The beam loss mechanisms seem now fairly well understood, one novel form of injection loss being due to H^0 atoms emerging from the stripping foil in certain unfavourable excited states. The current-limiting instability is now fairly firmly identified as an electron-proton instability, the electrons apparently being supplied chiefly by secondary emission from the foil; remedial measures are under way.

The proposals for new sources are listed in Table 2 (adapted from ref. 1). Two of these (AUSTRON, to be built near Vienna, and IREN, at JINR Dubna) offer capabilities similar to those of existing sources but to new user communities. The others all aim at much higher powers in the 1-5 MW range, and come in a variety of shapes, sizes and energies, though all can be reduced to the formula of linac+ring(s). The major design question is whether the ring should be an accelerator or a (fixed energy) compressor; this choice is correlated with that of top energy, accelerator rings being associated with high-energy and low-current designs and compressor rings with low-energy and high-current designs.

The major design considerations for these sources are minimizing the beam spill and minimizing the cost. It is the first of these that leads to the correlation mentioned above; assuming that the activity produced by beam spill is roughly proportional to the power loss, then to maintain the present activity levels in accelerators operating with an order of magnitude higher beam power, the fractional beam current spill must be reduced by an order of magnitude. What sources of beam spill are most important? The answer to this question is a major factor in steering the designer towards either the higher-energy accelerator or lower-energy compressor ring options.

Experience shows that the greatest current loss in a ring occurs during injection and trapping. Since many features of H^- injection (e.g. transport, painting, momentum ramping, and foil damage) get harder or worse at higher energies, it is desirable to keep the ring injection energy as low as possible. This logically leads to the lower-energy linac+accelerator ring option, as exemplified by the Argonne, Brookhaven and European RCS (rapid cycling synchrotron) and FFAG designs. (The historic term FFAG is misleading, for although the Field is Fixed, modern designs do not use Alternating Gradient but sector edge focusing; a better term would be ring synchrocyclotron, by analogy with the sector ring cyclotrons at PSI, Indiana, RIKEN, etc.).

Beam loss occurring during acceleration in a ring is intrinsically more dangerous than at injection because of the higher energy. Since the circulating currents will be an order of magnitude higher than at present, and the acceleration time will be around 10 ms compared to 1 ms for a compressor, a synchrotron may be much more difficult to operate than a compressor. These considerations have led Rutherford and Los Alamos designers to choose the full-energy linac+ compressor ring option.

The problem here is that to reach 5 MW with a reasonable current in the compressor ring its energy must be at least 2 GeV. This would make a conventional linac very expensive to build and extremely expensive to operate. For this reason the design of superconducting proton linacs is being actively pursued both in Europe and North America. The Santa Fe Workshop last February concluded that a superconducting linac looked very promising for a neutron source from both technical and economic points of view. At this meeting, however, it was pointed out that the duty cycle had incorrectly been assumed to be 10% rather than 3.3% and that the power required to pulse the linac cavities had been neglected, casting some doubt on the earlier conclusions. These questions will perhaps be resolved at the Superconducting Workshop to be held at Wuppertal next week.

An alternative approach, avoiding the need for either a very high energy linac or an accelerator ring, and providing some redundancy, is to use multiple compressor rings. Both Rutherford and Los Alamos have proposed options using three compressor rings with an 800 MeV linac for a 5 MW source.

I. Gardner[1], reviewing the choice of top energy, pointed out that the while high energies required only low average currents, the peak current requirement remains more or less the same, the difference lying in the duty cycle or the number of rings. His conclusion was "USE LOWEST POSSIBLE ENERGY, HIGHEST POSSIBLE INTENSITY".

Which of the above options is most cost-effective must await a detailed design and cost study. Meanwhile I can provide some guidance -- or perhaps fan the flames of controversy -- by proposing two speculative inequalities regarding accelerator costs C based on common prejudices:

1. For the same top energy, repetition rate and beam current

$$C(\text{FFAG}) > C(\text{synchrotron}) > C(\text{compressor})$$

2. For the same energy gain and five years' operation

$$C(\text{warm linac}) > C(\text{SC linac}) > C(\text{synchrotron})$$

Finally, I would like to thank the organizers for the opportunity to participate in this meeting and also to demonstrate a famous tradition of Abingdon, the Mayor's distribution of bread from the roof of the County Hall. In doing so I may have become the first speaker ever to throw buns at his audience -- rather than the other way around -- and I'm grateful that they resisted the temptation to respond in kind.

References

1. I.S.K. Gardner *"Accelerator Considerations for the Choice of Proton Energy"*, these proceedings.

Table 1: PRESENT SPALLATION NEUTRON SOURCES[1]

Facility	Energy	Rep. Rate	Beam Power Avg.	Beam Power Peak
KENS (Japan)	500 MeV	20 Hz	2 kW	2 kW
IPNS (US)	450 MeV	30 Hz	6 kW	7 kW
LANSCE (US)	800 MeV	20 Hz	40 kW	60 kW
ISIS (UK)	800 MeV	50 Hz	145 kW	160 kW
PSI (CH)	570 MeV	cw	1 MW	

Table 2: PROPOSED ACCELERATOR NEUTRON SOURCES

	Linac	Ring(s)		Beam Power
JINR (e^-)	0.2 GeV	--	Pu Booster	0.06 MW (eqvt.)
LBL	1.0 GeV	--	Indn. Linac	5.0 MW
AUSTRON	0.07 GeV	1.6 GeV	RCS	0.1 MW
ANL	0.4 GeV	2.2 GeV	RCS	1.0 MW
BNL	0.6 GeV	3.6 GeV	RCS x 2	5.0 MW
ESS	0.8 GeV	3.0 GeV	RCS	5.0 MW
INR	0.6 GeV	45.0 GeV	K Factory	5.0 MW
ESS	0.46 GeV	1.6 GeV	FFAG	5.0 MW
KEK/NEA	1.5 GeV	1.5 GeV	Comp x 1	3.0 MW
ESS	2.4 GeV	2.4 GeV	Comp x 1	5.0 MW
"	1.2 GeV	1.2 GeV	Comp x 2	5.0 MW
"	0.8 GeV	0.8 GeV	Comp x 3	5.0 MW
LANL	2.2 GeV	2.2 GeV	Comp x 1	5.0 MW
"	0.8 GeV	0.8 GeV	Comp x 1	1.0 MW
"	0.8 GeV	0.8 GeV	Comp x 3	5.0 MW

Reaching 200 μA on ISIS

C W Planner
Rutherford Appleton Laboratory, Chilton Didcot, Oxon, UK

Introduction.

On Friday 5 February 1993 the ISIS Pulsed Spallation Neutron Source just exceeded its design current of 200 μA at full energy of 800 MeV and repetition rate of 50 Hz. This is extremely good news for the experimental scientists who use the ISIS facility. Particularly so, for the scientists working on the neutrino collaboration KARMEN, since their need for higher intensity engendered additional financial support from the German Ministry of Science, which was particularly helpful in achieving this goal. It was also extremely gratifying for the accelerator physicists, because the full design specification was obtained in spite of the fact that the transverse acceptance of the synchrotron had to be reduced in the final design of the machine, resulting in the acceleration of beams with smaller transverse cross section, which enhances the effects of space charge.

From the beginning of 1986, when ISIS was first turned on for neutron physics, steady progress has been made, year by year, increasing the intensity as shown in Figure 1. By the end of 1991 the intensity had been raised to just over 100 μA and the start of 1993 saw a doubling of the current to 201.6 μA. As well as increasing the intensity, steady progress has also been made increasing the beam availability as can be seen from the plot of micro ampere hours irradiation on the spallation target shown in Figure 2.

Achieving 200 μA with greater machine availability has come from a combination of engineering improvements and better understanding in setting up, tuning and operating the accelerators. A brief account is given of the performance of the spallation source and the steps taken to reach the full design current.

Linac Development.

There has been a gradual and painstaking development[1] that has improved the output intensity and availability of the Penning H^- ion source, as illustrated in Figures 3 and 4. The rate of development of this ion source has been somewhat restricted, because the trial developments have been made on ISIS and not on an off-line test facility.

A significant reduction in the number of trips of the high voltage generator, following a spark down of the accelerating column, has been obtained by increasing the value of the resistor between the storage capacitor and the high voltage terminal from 10 kΩ to 1 MΩ. The column voltage recovers in 2-3 pulses and it is not necessary to shut off the beam into the column. A 'bouncer circuit' is fitted to the earthy terminal of the storage capacitor to inject a current into the 1 MΩ resistor to compensate the voltage droop from the beam loading of the column.

The installation of vertical and horizontal beam steering, at the start of the beam transfer line from the high voltage column to the linac, makes it possible to obtain over 60% transmission through the linac for any ion source fitted to the column. Transmission could at times be less than 50% before installation of the steering magnets

Improvements that allow the linac to be more easily set up for injecting into the synchrotron are the implementation of a ΔT system to optimise the accelerating field and phase of the rf accelerating cavities of the linac and a separate rf power system for the de-buncher cavity. The de-buncher was originally powered from a small loop coupled to the final accelerating cavity of the linac. The use of the de-buncher is critical for high intensity operation of ISIS, but it is found that it is optimum at a field significantly lower than that for maximum de-bunching.

Synchrotron Development.

Injecting into the synchrotron uses charge exchange and it is found that 'painting' the beam simultaneously in both transverse phase-planes is essential. In the horizontal plane injection is on the inside radius and starts a few hundred microseconds before field minimum. Painting is obtained by injecting beam at fixed energy at a point with a finite dispersion function together with a falling sinusoidal excitation of the synchrotron magnet field. In the vertical plane the painting is done by a small vertically deflecting dipole in the injection beam line powered from a programmable power supply. In the initial painting small amplitude horizontal betatron oscillations are correlated with large amplitude vertical oscillations and towards the of injection large amplitude horizontal are correlated with small amplitude vertical. However, it is found that as the intensity increases less particles with small amplitude oscillations can be injected. The maximum intensity injected to date is 4×10^{13} and the injected current rises linearly with time and shows no sign of saturation. However, not all the beam injected can be captured by the synchrotron rf. The intensity for 200 μA was obtained by injecting 3.05×10^{13} protons of which 2.52×10^{13} were trapped and accelerated to 800 MeV

Accelerating high intensities in the synchrotron has required the installation of an additional power tube in parallel with the existing tube at each of the six accelerating stations. Beam loading compensation is provided by a feed forward system[2]. The stability of the feed forward gain is now much improved with the fitting of solid state driver amplifiers to the synchrotron rf systems. For high intensity operation it is necessary to minimise phase transients and to have fine control of the time and amplitude of the accelerating voltage particularly during injection trapping and the early part of acceleration.

A major contribution to obtaining high intensities in ISIS is believed to be the combination of fast programmable supplies for both trim quadruple and dipole correction magnets together with the rf shielded ceramic vacuum chambers. This allows fast correction of betatron tunes and closed orbits during injection trapping and acceleration. The minimisation of closed orbits throughout the acceleration cycle is very critical to controlling and minimising beam loss around the ring.

The required rapid control of the betatron tunes is illustrated in Figure 5. During the injection interval the tunes are steadily raised in both planes to compensate for the large space charge tune shift. After trapping the vertical tune is moved rapidly away from the integer to avoid a vertical resistive-wall head-tail instability with mode m=1, see Figure 6. This is a lower mode

than predicted by accepted theory and a modified theory has been proposed by Rees to explain the low mode number. The betatron tune in the horizontal plane is gradually reduced after trapping and then rapidly moved closer to the integer in the latter half of the cycle to avoid a coupling resonance that is believed to be either the $Q_H + Q_V = 8$, or the $2Q_H + 2Q_V = 16$.

All trim quadrupoles are programmed initially with identical functions to produce the desired betatron tune profile. However, it has been found that compensating for gradient errors by superimposing small 7th and 8th harmonic variations in the gradients around the ring, reduces beam loss and allows more efficient trapping of the beam.

The only other coherent beam motion observed in the synchrotron develops during injection. This appears to be excited by residual rf structure on the injected beam at the linac frequency and its harmonics. The motion damps above an injected intensity of 4×10^{12}, but begins to grow again as the intensity approaches 1×10^{13}. The motion damps immediately injection stops and is also damped by a very small amplitude of the synchrotron rf, by use of the de-buncher to control the momentum spread and by increasing the vertical beam size, see Figure 7. To obtain the highest intensities it is necessary to optimise the amplitude and phase of the de-buncher, the amplitude and form of the excitation of the vertical sweep magnet, and also to have a small amplitude excitation of the synchrotron rf.

Several unsuccessful attempts have been made to excite in ISIS the instability observed on the PSR at Los Alamos.

The maximum tune shifts in ISIS, whilst accelerating 2.52×10^{13} , are estimated[3] to be approximately -0.4 in each plane. This assumes that the maximum tune shift occurs for particles with small horizontal but maximum vertical betatron amplitudes, which is considered a reasonable assumption due to the form of the ISIS H^- 'painting'. Thus it appears that at peak intensity some particles cross the resonances $Q_H = 4$, $Q_H = 8$ and $2Q_V = 7$.

Progress to full specification has been dictated in part by the need to control and reduce beam losses to an acceptable level. Beam losses in the synchrotron are confined to approximately one tenth of ring azimuth, between the injection and extraction dipoles, by a system of longitudinal and transverse beam scrapers and collectors. Typical beam losses at an intensity of 180 μA are shown in Figure 8. Some loss occurs at injection (2-3% H^0 from partially stripped H^-) and most of the remainder at low energy in the first 2 ms of trapping. Losses at high energy and in the transfer line to the target are less than 1 part in 10^4. The ability to effect rapid control over the closed orbit and betatron tunes are, as mentioned earlier, considered to be critical in controlling and minimising these losses. The beam loss in the extraction beam line at monitor 9-10 of Figure 8, results from a 1% beam loss at a full transmission carbon target, a little upstream of the spallation target, that is used to produce surface muons for the ISIS pulsed muon facility.

Tolerances on beam losses are shown in Figure 9. The tolerances operate on running averages and are classified into two categories. The first trips the machine and effectively forces it back to a repetition rate of 1 Hz until the beam spill is corrected. The second category is a warning system that does not trip the machine, but indicates that some parameter is beginning to drift and needs retuning. Action can be taken to correct this condition without reducing the output intensity or repetition rate of the machine.

Sets of sextupoles and octupoles have been installed in the synchrotron ring to control the focusing of particles with large momentum deviation and with large betatron amplitude. All attempts to excite these multipole elements at different times in the trapping and acceleration cycle have resulted in increased beam losses It would appear that in such high intensity machines there is a need to be as linear as possible and to avoid large orbit perturbations that produce a super period one condition.

Target Development.

The increased intensity and beam availability have increased the irradiation of the spallation targets. Neutron production has totalled 1.33 mg, but seven uranium targets have already been used and one tantalum target is currently operating, see figure 10. The lifetime of a uranium target is shorter than predicted, despite a large reduction in beam trips coupled with the ability to switch on the current gradually after a trip. The most probable cause of failure was considered to be the thermal fatigue/stress corrosion cracking induced by such beam trips. From measurements on the cooling of the targets[4] it appears that the tantalum target is following a similar pattern to the uranium and is also deteriorating and approaching the end of its useful life albeit after a considerably longer irradiation in excess of 1 mAh. Reasons for the failure of targets are under investigation and developments of the uranium target, such as smaller crystal size and alloying with molybdenum are to be tried as a possible ways of extending their useful life.

Acknowledgements.

The work reported here represents the successful culmination of several years of intense effort by all the staff of the ISIS facility.

References.

1. N D West, *Rutherford Appleton Laboratory.*
   Performance of the 70 MeV Injector to the ISIS Synchrotron.
   proceedings, 12th ICANS Workshop Abingdon UK May 1993.
2. P J S B Barratt, *Rutherford Appleton Laboratory.*
   The ISIS Synchrotron RF System at High Intensity.
   proceedings, 12th ICANS Workshop Abingdon UK May 1993.
3. G H Rees and H Zhang, *Rutherford Appleton Laboratory.*
   Maximum Space Charge Tune Shifts at ISIS.
   Internal report, Nov. 1992.
4. G Allen, T Broome, M Clarke Gayther, and C Planner, *Rutherford Appleton Laboratory.*
   Measurement of Cooling Characteristics of the ISIS Tantalum Target.
   proceedings, 12th ICANS Workshop Abingdon UK May 1993.

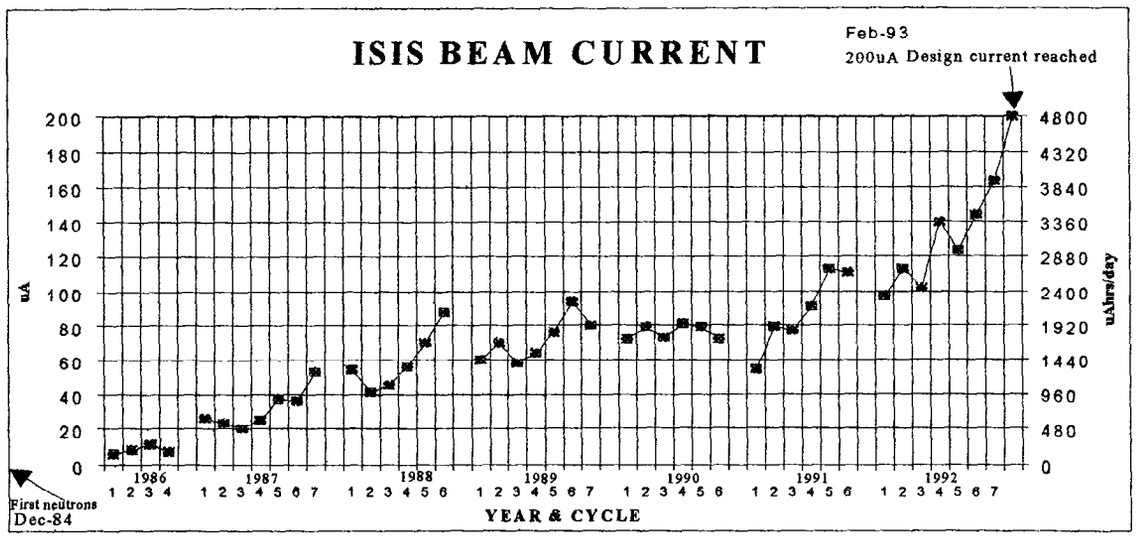

Figure 1. Increase in ISIS proton beam current.

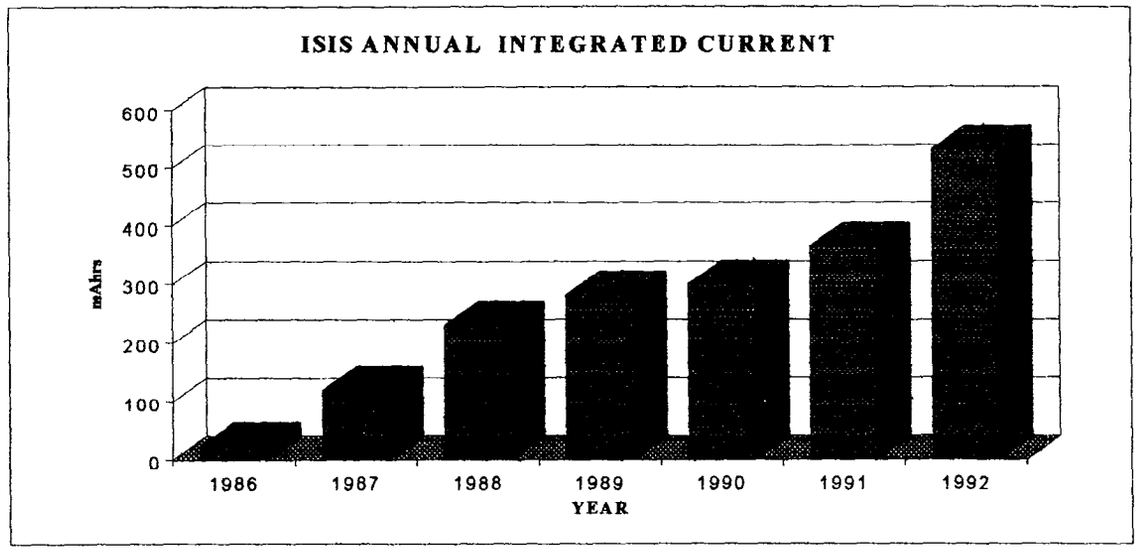

Figure 2. ISIS integrated proton irradiation

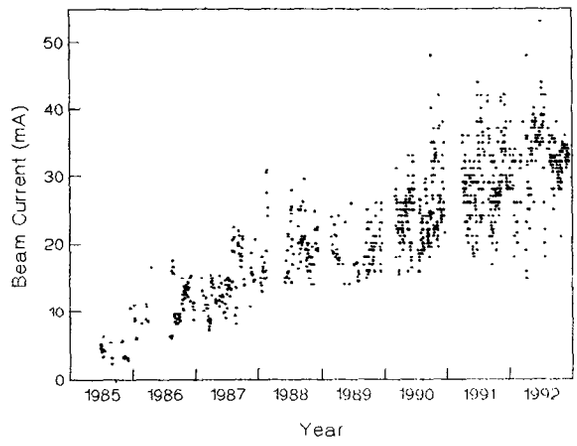

Figure 3. Development of output beam current for operational ISIS ion sources..

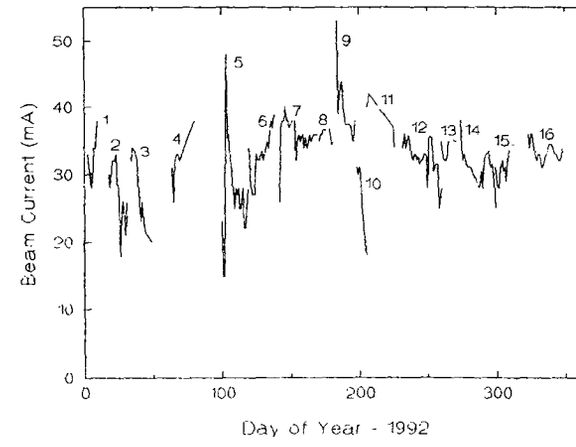

Figure 4 Beam current performance of ISIS operational ion sources.

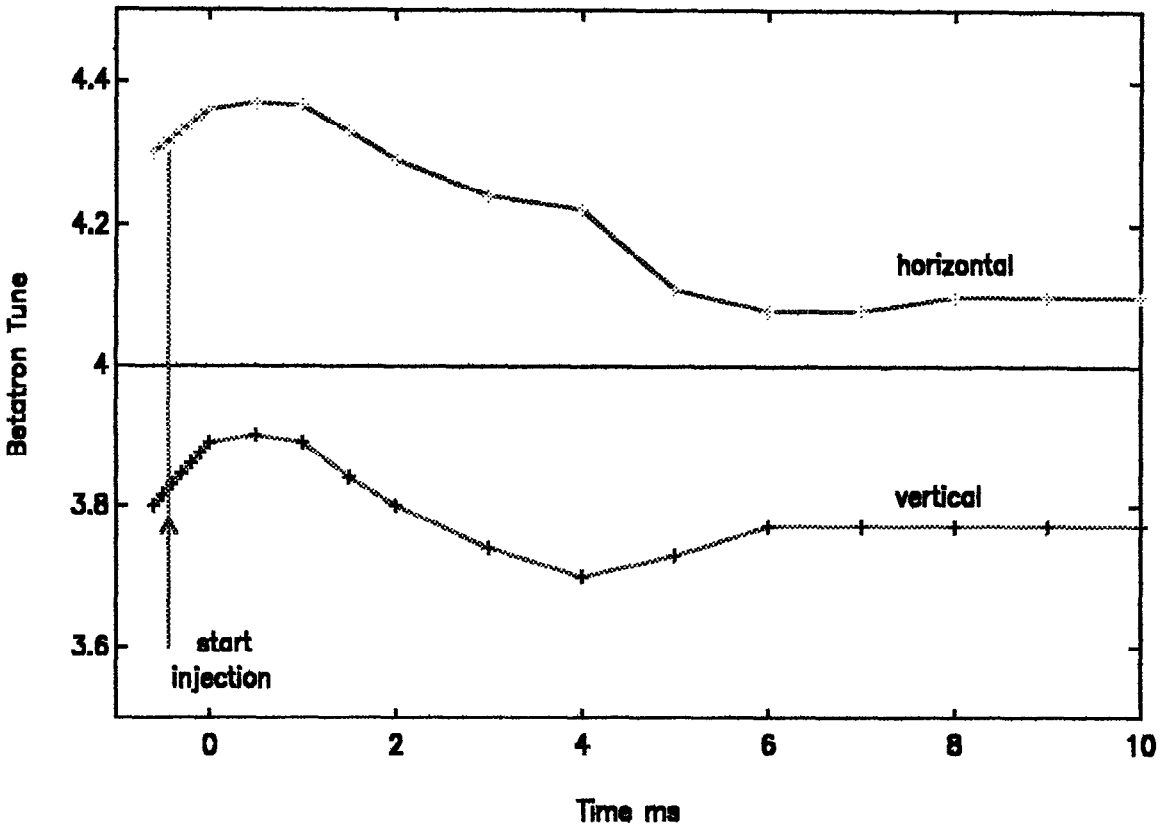

Figure 5. ISIS Betatron Tunes for high intensity operation.

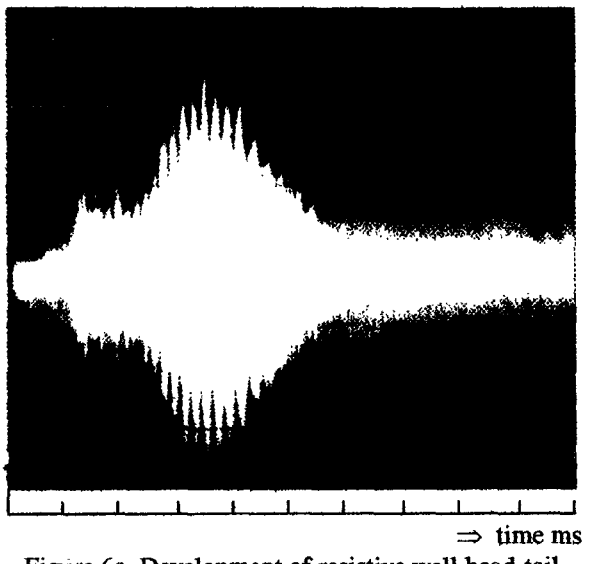

Figure 6a. Development of resistive wall head-tail instability.

Figure 6b. Resistive wall head-tail mode m=1.

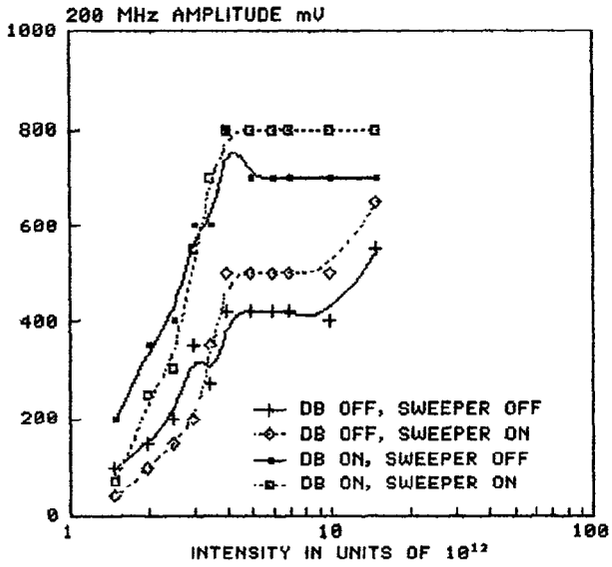

Figure 7. Growth of 200 MHz signal with increasing intensity

Loss at	Immediate Trip $\times 10^{12}$	Averaging Trip $\times 10^{12}$	Seconds Warning $\times 10^{12}$	Minutes Warning $\times 10^{12}$
Injection	4.9	1.1	0.80	0.6
Trapping	4.9	4.0	3.30	3.1
Acceleration	2.0	0.5	0.25	0.2
Extraction	1.0	0.5	0.20	0.1
Extraction Beamline	1.0	0.6	0.50	0.4
Total Loss	4.9	4.8	4.20	4.1
Period	3 pulses	25 pulses	30 secs	20 mins

Figure 9 ISIS Beam Loss Tolerances

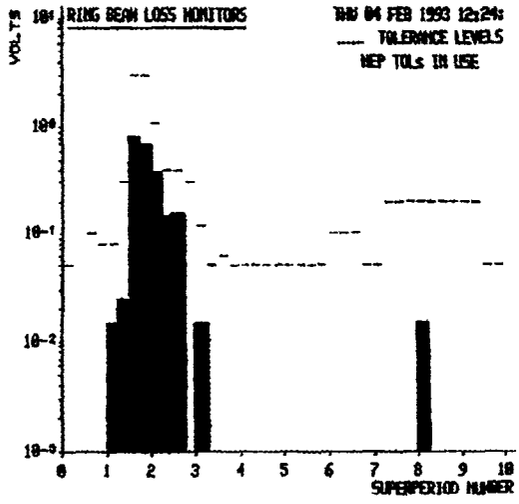

Figure 8a. Beam losses in ISIS synchrotron and tolerance levels.

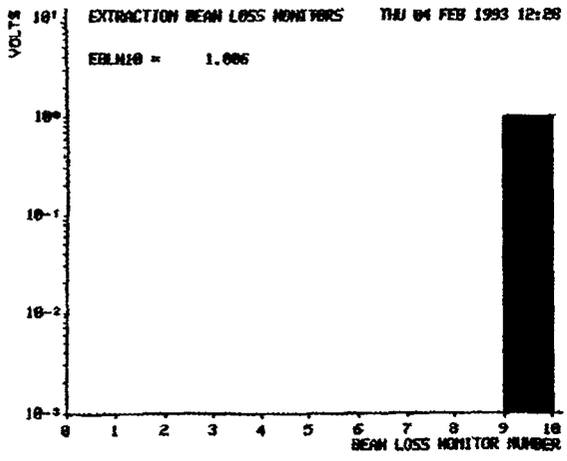

Figure 8b. Beam losses in extraction beam line to muon transmission target

Target Material	Gross Thermal Cycles	Integrated Current mAh	Neutron Production mg
U#1	Not Measured	92.4	75
U#2	40000	53.1	52
U#3	10389	174.9	163
U#4	4147	138.8	128
U#5	5074	295.6	273
U#6	2628	126.1	116
U#7	1805	107.2	99
Ta#1	43164	905.7	424
	Total	1893.8	1330

Figure 10. ISIS Target Performance Summary to 31/1/93

Studies of Dual Harmonic Acceleration in ISIS

C R Prior

Rutherford Appleton Laboratory, Chilton, Didcot, Oxon

Studies have been made of the addition of a harmonic number, $h=4$, radio-frequency system to the existing $h=2$ system in ISIS. The design aim is an improvement in the beam bunching factor for the acceleration of more intense beams. Use has been made of a longitudinal space-charge tracking code to define a set of parameters for the acceleration of 3×10^{13} protons per pulse, 240μA average. This corresponds to an increase of 20% in the maximum intensity achieved to date. Further studies indicate that it may in fact be possible to accelerate 3.7×10^{13} protons per pulse, 295μA, by these means.

Equations of Particle Motion

The motion of particles in a synchrotron is normally studied through the equations

$$\frac{d}{dt}\frac{\Delta E}{\omega_0}=\frac{e}{2\pi}\,[V(\phi)-V(\phi_s)+V_{sc}(\phi)] \tag{1}$$

$$\frac{d}{dt}\Delta\phi=\frac{h\omega_0\eta}{\beta^2E_s}\,\Delta E \tag{2}$$

where $\Delta E=E-E_s$; $\eta=1/\gamma_t^2-1/\gamma^2$; E and ϕ are the energy and phase of the particle; $V(\phi)$ is the accelerating waveform; and h is the harmonic number. The suffix s refers to the synchronous particle and, since the equations govern only the first-order variations from synchronous values, the revolution frequency ω_0 is the value for the synchronous particle to a first approximation. V_{sc} represents the space-charge forces generated within the beam and is given by

$$V_{sc}(\phi)=-e\,\frac{d\lambda(\phi)}{d\phi}\,[\frac{Rg_0}{2\varepsilon_0\gamma^2}-L\beta^2c^2] \tag{3}$$

where λ is the line density of particles, L is the total inductance per turn of the reactive wall, R the radius of the machine, and, for a beam with circular cross-section of mean radius a in a circular pipe of radius b, $g_0=1+2\ln(b/a)$.

Applied Voltage

When the applied voltage is sinusoidal, $V(\phi)=\hat{V}\sin\phi$, the behaviour of the particle beam, either in the absence of space-charge or in the case of simple particle distributions, is well known.[1,2] Here we wish to study the effect of introducing an additional acceleration component of harmonic number $2h$, giving a combined voltage which may be written in the form[3]

$$V(\phi)=\hat{V}(t)[\sin(\phi)-\delta\sin(2\phi+\theta)] \tag{4}$$

The problem is to find a continuous sequence of parameters, δ and θ, to find a stable system optimised in the sense of being able to contain intense beams with good bunching factor and low loss.

By balancing the energy gain to the effect of the guide magnetic field, we can find the synchronous phase through the equation

$$2\pi R\rho\dot{B}=\hat{V}[\sin\phi_s-\delta\sin(2\phi_s+\theta)]. \tag{5}$$

where ρ is the mean bending radius. For convenience, we shall denote by A the acceleration term $2\pi R\rho\dot{B}/\hat{V}$. When $\delta=0$, assuming $A<1$, there are two solutions of equation (4) in the range $[-\pi,\pi]$. One, $\sin^{-1}A$, defines the phase of the synchronous particle and the other, $\pi-\sin^{-1}A$, gives the maximum limit of stability. An example of the voltage shape when $\delta\neq0$ is shown in Figure 1, which is drawn for

$\delta = 0.58$ and $\theta = -60°$. This suggests that, for a limited range of values of A, it may be possible for four solutions to exist.

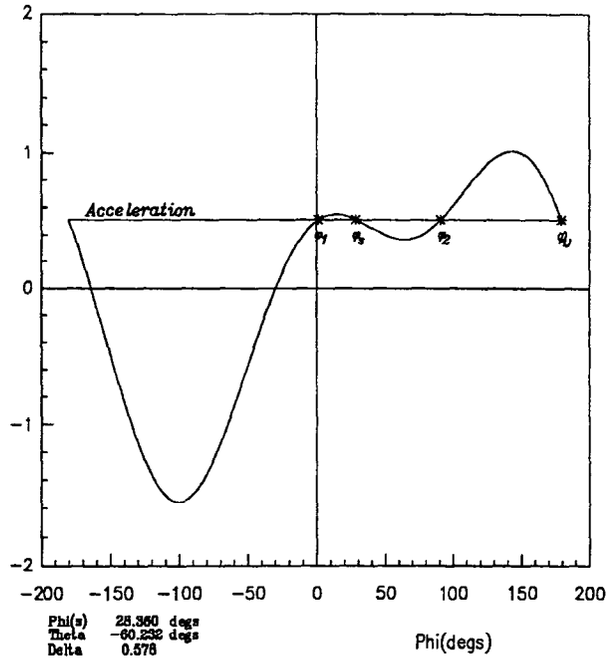

Figure 1. Shape of the Dual Harmonic Voltage Function

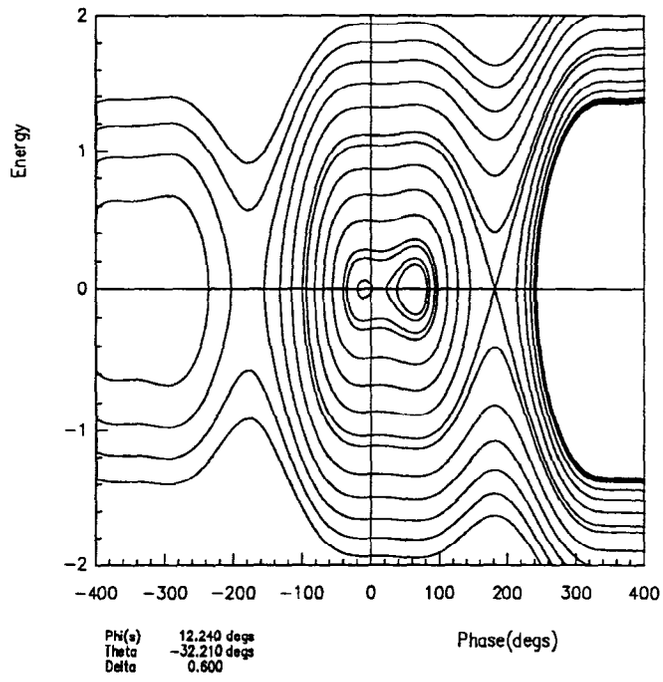

Figure 2. Phase-space Trajectories

The nature of these solutions may be found by looking at the the phase-space trajectories of particles, given by constant values of the Hamiltonian. Ignoring space-charge,

$$H = \frac{h\eta}{2\beta^2 E_s}(\Delta E)^2 - \frac{e}{2\pi}U(\phi) \tag{6}$$

where

$$U(\phi) = \int_{\phi_s}^{\phi} [V(\phi') - V(\phi_s)]d\phi'$$

$$= -\hat{V}[\cos\phi - \cos\phi_s - \tfrac{1}{2}\delta\{\cos(2\phi + \theta) - \cos(2\phi_s + \theta)\} + A(\phi - \phi_s)]$$

A typical plot, such as that shown in Figure 2, reveals that two of the points, ϕ_1 and ϕ_2, define stable synchronous particles. The solution ϕ_v defines the extreme unstable fixed point and the fourth represents a locally unstable fixed point near the centre of the stable region. It is this fourth solution that we take as ϕ_s.

Equation (5) is equivalent to the condition $dU/d\phi = 0$ and comparison of graphs of $U(\phi)$ for $\delta = 0$ and $\delta > 0$ (Figure 3) make clear that the introduction of the extra minimum leads to an extended region of ϕ over which stable oscillations are possible.

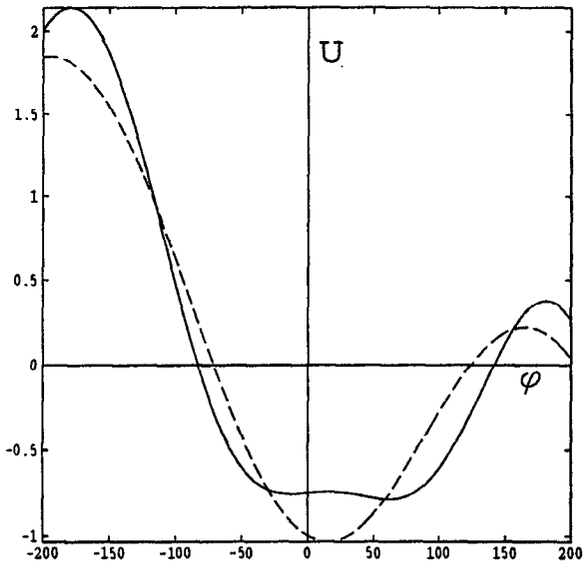

Figure 3. Potential Energy for $\delta > 0$ (continuous curve) and $\delta = 0$ (dashed curve).

Bunching factor, which is important since it is directly proportional to the maximum amount of beam that can be contained by the system, is also enhanced. Analytically this may be demonstrated by looking at the Hofmann-Pedersen particle distribution[2], which is a self-consistent model in which the space charge-forces have the same form as the applied voltages. For such a beam, the line density may be written

$$\lambda(\phi) = N_b \frac{U(\phi_v) - U(\phi)}{u_L}$$

where N_b is the number of particles in the bunch and

$$u_L = \int_{\phi_u}^{\phi_v} [U(\phi_v) - U(\phi)]d\phi$$

The bunching factor is then $N_b/2\pi\lambda(\hat{\phi})$, with $\hat{\phi}$ the value of ϕ corresponding to the peak value of λ (either ϕ_1 or ϕ_2). Defining

$$f(\phi_u, \phi_v) = \sin\phi_v - \sin\phi_u - \tfrac{1}{2}(\phi_v - \phi_u)(\cos\phi_v + \cos\phi_u)$$

this can be written most simply as

$$B_f = \frac{1}{2\pi} \frac{f(\phi_u, \phi_v) - \tfrac{1}{4}\delta f(2\phi_u + \theta, 2\phi_v + \theta)}{U(\hat{\phi}) - U(\phi_v)}. \tag{7}$$

These equations may be solved numerically and show that a non-zero δ can produce a bunching factor increased by as much as 50%. For example, when $\delta = 0$, $\phi_s = 28°$, $B_f = 0.29$, but with $\delta = 0.58$, $\phi_s = 28°$ and $\theta = -60°$, $B_f = 0.43$, an increase of 49.1%.

As a rough guide to the values of θ to use, we may note that $\theta = -2\phi_s$ will leave the synchronous phase unaltered when the additional voltage terms are introduced, but a more detailed analysis is needed to find the best scheme for the complete bunching process in a synchrotron. The quantity A for example depends critically on the ratio $\dot{B}/\hat{V}$ and, if the cavity voltages are not high enough to keep A less than about 0.7 it turns out that it is not possible to find a combination of θ and δ to give four solutions of (5). In addition, even when there are four solutions, the stable region can collapse at ϕ_s and degenerate into two separate, small, regions centred on ϕ_1 and ϕ_2. To investigate these effects in detail requires numerical analysis of equations (5) and (6). This reveals that for values of $A \leq 0.5$ most values of $\delta \leq 0.6$ and $\theta \leq 0.0$ give enhanced stable regions of phase-space, but as soon as A increases above 0.5, the range of acceptable δ and θ diminishes, and above 0.65 only a very limited range of δ and θ will work. The conclusion is that a suitable dual harmonic system can only be devised if the design voltages of the cavities are high enough to prevent A becoming too large, thereby allowing a complete set of continuous δ- and θ-values for the whole cycle. Given this, the condition for non-degeneracy of the stable region is

$$\eta U(\phi_v) > 0$$

where ϕ_v is the maximum phase excursion. For continuity under acceleration as A increases from zero (starting at time $t = 0$), we require

$$\phi_s = 0 \quad \theta = 0 \quad \delta = 0.5 \quad \text{at } t = 0. \tag{8}$$

The three roots ϕ_1, ϕ_s, ϕ_2 then coincide at the start of acceleration and immediately start to separate. For maximum area of the stable region, it is also found that θ, while always negative, should have as small an absolute value as possible.

Simulation Model for ISIS

The behaviour of the beam in ISIS from the start of injection through trapping and acceleration to an energy of $800MeV$, a timespan of just over 10msec, has been modelled by means of a one-dimensional tracking code based on the equations of motion (1) and (2). The injected beam has been assumed to be uniformly spread in phase from $-\pi$ to π and to have parabolic momentum spread corresponding to $\Delta p/p = \pm 2 \times 10^{-3}$. The simulation uses less than 20,000 particles in total but avoids the problem of having only a few unrepresentative particles for each injected turn by allowing particles to carry different charges and superimposing incoming beam onto existing beam by a weighted method of charge allocation onto an imaginary grid. Space charge is calculated from the line density according to equation (3) after a measure of smoothing has been carried out to remove statistical effects. Other parameters used in the model are

$$h = 2 \quad R = 26\text{m} \quad \rho = 7\text{m} \quad \gamma_t = 5.05 \quad g_0 = 1.75$$

$$B(t) = B_0 - B_1 \cos(2\pi f t) \tag{9}$$

where

$$B_0 = 0.4369T \quad B_1 = 0.2604T \quad f = 50Hz.$$

The first simulation runs were made with a beam of 2×10^{13} protons per pulse and a simple sinusoidal voltage ($\delta = 0$). These were used to determine the optimum voltage profile for $\hat{V}$ and also determine the point in the process at which the voltage should be switched on, so as to balance the requirements of low loss and small momentum spread. The result was a voltage profile looking broadly like that shown in Figure 4 but scaled to a peak of $140kV$. Loss was predicted to be under 5%, all occurring in the first 1.5msec of the cycle, and was found to be minimised by switching on the r.f. cavities as early in the process as possible. Maximum momentum spread was less that 7.7×10^{-3}.

For the dual harmonic model, the definition of A, equations (5) and (9) give the restriction

$$A_{\max}\hat{V}_{\max} \geq 2\pi R\rho\dot{B}\,|_{\max} = 93.54\ kV \tag{10}$$

If the maximum cavity voltage is $140kV$, A will exceed 0.67 and at this level it is at best extremely difficult to design a stable system. The full design capacity of the cavities must therefore be used and the voltage profile re-scaled to a peak of $160kV$ ($A \leq 0.6$) as shown in Figure 4 and the first two columns of Table 1.

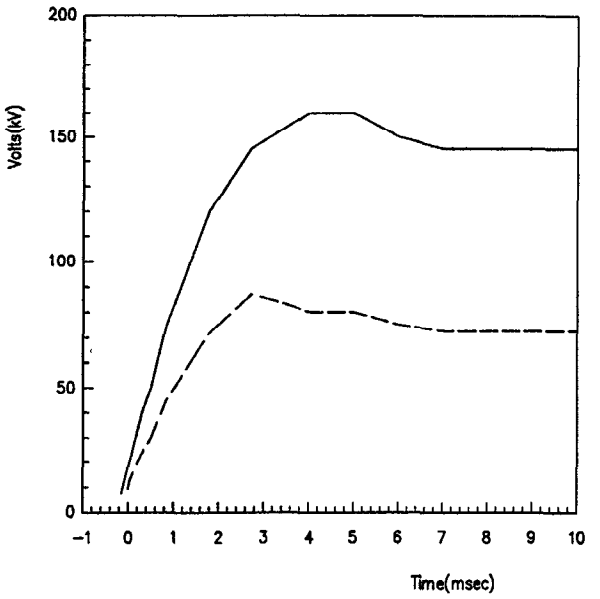

Figure 4. Cavity Voltages for ISIS Simulation Model
(The solid curve represents $\hat{V}(t)$; the dashed curve shows the second harmonic voltage $\delta\hat{V}$.)

A suitable set of values of θ and δ corresponding to the voltages can then be generated numerically. A fully optimised system (based on maximising the bunching factor) would not be practical since the parameters vary too rapidly and too widely to make economic sense, but we can follow the method used to control the cavity voltages. In ISIS these are prescribed as a set of values at fixed times between which the controlling computer carries out linear interpolation in the form of very small step functions. Similar schemes have been produced for δ and θ, keeping to the voltage data times where possible, and these are shown in Figures 5 and 6, with specific values laid out in Table 1.

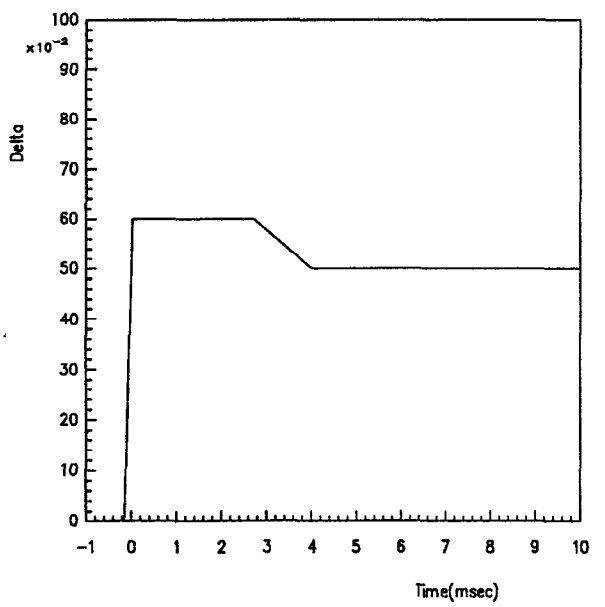

Figure 5. δ-ratio of Cavity Voltages.

With this model, δ is switched on at $t = -0.15$msec and rises through 0.5 at $t = 0.0$msec (equation (8)) to a maximum of 0.6. This peak value, determined by design and cost limitations, is maintained for just

under 3msec, but, because we also require that the $2h$-harmonic voltage does not exceed $80kV$, δ is brought down to 0.5 at 4msec and held at this level through to the end of the cycle. This maintains the extended bucket and allows the three fixed points ϕ_1, ϕ_2 and ϕ_s to coalesce smoothly to zero as $A \rightarrow 0$. Figure 6 also shows the limits between which θ has to lie for solutions to be possible with this choice of δ, and shows how the values have been chosen close to the upper limit to maximise the stable phase-space region. Note the severity of the restrictions for $t > 7.5$msec. Additional considerations are that the bunch at $800MeV$ should have approximately the same length as in the single harmonic model, and that the maximum momentum spread should not exceed previous values.

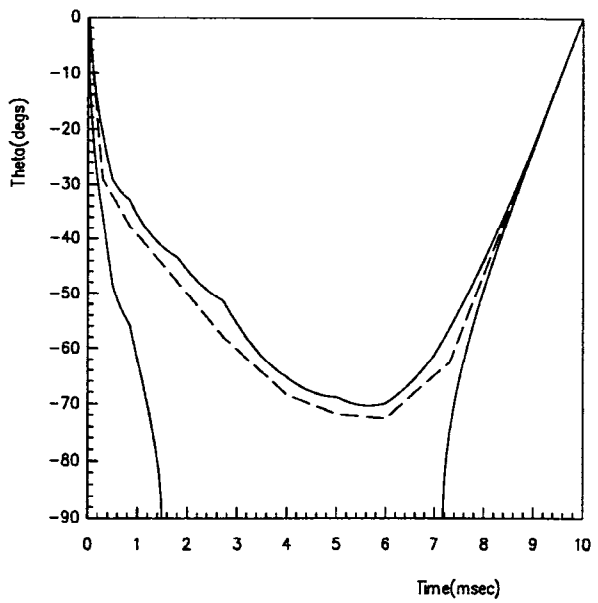

Figure 6. θ-values for ISIS
(The solid curves give the upper and lower limits of θ. The dashed curve shows the values used by the model for ISIS.)

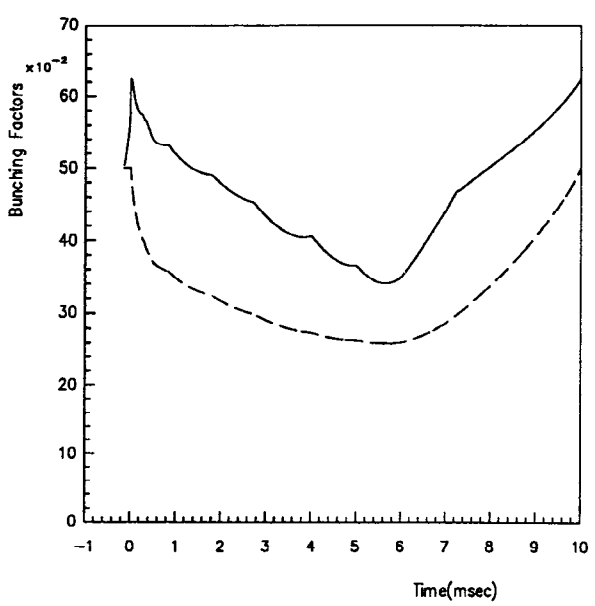

Figure 7. Bunching factors based on a Hofmann-Pedersen Distribution
($\delta \neq 0$: continuous curve; $\delta = 0$: dashed curve)

Bunching factors for this system, based on equation (7), are shown in Figure 7, with a superimposed dashed curve representing values when $\delta = 0$. Throughout the acceleration, the increase is well above 30% and between 0.5msec and 1.5msec is above 45%. In particular, at 1msec, which is the time in ISIS at which space-charge limiting effects are most critical, the bunching factor is increased by 49%. This suggests that it may in fact be possible to accelerate as many as 3.7×10^{13} protons per pulse using the dual harmonic system.

The main simulation runs, however, have been carried out for a beam of 3×10^{13} protons per pulse, 240μA average current. This compares with 200μA currently running in the machine. A selection of plots of phase-space is shown in Figure 9, with the superimposed limiting stable region calculated from the Hamiltonian via equation (6). Different colours are used to show the density of charge of the particles, ranging from red at high density through to blue at low density. From top left to bottom right, the plots show the initial formation of a single central core, just after injection but before acceleration and before the dual harmonic waveform is switched on. This develops into two centres as the particles start to orbit around the stable points, ϕ_1 and ϕ_2. Beam begins to spiral out and there is some loss (third and fourth pictures) but the 'arms' are largely confined by the separatrix as the bucket contracts. At 6msec, the bucket is expanding again, and as the acceleration slows, as 800MeV is approached, ϕ_1, ϕ_2 and ϕ_s coalesce and the bunch develops a fairly uniform line density stretching from −65° to 70° (or 120nsec in length). Total loss for the run was calculated to be as low as 3.5% but, whereas for the single harmonic, it was confined to the first 1.5msec, the simulation indicates that for the dual harmonic model, it may continue as far as 6msec into the cycle. One reason for this, as comparison of Figure 8 with Figure 5 suggests, is the reduction in δ from 0.6 to 0.5 between 3 and 4msec. It may however be possible to avoid the later loss by modifying the voltage profile slightly at earlier times. Such a modification should also reduce the maximum momentum spread, which although generally within 8.5×10^{-3} does briefly get as high as 1×10^{-2} and is larger than we would ideally like.

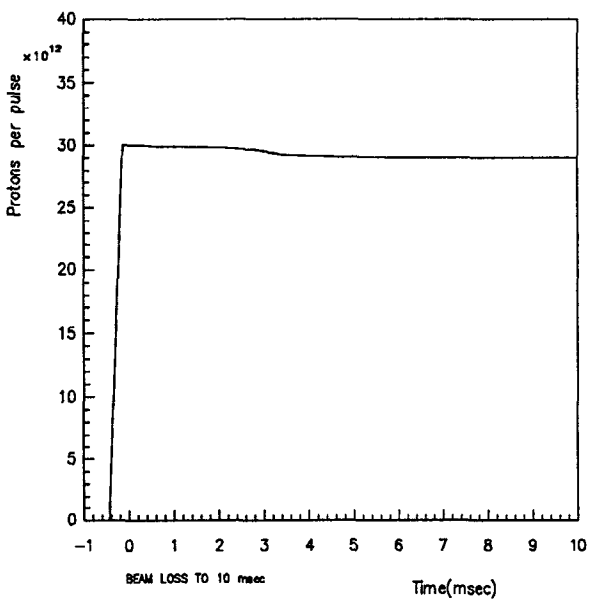

Figure 8. Simulated beam loss for the ISIS model

Initial runs have more recently been carried out for the simulation of 3.7×10^{13} protons per pulse. The results have been very encouraging. Loss is slightly greater and again takes place up to 6msec, but is still under 4%. Bunch length at extraction is about 130nsec and maximum momentum spread 8.8×10^{-3}. These predictions could also probably be improved by slight changes to the cavity voltages early in the cycle.

Conclusions

The study suggests that, by enhancing the bunching factor at critical times and increasing the stable regions of phase-space, use of the dual harmonic waveform should allow more intense beams to be accelerated in synchrotrons. For ISIS the design parameters produced here are within the specifications

of the r.f. cavities and it is hoped that some initial experiments may be carried out before the middle of 1994.

Time (msec)	*Peak voltage (kV)*	δ	θ *(degs)*	ϕ_s *(degs)*
-0.44	0.0	0.0	0.0	0.0
-0.35	3.0	0.0	0.0	0.0
-0.2	6.0	0.0	0.0	0.0
-0.15	7.5	0.0	0.0	0.0
0.0	18.3	0.5	0.0	0.0
0.03	20.5	0.6	-2.9	-5.0
0.3	40.0	0.6	-29.0	21.9
0.5	50.0	0.6	-32.2	12.2
0.84	75.0	0.6	-37.6	17.6
1.8	120.0	0.6	-48.0	21.6
2.72	145.0	0.6	-57.9	27.9
4.0	160.0	0.5	-68.4	36.0
5.0	160.0	0.5	-71.9	36.5
6.0	150.0	0.5	-72.6	35.6
7.0	145.0	0.5	-64.9	37.5
10.0	145.0	0.5	0.0	0.0

Table 1. ISIS Voltage Parameters

References

1. B W Montague: *Single Particle Dynamics - RF Acceleration* in Preceedings of CERN International School of Particle Accelerators, Erice, 1976.

2. A Hofmann and F Pedersen: *Bunches with Local Elliptic Energy Distributions*, IEEE Trans. Nucl. Sci, Vol. NS-26, No. 3, 1979.

3. G H Rees and J V Trotman: *Acceleration with combined use of R.F. Harmonic Numbers h and 2h*, RAL internal report SCS/MACHINE/10, 1970.

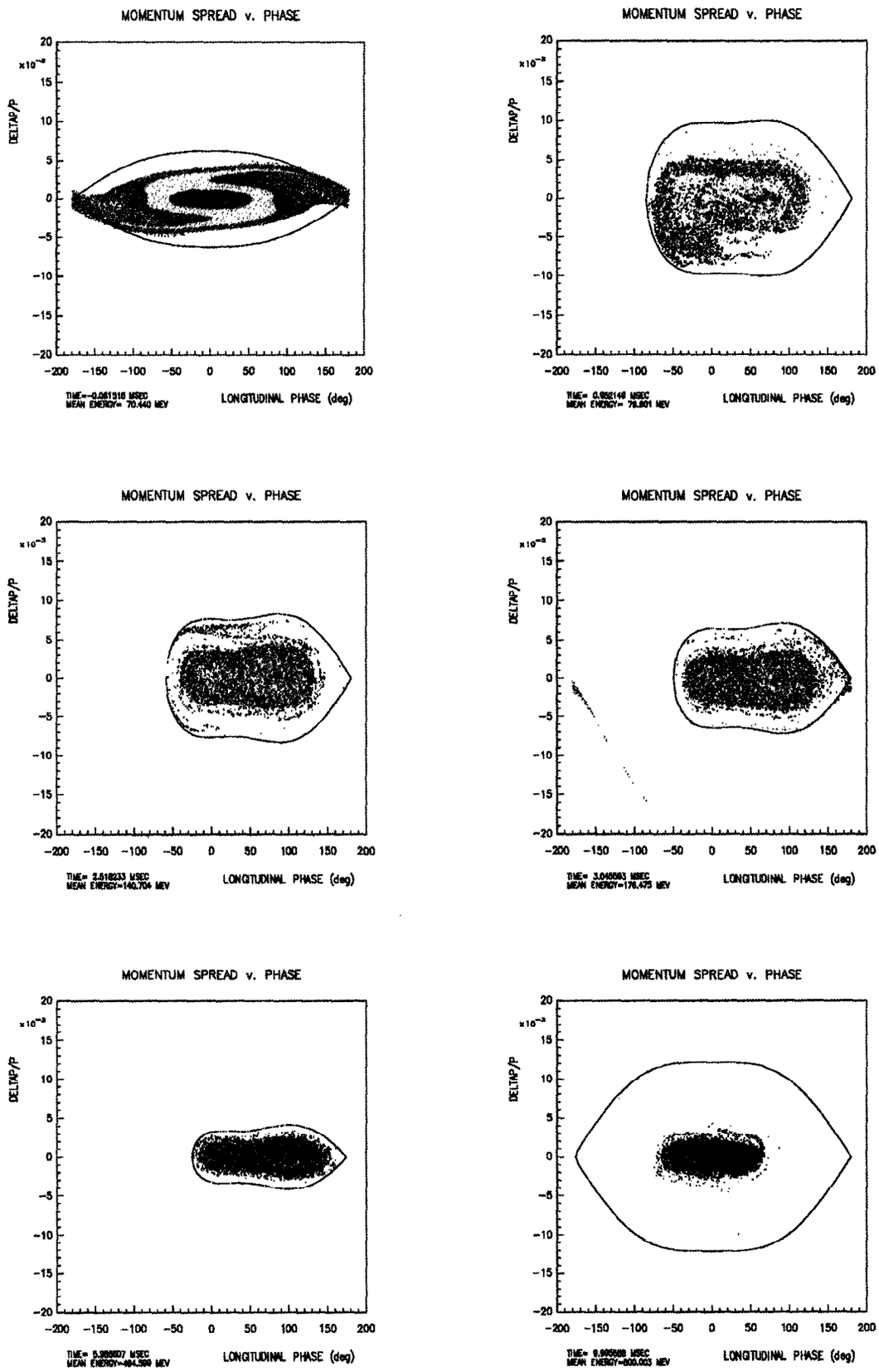

Figure 9. Phase-space plots for the injection and acceleration to 800*MeV* of a beam of 3×10^{13} protons per pulse in ISIS.

Preliminary Report on the BNL Spallation Neutron Source Design Study.*

L.N. Blumberg, for the BNL SNS Study Group
Brookhaven National Laboratory
Upton, NY 11973 USA

Abstract

A preliminary study of a 5-MW pulsed neutron source is presented based on a 600 MeV H^- linac injector and 2 fast-cycling synchrotrons, each of 3.6-GeV final proton energy and 30 Hz rep rate.

We have considered several options for an intense pulsed spallation neutron source (PSNS) based on an intermediate current H^- Linac and fast-cycling proton synchrotron (FCS) with design objectives of 5-MW beam power, pulse duration $\sim$ 1 μs, and 60 Hz total pulse repetition rate. A tentative architecture which satisfies these goals is schematically illustrated in Fig. 1, where we show a 600-MeV, 60 Hz, H^- Linac injecting into two identical FCS rings, each operating at 30Hz and independently powered 180° out of phase. The ring circumference of C $\simeq$ 363 m results in a pulse duration of $\tau \simeq 1.3$ μs from single turn extraction. A final energy of 3.6 - GeV is chosen so that the number of protons accelerated per ring can be reduced to $N_p = 1.4 \times 10^{14}$ protons/pulse, consistent with the bunched beam (B $\simeq$.3) Laslett space charge limit for a beam of emittance $\epsilon=200\pi$ mm - mrad and a space charge tune shift of $|\Delta\nu| = 0.21$. The extracted pulses from the rings are coalesced into a single external channel and then fast-switched onto two independent target stations T1 and T2 at a rate $R_1 + R_2 = 60$Hz; for example $R_1=10$Hz, $R_2=50$Hz.

The parameters of the Linac are summarized in Table I. The H^- ion source parameters are consistent with the present BNL source with peak pulse current of 80 mA and pulse duration $\tau_s=464$ μs; however, further work is required to attain 60 Hz operation. Two RFQ's are operated in tandem to obtain an injection energy of E = 2 - MeV into an 88-MeV drift-tube Linac (DTL) and a 510-MeV side coupled Linac (CCL) to obtain a final Linac energy of 600-MeV. The RF frequency of the CCL, 1280 -Mhz, is the 32nd harmonic of RFQ1 and the injection frequency of the ring, 40 -MHz. The Linac configuration is similar to that of the SSC although our duty factor of 2.8% is larger.

*Work performed under the auspices of the U.S. Dept. of Energy, Contract DE-AC02-76CH00016.

Table I. **Linac Parameters**

Final Kinetic Energy	600	MeV
Repetition Rate	60	Hz
Linac Beam Pulse	463.6	μs
Duty Cycle	2.8	%
Peak Current, in output	50	mA
Peak Power, to Beam	30	MW
Total Peak Power	60	MW
Beam Emittance	~ 1	π mm mrad
Δp/p of Beam (full)	~ 1×10^{-4}	

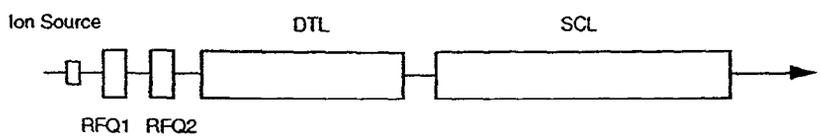

Ion Source (H-)	0.035	MeV	
RFQ1	0.2	MeV	40 MHz
RFQ2	2.0	MeV	160 MHz
DTL	90	MeV	320 MHz
SCL	600	MeV	1280 MHz
Synchrotron	3.6	GeV	40 - 50 MHz

The synchrotron ring is shown in Fig. 2 - a 2-superperiod FODO lattice with non zero dispersion straights for injection and near zero dispersion straights for sixteen 2-gap RF cavities. A ceramic vacuum chamber is planned for the ring with either a metallized interior surface or a metallic grid mesh similar to the ISIS design. The average circulating beam current at full energy is $\langle I \rangle = 19A$, lower than that attained in earlier proton storage rings such as the ISR. The final RF frequency of ~50 MHz is approximately that of the FERMILAB main ring.

We have also done preliminary studies at 1-GeV of a target configuration capable of sustaining the 5-MW beam power. As shown in Table II, a target consisting of either hexagonal rods or a particle bed of tungsten pebbles has been considered; an array of beds varying in thickness from 1cm to 5cm stacked axially in the beam direction provides the best heat transfer due to the more favorable area/volume ratio. Coolants studied were sodium, lead, helium and heavy water. Liquid sodium would provide the most attractive option in terms of lower pressure drop than liquid lead for axial flow.

Table II. Target Operating Conditions

• Power	5 MW
• Coolant Outlet Temperature	~800 - 900K
• Coolant Inlet Temperature	300K or Metal T_{mp}
• Proton Energy	1 GeV
• Rod Target:	
Rod OD (cm)	0.5
Rod Pitch (cm)	0.53
Solid Fraction of Target	~80%
Target Length (cm)	37.5
• Particle Bed Target:	
Particle OD (cm)	0.5
Solid Fraction of Target	~64%
Target Length (cm)	47

Rod Target

Coolant	ΔT (C)	ΔP (MPa)
Helium	500	1.17
Sodium	400	0.23
Lead	300	5.24

Co-axial Particle Bed Target

Coolant	ΔT (C)	ΔP (MPa)
Helium	-	-
Sodium	400	0.02
Lead	300	0.27

Initial neutronics calculations using the LAHET Monte-Carlo code have also been performed to compare neutron flux at higher energies to that expected at E_p = 1-GeV. In Fig. 3 we show the resulting integrated neutron flux (E_n<20-MeV) per incident proton at the surface of a 20-cm diameter tungsten rod for an incident 1 cm^2 beam of 1-GeV and 10-GeV protons, as a function of axial position along a 50-cm cylinder. Although the predicted flux per incident 10-GeV proton is less than 10 times that of an incident 1-GeV proton at the upstream end of the target, the higher energy proton gives more than 10 times of the 1-GeV flux at axial positions greater than Z=14-cm, and the axially integrated neutron flux is also greater than 10 times the 1-GeV flux. In Fig. 4 we show the radial integrated neutron flux per incident proton within a light water moderator at an axial position of Z=10 cm. The 10-GeV flux is comparable to 10 times the 1-GeV values at all radii. Comparable results at 3.6 - GeV are not yet available.

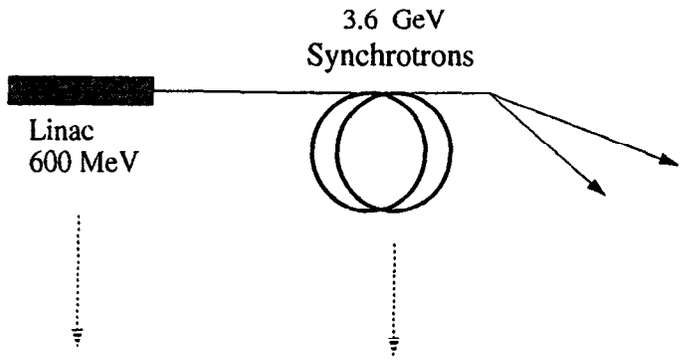

Rep. Rate = 60 Hz	Rep. Rate = 30 Hz
Duty Cycle = 2.8 %	Circumference = 363.2 m
Source Current = 80 mA	Beam Power = 2.5 MWatt / ring
Aver. Power < 2 MWatt	Pulse Duration = 1.3 μs
	Intensity = 1.4×10^{14} pr.s /ring/pulse
	No. of Turns injected = 303 / ring
	Emittance @ Injec. = 200 π mm mrad
	rf Frequency = 40 - 50 MHz

Fig.1 Schematic layout of pulsed spallation neutron source, parameters.

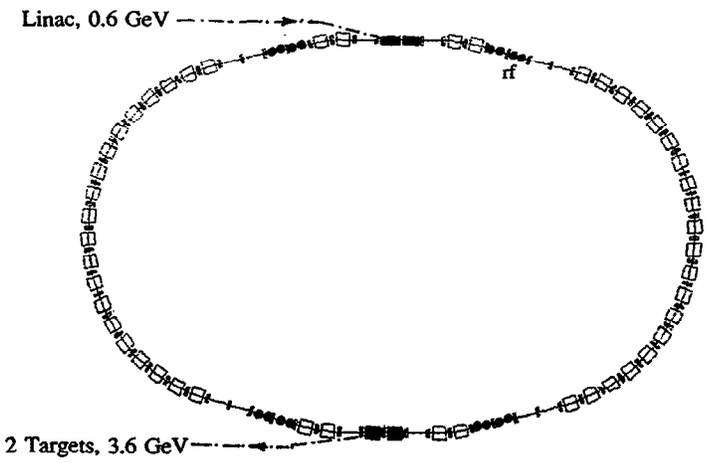

5 MW system
Linac plus 2 equal Fast Cycling Synchrotrons (FCS's)

Linac	Energy	(GeV)	0.6
	Current	(mA)	50
	Rep.Rate	((Hz)	60
	Np/pulse		1.4E14
FCS's	Energy	(GeV)	3.6
	Circ.current	(A)	19
	Rep.Rate	(Hz)	30
	Np/sec	(1/s)	2*4.2E15
	Circumference	(m)	363.2

Fig.2 Lattice and parameters of spallation source ring.

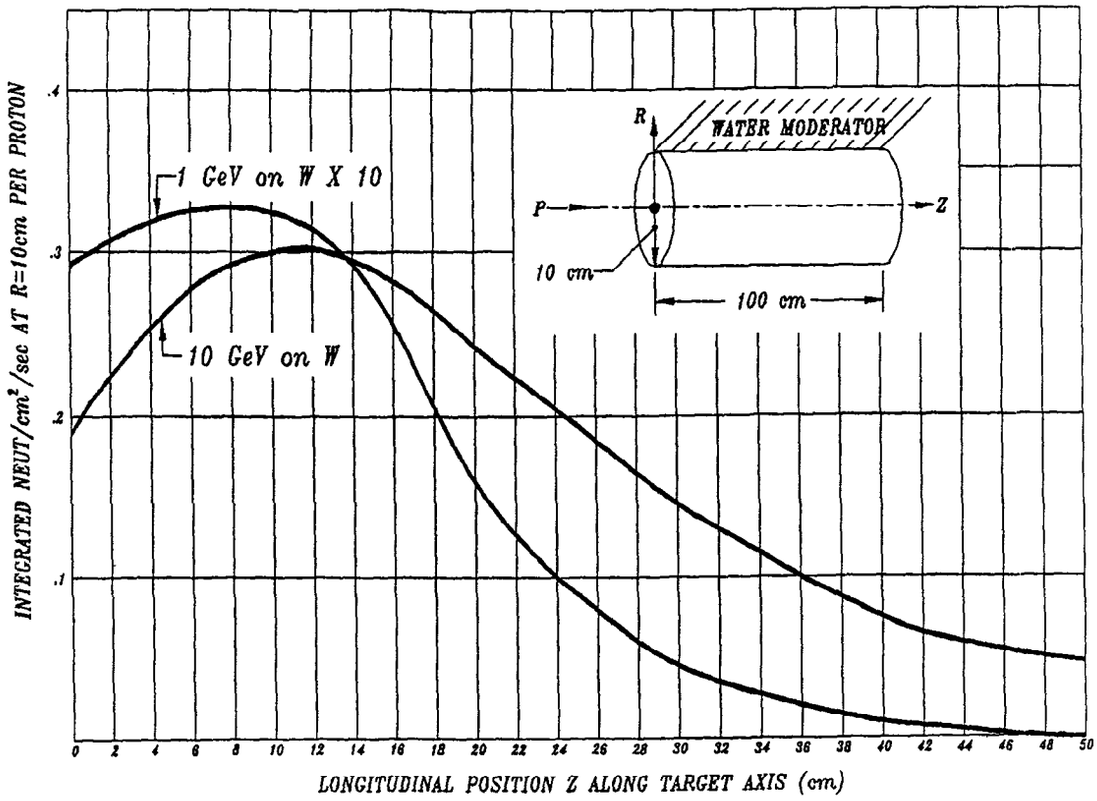

Fig.3 Integrated ($E_n < 20$ MeV) Neutron Flux at surface of 20 cm dia. tungsten target

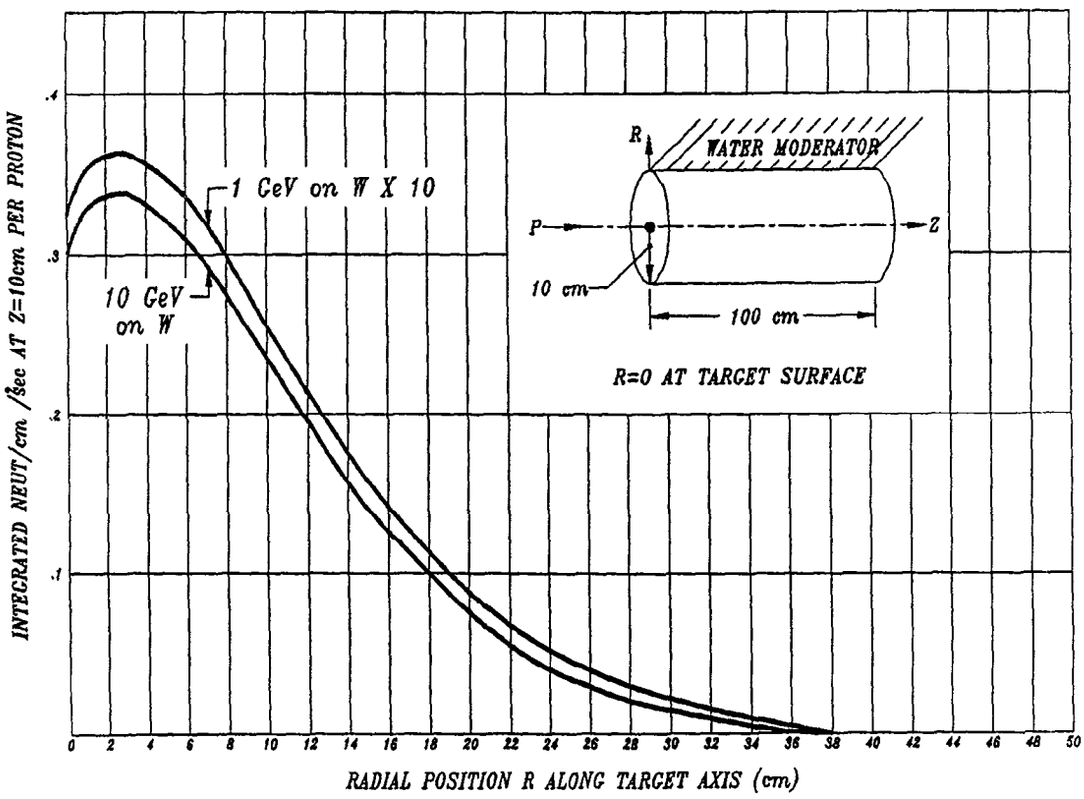

Fig.4 Integrated ($E_n < 20$ MeV) neutron flux vs. radial distance from tungsten target surface at Z = 10 cm.

Machine Studies at the Los Alamos Proton Storage Ring*

R. J. Macek and the extended PSR Development Team**
Los Alamos National Laboratory
Los Alamos NM, 87545

Abstract

Results from recent machine development studies at the Los Alamos Proton Storage Ring (PSR) are presented on the origin of the "first-turn" losses, the PSR instability, and volume H^- ion source development. An experiment has been performed to measure the production of excited states of H^0 when 800-MeV H^- ions impinge upon thin (70-300 μg/cm2) carbon foils. Preliminary results indicate yields of about 0.5% each for the n=3 and n=4 states. Much evidence has been accumulated supporting the hypothesis that the PSR instability is caused by coupled e-p oscillations, but a truly definitive and unambiguous test has not yet been performed. Plans for such a test include installation of hardware to suppress the most copious sources of electrons and experiments to measure the quantity of proton beam in the interbunch gap. Good progress is being made to test and evaluate two promising designs for a new high-intensity, high-brightness volume H^- ion source and on fast chopping of the beam by pulsing the plasma electrode.

Introduction

Machine studies and accelerator development efforts at PSR have in the past been focused on increasing the beam intensity, improving beam availability and correcting radiation protection deficiencies. However, during the past year with the prospect that LAMPF might be shut down after October of 1993, the emphasis shifted to studies of issues that are important to the design of a next generation spallation neutron source based on the linac and compressor ring concept. Therefore, the studies of first turn losses (now believed to be caused by the production of excited states of H^0 at the stripper foil[1,2,3] as first proposed by Richard Hutson) and the PSR transverse instability have assumed new urgency.

H^0 Excited States and First-Turn Losses

The losses of 0.2-0.3% on the first turn after injection have long been a puzzle but are now thought to be predominately caused by production of excited states of $H^0(n)$ (with principle quantum number, $n \geq 3$), which subsequently strip part way through the fringe field of the first dipole downstream of the stripper foil and fall outside the acceptance of the ring, as shown schematically in Figures 1 and 2.

In going some distance in the magnet fringe field before being created by stripping, the protons arising from $H^0(n)$ will not be deflected as much as protons that were created at the stripping foil and thus will have an angular displacement with respect to the central trajectory when projected back to the entrance of the magnet. At the PSR, the protons arising from excited states with $n \leq 5$ will have a large enough displacement that many will fall outside of the machine acceptance, as illustrated in Figure 2.

---

* Work performed under the auspices of the US. D.O.E.

** Includes the PSR development team of M. Borden, D. Brown, R. Cooper, R. Damjanovich, D. H. Fitzgerald, S. Frankle, T. Hardek, M. Zumbro, R. Hutson, R. Macek, D. Neuffer (CEBAF), M. Plum, C. Ohmori (visitor from Tokyo University), R. Ryder, D. R. Swenson, H. A. Thiessen, D. Tupa, T. F. Wang, C. Wilkinson, and R. York and the atomic physics group led by H. Bryant (University of New Mexico) that collaborated in the measurements of H^0 excited state production at HIRAB and includes J. Donahue, D. Clark, S. Cohen, E. Mackerrow, and O. van Dyck from LANL and H. Bryant, M. Gulley, M. Halka, P. Keating, and W. Miller from the University of New Mexico.

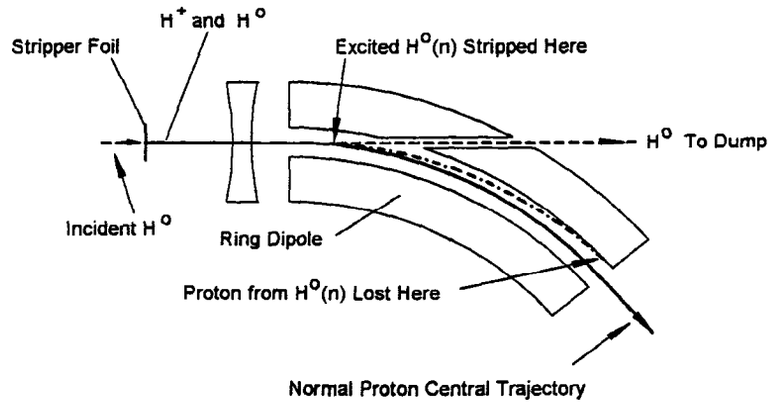

Figure 1. PSR injection region and the origin of "first turn" losses.

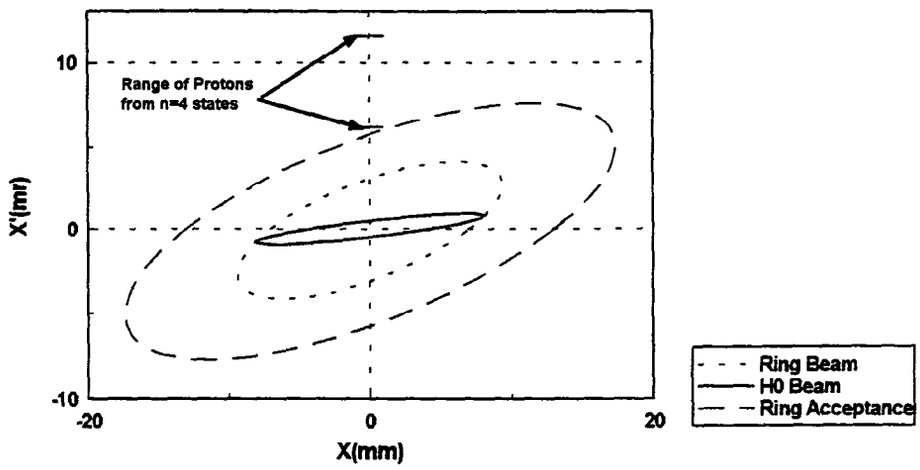

Figure 2. Beam ellipses and the ring acceptance at the entrance of the dipole downstream of the stripper foil. The H^o ellipse area is four times the rms emittance (2 sigma).

The behavior of excited states of H^o moving in a magnetic (or in an electric field in the rest frame of the atom) is well understood and can be calculated to good accuracy by a number of methods. For our purpose in tracking lost particles, the fifth-order perturbation theory of Damburg and Kolosov[4] is convenient and sufficiently accurate for calculating the energy and width (lifetime) of any H^o Stark state as a function of its quantum numbers (the parabolic quantum numbers, n1, n2, and the magnetic quantum number, m), its velocity, and the magnetic field in which it moves. For details on formulas for calculating lifetimes, see references 4 and 5.

The prescription of Damburg and Kolosov to calculate the central energy and width, Γ, of a given parabolic Stark state has been checked against numerical integration of the non-relativistic Schrodinger's equation with essentially no approximations for m=0,1. The agreement[6,7] on central energies is excellent (0.05%) and is better than 20% on the width for lifetimes of interest (1-100 picosecond) here. Furthermore, the perturbation theory results are in good agreement with laser experiments[8] at LAMPF on the hydrogen Stark effect.

The probability, P(z), for $H^o(n)$ to survive to a point located at coordinate, z, in the fringe field of the magnet is given by solution of the basic loss rate equation

$$\frac{dP(z)}{dz} = -\frac{P(z)}{\tau(z)\beta\gamma c} = -\frac{P(z)\Gamma(z)}{\hbar\beta\gamma c}; \quad \text{with solution } P(z) = \exp\left(-\frac{1}{\hbar\beta\gamma c}\int_{-\infty}^{z}\Gamma(s)ds\right).$$

Table I below summarizes results of calculations using the prescription described above along with the measured fringe field profile to compute the distribution of the angular displacement for protons from the field stripping of various excited states. The table also indicates location of proton loss and estimates of yield, which are taken as one-half of the measured yields (in an experiment described below) from H^- incident on the foil. It is plausible to assume that the yield of $H^0(n)$ from incident H^0 beams will be about half that for H^- beams since there are half as many "convoy" electrons traveling with the proton as they emerge from the foil where the proton can recapture an electron to form $H^0(n)$.

Table 1. $H^0(n)$ loss estimates

n	$\Delta\theta$ range (mradians)	Loss Location in the ring	Estimated Yield from 200-μg/cm^2 foil
3	22 - 50	in the first dipole	0.30%
4	6.1 - 12	after the first dipole but in the next 3 ring sections	0.20%
5	1.8 - 4.4	small fraction lost on the ring limiting apertures	0.15%

While theory provides a good prescription for the field stripping of excited states, at this time only experiments provide information on yields of various excited states from relativistic beams traversing thin foils. Fortunately, we were able to rapidly mount an exploratory experiment to measure the yields of excited states of H^0 produced when 800-MeV H^- ions impinge on thin carbons foils by using existing equipment and expertise provided by our collaborators from the University of New Mexico atomic physics research group, who have been conducting accelerator-based research using laser-ion colliding-beam experiments at LAMPF for the past twenty years.

The experiment layout is shown in the schematic of Figure 3. The main apparatus consisted of the foil box, the gradient magnet, a 5.27-m flight path and a detector system made up a scintillator telescope, a multi-wire proportional chamber, and a scanning scintillator. The scintillator telescope covered the entire beam so that the measurements could be normalized to the total beam. Standard beam diagnostics and phase-space tailoring equipment are not shown.

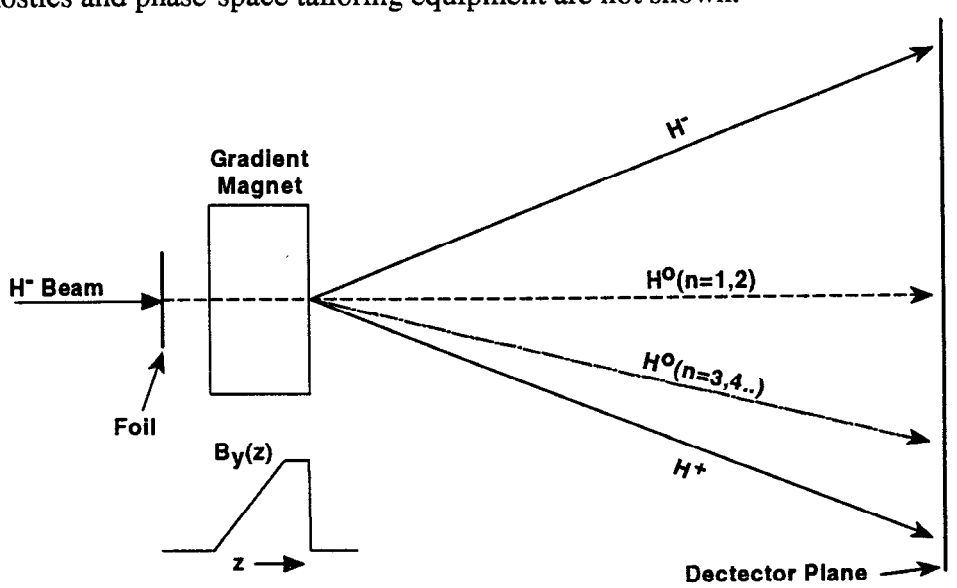

Figure 3. Schematic layout of the experiment to measure the production of excited states.

The gradient magnet is a half quadrupole turned sideways to the beam that enters through a hole in the return yoke and then encounters a vertical magnetic field whose strength increases linearly with distance. A maximum field of 1.9 T is available and the length of the gradient region is 0.20 m

When a given H^0 Stark state reaches a field in the gradient magnet where it has a high probability to ionize, it is stripped and the resulting H^+ is deflected in traversing the remaining downstream magnetic field. By measuring the position where the proton strikes the detector and using the field map of the magnet, one can reconstruct the value of the magnetic field where the proton was produced by stripping.

When the magnet is set to ionize a particular low-lying n-value manifold (n=3,4,5 or perhaps 6) in the linear gradient region of the magnet, each individual Stark state strips over a narrow range of field values that produce a peak separate from most of other substates, except for nearest neighbors and in some cases next-nearest neighbors. This offers the possibility that information on the distribution of substates within a given n-value manifold can be extracted from experimental data. We are in the process of analyzing the data to find the best-fit distribution of substates in the n=3 and n=4 manifolds.

A typical data set is shown in Figure 4 for the magnet set at 1.3 T and for foils of thickness 70 and 200 $\mu g/cm^2$. We are now persuaded that the sharp peak near x=17 cm is spurious (due to scattering from the scanning scintillator supporting plate) and not an excited state of H^0. Data are also available for a 300-$\mu g/cm^2$ -thick foil but are not plotted in Figure 4 to avoid obscuring the main features of the data from the other two foils.

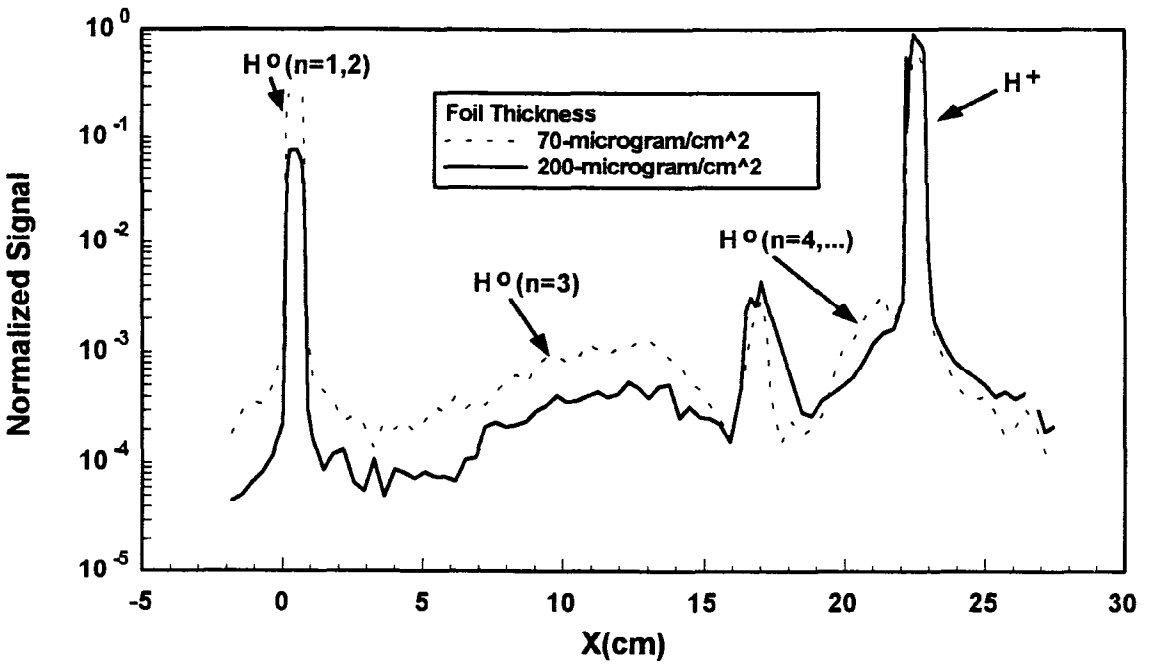

Figure 4. Scanning scintillator spectra for a peak field of 1.3 T.

In the spectra of Figure 4, the n=3 collection of states are separated from the n=1,2 group, as well as from the states n=4 and above. The n=3 collection can be summed to obtain the yield as a fraction of the incoming H^- and as a function of foil thickness. We also have data sets for n=4 collected at a peak field of 0.7 T. The preliminary results of the yield for n=3 states and the sum of n=1 and 2 are tabulated below and plotted in Figures 5a and 5b, along with curves (solid lines) that fit the shape of relative yield data published in reference 5. The curves of Figure 5 were obtained from the following formula which was derived for a simple model, assuming a series of interactions with individual (isolated) foil atoms.

$$Y(x) = N_i \cdot \frac{a}{a+b-c}\left[\exp(-c \cdot x) - \exp(-(a+b) \cdot x)\right].$$

The parameters a, b, and c are taken from reference 5 (a = 0.123, b = 0.00086, c = 0.0131 for n=3 and a = 0.0388, b = 0.00949, c = 0.0109 for n=1) with the overall normalization, N_i, adjusted for a good fit to the data from our experiment. The dependence of relative yield on foil thickness for our data are in good agreement with the curves of reference 5 as is evident in Figures 5a and 5b.

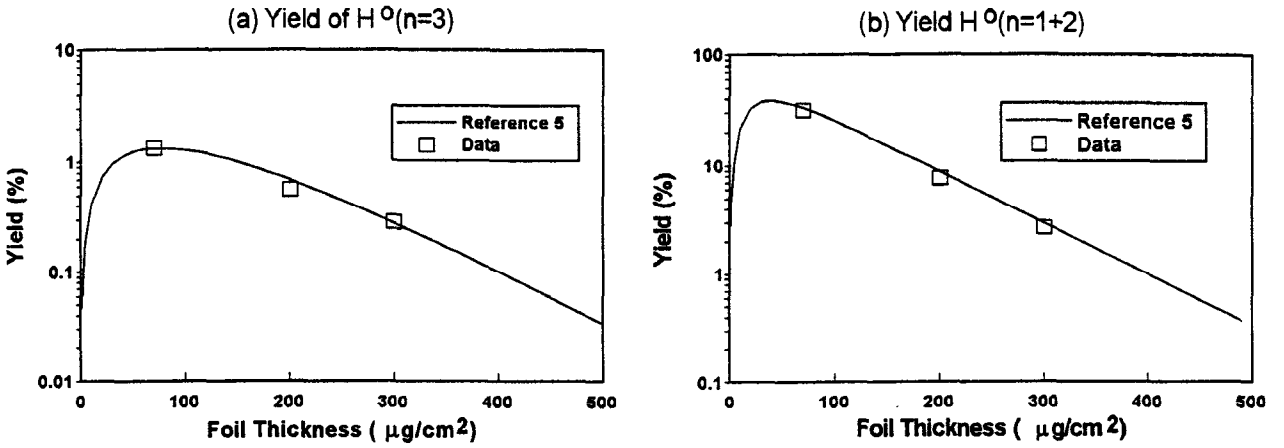

Figure 5. Yields of $H^o(n)$ as a function of foil thickness.

Yield data for the data set taken at 1.3-T peak field.

Foil thickness ($\mu g/cm^2$)	% yield for n=1+n=2	% yield for n=3
70	35	1.34
200	7.5	0.57
300	2.7	0.29

At this time, the best estimates of the percentage yield for other values of n in the range 2-5 are obtained by extrapolation from our results for n=3 using the power law distribution for n reported in reference 5. For a 200 $\mu g/cm^2$ carbon foil this implies $Y(n) = 0.0057(3/n)^{1.3}$.

Another experimental run to refine the measurements made in 1992, to measure yields for more n values and to study the effect of other foil parameters on yields is planned for September, 1993. It would be desirable to study other factors that might affect yields of excited states such as beam energy, the effect of other foil materials (Al_2O_3, Si...), the presence of a magnetic field at the stripper foil, the angle of foil with respect to the beam, and multiple, closely-spaced foils. However, the limited amount of beam time available for the study will restrict the number of factors that can be explored in the next run.

We are convinced that the excited states of H^o produced at the stripper foil are responsible for most of the first-turn losses. All of the available evidence is consistent with this explanation, including the location of the losses, the magnitude of the losses, and the behavior with foil thickness. An alternative explanation, halos on the incoming H^o beam, could explain some but not all of the evidence. It would take an unusual distribution of halo to spill at the observed locations of first-turn losses rather than at the limiting aperture (extraction septum). Most convincing is the reduction in first-turn losses with foil thickness. It is very difficult to see how the first-turn losses from beam halos would be reduced by the observed factor of two for a 300-$\mu g/cm^2$ foil of the same size placed at the same location as a 200-$\mu g/cm^2$ foil. If beam halos were the correct explanation, one would expect the first-turn losses (as a fraction of the H^+ beam) to remain the same.

The mechanism described above for the first-turn losses at PSR will generate some beam halo and possibly some losses for any machine employing charge exchange injection with a H^- or H^o beam incident on a stripper foil. Unless the foil is very thick, some H^o will emerge from the foil and

will be separated from H^+ in a magnetic field. The halo can be minimized but not eliminated in its entirety.

The PSR Instability

A strong, fast, transverse instability with high beam loss has long been observed at the PSR above a threshold of ~ 6×10^{12} protons per pulse (ppp) in a coasting beam and ~ $3\text{-}3.5 \times 10^{13}$ ppp for bunched beam conditions (12 kV on buncher)[9]. Transverse oscillations of the beam centroid at ~ 100 MHz are observed on stripline beam position monitor (BPM) pickups and increase exponentially with growth times of 10-50 μs for unstable beams at PSR.

Much evidence[10] has been accumulated indicating that the instability is driven by electrons trapped within the proton beam (referred to as the e-p instability seen in certain other proton machines). Plenty of electrons (shown below in the table of known sources of electrons at PSR) are available to provide neutralization at the 1-2 % level, which theoretical studies[10] and simulations[11] indicate is needed for the e-p instability. These studies[10] also show that a small amount of proton beam leakage into the inter bunch gap will cause trapping of electrons over successive passages of the beam bunch, although recent work[11] indicates that the instability may still occur (at perhaps a somewhat higher threshold) with a clean gap if the beam is sufficiently neutralized (a few percent) by fresh electrons created each turn.

Table 2. Known sources of electrons at PSR

Source	Electrons/accumulated proton
1. Electrons (400 keV) stripped from H^0 at the stripper foil	1 + secondaries
2. Secondary emission from stripper foil	5-10
3. Thermionic emission from stripper foil	< 0.1?
4. Secondary emission from beam spill on vacuum envelope	<0.1?
5. Residual gas ionization	~0.05
Total	**6-10 e/p**

Theory suggests that control of an e-p instability should be possible by suppressing the generation and/or trapping of electrons. Electron neutralization of the beam can be suppressed by various electron clearing fields. Leakage of protons into the interbunch gap and the resulting electron trapping can be suppressed by more effective RF bunching of the beam, say, by stronger RF fields at the buncher, a second buncher, or some form of barrier bucket. Since increasing buncher performance is not easily accomplished at PSR and since most (99% or more) of the electrons are produced in the injection straight section, we have chosen to focus on methods to suppress the electrons produced in the injection region.

The layout and configuration of electron collection devices recently installed in the injection straight section are shown in Figure 6. Collecting electrodes fill much of the space. The stripper foil

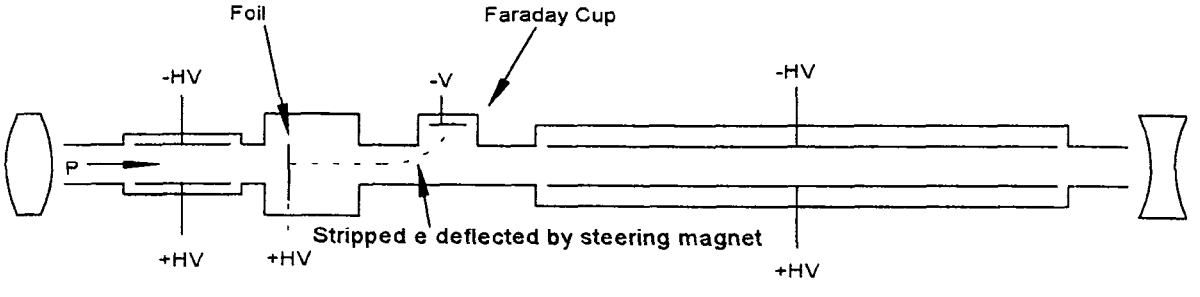

Figure 6. Layout of electron collection devices in the injection straight section of PSR.

can now be biased to ~ 10 kV to suppress secondary and thermionic emission from the foil. A small magnet will deflect the 400 keV electrons (stripped from the incoming H^0 at the stripper foil) onto a biased Faraday cup where they should be collected. Many of the more energetic delta rays from the foil will also be deflected to the Faraday cup. Studies of the efficacy of the newly installed devices will be undertaken in the summer of 1993.

Proton beam leakage at the 1% level into the inter bunch gap is not easily discerned with the existing beam diagnostics. A special beam current transformer with low undershoot is being developed for the 1993 instability studies. It will be placed in the extraction line for measurement of beam in the gap when the extraction kickers are timed to fully extract the gap region. Under these circumstances, beam will show up in the extraction line on either side of the "gap" with ~ 10% of the beam ahead of the "gap" and the rest of the beam coming after, as indicated in Figure 7. We expect to be able to detect and measure beam in the gap if it is ≥ 0.1% of the peak.

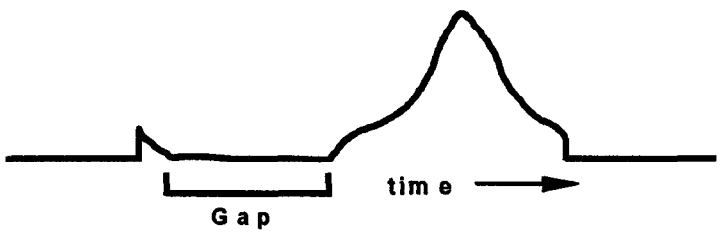

Figure 7. Beam current signal expected from extraction line monitor when "gap" is extracted.

H^- Source Development

Injection of higher peak current into the PSR will reduce the number of turns needed to accumulate a given charge and consequently reduce the number of foil traversals by the stored beam, thus reducing stored-beam losses. Development of a volume H^- source with twice the peak intensity and half the emittance of the present cusp-field source was judged to be feasible and considered to be the most cost-effective next step toward increased intensity. It has the added benefit of reducing the linac duty factor needed to serve the LANSCE program. Such a source would be required for any new spallation source.

A major effort is under way at Los Alamos to test and evaluate two promising options: (a) a dipole-filter design from LBL (Berkeley) and (b) a version of the BNL toroidal-filter volume H^- source engineered for high duty factor operation. Results to date are encouraging and have been reported elsewhere[12]. Both options show the potential to meet the goals discussed above. These studies will also include the use of RF to excite the source plasma for the dipole-filter source.

Design studies for an advanced spallation neutron source indicate that chopping the beam to provide 100-200-ns gaps before the beam reaches the linac will be difficult. Experiments by R. York[12] show that the beam intensity of the small LBL dipole-filter source can be modulated by biasing the plasma electrode. In tests with an arc current of 150 A, 90% of the extracted beam was suppressed when the plasma electrode was biased at -150 or +40 volts. Further tests were made using a simple modulator to pulse the plasma electrode to -150 volts with a rise time of ~ 100 ns. The time response of the source beam intensity followed the rise time of the modulator and the plasma discharge time of ~100 ns. Future tests with a faster modulator are planned to determine the time response limit of beam-intensity modulation.

Conclusions

Machine studies at PSR are highly relevant to development of the next generation of high-intensity compressor rings. All of the new machines will need to deal with the beam halos and beam losses generated by excited states of H^0 produced at the stripper foil. Brighter, more intense H^- ion

sources will be needed. The PSR instability could be a serious limitation if means to control it are not developed. Hopefully, the most important results of our proposed machine experiments will be obtained before PSR closes permanently. However, source development can still proceed without the linac and further studies of the production of excited states of H^0 at 400 MeV might be possible at the Fermilab linac.

References

1. This mechanism for the first-turn losses at PSR was first proposed by Richard Hutson in a PSR technical note in the summer of 1992. See R. Hutson, "First-Turn Losses in PSR: a Speculation About Their Origin," PSR Technical Note, PSR-92-015, August 12, 1992.

2. R. Hutson and R. Macek, "First-Turn Losses in the LAMPF Proton Storage Ring (PSR)," Conference Record of the 1993 Particle Accelerator Conference, Washington, DC, May 17-20, 1993, and Los Alamos National Laboratory report LA-UR-93-1868.

3. R. Hutson et al., "Stripper-Foil Scan Studies of the First-Turn Loss Mechanism in the LAMPF Proton Storage Ring (PSR)," Conference Record of the 1993 Particle Accelerator Conference, Washington, DC, May 17-20, 1993, and Los Alamos National Laboratory report LA-UR-93-1867.

4. R. J. Damburg and V. V. Kolosov, "Theoretical studies of hydrogen Rydberg atoms in electric fields," pp. 31-71 , **Rydberg States of Atoms and Molecules**, Edited by R. F. Stebbings and F. B. Dunning, (Cambridge Univ. Press 1983).

5. A. H. Mohagheghi, "Interaction of Relativistic H^- Ions with Thin Foils," Ph.D. thesis, University of New Mexico, 1990, also Los Alamos National Laboratory Report LA-11925-T. 1990; and A. H. Mohagheghi et al., "Interaction of Relativistic H- Ions with Thin Foils," Phys. Rev A, Vol. 43, pp. 1345-1365, (1991).

6. T. Bergeman and J. B. Donahue, private communications, 1992.

7. J. Donahue et al., "Measurement of H^0 Excited States Produced by Foil Stripping of 800-MeV H^- Ions," Conference Record of the 1993 Particle Accelerator Conference, Washington, DC, May 17-20, 1993, and Los Alamos National Laboratory report LA-UR-93-2038.

8. T. Bergeman et al., "Shape Resonances in the Hydrogen Stark Effect in Fields up to 3 MV/cm," Phys. Rev. Lett. 53, 775-8, (1984)

9. D. Neuffer et al., "Transverse Collective Instability in the PSR," Part. Accel. 23 (1988) 133.

10. D. Neuffer et al., "Observations of a fast transverse instability in the PSR," Nucl. Instrum. Methods A321,1-12 (1992).

11. T. F. Wang et al., "Recent Study of Beam Stability in the PSR," Conference Record of the 1993 Particle Accelerator Conference, Washington, DC, May 17-20, 1993, and Los Alamos National Laboratory report LA-UR-93-1874.

12. R. L. York et al., "Volume H^- Ion Source Development at LAMPF," Conference Record of the 1993 Particle Accelerator Conference, Washington, DC, May 17-20, 1993, and Los Alamos National Laboratory report LA-UR-93-1924.

OVERVIEW OF THE NCNR ACCELERATOR STUDIES

Andrew J. Jason
Los Alamos National Laboratory
Los Alamos, NM 87545

I. INTRODUCTION

Since the construction of the Los Alamos Proton Storage Ring (PSR) [1], there has been a strong program for neutron research at the Manuel Lujan, Jr. Neutron Scattering Center (LANSCE). The PSR was designed to provide 80 kW of beam power to the LANSCE spallation target. In view of a possible upgrade for this facility, we have undertaken a study to delineate a system capable of delivering 1 MW of beam power to an upgraded LANSCE facility with provision for a further increase in power to 5 MW. The project is known as the National Center for Neutron Research (NCNR).

The concept emerging from these studies features acceleration of H^- ions to an energy of 800 MeV and subsequent multiturn injection into an accumulator ring. The compressed pulse is then extracted in a single turn and transported to the spallation target. In all the studies we have stressed reliability and low beam loss.

II. GENERAL DESCRIPTION

The proposed scheme is shown in Figure 1. The existing side-coupled linac (SCL), which accelerates beam from 100 MeV to 800 MeV and comprises about 90% of the LAMPF linac, is retained as an integral part of the proposal. The present front end consists of three ion sources that provide H^+, H^-, and polarized H^- accelerated by Cockroft-Walton generators to 750 MeV. The three beams are merged, bunched, and matched to a 201.25-MHz drift-tube linac (DTL) for acceleration to 100 MeV. Our concept replaces the three sources with a single H^- source capable of providing up to 40-mA peak current at 100 keV. Beam is then matched to a 402.5-MHz radio-frequency-quadrupole linac that bunches and accelerates beam to 7.0 MeV. The next stage of acceleration is provided by a 402.5-MHz DTL to 20 MeV and subsequent acceleration by an 805-MHz DTL to 100 MeV for matching into the 805-MHz SCL. The many choices in this specification involved considerations of beam dynamics, reliability, and cost. Additionally, the configuration can be upgraded in current by funneling into the 805-MHz DTL.

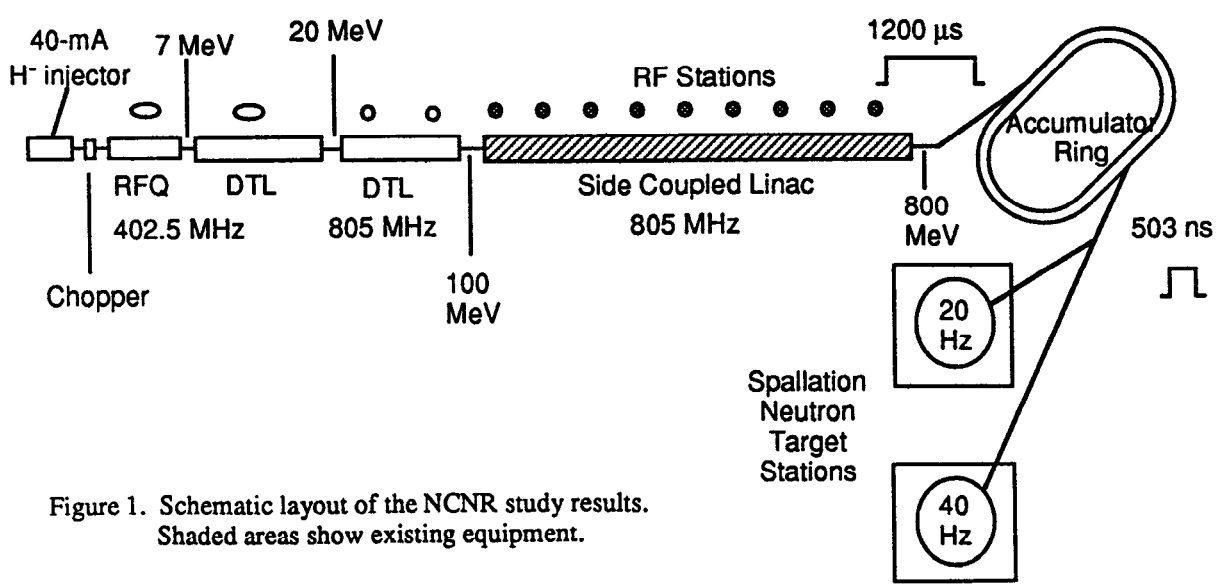

Figure 1. Schematic layout of the NCNR study results. Shaded areas show existing equipment.

*Work Supported by the US Department of Energy, Office of Defense Programs.

An achromatic transport line takes the beam northeast to the accumulator ring. The line also performs the function of dispersion scraping to remove off-momentum beam particles and contains magnets properly sized to avoid appreciable field stripping of the H^- beam. Beam is injected by single-stage stripping through a foil and, after accumulation for some 1790 turns, is immediately extracted. Beam is then transported to two spallation sources and inserted vertically upwards into the targets. Experiments at the neutron source generally require a regular pulse rate. Hence, pulsed equipment in the linac and ring must be capable of an 8.3-ms pulse repetition time to provide a uniform 20 and 40 Hz to the respective targets.

III. INJECTOR

Extensive development of high-current, high-brightness H^- ion sources has taken place at Los Alamos both for use at LAMPF [2] and for other projects such as the Ground Test Accelerator (GTA) [3]. We require currents near 40 mA with an rms normalized emittance of below 0.020π cm mrad and a duty factor near 9%. No existing ion source meets all these requirements although there are several applications for which one or more of the requirements has been exceeded. The 4X ion source developed for GTA has produced, for example, over 60 mA at about a third of the required emittance. However, the nominal duty factor for which it has been developed is 1%. The LAMPF ion source performs with adequate duty factor and emittance but produces a current of 20 mA. Similar comments also apply to sources developed at other institutions. With a modest development program, it is reasonable to extrapolate to the required performance.

A more difficult problem, for which no entirely satisfactory solution now exists, is that of chopping the beam at a 1.49-MHz rate (436 ns on, 235 ns off) to maintain an extraction gap in the compressor-ring stored beam. This is currently done for the PSR by a slow-wave deflector in the LAMPF injector region at 750-keV beam energy. Such a scheme will be difficult at the low-matching energy of the RFQ in the NCNR scheme. Several other options are being explored, among them fast beam switching at a source plasma electrode with modest pulsed-power requirements.

IV. LINAC

Specifications for the linac are given in Table 1

Table 1
Linac Parameters

Average current	1.4 mA
Average power	1.4 mA x 800 MeV=1.12 MW
Peak current	30 mA
Repetition rate	20 + 40 Hz
Beam duty factor	7.2 %
Macropulse length	1.2 ms
Micropulse frequency	402.5 MHz
Chopping frequency, duty factor	1.49 MHz, 65%

The RFQ selected is similar to previous four-vane designs constructed or proposed at Los Alamos [4]. The high output energy of 7 MeV requires an unusual length of 6.9 m. The RFQ features an integral copper vacuum, rf, and structural envelope and is constructed in eight electroformed sections. Each pair of sections forms a loop-driven rf segment resonantly coupled to the others in a coupled-cavity structure. The average structure power is 140 kW with a peak power (including beam) of 1.54 MW. Proven tuning algorithms have been developed for this type of device. Dynamics calculations show that the structure will have over 95% transmission with an emittance of 0.02π cm mrad (rms normalized) at 38 mA.

The 402.5-MHz DTL is designed with two tanks and a total length of 5.43 m. Permanent-magnet quadrupoles are used in an FFDD configuration. Drift-tube bores are 1.8-cm diameter, approximately 10 times rms beam size. The DTL is similar to designs tested at Los Alamos on GTA and other projects. The total peak power needed is 1.48 MW. This is to be supplied by a two-tube klystron module with each tube providing a nominal 1.25 MW of rf peak power. Beam-dynamics calculations show little emittance growth with a test current of 38 mA.

The 805.0-MHz DTL is similarly constructed with a total length of 54.7 m and consists of 15 tanks. The lattice is a FFFOOODDDOOO configuration using 1.8-cm-bore permanent-magnet quadrupoles. From our loss estimates and extensive testing of magnetic material, we do not believe that radiation-induced deterioration of the magnets will be appreciable over a period of many years. The ratio of aperture radius to beam rms size is greater than the factor of seven generally used at LAMPF as a "safe" value. Beam-dynamics calculations show small emittance growth with a current of 75 mA. The total peak rf power required is 5.8 MW to be supplied by a klystron module similar to that used for the 402.5-MHz DTL.

Matching between the four linac sections is done transversely with variable permanent-magnet quadrupoles and longitudinally with pairs of buncher cavities. The buncher systems require a total of 50-kW peak power and are supplied by six tetrode-driven supplies.

Studies and experimental results have shown that the LAMPF SCL (100 to 800 MeV) is quite adequate for NCNR purposes. Note that the LAMPF facility has functioned as a provider of beam at 1-MW levels at a repetition rate of 120 Hz with a micropulse frequency of 201.25 MHz. At these levels, it operates under low stress and has had a long history of high reliability. Our proposal nearly doubles the peak current. However, the increase in micropulse frequency to 402.5 MHz results in a similar charge per beam bunch; the single-bunch beam dynamics is hence unchanged. Because of the 65% chopping duty factor, the peak-average current is 19.5 mA, slightly above the present nominal current of 17 mA. Total peak power is then nearly 41 MW, to be supplied by the existing 44-klyston system. Taking into account the ratio of total supplied power to structure losses (~4/3), the additional average power to be supplied is some 4%, well within the present rf-system reserve capacity. Hence, no substantial upgrade is needed.

A remaining question is the SCL response to the chopping pattern. Beam to the PSR is currently supplied at about one-third the NCNR peak-current requirement and at twice the chopping frequency with no perceived perturbation to performance. Combined structure and beam-dynamics calculations show that, under NCNR conditions, the cavity fields will vary uniformly in each tank by about 1% during the chopping cycle but will have little effect on beam quality. This point will be tested in an upcoming series of experiments.

Recent advances in fast adaptive feed-forward control techniques [7], proven on operating systems, will be very useful in achieving low-loss beam control in the linac and will soon be tested on the SCL. Studies are underway for high-current adaptations to tuning techniques such as the Δt method. Programs are also in place to study halo growth and develop techniques that minimize beam loss [8].

V. ACCUMULATOR RING

A. Overview

The linac chopping pattern is superimposed on the stored beam by direct non-Liouvillean injection through a foil. Transverse injection painting is used to control the beam distribution, important for the ring stability. A gap is maintained by an rf system consisting of twelve cavities operating at first through fifth ring harmonic to produce a barrier bucket. At extraction, the gap is 168 ns, sufficient for a fast ferrite kicker to rise and cleanly remove the 503-ns beam bunch from the ring in single-turn extraction.

A ring closed-orbit energy of 790.0 MeV was chosen, slightly less than the nominal 800 MeV delivered by the accelerator, in order to provide for an energy sweep of ±4 MeV during injection. The ring circumference of 168.886 m was chosen so that the revolution frequency for 790-MeV protons is a subharmonic of 805 MHz; additionally, all five barrier-bucket rf harmonics are subharmonics of 805 MHz. A barrier bucket was chosen for its ability to keep the extraction gap free of protons (assuming successful chopping), avoiding extraction losses as well as a possible electron-proton instability. Additionally, the barrier bucket allows maximum beam capture and provides a bunching factor of 0.55 as compared to 0.25 for a first-harmonic cavity. The beam emittance necessary to keep the space-charge tune depression below a certain value is inversely proportional to the bunching factor.

Major design parameters are given in Table 2 and a schematic layout is shown in Figure 2.

Table 2
Accumulator-Ring Parameters

Ring circumference	168.886 m
Accumulated turns	1790
Ring period	671 ns
Extracted-beam-bunch length	503 ns
Stored protons	1.3×10^{14}
Peak stored current	57 A
Average extracted current	1.25 mA
Number of cells in achromatic arc	4
Number of cells in straight section	5
Length of straight-section cell	10.407 m
Length of arc cell	8.1 m

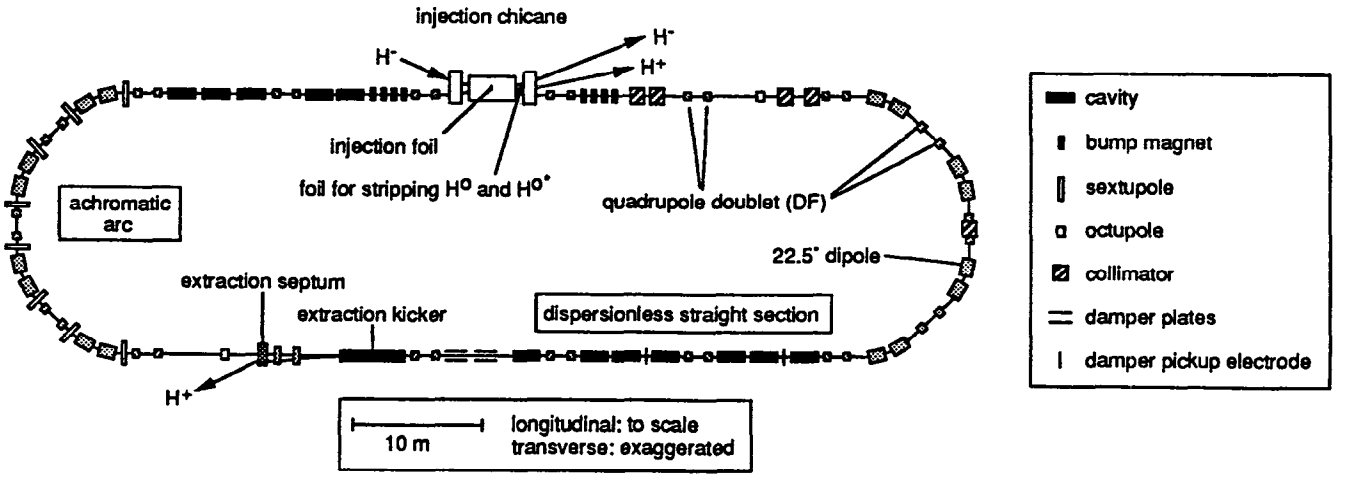

Figure 2. Ring layout

The ring features dispersionless straight sections and arcs in the configuration of second-order achromats. Straight sections house the injection chicane, bump magnets for injection painting, collimators for beam-halo control, bunching cavities, a transverse-damper system, linear and nonlinear corrector elements, and the extraction kicker and extraction septum. One achromatic arc houses chromaticity-adjusting sextupoles, the other a dispersion collimator. A full complement of diagnostics and orbit-correction steerers are included.

The desire to accomplish injection in a single drift mandated a minimum drift length of 8 m. This, together with the achromatic-arc design, suggested a doublet as opposed to a singlet lattice. Five cells per straight section were chosen because of tune considerations, because for the required ring circumference the long drifts are adequately dimensioned (8.407 m), and because the five long drifts in low-loss areas (upstream of the injection chicane and extraction kicker) can hold all rf cavities.

B. Linear Lattice

The lattice functions of the ring, slightly different from those of one superperiod because of the injection chicane, are shown in Figure 3. The undepressed tunes, $Q_x = 4.23$, $Q_y = 5.19$, correspond to phase advances per straight-section cell of 80.28° and 114.84°, respectively, near the value of 90° that minimizes aperture requirements. Stored-beam emittances are $\varepsilon_x = \varepsilon_y = 110\pi$ mm mrad to limit space-charge tune shifts to -0.15, thus remaining in a stable region of tune space. Apertures are dimensioned for transverse acceptances of 420π mm mrad and a momentum acceptance of ±1% $\delta p/p$. Ring dipoles and quadrupoles are described in Table 3.

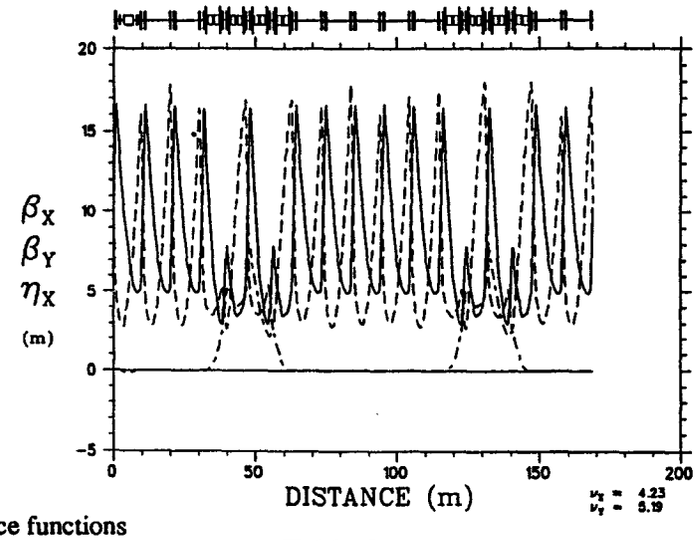

Figure 3. Ring lattice functions

Table 3
Ring-Magnet Description

Dipoles	
Arc length (m)	1.600
Field (T)	1.188
Straight-Section Quadrupoles	0.500
Defocusing-QuadrupoleGradient(T/m)	-4.541
Focusing Quadrupole Gradient (T/m)	3.990
Achromatic-Arc Quadrupole	
Effective Length (m)	0.500
Defocusing-Quadrupole Gradient (T/m)	-3.687
Focusing-Quadrupole Gradient (T/m)	4.366

C. Nonlinear Issues

The natural first- and second-order chromaticities and the anharmonicities for the perfect ring, without either random or systematic errors in the magnetic elements, are given in Table 4. The beam will cover a large area in the tune diagram, both from the tune shift of the reference particle due to space charge, and the tune spread around the central value, due to chromaticities and anharmonicities. Two families of four sextupoles each are placed in one arc to affect chromaticities. Two octupoles are placed at identical positions in the two superperiods to affect anharmonicities for control of tune spread.

Table 4
Nonlinear Ring Parameters

$\partial Q_x / \partial(\delta p/p)$	-4.86
$\partial Q_y / \partial(\delta p/p)$	-7.10
$\partial^2 Q_x / \partial(\delta p/p)^2$	182.07
$\partial^2 Q_y / \partial(\delta p/p)^2$	120.69
$\partial Q_x / \partial \varepsilon_x$ $(\pi \text{ m rad})^{-1}$	31.79
$\partial Q_y / \partial \varepsilon_y$ $(\pi \text{ m rad})^{-1}$	34.49
$\partial Q_x / \partial \varepsilon_y = \partial Q_y / \partial \varepsilon_x$ $(\pi \text{ m rad})^{-1}$	42.97

Adjustment of the tune spread by these methods and by shaping the beam distribution are means of controlling the ring stability via tune damping. If a large tune spread is maintained, the damper shown in Figure 2 may not be necessary or useful since the decoherence time will be small. Calculation of the form factors and impedances involved in a complete stability assessment is difficult and has not yet been accomplished. However, we now argue for ring stability by scaling from other rings, such as the PSR for which form factors and impedances are scalable, that have not shown a particular instability at a given charge-storage level. The PSR does, however, exhibit an electron-proton instability [10] which we believe can be avoided by keeping the extraction gap free of protons, by loss control, and by the possible implementation of clearing electrodes. Experiments are underway to assess some of these issues at the PSR.

The widths of the resonance lines in the presence of ring imperfections, such as quadrupole roll errors, and random and systematic higher-multipole errors in dipole and quadrupole fields, are a concern. Sets of Lambertson correctors are placed inside straight-section quadrupoles to affect the widths of resonance lines. Skew-quadrupole correctors to affect $Q_x - Q_y = 1$, normal-octupole correctors to affect $4Q_x = 17$, and normal-decapole correctors to affect $Q_x + 4Q_y = 25$, $3Q_x + 2\,Q_y = 23$ and $5Q_x = 21$ have been identified.

D. Ring Injection

The injection chicane, composed of two 5° septa and a 10° central dipole, moves the stored-beam orbit outward by 0.2 m. The injected H^- join the stored-beam orbit outward by 0.2 m. Unstripped H^- are deflected away from the stored beam and disposed of in a beam dump, causing minimal activation in the ring. Partially-stripped excited neutral atoms created by the foil stripping process have been identified as a source of activation [9] in the PSR. These excited atoms are stripped in the fringe field of a downstream magnet and are scattered by the field to outside the ring acceptance. It is possible in principle to reduce these losses from a few percent of the injected beam to $<10^{-5}$ by placing the stripper foil in a specially configured magnetic field.

Injection occurs in a nondispersive region; hence the painting process is uncoupled from beam momentum. Two independent sets of bump magnets relax the stored-beam centroid from near the injection point (e.g., ~2.5 cm, -4.0 mrad in the x plane) to the closed orbit during injection. Thus the initial bump coordinates define the final stored-beam emittance. The nominal bumping rate is adjusted so that the stored emittance grows linearly in time. The foil, configured as a small rectangle and supported by 5-micron carbon fibers, is positioned so that its corner just covers the injected beam. Injection painting keeps the number of foil traversals low, at an average of 10 per particle. Figure 4 shows a contour plot of the beam transverse distribution at the end of injection, assuming accumulation in the perfect ring and neglecting beam self-interaction. Because of the x-y correlation inherent in this bumping scheme, the distribution is rectangular and the X-shaped pileup noticeable in the figure engenders space-charge forces with octupolar components.

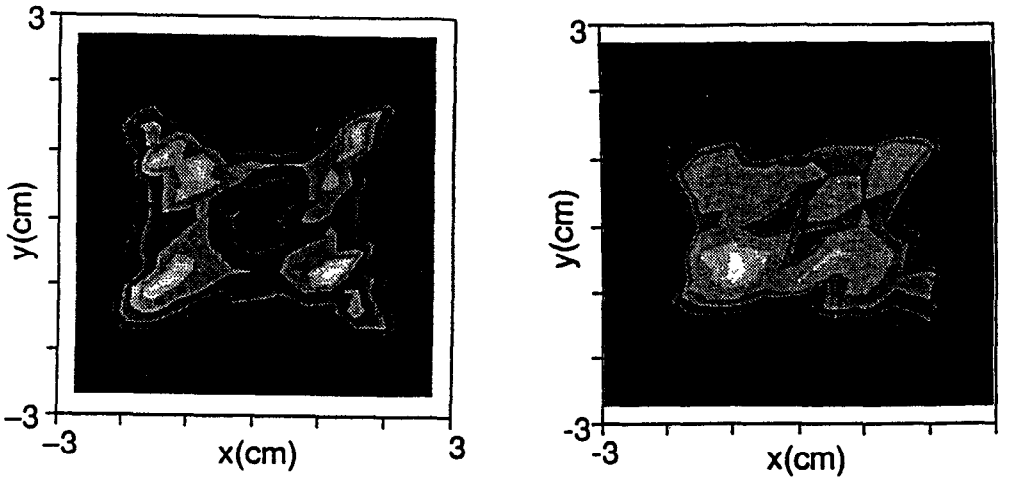

Figure 4. Left, transverse beam distribution after injection with neglect of space-charge forces. Right, evolution of this distribution for 100 turns including the forces derived from the distribution potential.

E. Particle Tracking

Figure 4 also indicates the effect of space charge forces. In the right-hand diagram the beam potential was calculated for the distribution on the left in the form of a fourth-order polynomial. Particles were then tracked with the high-order code Marylie for 100 turns. The resultant distribution shown is smoother and has slighty increased in size. Efforts are underway for a more self-consistent tracking capability.

The machine dynamic aperture was assessed by single-particle tracking to ninth order with the beam-optics code Tlie. We assumed random quadrupole-roll errors with a 10-mrad rms distribution, random sextupole errors of 0.01 T/m^2 rms and decapole errors of 1.0 T/m^4 rms in the dipoles, and octupole errors of 0.05 T/m^3 rms in the quadrupoles. The dynamic aperture as a function of particle momentum is shown in Figure 5. This strange looking diagram shows the fractal like nature of the nonlinear forces; were we to increase the resoulution, contours would further decrease in regularity. Improvements to the dynamic aperture will be made using first- and higher-order corrector elements.

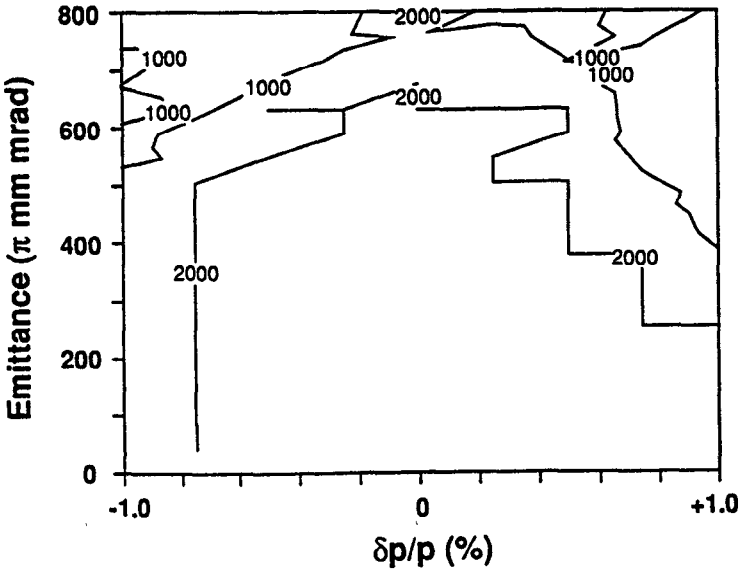

Figure 5. Contour plots for particles remaining within the emittance aperture on the vertical axis for 1000 and 2000 turns as a function of relative momentum deviation from the nominal. The particles were originally placed on the linear emittance contour corresponding to the ordinate value. Those particles that did not remain for the specified number of turns left the machine.

VI. UPGRADE OPTIONS

Although the major thrust of our study has been toward the 1-MW scenario, several options have been proposed for an upgrade to 5 MW and we have included features needed by these options in our design. The new linac front end is highly adaptable to funneling for increasing the current by the needed factor of 5 if a final energy of 800 MeV is retained. In this case further work is needed to establish the current-carrying capacity of the SCL and a multiple ring system would be needed.

The alternative, a higher beam energy of up to 2 GeV, is very attractive. Here a single ring, but with a substantially different lattice, appears feasible. Replacement of the CCL with a superconducting linac would use the existing LAMPF infrastructure and would ensure insensitivity to the chopping pattern that poses problems for a low-stored-energy room-temperature structure. Studies on upgrade alternatives are continuing.

VII. ACKNOWLEDGMENTS

We wish to thank the many individuals from LANSCE and AT and MP Divisions who contributed to this study.

VI. REFERENCES

[1] G. P. Lawrence, R. A. Hardekopf, A. J. Jason, P. N. Clout and G. A. Sawyer, "Los Alamos High-Current Proton Storage Ring; a Status Report," *IEEE Trans. Nucl. Sci.* NS-32, No. 5, 2662 (1985).

[2] R. York, D. Tupa, and D. Swenson, "Volume H^- Source Development at LAMPF," to be published in the Proceedings of the 1993 IEEE Particle Accelerator Conference.

[3] H. V. Smith, J. D. Sherman, P. Allison, "Pulsed H^- Ion Beams from Penning SPS Sources Equipped with Circular Emitters," *Proceedings of the 1988 Linear Accelerator Conference*, Newport News, October, 1988, p 164.

[4] L. Young, "Segmented Resonant Coupled Radio Frequency Quadrupole," these proceedings.

[5] K. Johnson, et al., "Commissioning of the First Drift Tube Linac Module in the Ground Test Accelerator," to be published in the Proceedings of the 1993 IEEE Particle Accelerator Conference.

[6] M. Lynch, et al., "Linac Design Study for an Intense Neutron-Source Driver," to be published in the Proceedings of the 1993 IEEE Particle Accelerator Conference.

[7] C. D. Ziomek, "Adaptive Feedforward in the LANL RF Control System," *Proceedings of the 1992 Linear Accelerator Conference*, Ottowa, August, 1992, p 685.

[8] R. Jameson, "Design for Low Beam Loss in Accelerators for Intense Neutron Applications," to be published in the Proceedings of the 1993 IEEE Particle Accelerator Conference.

[9] R. Hutson, R. Macek, "First-Turn Losses in the LAMPF Proton Storage Ring (PSR)," to be published in the Proceedings of the 1993 IEEE Particle Accelerator Conference.

[10] T. S. Wang, et al, "Recent Study of Beam Stability in the PSR," to be published in the Proceedings of the 1993 IEEE Particle Accelerator Conference.

ION SOURCE DEVELOPMENT

IN THE CULHAM LABORATORY OF AEA TECHNOLOGY

A J T Holmes
AEA Technology, Culham, Abingdon, Oxfordshire, OX14 3DB, UK

1. INTRODUCTION

Over the past eighteen years, Culham has been developing ion sources for various applications. In general these sources have had the task of injecting the maximum current into a defined solid angle which in effect defines a beam brightness and, more specifically, defines a beam current and emittance. Initially these sources were for producing proton beams for fusion heating experiments and more recently for H^- beams.

In this paper I describe the present achievements for both types of source and show how the same technology can be adapted for intense beams of both kinds of ion. There is a very close relationship between the production of H^- and H^+ which can be exploited to produce a high brightness beam of either ion. The paper also describes the accelerator technology and emittance of these beams. The ion source technology has been developed for continuous operation but it is possible to modulate the ion beam at frequencies up to 1 kHz using the source and in excess of 1 MHz using beam deflectors. A description of a novel low energy transport channel to the RFQ or DTL are also given.

2. THE PLASMA SOURCE

In this paper I will focus solely on the magnetic multipole or bucket ion source. This is shown in figure 1 and is a simple box lined on all sides except the extraction plane by rows of permanent magnets arranged in a N-S-N pattern as seen in figure 1. This box is the anode of the discharge and there are a number of hot wire filaments which act as cathodes. These filaments are usually heated by ac currents and are arranged in groups of three to minimise ripple. They are located at the back of the source, away from the extraction plane. The discharge forms between the anode and cathodes and is confined from the anode by the high order multipole magnetic fields. As a result a dense plasma forms ($n \geq 10^{12}$ cm^3) for arc currents in excess of 100 A/litre of volume. The discharge voltage is typically 100 V in H_2 pressures of a few millitorr.

However discharges in simple sources such as I have just described usually produce only low densities of H^+ or H^- ions. This arises from the fact that H^+ or H^- forms only in two-step ionisation processes. For H^+ formation the normal channel is:

$$e(E>15eV) + H_2 \rightarrow H_2^+ + 2e$$
$$e(E<5eV) + H_2^+ \rightarrow H^+ + H + e$$
$$H_2^+ + H_2 \rightarrow H_3^+ + H$$
$$e(E<5eV) + H_3^+ \rightarrow H^+ + 2H + e$$

A small amount of protons are formed directly by:

$$e(E>13eV) + H \rightarrow H^+ + 2e$$

To form a high fraction H^+ we must stop the ionisation process by excluding fast electrons and allow molecular ion break up by slow electrons.

A similar requirement exists for H^- production via dissociative attachment to vibrationally excited molecules, $H_2(v)$. Hence

$$e(E>13eV) + H_2(v=o) \rightarrow H_2(v>6) + e$$
$$e(E\sim1eV) + H_2(v>6) \rightarrow H^- + H$$
$$e(E>3eV) + H^- \rightarrow H + 2e$$

Again the presence of fast and slow electrons is essential with the fast electrons again being excluded from H^- production region to minimise H^- losses. This can be achieved by the magnetic filter.

2.1 The Magnetic Filter

This is shown again in figures 1 and 2. It is essentially a sheet of magnetic field separating two relatively field-free regions of plasma. Figure 1 shows an azimuthally symmetric system while figure 2 shows the simpler dipole type of filter. It works by modifying the diffusion coefficient of electrons in the plasma which is given by:

$$D_e = \frac{\nu kT}{m(\nu^2 + \omega^2)}$$

where kT	=	electron thermal energy		
ν	=	collision frequency	=	$C\,T^{-3/2}$
ω	=	cyclotron frequency	=	eB/m
m	=	electron mass		

Away from the filter we have $\omega = 0$, so:

$$D = \frac{kT^{5/2}}{mC}$$

while in the filter region $\omega >> \nu$, so:

$$D = mCkT^{-1/2}/e^2B^2$$

This means the normal order of events is reversed in the filter, fast electrons diffuse more slowly than slow electrons so we have a Maxwell's demon. Thus, dependent on the strength of B, we can choose the electron energy beyond the filter.

The requirements for proton production are not so stringent as for H^- production. In the former case we have to merely stop ionisation and have sufficient depth of plasma (typically 5 cm) such that molecular ions (for example H_2^+ and H_3^+) are broken up. In the latter case

we must exclude virtually all electrons whose energy exceeds 2 eV. Thus the filter for H11-production must have a higher value of $\int B^2 dl$, typically 5000 gauss^2 cm.

2.2 Proton Sources

Two fully developed proton sources have been designed and tested; the JET PINI source (55 x 31 x 22 cm^3) and the demonstrator source (18 x 30ϕ cm^3) which is also an H^- source. I will focus on the latter as it has a higher proton yield and is more suitable for single aperture applications. The proton yield is shown in figure 3 as a function of discharge current. At an ion current density of 100mA/cm^2, the proton yield is 87% (that for the PINI is only 80%). Higher proton fractions are possible with even stronger filters at the price of a lower available current density (because of the reduced value of the diffusion coefficient).

The discharge in long pulse mode is limited to around 80 A per filament (240 A) although this source has not been tested beyond about 140 A. The positive ion current density is linear with arc current over the full range. Higher discharge currents are feasible by adding extra filaments but accelerator perveance limitations limit j_+ to below about 200 mA/cm^2.

2.3 H^- Sources

In this case I will use the Type 4 H^- source as an example (19 x 10 x 10 cm^3 with three filaments). The extracted H^- current as a function of arc current is shown in figure 4. Unlike the proton source the H^- current tends to a limiting value and the peak value obtained for a 10 second pulse is 44 mA (22mA/cm^2) at an energy of 83 keV. Thus limitation is thought to be a result of the two step production process described earlier.

Addition of cesium as a catalyst adds an additional channel to the production process. We think this may be

$$Cs^* + H_2(v) \rightarrow Cs^+ + H^- + H$$

which overcomes the saturation effect. The effect on the discharge is shown in figure 5 where is can be seen that the H^- current is linear with arc current up to a maximum of 86 mA (43 mA/cm^2).

An additional problem with H^- sources is the suppression of co-extracted electrons. This is achieved by placing a transverse magnetic field across the aperture which effectively reduces the diffusion coefficient to a level where the electron flux is of the same order as the H^- current.

3. EMITTANCE

The beam emittance depends on many causes. These are:

- finite ion temperature in the plasma
- plasma ion emitting boundary aberrations
- accelerator aberrations
- LEBT emittance growth
- magnetic stochastic effects (H^- only)

We find no evidence for LEBT emittance growth or instabilities with multipole sources and the accelerator ray tracing codes show little sign of aberrations on transiting the accelerator. However the other three effects are non-trivial.

In earlier papers[1,2] I have shown that for a beam energy U and positive current density j_+ we have:

$$\varepsilon_n^2 = R^2 \left(\frac{1}{4} \left(\frac{T}{U} \right) + \frac{\gamma B^2 \lambda^2}{4U} + \alpha R^2 j^{2/3} / D^{2/3} \right)$$

where λ is the scattering length and R/D is the radius to extraction gap ratio. The first component arises from the finite ion temperature, T, the second component arises from the magnetic fields in the plasma and the last component depends on the plasma non-uniformity (also usually caused by the presence of magnetic fields. The second term is not usually very dominant unless these fields are very strong.

The above equation has been tested experimentally as seen in figure 6, where straight lines are obtained when ε_n^2 is plotted as a function of $j_-^{2/3}$ or $j_+^{2/3}$. This shows that the emittance of 8 mm radius H^- beams is 0.08 πmm mrad and rises with $j^{2/3}$ to a maximum of 0.26 πmm mrad. For He^+ beams (no proton data is available) the beam is largely dominated by its plasma temperature and the emittance is 0.02 πmm mrad.

4. THE ACCELERATOR

The accelerator is formed by a series of flat electrodes with circular apertures biased to potentials such that the beam gains the required energy and is collimated when it exits the last accelerating electrode. The first of these electrodes also forms one side of the plasma source as seen in figures 1 and 2. The beam is emitted from a curved plasma meniscus as seen in figure 7 which gives inward beam focusing. Subsequent electrodes create additional lenses of circular symmetry whose focal length is given by:

$$f^{-1} = (E_2 - E_1)/4U$$

where E_2 and E_1 are the downstream and upstream electric fields on either side of the electrode and U is the local beam energy.

It is possible to analyse the accelerator using matrix operators based on the above expression but it is much more convenient to analyse the problem using ray tracing codes such as IONTRAK which is a descendent of AXCEL. An example of the output is shown in figure 7 (note the geometry is distorted by conformal mapping).

The code can be used to analyse positive ion beams and also works very well for negative ion beams if the electron component is ignored. It models the ions from the plasma to the target and so forms the plasma meniscus self-consistently. This meniscus is responsible for a significant fraction of the total emittance growth if the plasma is non-uniform giving an aspherical shape to the meniscus.

5. THE LEBT

The beam transport to the RFQ requires two adjustable parameters per plane to match the beam emittance into the RFQ acceptance with maximum overlap. It is preferable to do this by circularly symmetric lenses as the accelerator gives at least one such lens as part of the acceleration process. Usually this is a solenoid just upstream of the RFQ. In addition beam alignment elements are also needed.

It is possible to use the accelerator alone to provide beam matching and alignment and a possible design is shown in figure 8. Here several extra lenses are created by having additional electrodes to create an accel-decel type structure. The focusing lenses become very strong under this situation and this particular example is designed for a 6° convergence into the RFQ, but is not fully optimised. Beam alignment is handled by segmenting one of the electrodes into four and applying weak dipole electric fields across the aperture to steer the main beam. Not shown in figure 8 is the electron separator which is two dipole magnets back-to-back which remove the H^- beam to be displaced sideways.

An advantage of this LEBT approach is compactness and simplicity and also the whole beamline path can be modelled by a single code IONTRAK, which eliminates many uncertainties.

6. CONCLUSIONS

Ion source development has now reached a stage that the requirements of future spallation sources can be met for both beam current and emittance for the initial beam. The novel designs of multipole sources lead to compact ion source systems whose power and cooling requirements are modest and can be operated over a wide range of beam pulse lengths, even continuous operation.

REFERENCES

1. Holmes A J T, Proc. IEEE Conf. on Particle Accelerators, Washington, p257, (1987).

2. Holmes A J T and Surrey E, Rev. Sci. Instrum., 62, p1173, (1991)

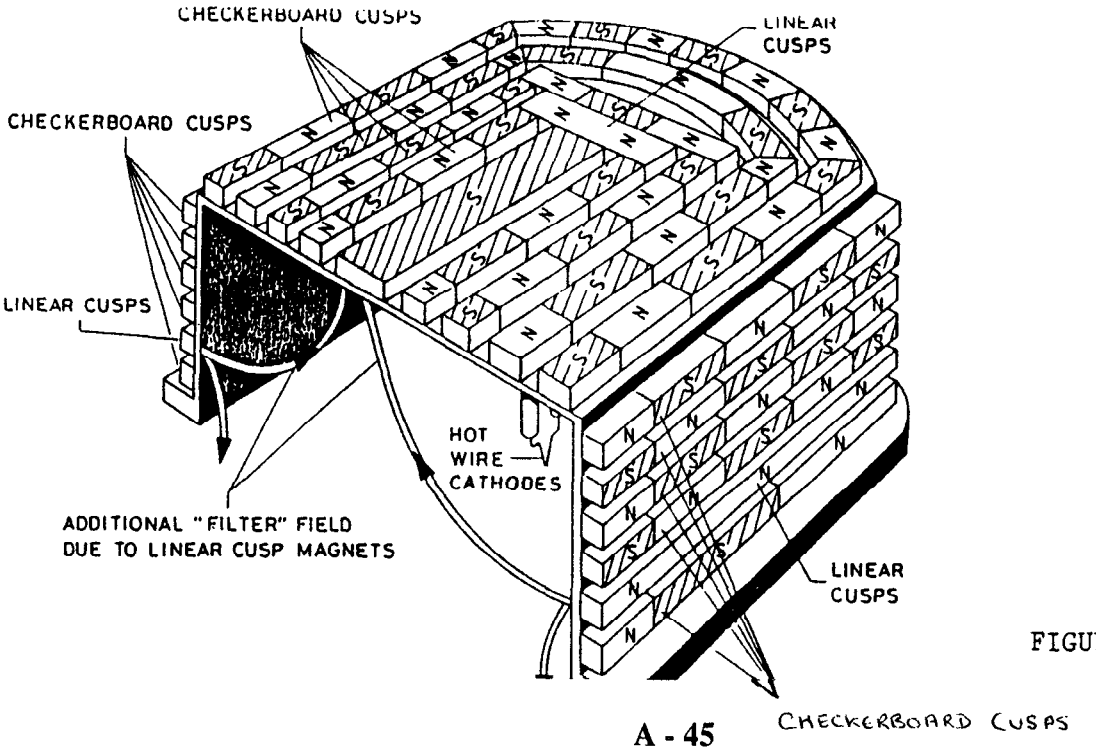

FIGURE 1

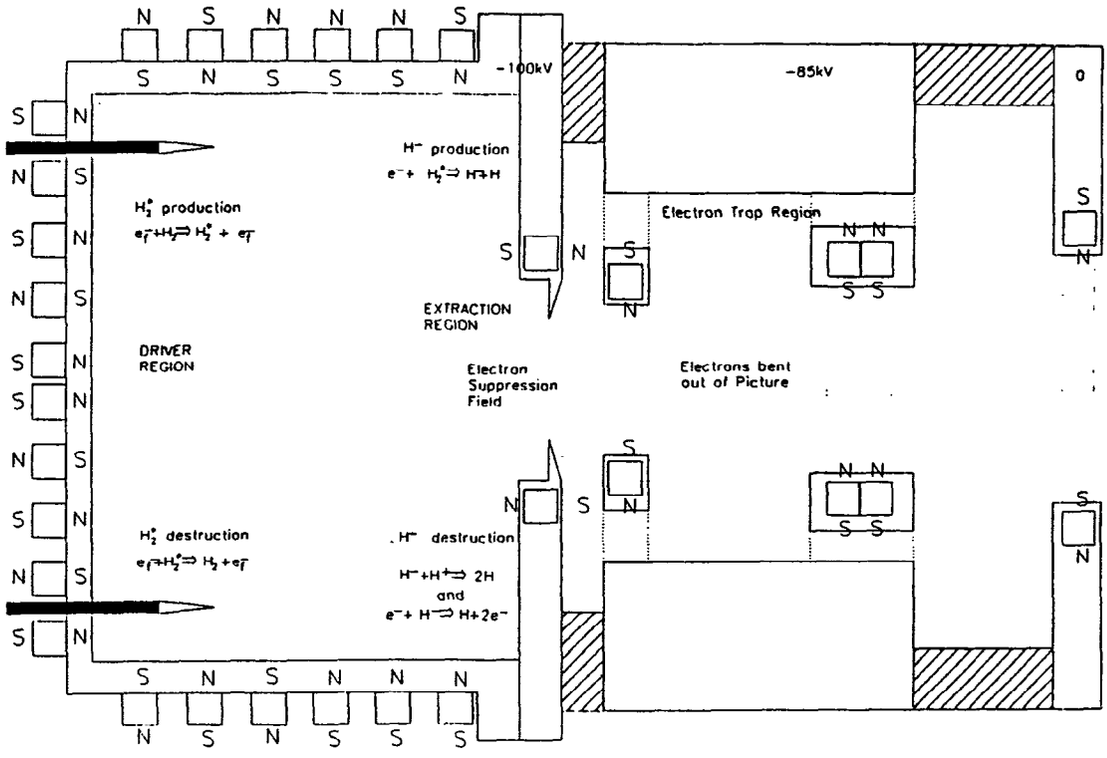

FIGURE 2

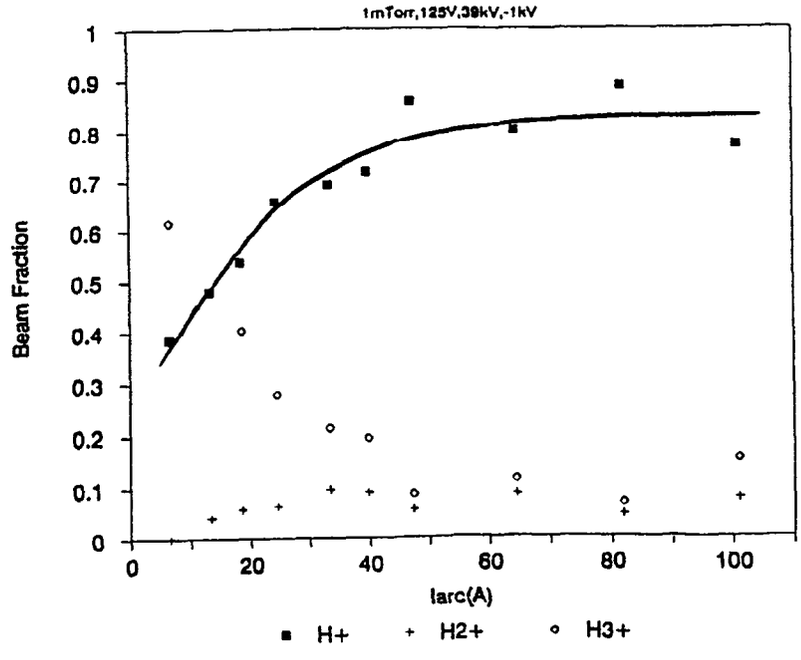

FIGURE 3

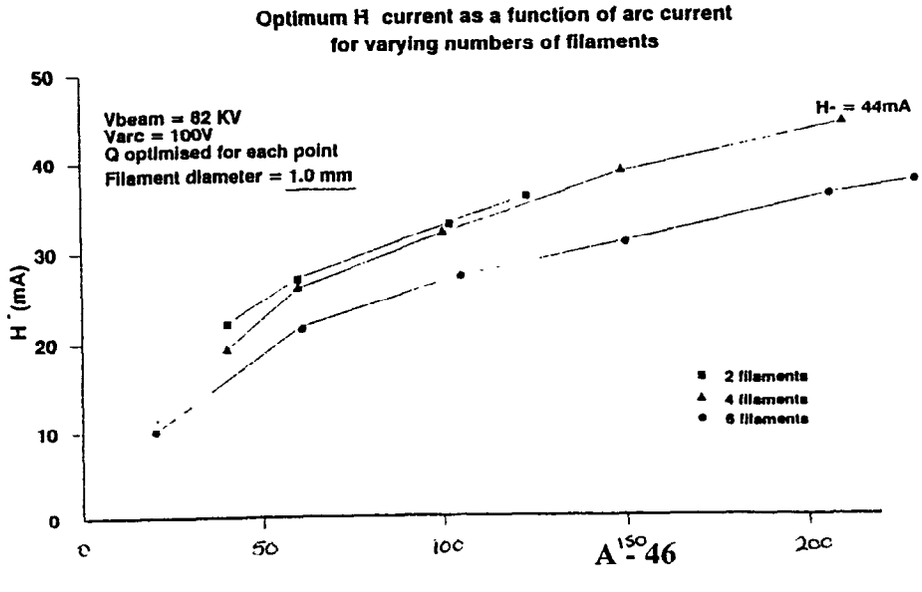

FIGURE 4

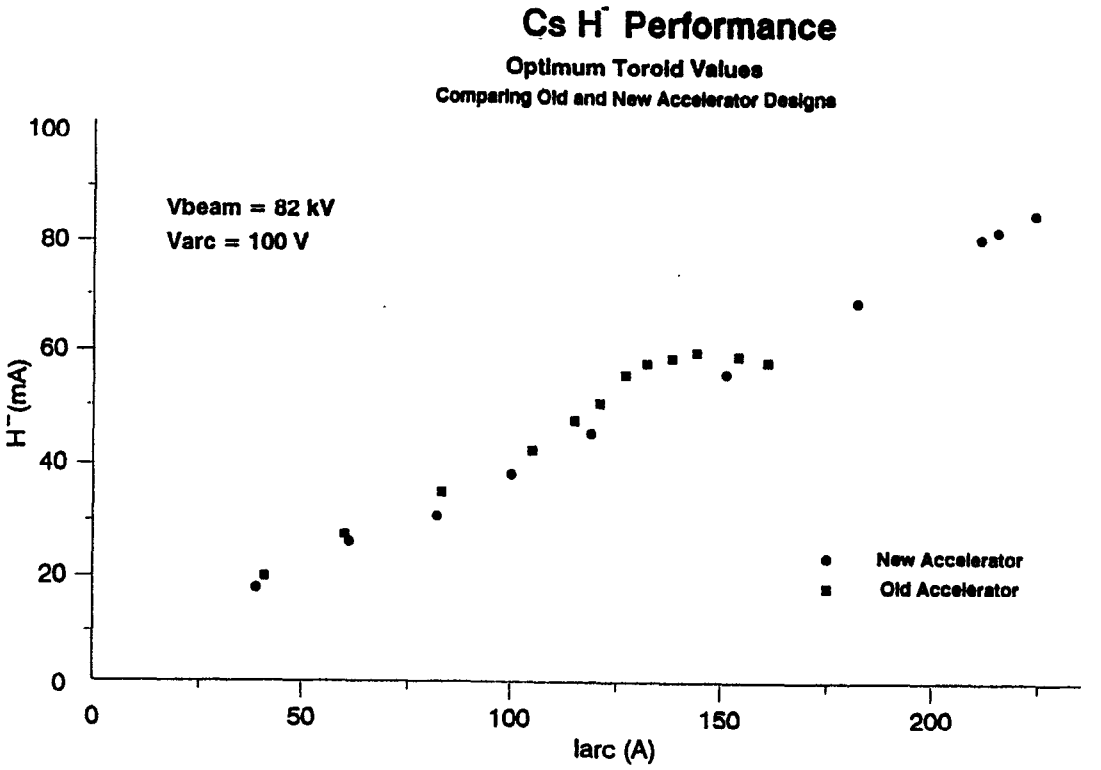

FIGURE 5

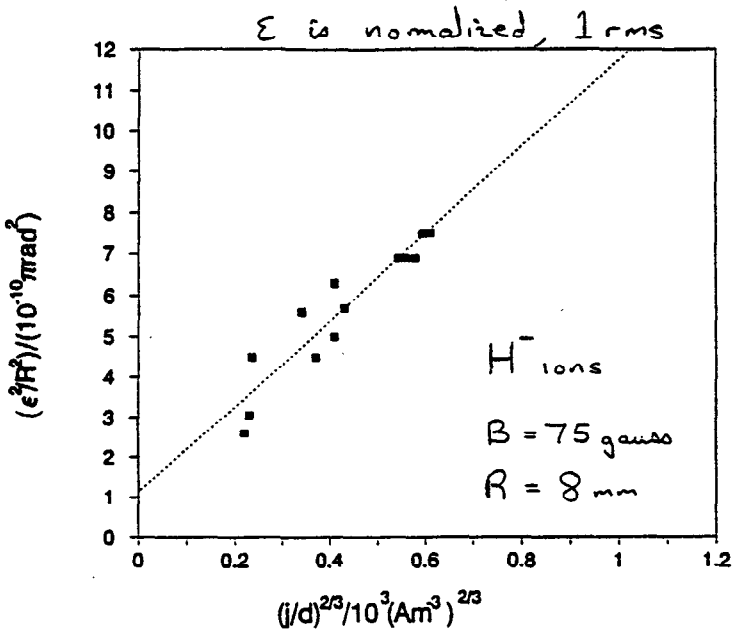

FIGURE 6

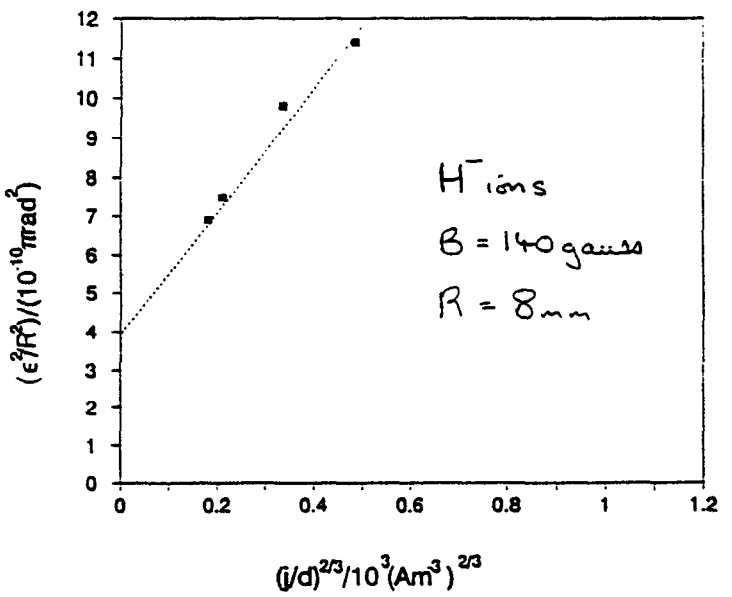

Current density = 100 mA/cm^2
Vext = 16KV
Vbeam = 90KV
Transported current = 220 mA

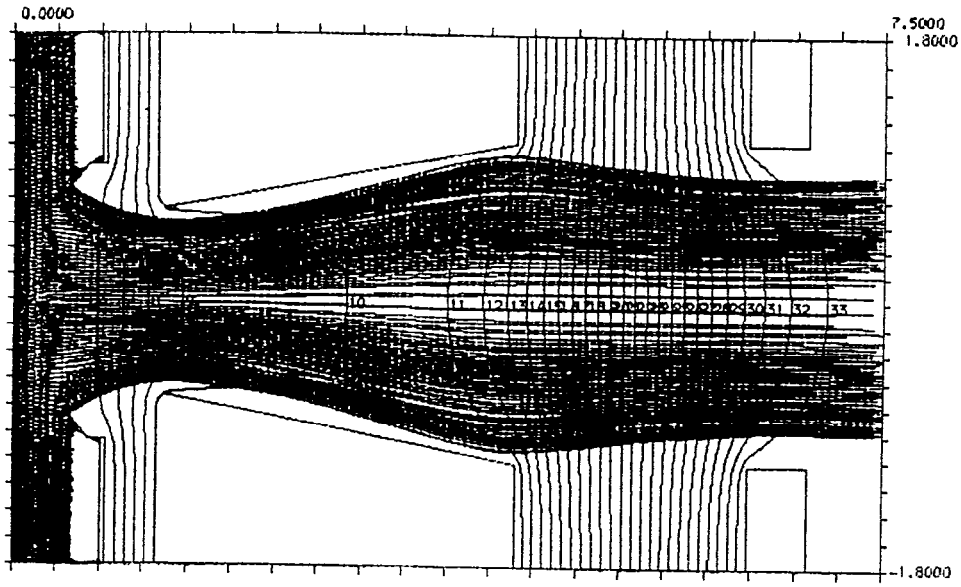

FIGURE 7

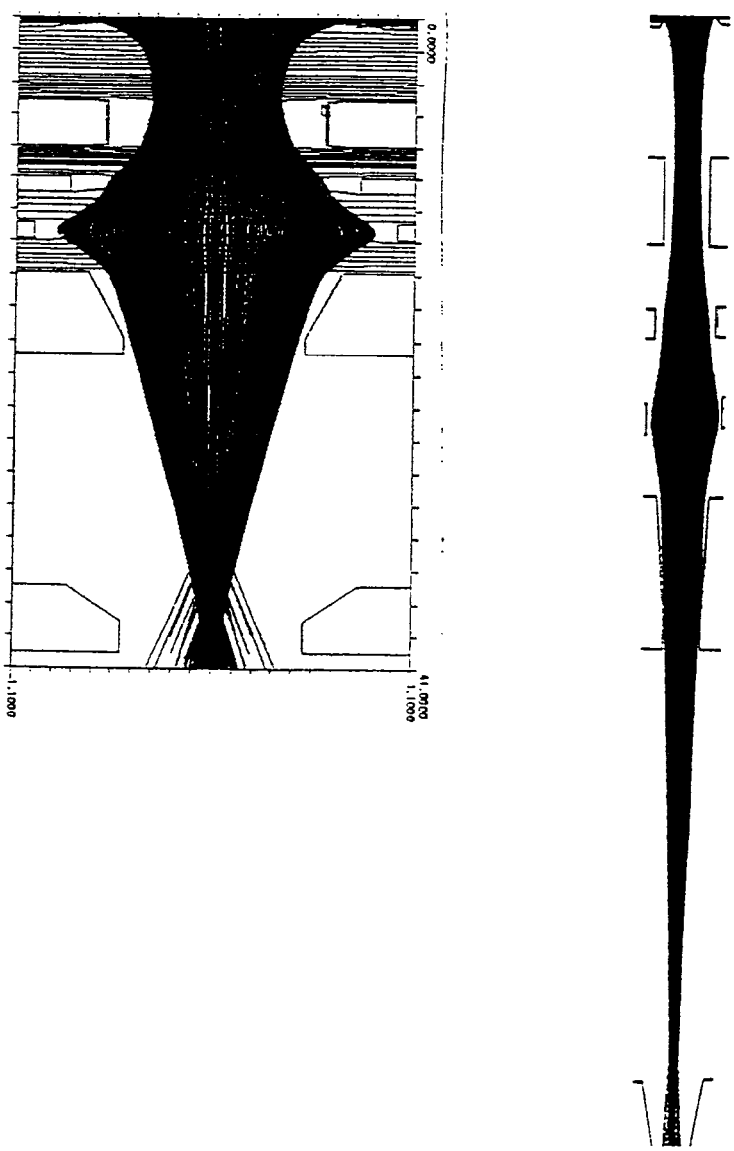

FIGURE 8

FUNNELING EXPERIENCE AT LOS ALAMOS: EXPERIMENTS AND DESIGNS*

Andrew J. Jason, Ken F. Johnson, and Subrata Nath
Los Alamos National Laboratory, Los Alamos, NM 87545

I. INTRODUCTION

Modern linacs are capable of accelerating high-current low-emittance beams input above a minimum energy. However, the ability of ion sources to produce such beams and the ability of low energy structures to accelerate high currents to this minimum energy is lacking. Funneling is a method of combining two or more beams to overcome this limitation. The process is simply illustrated in the sketch of Figure 1. It is very important to

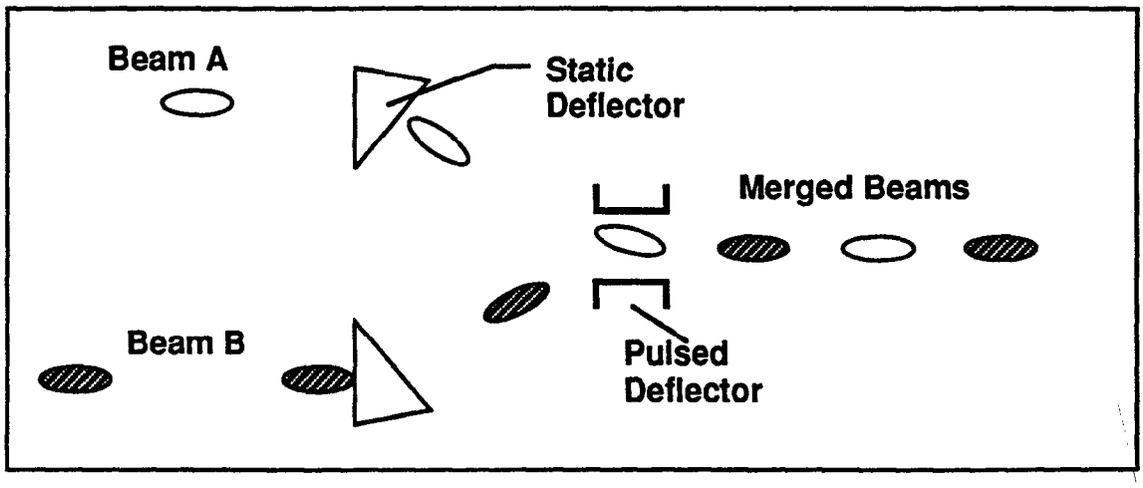

Figure 1. Schematic of basic funneling concept. Two separate beams, A and B, are merged by interleaving beam pulses to produce a beam of doubled frequency. The element labeled "pulsed deflector" must deflect alternate beam pulses in opposite directions.

note that the phase space of the two beams to be combined is not merged, in violation of Liouville's theorem. Instead beam micropulses from two sources are interleaved in time. It is also important to note that the micropulse frequency has doubled over that of the separate sources and must be accommodated by the linac following the funnel. Thus if the two funneled beams were accelerated by 400 MHz linacs, further acceleration must be done by an 800 MHz (or higher) linac. Other concepts are possible, but we concentrate on the one presented as the most feasible. The inclusion of further elements than shown in Figure 1 is needed for a practical device. In particular, the presence of both longitudinal and transverse focusing elements are crucial to device performance as are adequate diagnostic elements.

To attain the high peak currents needed for Los Alamos projects, such as the Ground Test Accelerator (GTA) [1], Accelerator Production of Tritium (APT) [2], Accelerator Transmutation of Waste (ATW) [3], or the 5 MW upgrade to the National Center for Neutron Research (NCNR) [4], a funneling scheme is needed. In these projects we consider funneling of two beams with peak currents of up to 100 mA and transverse emittances of the order of 0.02π cm mrad, rms normalized.

In this article we will discuss a funneling experiment done at Los Alamos and briefly mention a program at another institution that has demonstrated the concept. We will also discuss the funnel design for APT, now undergoing conceptual design.

*Work Supported by the US Department of Energy, Office of Defense Programs.

II. THE ATS FUNNEL EXPERIMENT

To demonstrate the funneling concept, a team at Los Alamos constructed a prototype device that explored the main issues inherent in the concept. Although we were certain of the *in principle* feasibility of funneling, it remained to be shown that, in practice, we could maintain emittance and steering control. Additionally, it was important to demonstrate the implementation of a pulsed deflector, which in this case took the form of a specialized rf cavity constructed to provide a deflecting mode by an rf field. We were also able to test the performance of several diagnostic systems that had recently been developed.

We had available a device called the Accelerator Test Stand (ATS) that could produce over 40 mA H^- peak current with an rms normalized emittance near 0.02π cm mrad at an energy of 5 MeV. The ATS consisted of a source, a radio-frequency quadrupole accelerator, and a drift tube linac (DTL). The funnel experiment was placed immediately downstream of the DTL.

A. Beam Characterization

Before going into detail about the equipment, we briefly discuss the diagnostics used to characterize the output beam during the various stages of the experiment. This is in contrast to the funnel permanent diagnostics that can measure only profile, position, and current. The diagnostics unit, known as the D-plate [5] is shown in Figure 2. At the

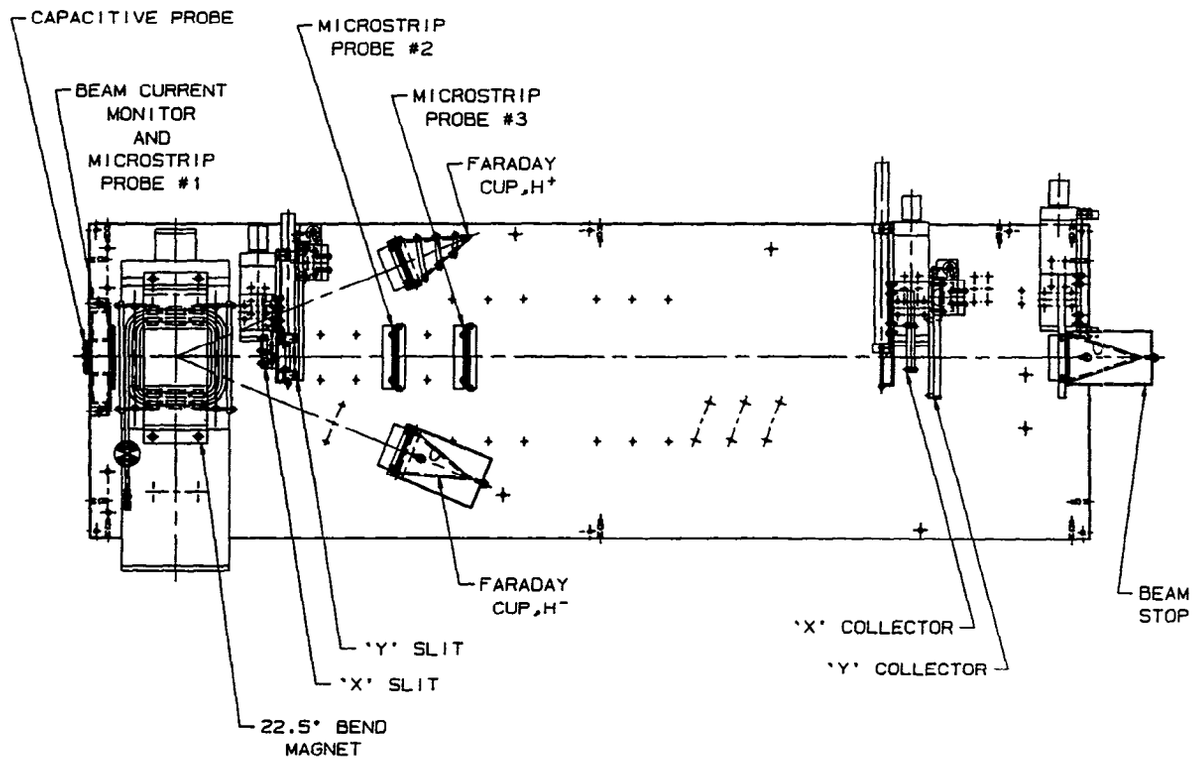

Figure 2. The GTA diagnostics plate. The length of the plate is 1.4 meters and beam direction is from left to right.

upsteam end of the D plate an additional assembly is mounted that defines the intersection of the Laser Induced Neutral Diagnostic Approach (LINDA) [6]. LINDA uses very fast 532-nm laser pulses to neutralize a longitudinal segment of a beam pulse. By timing across the length of the D plate, the energy and phase of the segment can be determined. Hence, the projection of the beam distribution onto longitudinal phase space can be fully determined. In a second mode, measurement of the transverse phase space is accomplished. Here,the intensity of a beam micropulse is reduced by a long partially-neutralizing laser pulse so that measurement diagnostics are not damaged and so that space charge forces do not affect the beam distribution during flight across the D plate. The transverse measurement is done by scanning a pair of slits (labeled x slit and y slit in Figure 2) across the beam to define position and a pair of segmented collector electrodes downstream to define angle. Thus the entire four-dimensional transverse phase space can be explored with a resolution of 0.1 mm by 800 μrad. The microstrip probes are short four-lobe directional-coupler pickups that determine beam position and are also used for timing. In both LINDA modes, unstripped beam is removed by a sweeping magnet shown in Figure 2.

As part of the diagnostics development program, sophisticated electronics modules were implemented and software developed for analysis of data. In particular a set of algorithms was established known as phase scans [7] to tune the linac and rf cavities. The resultant capabilities allowed complete characterization of beam from the linac and funnel.

- Distribution in longitudinal phase space - LINDA selects a narrow band of phase. Energy and phase values determined by timing signals from the microstrip probes. Signal is measured on a Faraday-cage beam stop.

- Distribution in transverse phase space - Slit and collector method defines angle and position of phase-space element. Collector signal measures relative intensity.

- Beam position - Difference measurements on the microstrip-probe lobes provides fast position information. The slit and collector measurements also gives centroid results on a slower time scale.

- Central energy and phase- Provided by microstrip-probe timing measurements.

- Beam current - Measured by a tape-wound-core toroid current monitor.

B. Funnel Beamline

The funnel beamline is shown in Figure 3. The transverse focusing elements, labeled Q1 through Q15 were samarium-colbalt permanent-magnet quadrupole lenses with a nominal 1 cm bore. They maintained a periodic focusing structure similar to that of the linac to prevent emittance growth by space-charge effects. Four of the quads were mounted on remotely moveable stages and hence could be used to steer the beam. Four permanent-magnet dipoles provided the (distributed) function of the static deflector shown in Figure 1. Additionally, Q13 and Q14 provided deflection since the beam passed through them off center. The first two bunchers R1 and R2 were resonant at 425 MHz while R3 and R4 were 850 MHz cavities. These cavities provided the necessary longitudinal focusing at the initial and final beam frequencies. The pulsed-deflector function was provided by R5, a 425 MHz resonant cavity with parallel plate geometry. Cavity deflection was approximately 36 mrad at a peak input power of 90 kW. The beamline configuration was determined by beam-dynamic considerations to minimize emittance growth and to optimize steering control. The beam line was mounted on four separate plates for staged commissioning and the entire assembly was placed in a cylindrical vacuum vessel.

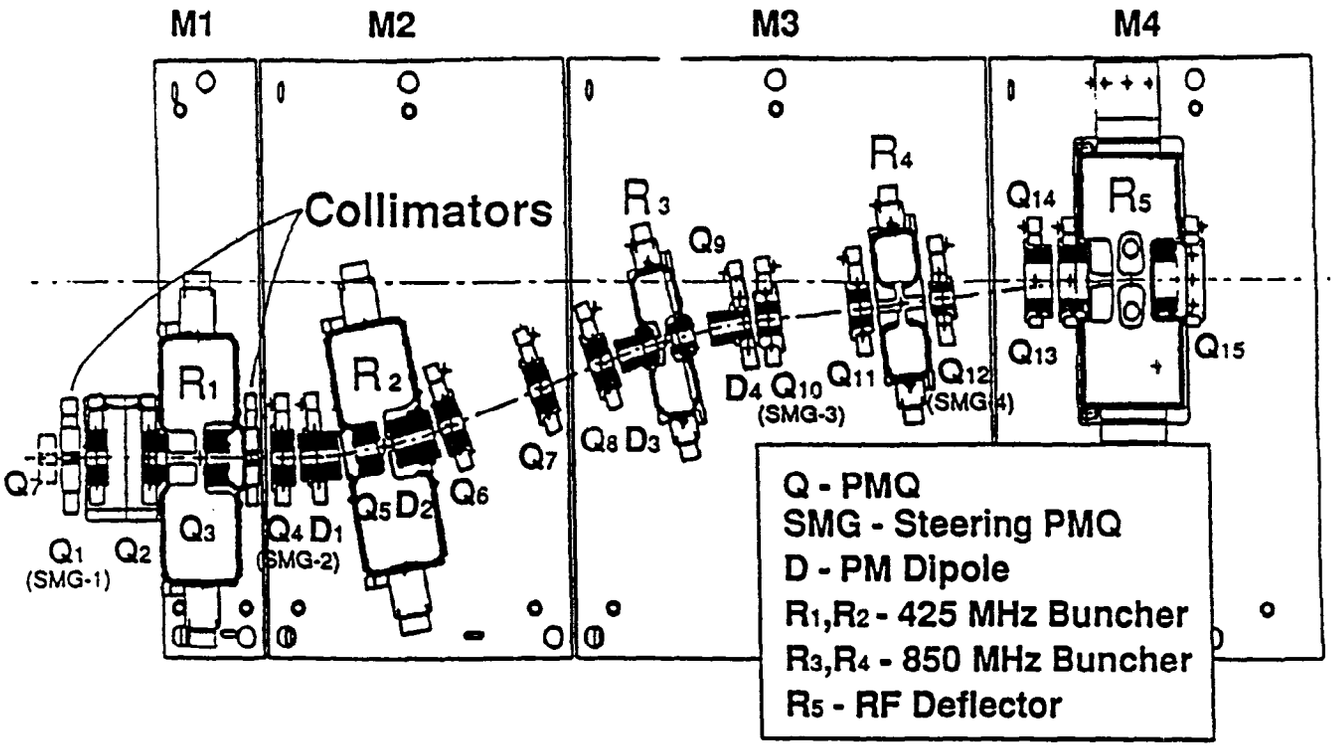

Figure 3. ATS funnel beamline schematic.

Several further permanent diagnostics, were incorporated into the funnel beamline. These consisted of eight microstrip probes to monitor position at critical points, approximately 90°in phase advance from the steering quads. Wire scanners at critical points in the beamline were used to measure the horizontal beam profile. A pair of toroid current monitors near the beamline extremes measured the transmission.

C. Experimental Results.

The experiment was staged in four parts. First the linac was tuned using the phase-scan technique and emittances were measured. Because the ATS transverse emittances had increased by a factor of two, collimators at the start of the M1 segment were used to define the transverse emittances to 0.021 cm mrad rms normalized. The beam from the M1 plate was then characterized to set the R1 cavity value and check the collimated emittances. Next M2 and M3 were installed with similar tests including the full repertoire of the D plate. The remaining three buncher cavities were set using LINDA and beam loading measurements. Emittances and deflections remained good. Finally, M4 was installed and the entire beamline tested at peak currents of from 25 to 40 mA.

All experimental goals were achieved. Dynamics calculations had shown negligible emittance growth and this was verified by the experiment to within the experimental error (about 7%). Transmission through the funnel was 100% and steering control was achieved. The rf deflection technique functioned as expected.

Some of the major experimental results [8] are shown in Figures 4 and 5. Figure 4 shows that the optimum value of cavity phase relative to the beam is 60°. In other parameterizations, longitudinal and transverse emittances varied weakly with cavity power. The emittances varied with rf phase but were minimized at the 60° phase setting. In Figure 5, the result of allowing the beam to drift without emittance control is shown. Substantial emittance growth is seen due to space-charge forces; with the control of the funnel beamline, little emittance growth is seen.

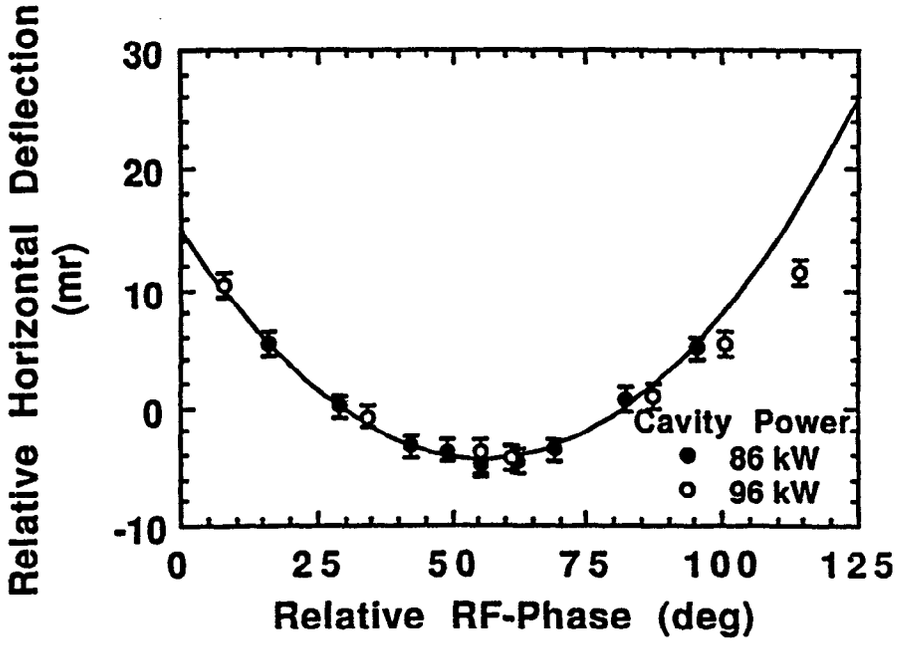

Fig 4. Horizontal deflection versus deflector cavity phase for two cavity powers. The optimum phase value was 60°. The deflection varied linearly with cavity power near the optimum values of phase and power.

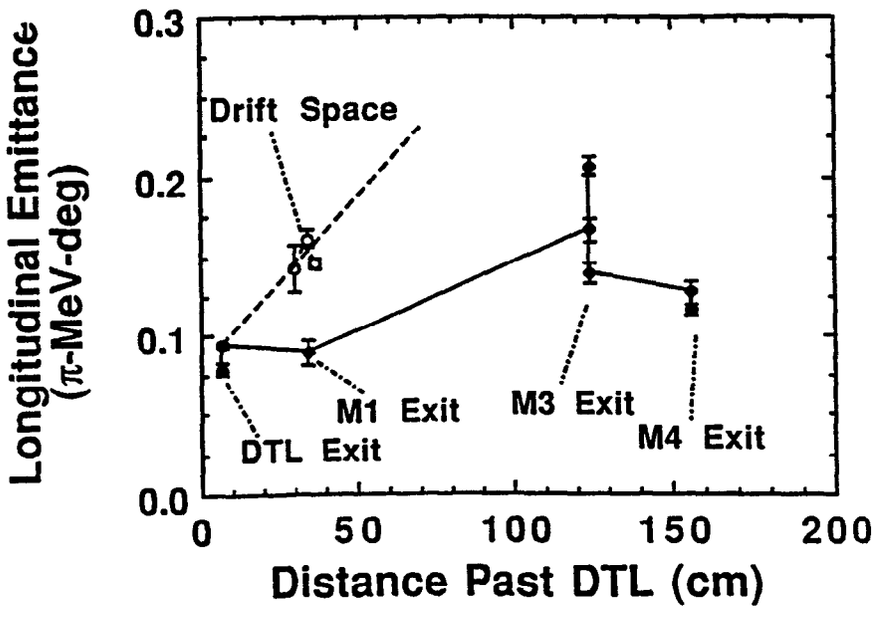

Fig 5. Longitudinal emittance versus distance from the DTL.

III. THE MCDONNEL DOUGLAS FUNNEL EXPERIMENT

The ATS funnel experiment was a good demonstration of beam control. However, to convince the many skeptics of the viability of funneling a two-beam experiment would be important. Such an experiment was done by the McDonnell Douglas Missile Systems Company. Though we have as of yet little details of their results, the experiment showed that two beam funneling at 2 MeV resulted in little emittance growth. The funnel design used is shown in Figure 6.

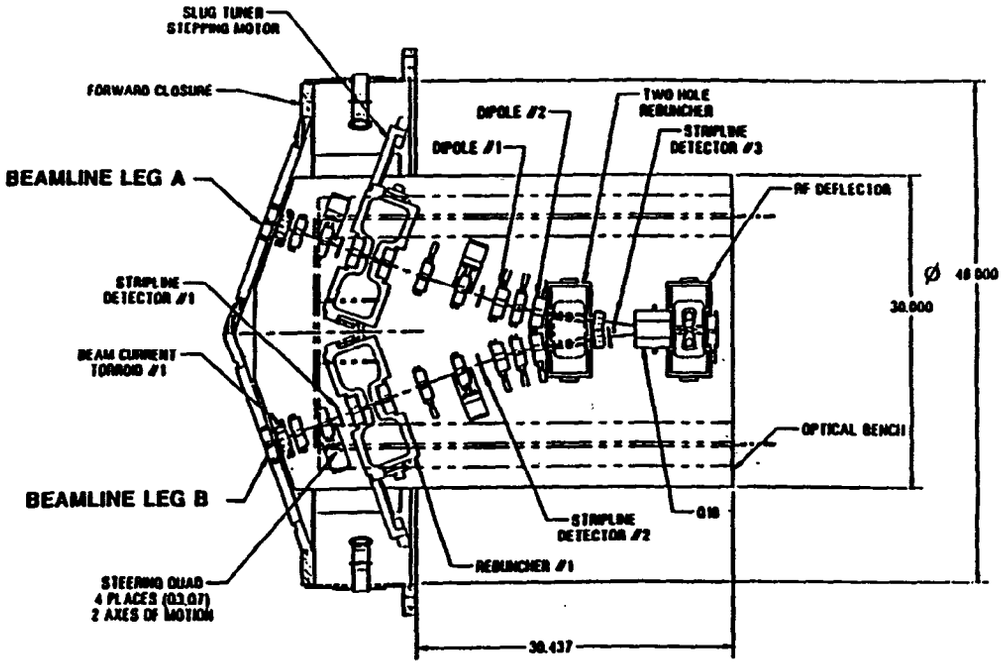

Figure 6. The McDonnell Douglas two-beam funnel beamline configuration.

One novel element in the design was the incorporation of a two-hole rebuncher. Note that in Figure 3, inclusion of a second leg would have resulted in an interference with buncher R4. The McDonnell Douglas experiment has resolved this and other engineering issues inherent in a two-beam funnel.

IV. APT FUNNEL DESIGN

Based on the results of these experiments, a conceptual design of a funnel for the APT project has been proposed and is highly applicable to the NCNR project. Here the funneling energy is 20 MeV with a current in each leg of 100 mA. The resultant 200 mA beam will be matched to a 700 MHz bridge-coupled drift tube linac (BCDTL). The linacs will run at 100% duty factor. The input beam has transverse and longitudinal rms normalized emittances of 0.023π cm mrad and 0.22π deg MeV respectively. The rms bunch length on entrance to the funnel is 5.5° of 350 MHz rf phase, to be reduced to 3.3° at the output for matching into the 700 MHz BCDTL. The proposed beamline is shown in Figure 7.

The concept is similar to the other designs discussed. The bends are distributed among focusing elements to avoid substantial dispersion effects. Novel buncher cavities and a high-field deflector cavity are being designed. Note that an angle between the entrance and exit beam is required to provide clearance between the low-energy linacs.

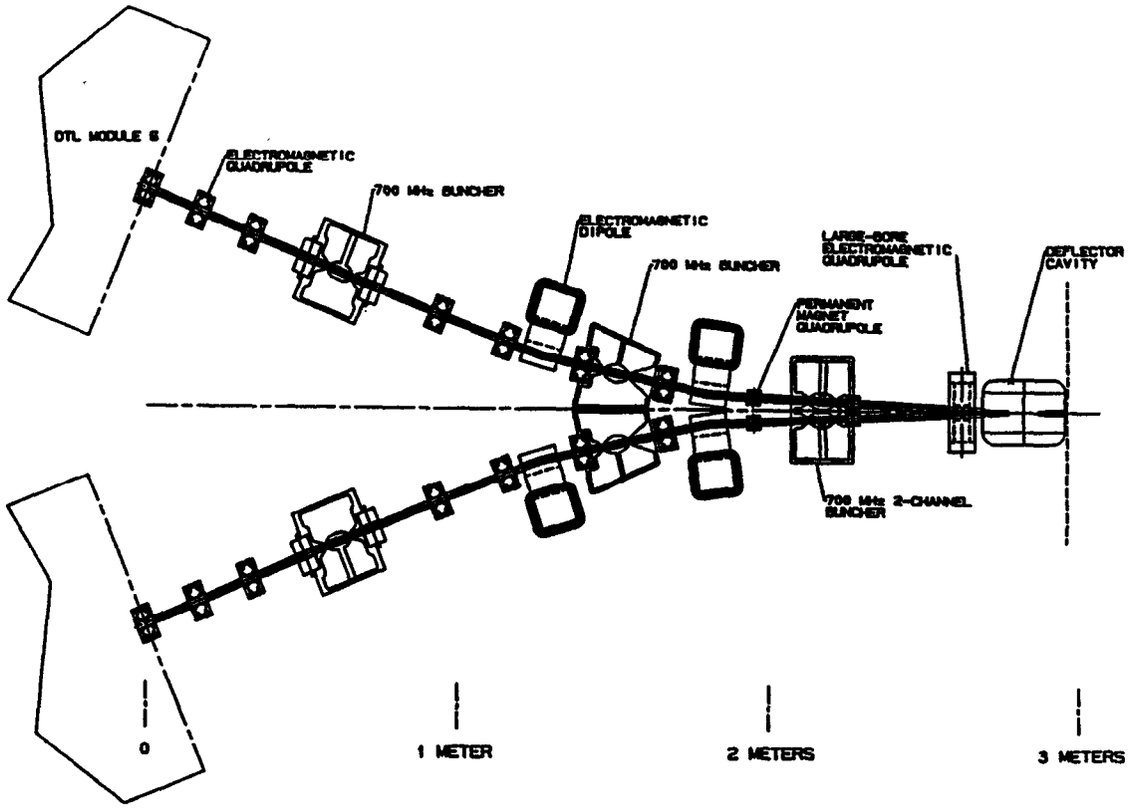

Figure 7. Layout of APT funnel conceptual design

A conceptual design for the deflector cavity has been proposed and the field distribution is shown in Figure 8. The deflecting voltage across the gap is 0.290 MV with a peak surface field of 1.3 Kilpatrick. The peak surface power density is some 60 W/cm^2, representing a challenge in thermal transfer. The two hole buncher cavity has undergone preliminary design using the axially symmetric code SUPERFISH and needs further work with a three-dimensional code. Similarly to the McDonnell Douglas experiment, it is a two-gap device. The peak surface power density is about 40 W/cm^2 and the peak electric field is 1.4 Kilpatrick.

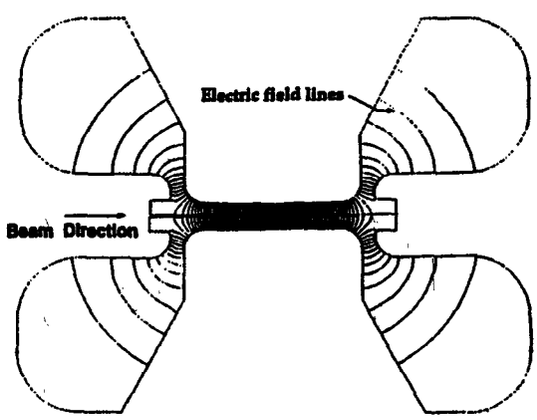

Figure 8. Sectional view of APT deflector cavity in the median deflecting plane. Electric field lines are shown. Each deflecting electrode is a rectangular prism wider in the diagram plane than in depth out of the plane. Otherwise, the diagram has azimuthal symmetry about a line perpendicular to the beam axis and in the plane of the diagram.

V. SUMMARY

It seems evident that the major physics issues in funneling have been experimentally resolved. It is necessary to match and confine the beam well both longitudinally and transversely in order to prevent emittance growth. This is a lesson learned from general studies in beam dynamics that tell us that emittance is conserved when matching is good and the beam is either entirely dominated by focusing forces (as in these designs) or dominated by space charge forces, as would happen for a large weakly focused beam. This is seen clearly in Figure 5 where a beam that has been freely allowed to expand experiences severe emittance growth. It still remains, however, to demonstrate further acceleration to the final higher energy. This would demonstrate that the funneling process has not coupled phase planes, e.g., through chromatic terms, so that beam emittances grow upon further transport.

Further challenges involve rf cavity design and resolution of other engineering aspects of funnels for efficient operation.. In particular, heat transfer from the cavities for CW operation is critical. Superconducting devices may be appropriate in this regard. Additionally, diagnostic devices and rf control are issues with respect to minimizing beam losses.

VII. REFERENCES

[1] O. R. Sander, *et al.*, "Commissioning the GTA," *Proc. 1992 Linear Accelerator Conference,* Ottowa, August, 1992, p. 535.

[2] "Accelerator and Beam Transport Design Information," APT Design Review, March 1993, Los Alamos Report LA-UR-93-980.

[3] G.P. Lawrence, "High-Power Proton Linac for Transmuting the Long-Lived Fission Products in Nuclear Waste," *Nucl. Instr. and Meth.*, **B56/57** (1991) p. 1000.

[4] A. J. Jason, "Overview of the NCNR Accelerator Studies," these proceedings.

[5] J. D. Gilpatrick, *et al.*, "GTA Beam Diagnostics for Experiments 1B through 2D," Los Alamos National Laboratory report LA-UR-91-341 (April 1991).

[6] W. V. Yuan, *et al.*, "Measurement of Longitudinal Phase Space in an Accelerated H^- Beam Using a Laser-Induced Neutralization Method," *Nucl. Instr. and Meth.*, **A239** (1993) p. 381.

[7] J. D. Gilpatrick, *et al.* "Synchronous Phase and Energy Measurement System for a 6.7 MeV H^- Beam," *Proc. 1988 Linear Accelerator Conference*, Newport News, October, 1988, p. 134.

[8] K. F. Johnson, *et al.*, "A Beam Funneling Demonstration: Experiment and Simulation, *Particle Accelerators*, 1992, **37-38**, p. 261.

[9] Private Communication, Bill Ard, McDonnell Douglas Missile Systems Company.

The submitted manuscript has been authored by a contractor of the U. S. Government under contract No. W-31-109-ENG-38. Accordingly, the U. S. Government retains a nonexclusive, royalty-free license to publish or reproduce the published form of this contribution, or allow others to do so, for U. S. Government purposes.

Conceptual Design for One Megawatt Spallation Neutron Source at Argonne*

Y. Cho, J. Bailey, B. Brown, F. Brumwell, J. Carpenter, K. Crawford, D. Horan, D. Jerng, R. Kleb, A. Knox, R. Kustom, E. Lessner, D. McGhee, F. Mills, H. Moe, R. Nielsen, C. Potts, A. Rauchas, and K. Thompson
Argonne National Laboratory, Argonne, IL 60439 U.S.A.

Abstract

A feasibility study of a spallation neutron source based on a rapid-cycling synchrotron which delivers a proton beam of 2 GeV in energy and 0.5 mA time-averaged current at a 30 Hz repetition rate is presented. The lattice consists of 90-degree phase advance FODO cells with dispersion-free straight sections, and has a three-fold symmetry. The ring magnet system will be energized by 20 Hz and 60 Hz resonant circuits to decrease the dB/dt during the acceleration cycle. This lowers the peak acceleration voltage requirement to 130 kV. The single turn extraction system will be used to extract the beam alternatively to two target stations. The first station will operate at 10 Hz for research using long wavelength neutrons, and the second station will use the remaining pulses, collectively, providing 36 neutron beams. The 400 MeV negative-hydrogen-ion injector linac consists of an ion source, rf quadrupole, matching section, 100 MeV drift-tube linac, and a 300 MeV coupled-cavity linac.

I. INTRODUCTION

During the past two years there have been several studies on accelerator-based pulsed spallation sources in Europe, the United States, and elsewhere. Studies in Europe include a 5 MW source called the European Spallation Source (ESS) [1] and the Austron Project [2] for the eastern European countries. The ESS concept consists of an 800 MeV linac and three pulse compressor rings capable of accumulating and compressing pulse length to the order of 1 μs and delivering over 2 mA of time-averaged current in each ring for a total of 6.25 mA. Studies in the United States include Los Alamos National Laboratory's LANSCE-II and Argonne National Laboratory's IPNS (Intense Pulsed Neutron Source) Upgrade. These two U.S. studies center around sources with 1 MW of beam power.

For over a dozen years the IPNS facility has been providing research opportunities for the neutron scattering research community. The IPNS facility consists of a 50 MeV negative-hydrogen-ion linac and a 30 Hz rapid-cycling synchrotron (RCS) which accelerates 50 MeV injected beams to 500 MeV. The RCS accelerates 3×10^{12} protons per pulse at a repetition rate of 30 Hz, resulting in a time-averaged current of some 15 μA. The 1 MW study described here is for upgrading the IPNS system.

With respect to the choice of the accelerator's peak energy, several studies have shown that the neutron yield is proportional to beam power almost independent of beam energy up to several GeV beam energy [1]. This fact provides an opportunity to compare the lower-energy/higher-current case with a higher-energy/lower-current machine. That is to say, for a 1 MW facility, the choice of beam energy can be traded with choice of the beam current.

*Work supported by U. S. Department of Energy, Office of Basic Energy Sciences under Contract no. W-31-109-ENG-38.

A decision was made to initially study a higher-energy/lower-current configuration of the accelerator system with a majority of the acceleration taking place in a circular machine. The other study option was to perform all acceleration in a linac with a circular machine acting as a pulse compressor. Since the cost of a high energy linac is relatively expensive, the latter scheme usually tends to have lower energy and high current. The decision to accelerate in a circular machine was based on past experiences with a high intensity circular proton accelerator; that beam loss always occurs during injection and capture processes and not during acceleration or extraction processes. Furthermore, the lost particles create residual radiation around the accelerator components. This residual radiation can be minimized by injecting lower energy protons and handling fewer particles.

A. Choice of Repetition Rate

For a given time-averaged current, a higher repetition rate would provide an easier condition by lowering the number of particles to be accelerated per pulse. On the other hand, a higher repetition rate necessitates higher acceleration voltage. Repetition rates commonly used in this kind of setting range from 30 Hz at IPNS to 50 Hz at the ISIS facility in the U.K. Discussions with the user communities indicate that many experimental programs require lower repetition rates in order to avoid the so called "frame overlap" problem, therefore a repetition rate of 30 Hz was chosen. In order to facilitate those experiments requiring an even lower repetition rate, it is proposed to have two target stations: one receiving a 10-Hz beam and the other using the remainder of the pulses.

B. Choice of Machine Type

RCS technology is a mature technology. There are several operating proton machines of this type. Since the plan is to inject a lower energy beam and accelerate to a higher energy, using a proven technology provides the advantage of reliability. Furthermore, IPNS personnel have accumulated over 10 years of experience in operating a 30 Hz RCS. If the desired repetition rate was much higher than 30 Hz, another type of machine, such as the FFAG (Fixed Field Alternating Gradient), would be appropriate.

C. Use of Existing Infra-structure

The IPNS facility occupies a small fraction of the former ZGS (Zero Gradient Synchrotron) complex area, and nearly all of about 500k square ft. of space is available for the 1 MW upgrade of IPNS. The ZGS ring building, which is heavily shielded, can accommodate a synchrotron 200 m in circumference, and several of the former ZGS experimental area buildings can house the two target stations mentioned earlier.

II. SYNCHROTRON

A. Lattice Type

The FODO-type lattice was chosen for simplicity and flexibility. A 90° phase advance was chosen to facilitate a missing-magnet-scheme dispersion suppression for the straight section area, and to provide relatively high transition gamma. Lattice functions are shown in Figure 1, which shows the normal cells, dispersion suppressor cell, and long straight section cells which are missing-magnet normal cells. After having decided on the normal cells and the dispersion cells, the straight section cells can be added or

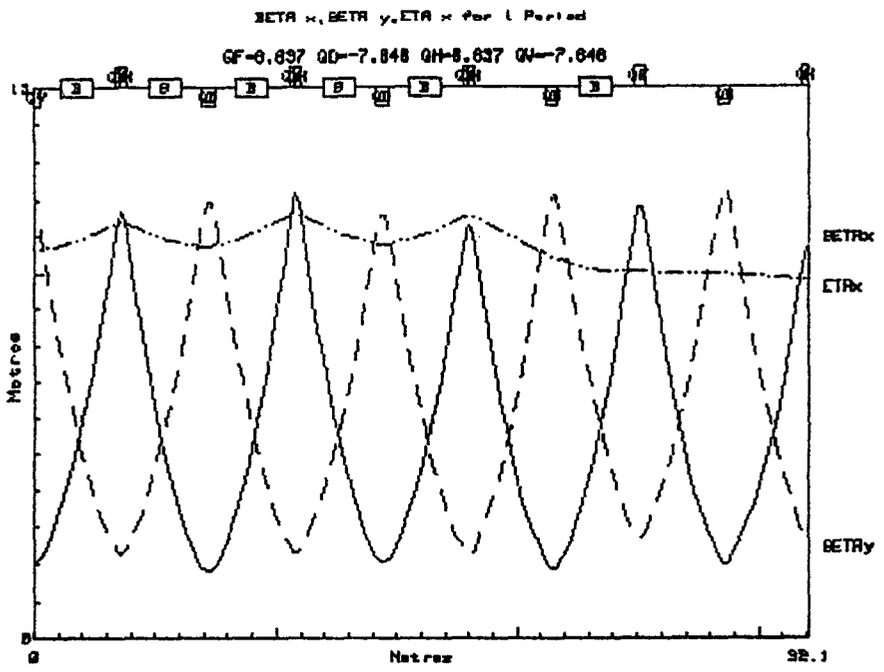

Figure 1. Lattice Functions (see text for details)

removed as the length of the straight section requires. (One half of the super-period is shown in the figure with the dispersion function displaced by 10 m for clarity.) For example, around the 1 MHz radio-frequency range, a typical cavity system provides about 10 kV rf voltage per meter of cavity. Thus if the required rf voltage is 120 kV, then there should be some 12 m of straight sections for the rf system.[3] A half-section diagram of the rf cavity is shown in Figure 2.

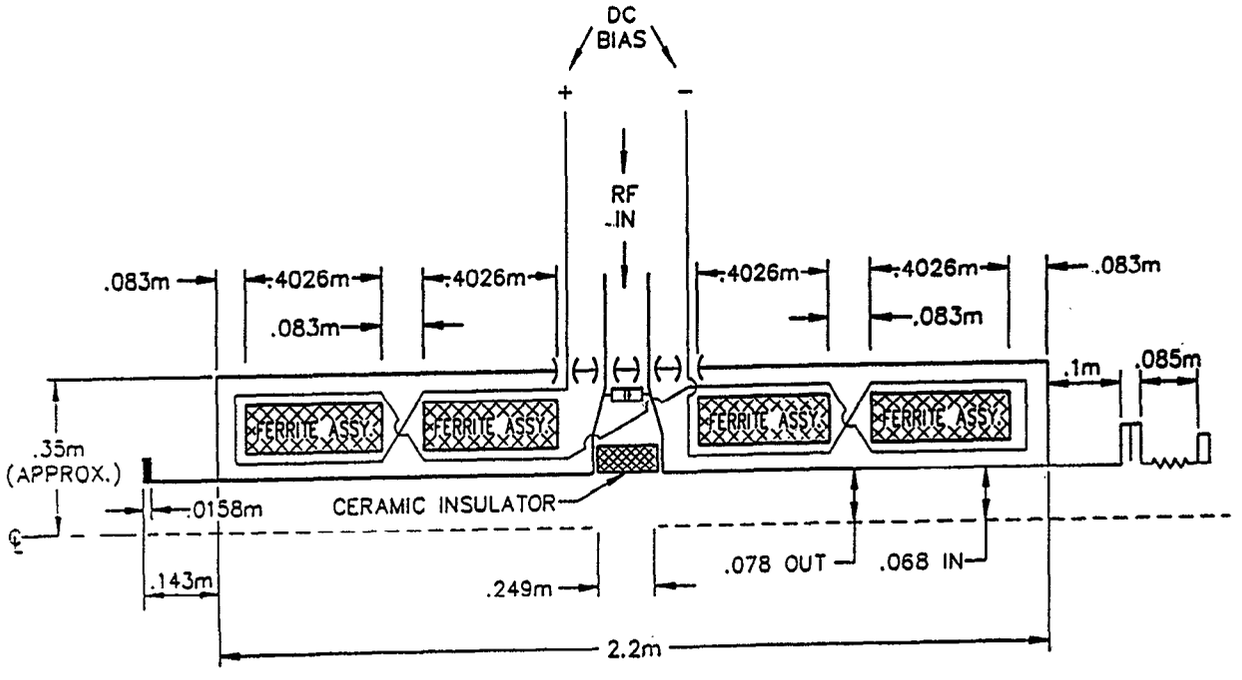

Figure 2. rf Cavity Half-section

B. Choice of B(t) and dB/dt

The lattice shown in Figure 1 can accelerate protons up to 2.2 GeV if the maximum magnetic field is about 1.5 T, which is commonly used value for this type of machine. It was decided to design a 2.2 GeV machine and to operate at 2 GeV for reliability reasons. The space charge limit discussed below implies the injection energy of the machine would be 400 MeV; this corresponds to the injection field of 0.417 T. A 30-Hz sinusoidal excitation of the ring magnets would require 180 kV of peak rf voltage. However, utilizing two (one 20-Hz and another 60-Hz) resonant power supplies for energizing the ring magnet with 20-Hz excitation and 60 Hz de-excitation enables the peak voltages to be lowered to some 120 kV.[4] The ring magnet excitation current and voltage waveforms are shown in Figure 3.

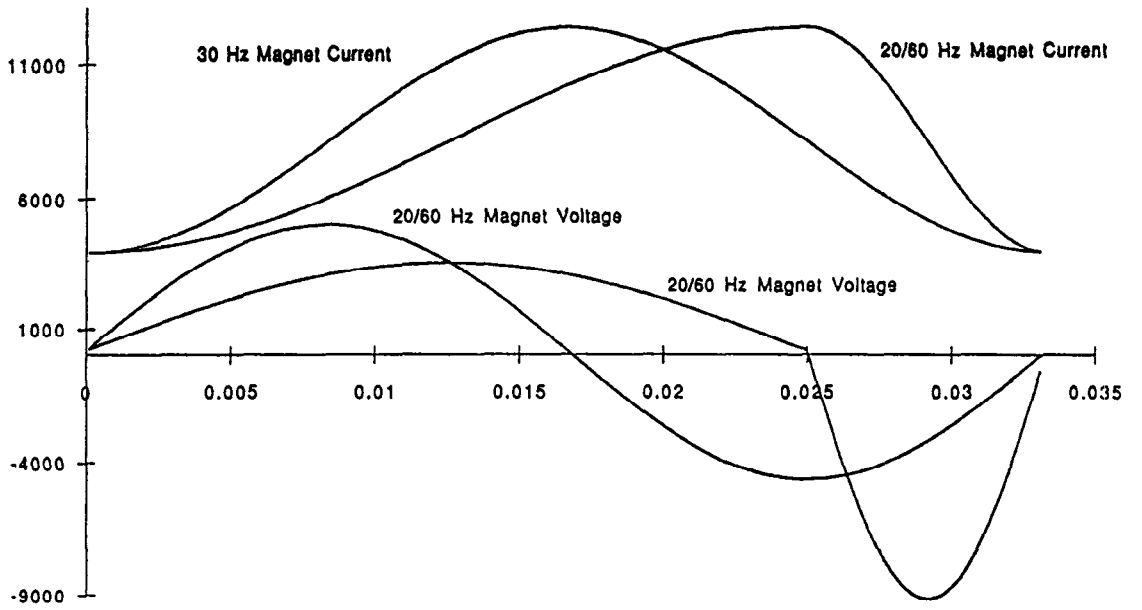

Figure 3. Ring Magnet Current and Voltage Waveforms

C. Space Charge Limit and Injection Energy

Typical transverse phase space acceptance of this type of accelerator varies from 200 π-mm-mr to 500 π-mm-mr. An iterative study using the beta-function shown in Figure 1 and reasonable apertures of quadrupole magnets showed that a choice of 375 π-mm-mr in both transverse planes is about optimum for the quadrupole magnet designs. The number of protons per pulse required to make a 0.5 mA time-averaged current is 1.04 x10^{14}. If the injection energy is 400 MeV, the acceptance of 375 π-mm-mr in both planes together with an assumption that the allowed space charge tune shift is 0.2, gives about 1.4 x 10^{14} protons per pulse. Therefore, 400 MeV was chosen as the injection energy. A cross-section of the ceramic vacuum chamber inside the quadrupole and sextupole magnet apertures is shown in Figure 4. The figure includes the beam envelopes in the quadrupoles and also shows the 5 mm allowance between the vacuum chamber and magnet pole tips.

D. Injection

In order to facilitate a multi-turn acceptance-filling injection into the synchrotron, a phase-space-painting

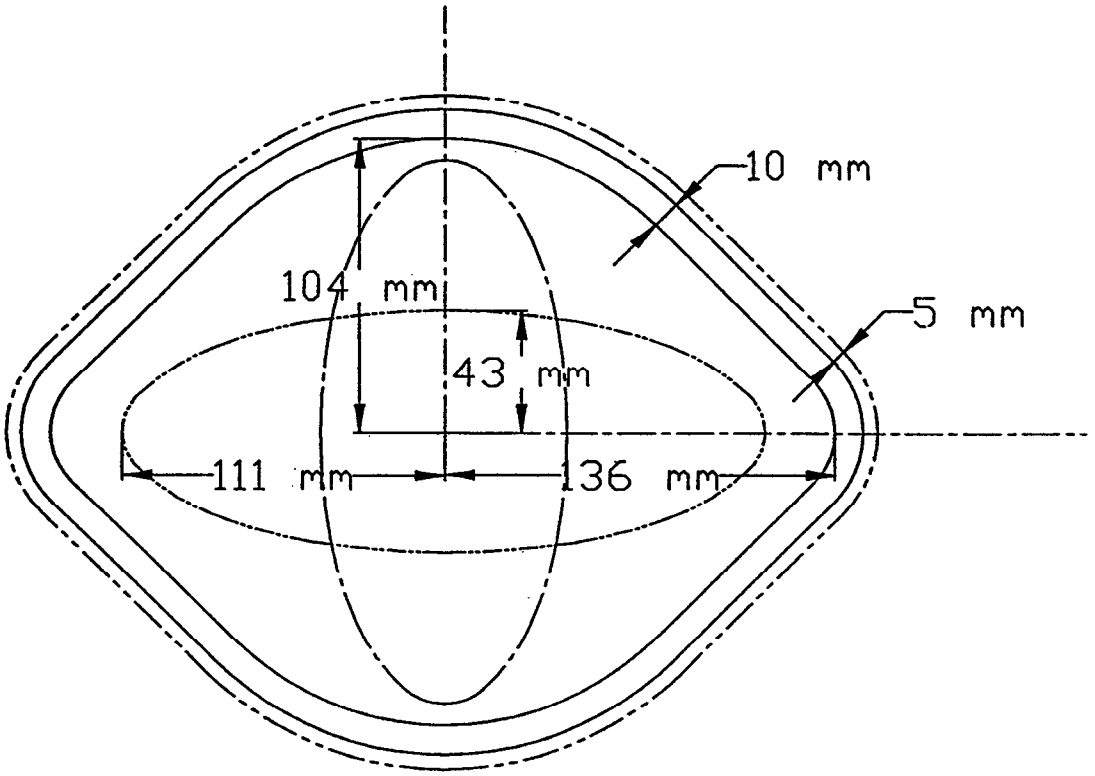

Figure 4. Vacuum Chamber Cross-section

scheme is used which incorporates a negative-hydrogen-ion beam and a "stripper foil" system. The stripper foil system "strips" the electrons and changes the negative-hydrogen ions to positive-hydrogen ions (charge exchange injection).

III. INJECTOR

A. Injector Requirements

The negative-hydrogen-ion source must deliver 1.04 x 10^{19} per pulse at a 30 Hz rate to provide 0.5 mA of the time-averaged current. This corresponds to a pulse current of 33 mA for a pulse width of 0.5 msec. If the available pulse current is 50 mA, then the pulse width could be 0.33 msec. Another implication here is that for a revolution period of 1 μs, 300 to 500 turns need to be injected. The space charge limit requires that the final energy of the injector should be approximately 400 MeV.

B. Injector Configuration

The injector system consists of the negative-hydrogen-ion source, a 2 MeV rf quadrupole, a beam chopper to facilitate loss-free capture, a 100 MeV drift-tube linac, and a 300 MeV coupled-cavity linac. It is contemplated that the frequency for both the rf quadrupole and the drift-tube linac will be 400 MHz and 1200 MHz for the coupled-cavity linac. This choice was made to take advantage of recent progress in linac technology from the SSC Laboratory and Fermilab.

IV. SUMMARY

Table 1 shows the parameters of the accelerator system, and the facility layout is shown in Figure 5. Figure 5 also shows the existing IPNS facility as well as the proposed two target stations. Further R&D continues on various hardware design studies, together with simulation studies of injection and capture. [3] The conclusion of the study team is that the RCS technology is appropriate and practical for a 1-MW pulsed spallation source.

Table 1 Major Parameters

Circumference	192.6	(m)	Horizontal Tune	7.28	
Injection Energy	400	(MeV)	Vertical Tune	6.21	
Maximum Energy	2.2	(GeV)	Transition Gamma	6.04	
Nominal Energy	2.0	(GeV)	Peak Rf Voltage	120	(kV)
No. of Protons/pulse	1×10^{14}		Harmonic Number	1	
Average Current	0.5	(mA)	rf Frequency @Injection	1.103	(MHz)
Injection Field	0.417	(T)	rf Frequency @Extraction	1.456	(MHz)
Extraction Field	1.341	(T)	Number of Cavities	6	
Bending Magnet Length	1.3	(m)	Maximum Beam Current @Extraction	61	(A)
Quadrupole Max. Gradient	8.6	(T/m)	Average Power Delivered to Beam	900	(kW)
Quadrupole Length	0.5	(m)	Number of Extraction Ports	2	
			Number of Target Stations	2	

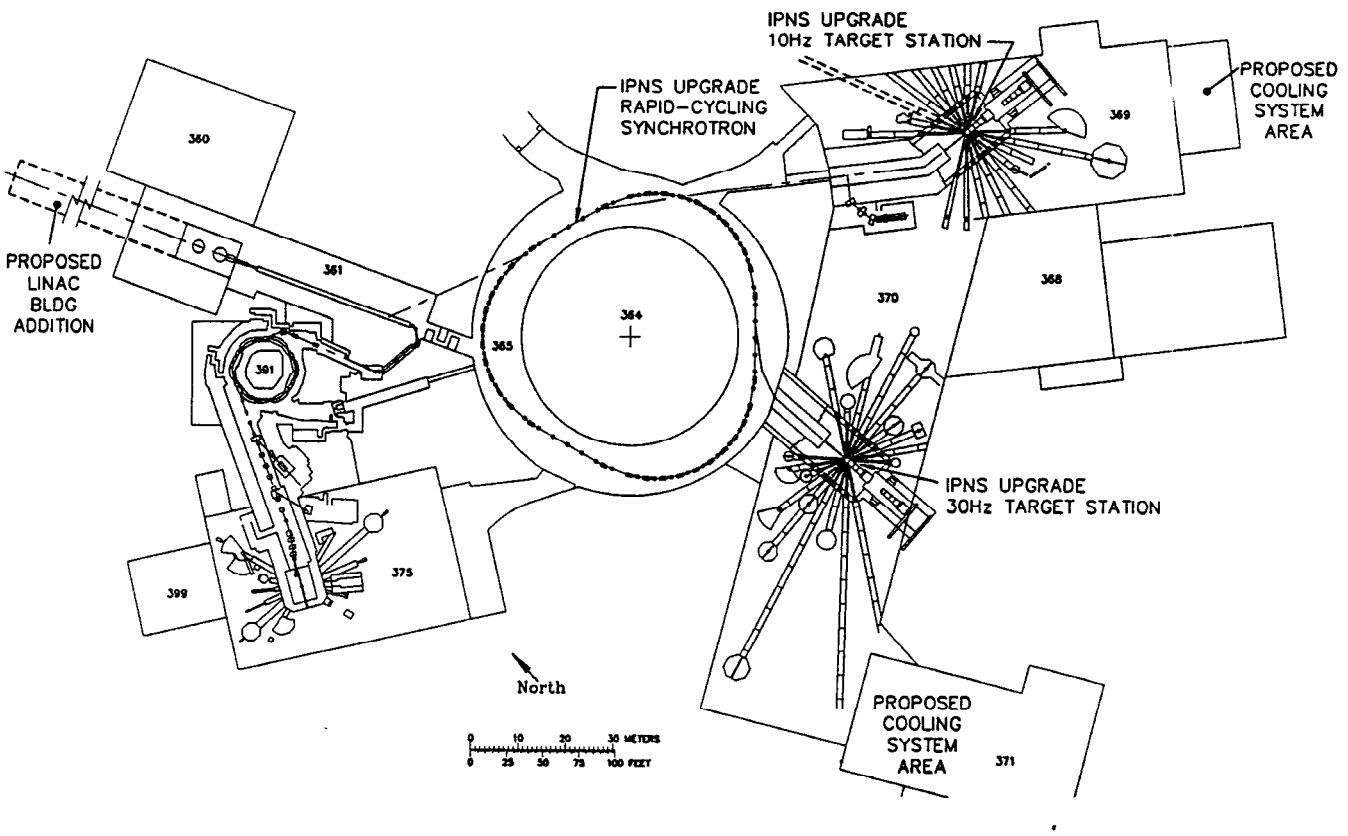

Figure 5. IPNS Upgrade Facility Layout

V. REFERENCES

[1] S. Martin and C. W. Planner, "Accelerator Design Parameters for a European Pulsed Spallation Neutron Source," 3rd European Particle Accelerator Conference, pp. 435-437 (1992).

[2] "AUSTRON" Machine Study Team, "A Pulsed Spallation Source in Central Europe," 3rd European Particle Accelerator Conference, pp. 432-434 (1992).

[3] R. Kustom, "RF System for the IPNS Upgrade", these proceedings.

[4] D. McGhee, "Power Supply Design for the IPNS Upgrade", these proceedings.

[5] E. S. Lessner and Y. Cho, "RF Capture Studies for Injection into a Synchrotron", to be published in the Proceedings of the 1993 Particle Accelerator Conference, Washington, D.C., May, 1993.

IPNS-UPGRADE RF System Design*

R. L. Kustom and D. Horan

The submitted manuscript has been authored by a contractor of the U. S. Government under contract No. W-31-109-ENG-38. Accordingly, the U. S. Government retains a nonexclusive, royalty-free license to publish or reproduce the published form of this contribution, or allow others to do so, for U. S. Government purposes.

I. Introduction

The RF System for the rapid cycling synchrotron proposed for the IPNS-Upgrade design must generate a minimum of 116.8 kV to be able to operate at a phase stable angle of 45° at B_{max} and must deliver an average power to the beam of 900 kW. The system is designed to provide this voltage and power with six double-ended cavities. The amplifiers are push-pull, cathode-follower types to handle the beam loading. The amplifiers and cavities might be split into single-ended types depending on computer calculations which are now being done. If so, however, the total amount of ferrite and the number of power tubes will remain the same. The RF system design parameters are listed in Table 1.

II. Cavity Design

Each cavity is designed to be 2.6 meters long from flange face to flange face and to have a single accelerating gap in the middle. A cross-sectional drawing of the cavity is shown in Fig. 1. There are four ferrite assemblies in each cavity, two on each side of the accelerating gap. Each ferrite assembly consists of a stack of 14 Philips 8C12 ferrite rings and water cooled copper disks as shown in

---

* Work supported by U.S. Department of Energy, Office of Basic Energy Sciences under Contract No. W-31-109-ENG-38.

Fig. 2. The ferrite rings are the same material and roughly the same size as was used in the GSI Heavy Ion Synchrotron[1]. The copper and ferrite disks in each assembly are stacked together and tightly clamped in the axial direction to provide good thermal contact between the copper plates and ferrite disks.

The four ferrite assemblies are wound with six turns of busbar to provide the dc bias field. The bias winding direction is reversed in each assembly providing the typical "figure-8" configuration[2] so that the induced RF voltage is cancelled at the input terminals of the bias windings. The physical parameters for the cavity are listed in Table 2.

The frequency varies from 1.1013 Mhz at injection to 1.4562 Mhz at extraction. The cavity resonance is adjusted by varying the incremental permeability of the ferrite from 120 to 67. These operating points are shown on the graph in Fig. 3. The bias current varies from 47.1 amperes to 77.6 amperes to achieve the change in incremental permeability.

The cavity gap is loaded with 600 pF of low-inductance capacitors to resonate with the cavity inductance. The capacitors will be mounted in conducting strips around the accelerator gap in the configuration suggested by M. Plotkin[3]. This technique achieves a coupling impedance, Z/n, of 1 to 10 ohms.

III. Power Amplifier

The power amplifier is a push-pull design as shown in Fig. 4. This configuration has been studied by Hardek[4] and Puglisi[5]. The output impedance of this device is extremely low over a fairly broad frequency range and will compensate for beam

loading due to the large circulating beam currents. There could be a problem with maintaining the proper bias on tubes in the push-pull configuration as indicated by Puglisi. This is being studied on the computer and, if necessary under our beam conditions, the cavities and amplifiers will be split into the single-ended configuration.

The RF output of the power amplifier is connected to the cavity by copper straps with blocking capacitors. The cavity and amplifier are designed to generate 23.1 kilovolts at $\dot{B}_{max}$. The plate voltage on the tubes is 25.0 kilovolts. The peak circulating beam current during acceleration is 61 amperes. In addition, the peak power at $\dot{B}_{max}$ into the ferrite is 27.1 kW, with 13.5 kW into the copper walls and cooling plates. The peak power delivered to the beam is 305.3 kW. The power to compensate for cavity losses adds as much as 19 to 20 amperes of plate current in the tube. In order to match these requirements, each cavity is supplied by a push-pull, cathode-follower amplifier using EIMAC 8973 tubes. The average power supplied by each tube is given by

$$\langle P \rangle = \frac{3}{4}\left\{\frac{1}{\pi}\int_0^{\pi} \sin^2\Theta \, d\Theta\right\}$$

where the 3/4 factor is a result of operating the synchrotron magnets with a 20 Hz acceleration cycle and a 60 Hz reset cycle. The average power from the amplifier under normal operation is 162.2 kW with an average beam current on

target of 500 μa and the cavities operating at 19.45 kilovolts. The parameters for maximum operating conditions are listed in Table 3 for the cavity and Table 4 for the amplifier.

1. K. Kasper and M. Emmerling, "Development of the RF Accelerating System for the GSI Heavy Ion Synchrotron", IEEE Trans on Nuclear Science, Vol NS-28, No 3, June, 1981, 3028.

2. C. Fougeron, et al., "RF System for "MIMAS"", IEEE Trans on Nuclear Science, Vol NS-28, No3, June, 1981, 3028.

3. M. Plotkin, "Isabelle Cavity Gap Assemblies", IEEE Trans on Nuclear Science, Vol NS-28, No 3, June, 1981, 2752.

4. Thomas W. Hardek and William E. Chyna, 1979, "Common Anode Amplifier Development," IEEE Trans. on Nuclear Science NS-26 No. 3 June.

5. A. Luccio and M. Puglisi, 1981, "Behavior of Single-Ended vs. Push-Pull Amplifiers for the Accelerating Systems of High-Current Beam Storage Rings," Particle Accelerator 11.

Table 1
RF System Design Parameters

RF Frequency @ Injection, MHz	1.1013
RF Frequency @ $\dot{B}_{max}$, MHz	1.3791
RF Frequency @ Extraction, MHz	1.4562
Maximum voltage per turn, kV	116.8
Maximum Beam Current @ Extraction, A	61.03
Average Power Delivered to Beam from RF, kW	900.0
$\sin \phi_s$ @ $\dot{B}_{max}$	0.707
Maximum Accelerating Voltage per Turn @ $\dot{B}_{max}$, kV	83.55

Table 2

Physical Parameters of Cavity

Physical Length of Cavity, flange-to-flange, m	2.6
Inside Length of Cavity, m	2.2
Length of Accelerating gap, m	.04
Outer Radius of Cavity (inside dimension), m	.35
Inner/ Outer Radii of Beam Tube, m	0.068/0.078
Type of Ferrite	Philips 8C12
μQ of Ferrite	6000
Ferrite Ring Dimensions:	
Inner Radius, m	0.125
Outer Radius, m	0.250
Thickness, m	0.0254
Type of Cavity	Double Ended, Single Gap
Number of Ferrite Rings	56
Volume of Ferrite/Cavity, m^3	0.21
Thickness of Copper Cooling Plates, m	0.003

Table 3

Operating Characteristics of Cavity for Nominal Operation

Maximum Flux Density, T	0.01264
Maximum Voltage per Cavity, kV	19.45
Peak Power in Ferrite, kW/m^3	91.8
Average Power in Ferrite, kW/m^3	34.4
Average Power in Ferrite per Cavity, kW	7.2
Peak Power to Copper, kW	9.56
Average Power to Copper, kW	3.6

Table 4

Amplifier Characteristics

Type	Push-Pull Cathode Follower
Tube Types	Eimac 8973
Plate Voltage, kV	25.0
Maximum Gap Voltage, kV	23.1
Peak Plate Current to Beam, A	61.0
Peak Plate Current from Amplifier, A	-80.0
Peak Power to Beam per Amplifier, kW	305.3
Peak Power to Ferrite per Cavity, kW	27.1
Peak Power to Copper per Cavity, kW	13.5
Average Power from Amplifier, kW	162.2

Figure 1

CAVITY DESIGN

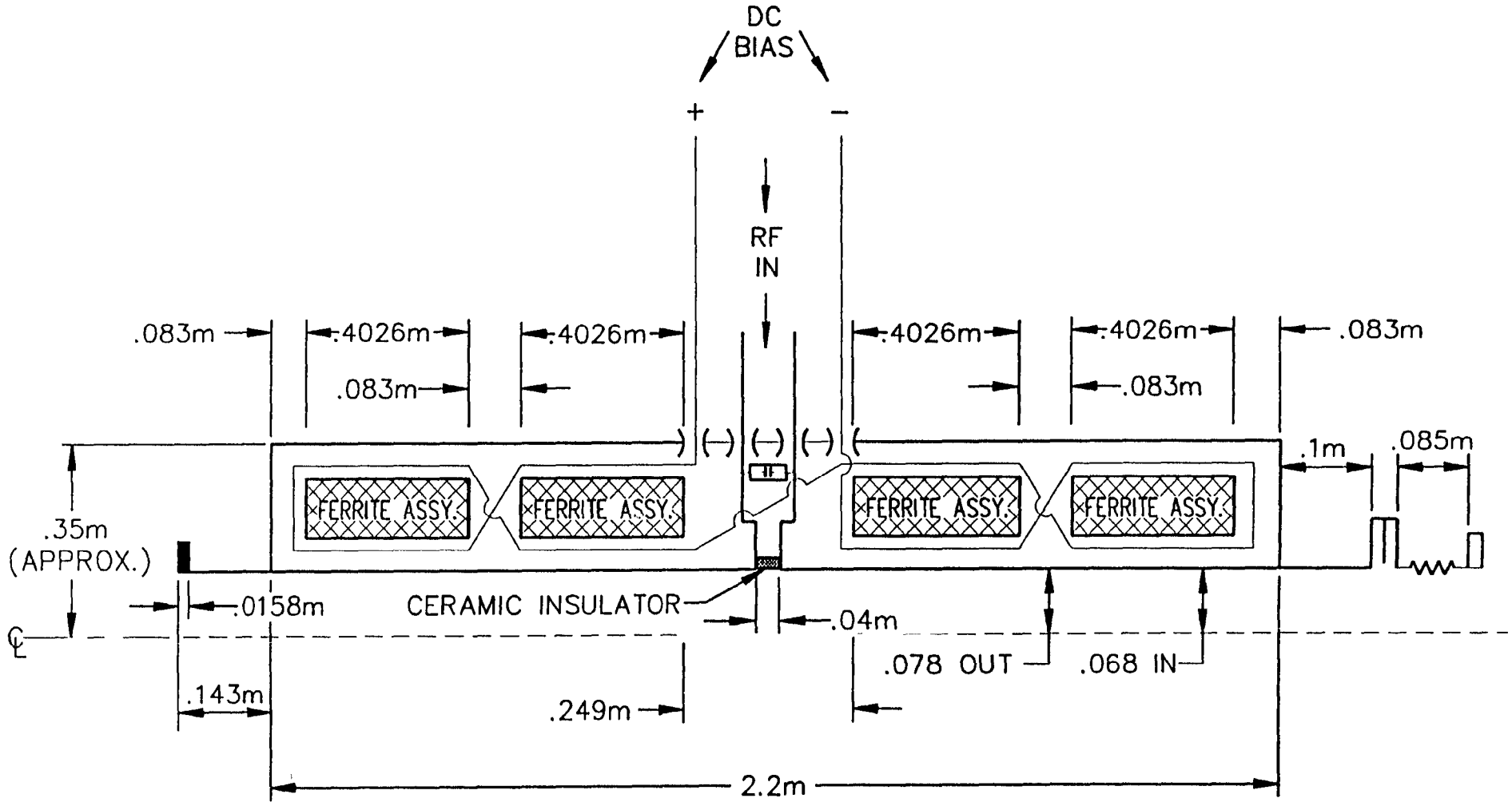

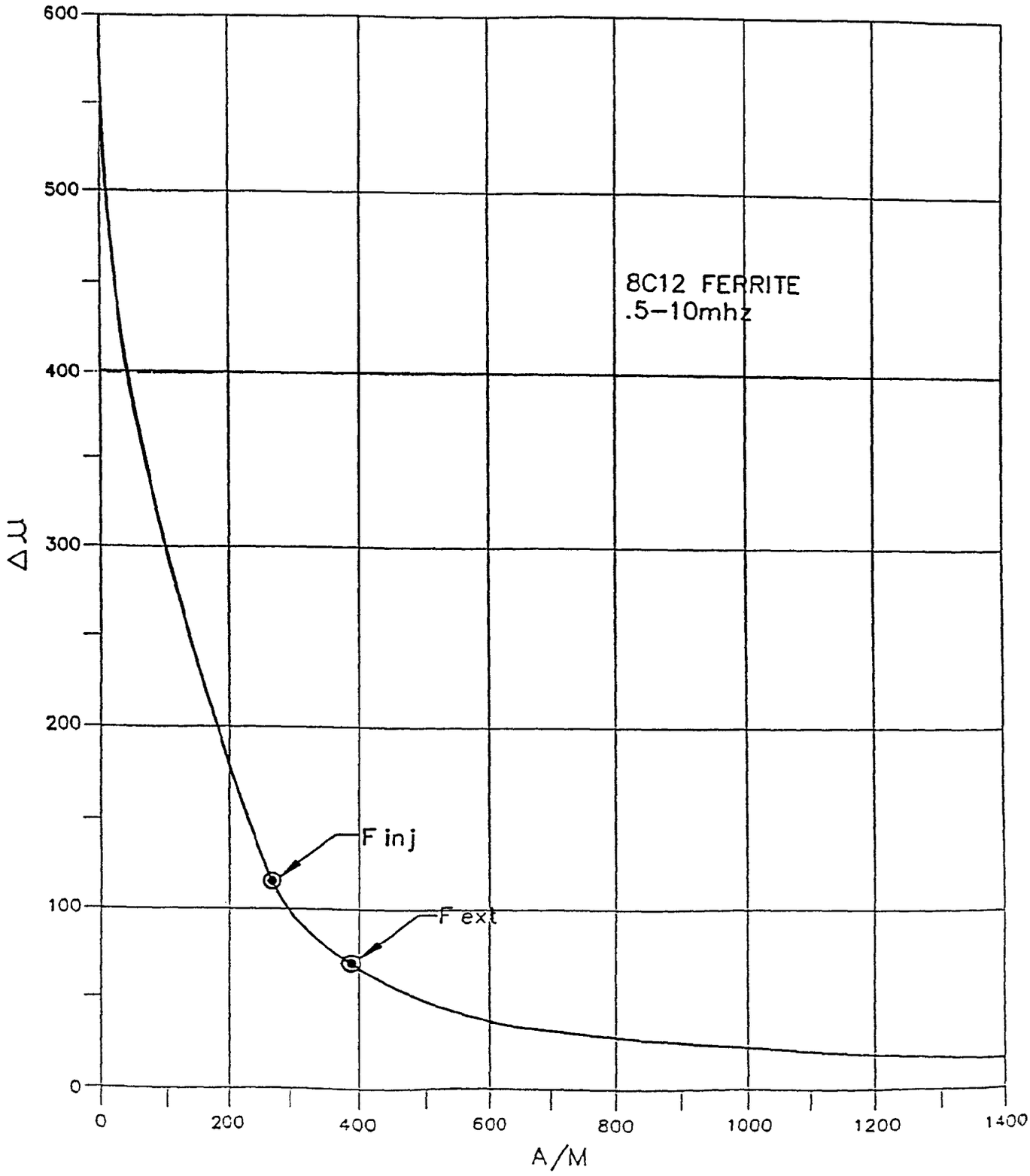

Figure 3 Incremental Relative Permeability vs DC Bias P003

Figure 2

FERRITE DISC DETAILS

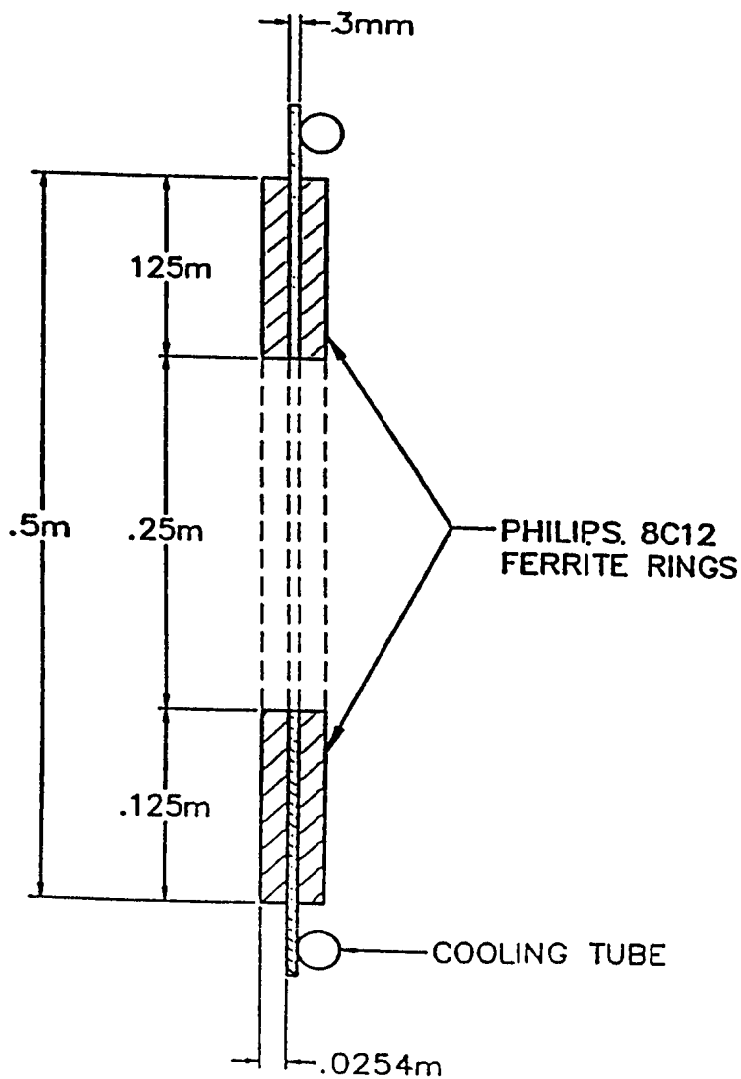

Figure 4

AMPLIFIER DETAILS

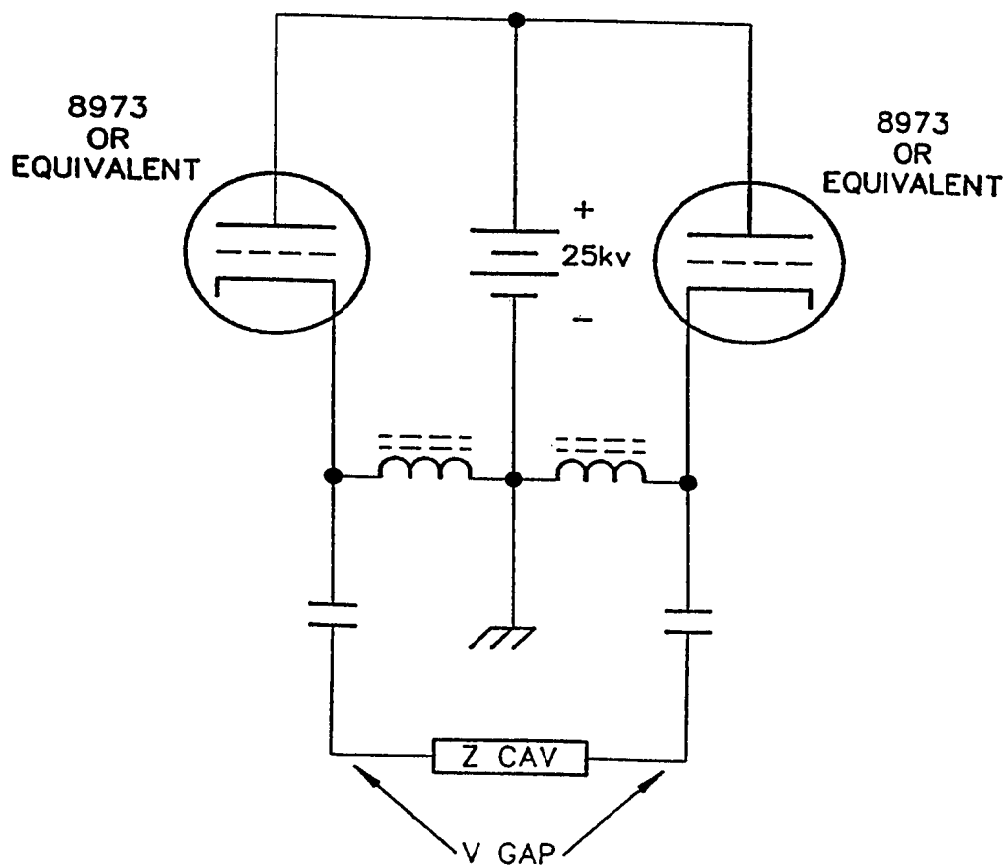

Study of 1 MW Neutron Source Synchrotron Dual Frequency Power Circuit for the Main Ring Magnets

D. G. McGhee
Argonne National Laboratory
9700 S. Cass Avenue
Argonne, IL 60439-4814

ABSTRACT

This paper describes the proposed design of the resonant power circuits for the 1-MW neutron source synchrotron's main ring magnets. The synchrotron is to have a duty cycle of 30 Hz with a maximum upper limit of operation corresponding to 2.0 GeV and a maximum design value of 2.2 GeV. A stability of 30 ppm is the design goal for the main bending and focusing magnets (dipoles and quadrupoles), in order to achieve an overall stability of 100 ppm when random field and position errors of the magnets are included. The power circuits of this design are similar to those used in Argonne's Intense Pulsed Neutron Source (IPNS) where the energy losses during each cycle are supplied by continuous excitation from modulated multiphase DC power supplies. Since only 50% of the 30-Hz sinewave is used for acceleration, a dual-frequency resonant magnet circuit is used in this design. The 30-Hz repetition rate is maintained with a 20-Hz magnet guide field during acceleration and a 60-Hz reset field when no beam is present. This lengthens the guide-field rise time and shortens the fall time, improving the duty factor for acceleration. The maximum B dot is reduced by 33% during acceleration and hence, the maximum rf voltage/turn is reduced by 56%.

I. INTRODUCTION

The main bending and focusing magnets, dipoles and quadrupoles, have an upper limit of operation corresponding to 2.1 GeV and a maximum design corresponding to 2.2 GeV for both the magnets and power supplies. The main dipole magnets are connected in series with six parallel resonant cells and six feed points as shown in Fig. 1. The energy losses for this circuit total 9 MW and are supplied continously through the six feed points. The quadrupole magnets are divided into two families and connected in the same manner but with three feed points per family as shown in Fig. 2. The total energy loss for both quadrupole families, connected as shown, is 11 MW.

The energy loss in the resonant circuits is made up by three 12-pulse power supplies phase shifted 10° by an autotransformer for each of the feed points. These power supplies are phase-controlled with their reference voltage digital-to-analog converters being serially counted up and down, creating the desired arbitrary current shape between a base current and the maximum current in each cycle.

Main Dipole Power Circuit

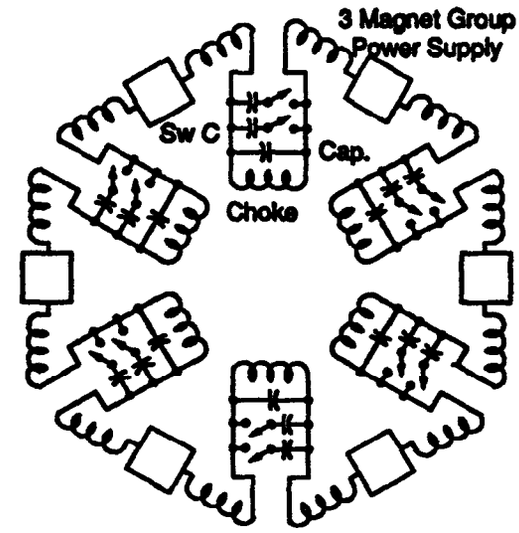

Fig. 1 Six parallel resonant cells and feed points

One Quadrupole Family Power Circuit

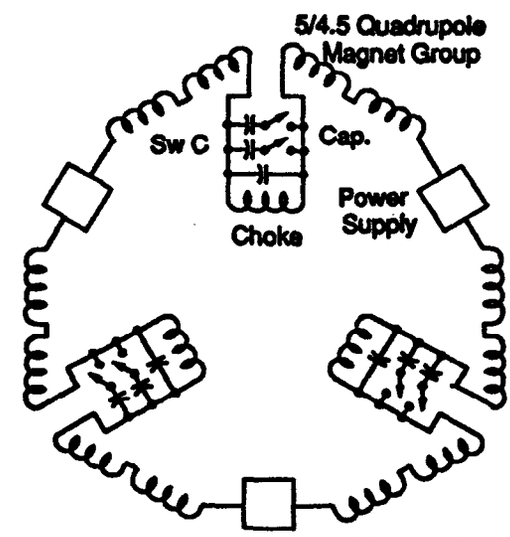

Fig. 2 Three parallel resonant cells and feed points

* Work supported by the U. S. Department of Energy, Office of Basic Energy Sciences, under Contract No. W-31-109-ENG-38.

The submitted manuscript has been authored by a contractor of the U. S. Government under contract No. W-31-109-ENG-38. Accordingly, the U. S. Government retains a nonexclusive, royalty-free license to publish or reproduce the published form of this contribution, or allow others to do so, for U. S. Government purposes.

II. GENERAL CONSIDERATIONS

The rapid cycling synchrotron is excited by a DC-biased sinewave current. Capacitors and chokes are used to resonate the magnets in order to save energy. The energy losses during each cycle are made up by a power source which provides continuous excitation from a modulated multiphase DC power supply, providing both DC and AC excitation from one source. It can operate over a wide frequency range and be readily phase-locked to the line or to a stable oscillator. Figure 3 illustrates the AC-DC power source comprised of three identical 12-pulse DC power supplies connected in series.

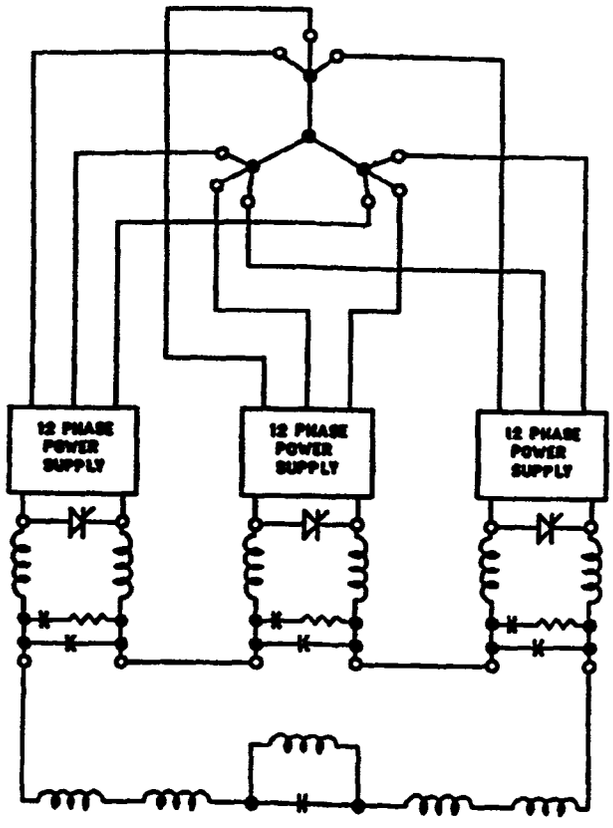

Fig. 3 Autotransformer, power supplies, and filter for one feed point.

An autotransformer is used to phase-shift the 3-phase AC inputs to each power supply by 10 electrical degrees with respect to each other. This combination provides a 36-pulse, phase-controlled DC power supply generating the desired wave shape. It operates into a slightly under-damped filter. The filter attenuates ripple above the circuit's operating frequency f_o. This configuration is repeated once for each feed point around the ring to reduce peak operating voltages. The circuit has been modified with the addition of capacitor switching for dual frequency operation, reducing the rf voltage required.

III. DUAL FREQUENCY CIRCUIT

Since only 50% of the 30-Hz sinewave is used for acceleration, a dual-frequency resonant magnet circuit has been chosen for the main magnets. The 30-Hz repetition rate is maintained with a 20-Hz magnet guide field during acceleration and a 60-Hz reset field when no beam is present. This lengthens the guide-field rise time and shortens the fall time, improving the duty factor for acceleration. The maximum B dot is reduced by 33% during acceleration and hence, the maximum rf voltage/turn is reduced by 56%. Figure 4 shows the comparison of magnet voltage and current between 30-Hz operation and the 20/60-Hz dual-frequency operation.

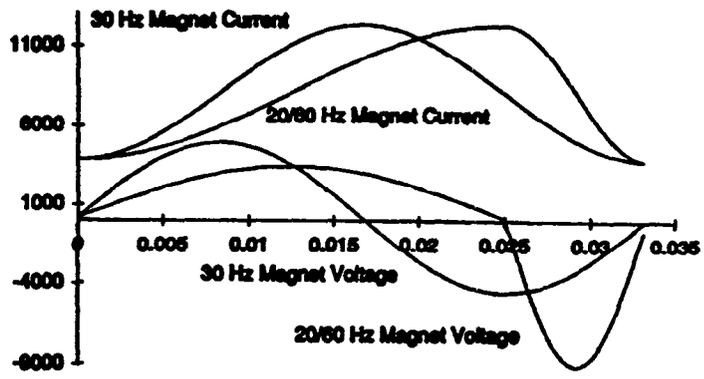

Fig. 4 Comparison of magnet voltage and current between 30 Hz and 20/60 Hz dual frequency operation.

A frequency f_1 during acceleration and a frequency f_2 during magnet reset results in a synchrotron repetition rate equal to frequency

$$f_o = \frac{2 \times f_1 \times f_2}{f_1 + f_2}. \qquad (1)$$

The fixed capacitors shown in Figs. 1 and 2 each represent capacitor bank C_2, and the sum of C_2 plus the switch capacitors per cell in Figs. 1 and 2 represent capacitor bank C_1.

The peak magnet voltage (during reset) is proportional to f_2. As f_o/f_1 increases, the capacitance value of capacitor C_1 increases while the capacitor voltage decreases. The opposite is true for the smaller capacitor bank C_2, the value of which decreases as f_o/f_1 increases, but with an ever higher voltage rating for capacitor C_2 and switch SwC, which is proportional to f_2.

For equal inductance values of the chokes and magnets, Fig. 5 shows the current waveforms and Fig. 6 shows the energy stored.

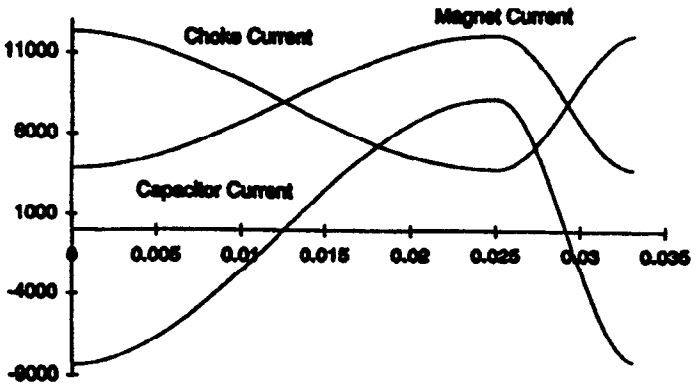

Fig. 5 Magnet, choke, and capacitor currents for circuits shown in Figs. 1 and 2.

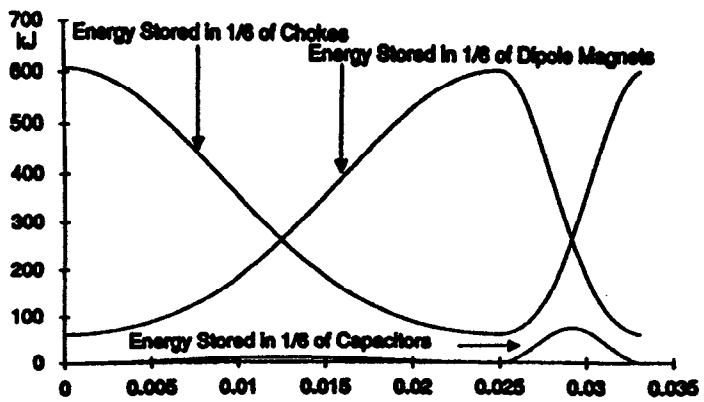

Fig. 6 Magnet, choke, and capacitor stored energy for the circuits shown in Figs. 1 and 2

The currents in the magnets and chokes are 180° out of phase. The magnet-stored energy is transferred to the choke and back again, once per cycle, through the resonant capacitor.

For equal inductance values for the choke and magnet we have

$$L_{ch} = L_m = L, \tag{2}$$

$$C = \frac{L_m + L_{ch}}{L_m \times L_{ch} \times \omega^2}. \tag{3}$$

Neglecting saturation effects, the time-variation of the magnet current during acceleration is

$$i_{magnet} = I_{dc} - I_{ac} \times Cos\ \omega t. \tag{4}$$

The choke and capacitor currents are given by

$$i_{choke} = I_{dc} + I_{ac} \times Cos\ \omega t, \tag{5}$$

$$\begin{aligned} i_{capacitor} &= i_{magnet} - i_{choke} \\ &= -2I_{ac} \times Cos\ \omega t \end{aligned}. \tag{6}$$

The capacitor and magnet voltages are given by

$$e_c = \frac{2I_{ac}}{\omega C} Sin\ \omega t, \tag{7}$$

$$e_m = E_{dc} + e_c. \tag{8}$$

IV. CIRCUIT LOSS BUDGET

To estimate the circuit parameters, a loss budget was established for the circuits in Figs. 1, 2, and 3 based on the dipole and quadrupole magnet designs. Table 1 shows the budget for the dipoles (Figs. 1 and 3). Table 2 shows the budget for the quadrupoles (Figs. 2 and 3).

Table 1 Synchrotron dipole resonant power circuit loss budget.

Ring Dipole Magnets	Chokes	Capacitors	Inter-connections	Filters	Power Supplies	Number of Magnets
0.32	0.32	0.05	0.10	0.05	0.16	
79765	79765	12463	24927	12463	39883	1
478591	478591	74780	149560	74780	239296	6
2871548	2871548	448679	897359	448679	1435774	36

There are six feed points, each has three 12-pulse power supplies, with their input phase shifted 10° from the next (see Fig. 3).
Each group of three power supples is required to make up 1495598 W.
Total system losses are 8973589 W.

Table 2 Synchrotron quadrupole resonant power circuits loss budget.

Ring Dipole Magnets	Chokes	Capacitors	Inter-connections	Filters	Power Supplies	Number of Magnets
32%	32%	5%	10%	5%	16%	
60101	60101	9391	18781	9391	30050	1
601005	601005	93907	187814	93907	300503	10
3606031	3606031	563442	1126885	563442	1803015	60

There are two families of quadrupoles, each having three feed points (this assumes half the quads per family). Each family's magnets are divided into six equal groups for a total of 4.5 magnets per group. To maintain symmetry, an extra magnet is added to make each group equal five magnets, for a total of 60. Each feedpoint has three 12-pulse power supplies, with their input phase shifted 10° from the next (see Fig. 3).

Each group of three power supples is required to make up 1878141 W.
Total system losses are 11268846 W.

From the loss budget and Eqs. 1 through 8, design values were established. They are listed in Table 3 for the dipole circuits and Table 4 for the quadrupole circuits.

V. FLAT-BOTTOM INJECTION

At injection into the synchrotron, a constant magnet field, $\dot{B} \approx 0$, may be required for 1 ms to 1.5 ms to reduce beam loss during injection. If this is needed, it is accomplished with either a passive or active crowbar as shown in Figs. 7a and 7b.

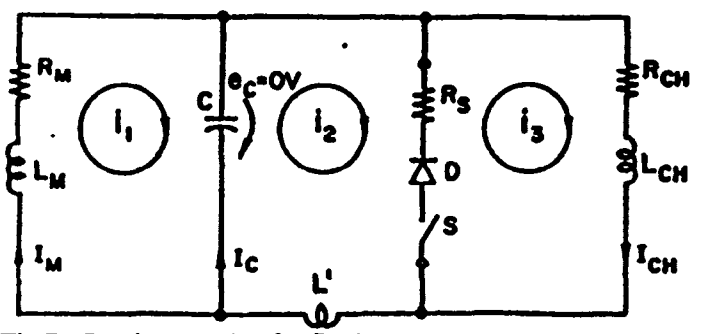

Fig.7a Passive crowbar for flat-bottom.

A flat-bottom magnet current for beam injection is initiated at times t_0, t_5, etc. when switch S is closed, as shown in Fig. 8. As illustrated in this figure, the power supply voltage maintains the magnet current until time t_1.

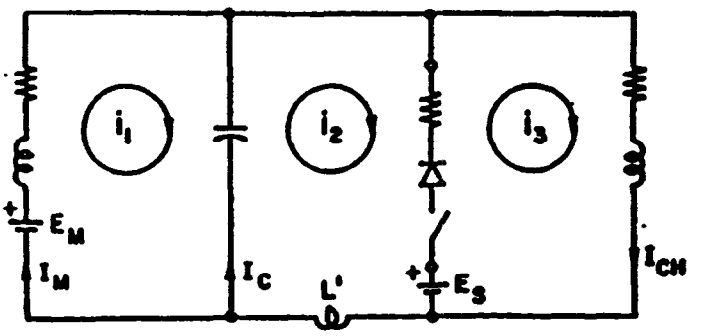

Fig. 7b Active crowbar for flat bottom.

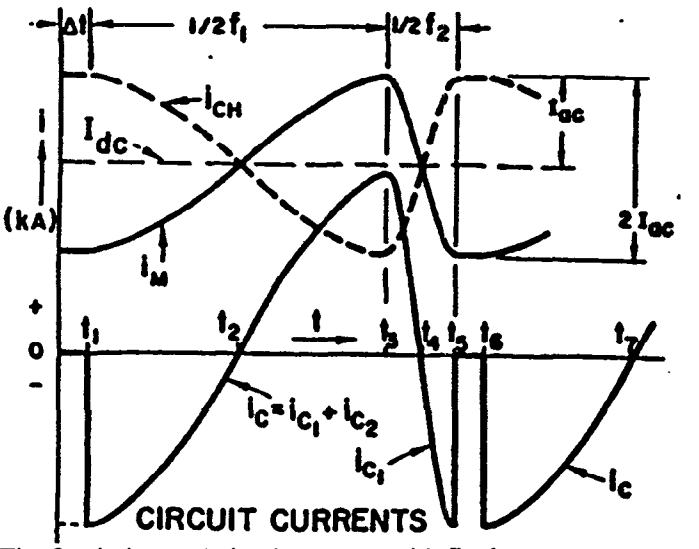

Fig. 8 Timing and circuit currents with flat bottom.

It is not essential to also maintain the choke current constant between times t_0 and t_1, which can be accomplished with a power source, E_S, in the crowbar.

Depending on the values of the DC voltages, $\dot{B}$ values of zero, positive, or negative, are possible.

For $t_0 \le t < t_1$, all the energy is stored in the circuit inductances. Crowbaring the ring magnets and the chokes requires the crowbar to carry the difference between these currents

$$i = i_{CH} - i_M = (I_{dc} + I_{ac}) - (I_{dc} - I_{ac}) = 2I_{ac}. \quad (9)$$

The crowbar may or may not contain a power source in addition to the 36-pulse power supply, requiring beam to be injected into:

a) A falling field (B<0, passive crowbar).
b) A rising field (B>0, active crowbar).
c) A constant field (B=0, active crowbar).
d) A combination of the above.

For magnets with a large L/R time constant, a passive crowbar is sufficient to keep the current flat within 0.1% for 1.5 ms. Magnets with small time constants require a DC driving voltage in the power supply and/or in the crowbar. Figs. 7a and 7b show equivalent circuits for passive and active crowbars. In these circuits, the crowbar switch S in series with diode D (unidirectional current flow) and resistor R_S is, for practical purposes, constant during the 1-ms injection time. The nominal crowbar current has the same value as the capacitor current at time $t = t_0$,

$$I = I_{CH} - I_M = 2I_{ac}.$$

Table 3 Operating parameters for the synchrotron dipole resonant circuit.

Circuit Values	20 Hz	60 Hz
Inductance of a magnet	0.001345	1.35E-03
Inductance of 1/6 of the total magnet	0.00807	8.07E-03
Magnet rms current	8616	8616
Magnet DC current	8092	8092
Magnet peak AC current	4181	4181
Capacitor bank peak AC current	-8362	-8362
Number of feedpoints	6	6
Total number of power supplies	18	18
Number of magnet families	1	1
Total number of magnets	36	36
Total DC resistance of 1/6 magnets, chokes, filters, interconnections.	0.0130308	0.0130308
Total AC resistance of 1/6 magnets, chokes, filters, interconnections and capacitors.	0.0654197	0.06541977
f_0	20	60
W_0	125.6637	376.9911
1/6 total capacitance	0.15694	0.001744
Select 550 kW (one power supply)	529	529
Voltage rms of one power supply based on the KW rating selected	64	64
Voltage peak of one power supply based on power supply selected	171	171
AC voltage peak across the tank	3318	9303
DC voltage across 1/6 of the magnets, chokes, interconnections, and filters	105	105
e_pT	3371	9356

Passive Crowbar

Without a driving voltage in the crowbar and with zero voltage on the capacitor, the magnet and choke currents change at time $t = t_0$ at the following rates. The magnet's current rate of change corresponds to

$$\frac{di_M}{dt} = -\frac{I_M R_M}{L_M},$$

and the choke's current rate of change corresponds to

$$\frac{di_{CH}}{dt} = -\frac{I_{CH} R_{CH}}{L_{CH}}.$$

With L' = 0, the current transfers form the capacitor to the crowbar in about 6 μs. With L' > 0, this transfer takes longer and is oscillatory with a frequency of

$$f = \frac{1}{2\pi\sqrt{L'C}}.$$

For L' = 0.2 μH the capacitor current i_C oscillates at 1 kHz around its steady state value of zero, for about 200 μs; the crowbar current oscillates at the same frequency and for the same duration with a steady state value of -8 kA. For L' = 1 μH, the oscillations are at 0.4 kHz for about 8 ms. These oscillations have a negligible effect on the magnet and choke currents. After the capacitor current has been transferred to the crowbar, the rate of change in

Table 4 Operating parameters for the synchrotron quadrupole resonant circuit.

Circuit Values	20 Hz	60 Hz
Inductance of a magnet	1.08E-03	1.08E-03
Inductance of 1/6 of the total magnet	1.08E-02	1.08E-02
Magnet rms current	4729	4729
Magnet DC current	4442	4442
Magnet peak AC current	2295	2295
Capacitor bank peak AC current	-4590	-4590
Number of feedpoints	6	6
Total number of power supplies	18	18
Number of magnet families	2	2
Total number of magnets	60	60
Total DC resistance of 1/6 magnets, chokes, filters, interconnections.	0.038759	0.038759
Total AC resistance of 1/6 magnets, chokes, filters, interconnections and capacitors.	0.31027	0.31027
f_o	20	60
W_o	125.6637	376.9911
1/6 total Capacitance	0.011727	0.001303
Select 550 kW (one power supply)	664.2688	664.2688
Voltage rms of one power supply based on the KW rating selected	142	142
Voltage peak of one power supply based on power supply selected	396	396
AC voltage peak across the tank	3153.991	7448
DC voltage across 1/6 of the magnets, chokes, interconnections, and filters	172	172
e_pT	3240	7534

the magnet current is,

$$\frac{di_M}{dt} = -\frac{I_M R_M - E_{crowbar}}{L_M}, \qquad (10)$$

while the choke current changes as

$$\frac{di_{CH}}{dt} = -\frac{I_{CH} R_{CH} + E_{crowbar}}{L_{CH}}. \qquad (11)$$

Note that the crowbar voltage drop reduces the current decay in the magnets but increases the current decay in the chokes.

Active Crowbar

For magnets with small L/R time constants, an active power source is required to hold the injection current to within 0.1%. The power source may be in the crowbar, the magnet circuit, or both, as shown in Fig. 7a.

Inductance of the crowbar power source must be small to not delay transfer of the current from the capacitor to the crowbar. This requires a low voltage capacitor bank in parallel with the crowbar power supply.

As in the passive crowbar circuit, L' causes an oscillatory delay during the transfer of current from the capacitor to the crowbar.

VI. CONCLUSIONS

The circuits covered in this paper meet the requirements for an IPNS upgrade to 1 MW.

The power loss estimates are conservative.

Effort should be made to reduce the losses in the final design.

A 1-1.5 ms zero $\dot{B}$ for injection should be obtainable.

VII. REFERENCES

1. W. Praeg, D. McGhee, "Ring Magnet Power Supply for 500 MeV Synchrotron," Conference Record Industry Application Society, IEEE-IAS-1978, 13th Annual Meeting, Toronto, Oct. 1978.

2. W. Foss,W. Praeg, "Shaped Excitation Current for Synchrotron Magnets," IEEE Transactions on Nuclear Science, Vol. NS-28, No. 3, June 1981.

3. W. Praeg, "Pulsed Magnet Systems for High Energy Physics Beam Lines," Proceedings of 5th International Conference on Magnet Technology, Rome, Italy, April 1975.

BASIS FOR THE POWER SUPPLY RELIABILITY STUDY OF THE 1 MW NEUTRON SOURCE

D. G. McGhee and M. Fathizadeh

Argonne National Laboratory
9700 S. Cass Avenue
Argonne, IL 60439-4814

ABSTRACT

The Intense Pulsed Neutron Source (IPNS) upgrade to 1 MW requires new power supply designs [1]. This paper describes the tools and the methodology needed to assess the reliability of the power supplies. Both the design and operation of the power supplies in the synchrotron will be taken into account. To develop a reliability budget, the experiments to be conducted with this accelerator are reviewed, and data is collected on the number and duration of interruptions possible before an experiment is required to start over. Once the budget is established, several accelerators of this type will be examined. The budget is allocated to the different accelerator systems based on their operating experience. The accelerator data is usually in terms of machine availability and system down time. It takes into account mean time to failure (MTTF), time to diagnose, time to repair or replace the failed components, and time to get the machine back online. These estimated times are used as baselines for the design. Even though we are in the early stage of design, available data can be analyzed to estimate the MTTF for the power supplies.

I. INTRODUCTION

The proposed reliability studies for the IPNS upgrade to 1 MW follow the format outlined during the Advanced Photon Source (APS) Reliability Workshop held at Argonne National Laboratory on January 29-31, 1992. Neutron source users establish a reliability or availability budget based on the number and length of disruptions experiments can sustain without data collection rates going below an acceptable level and 2) the operating experience of existing machines. These studies will concentrate on the reliability tools used for power supply designs: the main resonant magnet circuits and power supplies for the synchrotron of the proposed 1 MW IPNS upgrade. [1]. Based on the chosen budget for the machine, reliability budgets of the contributing subsystems will be determined using previous experience from existing machines, particularly IPNS, as it is and has been operating with a resonant magnet circuit similar to that proposed for the upgrade.

II. APS RELIABILITY WORKSHOP 29-31 JANUARY 1992

A workshop was held at APS to address reliability goals for accelerator systems. Seventy-one individuals participated in the workshop, including 30 from other institutions. The goals of the workshop were to:

1. Give attendees an introduction to the basic concepts of reliability analysis.

2. Exchange information on operating experience at existing accelerator facilities and strategies for achieving reliability at facilities under design or in construction.

3. Discuss reliability goals for the APS and how to attain them.

Data on the reliability of operating electron storage rings should be collected and analyzed to provide a database for more informed quantitative estimates of system reliability and maintainability.

The workshop included a series of lectures by Professors Rice and Hall of the University of Illinois at Chicago and the University of Illinois at Urbana-Champaign, respectively. They introduced mathematical definitions of availability (the fraction of time a system is performing its function as planned) and

* Work supported by the U. S. Department of Energy, Office of Basic Energy Sciences, under Contract No. W-31-109-ENG-38.

The submitted manuscript has been authored by a contractor of the U. S. Government under contract No. W-31-109-ENG-38. Accordingly, the U. S. Government retains a nonexclusive, royalty-free license to publish or reproduce the published form of this contribution, or allow others to do so, for U. S. Government purposes.

reliability in a time interval T (the probability a system will perform its function without interruption for an interval T). The effect of maintenance on availability and the effect of redundancy on reliability were also discussed.

Representatives from other laboratories presented information on the operating history of other accelerator facilities, e.g. Princeton Plasma Physics Laboratory's (PPPL) fault reporting procedures and the reliability planning activities for the Superconducting Super Collider (SSC), the Relativistic Heavy Ion Collider (RHIC), the Cornell Electron Storage Ring (CESR) B-Factory, and the Stanford Linear Accelerator Center/Lawrence Berkeley Laboratory (SLAC/LBL) B-Factory.

Working group discussions were held to address the following subsystems.

The rf working group felt that the reliability goal could be met. They studied the potential for improvement in availability and its effect on reliability by installing a fourth rf system to function as a "hot spare," should one of the originally planned systems fail. Participants from SLAC reported that this worked well at PEP; it was possible to shut down one rf station without interrupting operation.

The vacuum working group felt that the 99% goal is very difficult to achieve. They identified the potentially long recovery time from a vacuum accident requiring bakeout of the whole storage ring as an area to consider for improvement.

The power supply working group felt that the 99% goal is extremely difficult due to the large number of power supplies in the storage ring. Preemptive maintenance based on sophisticated testing procedures was considered the best approach to the problem.

The interlock and diagnostics working group proposed a conceptual design for the beam abort system, based on turning off the rf power in the storage ring. They stressed two points: first, redundancy to improve the reliability of the interlock function is at odds with overall facility reliability because redundant interlocks can trigger more false alarms; second, the magnitude of beam excursion defined as the beam abort trigger level should be made as large as possible to prevent noise-induced false alarms.

Another working group addressed the cost of unreliability in a synchrotron radiation facility. Several comparisons were made between the availability/reliability requirements of a particle physics accelerator and those of a synchrotron radiation facility. The largely fixed configuration and several-year duration of a high energy physics experiment do not demand very high reliability; the important figure of merit is availability averaged over a year or more. A one-week outage is not very long by these standards.

A synchrotron radiation user will typically be scheduled for 1-2 weeks of beam time to accomplish a specific experiment. About tenfold this amount of time is spent preparing for the experiment beforehand and analyzing data afterward. Even short interruptions near the end of the scheduled beam time might prevent the collection of enough data for a complete, definitive analysis. In this way the entire investment of time in the experiment is lost. Estimates derived from interviews of synchrotron radiation users indicated that even if the facility runs 75% of the time scheduled, experiments would take twice as long to do compared to a perfectly operating facility. This means the cost of research at a facility with 75% availability would be twice that of a 100% available facility.

III. POWER SUPPLIES WORKING GROUP SUMMARY AND CONCLUSION

1) The reliability and availability of the chopper power supplies were calculated. If 99% reliability is needed, the power supply MTTF must be about 900 years which is unrealistic. However, if scheduled maintenance is performed during refill and dumping of the beam, then an availability of 99% is attainable.

2) Most of the problems usually show up within the first two years of operation, and after debugging and improving the system, the reliability improves. Thus, a trial period is required to find and replace most of the components that cause failure of the system.

3) Unexpected problems caused by noise and

voltage transients can cause interruptions. Circuits should be designed and tested for such conditions in order to have more reliable power supplies.

4) Crews must be well-trained, and parts must be modularized for ease of repair.

5) Electronic boards should be tested for effects of vibration on cold solder joints according to Department of Defense procedures.

6) Some parameters of power supplies can be measured in order to anticipate failure. For example, in bipolar transistors, the gain [ß] can be measured at any time in order to predict the failure of the device. These devices should be replaced before failure.

7) Heat cycling should be performed on the electronic boards to speed up the infant mortality period of the devices.

8) When ordering power supplies from a vendor or a manufacturer, all the components should be specified by name and manufacturer.

9) In order to make maintenance safer and easier, buses should be covered.

10) An optimization program for the number of spare components on hand will be performed in order to determine the appropriate number of spare parts for the inventory.

11) Experiences should be shared with other laboratories.

12) Learn from operations, perform diagnostics, monitor signals, and analyze failures. Failure can provide valuable information for future plans.

13) In the design stage of a circuit, reliability analysis should be performed to predict the component or set of components most likely to fail.

IV. AVAILABILITY AND RELIABILITY TOOLS FOR POWER SUPPLY SYSTEMS

The power supply system is a series system with F1, F2, ••• Fn failure modes, where n = the number of modules. For the ring magnet power supplies, dipole and quadrupoles, we consider each resonant cell to be a module. Therefore, we have one series system with 12 modules. Series systems are non-redundant; that is, the failure of any one component will fail the system. At this early stage of design and drawing from Argonne's reliability workshop, we have assumed a failure rate of 1 per 1000 hrs of operation and a repair time of 2 hours per failure. From this, availability of the system is defined as:

$$AVAIL = \frac{SUT - UDT}{SUT}, \qquad (1)$$

$$= 1 - \frac{MTTR}{MTTF}, \qquad (2)$$

$$= 1 - MTTR \times \lambda_S, \qquad (3)$$

$$= 0.998,$$

where SUT is scheduled up time, UDT is unscheduled down time, and MTTR is the mean down time for repair. λ_S is the system failure rate; for the power supply system the failure rate is 1/1008 hours.

The system reliability function is

$$R(t) = e^{-\lambda t}.$$

R(t) gives the probability of survival over the time period t > 0.

The ring magnet power supplies (RMPS) reliability for a one-week experiment would be 84.7%.

V. DEVELOPING AN RMPS SYSTEM

In developing a ring magnet power supply system the following nine steps should be incorporated.

1) Determine the power supply system requirements.

2) Develop the preliminary design.

3) Calculate the failure rate using the part count method for a baseline failure rate.

4) Calculate failure rate, using the part stress method, with the military handbook MIL-HDBK-217F. [2]

5) Test the preliminary design.

6) Develop a final design.

7) Procurement/production.

8) Test the final design/production units.

9) Design upgrades.

VI. FAILURE DATA

Once the accelerator starts operation, failure records need to be maintained. Below is an example of IPNS's availability table for the last six years.

Our designs will be based on MIL-HDBK-217F, which assumes a constant rate of failure over the useful life of components ranging from ICs to solder joints. This is represented by the bathtub curve shown in Fig. 1.[2]

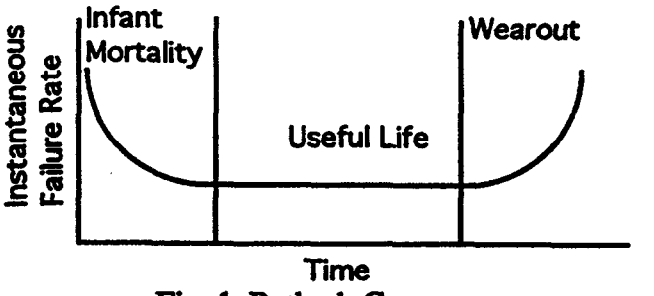

Fig. 1 Bathtub Curve

IPNS Availability Summary, FY 1988-FY 1993

Per 1000 Hours of Operation	FY'88 Failure Hours	FY'89 Failure Hours	FY'90 Failure Hours	FY'91 Failure Hours	FY'92 Failure Hours	FY'93 Failure Hours	Average Failure Hours	Power Supply Hours
H- Source	2.19	4.12	1.3	0.55	6.87	5.27	3.38	
Linac	4.58	6.91	4.42	1.27	2.84	7.5	4.59	
Stripper	0.23	0.36	0.28	0.14	0.13	5.27	1.07	
RF	4.98	1.5	8.85	8.84	6.67	18.15	8.17	
Bumper	1.66	6.32	0.79	0.07	0.35	0	1.53	1.53
RMPS	2.62	0.26	2.37	6.84	2.32	1.12	2.59	2.59
50 MeV	1.92	1.69	1.9	2.41	1.09	3.14	2.03	2.03
500 MeV	0.8	2.1	0.44	0.96	0.04	7.7	2.01	2.01
Magnets	0.43	1.14	1.17	0.41	0.39	3.35	1.15	
Vacuum	1.56	1.07	4.23	4.44	3.46	7.4	3.69	
Utilities	4.01	7.99	1.99	4.51	0.13	0	3.11	
Computer	17.28	1.36	3.25	0.76	1.97	1.12	4.29	
MCR Eqpt	0.07	0.88	4.42	1.41	0.48	0.71	1.33	
Septum	0.07	3.89	5.18	6.74	0.17	3.65	3.28	3.28
Kicker	11.28	8.61	4.74	5.74	8.18	7.2	7.63	7.63
Cool/Misc	0.4	0.17	0.85	3.47	4.81	2.13	1.97	
Total Failures Hours per 1000 Hours	54.08	48.37	46.18	48.56	39.9	73.71	51.80	19.06
Availability	95%	95%	95%	95%	96%	93%	95%	98%

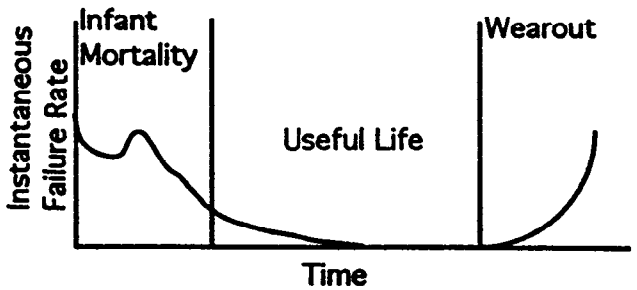

Fig. 2 Roller Coaster Curve

This curve assumes that between the initial period of infant mortality and a final wearout period, failures occur at a constant rate that can be minimized by choosing higher-quality components and reducing thermal and electrical stress. The predictions using the handbook should be thought of simply as tools for comparing design options. Possibly a better way to represent failure rates is the roller coaster curve, shown in Fig. 2. By keeping good records of failures, the job of designing a cost-effective maintance program will be greatly enhanced.

VII. CONCLUSIONS

It has been demonstrated that the approach and procedures outlined in this paper are key to achieving the proposed 99.9% availability goal of the IPNS 1 MW upgrade.

The results of the APS reliability workshop will be incorporated in the development of the magnet power supplies. As stated, the results are based on the experiences and operations of a number of facilities. Using this paper as a basis for the power supply design, it is anticipated that this goal is achievable within a scheduled time frame.

VIII. REFERENCES

[1] D.G. McGhee, "Study of 1 MW Neutron Source Synchrotron Dual Frequency Power Circuit for the Main Ring Magnets," these proceedings.

[2] Military Handbook (MIL-HDBK-217F), "Reliability Prediction of Electronic Equipment," Deparment of Defense, United States of America, 1990.

[3] IEEE Spectrum, "MIL Reliability: A New Approach," August 1992.

PERFORMANCE OF THE 70 MeV INJECTOR TO THE ISIS SYNCHROTRON

N D West
Rutherford Appleton Laboratory, Chilton, Didcot, Oxon, England

Abstract

The Injector to the synchrotron of the ISIS pulsed neutron source is a 70 MeV Alvarez linear accelerator which produces a 20 mA pulsed beam of H^- ions, at a pulse repetition rate of 50 Hz and pulse lengths of up to 300 μs. The accelerator has been in regular operation since 1985 during which time it has been under continuous development. The main features of the accelerator are described, together with data on its performance, and an account is also given of some of the problems experienced in its operation.

General Description Of The ISIS Injector

A description of the accelerator was last given in 1979[1] when it was in the process of being converted from a low duty cycle proton accelerator to a high duty cycle H^- ion accelerator. The historical background to the accelerator, given in the earlier paper, explains some of the unusual features of the present machine. For example, two of the accelerating cavities were built in the late 1950's and the remaining components, together with the building, were designed for minimum cost rather than for optimum operational performance or convenience. In short, the linac is far from representing the state of the art in the field, although it has been developed to give a satisfactory and competitive performance.

The accelerator is designed for a 20 mA pulsed beam current at 70 MeV, with pulse lengths up to 500 μs at a prf of 50 Hz. In practice, pulse lengths of greater than 300 μs have never been run at full prf. The H^- ions are produced by a Penning ion source[2], mounted on the high voltage terminal of a 665 keV, 444 mm long, accelerating column. High voltage is supplied by a commercial Cockcroft-Walton generator, to which are added a 0.01 μF storage capacitor and a 'bouncer' pulse voltage stabiliser. The 665 keV beam transport line is 4.7 m long and contains 3 quadrupole triplets, twin steering magnets and a single fundamental harmonic buncher cavity, together with an emittance measuring apparatus, beam current transformers and a beam stop. The buncher is a two gap coaxial resonator, fed from a pick-up loop in the first linac accelerator cavity, and is located 0.8 m from the linac. Beam transmission from accelerating column to linac output is normally just over 60%.

The linac has four accelerating cavities (tanks), the first of 10 MeV and each of the others 20 MeV. Tanks 1 & 4 are basically engineering copies of the appropriate lengths of the Fermilab linac, constructed from copper clad steel, while tanks 2 & 3 were taken from a former RAL 50 MeV linac and have fabricated sheet copper cavities mounted inside separate steel vacuum vessels. Evacuation of the tanks is by turbo-pumps. Tank 4 alone is fitted with post-couplers. The main parameters are given in Table I over page.

The quadrupole magnets in tank 1 are capable of operating in the FDFD focusing mode, but not at 50 Hz due to a limitation in power dissipation. Even with the lower strength FFDD mode, considerable ingenuity has been necessary in the design of the pulsed power supplies to keep the overall pulse length as short as possible whilst generating a good flat top pulse. Magnets in the remaining tanks are dc powered.

RF power to the tanks is provided by four identical amplifier chains consisting of:

(a) Two transistor stages amplifying from 10 mW input to 200 W maximum output;
(b) RCA 7651 tetrode stage of 4 kW maximum output;
(c) RCA tetrode stage of about 250 kW maximum output;
(d) Thomson TH 116 triode stage of about 2.5 MW maximum output.

Table I - Accelerating Cavity Parameters

Cavity Number	1	2	3	4
Construction	Cu clad steel	Vac vessel & Cu liner	Vac vessel & Cu liner	Cu clad steel
Length, m	7.15	11.96	11.24	12.11
Energy out, MeV	9.91	30.44	49.71	70.44
No of cells	56	41	27	24
DT aperture, mm	20-25	38.1	38.1	30
Acc rate, MeV/m	0.84-1.55	1.72	1.71	1.77-1.66
Q - theory	76,100	70,900	56,800	66,000
- measured	60,900	58,600	39,700	55,100
Power for ϕ_s=30°, MW - theoretical Q	0.44	1.31	1.40	1.51
- meas. Q + 20 mA beam	0.74	2.00	2.39	2.22
Focusing magnets - period	FFDD	FFDD	FFDD	FFDD
- excitation	Pulsed	DC	DC	DC
- gradient, T/m	40.0-15.0	7.5-6.1	4.6	5.3
- length, inches	1.0-2.75	4.5-6.0	9.0	7.5

The output stage is pulsed from a hard valve modulator which uses two CW1600 tetrodes in parallel and a 50 μF capacitor bank charged to a maximum of 40 kV. The timing of triggers to the thyristor controlled charging circuit is optimised by a microprocessor controlled adaptive loop, to equalise the current taken by each phase of the 3-phase supply while yielding the desired capacitor bank charged voltage. An additional rf system for the debuncher cavity employs a commercial 40 kW amplifier following stages (a) & (b) above.

RF power is fed to the linac cavity on a 300 mm diameter, aluminium, coaxial line, which is of an RAL design permitting a degree of misalignment between flanged sections. The line has four 90° elbows, a further stub-supported 90° bend, incorporates a trombone line-stretcher and uses cross-linked polystyrene disk supports. The cavity is fed by a remotely adjustable feed-loop located on the air side of a 25 mm thick, 300 mm diameter, cross-linked polystyrene vacuum window.

The 70 MeV beam-transport line, leading to the synchrotron injection system, is 50 m long and contains three horizontal and two vertical bending magnets, 22 quadrupole magnets and appropriate steering magnets. A single gap debuncher cavity of 410 keV peak design voltage is located 36 m from the linac. For beam diagnostic use, the line contains 5 beam current transformers, 14 combined horizontal and vertical wire beam profile monitors, a beam chopper and 8 ionisation chamber beam loss monitors. A further 9 chambers are distributed along tanks 2 to 4 of the linac.

The first two horizontal bending magnets of bending angles +63° and -64.5^o, together with associated quadrupole magnets, form an achromatic pair, and the third magnet of 24.69^o provides the desired beam dispersion at the point of injection to the synchrotron. Two vertical bends of +/- 6.3^o bring the beam to the correct height after passing over the sychrotron ring, to permit injection from the inner radius. In spite of some of the large bending angles, former High Energy Physics beam-line magnets with parallel edged poles have been used for all bends.

A number of developments and performance characteristics of the ISIS linac will now be discussed.

Ion Source Development

The main limitation on beam intensity has been the ion source although, as a result of steady improvement in the source performance, any further increase in beam current would begin to require a corresponding improvement in the present performance of the linac rf systems. Most of the ion source improvements have been described elsewhere(2) but a brief update of the source operational performance will be given. Fig 1 shows a scatter plot of 665 keV beam current readings over the operational life of ISIS and Fig 2 illustrates the operational life of individual ion sources during 1992. It is understood(3) that our Penning source, based on the Dudnikov design, should be capable of delivering pulsed currents of up to 100 mA and we intend to seek this by continued exploration of changes to the source dimensional parameters. Progress in this field has been limited by a lack of resources to maintain an ion source laboratory test rig, so that all trial developments have to made on the installed ISIS source.

Development of a multicusp volume H^- source was initiated at RAL some time ago, when it was thought that the Penning source would fail to meet the ISIS design requirements, but there have been no results of any interest to report so far. Results at other laboratories suggest that development of this source is not yet at a stage where it might be suitable for use on ISIS.

Accelerating Column Breakdown

Spark breakdown of the accelerating column occurs at a typical rate of about once per hour due to charging of the insulators by electrons stripped from the H^- beam(4). Such beam trips are damaging as they contribute to the total number of thermal quenches experienced by the ISIS neutron target, and these are thought to shorten the target life. Recently, it has been found possible to prevent the Cockcroft-Walton generator tripping on over-current, following a column spark, by increasing the value of the resistor between the 0.01μF storage capacitor and the column high voltage terminal from 10 kΩ to 1 MΩ. The CW voltage then recovers within 2 or 3 pulses and it is unnecessary to trip the linac beam. Since the effective capacity at the column high-voltage terminal is then much reduced, it is necessary to compensate for the much larger droop in the column voltage during the beam pulse and this is achieved by a bouncer circuit connected to the earthy terminal of the storage capacitor. During the beam pulse the voltage at the input end of the 1 MΩ resistor is increased by a pre-set value, to produce a current in the 1 MΩ resistor exactly balancing the beam current flowing down the column. A prototype bouncer circuit has been successfully used for some months and a final version of it should be in use by the time this paper is published.

Beam Parameters

Transverse emittance of the beam is measured at 665 keV using a single traversable slit 1 m upstream from an array of detector wires. These wires are at 10 mm spacing but the array is traversed in 10 steps of 1 mm during a measurement. Typical measured emittance plots for a 40 mA beam current are shown in Fig 3. The dots shown plotted are measurement points at which the detected signal is greater than a defined background noise level, and the irregular contour lines are equal intensity contours plotted at 0.05, 0.1, 0.3, 0.5, 0.7 and 0.9 of peak intensity.

Values normally quoted for beam emittance are often ambiguous when it is not made clear whether the contour enclosing the quoted area is regular or highly irregular in shape. Since in most accelerator applications the beam has to be accepted by equipment which has a beam acceptance shape close to an ellipse, beam emittance should properly be quoted for an elliptical area which encloses a given beam current or fraction of the beam, as has been suggested by Keller et al(5). Independently of their work a computer program has been written which, for a set of emittance measurement data, finds the parameters of the smallest area ellipse enclosing a specified fraction of the beam current. The ellipses shown plotted in Fig 3 have been calculated in this way for 40, 80 and 98% of the total beam current.

Plotting the emittance of the bounding ellipse against ln(1/(1-f)), where f is the fractional current enclosed by the ellipse, gives the result shown in Fig 4. The results lie approximately on a straight line which, as discussed by Allison[6], should be the case for a Gaussian phase space density distribution. A value for the rms emittance can be calculated from the slope of this line or directly from the original measurement data. Using Allison's notation, (where $\varepsilon_{4rms} = 4\varepsilon_{rms}$), and taking the momentum normalised values, emittances for the beam of Fig 3 are:

	H - plane	V - plane	
ε(norm) for 90% beam current in elliptical contour	1.46	2.24	πμmrad
ε_{4rms}(norm) from slope in Fig 4	1.20	1.82	πμmrad
ε_{4rms}(norm) from original measurement data	1.49	1.75	πμmrad

The 665 keV beam emittance figure for the horizontal plane, which is the plane normal to the long dimension of the ion source extraction slit, always shows a very significant degree of aberration but it is not clear where this originates. Possibilities are in the ion source extraction gap, in the 90° gradient bending magnet following extraction, in the electrostatic focusing at the entrance to the accelerating column or from non-linear space charge forces. A trial change to a more Pierce-like extraction geometry failed to produce any improvement.

Measurement of the 70 MeV beam emittance is made close to the linac output, using 3 beam profile monitors in a drift space, with the beam brought to a waist near to the drift space centre to provide good resolution in computing the emittance by beam tomography. A similar measurement can be made close to the injection point into the synchrotron, but accuracy here is poor due to momentum dispersion and unfavourable focal conditions. The shape of the 70 MeV measured beam emittance is generally good so ellipse fitting is not essential. Typical emittance figures for 99% of a 20 mA, 70 MeV beam are 25 πμmr in each plane, or 9.9 πμmr momentum normalised.

Momentum spread in the 70 MeV beam is measured using a simple magnet spectrometer. Excitation of the 24.69° horizontal bending magnet in the 70 MeV beam-line is increased to deflect the beam into a separate line at 50°. The upstream beam is defined by a slit and, with appropriate quadrupole focusing magnet settings, an image of the slit is formed at the position of a beam profile monitor in the 50° line. Beam momentum spread depends on the settings of the debuncher cavity, typical figures being:

	dp/p (Debuncher off)		dp/p (Minimum with debuncher on)	
	90% beam	100% beam	90% beam	100% beam
Measured beam	3.9×10^{-3}	6.0×10^{-3}	1.9×10^{-3}	3.2×10^{-3}
Computed beam (for axial dynamics & no space charge)	3.4×10^{-3}	5.5×10^{-3}	0.33×10^{-3}	0.44×10^{-3}

It is probable that the measured minimum value with debuncher on is significantly larger than the computed value due to limited resolution of the spectrometer. When the beam is set up for best ISIS synchrotron operation, with the debuncher field level and phase both freely optimised, it is generally found that the measured beam momentum spread ends up close to the value for the debuncher off.

Cavity Field Control

Stability of the linac beam, particularly in energy, has proved to be a very important factor in achieving reliable operation of the ISIS synchrotron, and this has required the development of adequate control over the amplitude and phase of the cavity fields.

Amplitude stabilisation is achieved using a feedback system in which a detected cavity field signal is compared with a reference level and the error signal used to modulate the drive to the rf system at the 10 mW level. During the cavity field rise-time, when the large error signal would heavily saturate the feed-back amplifier, the amplifier is automatically gated off and the

rf drive is preset to a separately controlled level. Typical rf cavity pulses are shown in Fig 5 for the acceleration of a 22 mA, 200 μs beam. The cavity feed-line forward wave signal shows the extra power being turned on for beam loading. The field level overshoot at the start of the flat-top and also after the beam switches off are of no operational importance. The only significant disturbance is a transient 1.5% dip in field level at the beginning of the beam pulse. It is known that this could be corrected by an appropriate feed-forward control signal, but operationally this is found to be unnecessary.

Cavity phase is similarly pulse stabilised with a closed loop gain of about 30. An important source of disturbance to the phase in tanks 2 & 3 is the effect of multipactor loading in these cavities at the operating field level which, with no feedback control, can produce a 10° phase change during the rf pulse. The main problem has been in achieving long term phase stability, allowing the linac parameters to be re-established quickly and repeatably following a shut-down and eliminating the need for periodic adjustments. This has been effected largely by installing semi-rigid, semi-air spaced cabling for all phase reference lines.

One further improvement has been the introduction of a technique(7), similar to the Δt method used at LAMPF, for setting-up the design settings of field level and phase in each cavity. This has eliminated a large amplitude coherent phase oscillation in the linac and has probably contributed to the improvement achieved in the ISIS operating intensity.

Beam Losses

In a high mean beam current linac, such as the ISIS injector, it is essential to keep beam losses to a minimum. In addition to prompt radiation and activation problems, the mean power in the beam exceeds 15 kW and can quickly cause serious damage if the beam goes astray. Beam loss protection is provided by the 17 beam loss monitors distributed along the Injector beam path. A beam trip can be initiated if the signal from any one monitor, integrated over a pulse, exceeds a pre-set value. For the 70 MeV beam the trip level is set for a beam loss of 0.05μC per pulse, equivalent to a local continuous loss of 1.2% full beam current. In practice the trip occurs if such a loss is detected on four of any eight consecutive pulses. This logic, carried out by a dedicated microprocessor, prevents any unnecessary beam trips due to single isolated bad pulses.

The signals from these monitors are also permanently displayed and used by the crew when tuning for minimum beam loss, since losses are too small to be resolved by the beam current transformers. Signals due to pulsed X-ray emission from the cavities are normally larger than those due to beam loss and so are arranged to be subtracted automatically from both the displayed and trip level signals.

An unusual feature of the ISIS Injector is the presence of beam collimation inside one of the cavities. At the time that ISIS was designed it was specified that the 70 MeV beam should not exceed a normalised emittance of 10π μmr. Some attempt was made to design the 70 MeV beam-line to incorporate suitable collimators, but the technical requirements could not be met within the beam path length available, and collimation at the input to the linac would not have been suitable because of emittance growth during the early stages of rf acceleration. As a compromise the collimation is installed in the apertures of the early drift-tubes of tank 2, where emittance growth is largely complete and yet where the beam energy is low enough for activation problems to be small. The collimation takes the form of a series of graphite tubes, of slowly decreasing aperture, which are split and made a slight interference fit in the drift-tubes in the hope of achieving some degree of thermal contact. The degree of beam interception is not known, but the 70 MeV beam emittance is within its specification and the collimators have not given any problems.

Activation of the injector has never seriously interfered with hands-on repair and maintenance of the linac or the 70 MeV beam-line. 18 hours after a recent operations cycle, the maximum measured radiation level along the linac was 100 μSv/hr on contact with the beam pipe between

tanks 3 & 4. On the 70 MeV beam-line, 35 hours after operation, measurements of 2000 μSv/hr on contact were made at two points, but these fell to 50 μSv/hr at 0.5 m.

Injector Reliability

Figures for the operation of ISIS during the 1992 operations year were as follows:

Scheduled user time	4182 hrs
Beam-on-target time	3564 hrs (85.2%)
Lost time	618 hrs
Equipment down-time	797 hrs (Allowing for concurrent equipment faults)
Total beam-on-target	533 mA.hrs

The Injector was responsible for 46% of the above equipment down-time and the loss of 8.8% of the ISIS scheduled user time. A breakdown of the figures amongst the different areas of the Injector, and between events of less than and greater than one hour's duration, are given in the following Table.

Events of duration:	All	< 1 hr	> 1 hr
Ion source	62.2 hrs	23.2 hrs	39.0 hrs
Source supplies	10.2	4.3	5.9
Cockcroft-Walton	0.7	0.7	0.0
Accelerating Column	7.0	7.0	0.0
Bouncer	2.5	0.3	2.2
Buncher cavity	0.9	0.9	0.0
Linac cavities	75.7	2.8	72.9
Modulators	25.1	10.7	14.4
RF systems	129.3	17.2	112.1
Magnet power supplies	4.7	3.7	1.0
Beam-line magnets	5.4	0.0	5.4
Debuncher	6.8	6.8	0.0
Cooling water	2.7	2.7	0.0
Beam-line vacuum	36.8	0.1	36.7
TOTAL	370.0 hrs =	80.4 hrs +	289.6 hrs

A large fraction (68%) of the Injector equipment down-time arose from a limited number of major events which are detailed below.

Ion Source: The 1992 ISIS scheduled operating time was divided into 7 operating cycles each of 3 to 4 weeks duration. During each cycle one change of ion source was normally required, accounting for 34 hrs down-time.

Linac Cavity RF Window: Tank No 3 suffered three consecutive failures of the cross-linked polystyrene rf vacuum window, at one week intervals, following a 4 year period without failure or change of window in this tank. Experience had shown that the only solution to this problem was to reduce the level of electron discharges by opening up the cavity to clean off all organic based coatings from the cavity and drift-tube surfaces. This process involved removal of the linac tunnel shielding roof, the cavity vacuum vessel lid and the upper half of the rf cavity. The work, including rf reconditioning the cavity, took about a week. This lost time does not appear in the statistics because it was accommodated by programme re-scheduling, but the window failures accounted for 73 hrs of down-time.

RF System Valve Changes: The 4 main rf systems including modulators contain a total of 20 thermionic valves. As yet it has not been possible to anticipate the end of life of any of these and hence valves are invariably replaced during operational periods, accounting for 62 hrs down-time in 1992. We have no test rig for the TH116 valve which has to be conditioned in use on the accelerator.

RF System Amplifier Circuit: The 4616 valve has always been a source of problems from parasitic oscillations, circuit breakdown and frequent re-tuning during valve ageing. Down-time

of 24 hrs resulted from a single incident requiring the replacement of a grid-circuit, in which the tuning mechanism had suffered mechanical failure after a life of nearly 20 years.

RF System Coaxial Lines: Down-time of 23 hrs resulted from two failures of the cross-linked polystyrene support insulator in the 12" coaxial rf feed-line to one cavity. This has been a recurring problem, but only for the insulator closest to the cavity coupling loop, and is probably associated with sparking across the line in the vicinity of the loop. Evidence of such sparking is often found on inspection of the lines even though not detected during operation, but it does not always result in a failure.

Beam-line Vacuum: Beam operation closely following a period in which the 70 MeV beam-line had been at atmospheric pressure gave rise to 37 hrs lost time during which the beam-line had to be vacuum conditioned. Above normal pressure in the line caused beam loss due to stripping which in turn created further outgassing. This limited the permitted beam current for a considerable period.

Summary

The Injector has been under constant development over its operational life but it is only fairly recently that it has been able reliably to meet its full design specification. Many of the difficulties have arisen from the fact that the original accelerator was never designed for high mean intensity operation. Development work will continue, in particular to improve its reliability and also to achieve a higher pulsed output beam current.

Acknowledgement

This paper describes the work of a large number of past and present members of the Linac Group, together with other ISIS accelerator staff, to whom the author makes grateful acknowledgement.

References

1. N D West, The Rutherford Laboratory 70 MeV Linear Accelerator, Proc 1979 Linear Accel Conf, BNL 51134, 88.

2. R Sidlow & N D West, Performance Of The Penning H^- Ion Source At ISIS, Proc 1992 European Part Accel Conf, 1005.

3. V G Dudnikov, Private communication to C W Planner.

4. H Wroe & N D West, High Current Commissioning Of The H^- Ion Accelerating Column Of The ISIS Injector, Proc 1988 European Part Accel Conf, 1439.

5. R Keller, J D Sherman & P Allison, Use of A Minimum-Ellipse Criterion In The Study Of Ion Beam Extraction Systems, IEEE Trans Nucl Sci, NS 32, 2579, (1985).

6. P Allison, Some Comments On Emittance Of H^- Ion Beams, Proc 4th International Symp On Production & Neutralisation Of Negative Ions & Beams, AIP Conf Proc 158, 465, (1986).

7. N D West & M A Clarke-Gayther, Optimisation Of ISIS Injector Linac RF Settings By Use Of A Beam Phase Monitoring System, Proc 1992 European Part Accel Conf, 1058.

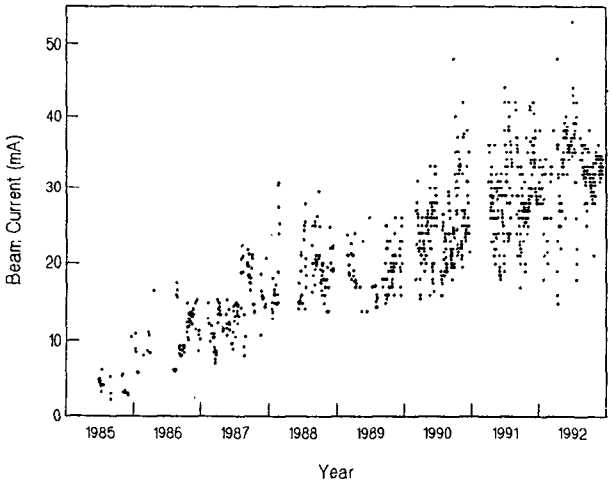

Fig 1 Pulsed current recorded from operational ion sources (at 665 keV).

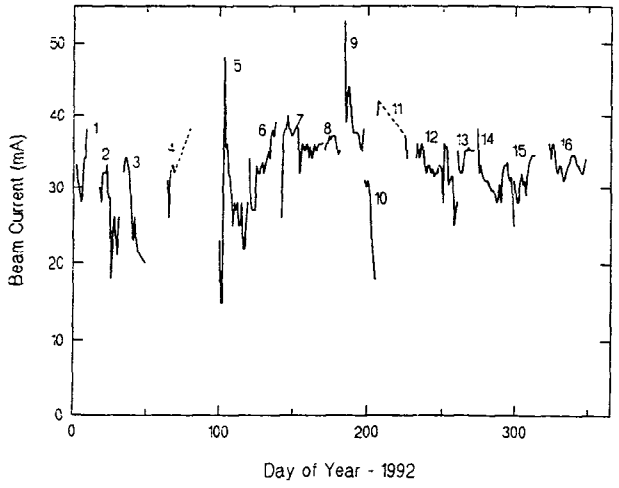

Fig 2 Record of current output from recent operational ion sources (at 665 keV).

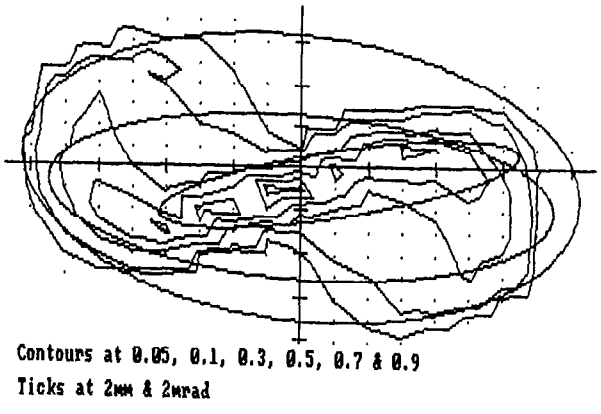

Fig 3a Emittance plot of 40 mA, 665 keV beam - H plane.
(See text for detailed description)

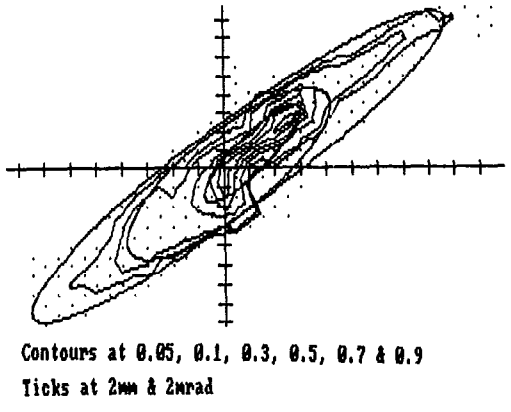

Fig 3b - V plane.

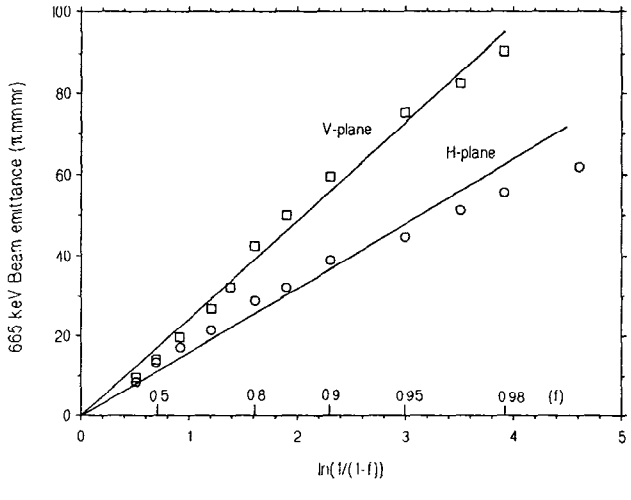

Fig 4 Emittance area of fitted ellipse as function of fractional beam enclosed (f), for beam of Fig 3.

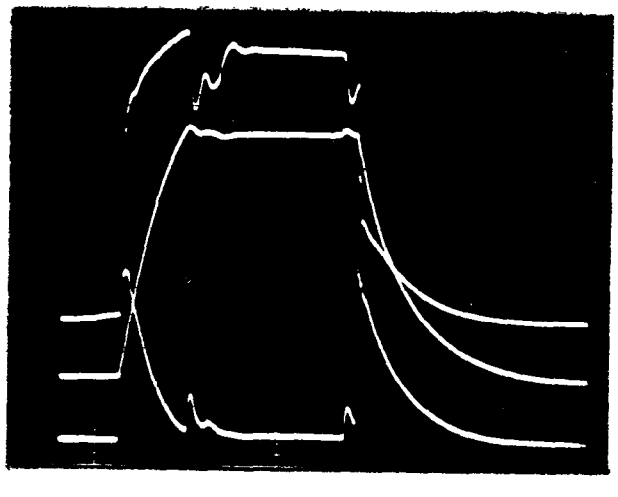

Fig 5 Cavity RF system oscilloscope pulses.

Top: Forward wave in cavity feed-line.
Middle: Cavity field level.
Bottom: Reflected wave in cavity feedline.

REPLACING A POPULAR ACCELERATOR CONTROL SYSTEM

R.P. Mannix

Rutherford Appleton Laboratory, DIDCOT, Oxon., OX11 0QX, U.K

Abstract

The ISIS computer control system has been both effective and well liked by its users. It is obsolete and very limited in power. The struggle to build a new system, using commercial software, that is at least as good as its predecessor (in spite of the advances in technology!) is described.

I. INTRODUCTION

ISIS is a 200μA, 50Hz, 800MeV proton synchrotron/heavy metal target spallation neutron source. The present control system has been used both during commissioning (1980-85) and operation. The design current of 200μA has recently been achieved.

A control system can be considered in two parts:

1. The environment, comprising-

    computer system(s)
    local control microprocessors
    equipment interface (i/o systems)
    man-machine interface
    system software
    equipment-specific software
    database organisation
    running environment for control programs
    commercial packages
    graphics language
    programming language(s)

The environment is always provided by or via a "controls group" of some sort and they alone make changes.

2. The implementation, comprising-

    control program specification
    control program authorship
    control program testing and installation
    control program availability
    implementation of commercial packages

The implementation is done to some extent by the users and from 0-90% by the controls group, depending on local preferences and precedence.

II. PRESENT SYSTEM

1. The environment.

computer system(s)-	GEC 4000 (1970's 16-bit minis)
local control microprocessors	Intel 8080
equipment interface (i/o systems)	Direct CAMAC/MPX,AWS
man-machine interface	CAMAC displays, touch screen, programmable knob
system software	GEC DOS (obsolete)
equipment-specific software	BABBAGE (GEC assembler)
database organisation	Rudimentary from BABBAGE
running environment for control programs	Semi-compiled interpreter
commercial packages	None
graphics language	) GRACES (interpreter)
programming language(s)	)

There are 5 GEC computers, connected via a CAMAC based star network (Figure 1). There are approximately 15000 lines of data module (equipment routine) source code. The equipment interface (MPX) consists of 700 modules in 70 crates. There are several hundred control programs in use. The Analogue Waveform Switching (AWS) system is run separately, via touch screens/PCs and CAMAC, to switch ~260 oscilloscope signals to the control desk.

The computers are very modest in power and are very limited in storage capacity. The operating system allows us to control hardware from a number of concurrent interpreter processes on each processor. High priority processes communicating with hardware completely lock out all others. Communication with other systems is non-existent, peripherals such as floppy disks are obsolete and unsupported, backups require shutting down the control system and maintenance is expensive (24hr cover is essential). The various branches of the interface hardware are tied explicitly to particular processors– reconfiguring after a processor failure is impossible– a serious disk drive fault can, and has, shut down the accelerator for a few hours. An average ISIS experiment lasts two days, within which several data taking runs, all of which are essential, must be performed. These sorts of breakdowns, although infrequent, are highly undesirable.

2. The implementation.

There are basically two schools of thought with regard to control system displays. The "crew" school like the use of colour, mimic diagrams, meters and dials etc. The "machine physicist" school like pages of numbers in monochrome with maybe an x-y plot for light relief every now and then, regarding all else as puritans regard the theatre- the devil's work. You have to allow both!

The guiding principle is "informed anarchy". The controls group rarely gets involved in implementation now (although we did start things off). Changes are made at will by machine physicists and crew members. The (dis)advantages of this approach are:

Advantages-

Extremely effective control system
Users "in touch" with machine
Changes to programs can be specified, implemented, tested and installed in under 5 minutes (for small changes) at any time by the person concerned.
Small (ie cheap!) controls group
Secure (due to use of idiot-proof interpreter)

Disadvantages-

Inefficient use of resources
No-one knows what all the programs do
Complicated programs difficult to maintain in author's absence.
Language limited to interpreter (slow, lacks facilities, needs to be learnt)

A final consequence- lack of well defined standards- is either an advantage or a disadvantage depending on who you talk to!

The decision was made to upgrade the environment with minimum impact on the implementation.

III. THE NEW SYSTEM

1. The environment.

computer system(s)-	DEC workstations
local control microprocessors	STEbus systems
equipment interface (i/o systems)	CAMAC/MPX,AWS (as now), connected via Ethernet.
man-machine interface	X-terminal
system software	Open-VMS
equipment-specific software	C functions
database organisation	Commercial package (see below)
running environment for control programs	Open-VMS process
commercial packages	Vsystem[1]
graphics language	Interactive screen generation OR port of existing commands.
programming language(s)	BASIC/FORTRAN/C

The Vsystem package provides a fully distributed database driven control system with a graphical interface over a number of DECnet nodes. Each control or monitoring object is referred to as a *channel* and, by using the *channel name*, control windows can be generated with an interactive draw package which interact with that channel via a number of control and monitoring "tools". Alarm handling, on-line database editing and logging facilities are also provided.

Access to the control and monitoring channels is also available from normal user programs written in VAX BASIC/FORTRAN or C. Such programs can be invoked from a ter-

minal window or from an interactively generated control window.

The use of channel names, database and handlers (equipment routines) maps very well on to our existing system based on Data Modules. The graphical interface provided with the new software should enable the functions of 75% of the control software to be replaced without recourse to writing code.

The system-wide nature of the databases and the networked nature of the CAMAC driver crates makes access to all equipment possible from any processor– something which was not previously possible. Up to 256 CAMAC crates can be accomodated on one Ethernet segment (Figure 2).

New and replacement microprocessor systems will be connected directly via Ethernet (at present they are connected to the MPX system.

Terminals with any level of access to the control system can easily be added anywhere on site (if desirable!). A control system for a new beam line can be provided by buying a workstation, another CAMAC controller and local interfacing hardware. The incorporation of this into the existing system is automatic (subject to the licensing agreement).

The current operator interfaces (touch sensitive screens , tracker balls, colour displays, knobs etc.) which are all obsolete or nearly so, will be replaced by high quality mouse/tracker ball and keyboard driven workstation type displays.

2. Implementation changes

The major changes the user will encounter (apart from the environment changes) will be in the specification, testing and installation of control programs and in the availability of the control programs.

The interpreter approach has been dropped and there is therefore no alternative to the edit/compile/link/run cycle, however streamlined. Choices have to be made as to whether the task is of sufficient complexity to warrant user code, or whether an interactively generated window would do the job and, if code is to be used, which language is appropriate. The specificity of devices on the control desk will disappear- all programs will be available from everywhere.

The requirement for users to update displayed information in their own programs has been dropped (at least for the interactively generated windows) database "readers" continually update the database values, changes being displayed as they occur.

No new system can look or behave as the old one did. Users are familiar with the old system and will be reluctant to change. Any shortcomings in the new system will be picked on and amplified, shortcomings in the old system having been assimilated years ago. Use of the new system from a user-written program is provided via a simple interface provided by the controls group.

IV. PROGRESS

Ten databases have been written, those for the injector magnets, the injector timing system, the injector general purpose status modules, target systems and extracted proton beam

magnets– a total of 2000 channels so far. Handlers for the programmable timing modules, magnet power supplies, function generators, equipment microprocessors and status modules have been written – conversion of BABBAGE to C is not too difficult. Control windows for the timer modules and magnet power supplies and the target station monitoring systems have been prepared and a suite of hardware test programs written for test access of interface modules via the ECC controller (external to the database).

A significant amount of time has been spent deciding how to modify the standard usage of the Vsystem software to suit our needs and in moving to new versions. Now this has been done, production of software should speed up.

V. OTHER APPROACHES

Well funded organisations can adopt the approach of doing everything themselves. The cost of this approach is high because of high level skills which need to be purchased- is the job of the controls group of a neutron source (for example) to push forward control system theory or to provide an engineering solution?

Various approaches have been described, using exclusively mass produced software on PC platforms (spreadsheets, DDE, LabView, etc). This approach may have many benefits, especially in smaller projects – I suspect such approaches are seldom glamorous enough to be given the full backing of their parent organisations.

VI. CONCLUSIONS

The choice of commercially available software must be correct for those establishments where lack of effort and staff turnover are problems. Good local support and constant updating of the product are also essential, as is the ability to feed requirements into the supplier's development plan. Even so the effort involved in changing to a new system is always underestimated, both by the customer and by the supplier. There is a lack of flexibility inherent in commercial systems- things have to be done "their way". This can be overcome by always having the option to tie in user programs in a variety of languages to the package concerned.

The licence and maintenance costs for such software, especially if not mass produced, are usually substantial, but must be compared with the staff-year costs in an organisation and offset against smaller staff requirements. Maintenance costs in our case equate to approximately 0.3 staff-year per year.

No commercial product will allow the easy assimilation of an existing control system. Whatever practises and methods prevail in an operating machine are the "right" ones by virtue of the fact that they are in use and familiar to those who use them. Any new system must be modified to fit what exists– not the best way to proceed. It is also clear that the only timing information of any interest to the user are the times taken to (1) present the control window required on the screen and (2) to operate a piece of hardware and see the effect on the screen, what happens underneath being irrelevant.

We are happy that the new control system will meet all our expectations with regard to extensibility, reconfiguration and communication and will perform as well as or better than

the existing system. It seems to be an unwritten law of control systems that, as the power of the processors increases, the complexity of the software rises until the perceived response time rises to the maximum acceptable. We would hope that the extra complexity in the new system will be achieved without a rise in perceived response time.

The suitability of Ethernet (or any general purpose network system) as the main i/o channel is unclear. On the one hand emerging computer systems are frequently only supplied with an Ethernet port and moving away from this becomes expensive. It is truly distributed and configuring the system and expanding it become trivial. On the other hand, the generality of the system means that it is slow. It is clearly unsuitable for a fast data acquisition system but should be well suited to a supervisory control system such as ours.

The key advantage over our old system (and over Q-bus, turbo-channel, SCSI controllers or even PCI interfaces) is the logical separation of the interfacing hardware from a particular processor and the similar distributed nature of the databases- this is a truly distributed system (aside from one disk which must always be available to the system). Directly connected systems force all access to be through the parent processor, whose failure will isolate that equipment entirely. It also allows the integration of PC's, CAMAC, VME, STEbus, and other systems in a controlled manner. Together with distributed software such as that described, it provides a system which is easily reconfigurable should a processor fail. The price paid for this flexibility is speed.

REFERENCES AND ACKNOWLEDGEMENTS

1. "Vsystem" is acknowledged to:

Vista Control Systems, Inc.
134 B Eastgate Drive
Los Alamos
New Mexico 87544

GEC Computers are now GPT Datasystems Ltd.

DEC, Open-VMS are registered trademarks of the Digital Equipment Corporation.

Ethernet is a registered trade mark of the Xerox Corporation.

LabView is a registered trademark of National Instruments.

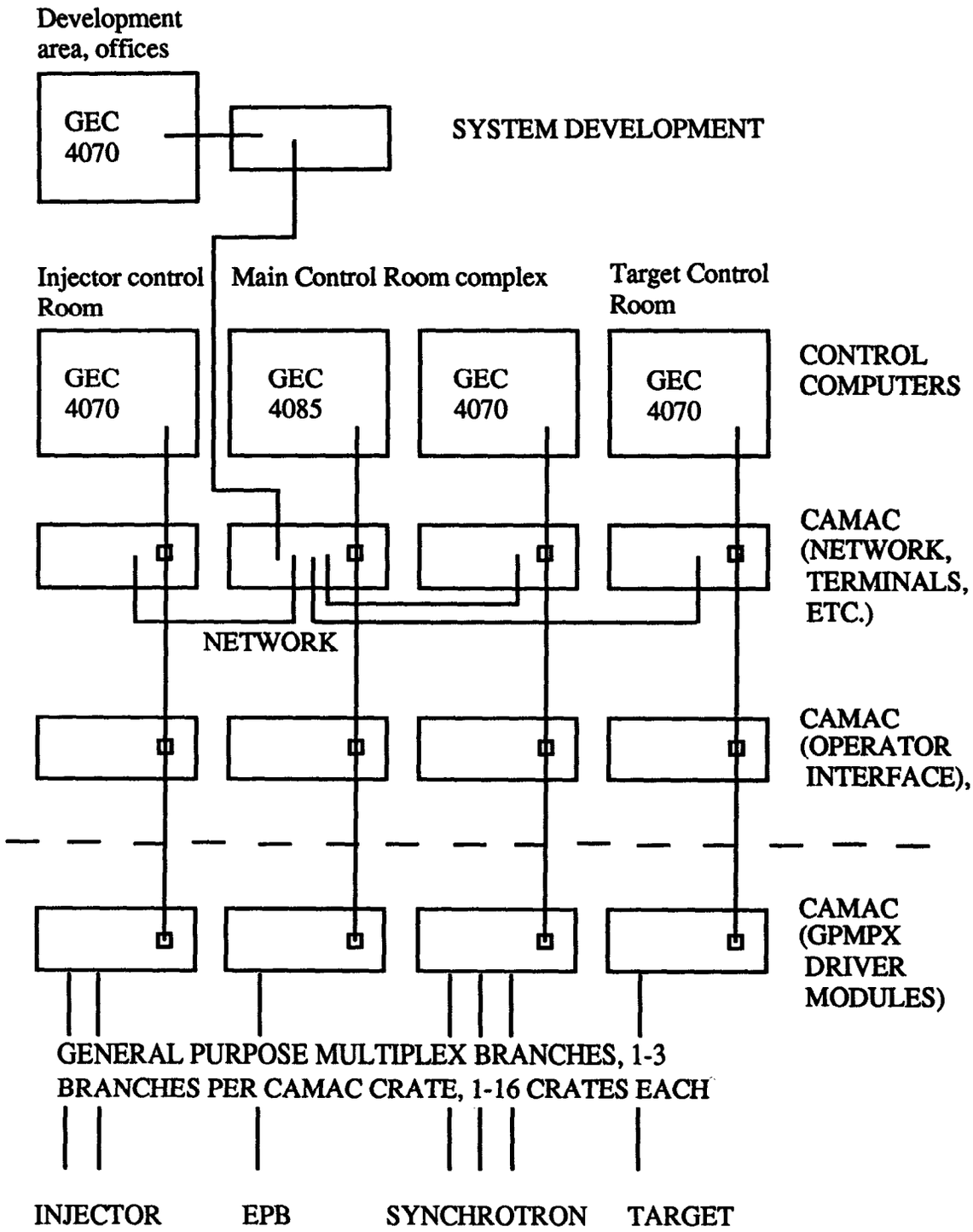

FIGURE 1. General arrangement of present system

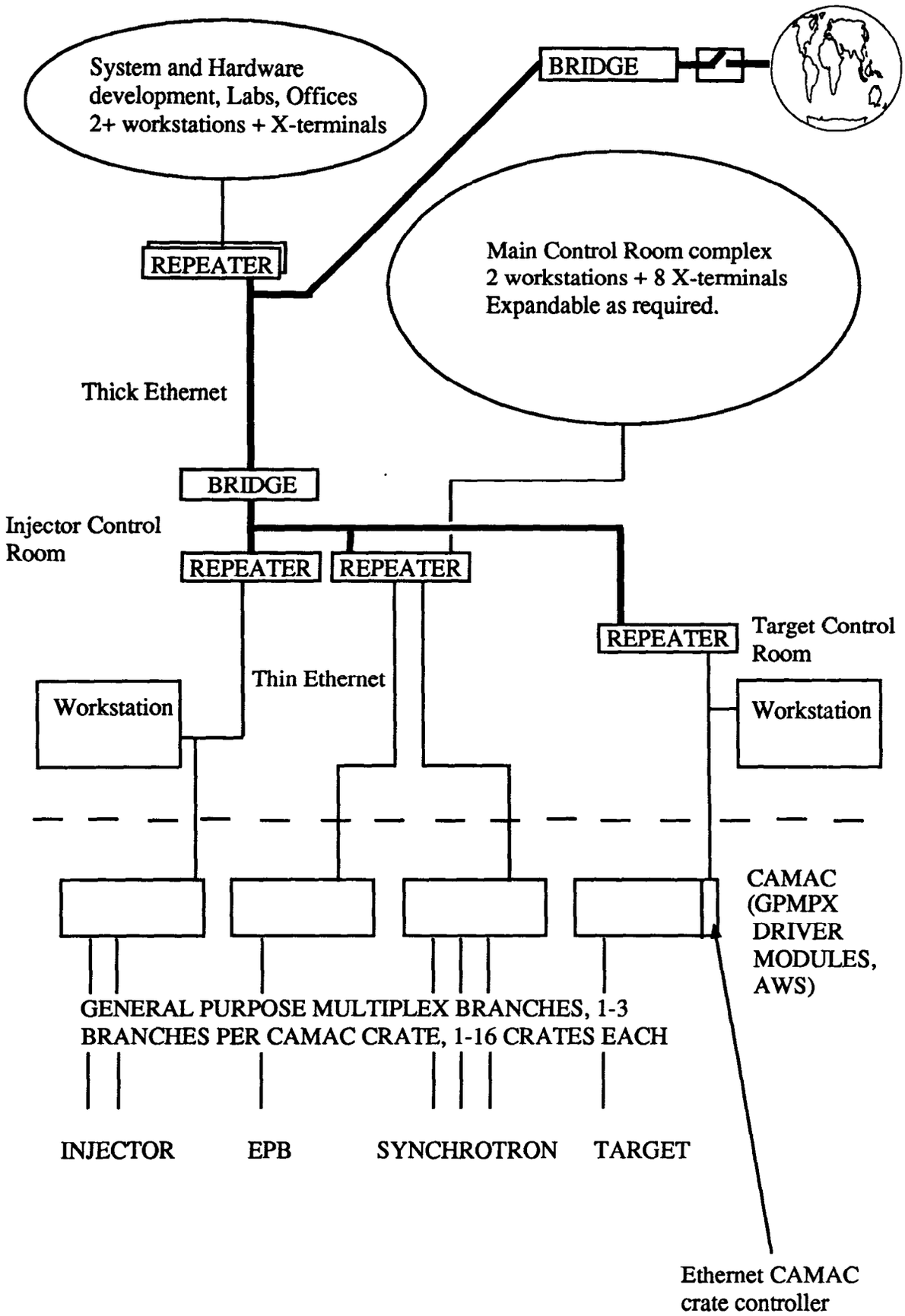

FIGURE 2. General arrangement of proposed system

LOW INTENSITY AND INJECTION STUDIES ON THE ISIS SYNCHROTRON.

C M Warsop.
Rutherford Appleton Laboratory, Chilton, Didcot, Oxon, England.

Abstract.

The use of chopped beams to study injected beam conditions and general low intensity behaviour of the ISIS Synchrotron is described. The difficulties associated with measurements at these relatively low intensities and development of the system for on-line diagnostics during operational running are outlined. Some results from ISIS are presented, along with their implications at high intensity.

Introduction.

The value of low intensity studies on a machine like the ISIS Synchrotron, designed specifically for high intensity, may not be immediately obvious, but they can in fact give much detailed information not otherwise available. At high intensity, the large amounts of beam filling most of the machine acceptance make detailed study of particle motion within the beam very difficult. Detailed motions of one part of the beam are obscured by the rest - as far as any practical diagnostics are concerned. However, motions of small beams, which fill a small fraction of the machine acceptance, can be observed directly - allowing detailed study of the beam dynamics in the low intensity limit. The information so obtained is of considerable value, facilitating checks on the lattice and investigations of the injection process, and measurement of properties of the injected beam - all of which have important implications at high intensities.

Background.

ISIS Injection and Beam 'Chopper'.

A high intensity beam is established in the ISIS Synchrotron by means of Multi-Turn, Charge-Exchange Injection [Ref. 1]. Under this scheme, protons are accumulated over about 200 machine revolutions from the 20mA, 25 π mm-mr H^- injector beam. To facilitate filling of the horizontal acceptance (540 π mm-mr), beam of constant energy is injected at constant horizontal angle and position while the (sinusoidal) main magnet field is falling; the resulting movement of the machine closed orbit leads to a suitable distribution in betatron amplitudes. In the vertical plane (acceptance 430 π mm-mr), a spread in betatron amplitudes is achieved by moving the vertical injected position and angle using a programmable steering magnet.

The beam 'chopper', an electrostatic kicker situated in the injection beam line, deflects all but a selected amount of beam, at a selected time, onto a beam dump. In this way, 'chopped' beam bunches of down to 100ns can be injected at any time during the ~200μs injection period. The motion of this relatively small beam (about 0.1% of full beam) can then be easily observed - giving information on the injection process itself, or on more general beam dynamics of the machine.

Measurements Possible with 'Chopped' Beams.

Chopped beams can be useful for a number of measurements, depending on the diagnostics used. In the transverse planes, position monitors and profile monitors allow the investigation of injection and basic beam dynamics. Suitable diagnostics can also measure the longitudinal profile of the chopped

beam bunch - thus giving information on motion on this direction. In particular, bunch lengthening measurements (with machine RF off) can give information on the momentum spread of the injected beam.

The main motivation behind chopped beam studies on ISIS is to investigate injection, and this naturally involves measurements on coasting beams (i.e. RF off). The possibility of developing more sophisticated measurements to include longitudinal oscillations, which would allow studies throughout the machine cycle, are not considered particularly profitable and have not been pursued. Work has thus concentrated mostly on transverse dynamics at injection. Measurements with position monitors have been particularly useful and justify some explanation (see below).

It should be emphasised that although much detailed and accurate information can be obtained with chopped beams, it is valid only in the low intensity limit. Essentially, they allow accurate determination of the 'initial conditions' at low intensity, but give no information on the way in which these may be modified by high intensity effects.

Position Monitor Measurements.

Transverse Motion.

Chopped beam measurements using position monitors (i.e. diagonally 'split cylinders', which measure transverse position of the beam centroid), are especially useful because of the amount of information they give. The method is essentially the same as that in [Ref. 2] and is as follows.

A small, chopped, beam bunch is injected into the synchrotron with a length which fills less than one turn or circumference. Such a beam is observed on a position monitor as a series of pulses as it circulates in the machine. Essentially, one sees sampled betatron oscillations of the bunch on each revolution, but these are modified by a number of effects. The changing main magnet field (with constant beam energy) during injection means that Q values and closed orbits change, though slowly, on successive turns. More significantly, the finite spread in betatron frequencies in the beam causes the oscillations to de-cohere after a finite number of turns; on a position monitor, which measures average values, this is seen as damping.

By assuming a functional form for the Q spread and allowing for the changing magnet fields, one can derive a theoretical function for turn by turn positions. Note that this assumes no longitudinal oscillations, i.e. synchrotron RF is off. In this work a Gaussian Q distribution is assumed and this leads to a function of the form [Ref. 2];

$$y_n = A \cdot \exp\left[\frac{-(\pi \cdot n \cdot \delta Q)^2}{2}\right] \cdot \cos\left[2\pi \cdot n \cdot \left(Q_0 + \frac{n \cdot \Delta Q}{2}\right) + 2\pi \cdot \Phi\right] + n \cdot \Delta R + R_0 \qquad \{E\ 1\}$$

where;

	y_n	- Transverse position on n^{th} turn
	A	- Initial Betatron Amplitude
	δQ	- Q Spread [due mainly to momentum spread in the beam]
	Q_0	- Initial Q value
	ΔQ	- Change of Q per turn
	Φ	- Initial Phase
	ΔR	- Change in closed orbit per turn
	R_0	- Initial close orbit

By least squares fitting measured positions to this function (see Figure 1), estimates of the above parameters are obtained, allowing values on the first turn to be calculated. These parameters give information on the lattice (Q, Φ), injection (A, R, Φ) and momentum spread (δQ), as will be detailed below. On ISIS, the particular values of momentum spread and chromaticity mean that the oscillations 'damp' out after about 30-40 turns; this gives enough data to obtain good estimates, with uncertainty in the betatron Q value being about ±0.002, and in position related measurements about ±1mm.

The short time over which the measurements are taken, 40 turns or 60μs, means that approximations in E1 associated with (i) the *assumed* Q spread distribution, and (ii) the changing magnetic fields, have minimal effect. The quality of fits obtained experimentally confirms that the approximations are reasonable.

Figure 1. Example of Least Squares Fit.

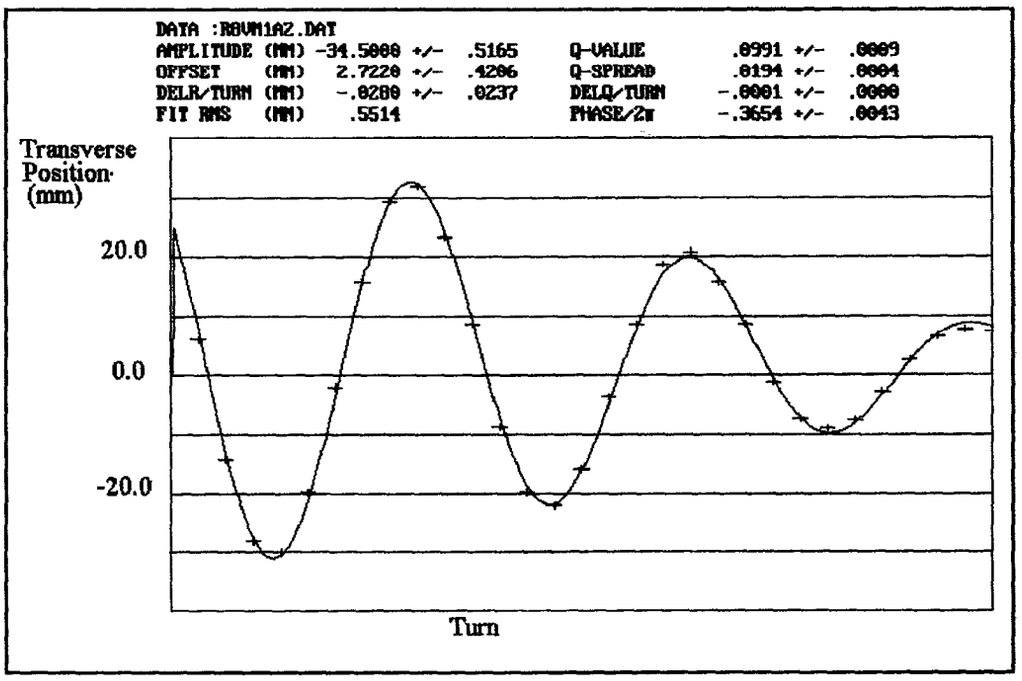

Momentum Spread.

The above method gives an estimate of the momentum spread of the injected beam, assuming that this is the only cause of Q spread and that chromaticity is known [$\Delta P/P=(\Delta Q/Q)/\xi$]. A better method is measurement of longitudinal debunching of coasting chopped beams, which can be observed conveniently on ISIS using the sum of position monitor electrode signals. Work is presently underway to allow such measurements.

Implementation.

The position monitor measurements are controlled by an IBM PC/AT compatible, which sets timing pulses, controls a digital sampling scope and processes the data (see Figure 2). A measurement time is selected and the PC sets up trigger pulses for the chopper and 'scope. The signals from the position monitor are passed to the sampling scope, where they are digitised, averaged and then transferred to the PC. After some processing, the turn by turn positions are determined, and fitted to the above

function. The process is automated, so that a 'scan' through the injection cycle, measuring parameters at time intervals down to 5μs, is possible - with speed being limited by the repetition rate of the chopper.

The chopper can be programmed to run at a number of repetition rates; the machine runs at 50Hz and the chopper can be triggered on one in every 32, 64 or 128 of these pulses. Loss of one pulse in 128 causes a tolerably small reduction in neutron production, and thus experimentation/optimisation is possible during normal running.

Figure 2. Schematic of Chopper System.

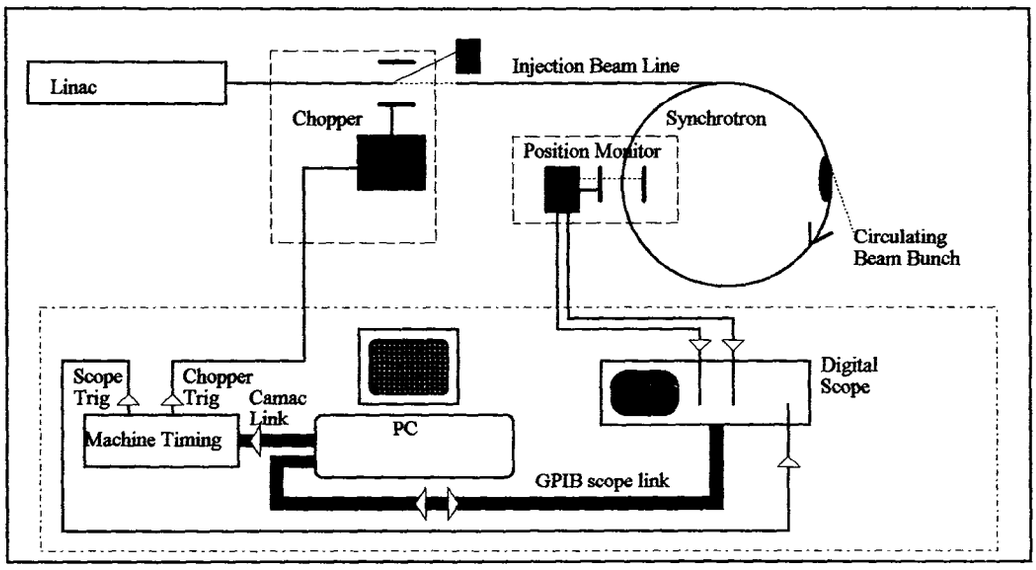

The 40 horizontal and vertical position monitors distributed around the ISIS Synchrotron were all originally intended for use with high intensity beams, and therefore give rather small, noisy (though just about usable) signals with 'chopped' beams (about 0.1% of normal beam). To overcome this problem, two 'dedicated' 'chopper' monitors, one for each plane, have been selected and the gain of their associated electronics increased. To allow measurements during normal running, where interleaved high intensity pulses would saturate electronics, some 'gating' of signals has also been necessary.

Profile Monitor Measurements.

Transverse Profiles and Matching.

Clearly, for any real understanding of injection, one needs information on beam widths. Use of profile monitors with chopped beams should give information on the matching of the injected beam into the synchrotron, and thus ultimately some idea of optimum conditions for high intensity.

Implementation.

Only a little preliminary work has been attempted with profile measurements on chopped beams to date, however it is worth mentioning the diagnostics installed and their intended use.

There are two types of profile monitor installed on the ISIS synchrotron, (i) residual gas ionisation monitors and (ii) a secondary emission grid or 'wire' monitor.

The residual gas ionisation monitors are regularly used with high intensity beams and have the advantage of being non destructive. Some initial tests indicate that these can be used with chopped beams despite the relatively small signals. Limitations to the speed of the electronics mean that profile measurements are averaged over about 10 revolutions of the chopped beam, but this still gives valuable information on the width of the injected beam.

The destructive secondary emission monitor is intended mainly for use with a beam stop also installed in the synchrotron. The beam stop prevents scattered, recirculating beam from distorting profiles. With the beam stop in (it is placed downstream of the profile monitor!), chopped beams of differing pulse lengths and at differing times can be injected, and their profile on the first turn seen directly.

Long Term Objectives.

Integrating the position monitor measurements with those of profile monitors, and with appropriate use of computer lattice programmes, it is hoped that a largely automated system for setting up and optimising all important aspects of injection will result. In addition, by allowing more machine parameters, e.g. steering magnet currents, trim quads etc. to be programmed with experimental values during the chopped/experimental pulse only, a system for doing far more experimentation during normal running is planned.

Measurements on ISIS.

Work with chopped beams is far from complete, however many useful results have been obtained with the position monitor measurements, and these are outlined below.

Figure 3. Typical Horizontal Injection

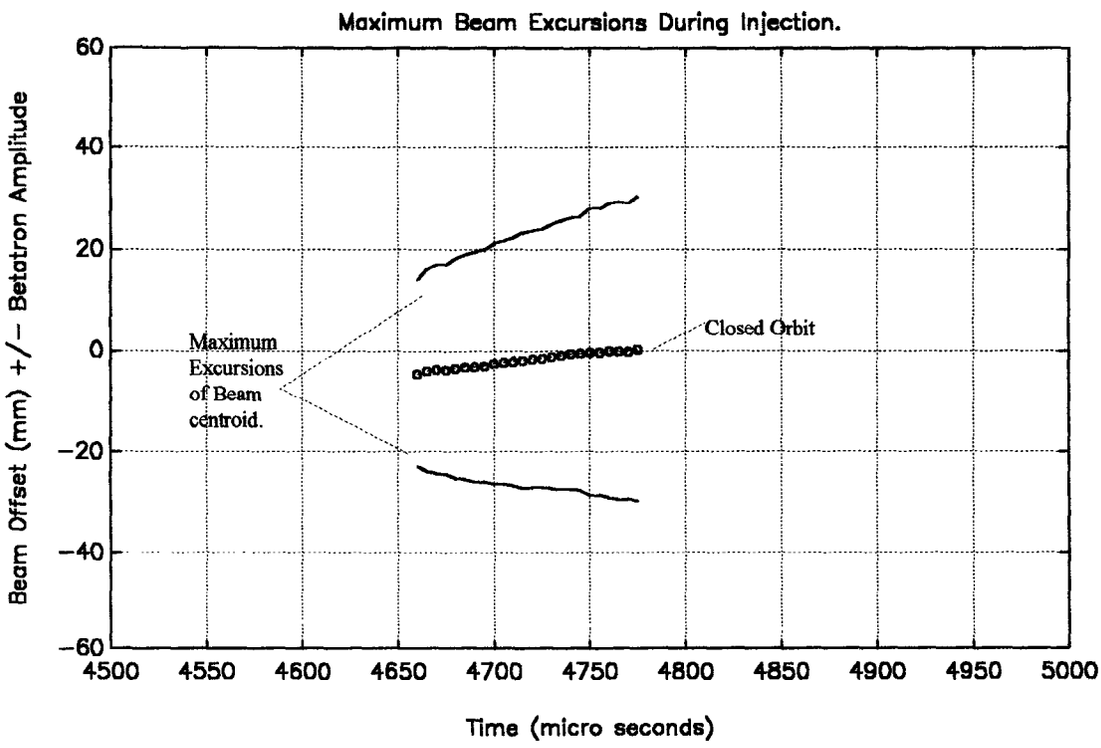

Injection Set up.

Repeating position monitor chopper measurements throughout the injection process, allows the betatron amplitudes of the injected beam, and the position of the closed orbit at the position monitor, to be obtained as a function of time. These show how the synchrotron acceptance is being filled or 'painted' in both transverse planes, in the low intensity limit. A typical example for the horizontal plane is shown in Figure 3, which indicates the maximum excursions of the injected beam centroid about the closed orbit, as a function of injection time. This information allows injection to be set up in a consistent way, with checks being possible during normal running.

It is known that at high intensity, the transverse beam distributions can change significantly from those 'predicted' by chopper measurements at low intensity. However it is also clear that the initial distributions at injection have a definite effect on trapping efficiencies etc. later on in the machine cycle. These measurements allow definite identification of the optimum set up, as well as showing whether injection alignment, closed orbits or other parameters are in need of correction. The planned profile measurements will give further essential information on the injection process.

Q Values at Injection.

Chopped beams allow accurate determination of the (low intensity) betatron Q values throughout injection, and thus provide a valuable check on the basic lattice and on the operation of the separately programmed trim quadrupoles [Ref. 3], as well as allowing optimum tuning to avoid resonances.

Figure 4. Q Values

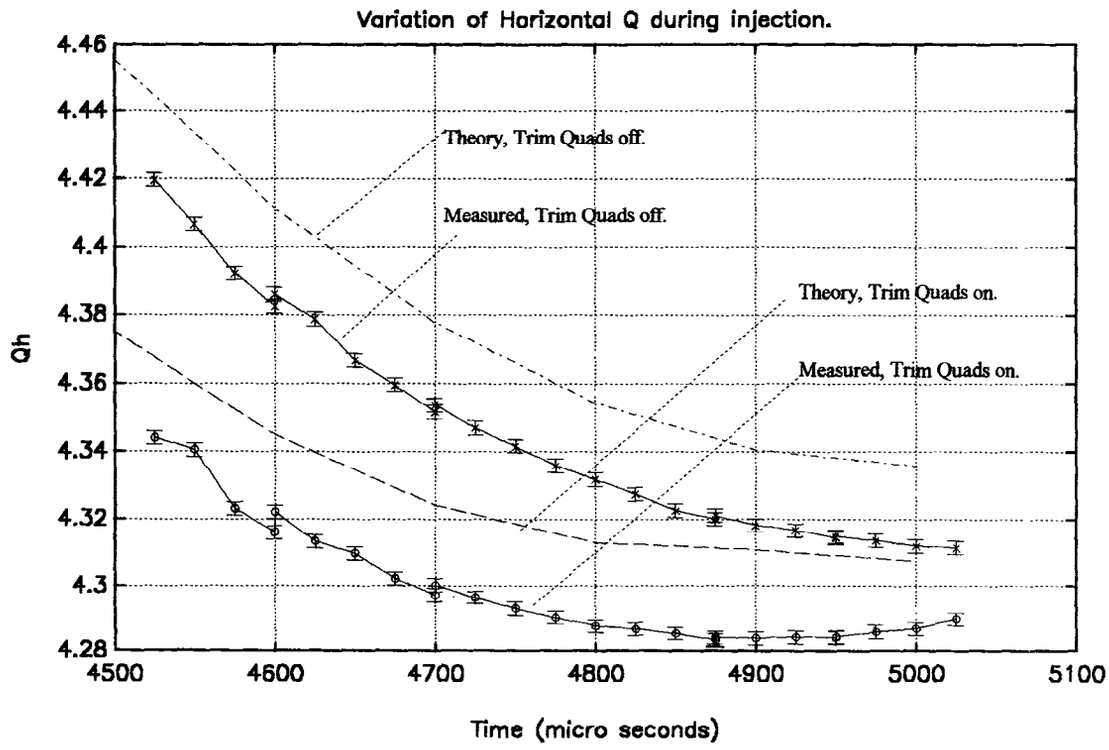

Typical results for the horizontal plane are given in Figure 4; these show measured and theoretical values for trim quads on and off. Similar results are found in the vertical plane, and indicate roughly constant offsets between measurement and theory of the order of -0.05, in both planes. Work is under way to explain these differences, as it is possible that the underlying cause may be affecting

high intensity performance. Ignoring the offset, the variation of Q with time and the change due to trim quads is in reasonable agreement with theory.

Chromaticity.

Switching trim quads off and measuring Q values as a function of the main magnet field (at constant beam energy), allows an accurate measurement of the machine chromaticities ξ.

$$\xi = \frac{\frac{\Delta Q}{Q}}{\frac{\Delta P}{P}} = -\frac{\frac{\Delta Q}{Q}}{\frac{\Delta B}{B}} \qquad \{E\,2\}$$

where P is the particle momentum and B the mean quadrupole field. Figure 5 shows the results in the horizontal with ξ_h= -1.41 ±0.09, a similar value of ξ_v= -1.42 ±0.08 was obtained in the vertical. These compare reasonably with theoretical values of ξ_h= -1.45 and ξ_v= -1.24, and indicate minimal errant sextupole components. It can be seen that the Q vs ΔB/B relation is highly linear, implying absence of significant octupole components.

Figure 5. Horizontal Chromaticity.

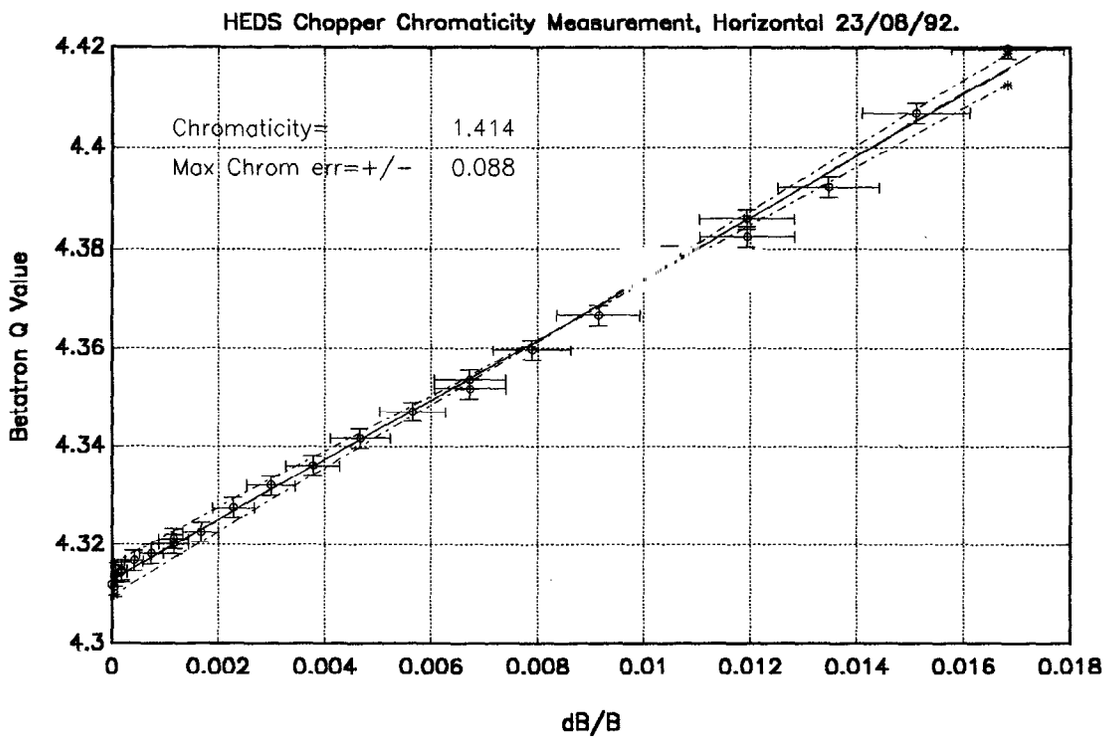

Closed Orbits at Injection; 'Many Monitor Measurements'.

Chopped beam measurements described so far have made use of the two specially modified 'high gain' position monitors. However it has been possible to take measurements at most other ('low gain') position monitors, albeit with lower precision, and this gives parameters in E1 as a function of azimuthal position around the synchrotron. This method has been used to measure closed orbits (R in E1) at injection, when the normal unbunched beam is difficult to measure using the AC coupled monitor system. Measurements of this type also have potential for detailed lattice checks, by giving betatron phase advances between monitors.

Momentum Spread Measurements.

As already mentioned, transverse position monitor measurements give an estimate of the injected beam momentum spread. Values for $\Delta P/P$ 95% full widths come out at about 4.5×10^{-3}, and this agrees reasonably with magnet spectrometer measurements in the injection beam line of about 4.0×10^{-3}, under similar conditions. These are to be checked with the bunch lengthening measurements mentioned above, and will provide valuable information on the operation of the debuncher cavity in the injection line, which is used to optimise injected momentum distribution for high intensities.

Commissioning of Non Linear Correction Elements.

Chopped beams are presently being used to check the installation of sextupoles and octupoles on ISIS. Fairly simple experiments, observing the changes in Q with radial beam position and multipole current, give clear indications of their operation.

General Applications.

The system has also been used to check the linearity and calibration of the position monitors, and to investigate amplitude dependence of Q.

Conclusions.

Low intensity, or 'chopped' beam studies on the ISIS Synchrotron have allowed many accurate and detailed measurements, not really possible with high intensity beams. The low intensity information these give is of great potential value in setting up the machine and 'trouble shooting' during operational running, as well as forming an excellent basis for high intensity work.

Acknowledgement.

The author would like to acknowledge the help and advice of A I Borden, I S K Gardner, M R Harold, C W Planner and G H Rees during the course of this work.

References.

[1] 'Injection Dynamics and Multiturn Charge Exchange Injection with Fast Cycling Synchrotron for the SNS.'; V C Kempson *et al.* IEEE Tr Nu Sci Vol NS-28, No 3 June 1981.

[2] 'A Method for Determining the Position, Angle and other Injection Parameters of Short Pulsed Beams in the AGS.'; L Ahrens *et al.* IEEE Tr Nu Sci Vol NS-32, No 5 Oct 1985.

[3] 'Spallation Neutron Source, Description of Accelerator and Target', B Boardman. Rutherford Appleton Laboratory Report, RL-82-006.

ICANS May 1993,
Rutherford Appleton Laboratory.

The ISIS Synchrotron RF System at High Intensity

P.J.S.B. Barratt

Abstract.

A summary of the RF system of the ISIS Synchrotron was published[1] in 1990 when the operating beam intensity was about half the present level and the extraction energy was 750 MeV instead of the current 800 MeV. A fuller description is given here reflecting the developments that have been carried out since then to facilitate operation with a beam of the design intensity of 200 μA.

Introduction.

The requirement to accelerate a beam of such a high intensity imposes some uncommon demands on the rf system. The ISIS synchrotron rf system allows a wide dynamic range of accelerating voltage which may be necessary to trap the coasting injected beam from the Linac into bunches of sufficient length to minimise space charge forces and peak momentum spread. The short acceleration time of 10 ms leads to a high maximum rate of change of accelerating frequency, necessitating the use of special techniques to keep the cavities in tune during acceleration. During the early stages of acceleration, the ratio of beam current to cavity current is such that the use of a fast feedforward beam compensation scheme is necessary to maintain stability. An additional constraint is that all components in the synchrotron ring must be radiation hard.

RF System Configuration and Parameters.

The synchrotron has ten superperiods; six of which contain a ferrite tuned rf accelerating cavity, three in adjacent superperiods on one side and three diametrically opposite. With a harmonic number of 2, there is then an rf phase angle of 72° between adjacent cavities of a group.

The ring dipole magnets have a dc biased, 50 Hz sinusoidal excitation giving a continuously increasing field over the 10 ms accelerating period. Injection from the 70 MeV Linac occurs during the 500 μs prior to the field minimum after which the unbunched beam is trapped and then accelerated by the rf cavity voltages. The large dynamic range of the accelerating voltage is achieved by supplementing the 200:1 dynamic range of a conventional amplitude control loop with an additional factor of 10:1 obtained by using a cavity phase loop that allows the phase angle between diametrically opposed cavities to be varied from -180° to 0°. Opposed cavities are thus brought rapidly into phase (in less than 30 μs) towards the end of the injection period.

Further rf system parameters are:-

Energy range	70 - 800 MeV
RF frequency range	1.3-3.1 MHz
Transition Gamma	5.032
Max Acceleration rate	124 GeV/sec
Max power transferred to beam	496 kW
No of gaps per cavity	2
Peak RF voltage per gap	14kV
Accelerating voltage per turn	168kV

The rf control electronics comprises:-

1. An oscillator whose frequency is controlled (from 1.3 to 3.1 MHz) by the contents of a block of memory that is interrogated according to the instantaneous central field in the ring gradient bending magnets.

2. Individual loops to control the amplitudes of each rf cavity voltage.

3. Individual loops to control the relative phasing of each cavity according to its position around the ring, the rf phase angle between adjacent cavities being 72°. It is this loop that is also used to "antiphase" opposing cavities during the injection period to reduce the vector sum of the accelerating voltage to zero.

4. Individual loops to tune each cavity by maintaining a 180° phase difference between the cavity voltage and an appropriate input drive voltage.

5. Three beam control loops which operate by varying the acceleration frequency: a radial loop to keep the beam on the correct orbit, a beam phase loop to damp beam coherent dipole phase oscillations, and another loop, driven by variations in bunch length, to damp quadrupole motion of the beam.

The Accelerating Cavity.

Fig. 1 shows the main elements of an ISIS cavity. The water-cooled plates which cool the ferrite can be seen separating the 35, 50 cm OD ferrite rings in each resonator. The centre is made from two co-axial tubes. The outer tube is made from copper to provide a low impedance path for the bias field current and the rf. The inner tube is made from nickel-plated mild steel to provide the vacuum pipe and to shield the beam aperture from any magnetic field produced on the beam axis by the bias field.

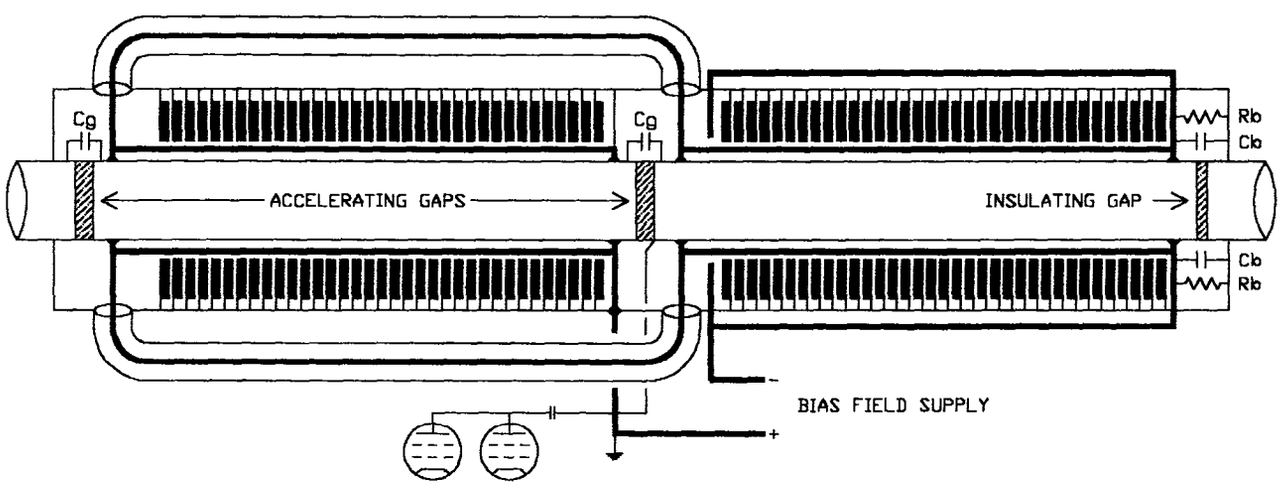

Fig. 1 The ISIS synchrotron accelerating cavity.

The two accelerating gaps are made from ceramic which is metallised on the ends and welded to the mild steel. Cg represents the total capacitance at a gap and is about 2.2 nF. The two gaps are connected in parallel by two 70 Ω co-axial lines which carry both the bias field current and the rf voltage. Cb is approximately 17 μF and forms an rf by-pass capacitor providing a low impedance for the circulating rf current in one of the resonators but allows the bias field current to be fed around both resonators which are in series to the bias current. The bias field is parallel to the rf field but in opposite direction in each resonator. With a gap voltage of 14 kV peak Cb limits the rf voltage appearing across the bias supply to less than a few volts. Cb and the two resonators form a tuned load for the bias supply. This resonance, at a minimum value of 10.4 kHz, is damped by Rb (6Ω).

The high Q-factor of the cavity ferrite results in an operational gap impedance of about 4 kΩ which would give rise to an excessively high beam-induced component of cavity voltage and thereby compromise the stability of acceleration. To avoid this, each gap is loaded with a Q-damping resistor in which the resistive element is formed from continuously pumped copper sulphate solution. By varying the concentration of the solution, the effective gap impedance can readily be controlled down to 1kΩ with a corresponding reduction in induced voltage. Each resistor can dissipate a peak rf power of 100 kW and presents very little reactive loading.

The High Power Driver Stage.

The high power driver stages are located adjacent to the cavities, and are now powered by a paralleled pair of RCA (Now Burle Industries inc) 250 kW tetrodes type 4648 operated in class AB with a grounded cathode and an anode voltage of 18 kV. No special matching of the tetrode characteristics is done; the standing currents of each of a pair are simply equalised (at 2A) by setting the grid bias. Each tetrode is required to deliver a maximum rf current of about 25 A peak into the cavity. The total current is nominally within the capabilities of a single tetrode of this type, and until recently only one was used, but operation at this higher level in our enclosure was then complicated by the sporadic onset of parasitic high frequency oscillations. These tetrodes have proved very reliable in operation. The shortest lived one so far was returned to Burle Industries for rebuilding after 16,000 hours of operation but another is still giving good service after 47,000 hours.

The rf drives for the tetrode grids of up to 150 v peak are provided from 2-channel 500 Watt water-cooled solid-state amplifiers, made by Herfurth GmbH of Hamburg, located in a low radiation environment in the centre of the synchrotron ring.

The Cavity Tuning Loop.

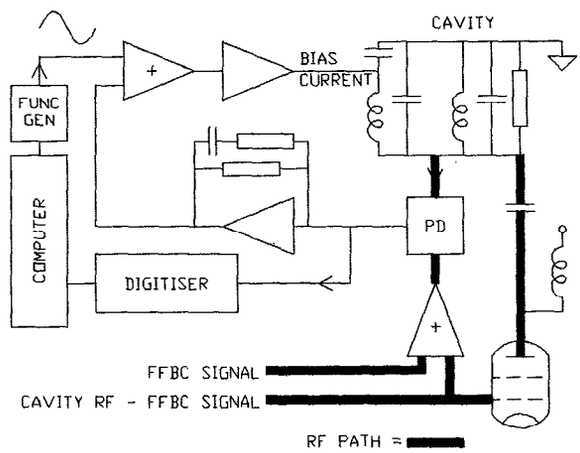

Fig. 2 The cavity tuning loop.

Due to the short acceleration time on ISIS, the cavity tuning loop has to cope with a rate of change of frequency of up to 330 MHz/s. This, coupled with a bandwidth of 5 kHz for the cavity bias current source and a similar bandwidth due to cavity Q, would lead to excessive cavity tune errors during the frequency sweep. The method used to correct this error, which is highly repetitive, is shown in Fig. 2.

The phase detector error is reduced by feeding a computer-generated analogue signal as a "demand" for the servo control. This is obtained as follows.

The phase detector signal is digitised at 2000 points throughout the full cycle. The signal is then Fourier analysed and each harmonic component is multiplied by an appropriate gain and phase, obtained from the measured closed-loop transfer function from the function generator output to the phase detector output, so as to reproduce the phase detector signal. These components are then subtracted from the existing function generator signal thus progressively reducing the phase detector error signal.

This procedure is normally carried out during maintenance periods with perhaps ten iterations being necessary to minimise a large tuning error but it is also practicable to use the system to reduce the beam-induced cavity tuning perturbations for any given operating intensity.

It can be seen from Fig. 2 that, while the FFBC (see below) is active, by nulling out the FFBC signal, the cavities are kept on tune as if no beam were present. Subsequently, they are detuned for reactive compensation. The tuning loop error, as monitored on the output of the tuning loop phase detector, is a useful indicator of the performance of the tuning loop, the beam compensation, and the general health of that rf system. During the acceleration period, the tuning error is generally less than ± 10° , the largest error usually occurring during trapping.

Feedforward Beam Compensation (FFBC).

FFBC is used to cancel the initial, beam-induced cavity fields so allowing the tuning loop to work effectively, for its 5 kHz bandwidth is not high enough otherwise to reduce the cavity tuning errors to a sufficiently low level during the bunching, trapping and initial acceleration period. Fig. 4 shows the principal components of the system.

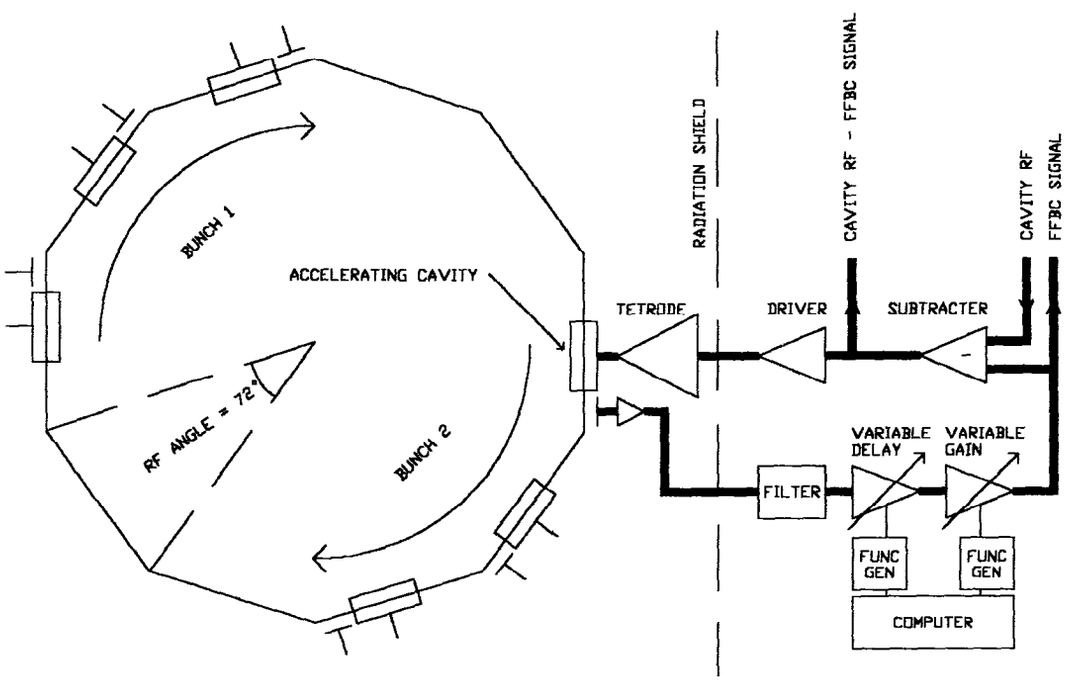

Fig. 3 The synchrotron ring layout and the feedforward beam compensation system.

The rf drive current to each cavity gap at the end of the injection period is about 1 A peak. At 200 μA (2.5×10^{13} protons per pulse), the injected beam will subsequently bunch to over 4 A peak. The FFBC system acts to compensate the resultant large beam-induced cavity voltage and thus preserve the critical acceleration voltage profile. This has the effect of reducing the cross-coupling between the various rf control loops thereby increasing the threshold of instability. Without the FFBC system in operation, it would not be possible to accelerate more than about 25 μA.

The instantaneous beam charge is sensed just downstream of each cavity and the signals are filtered to leave only the fundamental component. In each system, the signal is passed through a computer programmable variable delay - variable gain amplifier and then subtracted from the input signal to the driver amplifier. The purpose of the variable delay is to compensate for the revolution period that varies from 1.4 to 0.6 μs throughout acceleration, and that of the variable gain is to scale the charge signal into a current signal and compensate for variations in system gain with frequency.

The method used to determine the optimal delay and gain throughout the compensation period is to accelerate a low intensity beam (3×10^{12} ppp) with only five cavities powered and find experimentally the values that minimise the beam-induced voltage on the remaining unpowered cavity. Fig. 4 shows the envelopes of the resultant voltages induced in a cavity by such pulses with and without compensation.

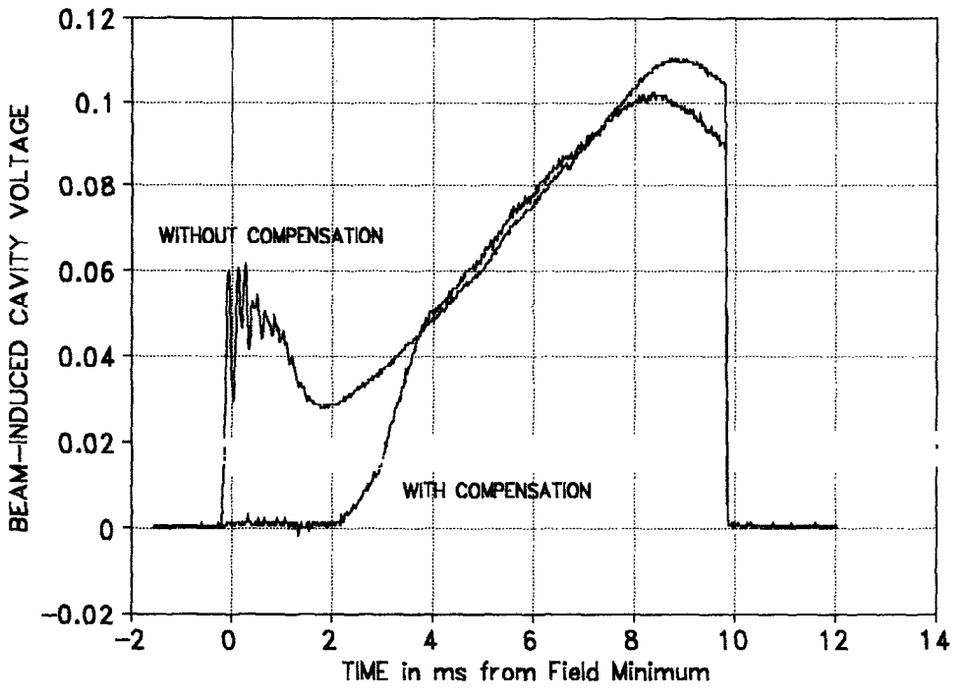

Fig. 4 - FFBC cancellation of beam-induced cavity voltage.

The cut-off frequency of the low pass filter in the FFBC signal path is chosen to give adequate suppression of the second harmonic component of the beam signal at the beginning of the acceleration period and its roll-off rate, together with that of the FFBC gain function, is chosen to give an orderly transition from FFBC to reactive compensation provided by the tuning loop which allows operation with less drive power. While the FFBC is active, the high power drive is working into an unmatched load.

Performance.

Fig. 5 shows the envelope of the rf accelerating voltage per cavity, the normalised beam intensity (a beam toroid signal divided by rf frequency) and the envelope of the peak beam charge signal derived from a pick-up. The acceleration efficiency at this intensity, about 2×10^{13} ppp, is around 90% with, as can be seen, most of the loss occurring at relatively low energy at trapping. Most of the untrapped beam is caught by the collectors in the ring.

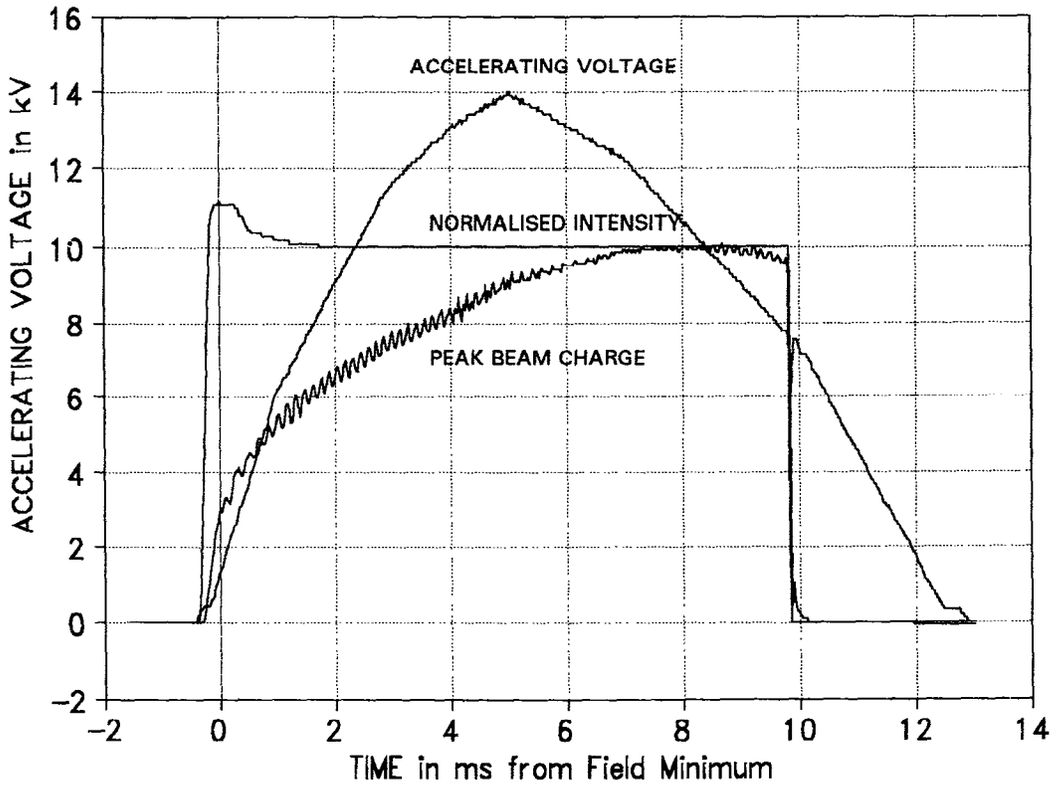

Fig. 5 RF voltage and beam intensity during acceleration.

It was anticipated that to minimise the loss at trapping, the rf voltage throughout the injection period should be kept as low as possible. However, at higher intensities, it is found experimentally that the trapping loss is lower if, as shown in Fig. 5, the accelerating voltage is turned on well before acceleration starts at the field minimum. This may be because the voltage suppresses the onset of a coasting beam instability during the injection period but this aspect requires further investigation.

The recorded trapping efficiency during the recent tests at 200 μA intensity was 86%. This figure is expected to improve with further experimentation and development. There is as yet no evidence that the performance of the present rf system will limit the efficiency.

Acknowledgements.

The author would like to thank I.S.K Gardner and other members of the ISIS accelerator division for their help and contributions to this work.

Reference.

[1] P. Barratt, I. Gardner, C. Planner, G. Rees, "RF System and Beam Loading on the ISIS Synchrotron" EPAC-90, Nice.

Matching Problems Between Linac and Compressor Ring

K. Bongardt
Institut für Kernphysik
KFA Jülich, D-52425 Jülich

Abstract

All accelerator schemes, discussed for a next generation spallation neutron source, start with a high current linear accelerator, injecting into a compressor ring or a rapid cycling synchrotron. For loss-free ring injection and extraction, the injector linac has to provide 200 nsec long voids every ring revolution time, typically 1 μsec. In order to keep the trapping voltage down, the outcoming linac bunches have to be rotated, and the energy has to be slowly ramped over the injection cycle. Solutions are presented for a low energy fast chopper, and for a high energy bunch rotator which also ramps the energy. Emphasis is given to the complications due to the high peak and average intensity required. For the beam chopper, different locations are discussed and one design shows how to incorporate the chopper after the RFQ, keeping the beam bunched.

In the transfer line from the linac to the compressor ring, longitudinal space charge forces influence the position and voltage for the bunch rotation cavity. Simple analytical formulae are given to calculate both effects. Longitudinal aberration effects, caused by the sinusoidal voltage, are substantial for energy ramping with the bunch rotation cavity. The correct rotation voltage may be controlled on-line by broadband pickups. In front of the cavity, an achromatic bending system should be installed which allows the scraping of longitudinal halo particles.

1. The Fast Beam Chopper at Low Energies

Next generation spallation neutron sources [1] such as the proposed European Spallation Source ESS [2], start with an RFQ, followed by a drift tube linac (DTL) at ~ 2.5 MeV. Both structures operate at a frequency of ~ 400 MHz and the H^--ion source has to deliver a pulse current of 50 mA at 100 keV. In order to minimize the injection loss in the following ring, a fast chopping device is needed with rise-fall times of about 10 nsec, creating a 200 nsec void every 1 μsec. For locating this device, 3 different positions may be considered:

a) <u>Chopper between ion source and RFQ</u>

Charge neutralization of the ion beam affects beam quality [3-5] so this chopping arrangement is not recommended (even though its chopper voltage requirements are least). However, a "prechopper" at this location reduces the heat load at a down-stream collector after the main chopper; such a "prechopper" should gradually decrease the beam intensity in the 200 nsec void without destroying the neutralization.

b) <u>Chopping at a medium energy</u>

By splitting the 400 MHz RFQ at 1 MeV, the chopper may be installed without affecting the beam quality. The main advantage here is the small chopper length, because the minimal product of voltage, U, length, L, given for a point like chopper by:

$$(U.L)_{min} \sim \quad \varepsilon_t^n \beta \qquad (1)$$

ε_t^n: normalized transverse rms emittance

$\beta \cdot c$ = particle velocity

is 175 V · m for an rms emittance of 0.2 π mm mrad and T = 1 MeV. For the minimal voltage · length value, the chopper and unchopped beam are just separated in phase space. Assuming a rise and falltime of 10 nsec (0-90%) and a voltage gradient of 100 V/nsec, obtained so far with existing chopping devices [3,6], then a chopper length of L = 2 · L min = 35 cm is needed to install a collector about 90° in betatron phase downstream, where the unchopped and chopped beam are well separated in real space. The collector is essential, because for an average current of 5 mA the average power density is ~ 300 W/cm^2.

For a 400 MHz bunched beam with a peak current of 50 mA at 1 MeV, the chopper and collector system is just not feasible. The arrangement cannot be ruled out completely, however, as chopping the coasting beam may be

considered. The coasting beam has to be trapped adiabatically in the downstream 400 MHz RFQ; detailed studies are required to assess this possibility.

c) Chopping between RFQ and DTL at 2.5 MeV

The minimum voltage · length value needed is increased to 275 V · m for the same emittance. In addition, the collector now has to absorb an average power density of 750 W/cm^2 for 5 mA average current. In spite of these demands, both chopper and collector may be installed in a transfer line, even for a bunched beam. In Fig. 1, the complete transfer line is shown for a 50 mA bunched beam at 2.5 MeV, including the matching section into the following 400 MHz DTL. A detailed description of this line is given in ref. [7].

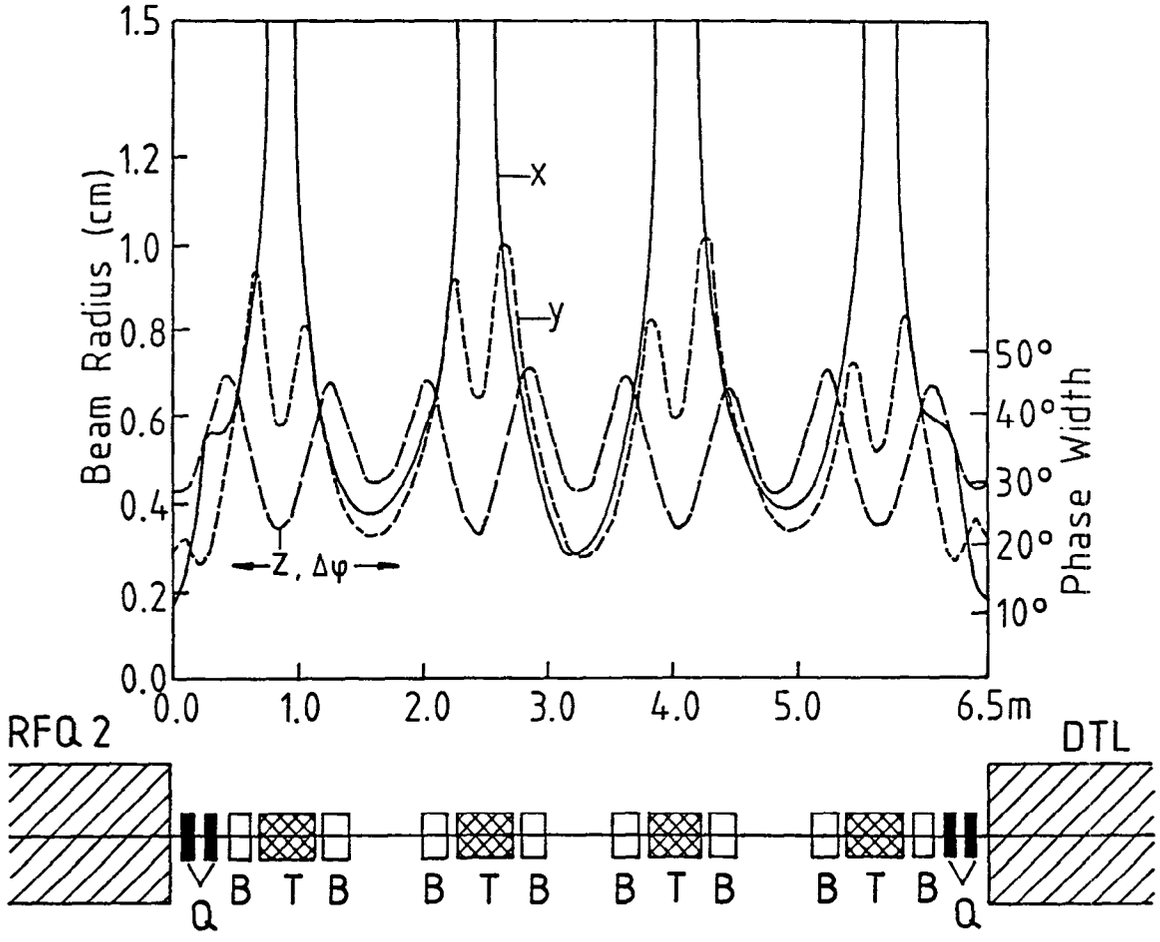

RFQ 2, DTL, B : 400 MHZ, Q quadrupole, T triplet

Fig. 1: Optical elements of the 2.5 MeV transport line, with beam envelopes ($\sqrt{5}$ · rms-value)

The design is basically a "triple waist" in the 0.6 m long drift sections between the buncher (B)-triplet (T)-buncher (B) elements. The fast beam chopper may be installed in the first drift section and the collector in the second. The third drift section is foreseen for moveable diagnostics. Fig. 2 shows the separation between the chopped and unchopped beam at the collector position, assuming a voltage · length value of 750 Vm, which is about 2.5 the minimum value. The transfer line was designed for the European Hadron Facility EHF [8], a Kaon facility with 100 μA average current. As the ESS needs about 5 mA average current, the beam separation at the collector has to be enlarged and care taken with the 4 bunches during the 10 nsec rise time. Both problems may be solved by increasing the chopper length to 0.9 m or 3.5 times the minimum. The voltage is assumed to be 100 V/nsec · 10 nsec = 1 kV. By doing so, the first kicked bunch stays in the linac with small, tolerable oscillations around the axis. Bunches 2 and 3 are destroyed in the transfer line, and bunch 4 is absorbed at the collector. The presented design in Fig. 1 allows 1 m long drift spaces for a peak current of 50 mA.

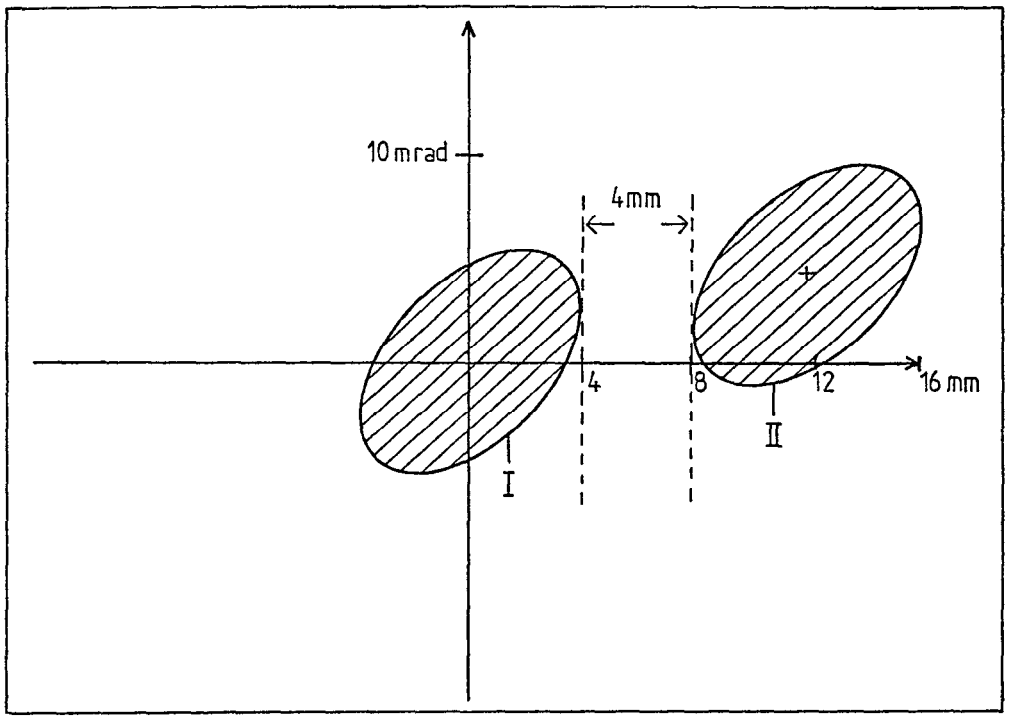

Fig. 2: Phase space diagram at the collector for the unchopped (I) and the chopped (II) beam.

The major disadvantage of this bunched beam transfer line is the emittance increase and the restrictions to the incoming emittances in all 3 planes. In the buncher cavities, both the transverse beam radius and the longitudinal phase width have to be limited. Transverse-longitudinal coupling, from the radial dependence of the transit time factor, and longitudinal aberration, due to the sinusoidal bunching field must be avoided. In order to install 1 m long drift spaces between the bunching cavities, the RFQ output normalised emittances have to be:

$$\varepsilon_t^{rms} \leq 0.2\,\pi \text{ mm mrad}, \quad \varepsilon_L^{rms} \leq 0.2\,\pi\,^\circ \text{ MeV (400 MHz)}$$

For the transverse plane, this limits the geometrical emittance of the 100 keV ion source beam to a value difficult to fulfil for a 50 mA H^-pulse current source [4]:

$$\varepsilon_t^{ion\text{-}source} \leq 55\,\pi \text{ mm mrad (geometrical, } 4 \cdot \text{rms-value)}$$

Due to the 50 mA peak current at 2.5 MeV, severe space charge forces are present. One quarter of the plasma wavelength, where most of the emittance increase occurs [9], is only about 0.3 m, and we cannot preserve the RFQ focusing period. Therefore the non-periodic transfer line suffers severe emittance increase caused by both the non-linear external bunching forces and the high internal space charge forces. Typically we find about 50% rms emittance increase in all 3 planes. It should be mentioned, that in the rms envelope equation the emittance term and the 50 mA space charge term are almost equal for the periodic part from the triplet (T) to triplet (T).

Most of the emittance increase may be reduced by shortening the line. For doing so, a more effective chopping structure with a voltage slope of about 200 V/nsec is needed. The now discrete buncher (B)-triplet(T)-buncher (B) combination should be replaced by a compact, non-accelerating RFQ-structure. A "pre-chopper" between ion source and RFQ should be installed to reduce the heat load at the collector.

The most promising alternative, however, is to use a coasting beam instead of a bunched beam. By doing so we can handle much larger transverse emittances, which put less demands on the development of high brilliance H^- sources. On the other hand, adiabatic trapping of a coasting beam in the DTL is a problem. Maybe it can be overcome by using first a bunch compression RFQ, where the coasting beam is compressed into a phase width of about ± 90° with almost no acceleration. This bunch can then be injected into the DTL by slowly increasing the synchronous phase from - 90° to - 25°. Studies are going on to evaluate this promising alternative in great detail.

2. Bunch Rotation and Energy Ramping at the Linac Output

The final linac energy of ≥ 0.8 GeV is achieved by changing the 400 MHz DTL structure at 100 MeV to a more efficient 800 MHz coupled cavity structure. Due to adiabatic phase damping, the outcoming linac bunches are narrow, with large values of energy spread. Typical numbers at 1 GeV are a phase width of ± 10° (800 MHz) or a bunch length of ± 75 psec and an energy spread of ± 2 MeV, corresponding to a momentum spread of ± $1.2 \cdot 10^{-3}$. As the bucket momentum height of the compressor ring is only about $\pm 5 \cdot 10^{-3}$, and as longitudinal painting [10] is essential for keeping the bunching factor small, the outcoming linac bunches have to be rotated in phase space and slow energy ramping used over the linac pulse. Both tasks may be fulfilled using a cavity which simultaneously rotates the bunch and slowly ramps the energy by varying amplitude and phase. The required cavity position and rotation voltage are strongly influenced by longitudinal space charge effects. Longitudinal aberration effects, caused by the sinusoidal voltage are discussed. The correct setting of the rotation voltage may be controlled on line by broadband pickups. In front of the cavity an achromatic bending system should be installed which allows the scraping of longitudinal halo particles.

a) Change of the Longitudinal Parameters Due to Space Charge Forces

As an example, Fig. 3 shows the increase of the phase width (in°) or the bunch length (in cm) in a longitudinal drift space for a 1.2 GeV beam, coming out of a 1200 MHz coupled cavity linac. The initial total phase width is assumed to be ± 6° (1200 MHz), the initial total energy spread to be ± 2.5 MeV. The solid line in Fig. 3 is the zero current case, whereas the broken line is calculated for 50 mA peak current in the 400 MHz DTL structure or 150 mA in 1200 MHz coupled cavity linac. The transverse beam radius is kept constant along the line. The space charge calculations are done with a numerical code, assuming linear space charge forces of a uniformly filled 3-dimensional ellipsoid. The variation of the phase width is taken into account. The code treats flat bunches with a large ratio of the longitudinal bunch length compared to the transverse beam radius. Due to the linear space charge forces, there is no emittance increase. Longitudinal space charge forces act as a linear defocusing lens with varying field strength along the line. They keep the longitudinal emittance constant, but they influence the phase width and the energy spread. The position of the bunch rotation cavity has to be changed, especially if the cavity operates at the 400 MHz DTL frequency. This would decrease the energy spread by a factor 8.

For most spallation source injectors, the energy spread has to be decreased only by a factor 2, allowing use of the same coupled cavity structure as before but now phased to - 90°. Fig. 4 and 5 show the use of such a 1200 MHz structure with somewhat changed input parameter ($\Delta\varphi = \pm 8°$ (1200 MHz), $\Delta W = \pm 2$ MeV), calculated for the 150 mA peak current at 1200 MHz. The bunch rotation cavity is placed after 65 m and with a voltage of ~ 6 MV; the phase width afterwards is constant to about ± 40°. For a zero current beam, not shown, a phase width of ± 40° occurs after 107 m.

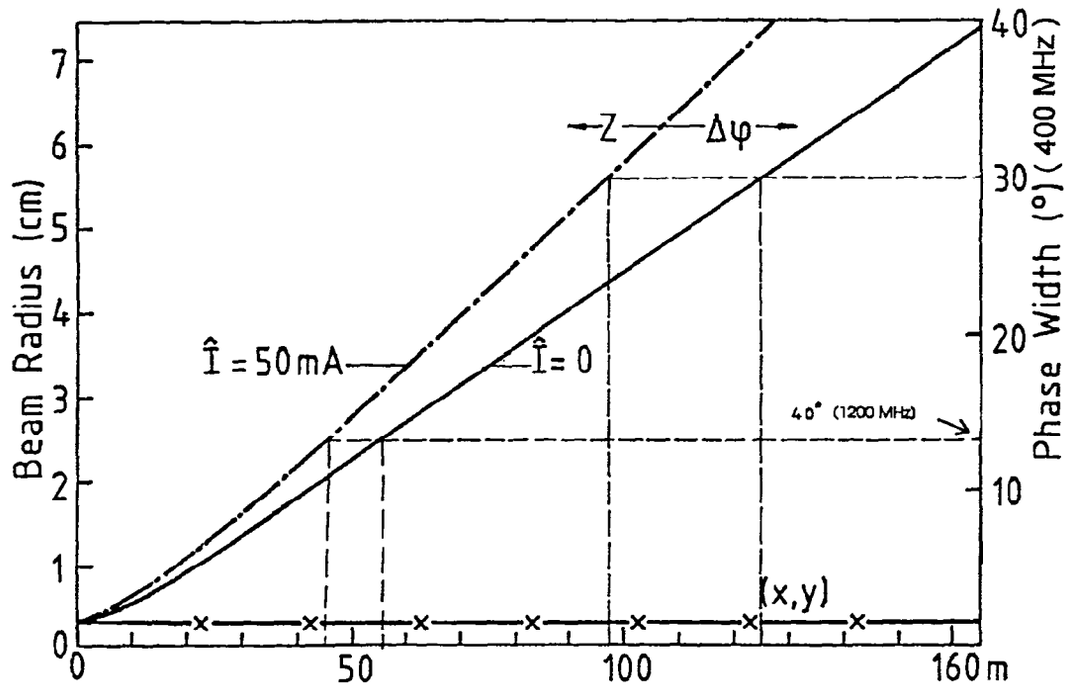

Fig. 3: Increase of the longitudinal phase width ($\sqrt{5}$·rms) for a 1.2 GeV beam with I = 0 and 50 mA

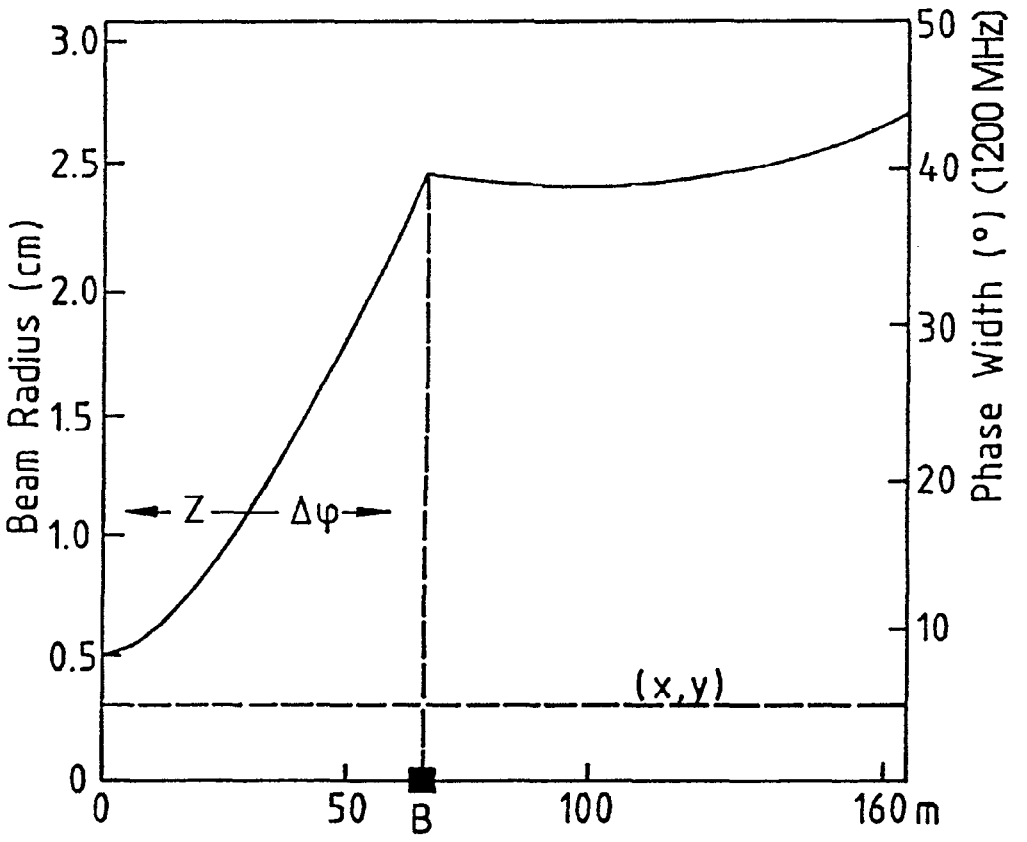

B: 1200 MHZ buncher L = 1.5m V ~ 6 MV

Fig. 4: Phase width ($\sqrt{5}$·rms) for 1.2 GeV and I = 150 mA using a 1200 MHz cavity

There is an accompanying increase of the energy spread, as shown in Fig. 5. Before the bunch rotation cavity, the energy spread is increased by a factor ~ 2; afterwards it is roughly constant, and at the end of the transfer line, the energy spread is reduced by more than a factor 2. The increase of the energy spread in front of the cavity doubles the required rotation voltage. If the space charge effects are ignored, the bunch rotation cavity is positioned incorrectly, with the cavity field non-linear. In addition, the foreseen voltage is too low, resulting in incomplete rotation, with longitudinal aberration effects as discussed later.

b) Analytical Formulae for the Description of the Longitudinal Space Charge Effects

As shown in Fig. 3 - 5, the phase width increases linearly at large distance, whereas the energy spread goes into saturation. This is expected because the space charge forces are getting weaker; the asymptotic behaviour may be described quite well by simple analytical formulae. For a longitudinal waist at the start, and for a final phase width $\Delta\varphi_f$ afterwards, the change of energy spread and the needed drift length L_D are given approximately by:

$$\left(\frac{\Delta W_f}{\Delta W_i}\right)^2 = 1+\left(\frac{\mu-1}{1+\alpha(I)\cdot\mu}\right)\left(1+\frac{1}{\alpha(I)\cdot\mu}\right) \tag{2}$$

$$L_D = \sqrt{\frac{\mu\cdot\beta_i}{f(I)}}\cdot \mathrm{sh}^{-1}\left(\sqrt{\frac{\mu-1}{1+\alpha(I)\cdot\mu}}\right) \tag{3}$$

with:

$$\mu = \left(\frac{\Delta\varphi_f}{\Delta\varphi_i}\right)^2 \qquad \frac{1}{\alpha(I)} = \beta_i\cdot f(I)$$

$$\beta_i = \frac{(\Delta\phi_i)^2\cdot\lambda\cdot(\beta\gamma)^3\cdot m_0c^2}{\left(E_z/\pi\right)\cdot 360^0} \qquad f(I) = \frac{120\cdot I\cdot 360^0\cdot\Omega\cdot q}{\beta\cdot\bar{a}\cdot\left(E_z/\pi\right)}$$

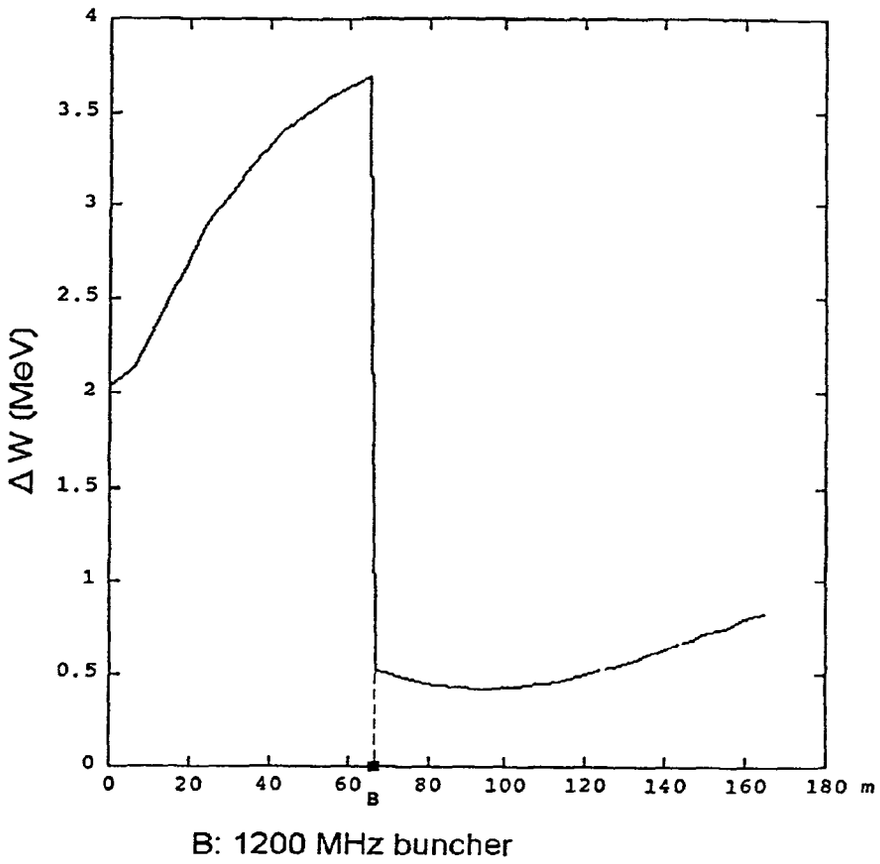

B: 1200 MHz buncher

Fig. 5: Energy Spread ($\sqrt{5}$·rms) for 1.2 GeV and I = 150 mA using a 1200 MHz cavity

$(\Delta\varphi_i,\Delta\varphi_f)$:	(initial, final) phase width (in°)
$(\Delta W_i,\Delta W_f)$:	(initial, final) energy spread (in MeV)
β_i:	initial longitudinal β-function (in m)
E_z:	longitudinal phase space area (in °MEV) = $\pi\cdot\Delta\varphi_i\cdot\Delta W_i$
λ:	wavelength of the rotating cavity
I:	peak current
$\bar{a} = \sqrt{a_x \cdot a_y}$:	average transverse beam radius
(β,γ)·	relativistic factors
(m_oc^2,q):	(rest mass, charge) of the particle
$(\Delta\varphi,\Delta W,\bar{a})$ =	$\sqrt{5}(\Delta\varphi,\Delta W,\bar{a})_{rms}$
E_z=	$5\ E_z^{rms}$

Eq (2,3) are correct for $\Delta\varphi_f > 3\cdot\Delta\varphi_i$.

They are derived by averaging the longitudinal space charge force over the drift distance [1] assuming a homogenous filled 3 dimensional ellipsoid. The final phase width $\Delta\varphi_f$ is treated as input parameter, giving the needed drift length L_D as an output parameter.

For very large values of $\Delta\varphi_f$, where the following holds, Eq (2,3) can be written as

$$\alpha(I)\cdot\left(\frac{\Delta\varphi_f}{\Delta\varphi_i}\right)^2 >> 1$$

$$\left(\frac{\Delta W_f}{\Delta W_i}\right)^2 = 1+\beta_i\cdot f(I) \tag{4}$$

$$L_D = \left(\frac{\Delta\varphi_f}{\Delta\varphi_i}\right)\cdot\sqrt{\frac{\beta_i}{f(I)}}\,sh^{-1}\left(\sqrt{\beta_i\cdot f(I)}\right) \tag{5}$$

This is the asymptotic case, where the energy spread becomes constant, depending only on the initial conditions. The phase width $\Delta\varphi_f$ increases linearly with the drift distance. The zero current case can be obtained from Eq (4,5) by setting the peak current to zero. These simple analytical formulae describe the longitudinal space charge effects quite well. For example with the same input data as for the numerical calculations of Fig. 4 and 5, we get:

$$\text{for } \hat{I} = 150\text{mA}, \Delta\varphi_i = \pm 8^o, \Delta W_i = \pm 2\text{MeV}, T = 1.2\text{GeV}, \bar{\alpha} = 3\text{mm}$$

$$\beta_i = 21.8\text{m} \qquad f(I) = 0.0144\,{}^1\!/_m \qquad \alpha(I) = 0.315$$

which means that we reach the final phase width $\Delta\varphi_f = \pm 40°$ after $L_D = 78$ m with an energy spread of $\Delta W_f = \pm 4.1$ MeV. The energy spread has almost reached its asymptotic value of ± 4.16 MeV. The numerical calculations, see Figs. 4,5, gives a driftlength of 65 m and a energy spread of ± 3.7 MeV. Also here the energy spread is approaching the constant asymptotic regime.

For a zero current beam, the drift length L_D is given by

$$L_D = \sqrt{\beta_i(\beta_f - \beta_i)} \tag{6}$$

where $\beta_f \sim \Delta\varphi_f^2$ is the final longitudinal β-function. A phase width of ± 40° is reached after 107 m. After the bunch rotation cavity, where the phase width stays almost constant, Eq (4) cannot be used. Here the change of the energy spread, see Fig. 5, can be described by a similar equation, using the longitudinal form factor of a "flat" bunch.

The simple analytical formulae allow the energy spread and the position of the bunch rotation cavity to be calculated for a given beam current and phase width at the cavity position. Beside the initial longitudinal β-function, only one current dependent factor must be calculated.

All numerical and analytical space charge calculations presented are made for linear forces without emittance increase. Longitudinal emittance increase has to be calculated by multiparticle codes, where the distribution at the linac output has to be taken as initial conditions. Thus, the beam has to be simulated throughout the linac, including the low energy matching sections. For locating the bunch rotation cavity and choosing the correct voltage, not much difference is expected from the presented linear space charge analysis.

c. Longitudinal Aberration Effects and Energy Ramping

The non-linear part of the voltage must be taken into account, especially for large voltages and bunch lengths. The sinusoidal voltage leads to longitudinal aberration effects and a dilution of the phase space area. For a linear voltage and an elliptical phase space boundary at the cavity entrance, there is an upright ellipse afterwards, where the outermost particles have no energy spread. The maximum energy spread is determined by the particles in the bunch centre. For a sinusoidal voltage, there is no longer an elliptical boundary afterwards. Keeping the same voltage as for the linear case, the outermost particles are no longer on axis. For the values of Fig. 5: U = 6 MV, $\Delta\varphi \pm 40°$, this gives for the outermost particle an energy spread of ± 300 keV compared to ± 550 keV for the bunch centre, which is acceptable.

The required slow energy ramping of the linac pulse, essential for the longitudinal painting [10], may be done by using either the bunch rotation cavity or the last part of the coupled cavity linac. In both cases, the synchronous phase (and the amplitude) are slowly changed during the linac pulse. If the bunch rotation cavity is used for energy ramping, aberration effects have to be taken seriously. Using the data of Figs. 4 and 5 as an example; by ramping the phase from - 65° to - 90° to - 115° and the voltage from 6.7 to 5.3 to 6.7 MV, the energy

can be varied from + 3 to 0 to - 3 MeV. The incoming bunches may still be rotated ($\Delta\varphi = \pm 40°$, $\Delta W = \pm 3.7$ MeV), but due to the strong aberration effects, the phase space boundary is no longer elliptical. For the energy ramped bunches, an almost rectangular phase space boundary is obtained, whereas the unramped bunches keep their elliptical boundary. The energy spread obtained, however, is still below ± 1 MeV for all bunches.

These results may be compared with the alternative of using the coupled cavity structure instead. Here aberration effects are almost non existent due to the small phase width around ± 10°. The synchronous phase may be changed adiabatically over many cells. Due to the use of large peakpower klystron units, the cells are grouped together in accelerating tanks having a common phase. Longitudinal mismatch effects cannot then be avoided. In a coupled cavity tank, where there is an energy gain of 18 MeV (total voltage 20 MV, synchronous phase - 25°), the energy may change only by an additional ± 1 MeV. Even then, the ramped bunches are mismatched at the linac exit and, due to the space charge forces, this longitudinal mismatch is increased up to the position of the bunch rotation cavity. After the rotation, all bunches have an elliptical boundary, but, due to mismatch, different energy spreads. This may be overcome by varying the amplitude of the bunch rotation cavity in an appropriate way, though for large values of the mismatched phase width, aberration effects have also to be considered. Detailed numerical calculations, including space charge and aberration effects, are proceeding to compare both possibilities for energy ramping to find the optimized voltage and phase programmes.

d) Online Measurements of the Longitudinal Beam Parameters and Longitudinal Halo Scraping

Due to the effects of space charge forces, it is important to measure the beam parameters online, especially to obtain the correct voltage setting. The online measurement may be done using broadband high frequency pickups (up to 6 GHz) and reconstruction methods in the frequency domain [12]. From the low frequency components of one pickup, the rms phase width is obtained, and by using, in addition, the high frequency content, the bunch distribution also. The reconstruction method has recently been confirmed with beam at the ISIS-facility [13]. With two identical pickups, the rms energy spread is obtained, and by placing identical broadband pickups before and after the bunch rotation cavity, the longitudinal beam parameters are measured on line for control of the rotation voltage.

Along the spallation neutron source linac, there is normally more longitudinal than transverse emittance increase. The longitudinal acceptance is too small at low energies and high intensities [14]. The frequency jump of the accelerating structures, in order to make the linac more cost effective, causes aberrations. To keep injection loss small in the subsequent rings, it is very desirable to scrape the longitudinal H^- halo particles, by stripping. This may be achieved by including an achromatic bending system in the high energy transfer line as in the PSR [15]. Care has to be taken in the design, as the bending field strength is limited to avoid unwanted Lorentz stripping of the H^-ions, and there is also length limitations. Due to the space charge forces, the energy spread is large and approximately constant only after the rotation cavity.

As an example, at 1.2 GeV, we can design a short 4 cell achromatic bending system, corrected in first order and only 36 m long [16]. This device has in the middle a dispersion value of about 1.6 m compared to the horizontal β-function value of 2.6 m, sufficient for doing the longitudinal halo scraping. The bending field is 0.3 T, which limits the stripping loss below 10^{-6}/m for the complete achromatic bending system. Over the total length of 36 m, the energy spread increases by 20%, see Fig. 5. Due to transverse-longitudinal coupling in the dispersive elements, only the 4-dimensional phase space area is conserved, but not the 2-dimensional projections on the transverse or the longitudinal plane. By choosing proper settings of the elements, we can preserve either the transverse or the longitudinal emittance [17]. Work is proceeding to find, under the space charge forces, the optimal parameters by looking at the transverse and the longitudinal plane simultaneously.

Summary

Major arguments are given on how to include a fast beam chopper at low energies and a bunch rotation cavity at high energies when both these linac areas are dominated by space charge forces. Careful design of these sections is important for loss-free injection and extraction in the subsequent rings for the next generation spallation neutron source.

Acknowledgement

Most of the work presented resulted from lively, exciting, fruitful discussions with colleagues from the former EHF study group, which was led by F. Bradamante, who is accordingly thanked.

References

[1] G. Rees, "Overview of Future Spallation Neutron Sources", to be published in: Proc. of the US Particle Accelerator Conferences, 1993.

[2] H. Lengeler, "The European Spallation Source Project ESS", invited talk at ICANS XII

S. Martin, C. W. Planner "Accelerator Design Parameters for a European Pulsed Spallation Neutron Source", Proc. EPAC Berlin 1992, p, 435

[3] J. M. Brennan, L. Ahrens, J. Alessi, J. Brodowski, J. Kats "A Fast Chopper for Programmed Population of the Longitudinal Phase Space of the AGS Booster", Proc. EPAC Rome 88, p. 1003

[4] D. Schneider "Summary Report: Ion Source", Proc. Spallation Source Workshop, Santa Fe 1993, Los Alamos Conference Report, LA-UR-93-1356, p.1

[5] T. Weis, J. Wiegand, R. Dölling, J. Pozimski, F. Fenger, H. Klein "Evaluation of Space Charge Neutralization in a High Perveance Injector System with Solenoids" Proc. EPAC Nice 1990, p. 809

[6] J. S. Lunsford, R. A. Hardekopf "Pulsed Beam Chopper for the PSR at LAMPF", Proc. 1983 Particle Accelerator Conference, IEEE NS-30,(1983) p.2830

[7] K. Bongardt, M. Pabst, R. Wagner "The 2,5 MeV Low Energy and the 1,2 GeV High Energy Transfer Lines", Proc. International Workshop on Hadron Facility Technology, Santa Fe 1987, Los Alamos Conference Report LA-11130-C, p. 184

[8] F. Bradamante "Meson Factories", Proc. EPAC Rome 1988, p.70

"Proposal for a European Hadron Facility", Edited by J. F. Crawford, EHF-87-18, May 18, 1987.

[9] T. P. Wangler, K. R. Crandall, R. S. Mills "Emittance Growth from Charge Density Changes in High-Current Beams", Proc. Heavy Ion Inertial Fusion 1986, AIP conference proc. 152, (1986), p. 166

[10] E. Gianfelice, H. Schönauer "Strategies for Longitudinal Painting in the EHF Booster at Injection", Proc. EPAC Rome 1988, p. 860.

[11] K. Bongardt "Design Formulae for a Space-Charge Dominated Transport Line", internal KFA Jülich note, Nov. 1988.

[12] K. Bongardt, A. K. Mitra, M. Sauer, H. Stockhorst "The Deflector-Pickup System: A Novel Approach to Measure Online the Energy Spread of DC Ions Beams", NIM A 287, (1990), p. 273.

K. Bongardt, K. Kennepohl "Determination of 100 psec Short Linac Bunches by Broadband Pickups and Reconstruction Technique", Proc. EPAC Rome 1988, p. 976.

[13] M. Clarke-Gayther, private communication

[14] M. Pabst, K. Bongardt, U. Funk "An Improved Definition of the Longitudinal Acceptance for High Intensity Bunched Beams", Proc. Workshop on High-current, High-Brightness and High-Duty-factor Ion Injectors, AIP Conference Proceedings 139, (1985), p. 193.

[15] G. P. Lawrence, R. A. Hardekopf, A. J. Jason, P. N. Clout, G. A. Sawyer "Los Alamos High-Current Proton Storage Ring: A Status Report", Proc. Particle Accelerator Conference 1985, IEEE NS-32, (1985), p. 2662

[16] J. Crawford "Achromat Between the EHF Linac and Booster", EHF-88-4, Feb. 1988

[17] A. J. Jason, E. M. Svaton, B. Blind, E. A. Heighway "Design of Achromatic Bending Systems in the presence of Space Charge", Proc. Particle Accelerator Conference 1987, p. 1767 .

ACCELERATOR STUDIES AT THE KEK-PS BOOSTER , PROBLEMS RELATED WITH HIGH INTENSITY BEAM

Isao Yamane

National Laboratory For High Energy Physics (KEK)
Oho 1-1, Tsukuba-shi, Ibaraki-ken, 305 Japan

Abstracts

The beam intesitry of the KEK-PS booster attained a level over 1.5 x 10^{12} ppp by a comprehensive and systematic tuning. Accompanying with beam intensity upgrade, residual activity around the booster ring and vertical beam blowup in the booster become two important problems to be solved before the booster beam intensity is increased higher.

1. Introduction

Increase of the booster beam intensity is a main theme of accelerator study that has been consistently undertaken since 1985, when the injection scheme was changed from the proton multiturn injection to the H^- charge exchange injection and the injection energy was upgraded from 20 to 40 MeV. Booster beam intensity gradually increased as the accelerator tuning was advanced. But beam intensity of the main ring did not increase as that of the booster. After a few years, it was made clear that beam intensity of the main ring had some limitations related with the injection porch and the transition energy. Then the aim to increase beam intensity of the main ring was changed to increase efficiency of data taking in physics experiments by expanding the length of the beam spill.

As for the booster, studies to increase beam intensity was continued as a project not only because BSF (the Booster Synchrotron Utilization Facility) eagerly required a beam as intense as possible, but also experience of those studies was considered to be very helpful for the future construction and operation of the high intensity proton accelerator that was planned in JHP (the Japan Hadron Project).

The target of the booster beam intensity was set as 2 x 10^{12} ppp, and this value was attained in 1989 as an instantaneous intensity. The standard intensity of routine operation, however, has been kept at a level a little over 1.5 x 10^{12} ppp, because residual radioactivity around the booster ring becomes harmful at some locations.

Two serious problems have come to the fore in this series of studies. One is the expected high level residual radioactivity around the booster ring and the other is abnormally large vertical emittance of the 500 MeV beam accelerated by the booster synchrotron. This latter problem was first indicated with respect to the bad condition of beam injection into the main ring. It also implied vertical beam blowup during acceleration in the booster, which would cause harmful beam loss in the ring.

Improvement of the RF system that played a very important role for increase of the booster beam intensity will not be mentioned in this report. But it will be reported in another paper of this proceedings [1].

2. History of the booster beam intensity

Figure 1 shows the history of the booster beam intensity averaged in each operation cycle. A series of systematic tuning was undertaken in order to increase the booster beam intensity during '87 - '89. Main items of the tuning were

- correction of the booster injection error in both horizontal and vertical planes,
- adjustment of ionoptical parameters in the 40 MeV beam transport line,
- adjustment of RF power and phase of each linac tank,
- adjustment of ionoptical parameters in the linac injection beam line,
- adjustment of H^- beam intensity extracted from the ion source, and
- adjustment of the booster RF voltage program at the first stage of acceleration.

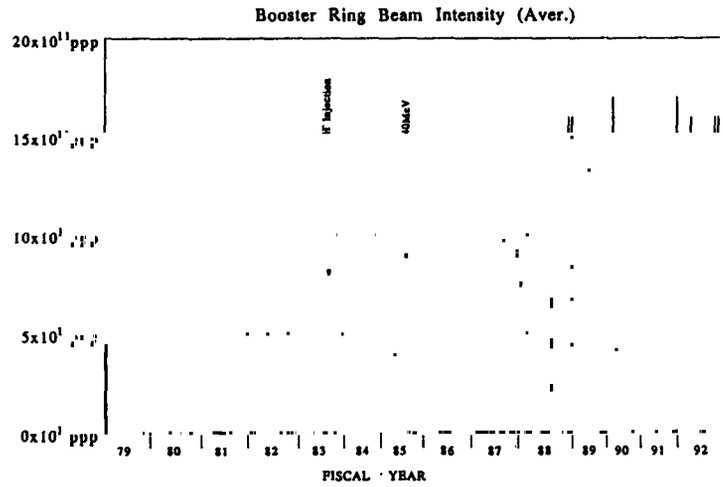

Fig. 1 Progress of the KEK-PS Booster beam intensity averaged in an operational cycle

In these tuning following items were monitered as criteria for good tuning.

- Vertical and horizontal beam size observed by the profile monitor Pr5V or Pr6H respectively was sufficiently small.
- Injection efficiency of the booster was sufficiently high as.
- Beam loss during acceleration was sufficiently little as.

By this tuning booster beam intensity was gradually increased and in Feb. '89 the maximum beam intensity recorded 2.2 x 10^{12} ppp. Roughly speaking, this intensity is near to the space charge limit, 2.6 x 10^{12} ppp, that was calculated by T. Suzuki [2] .

Although intensity of proton beam showed temporary decrease, after the booster RF system was modified to cope with acceleration of a deuteron beam in '90, it recovered former value in '92 by efforts of the RF group. Recently the average intensity is cntrolled as a little over 1.5 x 10^{12} ppp in order to supress increase of residual radioactivity.

An important point to be mentioned with respect to beam intensity of the KEK-PS booster is the reliability of machine, (actual beam-on time) / (scheduled beam time). Reliability at BSF is usually no less than 95 % and this high reliability is considered to make for such a low average beam current as 5μA.

3. Distribution of residual radioactivity around the booster ring and monitoring beam losses

Figure 2 shows a recent distribution of residual radioactivity on surface around the booster ring. These data are usually measured three days after the end of an operation cycle 16 days long by persons of the radiation administration section. Distribution indicates three kinds of characteristic peak which should be harmful in the maintenance service.

peak A ----- peak at the beam extraction straight section (S3)
peak B ----- peak at the synchrotron magnet (M1) immediately downstream of the injection straight section
peak C ----- peaks at central part of the magnet M2 and M5

Beam loss distribution during acceleration along time axis is observed by loss monitors using ionization chamber [3] which are disposed around the booster ring as shown

in Fig. 3. A typical variation of proton number during acceleration is shown in Fig.4 together with times when beam loss is observed. Beam losses are observed at following 6 times,

during injection,

at the instant when the injection bump magnet is turned off,

100 - 200 μsec after the start of injection,

about 1 msec after the start of injection,

some time later than fifteen msec after the start of injection, and

at the beam extraction instant.

These losses are called for the sake of convenience as " loss 1", " loss2 ", ---, " loss 6 " in order .

The peak A is obviously due to loss accompanying with the beam extraction , and corresponds to the loss 6. At the extraction, beam loss measured by current transformers is usually no more than a few per cent. Inspecting radioactivity distribution of the extraction septum, it was confirmed that a significant radioactivity was localized at the upstream end of the septum coil. At the extraction instant, the interval of two bunches is 167 nsec and the bunch length is typically 80 nsec. On the other hand, the rise time of the kicker magnetic field pulse is 80 nsec. Therefore the gap between two bunches does not have a sufficient margine and some fringe part of the beam bunch comes in the rising edge of the kicker magnetic field pulse. Such a part is insuficiently kicked and hits the septum coil.

The cause of peak B has two conponents : the incompletely stripped H^0 atoms and the part of H^- ions which missed the stripping foil. It took place after the change of injection scheme and consisted of two constituent peaks. Using a loss distribution monitor [4], it was confirmed that the beam loss occured at the time of loss 1 and at two different but near locations as is shown in Fig. 5. The H^- ion part of the loss 1 can be controlled by adjustment of the foil position. The H^0 part also can be decreased to an allowable level by using a little thicker.foil

Observing loss monitors arranged near the peak C, it was found that beam loss causing it occurred at the time of loss 2. The beam loss increases as the beam intensity

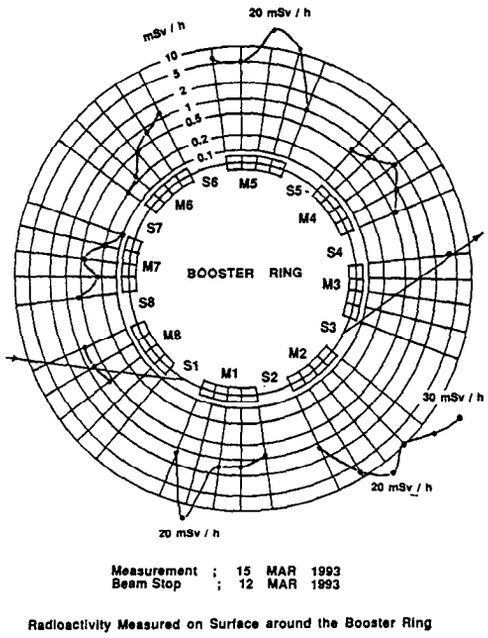

Fig. 2 Recent distribution of residual radioactivity around the KEK-PS Booster

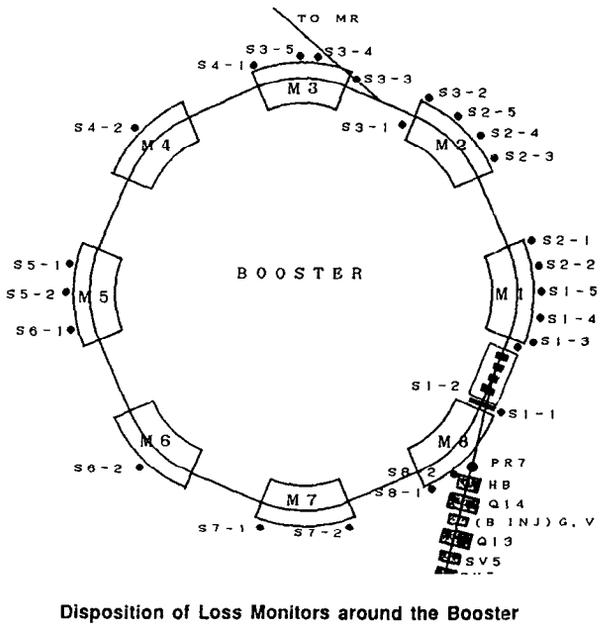

Fig. 3 Loss monitors around the KEK-PS Booster ring

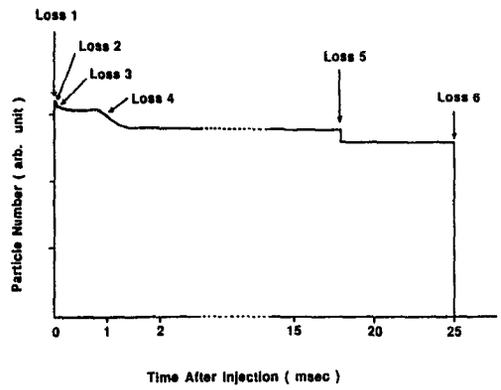

Fig. 4 Typical variation of the proton number during acceleration in the KEK-PS Booster and times when beam loss is observed

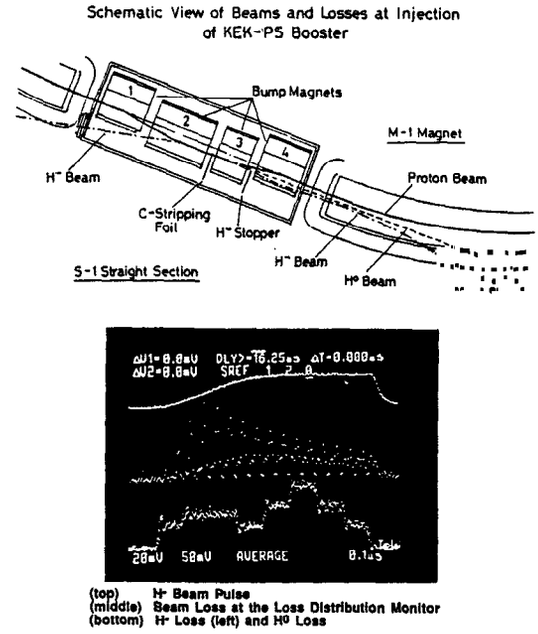

Fig. 5 (upper) relation among H^- ion loss, H^0 atom loss and the loss distribution monitor. (lower) a display of loss signals

causing it occurred at the time of loss 2. The beam loss increases as the beam intensity stacked in the booster. It starts to decrease when the H^- bump magnet is turned off and soon disappears. As the peak C takes place at the location where the vertical betafunction becomes large, it is cosidered that the vertical beam size becomes large while the beam circulates on the bumped orbit. Anyway, we dont know much about the cause of the peak C.

The time of loss 3 is that a beam bunch is first formed from the continuous beam after injection. It usually occurs when the beam intensity is as high as 1.5 x 10^{12} ppp. When the beam intensity is not so high, this loss can be avoided by adjusting the RF voltage.
The loss 4 is considered to come from the part of beam that is not captured by the RF bucket. Because the part is not accelerated, its orbit radius becomes amaller as the magnetic field rises and at last it hits the inside wall of the vacuum chamber. Loss signal corresponding to this beam loss is not observed, because the beam loss occurs very slowly and instantaneous loss is too little to make a signal in a loss monitor. Although the total amount of this loss is considerable, it does not make a peak of residual activity not only because the energy of lost particle is as low as 40 MeV but also because the loss is scattered all around the ring.

The loss 5 occurs when the RF system becomes unstable with a parasitic oscillation. When the RF system is in a bad condition, this phenomenon occurs as the beam intensity becomes high and limits the beam intensity. After this problem is overcome by improvement of the RF system, the booster beam intensity becomes stable at a level as high as over 1.5 x 10^{12} ppp.

4. Vertical beam size of the booster beam

Vertical beam size observed by the beam profile monitor Pr-5V in the 500 MeV beam line is typically about 40 mm in the full width including 99 per cent of beam, even after the injection and acceleration condition of the booster is carefully adjusted. As the beta function at the point is calculated to be 16 m, the vertical emittance is estimated to be about 25

πmmmrad. Although the value 16 m is only a calculated value, the emittance value is considered to be sufficiently resonable. This emittance is too large compared to the acceptance of the main ring, 20 πmmmrad.

On the other hand, the acceptance of the booster is about 50 πmmmrad. Theoretically, beam emittance is damped by a factor, $\beta\gamma$(40 MeV) / $\beta\gamma$(500 MeV) = 1/4, during acceleration from 40 to 500 MeV. Emittance of 500 MeV is expected to be 12.5 πmmmrad, even if the acceptance of the booster is fully occupied by the beam. Therefore, the observed emittance of 500 MeV beam is cosidered to be abnormally large. Moreover, the typical value of 40 MeV H^- beam is 20 πmmmrad and the injected beam is not scattered all over the acceptance artificially. So it is considered that some beam blowup occurs at the injection and/or during acceleration.

This problem had been indicated with respect to the main ring injection. It is now evident that the problem is also related with beam loss in the booster. It is necessary to make clear and remove, if possible, the cause of vertical beam blowup before the booster beam intensity of routine operation is increased higher than the present. Studies on this problem are being steadily continued and some results are already obtained as follows.

i) Matching of the injected beam to the booster optics

The taken procedure for beam matching is as follows.

step-1 Twiss parameters of the 40 MeV H^- beam are obtained from the phase space distribution measured with an emittance monitor in the 40 MeV beam line.

step-2 Twiss parameters of the beam at the exit of the linac are calculated using the inverse matrix of the transfer matrix from the exit of the linac to the emittance monitor.

step-3 Current set of the quadrupole magnets in the 40 MeV beam line are calculated so as to fit the beta functions of beam to those of the booster ring at the injection point.

step-4 After currents of beam line quadrupole magnets are adjusted to the calculated values, the phase space distribution of the beam is measured again by the emittance monitor in order to check if the distribution is actually same as the expected by calculation. When the distribution satisfactorily coinside with the expected, the matching procedure is completed. If it does not, the procedure above mentioned are repeated again.

Although this procedure seemed to be adequit to fit Twiss parameters of the injected beam to those of the ring at the injection point, following two problems were also found.

problem-1 Since the phase space distribution of the beam accelerated by a linac has a very complicated shape, the beta function can not be determined straightforward and its determined value has some uncertainty.

problem-2 It was found that the beta function of the ring is deviated from the designed value during injection by edge effect of the injection bump magnets as is shown in Fig. 6. So measurment is necessary to get correct values of the ring beta function.

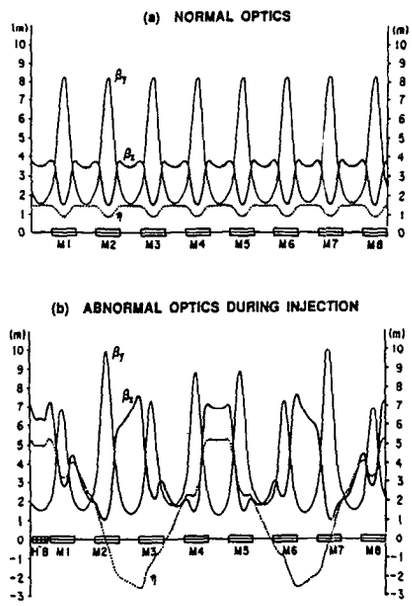

Fig. 6 Distortion of the booster optics due to edge focussing effects of the injection bump magnets

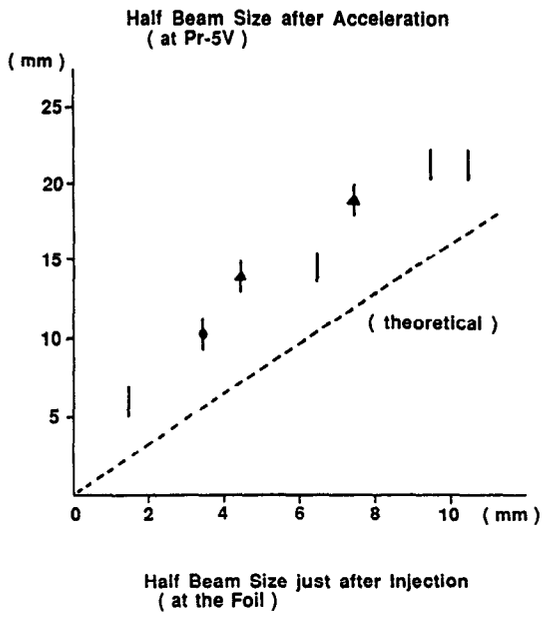

Fig. 7 Dependence of the beam size after acceleration upon that just after injection

Thus beam matching at the booster injection is very complicated process and a considerable beam blowup due to mismatch seems to remain at present.

ii) Correction of the vertical injection error

Two steering magnets in the 40 MeV beam line are used in order to correct the vertical injection error. Since locations of those steering magnets are not suitable, displacement and angle are not adjusted independently. Therefore a map of height of the beam profile observed by the Pr-5V is measured in a plane with currents of those steering magnets as two variables. Then currents are adjusted to the values at the peak of height distribution. This procedure turned out to work well.

iii) Size of 500 MeV beams accelerated from small beams formed at the booster injection

The initial beam size just after injection at the foil location can be defined with a scraper attached on a frame of stripping foil. Figure 7 shows dependence of the beam size at the Pr-5V profile monitor on the initial beam size. The beam size observed with the Pr-5V profile monitor is systematically larger than that theoretically calculated from the initial beam size (the dotted line). This fact is considered to indicate there is a vertical beam blowup halfway of acceleration.

iv) Emittance growth due to foil traverse

Variation of the beam size at the Pr-5V profile monitor was observed, changing the duration while the injected beam traverses the foil. The duration can be changed by changing the time of the H^- beam pulse with respect to the cut off-time of the injection bump pulse. The result is that there is appreciable emittance growth due to foil traverse but its amount is not significant.

v) Space charge effect

Beam blowup due to the space charge effect, if exists, is considered to occur most clearly when a beam bunch is first formed from the continuous beam just after injection by the RF voltage, namely at the time of loss 3. At first a vertical scraper at the straight section S3 is set at a position where the scraper edge is very near but does not scrape the beam with the RF voltage off. Beam intensity can be varied by changing size of the beam mesh or length of the H^- beam pulse. The beam mesh is installed in the 40 MeV beam line. It can only thin particle density of the beam but not change the beam shape. After a beam intensity is set, the RF voltage is turned on and the beam loss is searched for at the time of bunch formation. Of course, the RF voltage and frequency must be enough adjusted in advance not to excite a quadrupole oscillation in the longitudinal phase space. By this method, it was found that the beam blowup due to space charge effect certainly occured with a beam intensity about 1.5×10^{12} ppp or more.

5. Summary

At the KEK-PS booster, the beam intensity at the routine operation has recently attained a level over 1.5×10^{12} ppp by a series of comprehensive and systematic tuning for a

few years. Although a higher beam intensity is available, it is controlled at the present level because the residual radioactivity around the ring becomes serious at some points.

Two problems has come to the fore in this process. One is the residual radioactivity around tha booster ring, and the other is vertical beam blowup at the beam injection and during acceleration in the booster. As for the residual radioactivity, there are three kinds of harmful peaks. Two of these turned out to relate with the beam extraction and injection. Peaks of the third kind are at the center of the synchrotron magnet M2 and M5 and are not well known about the cause of production.

The vertical beam blowup in the booster is considered to occur at the injection and at an early stage of acceleration. At present, there is considerable mismatch between the injected beam and the ring optics. Blowup due to space charge effects is appreciable when the beam intensity becomes as high as 1.5×10^{12} ppp or more.

These problems are now being actively studied and when they are solved the booster beam intensity will be increased to the level of 2.0×10^{12} ppp.

References

[1] S. Ninomiya, " Operation of the RF System at the KEK-PS ", another paper in this proceedings.
[2] T. Suzuki, KEK Report KEK-74-4, JUNE 1974
[3] H. Yamaguchi, I. Yamane, H. Nakagawa and K. Nigorikawa, KEK Report 88-13 A (in Japanese)
[4] H. Someya, Y. Satoh and I. Yamane, Proc. of the Workshop on Advanced Beam Instrumentation, April 22-24, 1991, KEK, Tsukuba, Japan, p333-338

VERY LOW OUTPUT IMPEDANCE RF SYSTEM FOR HIGH INTENSITY ACCELERATORS

Y. Irie

KEK National Laboratory for High Energy Physics
Oho 1-1, Tsukuba-shi, Ibaraki-ken, 305 Japan

abstract : A model RF system with a cathode follower was tested under frequency modulation in the 1-3.5 MHz range. The repetition rate was 40 Hz. The oscillation was stable, and no liability to parasitic oscillations has been observed. An energy problem associated with this scheme is also mentioned.

1. Introduction

The cathode follower RF system was first implemented as a beam buncher in the Proton Storage Ring at the Los Alamos National Laboratory.[1] For further applications to synchrotrons, it is necessary to study the feasibility under frequency modulation. A model RF system with a cathode follower[2] is being tested for this purpose. This report describes the results of the preliminary tests.

2. Stability analysis

The cathode follower is inherently liable to spurious oscillations when the cathode load is capacitively tuned (Fig.1). If the grid current (i_g) is negligible compared to the other branch currents, the cathode voltage (e_k) is given by

$$e_k = \frac{\mu}{\mu+1} e_{in} \frac{Z_k}{r/(\mu+1)+Z_k},$$

where Z_k is the cathode load, μ the amplification factor, r the plate resistance and the beam is assumed to be absent for the moment. Since $-i_g = j\,\omega\, C_g (e_k - e_{in})$, where C_g is the cathode-grid capacitance, the scalar product of e_{in} and $-i_g$ is negative for an inductive load and is positive for a capacitive load (Fig.2). The energy is then fed back to the driver stage through C_g for the latter case and the system possibly becomes unstable. Since this phenomenon is transient, a stability criterion should be used for the analysis.

Suppose that the driver stage comprises a tank circuit (L_d, C_d), and the cathode load an RF cavity with beam current (i_b). The driver voltage with an initial charge Q_0 in C_d is then written as

$$e_{in} = Q_0 \frac{s^3 (C+C_g) L_d r + s^2 (\mu + 1 + r/R) L_d + s\,\omega_0^2\, C\, L_d\, r}{a_0 s^4 + a_1 s^3 + a_2 s^2 + a_3 s + a_4}$$

$$- \frac{I_1 s + I_2 \omega}{s^2+\omega^2} \frac{s^3 C_g L_d r}{a_0 s^4 + a_1 s^3 + a_2 s^2 + a_3 s + a_4},$$

where $i_b = (I_1 s + I_2 \omega) / (s^2 + \omega^2)$, ω_0 is the cavity resonant frequency $(\sqrt{L\,C})^{-1}$, R is the shunt resistance, and the coefficients in the denominator are:

$$
\begin{aligned}
a_0 &= [C_d C_g + C(C_d + C_g)] L_d r, \\
a_1 &= C_g L_d + (\mu + 1) C_d L_d + (C_d + C_g) L_d r / R, \\
a_2 &= [C + C_g + \omega_0^2 C (C_d + C_g) L_d] r, \\
a_3 &= \mu + 1 + r / R,
\end{aligned}
\tag{1}
$$

and

$$a_4 = \omega_0^2 C r.$$

It is interesting that no beam component appears in eq.(1), ie the beam loading has no influence upon whether or not the pole has a positive real component. According to the Hurwitz criterion, the following terms should have positive sign for stable operation:

$$b_1 \approx \omega_0^2 C C_d L_d r \ > 0$$

and

$$c_1 \approx \frac{\mu C_g (\omega_0^2 C_d L_d - 1)}{\omega_0^2 C_d^2 L_d} \tag{2}$$

where we have assumed that C_g is small compared to C and C_d. Corresponding to the difference in the resonant frequency between the driver circuit and the cathode load, c_1 changes sign. For a capacitive load, it is negative and the system becomes unstable, which is consistent with the discussion above. Hence, it seems that cavity tuning control is effective for stable RF operation.

3. RF system

Figure 3 shows the system setup. Two cavities are connected by a single-turn bias winding, either of which is directly coupled to the cathode of the final amplifier. Five ferrite rings with cooling plates are stacked in each cavity. A 30-ohm resistor is installed at the grid input of the cathode follower to prevent the likelihood of vigorous oscillations. In the driver stage high power tetrode (max. plate dissipation 90 kw) was used to drive a 500-ohm resistor across the grid input. Table 1 summarises the parameters.

The bias power supply for cavity ferrites comprises a dc plus a resonant power source, which was originally purchased to study a ring magnet power supply at a high repetition rate. The output current has a shape of the dc-biased sinusoidal wave at a 40 Hz repetition. The power supply has just been provided with a self-trigger system to maintain the oscillation at resonance. Since the ac amplitude was limited to 250 A, the bias current was divided into three groups (200-700 A, 700-1200 A and 1200-1700 A) to cover the entire range of the RF frequency of interest.

A Tektronix programmable arbitrary/function generator produces a predetermined reference voltage for a voltage-controlled oscillator (VCO) at a constant clock rate. The waveform is generated with 12-bit resolution and the full scale of memory is 8192 points. The start of the generator cycle is synchronized with the repetition of the bias power supply. The phase difference between the grid voltage and the cathode current, the sensor of which is a Pearson model 150 current transformer, is also fed into the VCO. The level control loop is incorporated only to keep the preamplifier output constant.

4. Output impedance and high power results

A Hewlett Packard 4195A network analyser was used to measure the output impedance; the probe was connected to the 'cold' gap where no quiescent current flows. Figure 4 shows a typical result compared with calculations using an electronic circuit simulation program, Spice. In the

calculation, $\mu = 18$, $r = 370$ ohm, $C_g = 70$ pF and any stray capacitances (C_{stray}) across the grid input were estimated to be 83 pF. The bias current for ferrites was adjusted to the resonance at 2.5 MHz. The peak at 4.5 MHz showed a parasitic resonance through the inductance (0.3 μH) of the bias winding loop, where the gap voltages of the two cavities swung 180° out-of-phase with nearly the same amplitudes.[2] The calculation also fits the other spikes and the steep slope at higher frequencies, where contributions are from the lead inductance of the measuring probe and the cavity capacitors, as well as the bypass capacitor at the feeding point of the cavity bias current. The output impedance seen by the beam is summarised in Fig. 5. Inadequate grounding of the anode circuit is thought to be a reason for the large amplitude near 1 MHz. A slight increase of the impedance with frequency is due to the fact that less voltage is developed between the grid and the cathode as the frequency becomes higher; hence, the characteristic of low output impedance will be diminished. To make the calculation independent of the cavities, we directly look into the cathode and the cathode-grid reactance in series with whatever appears between grid and ground in the driver stage (Fig.1). The impedance thus seen gives $r/(\mu+1)$ at a lower frequency, and increases with frequency. The results for the present system are 20 ohm∠5° at 500 kHz and 33 ohm∠-16° at 50 MHz. These values are still low.

The same resonances can be seen for the grid input impedance. Figure 6 shows the result of a Spice calculation, in which the cavity inductance is taken to be same as in Fig.4. In the figure, the dashed line indicates the approximate impedance of a 500-ohm resistor in parallel with the total capacitance across the grid input. The total capacitance (C_{gg}) is given as

$$C_{gg} = C_{stray} + C_g\ (1 - A),$$

where A is the voltage gain of the cathode follower.[3] However, the second term in the right-hand side was approximated by C_g in the calculation, which is really the case except for the resonance region.

Figure 7 displays RF wave forms over the range of 1.1-2.3 MHz. The voltages are lower by half or less than expected from the low-level measurements of the cavity shunt impedance.[2] The preliminary result for an RF voltage is at most 500 V per two gaps at 1.2 MHz. However, the oscillation was stable and no liability to parasitic oscillations has been observed. In order to see the effect of cavity tuning as discussed in section 1, a test was also made under fixed frequencies, which were slightly shifted from the resonance. However, contrary to eq.(2) the result indicated no buildup of oscillations.

5. Discussions

It seems worthwhile at this point to mention the power consumption at the driver stage,[4] since the voltage gain of the cathode follower is less than unity. At higher frequencies, the reactance due to the total capacitance between the grid and ground becomes a dominant term (Fig.6), and a much higher current will be required than that of the final stage amplifier. The cathode follower should be therefore used far below the frequency $\mu/(2\pi r C_{gg})$, where the output impedance is equal to the driver-stage reactance. The choice of cathode follower to high intensity accelerators depends upon the beam loading and necessary RF voltage.

Acknowledgments

The author would like to express his gratitude to Messrs Y. Yano, N. Kaneko and Y. Kobayashi for their cooperation.

References:

1) T. Hardek: Preprint LA-UR-84-1935.
2) Y. Irie, N. Kaneko, H. Baba and M. Miki: KEK Report 87-28, 1988.
3) F. Clapp: Proc. I.R.E., 37, (1949) pp.932-937.

4) Y. Irie: Proc. Int. Workshop on Hadron Facility Technology (LANL,1987) pp.349-358.

Table1. Parameters of the cathode follower RF system

Repetition frequency	40	Hz
RF frequency	1-4	MHz
Cavity		
Inductance	2.4-0.15	μH
Resonating capacitance	10.5	nF
Ferrite material	TDK SY-5	
inner radius	0.12	m
outer radius	0.22	m
thickness	0.025	m
No. of ferrite rings / cavity	5	
Bias loop	1	turn
Bias current	200-1700	ampere
Final Amplifier		
Class of operation	A	
Type	Cathode follower	
Configuration	single-ended	
Power tube	Eimac 3CW40,000H3	
Driver Amplifier		
Class of operation	A	
Type	Grounded cathode	
Power tube	Ziemens RS2058CJ	

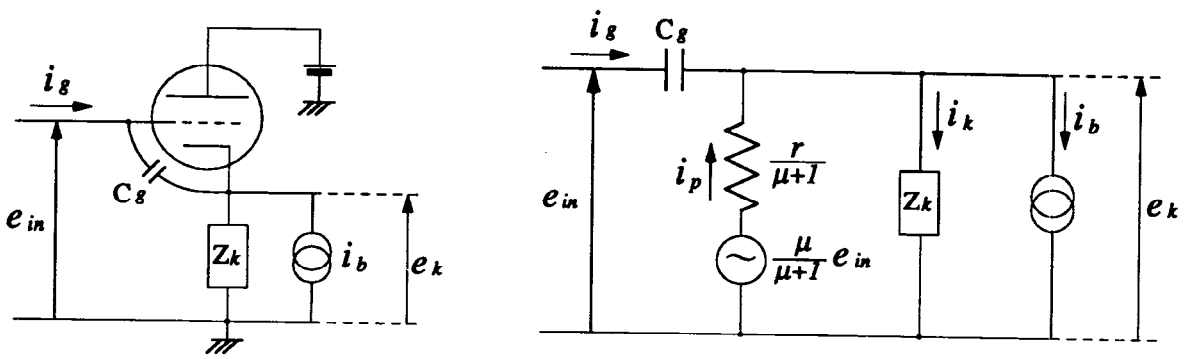

Fig.1 Cathode follower and its equivalent circuit.

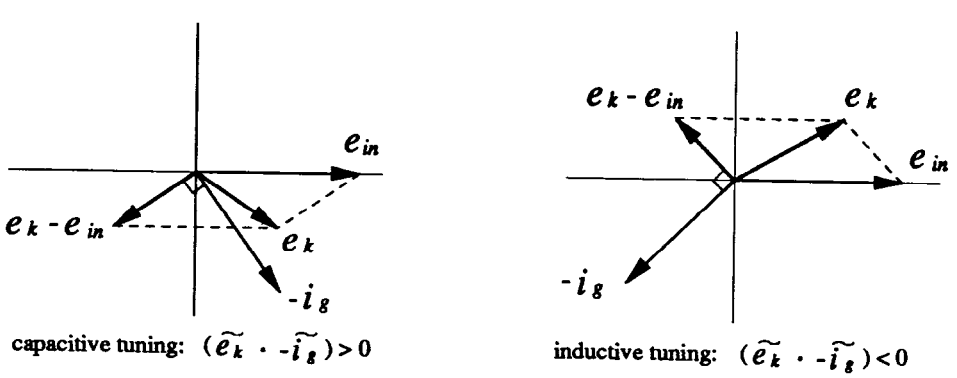

Fig.2 Phasor diagram for the cathode follower.

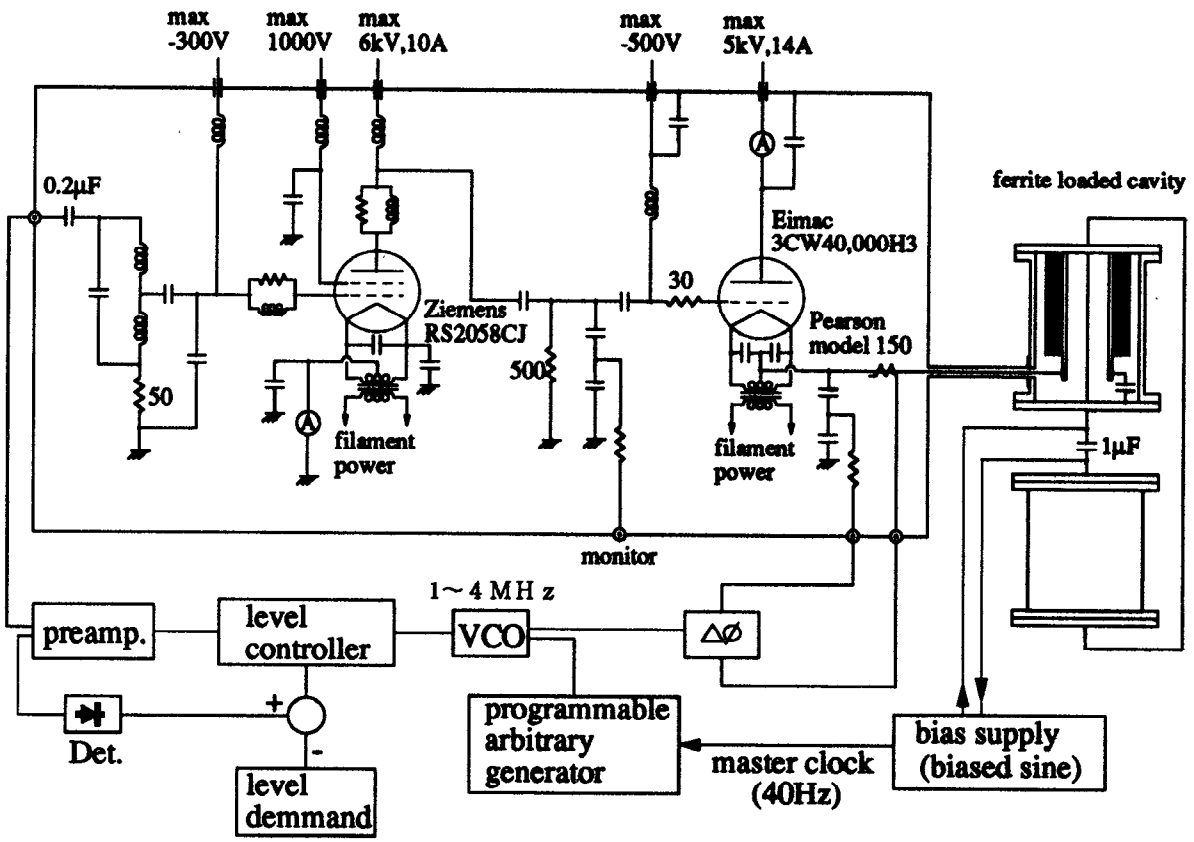

Fig.3 Setup of the RF system.

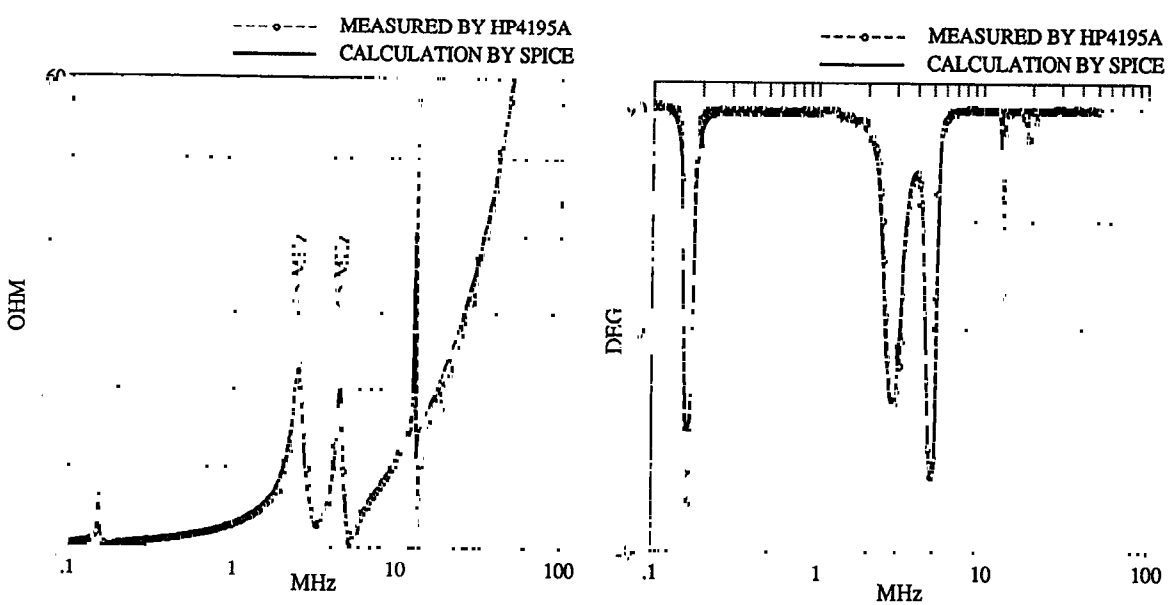

Fig.4 Typical result of an output impedance measurement.

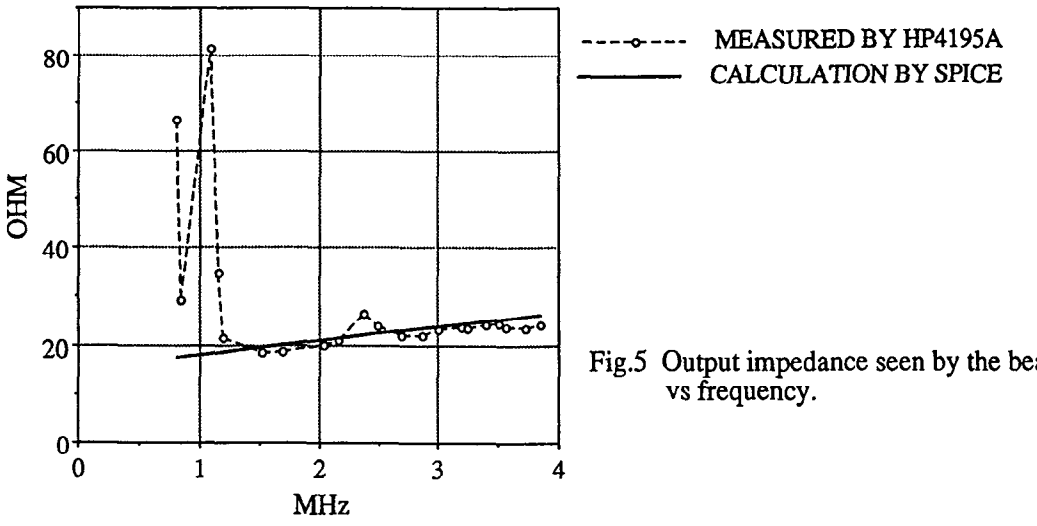

Fig.5 Output impedance seen by the beam vs frequency.

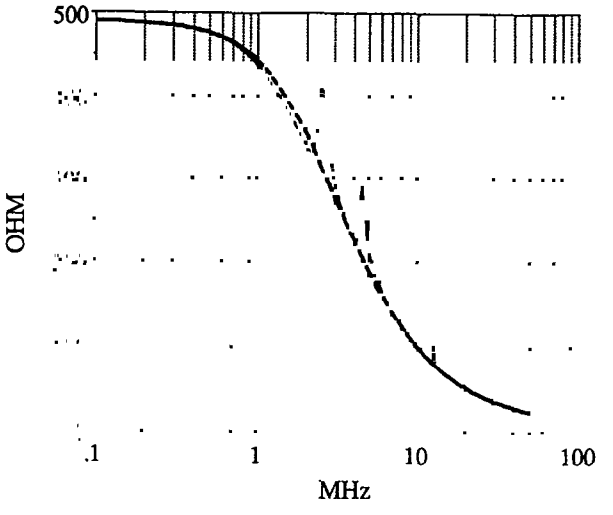

Fig.6 Grid input impedance (solid) and approximation by Cg (1-A) ~ Cg (dashed).

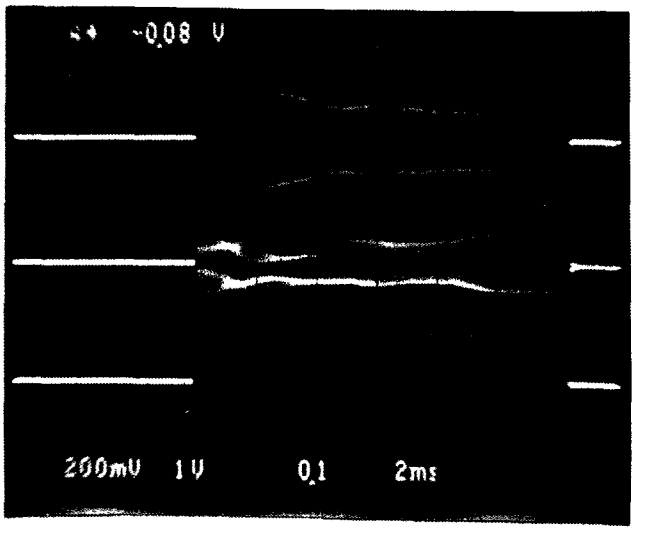

Fig. 7
From the upper to the lower traces: the grid input voltage (200 V/div), cavity input current (2 A/div), and cathode voltage (100 V/div) over the range of 1.1-2.3 MHz.

OPERATION OF THE RF SYSTEM AT THE KEK PS

Shigeshi NINOMIYA

National Laboratory for High Energy Physics
Oho 1-1, Tsukuba-city, Ibaraki, 305 Japan

ABSTRACT: The development of the KEK-PS rf system for this 10 years and the recent operation are summarized.[1] The measured emittance variations during acceleration are also presented.

DEVELOPMENT OF THE KEK-PS RF SYSTEM

The operation of the KEK-PS for physics experiments started in 1977. In 1980, the Booster Synchrotron Utilization Facility(BSF) started operation. The beam intensity of the Booster and that of the Main Ring were $\sim 6\cdot 10^{11}$ppp and $\sim 4\cdot 10^{12}$ppp, respectively. The ion source was changed from proton to H^- ion with employing the charge-excahnge technique at the Booster injection in 1983. In 1985, the 40MeV linac was installed. This improvement has increased the intensity of BSF beam to $\sim 2\cdot 10^{12}$ppp at the Booster injection. For an increased beam intensity at the Booster, the stability of the rf system becomes substantial for steady operation of the KEK-PS.

We have analyzed the feedback loops in the rf system on the basis of control theory. Fig.1 shows a signal flow diagram of the KEK-PS rf system. The diagram shows all of the connections of the feedback loops in the system. The analyzed systems are the cavity tuning loop, the Automatic Voltage Control loop (AVC), and the beam feedback system[1]. The stability of the cavity tuning system is essential for a steady operation of the rf system. In order to increase the loop gain of the automatic cavity-tuning system, an improvement of the bias power supply was necessary. The adjustment of the control circuit in the bias power supply increased the bandwidth of the cavity-tuning loop to ~1kHz. For the Main Ring cavity-tuning system, the bandwidth is ~3kHz.

Parallel operation of the two accelerating stations in the Booster has started from 1979.

In 1983, we installed the cavity phase-lock loop both for the Booster and the Main Ring. The system can be used for a counter-phasing technique with which the effective accelerating voltage per ring can be reduced without a reduction of the rf voltage at rf cavities.

In the above analyses of the feedback loops, we had neglected the beam loading effect. We started the analysis of the stability of the rf system in the presence of the beam loading since 1986. The analysis is based on the transfer function method.[2] The analysis shows that the beam loading shifts the cavity resonating frequency to several-10kHz higher than the accelerating frequency(before transition). This phenomenon is clearly observed at the transition in the Main Ring ferrite bias current; the bias current(the resonating frequency of the cavity) suddenly decreases at the transition(Fig.2b). This analysis also shows that the transfer function of the cavity for a modulation signal reduces its value with increasing loading beam current.[3] This means that feedback loops in the rf system reduce their open loop gains with increasing the circulating beam current. Therefore, even under an operating condition of below the loading stability limit, the gain of the feedback loop must be made to be as large as possible.

The KEK-PS has also been accelerating deuteron beam since 1991. The accelerating frequency range of the Booster is reduced from 2.25MHz ~ 6MHz to 1.16MHz ~ 4MHz by connecting vacuum capacitors across the accelerating gap. For the Main Ring, the frequency range is extended from 6 ~ 8MHz to 4 ~ 8MHz by installing a new bias power supply having a output current of 1500A. The lowest frequency is also reduced by connecting vacuum capacitors across the gap.[4]

In 1992, the following electronic modules were moved from the Booster accelerator room to an auxiliary control room for the Booster apparatus. The moved modules are the low level electronic circuits of the cavity-tuning system, that of the AVC and the cavity phase-lock system. These circuits had suffered from a noise from the high power rf system. This improvement has eliminated the noise from the circuits.

RECENT OPERATION OF THE KEK-PS RF SYSTEM

The scheduled operation of the KEK-PS repeats with a period of three weeks. The intensity of the Booster beam is $\sim 1.2 \cdot 10^{12}$ppp at the start of the operation and increase to $\sim 1.6 \cdot 10^{12}$ppp within a few days. The KEK Booster steadily accelerates the beam with an intensity of $1.6 \cdot 10^{12}$ppp, which corresponds to a 1.54A average beam current at 500MeV-top energy. Since the accelerating system has 2 gaps, the amplitude of the loading current(I_L) onto the power amplifier amounts to 4.6 ~ 6.2A depending upon the bunch width. The shunt impedance at the drive terminal is 600Ω, therefore the drive current of the rf cavity(I_D) is 5A at a 6kV accelerating voltage. The relative loading Y, defined by $Y = I_L/I_D$, is 0.94.

The beam loading effect reduces the cavity transfer function for a modulation signal. The analyses in Refs. 2) and 3) say that the rf system becomes unstable for a loading of $Y \sim 2$. The rf system of the Booster at the top energy is still free from the loading instability.

At beam injection average circulating current is 0.51A and the loading current(I_L) is ~1.54A. The shunt impedance of the cavity at the drive terminal is ~1kΩ; therefore, we must increase the accelerating voltage to a value greater than 3kV by the time a bunch is established(~100μs after the beam injection). In order to reduce the relative loading at the beam capture process, we keep the rf voltage at an accelerating station to 5kV and reduce the effective accelerating voltage by the counter-phasing technique(Fig. 3(a)). This technique is effective for an operating region where the relative loading has a value of less than 1.[3]

Adoption of the counter phasing technique solves three difficulties in the Booster rf system, one is the loading problem at beam injection(explained above); the other two difficulties come from a limitation of the bandwidth of the bias power supply. At beam injection, the bias power supply experiences two perturbations: the first one comes from a shift in the cavity resonating frequency due to the beam current; the second one comes from the dependence of the ferrite permeability on the flux density. An abrupt increase of the accelerating voltage increases the bias current. At the beam injection, the output current of the bias power supply is minimum, and its bandwidth is also narrow. Therefore, the beam injection period is the most unstable operating time for the cavity-tuning system. The unstable oscillation of the bias current due to the perturbations at the beam injection was observed at the output of the phase detector in the cavity-tuning system. The oscillation had reduced the capture efficiency of the injected beam. This unstable oscillation has been removed by increasing rf voltage to 5kV before the beam injection and by employing a second-order compensation technique[1] for the cavity-tuning loop.

The problem concerning the longitudinal beam emittance is a serious problem for the Main Ring injection and for the extraction system of the Booster at high intensity.

The emittance of the beam from the linac is typically 0.35eV·s which is calculated from $\Delta p/p$ of linac beam. As shown in Fig.4, the emittance blows up to ~ 0.6eV·s for the BSF beam at an intensity of $1.6 \cdot 10^{12}$ppp. The blow-up occurs during both an adiabatic capture process and acceleration. These emittance values are

calculated from the measured bunch width(in the unit of rf phase) and the accelerating voltage. In the calculation, an ellipse approximation of the bunch in the phase space is employed. In the case of the Booster, the space charge force in the bunch is not substantial. Since the width of the bunch is not so short, it gives an error of nearly 10%. The results at 15ms and 20ms in Fig.4 contain errors in the approximation. The dependence of the longitudinal emittance at 1ms on the date of the measurement comes both from variation of the linac emittance and from the adjustment of the growing bucket. For a low intensity, the emittance growth during the acceleration is small. The quadrupole mode damping system[1] is used from the start of the capture process. Fig.3(b) is an example of the fast intensity monitor during the capture process. When the ramp speed of the accelerating voltage is faster than the example, a strong quadrupole oscillation is observed.

The longitudinal acceptance of the Main Ring is determined by the effective rise time of five kicker magnets at the Main Ring, and the value is ~0.4eV·s. The emittance of the Booster increase to 0.4eV·s at $4.5\cdot10^{11}$ppp for the Main Ring beam. The injection phase error and the mismatch between the rf buckets of the Booster and the Main Ring increase further the phase space area of the injected beam. As a result, the width of the bunch circulating in the Main Ring increases, and a certain part of the protons in the bunch are kicked by the rising head of magnetic field of the kicker magnets at the next beam injection. This effect causes a beam loss at the beginning of the acceleration, where the dynamic aperture of the Main Ring is minimum.

The emittance at an intensity of $1.6\cdot10^{12}$ppp for the BSF is ~0.6eV·s. On one hand, the rise time of the magnets is designed to be ~80ns. On the other hand, the large emittance value results in a smaller bunch-to-bunch space of the circulat-ing beam in the Booster and limits the permitted rise time of the extraction kicker magnets. In order to maintain an 80ns bunch-to-bunch spacing, we must increase the accelerating voltage at the extraction for the BSF to 12kV. As a result, the momentum spread of the extracted beam for the BSF is far larger than that of the Main Ring beam.

At the phase transition of the Main Ring, both the micro-wave instability and the longitudinal quadrupole mode oscillation are observed. This quadrupole mode oscillation is caused by the mismatch between the rf bucket and the bunch due to the space charge force. The longitudinal emittance blows up to nearly 5-times as large as the value before the transition. The project to shift the transition

energy to above 12GeV-top energy has been stopped, because of the requirement of physicists on the internal target channel, where one of four quadrupole doublets has to be installed. The four quadrupole doublets vary the dispersion function in the Main Ring and shift the transition energy.

The following list is an operational result for this 10 years.

Operation time from April 1982 to March 1993; 37270h

The time stopped due to machine troubles; 1426h(3.8% of the operation time)

The time of trouble due to		Linac;	354h(24.8% of the trouble-time)
40MeV BT;	265h(18.6%)	500MeV BT;	187h(13.1%)
@ Booster RF;	110h(7.8%)	Pre-inj.;	119h(8.3%)
Main Mag. PS;	98h(6.9%)	@ Main Ring RF;	63h(4.4%)

The time of the machine troubles due to the Booster and the Main Ring rf systems is more than 12% of the total machine trouble time. It could be reduced to less than 10%, if a more systematic diagnostic procedure was established.

CONCLUSIONS

The elementary analyses[1] based on control theory help the diagnosis and the tuning of the rf system. The reliability of the rf system at the KEK-PS is achieved by the effort of all members of the KEK-PS RF Group.

ACKNOWLEDGEMENTS

The author would like to express his thanks to Professor N.Watanabe. He give me the opportunity to join this meeting. And I would also like to express thanks to Professors M. Kihara, I. Yamane, and K. Muto for the encouragement and valuable discussions. Prof. K.Muto has established the technology concerning daily operation of the rf system and the parallel operation of the two rf stations in the Booster.

REFERENCES

1) S.Ninomiya et al, "DEVELOPMENT OF THE RF SYSTEM AT KEK-PS." KEK Report, 1993.
2) F.Pedersen, IEEE NS-22, p.1906, 1975.
3) S.Ninomiya, "Beam Loading Effect on RF ....(in Japanese)" KEK Report, 89-18.
4) S.NINOMIYA et al, "Improvement of the RF System .... for Deuteron Accel." Proc. of 8th Symp. on Accel. Sci. and Tech., p.167, 1991.

FIGURE CAPTIONS

Fig.1 Signal flow diagram of the KEK-PS RF system.

Fig.2 (a) Booster bias current changes from 300A to 2300A sinusoidally with a repetition of 50ms. Variation of the cavity tuning phase error is also shown in a scale of 40°/div. (Horizontal; 5ms/div.)

(b) The upper trace is the variation of the accelerating frequency from 6MHz to 8MHz at the KEK-PS Main Ring rf system. The middle is the bias current. It shows the jump in the resonating frequency at the transition. The lower trace is the cavity tuning error in 20°/div. (Horizontal; 0.2s/div.)

Fig.3 (a) Counter-phasing technique at the Booster beam injection reduces the rf voltage at the Booster accelerating gap(lower trace, 5kV/div.) and makes the effective accelerating voltage per revolution(upper trace, 6kV/div.) Horizontal; 0.5ms/div.

(b) Growth of the bunch(lower trace) at the Booster injection is compared to the accelerating voltage(upper trace).

Fig.4 Variation of the longitudinal emittance of the Booster beam during the acceleration.

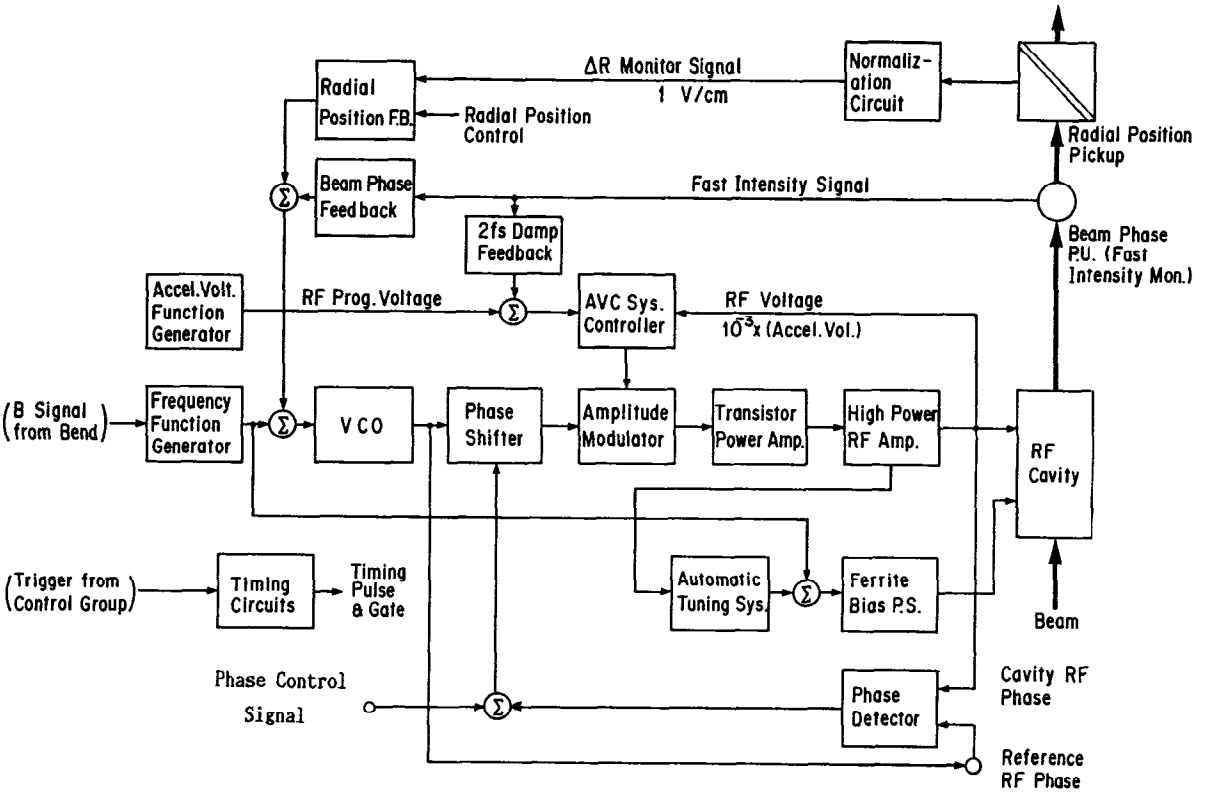

Fig. 1

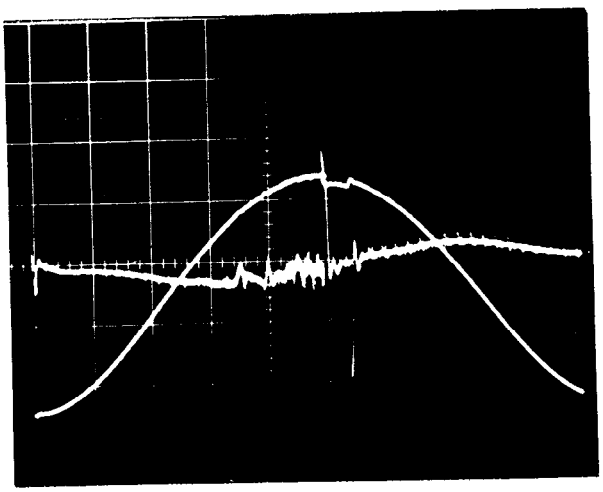

Fig.2(a)

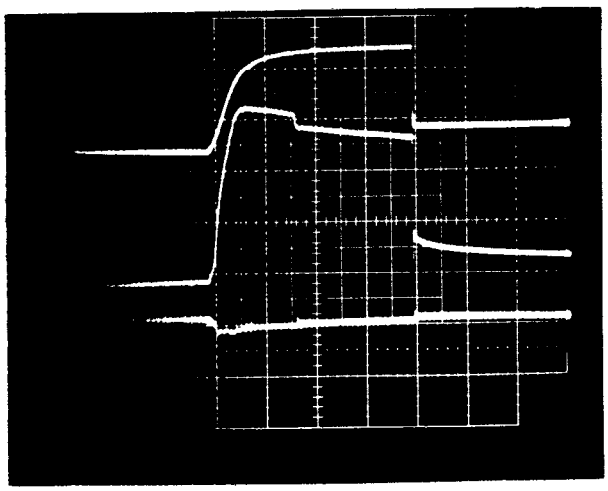

Fig.2(b)

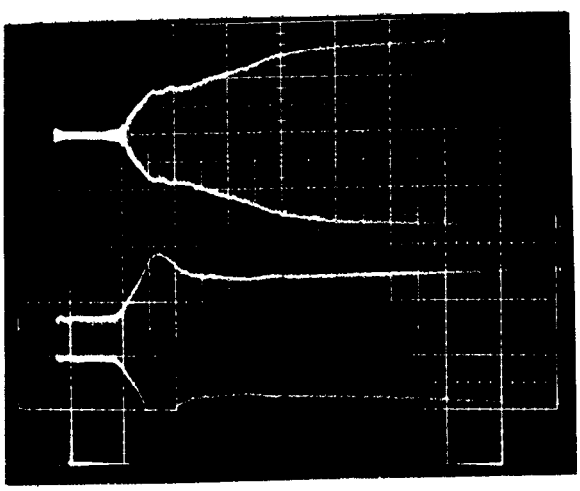

Fig.3(a)

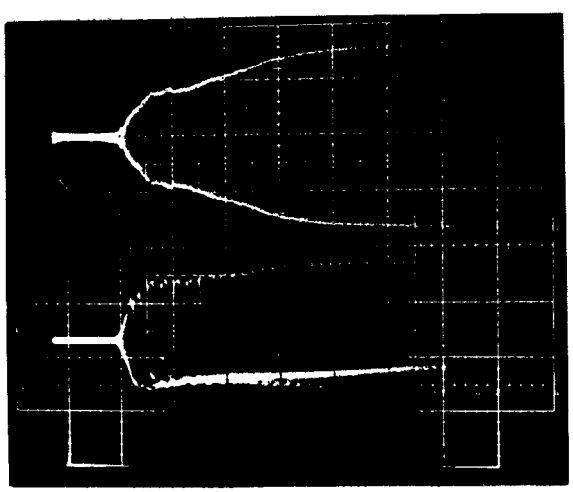

Fig.3(b)

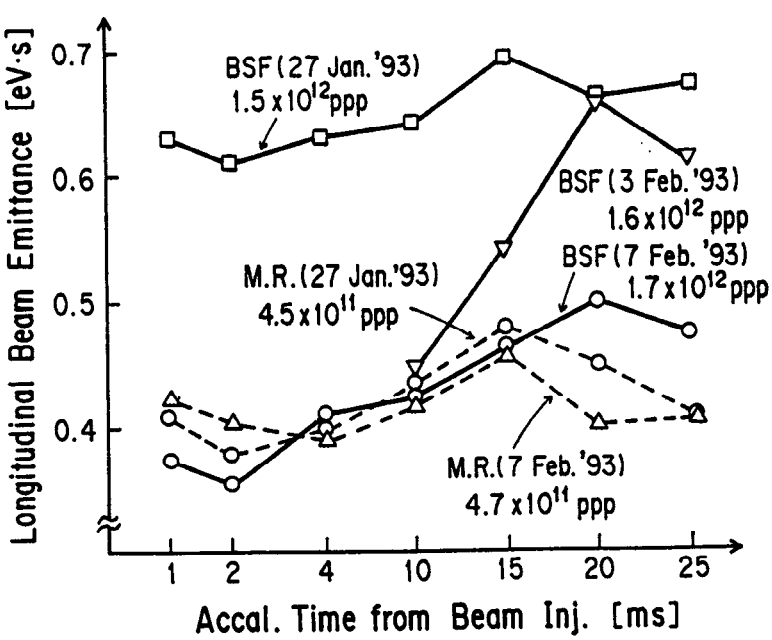

Fig. 4

Room Temperature Vs Superconducting LINACS

Horst Heinrichs
Bergische Universität-Gesamthochschule Wuppertal
42097 Wuppertal, Germany

Abstract

For the proposed accelerator based, pulsed spallation neutron source a linear accelerator is needed. Starting from fundamental relations for the characteristic properties of cavities and linacs a comparison of a room temperature with a superconducting linac is presented. It turns out that the superconducting linac is superior in nearly all parameters, and a rough estimate shows that it is cheaper in investment and in operational costs. The room temperature linac has the advantage of a simple technology. On the other hand it has been shown during operation of superconducting cavities in storage rings that the maintenance of these structures can be carried out by the staff of the room temperature cavities.

Introduction

The initial aim of an accelerator based, pulsed spallation neutron source is a beam power of 5 MW, a beam pulse length of 1-2 μs, and a repetitions rate of 50 Hz. At the Workshop on Accelerators for Future Neutron Sources held at Santa Fe it turned out that the optimum energy of the proton beam is ~ 2 GeV. Different types of accelerators can fullfill these requirements. One option is the linear accelerator followed by one or more accumulator or compressor rings. Some aspects of the question whether this linear accelerator should be a normalconducting or a superconducting one will be discussed in this paper. It cannot be the aim of this paper to present a real and fair comparison, to do so an optimum design of both types must be developed by independent expert groups. The two designs presented here should be looked at as a starting point for further discussions.

History of Technological Progress

The development of room temperature linear accelerators started after world war II when microwave power sources were available. The physics of microwave resonators was known since long time. The iris loaded structure for electron linacs and the Alvarez structure for proton linacs were investigated. Due to a simple handling the structures were manufactured from copper. It was a big step to go from laboratory tests of single resonators to a series production of structures. The small tolerances in the production of structures and in its alignment were severe problems. Moreover the particle sources, the injection and ejection, the focusing system, and last but not least the vacuum system for an up to several hundred meters long accelerator had to be developed. On the way to reach high energy proton beams the biperiodic and side coupled structures were developed by Knapp at Los Alamos National Laboratory [1]. Structures of this type are installed in LAMPF which went to operation in

1972. In the following time the performance of all components have been improved and other types of structures have been developed. But the side coupled structure of the Los Alamos type is still a favoured structure and is designed for new proton accelerators like the injector for SSC [2] or the linac of the Japanese Hadron Project [3] or the 400 MeV upgrade for the Fermilab linac [4]. Among the normalconducting linac types the coupled-cavity linac (CCL) is the simplest, provides the highest gradient, and is the least expensive per meter to fabricate.[2]

The investigation of the properties of superconductors under RF fields was started in 1940 by H. London. About twenty years later the BCS theory gave an insight to the physical origin of the surface resistance of normalconducting and superconducting materials. According to this theory the microwave power losses in superconducting cavities are four to five orders of magnitude smaller than those in normalconducting ones. The first laboratory tests of niobium single cell cavities were done in 1963. Though the first laboratory measurement of high fields (~ 45 MV/m) at a Q-value of ~ 10^{10} in a superconducting single cell cavity were reported in 1968 [5] a proposal for a 2 GeV electron accelerator was presented in 1963 and for a 1 and 7 GeV proton accelerator was published in 1967[6]. In the following time many superconducting structures have been operated in electron, proton, and heavy ion accelerators at field levels of 2-3 MV/m.

A big step forward in getting high accelerating fields was done in 1978 when one side electron multipacting could be analysed. It was shown that this field limiting barrier was absent in cavities of round shape as they are now used in electron machines. From about 1980 there was great interest in operating superconducting cavities in electron storage rings. Unfortunately there was no need to install a superconducting cavity in a high energy proton accelerator.

The next milestone on the way to high fields was the invention of high thermal conductivity niobium sheet metal which was developed in collaboration with industry. Defects and impurities which produce heat on the inner surface or in the bulk near the surface can be stabilized by use of high thermal conducting material. The breakdown or quench field can be increased. As a measure of the temperature dependent thermal conductivity the value of RRR (residual resistivity ratio: R(300K)/R(4.2K)) is often quoted. The niobium material which was delivered from industry till 1983 had an RRR of 30, now it has an RRR of 300-400, i.e. the quench field is increased by a factor of ~ 4. Moreover a further increase of the thermal conductivity can be reached by firing the complete cavity together with Titanium solid state material in a furnace at 1400 C. This purification is especially usefull to cure mistakes during fabrication or to heal after accidents.

When the accelerating field reaches 10 MV/m or more - the surface field is still a factor of 2 higher - field emission becomes the dominant field limiting effect. The superconducting surface is very sensitive against additional heat input so that field emitted currents can produce a quench. The most likely sources are metallic or dielectric dust particles on the surface. But also "irregularities" like etch pits or intrinsic surface properties can emit electron currents. Special cleaning techniques and preparation methods like those known from micro chip production have been developed. Recently field level of 25 MV/m could be reached in single cell 1.5 GHz cavities reproducibly. Fianally with the high power processing method there is a tool to repair cavities after a dust accident. High peak power RF pulses (300KW to 1MW and 100μs to 1ms) are fed via an adjustable input coupler into the cavity. From several tests it is concluded that the dust particles are heated during the RF pulse so that they evaporate immediately.

This short overview [7] shows that superconducting cavities are under use in electron and heavy ion accelerators since more than ten years in several laboratories. The cavities run under routine conditions and the operating experience exceeds 10,000 h. Also the decision to build CEBAF as a fully superconducting machine shows that the superconducting technology is available and reliable.

Basic Relations

The main differences between the normalconducting (nc) and the superconducting (sc) structure are demonstrated by the calculation of the power loss in the structure walls. If P is the rf power per unit length necessary to maintain an effective accelerating field E_a in an unloaded cavity and r is the shunt impedance per unit length of the accelerator structure then it is (by definition of r)

$$P = \frac{E_a^2}{r}. \tag{1}$$

The quality factor Q of a cavity is defined by the relation

$$Q = \frac{\omega W}{P} \tag{2}$$

where ω is the angular frequency, W is the stored energy, and P the power loss (per second) of the cavity. As the stored energy is proportional to $\int E^2 \, d\tau$ over the volume of the cavity it can be shown that the quantity r/Q is a geometrical constant, independant of the material of the walls. So the above relation can be written as

$$P = \frac{E_a^2}{\frac{r}{Q} Q}. \tag{3}$$

This shows that the power loss is inversely proportional to the specific shunt impedance r/Q and the quality factor Q. The r/Q can be expressed as r/Q *d ~ 150 Ω, where d is the length of a cavity cell, which is $\beta\pi c/\omega$. As the power loss P in equation (2) is given by

$$P = \frac{1}{2} R_S \int H^2 \, ds \tag{4}$$

where R_S is the surface resistance - which is assumed to be homogenous over the surface of the cavity - and E is proportional to H the quality factor Q can be expressed as

$$Q = \frac{G}{R_S} \tag{5}$$

where G is the geometrical factor (by definition).
For a normalconducting high frequency cavity the surface resistance is given by

$$R_S = \sqrt{\frac{\mu\omega}{2\sigma}} = \frac{1}{\sigma\delta}. \tag{6}$$

If the mean free path length l is greater than the skin depth δ the surface resistance is determined in the Pippard limit by the relation

$$R_S = \frac{8}{9} \left(\frac{\sqrt{3}}{16\pi} \frac{\mu_0^2 \omega^2 l}{\sigma}\right)^{1/3} \tag{7}$$

where σ is the conductivity.
This gives for copper at 500 MHz a value of R = 5 mΩ. The Q is of the order of $3*10^4$.

The superconducting surface resistance is given by

$$(8) \qquad R_s = A(\lambda, \xi, l, v_F)\frac{\omega^2}{T}\exp\{-\frac{\Delta(0)}{kT_c}\frac{T_c}{T}\} + R_{res}$$

or approximately for niobium with $\Delta(0) = 1{,}95\ kT_c$ and $T_c = 9{,}25$ K for commercially available niobium

$$(9) \qquad R_s(n\Omega) = 10^5\ f^2(\mathrm{GHz})\frac{1}{T(K)}\exp\{-\frac{18}{T(K)}\} + R_{res}$$

A typical value is R = 30 nΩ at 4.2K, the residual resistance is about 20nΩ, best values are 1 nΩ. The Q is of the order of $5*10^9$.

This simple analyses shows that the power loss is reduced by 4.5 orders of magnitude in a superconducting cavity compared to a normalconducting one with the same shape. Quantitatively at an effective accelerating field level of 10 MV/m and an r/Q of 1000 Ω/m the nc cavity dissipates in cw operation 400-500 KW/m whereas the sc cavity only several W/m. This shows a cooling problem for the nc cavity which has to be operated in a pulsed mode, i.e. at a low field level for a long pulse duration or at a high field level for a short pulse duration. The sc cavity can be operated in a cw mode because the cooling limit of 1 W/cm^2 is by far not reached. Field limitations are caused by other effects as mentioned above. In pulsed operation the lower limit for the pulse duration is given by the filling time of the cavity which is in the range of 1 ms. With respect to the efficiency and to the effective wall plug power one has to keep in mind that in the superconducting case the losses are produced at a temperature of 4.2 K. Assuming an efficiency of the refrigerator of 20% of a carnot cycle the power consumption is 350W at room temperature per Watt at 4.2K. Nevertheless the sc linac needs less power than the nc one. If one defines the efficiency as the ratio of beam power and the net wall plug power the efficiency of a nc linac is given by

$$(10) \qquad \eta_{nc} = \frac{P_{beam}}{\frac{P_{beam} + P_{diss}}{\eta_{rf}}},$$

with $P_{beam} = i_{av} * E_a * \cos(\Phi)$ and $P_{diss} = (E_a^2/r)*dc$. Here i_{av} is the average current, $E_a*\cos(\Phi)$ the effective accelerating field seen by the particle, and dc the duty cycle. As the power dissipated in the cavity scales with E_a square but the beam power only with E_a the efficiency decreases rapidly with increasing E_a. The efficiency has a maximum equal to the efficiency of the RF for $E_a = 0$. The efficiency of a sc linac is given by

$$(11) \qquad \eta_{sc} = \frac{P_{beam}}{\frac{P_{beam} + P_{diss}}{\eta_{rf}} + \frac{P_{diss} + P_{stat}}{\eta_{cryo}}}$$

Due to the static losses P_{stat} the efficiency is zero for vanishing fields but increases rapidly. It shows a maximum and decreases slowly because of the increase of the cavity losses at very high fields. For the parameters given in the following Table 1 the efficiencies of the nc and the sc linac are shown in Figure 1. It should be mentioned that these arguments are based only on the power consumption of the linacs, there are up to here no capital costs included. These

would ask for even higher accelerating fields because of saving costs due to a short length of the accelerator.

		pulsed nc linac	pulsed sc linac
Average current i	mA	2.5 (6.25)	2.5 (6.25)
Shunt impedance (av) r	Ω/m	$4.29 * 10^7$	$1.95 * 10^{12}$
Phase angle Φ	deg.	24	24
Pulse duration t	ms	2	2
Filling time t_f	ms	0.05	1
Repetition rate	1/s	50	50
RF-efficiency		0.6	0.6
Cryo-efficiency		-	$2.8 * 10^{-3}$
Static power loss	W	-	5

Table 1.: Typical parameters of nc and sc linacs. These parameters were used in efficiency calculation

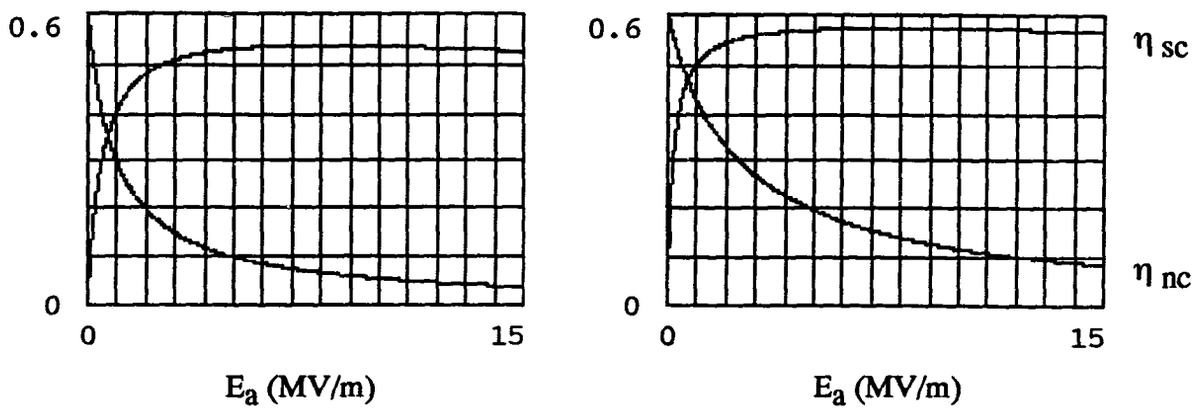

Fig. 1: Efficiency of nc and sc linac as a function of accelerating field; left for i_{av} = 2.5 mA and right for i_{av} = 6.25 mA. Further parameters see Table 1.

The question whether to operate a sc linac at 4.2K or at 2K can be answered by the ratio of the BCS part of the surface resistance to the residual resistance. As the BCS part increases with the square of the frequency one can conclude that cavities at 500 MHz and below can be operated at 4.2K whereas cavities at 800 MHz and above should be operated at 2K. From the cryogenic point of view an operation at 4.2 K is favoured because of its simple construction and handling

The amount of the power dissipated in the walls of a nc cavity asks for a high shunt impedance. In former time cavities were optimized with respect to increase shunt impedance. This gave a strong condition to the shape of the cavity. One consequence was the small bore hole of the irises. As the surface resistance of a sc cavity is orders of magnitude lower there is not such strong impact for shunt impedance optimization. On the other hand the sc cavity is much more sensitive against additional power losses on the surface as they are caused by

multipacting or field emitted currents the shape of a sc cavity was optimized long ago to be multipacting free and to lower the field enhancement factors E_{peak}/E_a and H_{peak}/E_a. This is now also true for nc cavities which shall be operated at high field level and short pulse duration (like SSC and JHP).

Figure 2 shows the shape of the nc cavity for the 400 MeV upgrade of the Fermilab linac. It operates at a frequency of 1284 MHz. This shape is typical for nc cavities for proton accelerators. The typical shape of a sc structure for two different phase velocities is shown in Figure 3. Significant is the simple shape without nose cones and the large bore hole which may have a diameter of 20 cm in a 350 MHz cavity compared to about 3 cm in the nc cavities. This is essential for a low loss beam transport through the structures because the typical transverse dimensions of a proton beam are 1 - 2 cm [10]. For the reason of radiation protection and hands on maintenance losses of the order of 10^{-7} are required. Careful particle dynamics calculations have to be carried out but it seems that a beam tube size of several standard deviations of the beam is favourable.

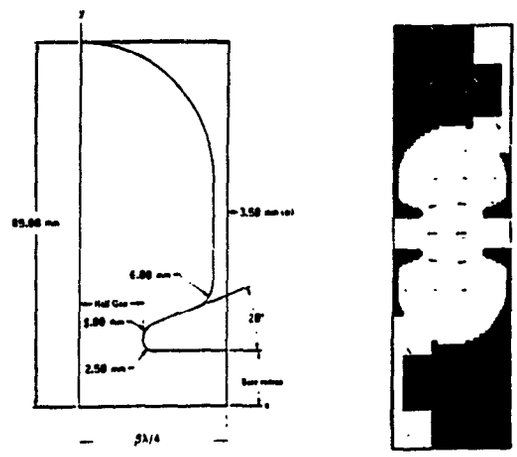

Fig. 2: Typical shape of a normalconducting cavity (injector linac for SSC)

The surface resistance of the nc material scales with $\omega^{1/2}$ resp. $\omega^{2/3}$ according to equation (6) resp. (7) whereas the surface resistance of a super-conductor scales with ω^2 according to equation (9). Consequently according to (2) the power loss scales with $\omega^{-1/2}$ resp. $\omega^{-1/3}$ for a nc linac and with ω for a sc linac. Therefore nc cavities favour high frequencies, and sc cavities favour low frequencies. This is important specially for high current machines because also space charge effects are reduced in low frequency structures. The spacing of two bunches in a train is proportional to the wavelength, and the dimensions of a bunch can be chosen larger in low frequency cavities so that the space charge density is reduced. The space charge forces scale with ω^2.

Due to the simple shape of the sc cavity the overall parasitic mode loss factor as it can be calculated with the TBCI code is considerably (a factor of three or more) smaller for the sc cavity than for the nc one. In addition due to the high accelerating field level that can be achieved in sc cavities the amount of structures - that is the number of sources for wake fields - is in a sc linac a factor of three lower than in a nc linac.

Another important difference between nc and sc linacs is the stored energy which is much higher in sc cavities than in nc ones. Specially in pulsed high current accelerators a high stored energy is needed because as the stored energy is proportional to the square of the field it

"stabilizes" the accelerating field when the bunch takes energy from the cavity. It can be shown [8] that the energy spread ΔE/E of a chopped beam can be expressed as

$$\frac{\Delta E}{E} = \sqrt{1 + \frac{P_{beam}}{W} * \frac{\Delta t1 * \Delta t2}{\Delta t1 + \Delta t2}} - 1 , \qquad (13)$$

where Δt1 und Δt2 are the time intervalls for "beam on" and "beam off". It can be seen that the bigger the stored energy W the smaller the energy spread.

Comparison of Linear Accelerators

The following Table 2 summarizes the main parameters for three types of linacs for a 5 MW spallation neutron source.

		normalc. pulsed	superc. pulsed	superc. cw
Beam power	MW	5		
Endpoint energy	MeV	2000		
Repetition rate	Hz	50		
Pulse duration	ms	2		20
Duty cycle	%	10		100
Chopping cycle		0.86		
Average current	mA	2.5		
Peak current	mA	33		3.3
Accelerating field	MV/m	3	10	

Table 2: Main parameters of three high energy linacs

For a comparison of a nc and a sc linac which fullfill the above requirements only the high β-part of the linacs will be taken into account. The energy range will be from 100 MeV to 2 GeV, which corresponds to a range of β=0.43 to β=0.95. These linacs are by far the largest part of the whole accelerator. All of the arguments which are given below for the high energy part also hold for the low energy part.

The parameters of Table 2 characterize three different linacs: a pulsed nc, a pulsed sc, and a sc linac operated in a cw mode. The main advantage of the latter is that the peak current is reduced to the value of the average current. It can be used in pulsed spallation source only if the following accumulator ring is designed to accept an injection over a factor of at least ten times more turns. Such an accumulator ring is presently under design [9]. Moreover such a cw linac is a powerful device - for example - for the application of accelerator transmutation of waste (ATW) because it seems to be quite easy to increase the beam power by a factor ten by increasing the current to the value of the pulsed linacs. As there is no need for an accumulator ring in this application the chopping cycle is not necessary. Therefore possible design parameters for a 200 MW cw linac could be 3 GeV and 67 mA.

Table 3 summarizes the main design parameters of a pulsed nc and sc linac for a 5 MW spallation neutron source.

		nc linac	sc linac
Frequency	MHz	800	350
Number of cells/cavity		12	2
Acc. field Ea	MV/m	3	10
Number of cavities		396	277
Unloaded Q		21400	$5*10^9$
Shunt impedance (av)	Ω/m	$4.29*10^7$	$1.95*10^{12}$
Joule losses during pulse	W	37800	5
peak rf input powe	KW	500	175
klystron power	MW	2	2.8
Cavities per klystron		4	16
Number of klystrons		100	18
Wall plug power (rf)	MW	33.3	8.4
Operating temperature	K	290	4.2
Stand by losses	W	-	5
Total cryogenic loss	W	-	3200
Design capacity	W	-	4800
Wall plug power	MW	-	1.62
Total wall plug power	MW	33.3	10.02
Effect. length of structure	m	717	220
Length fill factor		0.75	0.5
Total length	m	960	440

Table 3: Parameter list of a normalconducting and a superconducting pulsed high beta linac for a spallation neutron source

Due to the high accelerating field the number of structures in the sc linac is lower than in the nc linac. The high shunt impedance reduces the peak input power. Both effects together reduce the number of klystrons remarkable. Also the effective accelerating length of all sc structures is much shorter - 220 m to 717 m. As can be seen from Figure 3 each sc structure needs "cut-off tubes" on both sides. The "length fill factor" which is the ratio of the total linac length to the structure length is smaller for the sc linac. The total length is therefore "only" a factor of two shorter. The consumption of wall plug power is a factor of three lower, the efficiency of the sc linac is about 50%, that of the nc linac about 15%.

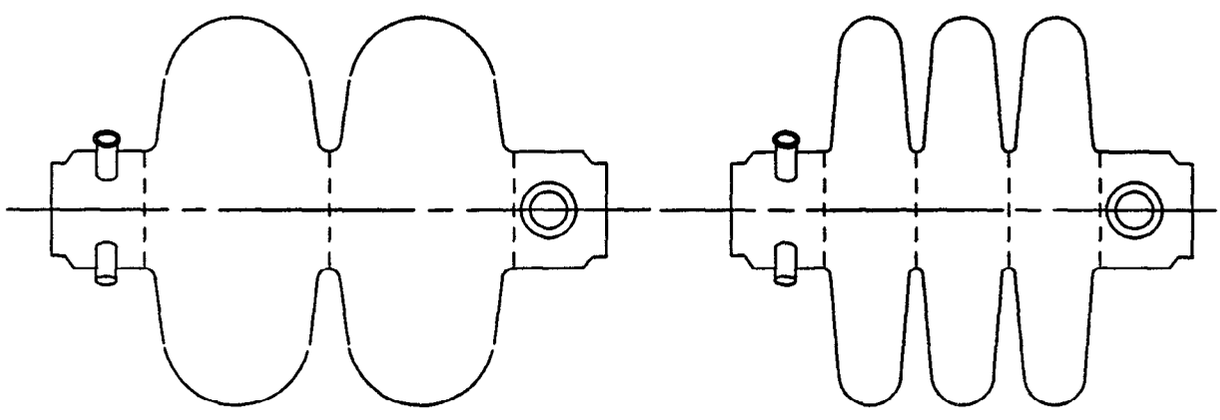

Fig.3: Shape of superconducting structures for two different phase velocities

A rough estimate of the investment cost with the presently available prices ends up at about 200 M$ for the superconducting linac while the normalconducting one is more than twice as expensive. The power bill for 10 years operation (accelerator 5000 h and refrigerator 8750 h per year) will be about 45 M$ for the superconducting and about 130 M$ for the normal-conducting linac.[11]

Conclusion

On the basis of fundamental relations of cavities and linacs the advantages of a superconducting pulsed high current linac over a normalconducting one are discussed. Besides the advantage of being cheaper in investment and in operational costs it seems that the superconducting linac has less beam losses due to the large bore hole and the excellent vacuum at cryogenic temperatures.

References

[1] B.C. Knapp et al., IEEE Trans. Nucl. Sci., **NS-12,** 159 (1965)

[2] J. Watson et al.., Proc. IEEE Part. Acc. Conf., San Francisco, 1991, p.572
C.R. Chang et al., ibid. p.2993

[3] M.Kihara, Proc. XIVth Intern. Conf. High Energy Acc., Tsukuba,1989, and Part. Acc., 1990, Vol. 32, pp. 1-8

[4] D.E. Young and R.J. Noble Proc. XIVth Intern. Conf. High Energy Acc.,Tsukuba,1989, and Part.Acc.,1990, Vol.26, pp.205-210

[5] J.P. Turneaure and I.Weissmann, J. Appl. Phys. 39, (1968), p.4417

[6] A. Citron and H. Schopper, in Linear Accelerators, Ed. P. Lapostolle and A. Septier, North Holland Pub.,1970

[7] The progress in RF superconductivity is well described in the Proceedings of the RF Superconductivity Workshops. Up to May 1993 there were five workshops: 1st 1980 at Karlsruhe, 2nd 1984 at CERN, 3rd 1987 at Argonne, 4th 1989 at KEK, KEK Report 89-21, and 5th 1991 at DESY, DESY M 92-1. The 6th will be held Oct. 1993 at CEBAF.
H. Piel, Proc. CERN Accelerator School, Oxford 1985, CERN 87-03, p.736
W. Weingarten, Proc. XVth Intern. Conf. High Energy Acc., Hamburg, 1992, p.678

[8] G. Spalek, Proc. Workshop on Accelerators for Future Spallation Neutron Sources, Santa Fe, 1993

[9] S.A. Martin et al., Proc. Part. Acc. Conf., 1993, Washington, to be published

[10] SNQ Project Proposal, 1984

[11] H. Heinrichs, Proc. Workshop on High Intensity Proton Linear Accelerators for Future Spallation Neutron Sources, Witten, 1993, to be published

FFAG STUDIES FOR A 5 MW NEUTRON SOURCE

S. A. Martin
IKP, Forschungszentrum Jülich GmbH, Postfach 1913, D-5170 Jülich, Germany

P. F. Meads
7053 Shirley Drive, Oakland, CA 94611-1631 USA

G. Wüstefeld
BESSY-Berlin GmbH, Lentzeallee 100, D-1000 Berlin 33, Germany

E. Zaplatin†, K. Ziegler
HMI-Berlin GmbH, Glienicker Strasse 100, D-1000 Berlin 39, Germany

Abstract

Based on the requirements for a future European Spallation Neutron Source: 5 MW of beam power, a pulse repetition rate of 50 Hz, and a pulse length of less than 3 μs, we looked into the possibility of using different FFAG options for this source. Starting with an H^--linac, the beam will be accelerated to an energy between 400 MeV and 500 MeV and then transferred into an FFAG using stripping injection. We have looked at FFAG options giving final energies between 3.2 GeV and 1.6 GeV.

1. Introduction

The FFAG (Fixed Field Alternating Gradient)-Accelerator was invented in the fifties by the MURA group[1]. This group built a working electron model accelerator and performed a lot of beam studies with this machine, including beam stacking experiments. Unfortunately however a proton version was never built, because of the successful operation of the proton synchrotrons. We feel however, that it is necessary to look if an FFAG could be an option for a high intensity accelerator needed for a high power spallation neutron source. The FFAG can be considered as a ring synchrocyclotron (in the Russian literature: ring phasotron[2]) which like the synchrotron has a fixed working point in the resonance diagram. In the following we want to explain the general features of FFAG accelerators and give reasons why we think it worthwhile to investigate the possible usefulness of such an accelerator for a spallation neutron source.

2. General Features of FFAG Accelerators

We will first list what we consider advantages of the FFAG and then look at the points which can be made against using such a machine for a spallation neutron source facility.

† Guest Scientist from JINR, Dubna, Moscow Region, Russia

-The more powerful existing spallation sources are limited by the beam losses encountered during operation. Therefore the limitation of beam losses must be an essential design criterion for a new facility. Because of the required pulse structure, and the short beam bursts demanded, a linear RF-accelerator alone cannot fulfill these specifications. Therefore a storage ring or a ring accelerator must be added to provide the time structure. An induction linear accelerator recently discussed[3] as an option which would eliminate the need for a ring, seems not to be competitive for cost reasons. Experience has shown, that in the stripping injection process of the H^--ions into the ring accelerator about 2% of the beam is lost. Because the neutron production and therefore the activation of accelerator parts is proportional to the beam power, it is advantageous, to inject into the ring at the lowest possible energy acceptable by space charge considerations, and to gain the major part of the beam power during acceleration in the circular machine as it is done in an FFAG.

- The magnetic field of the FFAG is constant in time and therefore only the RF-frequency needs to be varied and losses due to incomplete tracking of magnetic field and RF-frequency do not occur. It is a generally accepted assumption, that in the FFAG there will be essentially no losses during acceleration.

- Assuming we will inject the linac beam into the FFAG with the RF-voltage turned of and then adiabatically trap the beam, the time structure for the injector linac is quite relaxed because no chopping will be needed. Preliminary studies indicate trapping losses at about the 1% level[4], and furthermore these losses are again at low power and they can be dumped into a specifically designed beam stop.

-Accelerating in the circular machine to a higher energy means one can for the equivalent power accelerate less current and therefore intensity dependend critical effects will be reduced.

-The radial aperture of an FFAG is large and so is the momentum acceptance.

-Stability conditions are good, because the beam does not see the extraction kicker ferrites except for the last few turns. Coherent instability problems are therefore relaxed.

-The FFAG can easily be upgraded to a higher repetition rate thus possibly serving additional targets simply by adding RF-cavities.

-Another option for the future is the possibility of beam stacking for intensity upgrading and reduction of the repetition rate. The option of stacking however hinges very much on the control of beam losses, and therefore again these questions need to be addressed seriously.

We think that all these properties of the FFAG clearly indicate, that a carefull evaluation of this type of accelerator needs to be made, before one can rightfully say that the FFAG is not an option for the spallation source.

The main argument against the FFAG is, that it has never been built, and therefore lacks the the experience of over 30 years of engineering and developments which synchrotrons have received. The design and development of synchrotrons and storage rings is well understood, while designing and building an FFAG means we are entering into a field where some unknown difficulties might be expected. Even so all the individual components are well understood the combination of all of them into one machine, and the need for all of them to work simultaneously to make the FFAG perform, is a scary thought for many, especially when a facility has to be built, which should have a very high reliability.

-Any evaluation of reliability and performance can therefore not be based on the experience of an existing machine but rather needs special discussion.

-The FFAG magnets are very large, superconducting, with a high flux of up to 4 Tesla. The radial type magnets are not complicated, but so far no prototypes have been built and studied.

-The operation of superconducting coils close to a high intensity beam requires again special attention to particle losses, and their effect on the superconducting coils.

-The working point of the FFAG is determined by the hardware of the magnets, and special systems like e.g. pole face windings need to be built for fine tuning.

-The ferrite tuned-cavities require large ceramic windows for the acceleration gap. Other concepts for tuning of the cavities need to be looked into and require additional studies.

-The high beam intensity requires special studies of beam loading effects.

-The shielding for the higher beam energy is more costly.

-Operational costs for an FFAG cannot be based on experience, but again require special discussion and study.

3. Discussion of FFAG Options

In the range between 1 GeV and 3 GeV, the required proton beam power for a given thermal neutron flux is approximately independent of the proton energy. We have therefore concentrated on this range of energies with a preference toward the higher energy because this requires lower beam intensities. The repetition rate of 50 Hz is specified by the user community. For the RF harmonic we select the first or second in order to avoid the coupled bunch instabilities. So far we have concentrated on scaling FFAG options, where the average magnetic field increases with average radius as $\langle R \rangle^k$. Gamma transition is given by $\gamma_{tr} = \sqrt{(k+1)}$. We choose the FFAG ring parameters such to prevent the crossing of γ_{tr} in order to avoid the excitation of strong longitudinal beam oscillations, possible beam blow-up, and, in the worst case, particle losses. If we assume 2×10^{14} accelerated particles - a number achieved in the CERN synchrotrons - the final energy at 50 Hz repetition rate must be 3.12 GeV. For a Laslett tune shift of 0.2 we get with 2×10^{14} protons an injection energy of 430 MeV. Using these data we have looked into the possible FFAG options, which we will describe in the following.

3.1 The 3.2 GeV FFAG

The relativistic γ at 3.2 GeV is about 4.4, consequently we want the field index k to be not

Inj. Energy	430 MeV	Q_x	5.75
Max. Radius	45 m	Q_y	2.75
Radial Width	2.8 m	Max. RF-Frequency	1.03 MHz
Field Index	21	Frequency Swing	25 %
Nr. of Sectors	20	Min. Orbit Period	968 ns
Max. B_+-Field	4 T	Cavity Voltage	20 kV
Max. B_--Field	2 T	Min. Nr. of Cavities	10
Spiral Angle	17 °	Repetition Rate	50 Hz

Table 1. Parameters for a 3.2 GeV FFAG

smooth beam envelope), we will need about 20 sectors. The radius should be larger than 40 m in order to provide adequate space for the RF cavities, the injection and the extraction systems. The radial width of the magnets is determined by the field index, k, and the injection and extraction energies. The parameters of a version of a 3.2 GeV FFAG are shown in table 1. Further details of this machine have been given earlier[5] A closer look at a machine with these parameters convinced us, that it would be to much of a challenge to try to build this accelerator. The magnets with a 2.8 m radial extent of the usefull field were calculated and the required field seemed to be achievable. However a rough estimate of the magnet cost resulted in a price of about 10 million DM. Also the amount of ferrite needed for the 10 cavities came to over 24 m^3. Calculations of the dynamical aperture of this machine also indicated a rather large reduction in the aperture as soon as we introduced sizeable vertical oscillations. We attributed this to the rather strong nonlinearities due to the large field index and the spiral angle. Therefore we looked into another option, namely a FFAG with a maximum energy of 1.6 GeV.

3.2 The 1.6 GeV FFAG

The reduction of the maximum energy to 1.6 GeV at the same injection energy of 430 MeV and the same repetition rate results in a beam power of 2.5 MW. We therefore considered to design the FFAG for a repetition rate of 100 Hz, with the possibility to start with 50 Hz at 2.5 MW and then try to investigate the option of beam stacking at an intermediate energy. With a two to one stacking we could then again deliver 5 MW at 50 Hz, provided the losses in the stacking process can be kept small and under control. The following table shows the parameters of the 1.6 GeV FFAG. Further information on this option has been presented elsewhere[6]

Inj. Energy	430 MeV	Q_x	4.26
Max. Radius	26 m	Q_y	3.26
Radial Width	1.8 m	Max. RF-Frequency	1.72 MHz
Field Index k	11.8	Frequency Swing	19 %
Nr. of Sectors	16	Min. Orbit Period	586 ns
Max. B_+-Field	4 T	Cavity Voltage	20 kV
Max. B_--Field	2 T	Min. Nr. of Cavities	10
Spiral Angle	0 °	Repetition Rate	100/50 Hz

Table 2. Parameters for a 1.6 GeV FFAG

Another option could be not to try to gain the total energy in one ring, but rather to use two rings instead. By operating the first ring on the first harmonic of the RF frequency and the second ring then on the second harmonic, one again could get a two to one reduction of the repetition rate. The extraction energy of the first and thus the injection energy of the second ring would need to be optimised, for either a phased construction or the cost. This aproach is considered by the Argonne people. The parameters for the 1.6 GeV FFAG appear quite acceptable, as far as building such a machine is concerned. With the considerably lower field index k and the absence of any spiral angle the dynamic aperture is not as sensitive to vertical oscillations and reasonably large.

4. Conclusions

The next steps we need to take are to settle on the best option for a 5 MW source, and then to investigate in detail all the questions which have not been addressed so far. We have convinced ourselves, that the construction of all the hardware is possible, with all the required properties given by the parameters shown. The magnets with the required fields are possible (see Fig. 1), the RF-systems with the necessary frequency swing can be built (see Fig. 2) and it is possible to inject the beam into and extract it from the accelerators. However none of the details has been worked out yet. An optimised injection scheme can only be calculated, when the ring parameters are settled, and the same is true for the extraction scheme. It might be necessary to even deviate from the circular shape of the FFAG and include dispersion-free long straight sections, as described earlier[7]. This might be quite helpful for the design of an optimised injection system.

Clearly there are a host of details which need to be looked at, and it appears to us it would be an act of negligeance if one would not study these questions and then decide for or against the FFAG after a reasonable basis for this decision has been found.

5. Acknowledgements

We greatly appreciate the many helpful discussions and suggestions and want to thank our colleagues G. Hinderer, U. Trinks (TU Munich), H. Klein, A. Schempp (Univ. Frankfurt), G. Bauer (PSI), H. Conrad, G. Müller, U. Sieling (KFA Jülich), H. Henke (TU Berlin), W. Pelzer (HMI Berlin),I.S.K. Gardner, M. Harold, C.W. Planner, G.H. Rees (RAL), V. Vaccaro (Univ. Naples), A. Susini (CERN), V. Dimitriewski (Dubna), U. Senichev (Troizk), J. Botman (TU Eindhoven), Y. Cho, B. Kustom, F. Mills (ANL), and K. Erdman (UBC).

6. References

1. F.T. Cole, R.O. Haxby, L.W. Jones, C.H. Pruett and K.M. Terwilliger, Electron Model Fixed Field Alternating Gradient Accelerator, Rev.Sci.Instr.28, Nr.6, 403,1957
2. A.A. Kolomensky and A.N. Lebedev, Theory of Cyclic Accelerators, Translated from Russian by M. Barbier (CERN), North Holland Publishing Company , Amsterdam, 1966
3. A. Faltens, Induction Linacs for Neutron Generation, Proc. of the Workshop on Accelerators for Future Spallation Neutron Sources, Los Alamos Report LA-UR-93-1356, Vol. IIB, 1284, Feb. 1993
4. Private communication, Eliane Lessner, Argonne National Laboratory, Feb 1993
5. S.A. Martin, P.F. Meads Jr., G. Wüstefeld, E. Zaplatin and K. Ziegler, Study of an FFAG Synchrocyclotron for a Pulsed Neutron Source, Proc. 13th Int Conf. on Cycl. and their App., World Scientific, Singapore, p. 701, 1993
6. S.A. Martin, P.F. Meads, G. Wüstefeld, E. Zaplatin and K. Ziegler, Study of FFAG Options for a European Pulsed Neutron Source (ESS), Proc. of XIII National Particle Accelerator Conference, Dubna, Oct 13-15, 1992, to be published
7. P.F. Meads, A Dispersion-Free Long Straight Section For a Fixed-Field Alternating Gradient Synchrotron, IEEE Vol. NS-30, No.4, p.2448, 1983

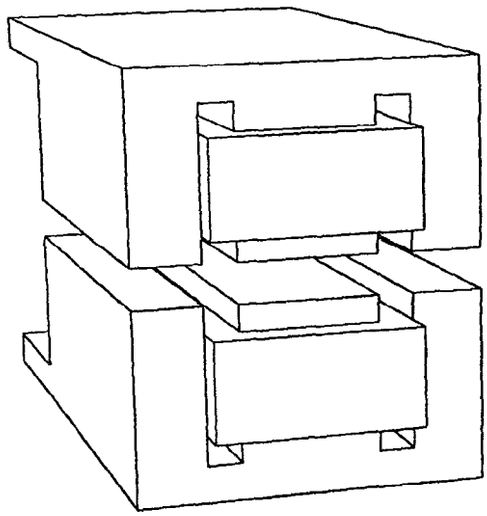

Fig. 1 FFAG magnet scheme with 4 T peak field and reverse "gulley" fields to -2 T.

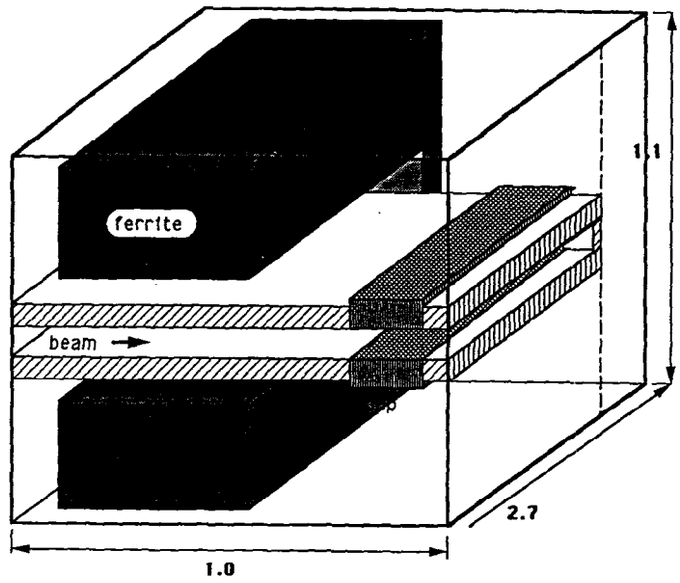

Fig. 2 Geometry of a possible FFAG cavity.

A 2-stage, 5-MW FFAG

R. Kustom
Argonne National Laboratory
9700 S. Cass Avenue
Argonne, IL 60439

The submitted manuscript has been authored by a contractor of the U. S. Government under contract No. W-31-109-ENG-38. Accordingly, the U. S. Government retains a nonexclusive, royalty-free license to publish or reproduce the published form of this contribution, or allow others to do so, for U. S. Government purposes.

Abstract

The Fixed-Field Alternating Gradient (FFAG) accelerator has DC-excited magnets whose field strength varies with radius as $B_o(R/R_o)^k$, where B_o is the injection field, R_o is the injection radius, and k is a constant which is called the field index.

Typically, injection energy into an FFAG is between 250 and 400 MeV and extraction energy is between 1100 and 2200 MeV. Because of the DC-excited magnetic fields, the FFAG can be operated with repetition rates as high as 250 to 400 Hz. The optimum repetition rate for neutron-scattering users is usually lower, 30-100 Hz. Techniques such as internal stacking, an external stacking ring, or staged FFAGs for lowering the extraction rate will be discussed. A 2-stage design will be described which uses a 100 Hz, 250 to 800 MeV machine and a 50 Hz, 800 MeV to 2000 MeV machines. With additional installed RF, the machine could be designed to operate at even higher repetition rates to deliver multi-megawatt beams to more than one target facility.

I. Introduction

Conceptual designs for a 5-Megawatt FFAG accelerator have considered using relatively low energy (250-350 MeV) linac injectors at a high repetition rate (250 Hz) with internal stacking at an intermediate energy[1] or an external isochronous storage ring to store several bunches[2] in order to lower the repetition rate on the target. Another option is suggested here. The proposal is to use two FFAG accelerators; the first operates at a 100-Hz repetition rate at the first RF harmonic and the second FFAG operates at a 50-Hz repetition rate on the second RF harmonic. With this configuration, two one-bunch extractions from the first FFAG are injected into two waiting buckets in the second FFAG.

The concept which is outlined in this paper is not represented as a design since one has not been done. What is presented is the basis on which the design would be pursued using components that have been designed for previous machines.

II. 2-stage FFAG Parameters

The proposed facility layout is shown in Figure 1. Injection into the first FFAG would be at 400 MeV with a 100-Hz repetition rate. The first, or low energy, FFAG would accelerate the beam to 800 MeV at a 100-Hz repetition rate. The injection radius would be about 12.0 meters and the extraction radius would be about 12.7 meters. There would be 16 sector magnets each of which would provide the field strength along the particle orbit shown in Figure 2[3]. The variation of magnetic field with radius would be

$$B = B_o \left(\frac{R}{R_o}\right)^k$$

where R_0 is the injection radius, B_0 is the magnetic field at injection, and k is a constant known as the field index. The value of k for the first machine would be between 12 and 13. The betatron tunes would be 3.25 in the horizontal plane and 2.75 in the vertical plane. The inside height of the vacuum chamber at the injection radius would be about 20 centimetres. The injected charge would be 1.58×10^{14} protons per acceleration cycle. This would result in a betatron tune depression of 0.17 assuming a bunch factor of 0.375 and a form factor of 1.35, which corresponds to reasonably uniform painting in the horizontal plane and parabolic in the vertical plane.

The RF frequency would swing from 2.835 MHz at injection to 3.16 MHz at extraction. The peak voltage required would be 40 kilovolts which allows operation at a 30° phase stable angle.

The second stage FFAG would take the beam from 800 MeV to 2 GeV. The first bunch from the low energy FFAG would either be 1) injected into one of the two RF buckets in the second stage FFAG and held in a stationary orbit until the second bunch from the low energy FFAG is injected into the other RF bucket, or 2) accelerated very slowly to keep the particles in the bucket until the second bunch is injected. Then, the two bunches would be accelerated in about 10 milliseconds to 2 GeV and both extracted in one turn into the spallation target.

The injection radius for the proposed second stage would be about 36 meters and the extraction radius about 37.3 m. The number of sectors would be between 24 and 26, the field index, k, about 18, the horizontal tune would be 5.25, and the vertical tune 4.25.

The RF frequency at injection would be 2.16 MHz and at extraction would be 2.43 MHz. The peak RF voltage would be 280 kilovolts, which would allow for operation at a phase stable angle of 30°.

Table 1 lists the parameters for the two FFAG stages.

III. Magnet Design

The design of the magnets for the 2-stage FFAG accelerators would be similar to the magnet designed for a 1500-MeV FFAG[2]. Figure 3 shows the field variation that must be matched in the 1500-MeV FFAG at the extraction orbit. The peak field in the focusing section would be 4.1 T and peak fields in the defocusing section would be 1.9 T. A 6-coil core configuration that provides correct field pattern is shown in Figure 4. Figure 5 shows the required, or target, field over the radius at the plane of symmetry along with that achieved with the 6-coil configuration. Figure 6 shows the target and achieved azimuthal fields at the extraction radius for the same coil configuration. The coil sizes and required excitation currents are listed in Table 2.

Coil 1 in Table 2 corresponds to the large coil that is furthest above (and below) the vacuum chamber. These are the upper and lower coils shown in the upper view of Figure 4. The coordinate x is the radial direction in the FFAG and z is the plane perpendicular to the orbital plane. The coordinate Y is the distance along the beam orbit measured from the median plane of the magnet. The reverse field coils (coil 2) are closer to the vacuum chamber in the top view and straddle coil 1 (the heavy black coil) in the bottom view of Figure 4. A long thin coil (coil 4) is located inside coil 1 and is shown as the smaller rectangle inside coil 1 in the bottom view of Figure 4. Finally, two smaller coils

are shown in the upper view (coil 3) at the extraction side of the coils. They are located on each side of the median plane of the coil.

The conductor for the coil would use high purity aluminium (HPAL) stabilizer with NbTi strands as shown in Figure 7. The conductor would be embedded in a high-strength alloy aluminium (HSAL) as shown in Figure 8.

It is proposed that the vacuum jacket and heat shields also be made out of aluminium to minimize the possibility of generating long-life residual radioactivity.

Normal-conducting, aluminium pole-face windings would be placed between the beam vacuum chamber and outer cryostat wall of the sector magnets to fine tune the magnetic field and the beam as a function of radial position in the FFAG.

IV. RF System

The cavities for the FFAG would be a picture frame design using ferrite blocks in a construction technique similar to the RF cavities of the old weak-focusing synchrotrons[4]. The cavities for the second stage FFAG would be about 50% larger than the cavities for the weak-focusing synchrotrons, but basically would not pose any real construction problems. The beam loading, however, requires the use of cathode-follower amplifiers to avoid distortion of the RF bucket. This type of amplifier maintains a low output impedance, 20 to 80 ohms, over a large frequency range[5]. Also, the power tubes must be able to provide sufficient output current to match the peak circulating current of the beam and to be able to supply the peak RF voltage on the cavity. These conditions result in an average power per tube that is only 25 to 50% the cw power rating of the tube.

Typically, twenty cavities with a physical length of 1.25 meters each would be used. Each cavity would generate 14 kV with 0.012 T peak RF field in the ferrite. The active length of ferrite would be about 0.8 m, in the direction of the beam.

References

1. T. K. Khoe and R. L. Kustom, "ASPUN Design for an Argonne Super Intense Pulsed Neutron Source," IEEE Trans. on Nuclear Science, NS-30, No. 4, 1983.

2. R. L. Kustom, "The ASPUN Project," Advanced Neutron Sources 1988, Institute of Physics Conference Series Number 97, Institute of Physics, Bristol and New York, 1989.

3. P. F. Meads, Jr. and G. Wustefeld, "An FFAG Compressor and Accelerator Ring Studied for the German Spallation Neutron Source," IEEE Trans. on Nuclear Science, NS-32, No. 5, 1985.

4. L. A. Klausner, et al., "Zero Gradient Synchrotron RF System," IEEE Trans. on Nuclear Science, Vol NS-12, No. 3, 1965.

5. Thomas W. Hardek and William E. Chyna, "Common Anode Amplifier Development," IEEE Trans. on Nuclear Science, Vol NS-26, No. 3, 1979.

Table 1

Parameters for 2-Stage FFAG

800-MeV FFAG

Number of Sectors	16
Injection Radius, m	12.0
Extraction Radius, m	12.7
Magnetic Field Index, k	12 to 13
Radial Tune, ν_x	3.25
Verticle Tune ν_y	2.75
Harmonic Number	1
RF Frequency @ Injection, MHz	2.835
RF Frequency @ Extraction, MHz	3.16
RF Voltage, kV, ϕ_s=30°	40
τ Bunch at Extraction, nsec	158
Q_{inj}	1.58×10^{14}

2000-MeV FFAG

Number of Sectors	24 to 26
Injection Radius, m	36
Extraction Radius, m	37.3
Magnetic Field Index, k	18
Radial Tune, ν_x	5.25
Verticle Tune, ν_y	4.25
Harmonic Number	2
RF Frequency @ Injection, MHz	2.16
RF Frequency @ Extraction, MHz	2.43
RF Voltage, kV, ϕ_s=30°	280
Q_{ext}	3.16×10^{14}

Table 2

SIX-COIL CONFIGURATION - Dimensions and coil currents

COIL COORDINATES

Coil #	X	Y	Z	X	Y	Z	W/H
1	25.800	.360	1.100	28.800	.402	.500	.400
	28.800	.000	.400	25.800	.000	1.000	.250
2	25.800	.540	.450	28.800	.603	.250	.300
	28.800	.855	.250	25.800	.766	.450	.150
3	27.800	.243	.250	28.800	.251	.250	.080
	28.800	.503	.250	27.800	.485	.250	.100
4	26.000	.113	.250	28.400	.124	.250	.040
	28.400	.000	.250	26.000	.000	.250	.100

COIL CURRENTS (AMPERE-TURNS)

Coil#	Current	J (kA/cm^2)*
1	6.449E+06	6.45
2	2.372E+06	-5.27
3	-4.242E+05	5.30
4	-2.462E+05	-6.16

* Positive current denotes a force directed towards the center of the FFAG

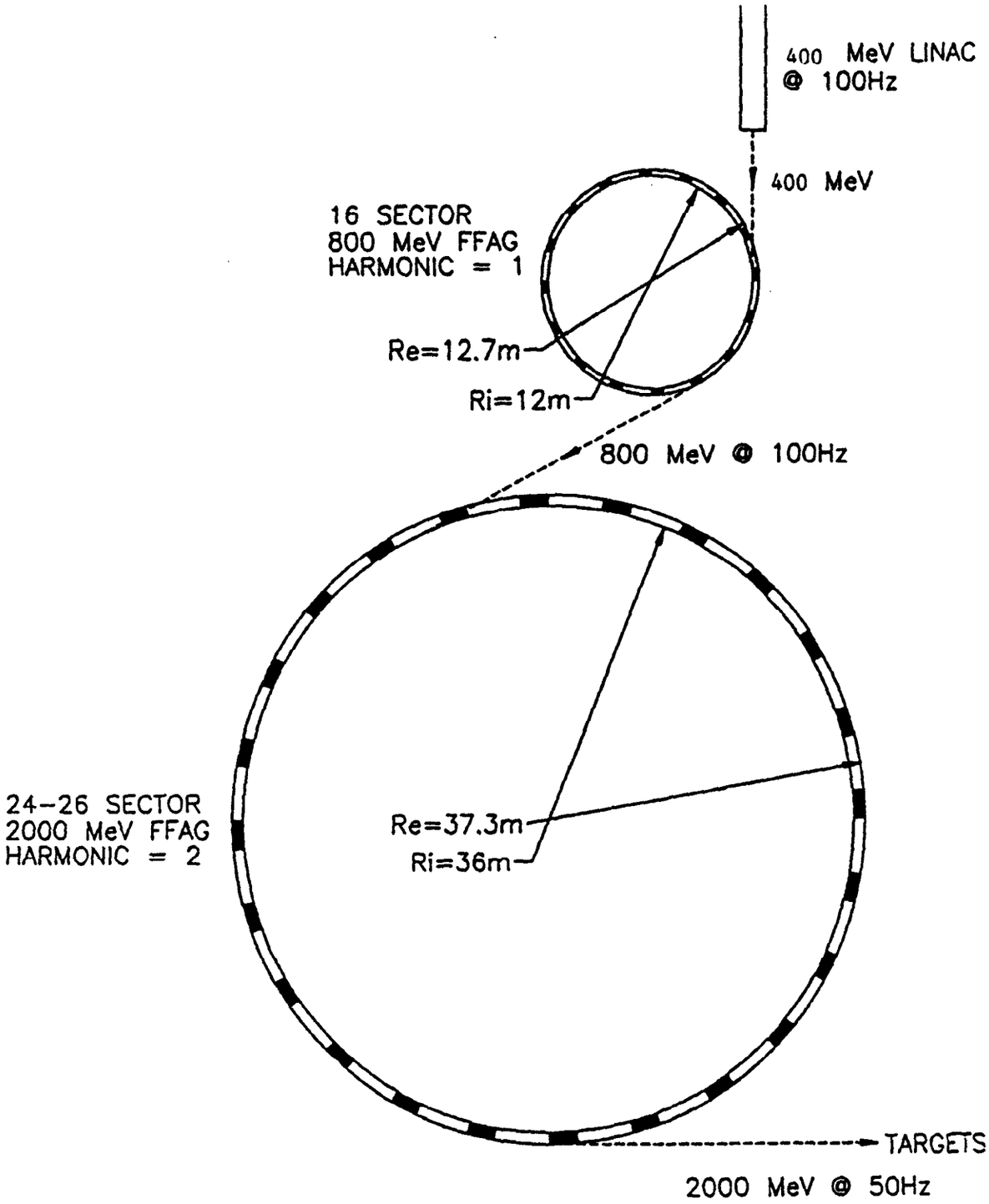

Figure 1 - Layout of 2-stage 5 MW FFAG

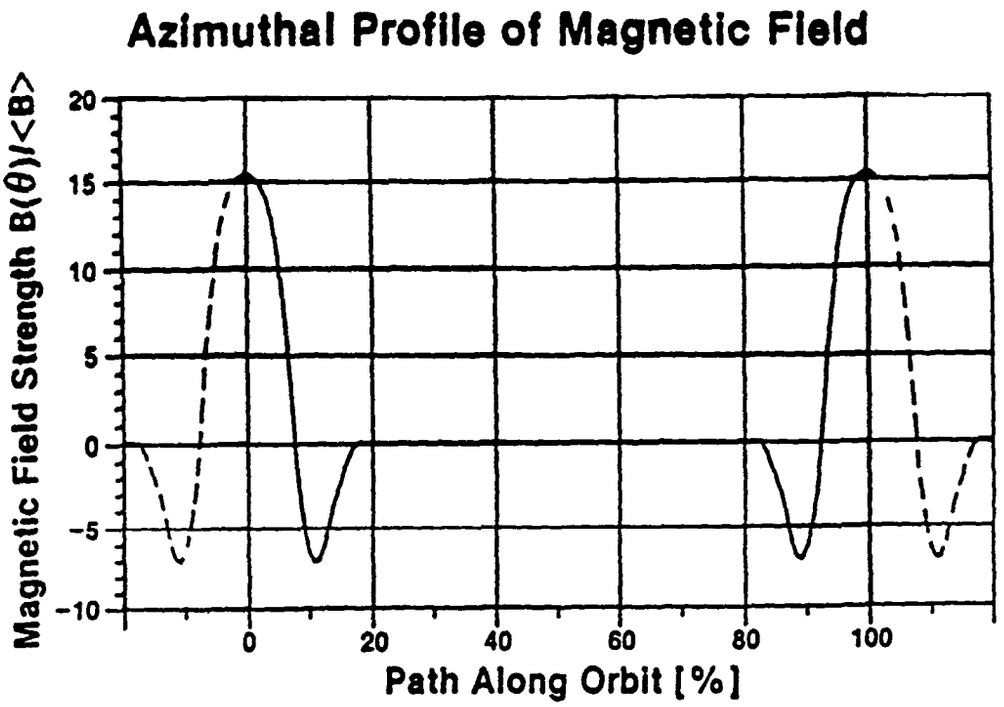

Figure 2 - Magnetic Field Strength along particle orbit through one sector of FFAG

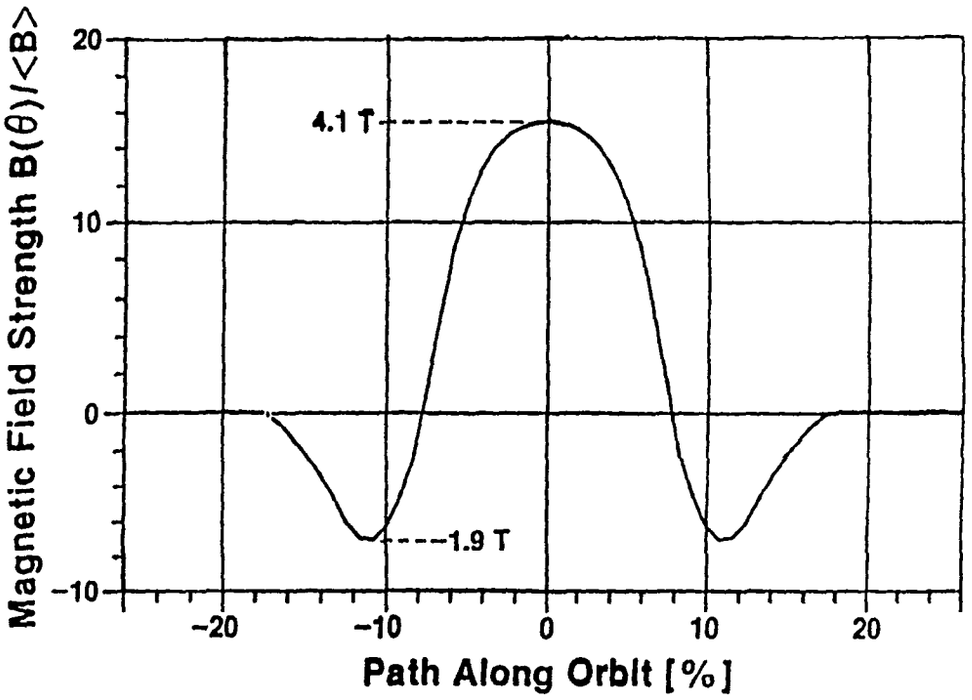

Figure 3 Azimuthal profile of magnetic field along the path of one cell

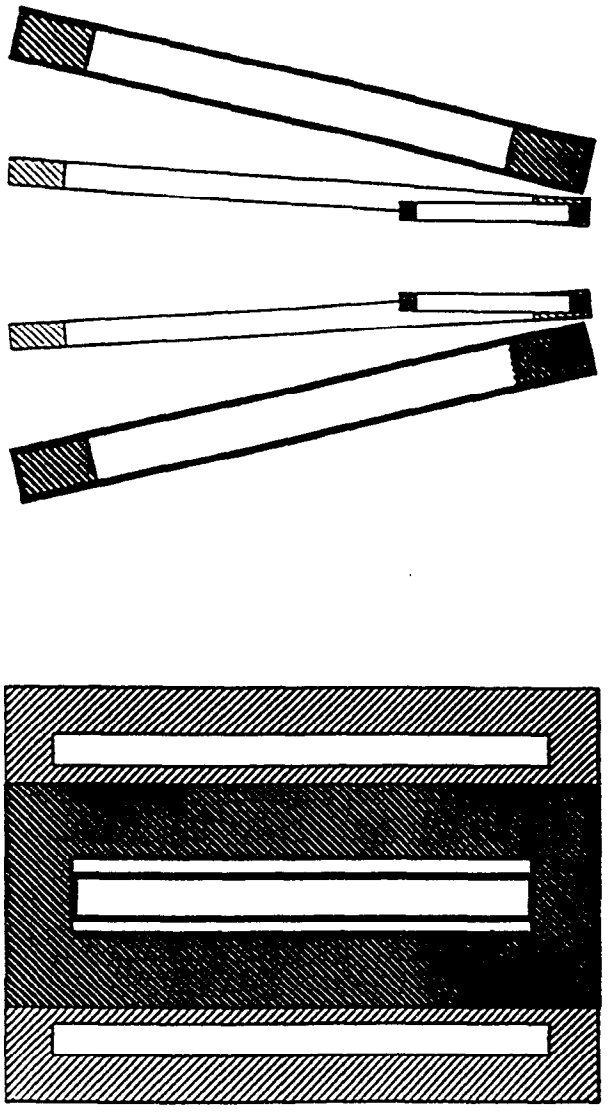

Figure 4

6 COIL–CONFIGURATION for a 1500-MeV FFAG - top view is looking in the direction of the beam and bottom view is looking down on the beam. The left side is the injection radius and the right side is the extraction radius.

Figure 5 FIELD AT PLANE OF SYMMETRY FOR THE 6-COIL DESIGN

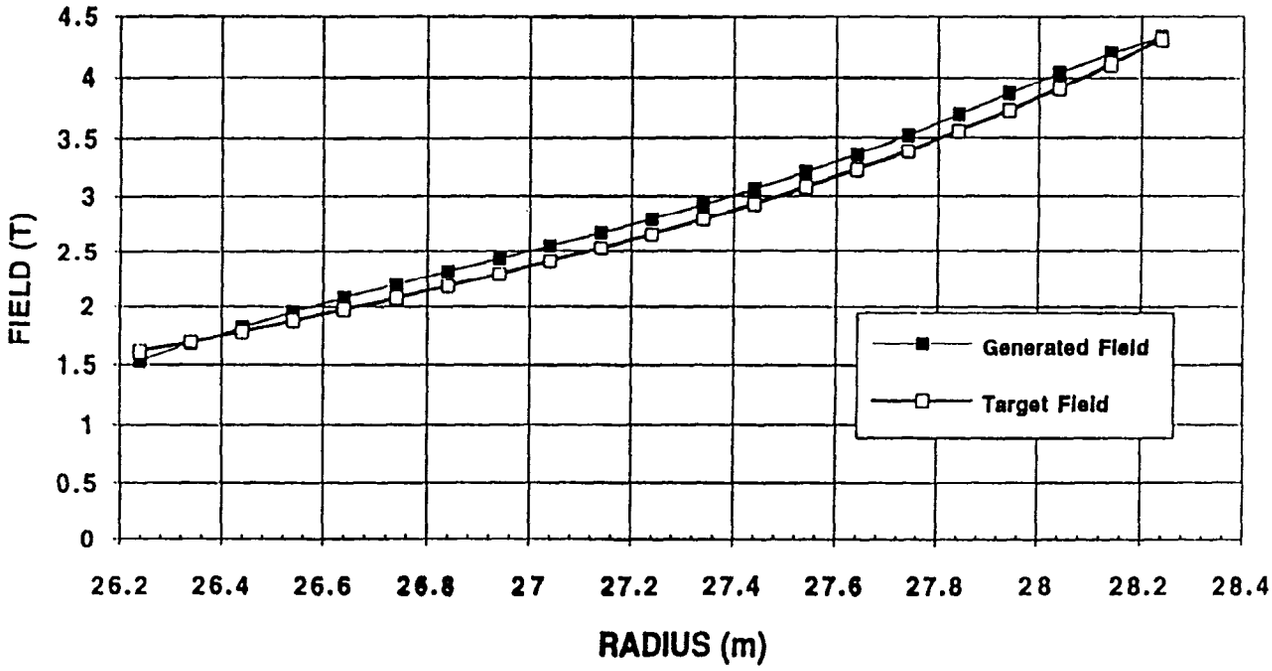

Figure 6 FIELD AT OUTER RADIUS FOR THE 6-COIL DESIGN

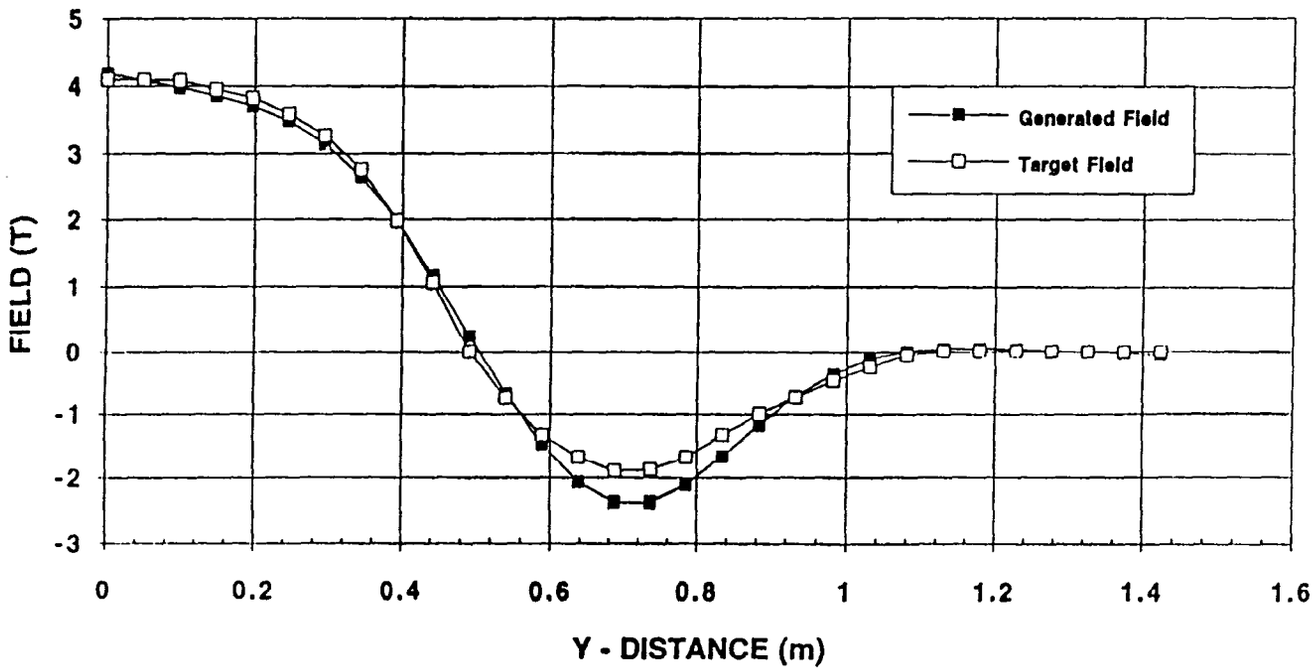

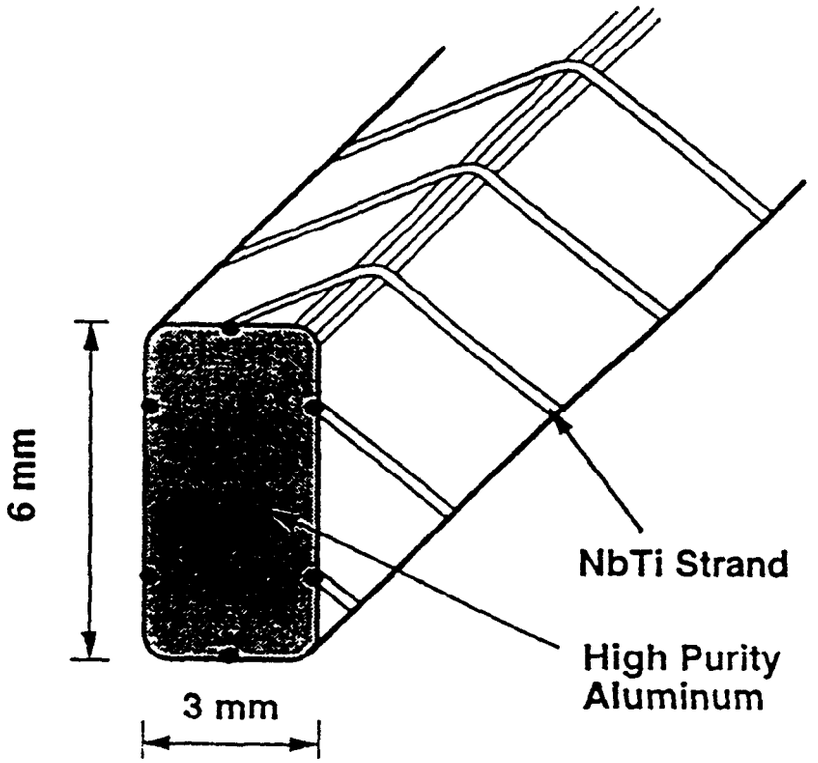

Figure 7 5 KA HPAL Stabilized Conductor

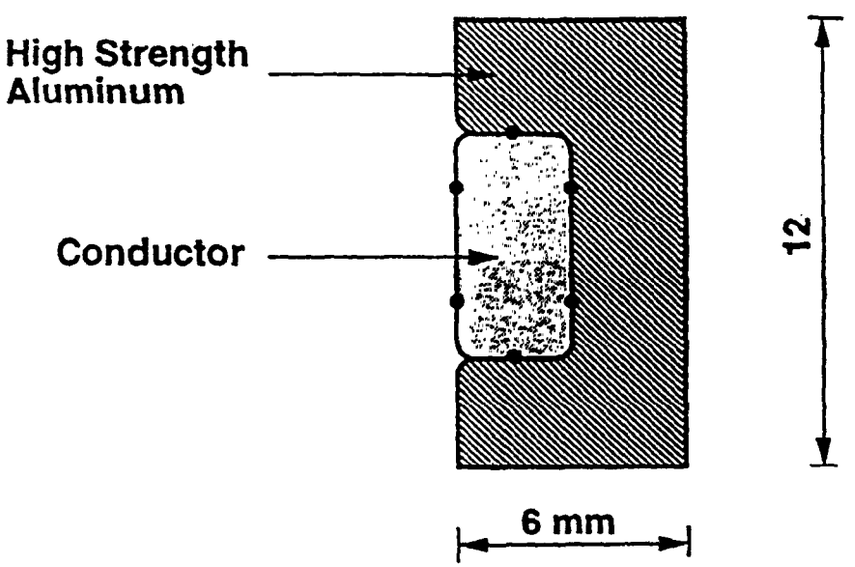

Figure 8 CONDUCTOR EMBEDDED IN HSAL STRUCTURE

Compressor Ring Studies for a 5 MW Spallation Neutron Source

G H Rees, Rutherford Appleton Laboratory, U.K.

Abstract

An outline design has been made of Compressor rings for a 5 MW spallation neutron source. Aspects of the design are discussed: magnet lattice, H^- injection, radiofrequency containment, extraction, beam loss collection, beam instability considerations and linac current levels.

1. Introduction

Three options have been considered for compressor rings fed from H^- linacs: 3 rings at 0.8 GeV and 1.7 MW each, 2 rings at 1.2 GeV and 2.5 MW each, or 1 ring at 2.4 GeV and 5 MW. The 3 or 2 ring option is favoured for the following reasons:

a. Cost.
b. Reliability (lose a ring and operation is still possible at $^2/_3$ or ½ intensity).
c. There is a longer linac to maintain for 2.4 GeV.
d. Debunching of the linac microbunches is slower at 2.4 GeV.
e. Momentum ramping for the linac is more difficult at 2.4 GeV.
f. The beam lines to the rings and target are more expensive at 2.4 GeV.
g. Beam loss collimation and collection is more difficult at 2.4 GeV.
h. More shielding is required for higher energy.
j. All rings have the same number of particles and, at the lower energies, more loss per ring is allowed due to the lower ring beam powers.
k. The ring has to be larger for 2.4 GeV, and since a linear lattice is preferred, there is a larger Q, and a larger chromatic Q spread.
l. Extraction is more difficult at 2.4 GeV as the ring aperture may not be reduced much with energy without increasing the transverse impedance.
m. H^- injection is more difficult at 2.4 GeV; there is a longer injection region, tighter tolerances, greater radiation damage to the foil, and more uncertainty about the metastable H° excited states.
n. The only target experience is at 0.8 GeV or less.

Against all these advantages for the lower energy rings must be weighed the difficulties associated with longer linac duty cycles, caused by the constraint of a given linac peak current. The effect of relaxing this constraint is discussed in the final section of the paper. Elsewhere, other ring features are described but with the 0.8 GeV case only considered.

2. Magnet Lattice

A lattice of 3 superperiods is chosen, as shown in Figure 2. There are separate regions of high dispersion for H^- injection and momentum collimation, and separate regions of zero dispersion for betatron collimation, extraction and radiofrequency systems. Each superperiod has 5 triplet cells, arranged with mirror symmetry about

FIG. 1

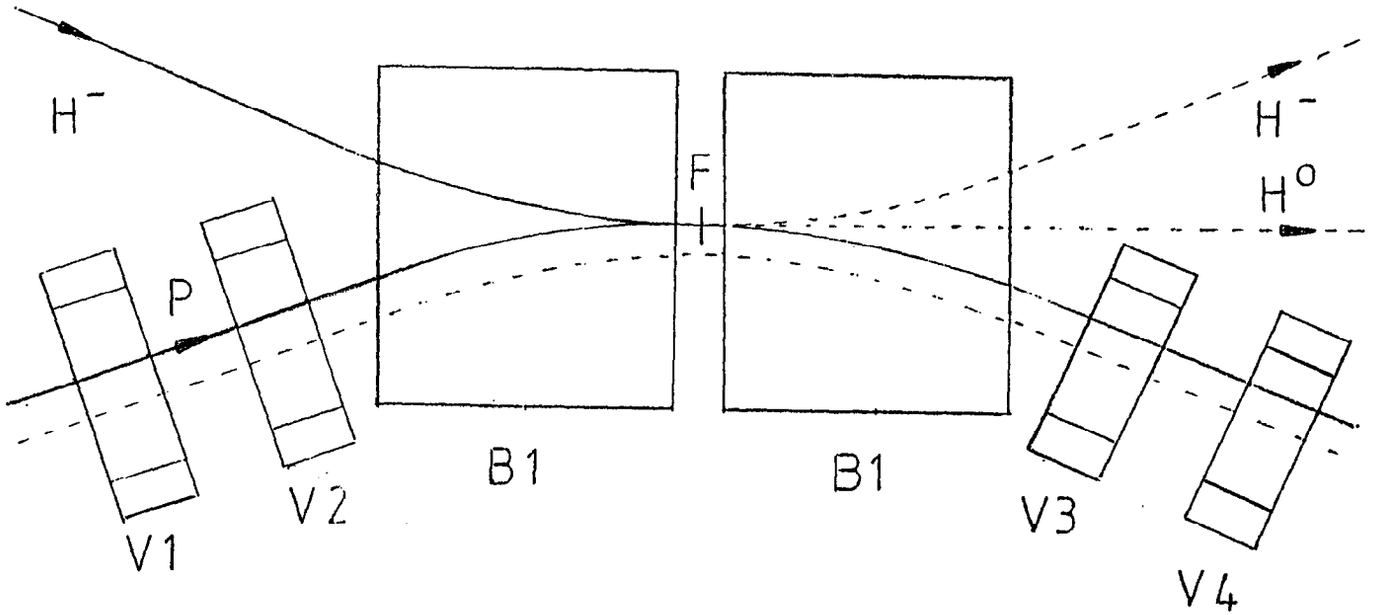

OPTIMISED H⁻ INJECTION

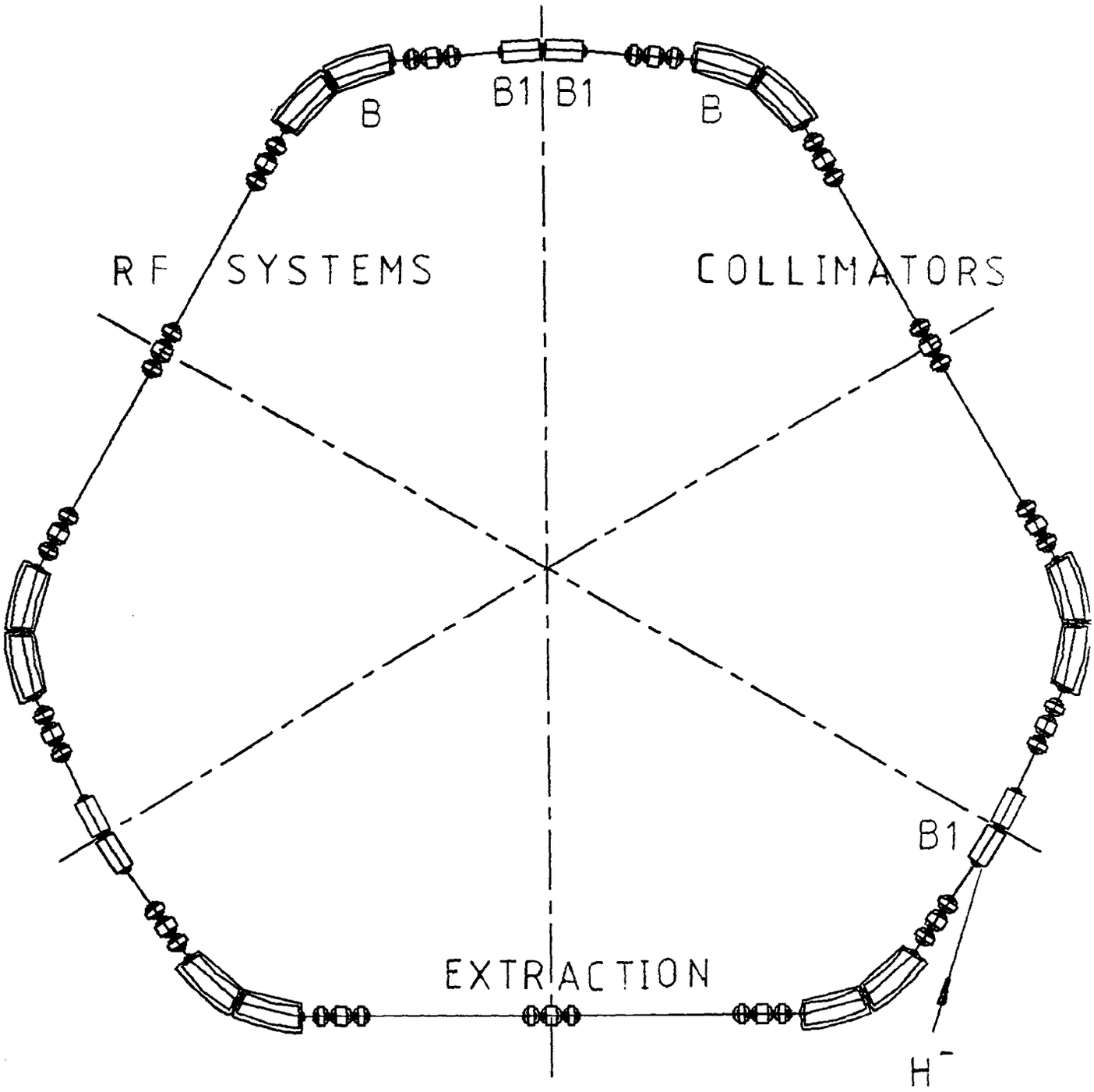

FIG. 2 LATTICE

the point where the parameters for the injection stripping foil are specified. Thus, only 3 of the 5 triplets are independent, and the 6 independent quadrupole gradients are adjusted to give $Q_x = 3.7$, $Q_y = 4.24$, β_y(peak) = 22.0 m, D_x(long straight) = 0, $\mu_x = \mu_y \geq 170°$ (long straight) and $D_x/\sqrt{\beta_x} = 2.7$ m $^{1/2}$ (foil). The last condition is required for optimised H^- injection, and the last but one for optimised beam loss collection. Rectangular bending magnets are used, of a relatively short length, and these contribute some vertical edge focusing. There are main bending magnets, B, and subsidiary units, B_1; the latter allow direct merging of the incoming H^- beam with the circulating protons. The operating point in the Q-diagram is located carefully with respect to fourth order betatron resonances excited by space charge; in this respect, the lattice is superior to one of superperiodicity 2. Lattice functions are shown in Figure 3.

3. H^- Injection

The H^- charge exchange system is the most critical item for the successful operation of the rings. The scheme proposed is shown in Figure 1, and occupies a region of approximately 9.1 m. There is a central stripping foil, the B1 lattice dipoles, and 4 identical dipoles to create a symmetrical vertical orbit bump. Use is made of a foil with 2 free, unsupported edges, and there is simultaneous 'painting' in the longitudinal and both transverse planes. Vertical painting is obtained by programming the vertical bump magnet system, and the horizontal and longitudinal painting by a ramping of the momentum of the input H^- beam. For the longitudinal painting, there is, in addition, a programming of the amplitudes of the radiofrequency containing fields. Optimised injection [1] is achieved by the use of the special foil, and by appropriate choices of the dispersion and betatron parameters in the injection region, together with mismatching for the injected beam. The proposed parameters reduce the average number of proton foil traversals during a 1000 turn injection interval to ~ 5. Beam loss in the rings is further minimised by chopping the H^- beam in the linac, with a duty cycle of ~ 60%, at the ring revolution frequency. A foil thickness of 275 μgm cm^{-2} is proposed, which strips ~ 98% of the 800 MeV H^- particles to protons, leaving most of the remainder as partially stripped H^o particles, in a range of quantum states. The fate of these H^o particles depends on their quantum state and the local value of the magnetic field (1.25 to 2.5 kG); the particles of low principal quantum number ($n < 5$) remain unstripped and pass out of the ring for external collection; the particles of $n \geq 7$ strip almost immediately in the magnetic fields at the foil, and are accepted as protons; there remain some $n = 5$ and 6 states, which strip after some delay, and so may be accepted, or lost, or pass into the beam halo. The choices of the field levels at the foil and B1 units are therefore very important. They are provisionally selected at 1.25 and 2.5 kG, respectively, which allows the foil stripped electrons to be intercepted in an adjacent collector, before they recirculate through the foil. An alternative arrangement is to replace the two, 2.5 kG, B_1 magnets by a long common unit with a uniform field of 1.25 kG, which is the optimum field level with respect to the $n = 5$ and 6 quantum state lifetimes. The foil is then at the centre position of this 1.25 kG magnet.

FIG. 3

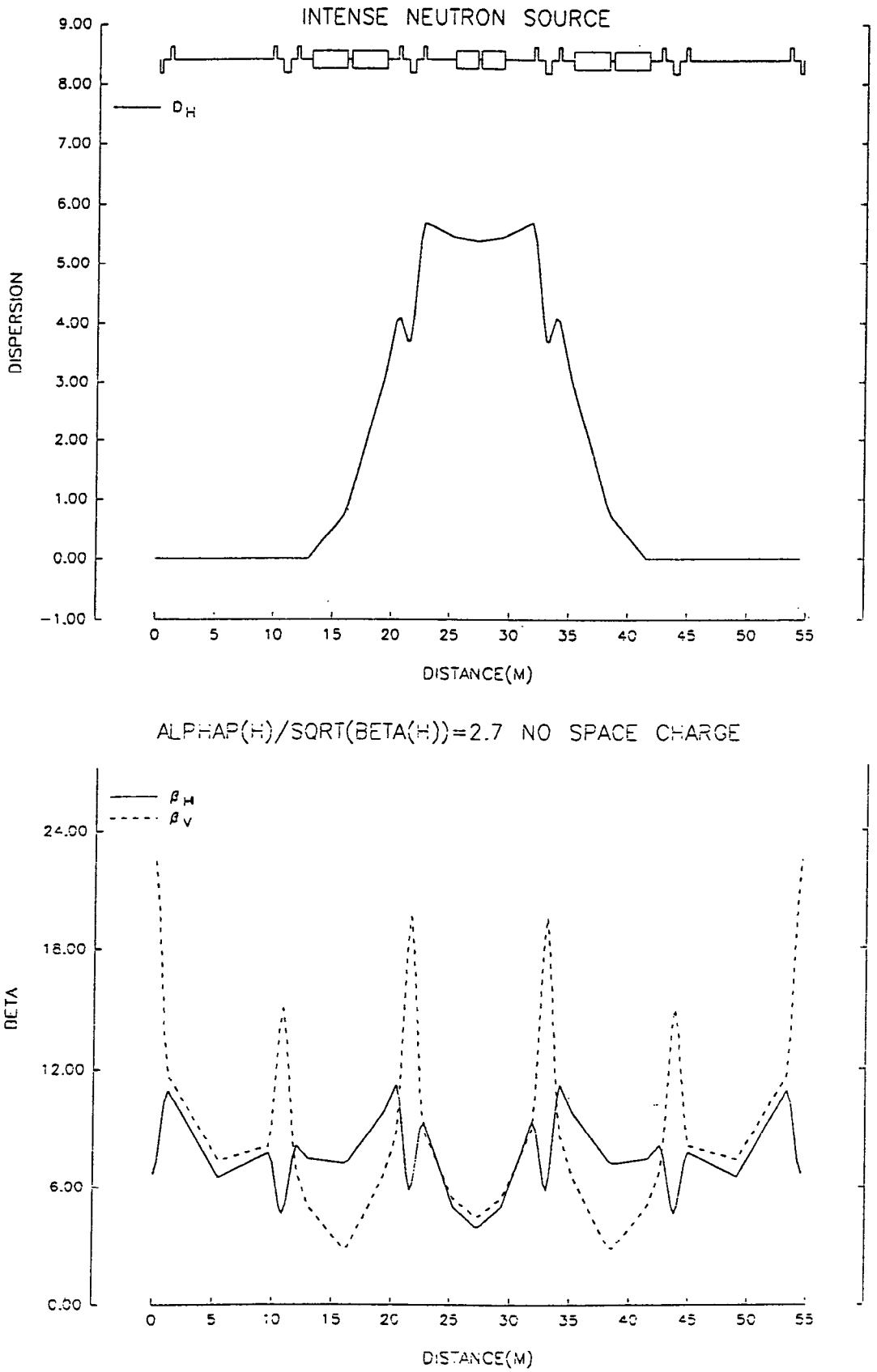
INTENSE NEUTRON SOURCE
DISPERSION
D_H
9.00
8.00
7.00
6.00
5.00
4.00
3.00
2.00
1.00
0.00
-1.00
0 5 10 15 20 25 30 35 40 45 50 55
DISTANCE(M)
ALPHAP(H)/SQRT(BETA(H))=2.7 NO SPACE CHARGE
BETA
β_H
β_V
24.00
18.00
12.00
6.00
0.00
0 5 10 15 20 25 30 35 40 45 50 55
DISTANCE(M)

4. Radiofrequency Containment

The basic requirements for radiofrequency (rf) containment are set by the level of the longitudinal space charge forces in the rings. These forces may be reduced by ensuring that the stored beam has a reasonably uniform transverse density distribution, and by profiling the vacuum chamber envelope to follow a shape which is a fixed ratio to that of the adjacent beam envelope. The ratio cannot be too small or it will prevent the efficient action of a beam loss collection system; the ratio chosen is $4/\sqrt{5}$, leading to a longitudinal space charge parameter, g, of ~ 1.75. A low value of g is advantageous for it reduces the requirements for both the amplitude of the rf containing field and the amount of momentum ramping for the injected beam. The waveform of the rf containing field is non-sinusoidal, either rectangular for a barrier bucket, or that of a dual harmonic, h = 1 and h = 2 system. Assuming a phase extent of $\pm 0.691\ \pi$ in the rings, and longitudinal elliptical 2 - D density distributions, the required voltage amplitude/turn for these waveforms are ± 51.4 kV for the former, and ± 29.5 and ± 17.7 kV for the latter. The related fractional peak beam momentum spread is ± 5.5 10^{-3}. The barrier bucket waveform may be generated approximately on an induction linac type cavity, or on a number (~ 5) of separate, harmonically related, resonant cavities. The latter is an extension of the arrangement proposed for the dual harmonic rf system. Initial ideas assume single, not twin, gapped cavities for reduced beam loading, and with ferrite and capacitive loading. A gap capacity of ~ 3500 pF leads to an R/Q value of ~ 30 Ω for the h = 1 system, and ceramic vacuum capacitors are available for gap voltages of ~ 15 kV. It may be sufficient to operate the cavities at a fixed tuning, at approximately half the detuning required for full reactive beam loading compensation. Alternatively, it may be possible to find a ferrite that is approximately optimally detuned by the proposed level of beam current. Control for the beam loading will also involve beam feed-forward or rf feedback systems.

5. Extraction

A fast extraction system is required, with beam loss less than 1 part in 10^4. This figure is achieved on the ISIS synchrotron, and a similar extraction system is proposed for the compressor rings. There are 3, push-pull, lumped kickers, with a total kicker rise time of ~ 180 ns, provided by 6 pulse generators per ring, at impedance, voltage and current levels of 8.33 Ω, 42 kV and 5000 A, respectively. A longitudinal ground plane threads each kicker, which is back terminated at the source, so that pulse forming networks are at an impedance level of 8.33/2 Ω. Induced volts for a centred beam in the kicker are estimated at < 5 V. More straight section space is available than in ISIS, so the extraction septum magnet design is simplified. An additional difference from ISIS is that there is no slow orbit bump, which has proved a complication for ISIS operation.

6. Beam Loss Collection

Activation and radiation damage of ring components may be reduced by localising the beam loss in betatron and momentum collectors. Such a system has proved very effective on the ISIS synchrotron, in particular the momentum collectors for untrapped 70 - 85 MeV protons. Collimation in the Compressor rings is more difficult because the beam energy is $\geq$ 800 MeV, and because growth in beam size is expected to be due more to transverse betatron than longitudinal synchrotron motion. Again, however, the use of collimators and collectors is proposed. Optimum criteria for betatron collection in a dispersion free region may be derived from a normalised betatron phase space diagram. It may be shown that if a primary collimator is located at a normalised transverse position, Z, and secondary collectors at positions Z_1 and $- Z_1$, after betatron phase shifts, μ_1 and μ_2, respectively, then optimum values are $\mu_1 = \cos^{-1} (Z/Z_1)$ and $\mu_2 = \cos^{-1} (- Z/Z_1)$, with Z_1 a few percent larger than Z. For high collection efficiency, it is necessary for the dispersion free region to extend over a μ range > 160°, and for there to be equal values of μ_2 in the 2 transverse phase planes. It is also advantageous to angle the upper or lower half of the collimator and collectors to improve the interception efficiencies. The optimised H^- injection process correlates large synchrotron oscillations with small horizontal betatron motion, so momentum collimation may be unnecessary. However, for protection, momentum collimators will be installed at a position where $D_x/\sqrt{\beta_x}$ is a maximum. It is proposed to use graphite collectors, where possible, to reduce the activation levels, with lengths of ~ 1 m to stop 800 MeV protons. The first collector is immediately downstream of the collimator, with the surface, Z_1, set back progressively as the distance downstream increases, with a maximum end value for $Z_1 \sim 1.02$ Z. A material of higher atomic number than graphite is preferred for the collimator, to reduce the amount of beam outscattered from its front surface.

7. Beam Instability Considerations

Bunched beam instabilities, only, need be considered. The maximum stored beam, N, is 2.6 10^{14} protons per ring, which is a factor 6 larger than has been achieved on ISIS at 70 MeV, where there has been no sign of a bunched or unbunched electron-proton instability. The momentum spread of the ISIS beam at 70 MeV is $\pm$ 2 10^{-3}, a factor of ~ 3 smaller than that proposed for the 800 MeV compressor rings. At LANL, however, an e-p instability has been observed on the Proton Storage Ring, at intensities comparable to those of ISIS. The differences between ISIS and the PSR include for ISIS; smoother chamber transitions, larger transverse emittances, a somewhat larger circumference, and collection of the foil stripped electrons. All these safeguards are proposed for the Compressor. For bunched beam longitudinal stability, it is advantageous to profile the vacuum envelope to reduce the g parameter, and to improve the transverse distributions by the H^- painting process, as mentioned previously. Since the injection interval corresponds to ~ 1.5 synchrotron periods, it is considered unlikely that a coherent longitudinal or a coherent head-tail transverse mode has time to develop. The latter would have to be a very high order mode because it is planned to operate with the natural value of the ring chromaticities.

8. Linac Current Levels

The maximum injection duty cycle of each compressor ring is limited to ~ $3^1/_3$%, so if the rings for the 800 MeV option are fed sequentially, the total linac duty cycle is 10%. The average linac beam current during the pulse is then 62.5 mA and the peak value, due to the chopping at the ring revolution frequency, is 105 mA. A reference H^- linac may be defined for this current, using funneling at low energy to reduce the ion source requirements. Such a linac may be room temperature (RT) or superconducting (SC). The optimum ratio for the total rf power to the beam power, during the beam pulse, may be expressed as $1 + (R_b/R_c)$, where R_b and R_c are transit time corrected beam and cavity shunt resistances, respectively, with $R_b = V/(I_b \cos \phi_s)$ and $\phi_s \sim -25°$. For a SC linac, the total rf power to provide the beam pulse is thus ~ 5 MW, and for the proposed, 440 m, 700 MHz, RT linac ~ 10 MW. In addition, the klystrons, circulators and loads must introduce additional power during the on and off pulsing of the cavity fields. For the suggested SC linac, this power is considerable, as the parameters considered are cavity frequencies of 350 MHz and loaded cavity Q-values of 10^6, corresponding to cavity filling times of 1 ms, and total rise or fall times for the cavity fields of ~ 4 ms. The filling time is reduced by an order of magnitude by raising the frequency to 700 MHz and lowering the loaded Q to 2 10^5; even so, this is still an order of magnitude larger than for the RT linac. Finally, the effect of relaxing the peak current constraint for the RT linac may be considered, hence reducing R_b. In one scheme envisaged, the duty cycle of the chopping may be changed, and the linac current increased to ~ 200 mA, eg by adding a further stage of funneling and using special high duty cycle chopping at low energy, correlated with 3-way switching at high energy for repeated sequential filling of the 3 rings at a 60% duty cycle, every second turn. In this mode, the linac duty cycle is reduced to $3^1/_3$%. The proposed scheme is of interest because of the potential cost saving, but for it to be feasible, higher peak power klystrons have to be developed, and also a low beam loss, high energy beam chopper. Peak currents in the main linac are approximately doubled. Some increase in the cavity fields may also be considered to reduce the length of the linac.

Reference

[1] G H Rees and H Zhang, RAL design notes for the ESS, EPNS/RAL/A2-91 and A4-92, 1991-92.

CHOICE OF PROTON ENERGY FOR NEW SOURCES

I S K Gardner

Rutherford Appleton Laboratory, Chilton, Didcot, Oxfordshire, England.

Abstract

Some of the accelerator design factors affecting the choice of proton energy for a future spallation source are identified and discussed.

Introduction

The final selection of the proton beam energy for a future higher intensity spallation neutron source must take into account factors from the target design and the neutron scattering instrument design as well as the accelerator design. Only accelerator design factors affecting the performance, construction cost and operating cost of a 5 MW Spallation Neutron Source are outlined in this paper as a preliminary to a discussion on these topics.

Conclusions of Prior Meetings

Initial meetings on a possible, new European Spallation Source concluded that a suitable set of parameters would be those shown in Table 1.

Beam Energy	0.8 - 3.0 GeV
Beam Power	5 MW
Proton Beam Pulse Length	< 3 μs
Target 1	4 or 5 MW @ 50 Hz
Target 2	1 MW @ 10 Hz

Table 1

It was also concluded that a future study would need to design and cost an accelerator and two target configuration consisting of the following:

1. An 800 MeV linac of 6.25 mA mean current and 100 mA or more peak current.
2. Three compressor rings.
3. A 5 MW Tantalum target and target station.
4. A 1 MW target and target station.

In addition a future study would need to assess the possible benefits that could be derived from the use of :

1. Superconducting Linacs.
2. Fixed Field Alternating Gradient Accelerators (FFAG).
3. Use of Higher Proton Energy.
4. Different Target Designs.
5. Other Types of Accelerators.

Existing Experience

Table 2 (Ref. 1) outlines the parameters of some of the accelerators used for existing pulsed, spallation neutron sources. An exception is the cyclotron at PSI where the high power spallation target is still under construction and the beam is continuous and not pulsed. It is included here because the beam power is expected to reach the 1 MW level this year.

FACILITY	ENERGY (MeV)	Repetition Rate (Hz)	Operating Beam Power (kW)	Highest Achieved Beam Power (kW)
KENS (Japan)	500	20	2	2
IPNS (US)	450	30	6	7
LANSCE (US)	800	20	40	60
ISIS (UK)	800	50	145	160
PSI (S)	570	CW	1000 (Design)	

Table 2.

Figures for beam losses at the two most powerful pulsed spallation sources currently in operation are given in Table 3. It is interesting to note that one, ISIS, is a linac and rapid cycling synchrotron and the other, LANSCE, is a linac and compressor ring.

	ISIS	**Beam Energy**	**LANSCE**	**Beam Energy**
Beam Current	190 μA	800 MeV	80 μA	800 MeV
Losses				
Injection	3 μA (c)	70 MeV	6 μA (c)	800 MeV
Trapping	28 μA (c)	70 MeV	0.5 μA	800 MeV
Acceleration	1.5 μA (c)	120 MeV	-	
Extraction	<10 nA	800 MeV	160 nA	800 MeV
Transport	<1 nA	800 MeV		

Table 3. Beam losses at ISIS and LANSCE PSR. (c) indicates that the lost beam is picked up by a beam collector.

As both these machines run reasonably close to the induced activity levels that can be tolerated for hands on maintenance it is clear that uncollected beam loss at energies above

120 MeV must be kept below 100 nA in future higher intensity machines. It is also clear that wherever possible lost beam must be captured on beam collectors specifically designed for this purpose.

New Spallation Source Proposals

Table 4 lists the main parameters of proposed designs of new spallation sources where the proton beam energies range from 800 MeV to 45 GeV. As can be seen, different accelerator options favour different proton beam energies, bearing in mind that the maximum current in a ring is likely to be limited to the levels achieved in the CERN ISR due to the instability limit.

	Linac Energy GeV	Ring Energy GeV	Ring Type	Beam Power MW
AUSTRON	0.07	1.6	RCS	0.1
ANL	0.4	2.2	RCS	1.0
ESS - 1	0.46	1.6	FFAG	5.0
ESS - 2	0.8	0.8	COMP X 3	5.0
ESS - 3	1.2	1.2	COMP X 2	5.0
ESS - 4	2.4	2.4	COMP X 1	5.0
ESS - 5	0.8	3.0	RCS	5.0
LANL	0.8	0.8	COMP X 1	1.0
INR	0.6	45.0	KAON FACTORY	5.0
LBL	1.0 (Ind linac)			5.0

Table 4. New spallation source proposals.

5 MW Rapid Cycling Synchrotron (RCS)

This is an extrapolation of ISIS by a factor of 30, taking the stored energy in the beam from 3 kJ to 100 kJ. The minimum final energy of the proton beam would be 3 GeV and for a 50 Hz machine the beam would need to be in the ring for at least 10 ms as compared with the 1 - 2 ms of the Compressor Ring options (CR). The required value of peak current from the 0.8 GeV Linac injector is similar to the CR options. Most of the RCS components will be technically more difficult than for the CR options with, for example, all the ring magnets having RF screens of low eddy current design inside the vacuum vessel to maintain a low impedance for the beam. It may be beneficial to consider two 25 Hz RCS to alleviate some of the design problems.

Beam loss from the injection, trapping and acceleration processes will all take place at energies well above the neutron production threshold, making beam collection considerably more difficult than on ISIS. Graphite collectors would need to be about 1 m long instead of a few centimetres.

5 MW Compressor Ring Options

Three energies have been proposed for the Compressor Ring options, namely:

3 Rings at 0.8 GeV and 1.7 MW each,
2 Rings at 1.2 GeV and 2.5 MW each,
1 Ring at 2.4 GeV and 5.0 MW.

Of these options the lower energy, three or two ring version, appears as a more favourable choice for the following reasons.

1. Cost

The cost of the rings will almost certainly scale with the beam momentum giving scale factors of 2.2, 1.3, and 1 for the 2.4, 1.2, and 0.8 GeV energies respectively. In addition there will be a much longer linac to build for 2.4 GeV energy.

2. Reliability

A multi ring version will allow continued operation at 2/3 or 1/2 intensity even if one ring fails, although it could be argued that the multi-ring version requires more components in working order if it is to operate at full intensity. However, it is likely that the 2.4 GeV version will have nearly the same number of components as the multi-ring version but they will be connected in series rather than in parallel.

Also for the 2.4 GeV linac there will be a much longer linac to maintain.

4. Buildings and Shielding

Figure 1 indicates the size of building required for achieving hands on maintenance with levels of induced radioactivity similar to those at ISIS and LANSCE. The shielding is that estimated to allow personnel occupation of the areas outside the compressor ring or beam transport line carrying the 5 MW beam. With present day prices a structure of this large cross section will cost about £400k/m. Cost savings may be made by use of tunnels but clearly the lower the energy the lower the cost of the buildings and shielding will be.

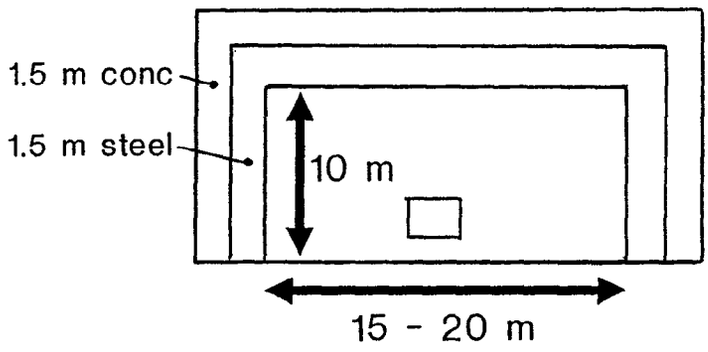

Fig 1. Shielding and building size required for hands on maintenance.

5. Lost Beam

Beam collection and collimation will be much harder at 2.4 GeV and, since the number of particles per ring is the same in all three cases, then each lower energy ring can tolerate a larger fractional loss.

6. Injection

H-minus injection becomes more difficult at 2.4 GeV where there is more uncertainty about the excited H-zero states. At the higher energy, stripping foil radiation damage will be greater, the required linac momentum ramping will be more difficult and the debunching of the linac micro bunches will be slower.

7. Extraction

For a high energy ring the aperture cannot be reduced much because of the impedance increase, thus the extraction will be more difficult.

8. Beam Transport

2.4 GeV beam transport lines will be more expensive to build and to operate than for the lower energies. On ISIS almost half the total electrical power is used by the 800 MeV beam transport line.

Conclusion

From the above considerations, it is probable that the accelerator design that will be of the lowest cost, to build and to operate with high reliability, will be that which has the lowest possible output energy and the highest achievable beam intensity. However, the final choice of energy can only be made when more detailed designs have been produced and costed.

References

1. G H Rees , Overview of Future Spallation Neutron Sources, Proc. of the US National Accelerator Conference, IEEE Trans. Nucl. Sc, 1993.

EXPERIENCE WITH IPNS TARGETS

J. M. Carpenter and A. G. Hins
Argonne National Laboratory

Abstract

Three targets have operated in the IPNS Neutron Scattering Facility. The first, a depleted Uranium target, served from 1981 until it was replaced in 1988 by the Enriched Uranium Booster Target. The Booster Target had operated for nearly three years when it suffered a cladding leak and was replaced with the retired depleted Uranium target. That target reached its end-of-life after less than one year's further operation, and was replaced with an identical one newly assembled from spare components, which is still operating satisfactorily.

This paper reviews the operating history of the IPNS targets and the findings reached during analysis of the failures. Similarities with ISIS target experience, preliminary conclusions and plans for providing spares and improved targets are discussed. We present some preliminary results from the hot cell examination of the failed depleted Uranium target.

Introduction

Figure 1 shows the design of the IPNS Enriched Uranium Booster Target. The depleted Uranium target is similar, but all disks are nominally 25 mm thick. The core material of both targets is α-phase Springfield adjusted alloy, with HIP bonded 0.5 mm thick Zircaloy-2 cladding. The designs of the targets have been described earlier.[1-4]

Figure 2 shows the average proton current on the IPNS target from turnon in May, 1981 until the present. IPNS ran about 26 weeks per year in the early years and 18 weeks per year in FY 1992, diminishing about linearly in between. For most of this time, the proton energy was 450 MeV. Through 1984, the Neutron Scattering Target received beam 75% of the time; the Radiation Effects Facility received the remaining 25%. The targets suffered between 10 and 100 full thermal cycles each day.

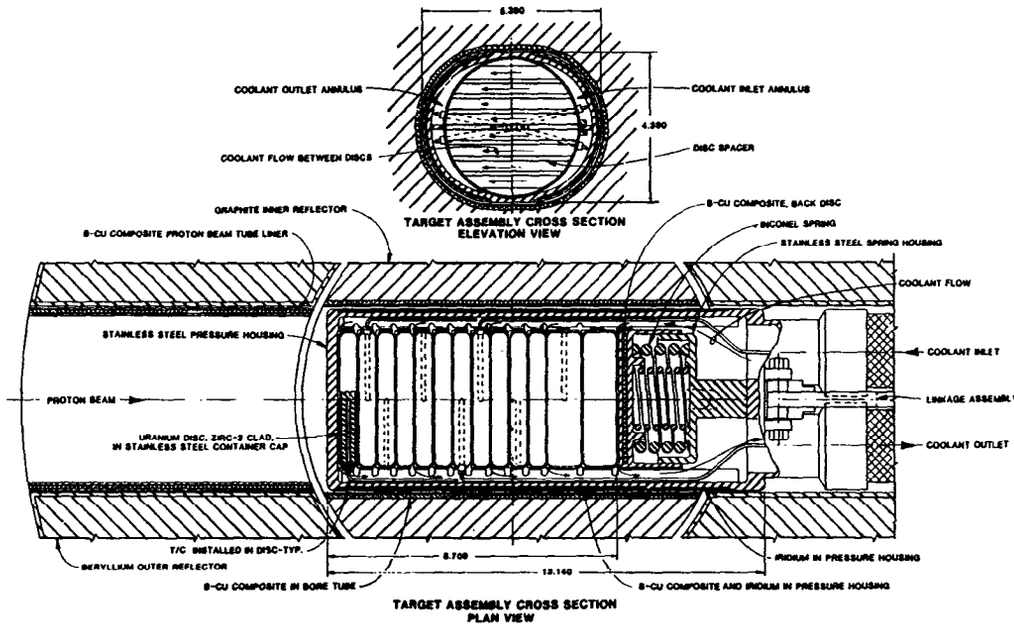

Figure 1 The IPNS Enriched Uranium Booster Target

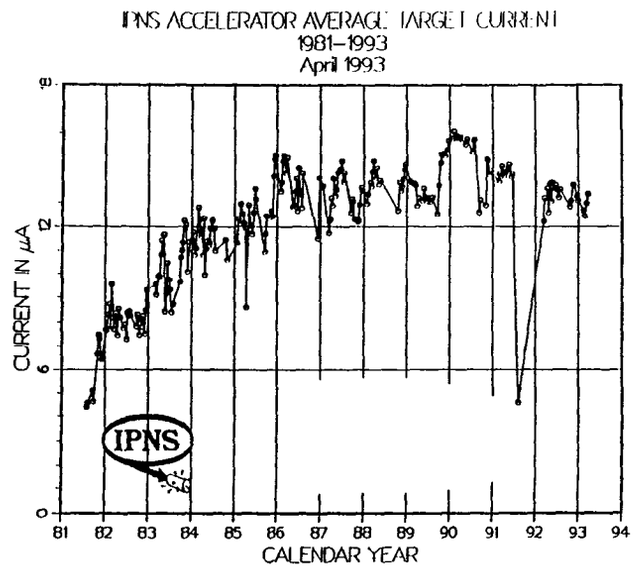

Figure 2 Weekly averaged proton current on the IPNS targets.

The original depleted Uranium target operated in the Neutron Scattering Facility from the beginning until it was replaced in October, 1988 by the Booster Target. In June, 1991, the target monitoring system displayed an increase in the concentration of Xe-135 in the cover gas of the primary coolant surge tanks, indicating a leak in the cladding after nearly three years of trouble-free operation.

Figure 3a shows the counting rate in the monitors (there are two systems, interrogated alternately) around the time of the Booster Target failure. The counting rate rose linearly from its long-term background level up to the conservatively-imposed upper limit where operation terminated.

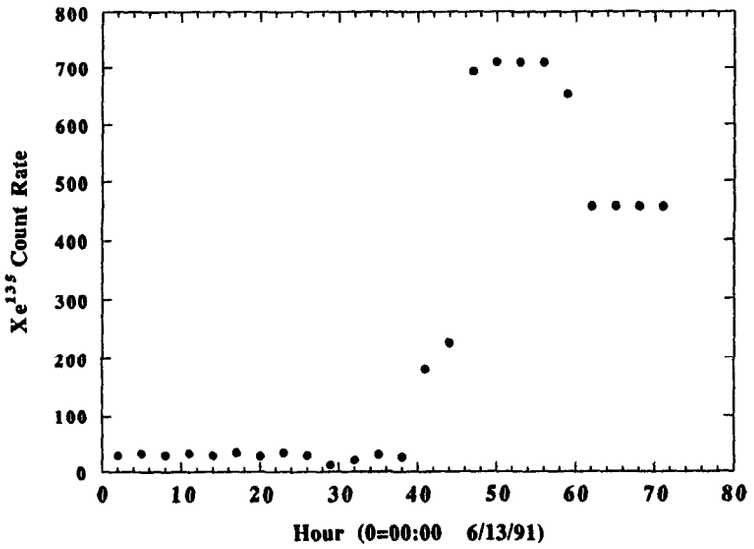

Figure 3 a Counting rate in the Xe-135 monitoring system.around the onset of the Booster Target leak.

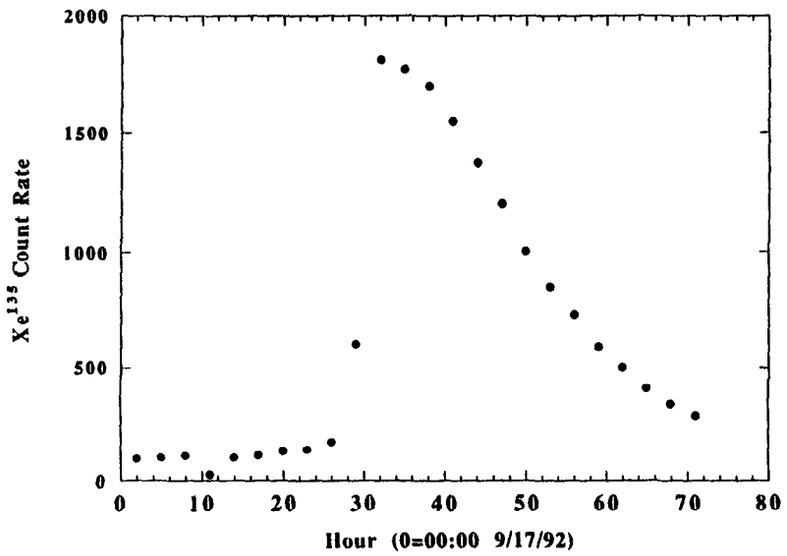

Figure 3 b Counting rate in the Xe-135 monitoring system.around the onset of the depleted Uranium target leak.

Extensive tests followed to establish that the increase was due to Xe-135 leaking from a breach in the cladding and to quantify the leak. After further extensive investigation of the consequences of continuing operation with the leaking clad[5], we concluded that it was necessary to remove the Booster Target and replaced it

with the original depleted Uranium target previously operated in the Neutron Scattering Facility. That target ran successfully until August, 1992, when it, too, sprang a leak and Xe-135 was seen in the surge tank cover gas. Figure 3b shows the counting rate around the time of the failure. In this case, the rate increased at first slowly, then more rapidly until it reached the limit where operation was terminated. The target was replaced with a spare which continues to operate normally. We have assembled another spare depleted Uranium target. We are designing a replacement enriched Uranium target, based on U-10%Mo alloy.

Figure 4 shows the specific activity of Xe-135, Xe-133 and La-140 observed in samples of cooling water removed from the cooling system during test operation with the failed Booster (we remain uncertain about the identity of the La-140.) In these tests with the demineralizer connected in the coolant system, we were unable to detect many expected chemically-active fission products. When the demineralizer was isolated from the system, the full range of fission products became observable, as Figure 5 shows in the case of the Iodine isotopes. The demineralizer efficiently removes chemically active elements from the water stream, as demonstrated by the rapid decrease in Iodine activity when it was reconnected to the system. From kinematic model analysis and from data from these and other tests, we could determine the absolute leak rates of various isotopes, and the partitioning of volatile elements between water and cover gas.

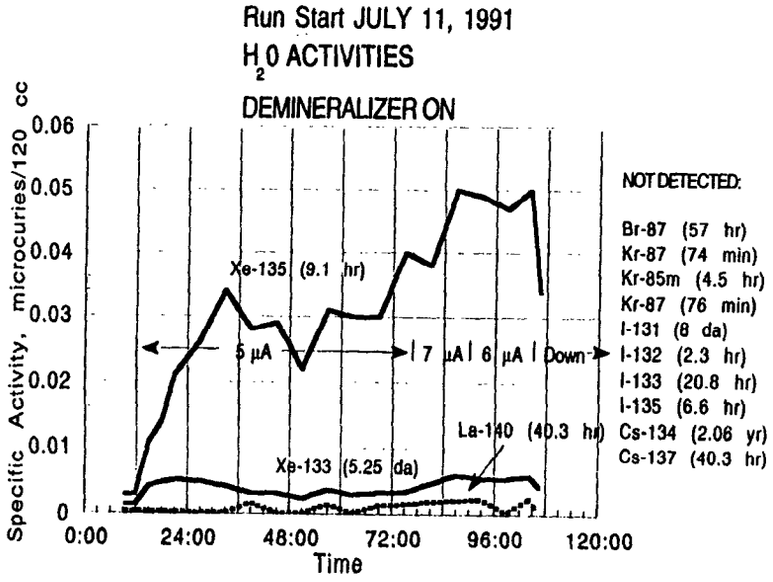

Figure 4 Xe-135 and Xe-133 activities, demineralizer on

We removed the leaky depleted target into a hot cell for destructive examination. Sawing away the vessel, we were easily able to remove the target disks. We have completed a series of preliminary examinations and non-destructive tests. Figure 6 shows the gamma-ray dose rate measured 8 cm from the surfaces of the individual

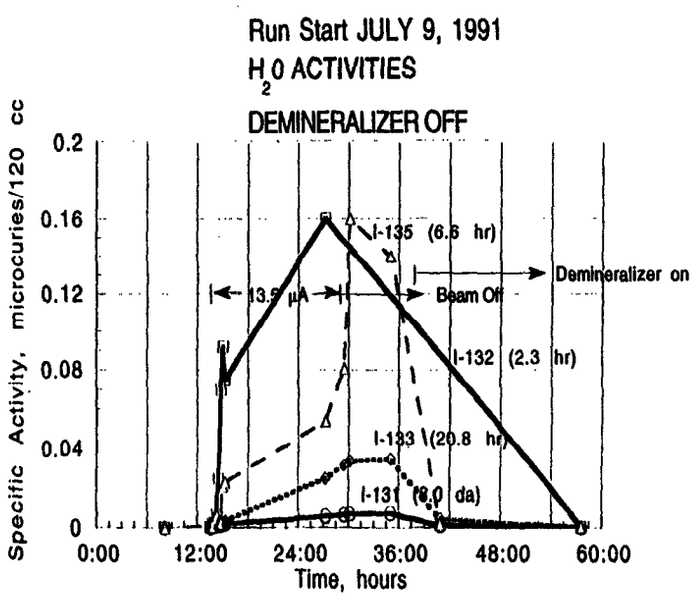

Figure 5 Activities with demineralizer on and off

disks, a measure of their activation by proton irradiation. As expected, the highest activity is confined to the front of the target. The figure also shows the power density calculated for 500 MeV protons. The fall-off at the end of range (13.4 cm of U metal, 11.4 cm for 450 MeV) occurs farther downstream than the fall-off in the measured dose rates; as of the time of writing, we do not understand this.

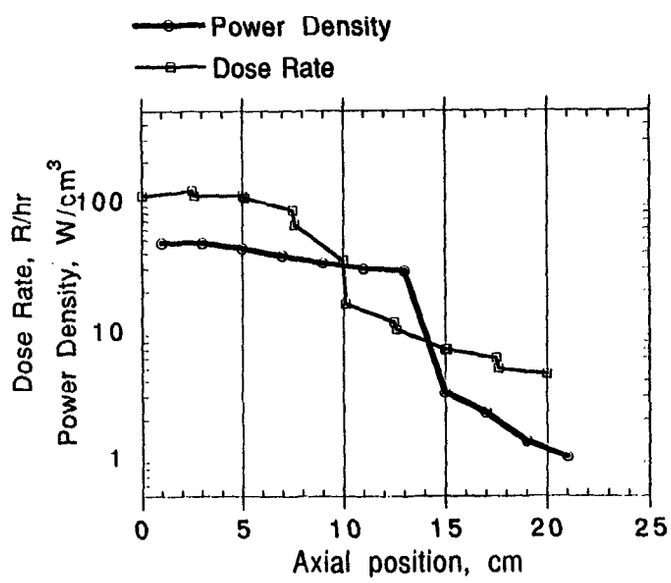

Figure 6 Gamma-ray dose rate as a function of disk position in the depleted Uranium target, and power density calculated for 500 MeV protons.

Progress in Examining Disk Surfaces

After opening the welded vessel, most of the disks, in their flow guides, easily slid down the housing guideways, but the front disk required slight additional manipulation. All eight disks were easily removed from the flow guides by force of gravity, or with a few pounds of force from an extraction fixture. Thermocouples in disks 3, 5 and 7 fell from their wells during the course of handling. The thermocouple in disk #1 remained stuck in the well and later broke off at the disk during repeated handling.

Photographs were taken of both faces of all 8 disks. Angled views provide the best lighting to accentuate disk surface irregularities. Witness of the flow channel guide bars is apparent on the front faces of all disks.

The front face of disk #1 shows a 1-inch long crack running across the approximate center of the disk in the direction of the thermowell tube exit, Figure 7. The crack appears to be imbedded in a narrow depression channel that is visible on the disk surface. The depression channel is more than 2 inches long and extends to the thermowell tube exit point. In the central region of the disk, a pattern of surface undulation and apparent blistering are easily seen. The surface damage pattern apparently outlines target beam location, which is somewhat off-round and off-center. Figure 8 shows a magnified view of the central portion of the disk face.

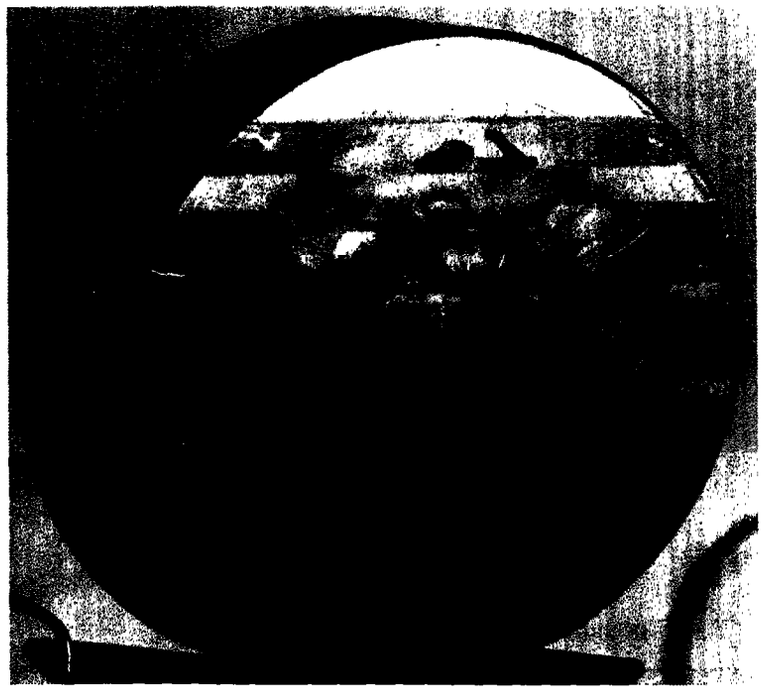

Figure 7 Front face of Disk #1 (ANL photo #283811)

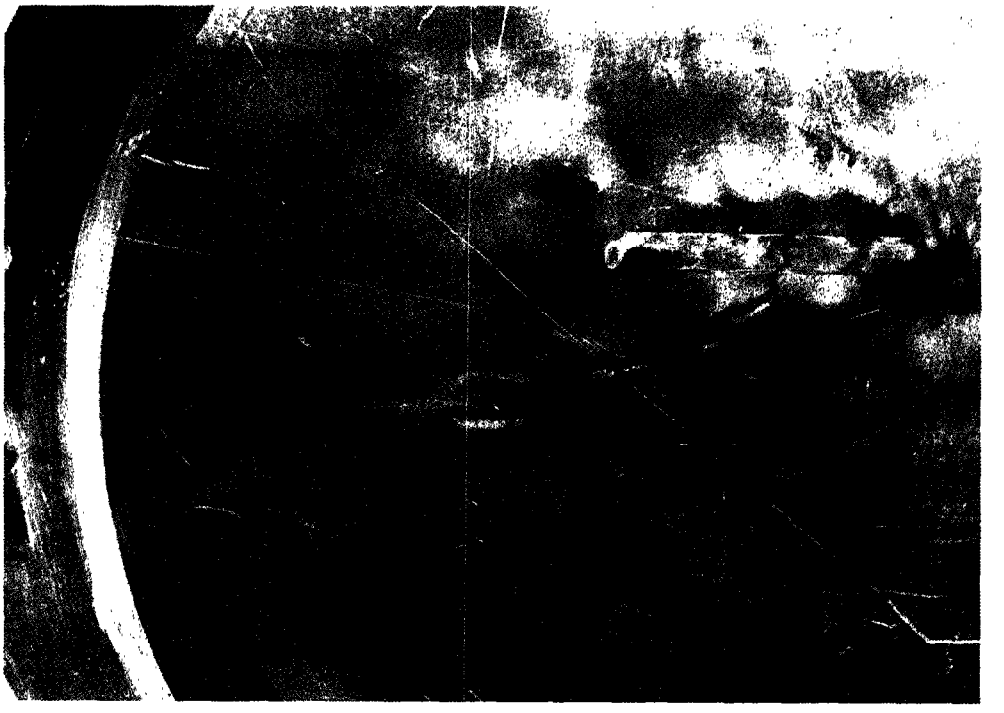

Figure 8 Front face of Disk #1, enlarged view (ANL photo #283895)

Figure 9 shows the rear face of disk #1. In this view the disk is still housed in the flow guide cup. Imprints from the adjacent flow channel guides are

Figure 9 Back face of Disk #1 (ANL photo # 283713)

pronounced in the central region of the disk face. A major elevated surface projection (blister??) has occurred within 1/8" of the center of the face. A 1/8"-long blunt crack can be seen at the midpoint down one slope of the blister. Figure 10 is a 3X magnified view of the disk central region, which shows the blunt crack in detail.

Figure 10 Back face of Disk #1, enlarged view (ANL photo # 283696)

Figure 11 is a profile view of the back face of disk #1 and it shows the elevation of the major blister on that face. By rough measurement, the blister elevation is seen to be about 0.066" from its base. By oblique light, surface rounding (blisters?) can be seen in random areas throughout the face--with some blisters extending nearly to the outside edge of the disk. However, the undulating surface is most pronounced in the central region of the face. Depression channels, generally in line with the axis of the thermowell tube, are seen on this face also.

Disk #2 front face photographs show an obvious elevated surface projection in the central region of the face. This (blister) is nearly opposite the major blister that occurred on the back face of disk #1. No surface crack is visually apparent on this face. The central region of the face shows general surface undulation as does the central region of the back face of disk #2.

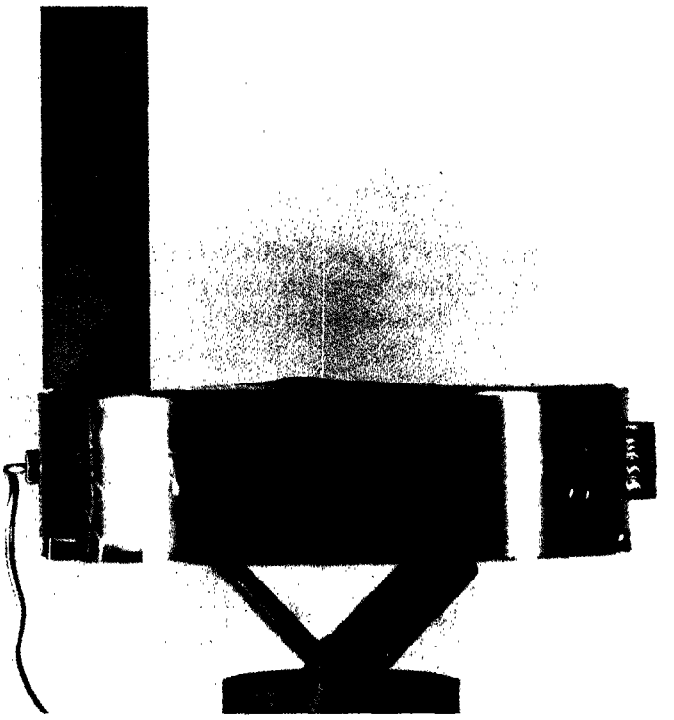

Figure 11 Back face of Disk #1, profile view (ANL photo # 283712)

Both faces of disk #3 and the front face of disk #4 show some visual evidence of surface undulation in the central region. The disk faces farther back in the target stack show very little visual evidence of surface undulation.

We plan destructive metallurgical examination of the disks and cladding to begin in the near future.

Relationship to ISIS Target Experience

Table 1 represents an attempt to relate failure data on ISIS and IPNS targets[6]. In many instances, the table entries are only best estimates.

Table 1

ISIS and IPNS Target Failure Data
Thermal cycles to failure, Total protons to failure and
Total fissions to failure

Target	Thermal Cycles	Total Protons, mAhrs	Peak Temperature, °C	Relative Total Number of Fissions
ISIS#1		92.4		0.31
ISIS#2	40000.0	53.1	120.0	0.18
ISIS#3	10389.0	174.9	130.0	0.59
ISIS#4	4147.0	138.8	150.0	0.47
ISIS#5	5074.0	295.6	165.0	1.00
ISIS#6	2628.0	126.1	180.0	0.43
ISIS#7	1805.0	107.2	215.0	0.36
IPNS Depleted#1	89600.0	240.0	225.0	0.39
IPNS Booster#1	28000.0	128.8	175.0	1.07

The data suggest the following observations. The lifetimes of the targets, while variable, are not dramatically different in terms of total protons or fissions. There is much less consistency in the lifetime expressed as thermal cycles. While the statistics are poor, a reduction in target lifetime as the peak temperature increases seems to be indicated. If this is confirmed by future targets then increased lifetime can be achieved by a change of design to give lower peak temperatures, which would, most likely, result in only a small reduction in neutron production .

References

1. J. Carpenter, H. Ahmed, B. Loomis, J. Ball, T. Ewing, J Bailey and A. F. D'Souza, "An Evaluation of Structural Integrity of IPNS-I and ZING-P' Targets", Argonne National Laboratory Report ANL-83-14, December, 1982.

2. B. A. Loomis, H. R. Thresh, G. L. Fogle, and S. B. Gerber, "Design, Production and Evaluation of a Zircaloy-Clad Uranium Target for an Intense Pulsed Neutron Source Application:, *Nuclear Technology* **55**, 617-627 (1981).

3. A. E. Knox, J. M. Carpenter, J. L. Bailey, R. J. Armani, R. N. Blomquist, B. S. Brown, D. R. Henley, A. G. Hins, B. A. Loomis, A. W. Schulke, and H. R. Thresh, "Progress on the IPNS Enriched Uranium Booster Target", ICANS IX,

Proceedings of the Ninth Meeting of the International Collaboration on Advanced Neutron Sources, Villigen, Switzerland, 22-26 September, 1986, SIN Report ISBN 3-907998-01-4, July, 1987, page 557.

4. A. G. Hins, R. F. Simandl, L. R. Walker, H. L. Richards, and A. E. Knox, "A Study of Core/Cladding Bonding in IPNS Booster Target Disks", Hot Isostatic Pressing: Theory and Applications, Proceedings of the Second International Conference, Gaithersburg, Maryland, 7-9 June, 1989, ASM International, Materials Park, Ohio (1991), p 281-291.

5. Harold F. McFarlane, "Safety Evaluation Summary: Report of the Laboratory Director's Special Task Force on IPNS Operation with Leaking Booster Target", Argonne National Laboratory internal report, March 4, 1992.

6. Private communication, T. A. Broome, J. M. Carpenter and M. Holding, 1992.

Measurement of Cooling Characteristics of the ISIS Tantalum Target.

G M Allen, T A Broome, M A Clarke Gayther, and C W Planner
Rutherford Appleton Laboratory, Chilton, Didcot, Oxon, UK.

Introduction

An ISIS spallation neutron target, shown schematically in Figure 1, comprises 23 heavy metal discs of different thicknesses, separated by narrow water cooling channels. Two types of target disc are used on ISIS, depleted uranium clad in zircaloy-2 and pure tantalum. The target discs have stainless steel frames shrunk on to them, and the assembly of frames is electron beam welded to form a solid structure, to which heavy-water cooling manifolds are fitted. Coolant is fed via three loops that are pressurised to supply approximately the same high velocity flow rate for each of the inter-plate coolant channels. Plate temperature is monitored by a thermocouple at the bottom of a radial hole, that extends to the centre of each plate. For the tantalum target only every other plate is fitted with a thermocouple.

This report describes measurements of target plate cooling before and after irradiation of targets. The deterioration in cooling of uranium targets has been shown to correlate with the onset of target failure. Cooling measurements on the tantalum target indicate a steady decrease in cooling efficiency with proton irradiation. The reasons for such a deterioration can only be speculative, until the cooling measurements can be correlated with a post-mortem examination of an irradiated target. However, the measurements indicate that some care must be exercised when considering the use of tantalum for the much higher power targets of the proposed European Pulsed Spallation Neutron Source.

ISIS Target Cooling

The ISIS target is force cooled using heavy-water as the coolant. A hot body under conditions of forced cooling should obey Newton's Law of Cooling, which states that the rate of heat loss is proportional to the temperature difference between the hot body and the coolant stream.

If -dH corresponds to the heat loss

then $$-\frac{dH}{dt} = \kappa(\theta - \theta_o) \qquad (1),$$

where θ is the temperature at any instant,
θ_o is the coolant temperature (assumed constant)
and κ is a constant for a given body under given conditions.

A small loss of heat $-\delta H$ in a time δt correspond to a temperature change $-\delta\theta$

and $$-\delta H = -ms\delta\theta \ ,$$

where, m = mass of body, and s = specific heat of body.

The average rate of heat loss over the interval is

$$-\frac{\delta H}{\delta t} = -ms\frac{\delta\theta}{\delta t} \quad ,$$

which in the limit δt very small becomes

$$-\frac{dH}{dt} = -ms\frac{d\theta}{dt} \qquad (2).$$

Substituting from equation (1) into equation (2) for $\frac{dH}{dt}$,

then
$$-\frac{d\theta}{dt} = -\frac{\kappa}{ms}(\theta - \theta_o)$$

Integrating with initial conditions, $\theta = \theta_{max}$ at $t = 0$, gives:

$$\ln\left\{\frac{\theta - \theta_o}{\theta_{max} - \theta_o}\right\} = -\frac{\kappa}{ms}\cdot t$$

or
$$\theta = \theta_o + (\theta_{max} - \theta_o)e^{-t/t_c} \quad ,$$

where $t_c = \frac{ms}{\kappa}$ = characteristic cooling time (CCT).

The plates in the spallation target all have the same face area, but there are four sizes of plate thickness. The mass of a plate is therefore proportional to the plate thickness. Assuming that cooling at the plate edges is small *c.f.* cooling from the disc faces then the characteristic cooling time may be normalised to plate thickness. The thickness normalised characteristic cooling time (TNCCT) should then be a constant for all target plates.

For a given material the TNCCT is directly proportional to its specific heat and inversely proportional to its thermal conductance. If it is assumed that the thermal conductance is directly proportional to the thermal conductivity in target plates of different materials but with the same geometric design, then it is possible to make the following comparison for the TNCCT's of tantalum and uranium targets before irradiation:

$$Ta_{TNCCT} = \frac{Ta_{specific\ heat}}{U_{specific\ heat}} \cdot \frac{U_{thermal\ conductivity}}{Ta_{thermal\ conductivity}} \cdot U_{TNCCT}$$

It must be borne in mind when making such a comparison that the uranium is clad in a very thin coat of zircaloy-2 and the effective thermal conductance will be affected by the quality of the adhesion at the interface between the two metals. In addition there are three small zircaloy ribs 1.0 mm wide by 1.5 mm high on one side of the zircaloy clad plates that are not included in the mass normalisation.

Measurements of Target Cooling

Cooling of the target plates is measured by recording the temperature indicated by each of the thermocouple monitors as a function of time, immediately after switching off the proton irradiation of the target. Typical Plate cooling curves are shown in Figure 2. The measurements are made using a Hewlett Packard HP54510A Digital Sampling Oscilloscope.

Apart from the initial 'knee' of the curve, it is found that for all plates, the cooling curves fit very closely the exponential decay of temperature with time predicted by Newton's Law of Cooling.

Measurements of the thickness normalised characteristic cooling time are plotted in Figure 3 for a uranium target before proton irradiation. At the time these measurements were started, the tantalum target had already received approximately 400 mAh proton irradiation. The measurements on the non irradiated uranium target show that the constancy of the TNCCT's is in close agreement with prediction. The measurements give an average value of $U_{TNCCT} = 0.1967$ s mm^{-1} for uranium before irradiation . The measurement error for the characteristic cooling time is estimated to be very small, ±0.03%, but the tolerance on plate thickness of ±0.35 mm must be added to this. Also, the normalisation assumes that the specific heat is a constant and the thermal conductance κ is constant. The discs are a layered structure of two materials, zircaloy-2 (specific heat 276 J °C^{-1} kg^{-1}) and uranium (116 J °C^{-1} kg^{-1}). The thickness of zircaloy-2 on each plate is non uniform, ranging from 0.25 mm to 0.6 mm and the zircaloy-2 forms a smaller fraction of the thicker plate composition. The thermal conductance has a dependence on how well the zircaloy-2 is bonded to the uranium and no allowance is made for the perturbing effect of the additional mass of the zircaloy-2 ribs. However, the simple thickness normalisation does show a remarkable constancy of value from plate to plate.

Also plotted in Figure 3 are TNCCT's measured for a uranium target after a 295 mAh, 800 MeV proton irradiation. These measurements show relatively large changes to the TNCCT values for Plate #2 and #3. Plate #8 also has a value that is above the average. The remainder of the values are only slightly higher than the average value for uranium before irradiation. This target was replaced shortly after making these measurements when plate temperature and coolant flow rate measurements confirmed critical damage to the target.

In Figure 4 the TNCCT's for a tantalum target are plotted for several levels of proton irradiation. The dotted line plotted on the graph is for the scaled value of the average TNCCT measured for uranium before irradiation. Thus, using the following tabulated values for the specific heat and thermal conductivity:

Metal	Specific Heat J K^{-1}Kg^{-1}	Thermal Conductivity W m^{-1} K^{-1}
uranium	116	27.5
tantalum	140	57.5

together with the measured value of U_{TNCCT}, the scaling for tantalum before irradiation becomes:

$$Ta_{TNCCT} = 0.5772\,U_{TNCCT} = 0.1135\ \mathrm{s\ mm^{-1}}$$

From the measurements shown in Figure 5 it can be seen that for the lowest proton irradiation of 417 mAh, the values of TNCCT lie very close to the scaled value for Plate #17 and #19 at the downstream end of the target. This may be coincidence, but the downstream plates might be expected to be closer to the value with no irradiation since the downstream end of the target would suffer a lower irradiation by a factor five less than the thinner upstream plates. The thicker downstream plates should also be less prone to mechanical distortions resulting from heat and/or irradiation. Measurements on all plates upstream of Plate #17 show a large increase in the values of TNCCT relative to the scaled value. The measurements also show a steadily increasing deviation with increasing irradiation as shown in Figures 5 and 6. The rate of deterioration in cooling appears to be roughly similar for the plates with a large change in their TNCCT.

For the irradiated uranium target, critical damage occurred when the TNCCT of one of the plates had increased by a factor ~ 4. The measurements on the irradiated tantalum target are already showing a similar factor increase, but from an initial value approximately half that of uranium.

Conclusion

The cooling of the target plates in the ISIS spallation neutron target appears to obey Newton's Law of Cooling. A single parameter, the thickness normalised characteristic cooling time, may be used to characterise the cooling of all target plates. There is some evidence that the parameter scales appropriately with the thermal properties of the materials. Measurements of the parameter for plates in a tantalum target indicate considerable reduction in cooling efficiency after an irradiation of nearly 1 Ah, with 800 MeV protons. It cannot be ascertained without a detailed examination of the irradiated target plates, whether the deterioration is due to mechanical distortion, crystal growth or gas swelling, or due to changes in the thermal properties of the material or a change in thermal conductance from some form of corrosion. Such an examination would seem to be essential if tantalum is to be considered for the higher power targets of the proposed European Spallation Neutron Source.

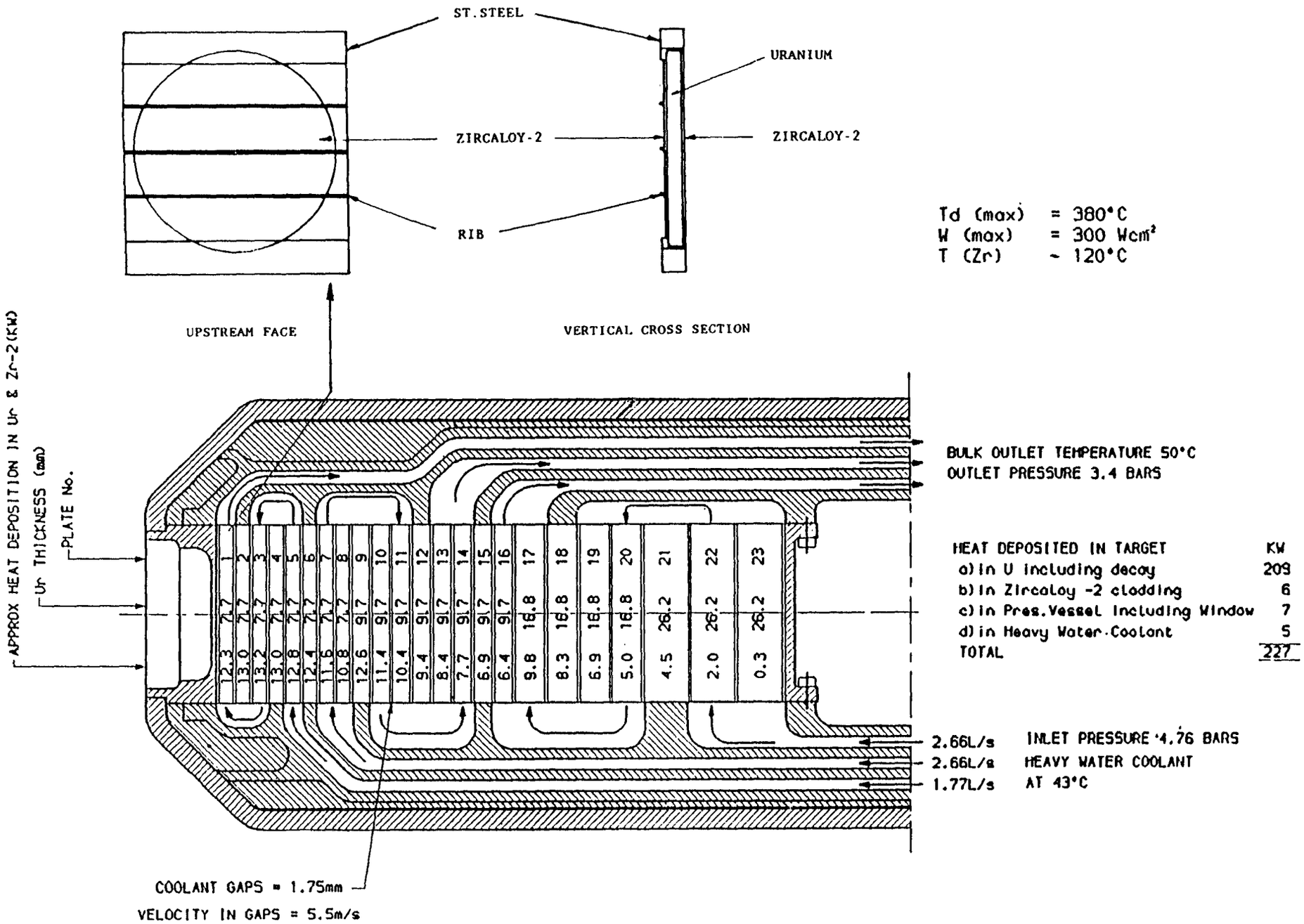

FIGURE 1 SCHEMATIC DIAGRAM OF ISIS URANIUM TARGET

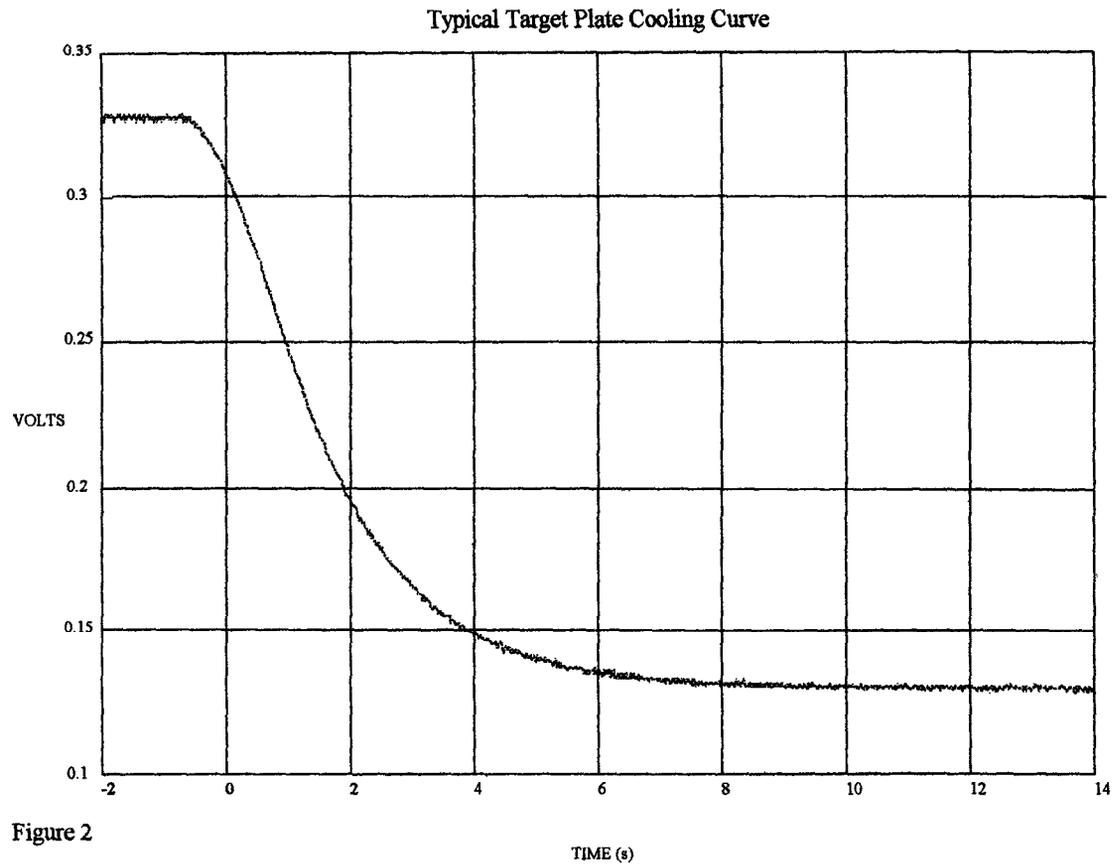

Figure 2

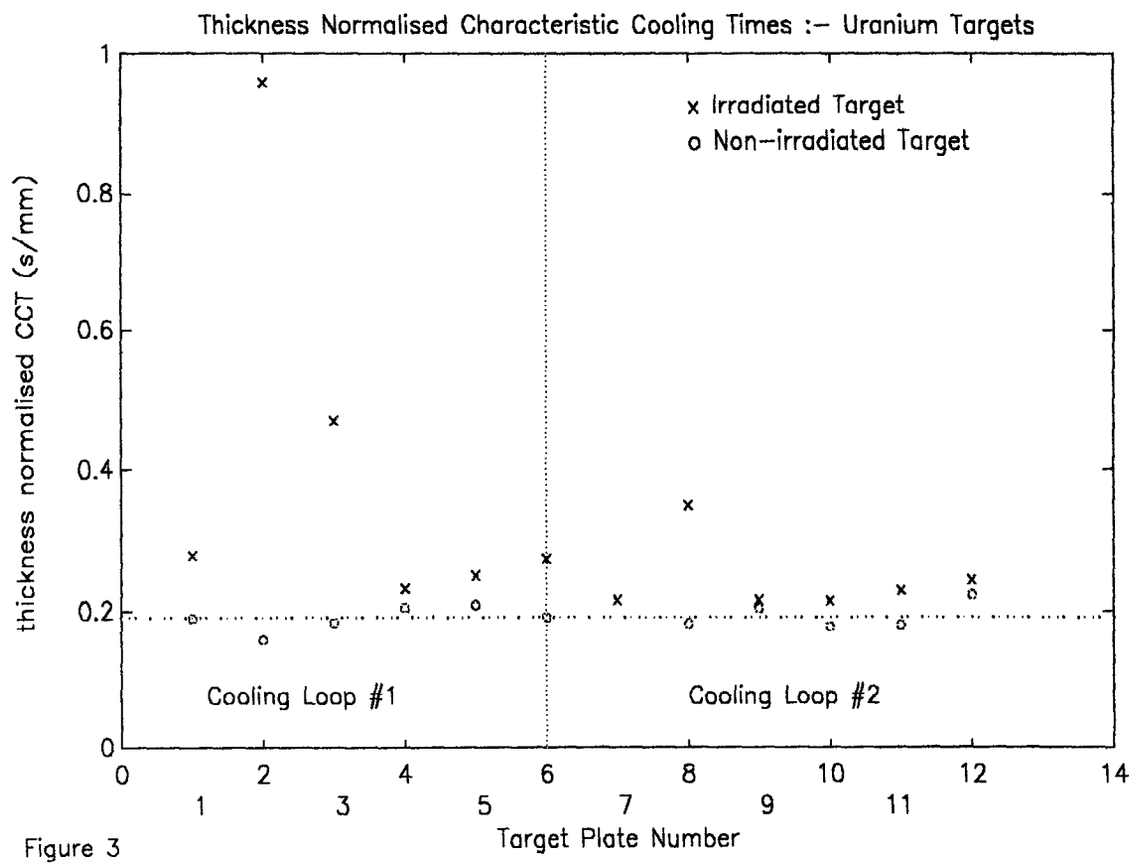

Figure 3

Thickness normalised characteristic cooling times for irradiated tantalum target.

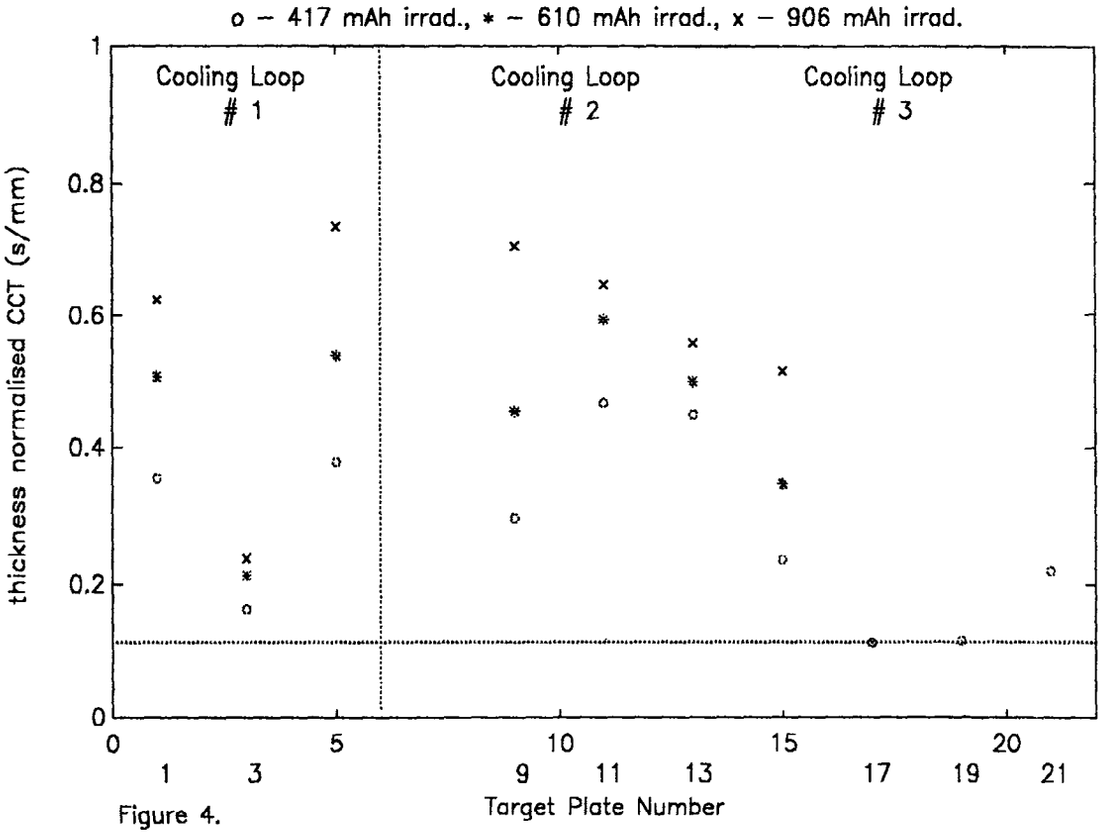

Figure 4.

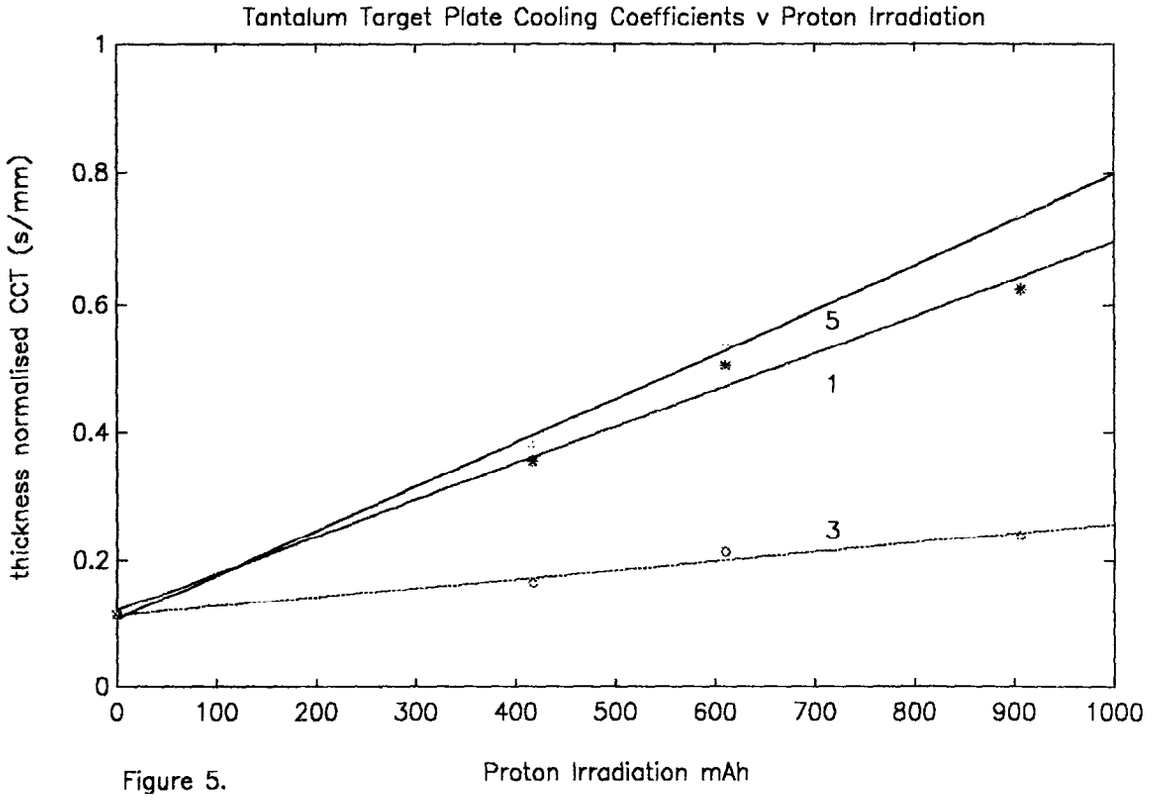

Figure 5.

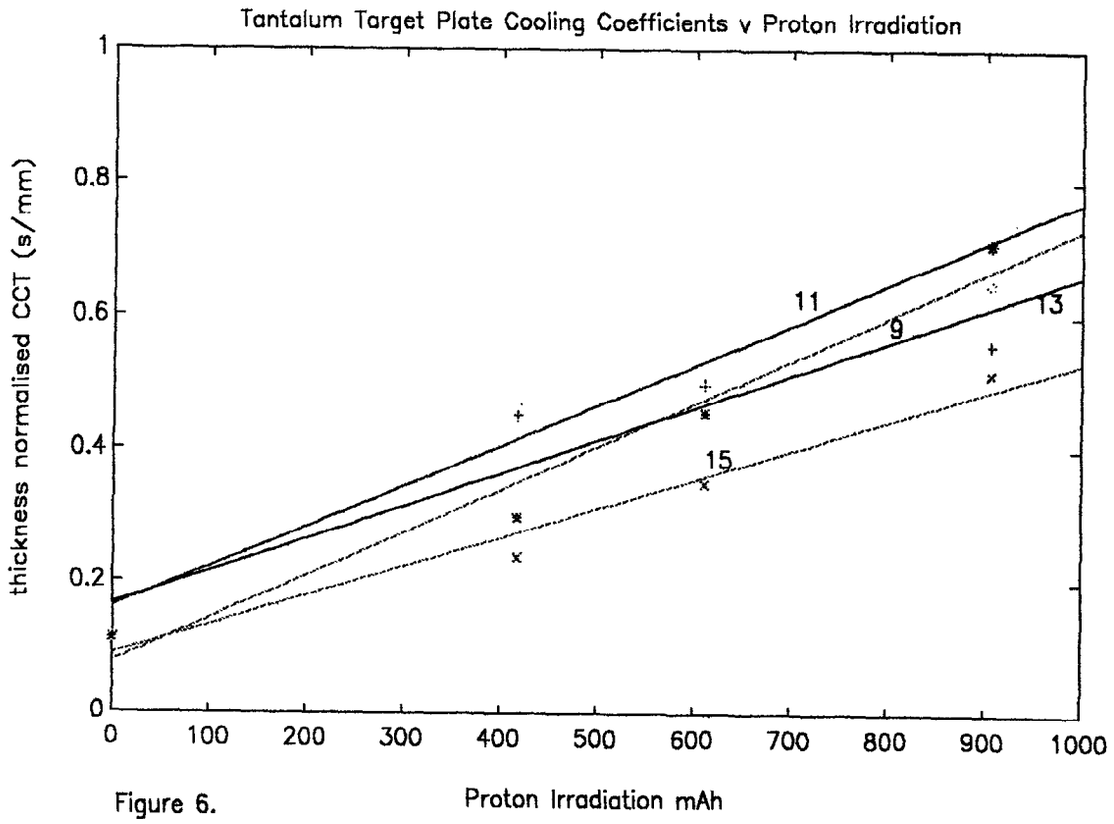
Tantalum Target Plate Cooling Coefficients v Proton Irradiation
thickness normalised CCT (s/mm)
Proton Irradiation mAh
0
0.2
0.4
0.6
0.8
1
0
100
200
300
400
500
600
700
800
900
1000
11
9
13
15

Figure 6.

OPERATIONAL CONSEQUENCES OF INDUCED ACTIVITY ON THE ISIS TARGET STATION

T. A. Broome
Rutherford Appleton Laboratory

1. INTRODUCTION.

ISIS has now been operating for several years at progressively increasing proton currents. This report examines the operational difficulties encountered as a consequence of the levels of induced activity in the components of several systems. In particular difficulties with maintenance of the water cooling systems, remote handling of the target, reflector and moderator assembly and discharge of radioactive gases to the environment will be discussed.

The hazard from induced activity is radiation dose to the staff working on the active systems. At ISIS the policy is to minimise both the radiation doses to individuals and the collective dose. The limit set for an individual is 5 mSv/y. The typical annual dose is less than 1 mSv. This has been achieved mainly as a result of the development of detailed working procedures.

The consequences of the experience at ISIS (160 kW of beam power) for the high intensity sources (beam powers up to 5 MW) discussed at this meeting are potentially serious and present a challenging design problem.

For reference figure 1 shows a schematic layout of the ISIS target station.

2. MAINTENANCE OF THE WATER COOLING SYSTEMS.

The plant which provides cooling for the target, moderators and reflector is both complex and compact. The pipework, pumps, filters and ion exchange columns, illustrated in Figure 2., are located in a shielded enclosure called the Services Area which has a volume of 1200 m^3. Regular maintenance is required to service pumps, renew ion exchange columns and replace components such as pumps and instrumentation sensors.

The dose rate around the pipework, even when empty, is typically 200 - 500 μSv/h. This is due to contamination of the inside of the pipes by Be^7 which is produced by spallation of Oxygen. All the active water circuits incorporate an ion exchange column which does trap a proportion of the Be^7. However. only a fraction of the total flow, typically 10%, passes through the columns with the result that the Be^7 is deposited on the pipe surfaces.

Meticulous planning of maintenance work is required to achieve acceptably low radiation doses to the staff involved. It is vital that the time spent in the areas where the dose rate is relatively high is minimised. This is particularly important for access into the more congested areas in the centre of the plant. Accurate documentation of the plant has proved crucial. A useful aid to this at ISIS is a comprehensive and detailed set of annotated photographs of the plant. This is illustrated in figures 3 and 4

which show a photograph of part of the pipework together with an overlay giving component and pipe numbers. Using these the individual can become very familiar with the task and the layout of the equipment before entry to the area. An extension of this facility using video film is being considered.

Early in 1992 all the rubber diaphragms in 150 control valves were examined and the damaged ones replaced. This involved 90 man days of work and the collective dose was 0.7 mSv.

The dose rate on the pipework will scale with the proton beam current for a water cooled system similar to the ISIS assembly. Even if a design can be developed where the proton beam does not pass through the water the likelihood is that the water will be in a substantial flux of high energy neutrons close to the target. In fact the activity of the reflector coolant at ISIS is only half that of the main target cooling circuit. For a 1 MW source dose rates around the empty pipework could well be as high as 1 - 4 mSv/h unless some method can be found to prevent the Be^7 from depositing on the pipes. The design of the high power cooling systems must take this into account so that the need for access is minimised. For a 5 MW source it may be necessary to consider limited remote handling.

3. REMOTE HANDLING.

Since start-up in 1986 there have been 12 target changes, three moderator replacements and other detailed work carried out in the remote handling cell. While these tasks are regarded as relatively routine some observations can be made which may be useful to those designing new sources.

Good engineering practice often requires a known torque to be applied when tightening bolts and nuts. This is particularly important when making sealed joints. Many devices are commercially available for this and several have been used in the remote handling work at ISIS. However, nearly all these require the friction between the threads to be definable and this generally means lubrication. The dose rate around the target assembly is high and the use of conventional lubricants is problematic. At ISIS the decision was taken to use no lubricants. Many of the nuts and bolts are now very stiff to turn. Visually there is little evidence for corrosion on the stainless steel and the reason for the stiffness is not clear. However, this effect has been progressive as the total proton dose on the target assembly has increased and it may well be necessary to replace some of the bolts and nuts. A consequence is that it is not possible to use conventional equipment to apply known torques which has had the result of much more difficulty than expected in achieving leak tight joints.

It can reasonably be expected that this effect will be much more severe for high power sources and this should be taken into account when designing the remote handling for the components.

The approach at ISIS in the design for remote maintenance of the target moderator and reflector assembly was to replace individual components. This requires water, cryogenic and vacuum joints to be made remotely. In general the flanged joints have, in

practice, presented no great difficulty except the problem of applying the correct torque discussed above. However, the joints on flexible line have not been as reliable as had been expected. A bayonet connector illustrated in figure 4 is used. This works very well in laboratory conditions. Handling it remotely is also easy. However, occasional leaks have occurred and more development of this component is required. This illustrates the difficulty in design of remote handling equipment. Rigorous testing and development is essential and the design must be sufficiently flexible to allow changes in the installed equipment after operation as some problems will only appear on the real assembly.

4. RADIOACTIVE GAS RELEASES.

Difficulties with Tritium releases to the atmosphere from the ISIS target station have caused serious disruption to the user programme in 1992 and 1993. Between 30 and 40 days of scheduled operation have been lost.

The regulatory constraints are becoming ever more stringent. RAL has a Certificate of Authorisation to release no more than 30 GBq per month of Tritium in any form. This limit is based on pollution considerations as even at the maximum level there is no conceivable safety hazard. This is a very low limit compared to that allowed at other laboratories but given the very much higher Tritium concentrations expected at the high power sources being planned they may well face similar operational difficulties to ISIS.

The dominant production mechanism for Tritium in the cooling circuits is spallation of Oxygen. The concentration in the target cooling water is currently 8 TBq m^{-3} giving a total inventory of 6 TBq. This represents a production rate of 0.15 Tritium nuclei per incident proton.

On line measurement of Tritium in an active air ventilation stream is very difficult and to date no commercial solution had been identified.. The low energy tail of the β spectrum (i.e. less than the end point energy of the Tritium β decay) from the other active radionuclides (O,N) gives, typically, 100 times the count rate of Tritium. At ISIS a fraction of the ventilation stream is passed through a water bubbler to absorb the Tritiated water vapour for later off line measurement. This then places extreme demands of leak detection in the water systems for giving prompt warning of a problem. For ISIS this requires a knowledge of the water inventory to better than 0.5% which is at the limit of the sensitivity of the instrumentation. Small leaks have resulted in releases of Tritium which are close to the monthly discharge limit. This has required the facility to be shut down for investigation and repair.

There are systems for collecting both Tritium gas and Tritiated water vapour. However, such equipment is very expensive on the scale required to deal with the active air ventilation systems at ISIS (flow rate about 7 m^3 s^{-1}).

It will be essential for future designs to anticipate the likely downward pressure on discharge limits.

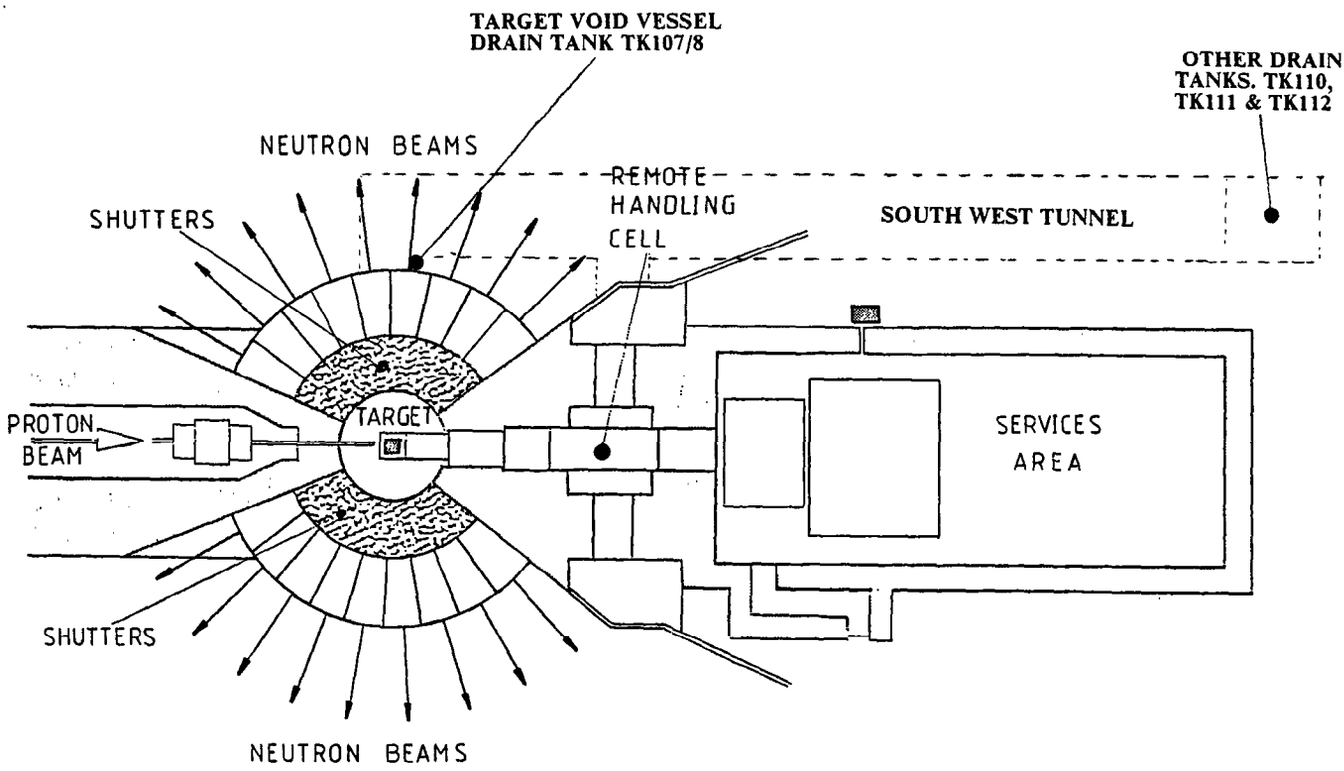

Figure 1. Schematic Layout of the ISIS Target Station

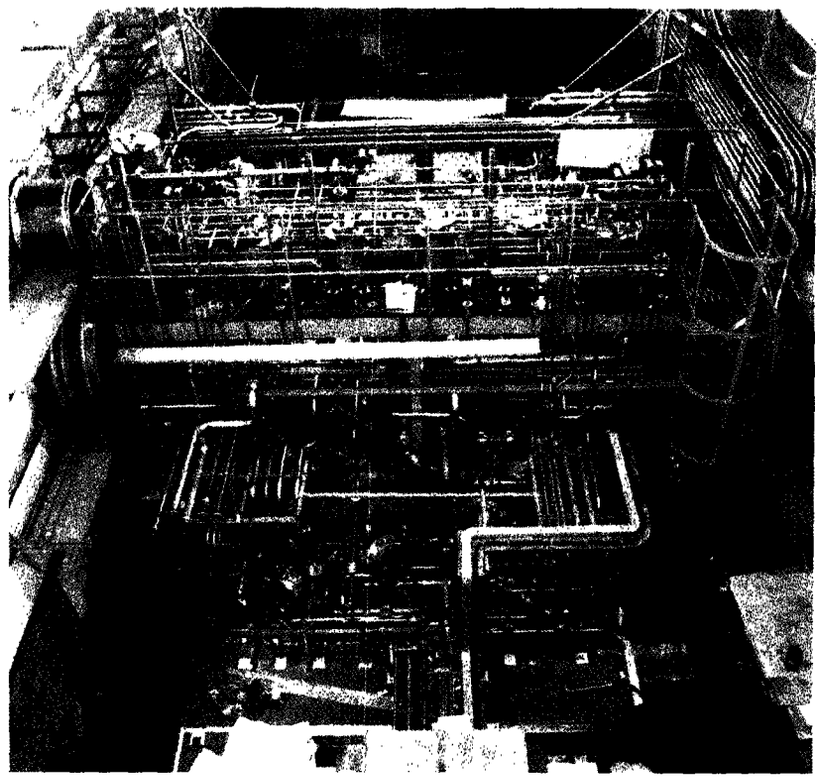

Figure 2. A View of the Water Cooling Plant

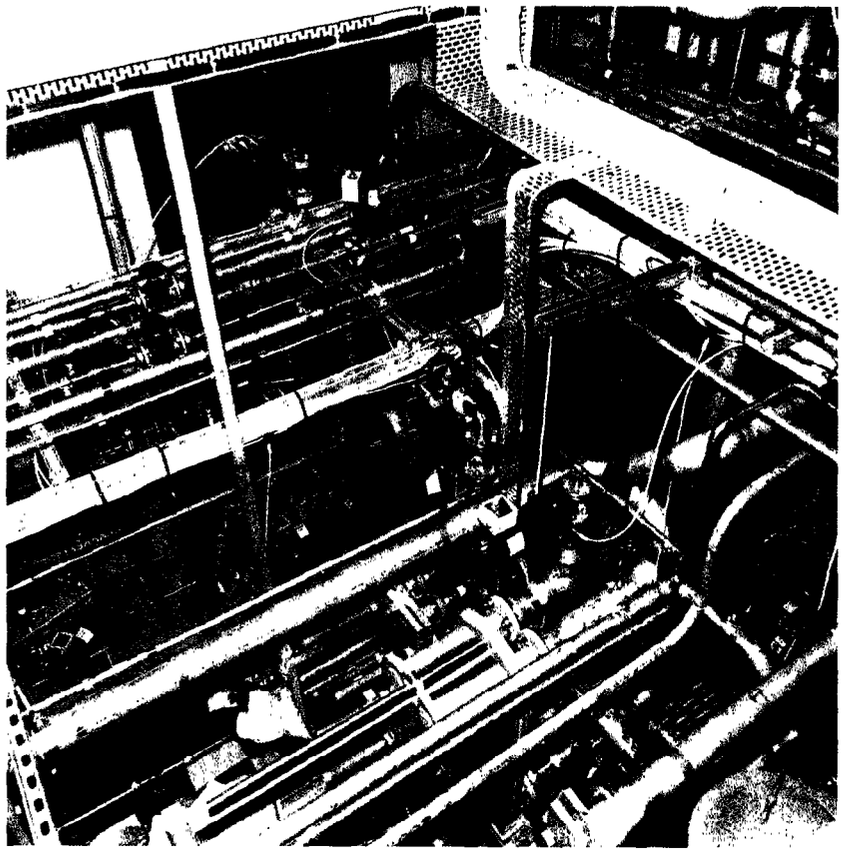

Figure 3. Detail of one Area of the Water Cooling Plant

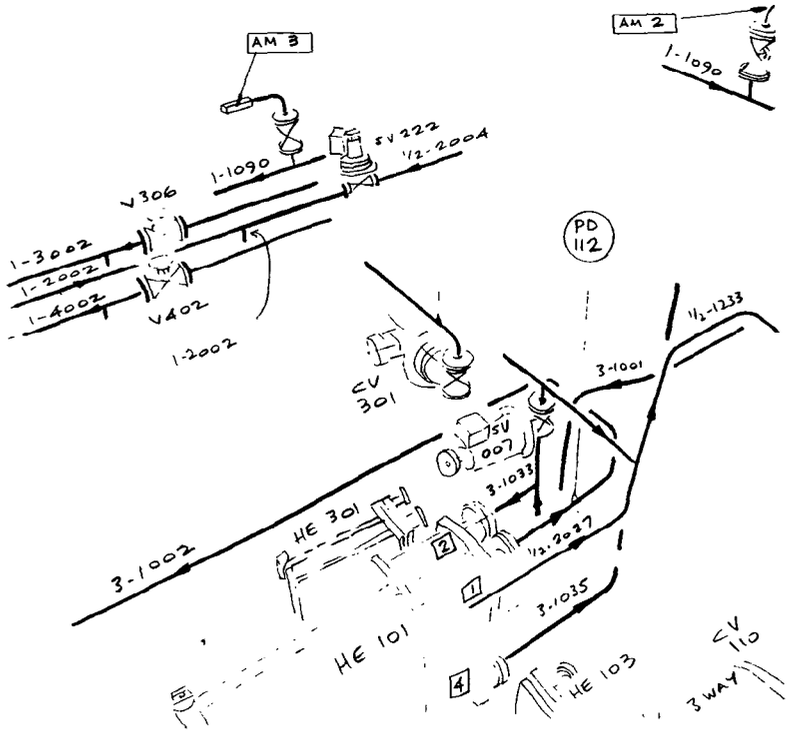

Figure 4. Overlay of Plant Photograph Defining Individual Components

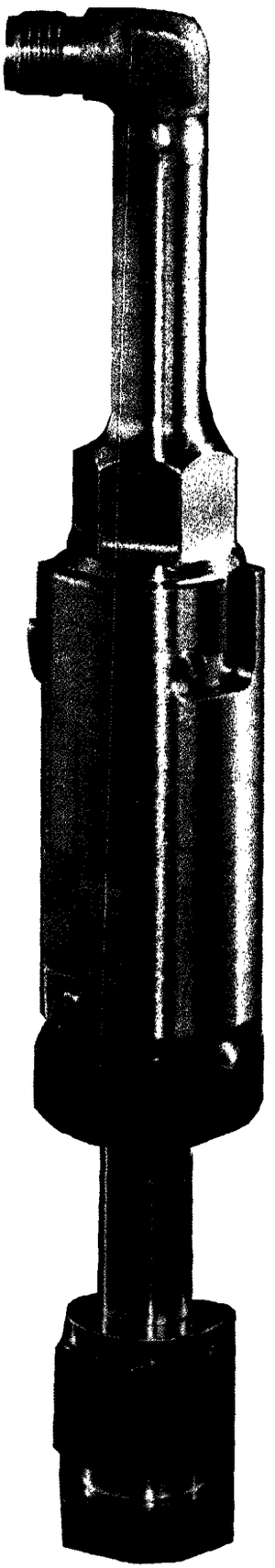

Figure 5. A Typical Bayonet Coupling for use in the Remote Handling Cell

Twelfth Meeting of the International Collaboration on Advanced Neutron Sources
24-28 May 1993, The Cosener's House, Abingdon, Oxfordshire, U.K.

LAHET Code System/CINDER'90 Validation Calculations and Comparison With Experimental Data

T. O. Brun, C. A. Beard, L. L. Daemen, E. J. Pitcher, G. J. Russell, and W. B. Wilson
Los Alamos National Laboratory
Los Alamos, NM U.S.A.

We use the Los Alamos LAHET Code System (LCS)/CINDER'90 suite of codes in a variety of spallation neutron source applications to predict neutronic performance and as a basis for making engineering decisions. We have broadened our usage of the suite from designing LANSCE and the next generation of spallation neutron sources for materials science and nuclear physics research to designing a target system for Accelerator Production of Tritium and Accelerator Transmutation of Waste. While designing, we continue to validate the LCS/CINDER'90 code suite against experimental data whenever possible. In the following, we discuss comparisons between calculations and measurements for: integral neutron yields from a bare-target of lead; fertile-to-fissile conversion yields for thorium and depleted uranium targets; dose rates from the LANSCE tungsten target; energy deposition in a variety of light and heavy materials; and neutron spectra from LANSCE water and liquid hydrogen moderators. The accuracy with which our calculations reproduce experimental results is an indication of our confidence in the validity of our design calculations.

Introduction

At Los Alamos, we have world-class Monte Carlo computational capability, which can be used for a variety of spallation-neutron-source design applications in environments with requisite computer hardware and experienced people to set up and run the codes and interpret the results. One part of our computational tool is based on the LANL version of the HETC Monte Carlo code for the transport of nucleons, pions, and muons, which was originally developed at ORNL [1]. Because of major modifications and additions made to the HETC code at LANL, our version of HETC has been renamed LAHET, and the system of codes based on LAHET (which we use in spallation neutron source design) is designated the LAHET Code System (LCS) [2]. The LCS is a sophisticated code system based on several sub-components, among which LAHET and the Los Alamos continuous energy neutron, photon, electron monte carlo code MCNP are the major players. CINDER'90 describes the temporal concentrations of nuclides depleted and produced in materials subject to spallation and neutron reactions [3].

In the following, we offer a brief description of the LCS and CINDER'90 codes and indicate the breadth of capabilities that this suite of codes puts at the users' disposal. We compare calculated predictions to measured values for a variety of "benchmark" experiments including

- integral neutron leakage from lead targets bombarded by protons with energies from 800 MeV to 3 GeV;
- fertile-to-fissile conversion yields for bare targets of thorium and depleted uranium bombarded by 800-MeV protons;
- neutron dose rates from the LANSCE tungsten target;
- energy deposition in a variety of target materials as a function of proton energy; and
- neutron spectra from the LANSCE water and liquid hydrogen moderators.

Calculational Methodology

Overview of the LAHET Code System

Group X–6 at LANL develops, maintains, and supports the LCS and distributes the code system worldwide. LAHET itself is used for the transport and interaction of nucleons, pions, and muons at high-energies (20 MeV<E<~4 GeV). LAHET uses the Bertini [4] or the ISABEL [5] model to describe the physics of the intranuclear cascade and uses the Dresner evaporation model [6] for the last phase of the nuclear interaction. (The Fermi breakup model [7] replaces the Dresner model for describing the evaporation process for light nuclei.) Group X–6 recently added a preequilibrium model [8] as an intermediate stage between the intranuclear phase and the evaporation phase; two fission models (Rutherford-Appleton [9] or ORNL [10]) complement the set of physics models LAHET uses.

The MCNP code (developed at LANL over the past 40 years or so) is a design-production code for low-energy neutron/photon/electron Monte Carlo transport [11]. The code is distributed and used internationally by nuclear-systems designers. The MCNP code is geared toward the transport of neutrons, photons, and electrons in matter and uses very detailed cross sections for several hundred isotopes to describe the interaction of neutrons and photons with matter down to thermal energies. MCNP makes use of ENDF/B–V cross section for neutron and photon reactions. We describe thermal neutron reactions using the free gas model or, when available, detailed scattering kernels, the $S(\alpha,\beta)$ treatment. For photons, the code takes coherent and incoherent scattering, fluorescent emission after photoelectric absorption, and various other physical processes into account. Contrary to multigroup codes, MCNP is a general-purpose, continuous-energy, generalized-geometry, and time-dependent Monte Carlo transport code. It is capable of handling arbitrarily complex three-dimensional geometries. The output MCNP produces ranges from neutron and gamma-ray fluxes and currents to energy deposition; from energy fluxes to gas production; and from radiation doses to criticality eigenvalues.

Particle transport in both LAHET and MCNP is based on Monte Carlo techniques. The philosophy used in the LAHET code is to treat all interactions by protons, pions, and muons within LAHET but to treat neutron interactions only above a cutoff energy, typically 20 MeV, at Los Alamos. Any low-energy (<20 MeV) neutron emerging from a reaction has its kinematic parameters recorded on a neutron file (NEUTP) for subsequent transport. For LAHET, a version of MCNP (called HMCNP) has been modified to accept the NEUTP file as an input source to complete the low-energy neutron transport using continuous-energy, ENDF/B-based, neutron cross-section libraries. Low-energy transported neutrons can participate in nuclear reactions and produce additional particles.

During a LAHET calculation, we record a large quantity of information on a separate file, which another piece of code, PHT—a photon source generating code—can subsequently analyze to produce a source for HMCNP. We can then execute the HMCNP phase of the calculation as a coupled neutron/photon transport problem. The photons originate either from the decay of neutral pions produced in the intranuclear cascade phase or by the deexcitation of residual nuclei after the evaporation phase. In a coupled neutron/photon problem, we merge the neutron file NEUTP and the gamma-ray file GAMTP (by the MRGNTP code in the LCS) to produce a combined neutron/photon file COMTP that describes the low-energy neutron source and high-energy-produced gamma-ray source for the entire system. We then use HMCNP to transport these neutrons and photons plus gamma rays produced from neutron-induced reactions below 20 MeV. In addition, both LAHET and HMCNP can write history files, called HISTP and HISTX, respectively, that contain a (nearly) complete description of events occurring during the computations. We postprocess the HISTP and HISTX files with another code (in the LCS suite of codes) called HTAPE. The edit options available with HTAPE include surface current and flux; cell-average neutron flux particle production spectra; residual mass production; mean excitation

energy; mass-energy balance, gas production and energy deposition by cell or material; pulse shape analysis of surface current; and global emission spectrum in polar and azimuthal bins.

The relationships of the various codes in the LCS and the files that carry information from one to another are shown in Figure 1. We use the LCS for a variety of applications including Spallation Neutron Source Design, Accelerator Production of Tritium (APT), and Accelerator Transmutation of Waste (ATW).

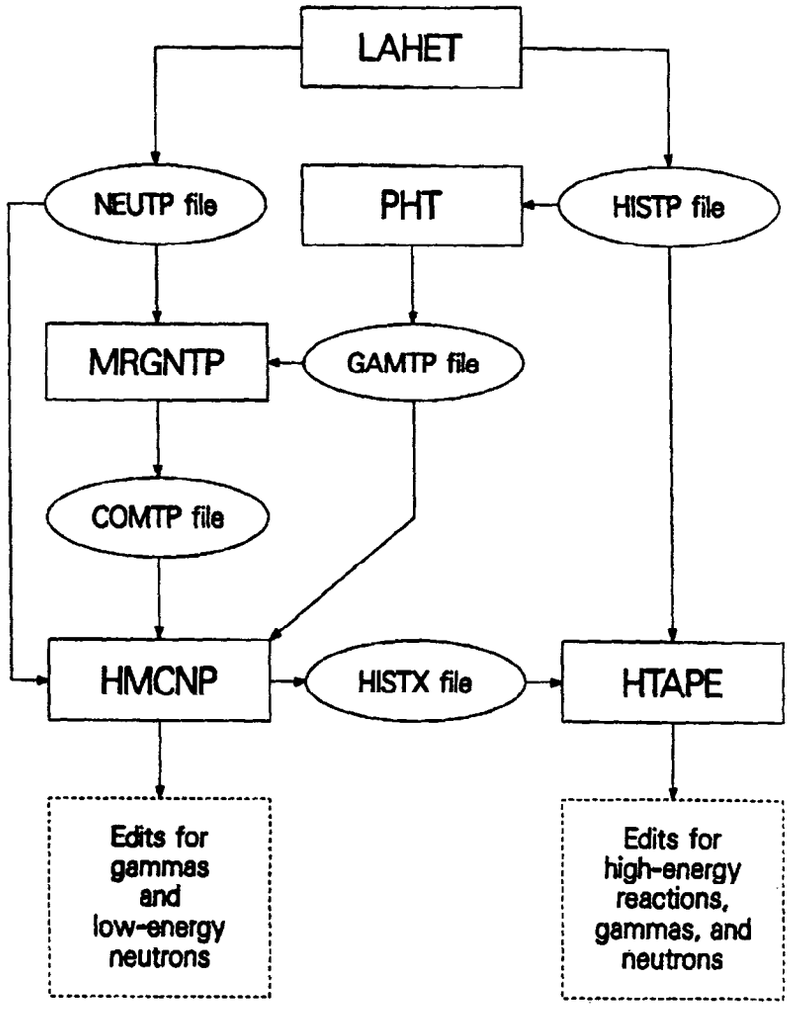

Fig. 1. LCS codes and data files.

Overview of CINDER'90

We describe the temporal concentrations of nuclides depleted and produced in materials subject to irradiation by a large set of coupled differential equations; and we determine each nuclide's concentration by a history of gains from neutron absorption reactions [spallation, fission, (n,γ), (n,2n), etc.] and radioactive decay of parent nuclides, as well as losses from its own decay and particle absorption. The solution for these nuclide concentrations was simplified in 1962 with the CINDER code, which resolved the complicated nuclide couplings into linear chains, each chain representing a unique path from nuclide to nuclide, resulting in small independent sets of

differential equations describing the rate of change of partial concentrations of nuclides in each chain. This reduces the solution of a large set of coupled differential equations to the solution of a number of small sets of differential equations, each characterized by a single generalized form. Because of the linear nature of the chain (a result of the Markov process), we may solve the generalized equations sequentially for the partial concentration of each linear nuclide in the chain. We then obtain nuclide concentrations by summing partial concentrations.

Calculations of radionuclide inventories in high-current, medium- and high-energy accelerator targets have required the development of a new inventory code (CINDER'90), evolved from earlier versions of CINDER [3, 12 through 16] and REAC, [17 through 20] and continuing development of cross-section and decay data. CINDER'90 uses these data with problem-specific spallation production and neutron-flux data calculated using LCS.

The CINDER'90 code differs from earlier CINDER versions in that earlier versions required the development of a library of transmutation chains before a calculation. Users selected chains of such libraries to follow transmutation paths that the user considered necessary and sufficient for the problem, and chains developed for one problem were not necessarily applicable to others. The CINDER'90 code uses a library of basic nuclear data to trace all possible transmutation paths, determining the partial concentration and associated activity of each linear nuclide as well as the integrated transmutation of each linear nuclide during a time increment. A linear nuclide's integrated transmutation, called the passerby, indicates the sum of subsequent partial concentrations in chains continuing from the nuclide. CINDER'90 examines each linear nuclide's partial concentration, activity, and passerby to determine whether a chain should be terminated relative to input significance criteria.

CINDER'90 accumulates nuclide concentrations and activities from linear nuclide properties as they are calculated. It then combines the postprocessing data with decay and neutron absorption data to obtain density (atoms/barn-cm and kg); activity (Ci/cm^3 and Ci); decay power (W/cm^3 and watts); macroscopic neutron absorption (cm^{-1}); and decay spectra properties listed by nuclide, element Z, and mass A. The code also tabulates major contributors ($\geq$0.1%) to mass, activity, decay power, and macroscopic absorption.

Many applications of these calculations are addressed with the direct utilization of the individual-nuclide and aggregate results—activity inventory, decay power, macroscopic neutron absorption, etc. Some applications require the tranport of the decay source γ's to obtain a desired response, such as dose or dose-equivalent rates.

Since target activity and nuclei inventory are very important for evaluating personnel safety risks and environmental impact of waste stream from a spallation target, the capability of predicting target activation and waste stream is extremely useful for target operations. Some applications require the transport of the decay source to obtain a desired response, such as dose or dose-equivalent rates. Transmutation calculation results are, of course, limited in accuracy by appropriate problem definition and by the validity of the nuclear data used in the calculation (i.e., neutron-absorption cross sections, decay constants for each nuclide transmutation path, and associated branching fractions to ground and isomeric states produced). Additional data describing the energy spectra and toxicity associated with the decay of radionuclides are required. The collection, calculation, and evaluation of the data are ongoing efforts currently involving dozens of scientists internationally. A detailed description of current CINDER'90 development activities is given in References 21 and 22.

Comparison between LCS Calculations and Experimental Data

The LAHET Code System is used worldwide for a variety of spallation neutron source applications. It is a premier design tool. As such, we must continue to evaluate the LCS against all types of basic and applied experimental data. The accuracy with which our calculations

reproduce experimental results is an indication of our confidence in the validity of our design calculations. We discuss below several comparisons we have made between LCS/CINDER'90 calculations and a variety of experimental data.

Bare-Target Integral Neutron Leakage

A simple test for the LAHET Code System consists of estimating neutron yields from simple targets. This particular test, although straightforward, is very important because it relates directly to the ability of LCS to reliably predict absolute neutron yields in the energy range of interest for spallation source applications. Other tests, even more stringent in nature, are described in subsequent sections.

Recent measurements by Vassilkov, et al. [23] in Dubna define an excellent test problem for LCS. They measured absolute neutron yields from a thick cylindrical lead target at various proton beam energies. More precisely, the target was a natural lead cylinder, 20 cm in diameter and 60 cm long. The JINR synchrocylotron in Dubna was used to produce a focused proton beam at various energies ranging from 990 to 3650 MeV. The proton beam characteristics are not known with great accuracy. In all our calculations, we assumed a circular, centered beam spot on target with the beam spot having a full width at half-maximum of 20 to 30 mm. In the experiment, absolute neutron yields were measured with threshold fission detectors.

Our simulations of the experiment with LAHET made use of the Bertini intranuclear cascade model followed by the application of a multistage preequilibrium model. This phase was in turn followed by the application of the Dresner evaporation model. The use and interfacing of these different models is not very crucial for total-yield calculations but could affect the details of the emission spectrum, for instance. Figure 2 shows the results produced by LCS, as well as the experimental data of Vassilkov, et al. Clearly, the agreement between the LCS results and the

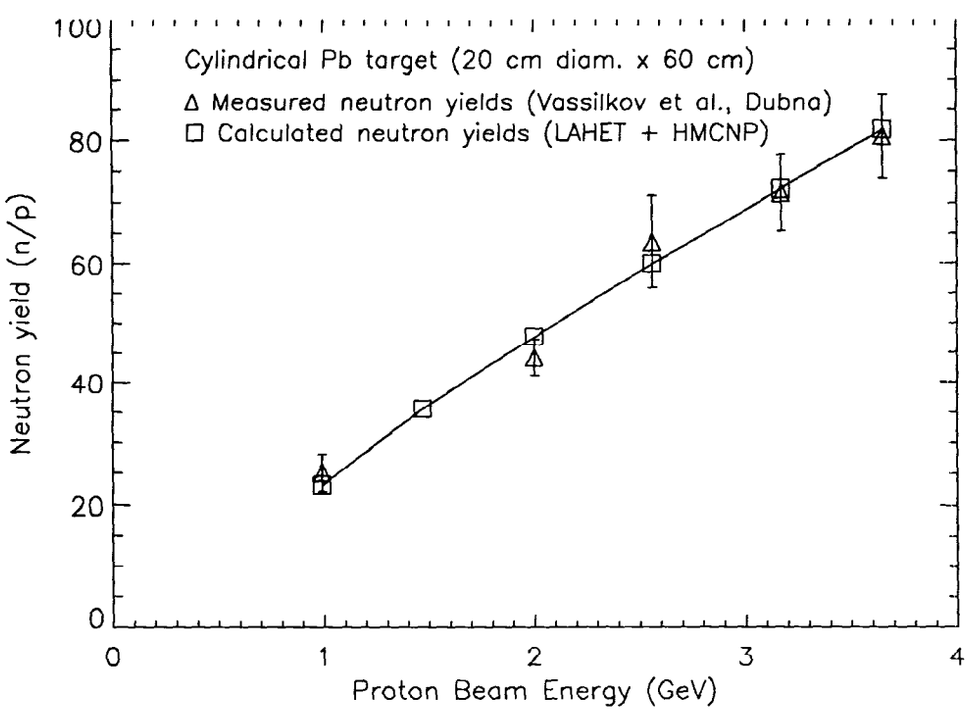

Fig. 2. Absolute neutron yields from a cylindrical (stopping length) Pb target 20 cm diam. × 60 cm long. Squares denote LCS results; triangles denote experimental results by Vassilkov, et al. The solid line is placed to guide the eye.

experimental data over the entire energy range is excellent, using models and parameters for those models that are the same as for our standard design calculations.

Los Alamos FERFICON Conversion Measurements

As part of the Fertile-to-Fissile Conversion program [24] at LANL, we measured the axial distributions of fissions and of fertile-to-fissile conversions in thick depleted uranium and thorium targets bombarded by 800-MeV protons. Table 1 gives the physical characteristics of the targets, and Fig. 3 illustrates the clustered target arrangements used in the experiments. We determined ^{239}Pu production from the amount of ^{239}Np formed and ^{233}U production from the amount of ^{233}Pa formed. We deduced the number of fissions from fission product mass-yield curves. We integrated the axial distributions to get the total number of conversions and fissions occurring in the targets. Table 2 shows measured conversion results compared to calculated predictions. The results are gratifying and indicate that the "source term" for low-energy (<20 MeV) neutron production is being handled well by LAHET. We are repeating the calculation with the latest model-values being used in LAHET.

Table 1 Physical Characteristics of the Targets

Material	Number of Rods	Density (g/cm^2)	Diameter (cm)	Length (cm)
Depleted Uranium*	37	19.04	19.70**	30.46
Thorium	19	11.38	18.28***	36.31

*0.251 wt% ^{235}U.

**Effective diameter of the clustered target ($D=d\sqrt{n}$) with an individual rod diameter of 3.239 cm.

***Effective diameter of the clustered target with an individual rod diameter if 4.194 cm.

Table 2 Comparison of Measured and Calculated Conversions for Thorium and Depleted Uranium Targets Bombarded by 800-MeV Protons

Target	Measured Conversion (atoms/protons)	Calculated Conversion (atoms/protons)
Thorium	1.25 ± 0.01	1.27 ± 0.01
Depleted Uranium	3.81 ± 0.01	3.88 ± 0.03

Russian Energy Deposition Measurements

Because we based our ^{3}He target/blanket system thermal-hydraulic design on calculated energy deposition, it is one of the most important pieces of information transferred to the engineering task. To estimate the accuracy of the LCS with regard to energy deposition, we compared LCS predictions with experimental results of Belyakov-Bodin, et al. [25-27]. We performed these comparisons for protons with energies of 800, 1000, and 1200 MeV on lead, bismuth, beryllium, carbon, aluminum, and uranium. The results for lead, bismuth, and uranium showed good agreement between the experimental results and the calculated values. For the lighter materials, however, the LCS inconsistently matched the experimental data.

The experimental apparatus used by Belyakov-Bodin, et al. consisted of 24 blocks, each 2.5 cm thick, 20 cm in diameter, and fabricated with internal thermocouples for temperature

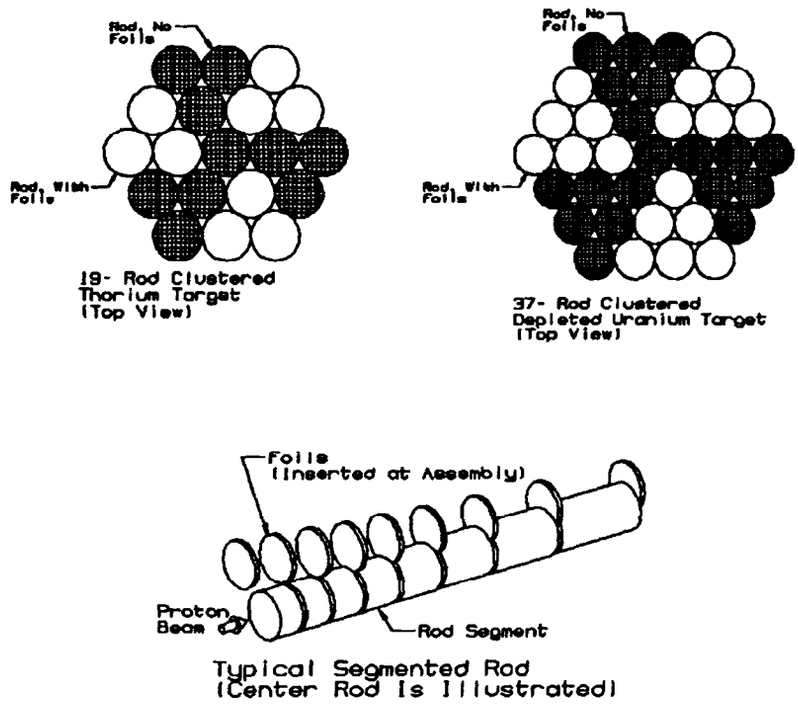

Fig. 3. Illustration of clustered target used in the conversion measurements, the location of the foils in an array, and the foil position within a rod.

measurements. Belyakov-Bodin used two techniques for fabricating the thermocouples into the target. The first, called the whole measuring block technique, involved inserting 12 measuring ends of differential thermocouples into a central disk and sealing them to derive the instantaneous temperature in 2 orthogonal directions at radii of 0.5, 1.3, 2.7, 5.0, and 9.4 cm. They converted temperature to energy deposition by an analytical solution to the linear-heat-transfer equation. Using a second method, named the cut measuring block technique, they divided the block into insulated rings with outer diameters of 2.0 cm, 5.0 cm, 10 cm, and 20 cm. They inserted three ends of differential thermocouples into each ring and directly measured the energy deposition as the integrated temperature variation of a chosen thermally insulated ring.

The LAHET/MCNP geometry, which we set up to model the experimental configuration, consists of a cylinder divided into a total of 48 cells, each 2.5 cm thick, divided into two radial regions ($r<5$ cm and 5 cm$<r<$10 cm), as shown in Fig. 4. We calculated the total energy deposition in each cell by adding the LAHET energy deposition, determined by an HTAPE analysis of the history tape (Type-6 edit with the contributions from nuclear excitation and π^0 decay subtracted), to the coupled neutron-photon energy deposition from MCNP (type 6 tally). To match the quantities determined in the experiment, we determined the total energy deposited to a radius of both 5 cm and 10 cm for each axial cell and divided these values by 2.5 cm to yield the units of energy/unit length. We assumed the axial locations for these values to be the axial midpoints of each cell.

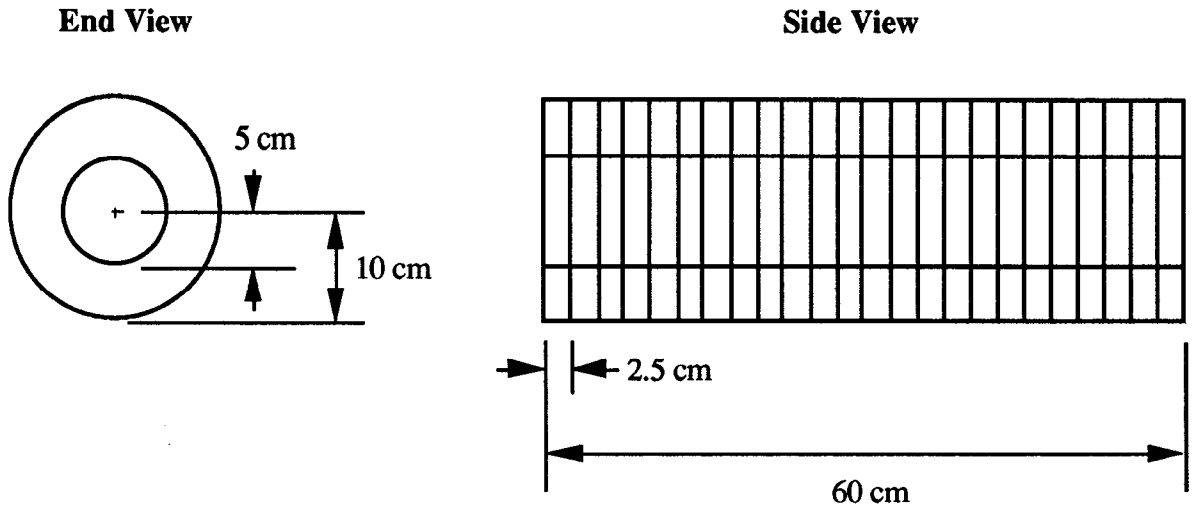

Fig. 4. LCS geometry for energy deposition calculations.

The proton beam distribution in the experiment was approximately Gaussian with FWHM= 2.4 cm that we modeled using a Gaussian distribution with a σ=1.0213 cm for the LAHET calculations. Belyakov-Bodin et al. stated that in their experiment, the beam had an inclination of 2°±1° and a beam divergence of 0.5°±0.2° for the lead and bismuth experiments. We did not account for these effects in the LAHET calculations.

We used the BERTINI nuclear cascade model for all of the LAHET calculations with many default input parameters. Exceptions included the implementation of the preequilibrium model, the inclusion of elastic scattering, and allowing for the transport of heavy charged particles (for which the BERTINI model only includes slowing down). Belyakov-Bodin, et al. did not give the densities of the materials used in the experiments; therefore, we assumed the densities were the natural densities of the pure materials and used the values shown in Table 3 in the LCS model.

In our study, we investigated both the experimental and LCS values for lead, bismuth, and uranium targets in respect to preselected proton energies and radii. We considered the total energy deposited over the entire length of the targets out to their 5-cm and 10-cm radii (Table 4). We investigated other targets, including beryllium, carbon, and aluminum targets, although we did not investigate their total energy deposition values. The relative errors using LAHET were approximately 0.04 and 0.05 using MCNP with regard to energy deposition in each cell, although some larger values resulted for the lower beam energies at large distances into the target. The relative error for total energy deposition using LAHET was 0.001.

We could not identify specific trends that encompass the results for all of the elements; the results are summarized below for each target material. However, we conclude that, for heavy

Table 3. Assumed Densities for the LCS Calculations

Material	Density (g/cm^3)
Beryllium	1.85
Carbon	1.60
Aluminum	2.70
Lead	11.30
Bismuth	9.80
Uranium	18.90

Table 4. Total Energy Deposited over Axial Length for Radii of 5 cm and 10 cm

Material	Proton Energy (MeV)	Radius (cm)	According to Exp. (MeV)	Quoted Experimental Error (%)	According to Calc. (MeV)	Deviation between Calc. and Exp. (%)*
Lead	800	5	380	7.0	475	25.0
Lead	800	10	460	10.0	523	13.7
Lead	1000	5	450	7.0	540	20.0
Lead	1000	10	520	10.0	608	16.9
Lead	1200	5	530	8.0	611	15.3
Lead	1200	10	600	11.0	687	14.5
Bismuth	800	5	430	4.0	469	9.1
Bismuth	800	10	520	6.0	525	1.0
Bismuth	1000	5	470	4.0	526	11.9
Bismuth	1000	10	570	6.0	600	5.3
Bismuth	1200	5	470	8.0	589	25.3
Bismuth	1200	10	570	10.0	672	17.9
Uranium	800	5	1090	4.4	1205	10.6
Uranium	800	10	1570	5.8	1622	3.3
Uranium	1000	5	1460	6.7	1497	2.5
Uranium	1000	10	2170	7.2	2083	-4.0
Uranium	1200	5	1700	3.5	1784	4.9
Uranium	1200	10	2530	4.1	2540	0.4

*Error defined as (Calc. Value - Exp. Value)/(Exp. Value).

materials, the LCS accurately predicts energy deposition values for both total deposition and deposition at specific locations within the targets with the total energy deposition being correct within approximately 20% and energy deposition values at specific locations being even more accurate. However, for lighter elements, the uncertainty in the predictions is greater. This is partly because the Bertini intranuclear cascade and Dresner evaporation models are statistical in nature and work better for heavier nuclei. Also, nuclear density is not modeled as well for light nuclei.

LANSCE Activation Measurement

To test the accuracy of the LCS coupled with CINDER'90 with regard to predicting residual nuclide activity due to long-term proton bombardment, we performed a comparison of calculational predictions and experimental residual dose rate measurements of the LANSCE target after removal for storage [28]. From November 1985 through October 1990, the LANSCE spallation target received an integrated beam current of about 0.25 amp-hour of 800-MeV protons with a documented operational history. Personnel removed the target on April 7, 1991, and measured gamma dose rates due to the decay of activation products in the target along the outside surface of the target and within the center of the flux trap.

The model we are using for the LCS calculations is a modification of the LANSCE target-moderator-reflector-shield geometry developed by H. G. Hughes and H. Lichtenstein [29–30]. The only modifications we made to this model are the alteration of the cell divisions within the regions of interest (upper tungsten target, lower tungsten target, beryllium, and steel around the central target region) (Fig. 5). We obtained the isotopic concentrations for the LAHET calculations by taking the MCNP material specifications in the Hughes/Lichtenstein model and modifying them when necessary by the isotopic abundances in the Chart of the Nuclides, Thirteenth Edition [31].

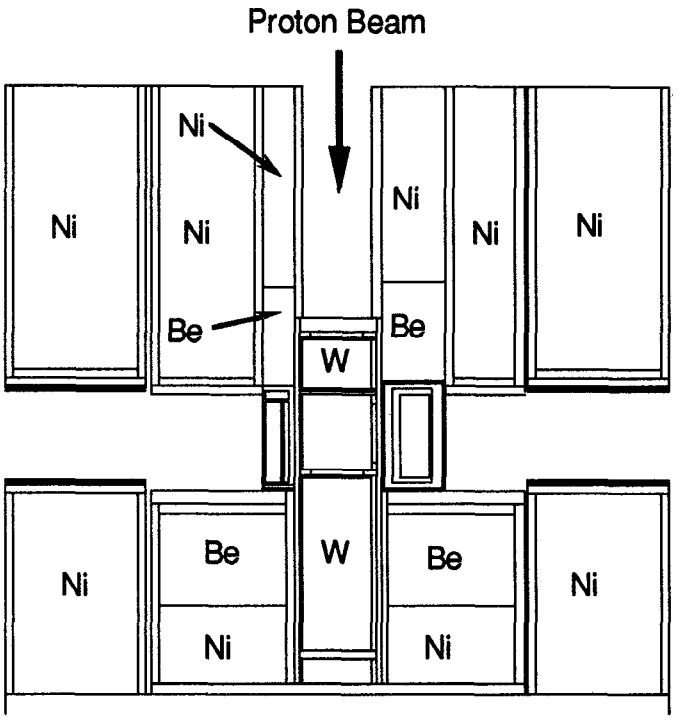

Fig. 5. LCS geometry for LANSCE activation calculations.

In the calculational procedure, we used the LCS to predict the spallation product production and nuclide destruction rates, as well as the flux levels generated in the LANSCE target and surrounding regions during operation. We then used this information to perform subsequent isotopic depletion calculations using CINDER'90. Using CINDER'90, we determined the gamma-source distribution corresponding to the time of the LANSCE target measurements and then inserted the source into the LCS model and transported it using MCNP to determine the dose rates at the measurement locations.

For the LAHET calculation, we ran 50,000 source protons. We then used HTAPE to determine the nuclide production, nuclide destruction, and gas production in the system. We then added the gas production results to the nuclide production files. We transported the resulting generated neutrons in MCNP and tallied the fluxes for the upper tungsten target, the lower tungsten target, and the beryllium and steel, which directly surround the target (everything inside the beryllium sheath). This material was removed as a unit-target-assembly when the measurements were taken.

For the subsequent gamma-transport calculations, we entered the gamma distributions predicted by CINDER'90 (refer to the target/blanket technical report) as homogeneous gamma sources, in the respective regions in which they were generated, by defining a volume for source-point sampling in MCNP and using cell rejection so that particles would only be initiated in the appropriate regions. We used one million source particles for each transport calculation, and we performed a separate calculation for each region so that we could determine the contribution from the various regions. We took point detector tallies in the center of the flux trap and 5.1 cm from the beryllium sheath in the center of the 12.22-cm-wide vertical face, located vertically 11.4, 22.4, and 33.4 cm from the center of the flux trap along the lower tungsten target, and 12.6, 29.5, and 46.4 cm from the center of the flux trap along the upper tungsten target. The tally results were normalized to the total gamma source for each individual region obtained from the CINDER'90 results. These gamma sources are given in Table 5.

Table 5. Decay Gamma-Source Strengths	
Region	**Source Strength (gammas/(s/cm^3))**
Upper Tungsten	4.871e+10
Lower Tungsten	9.680e+09
Beryllium	2.995e+05
Steel	2.095e+09

The greatest error in the LCS results when compared to the experimental values occurred at the bottom of the lower target assembly, where the LCS prediction was 2.4 times greater than the experimental measurement (Table 6). This was also the only value predicted by the LCS that was greater than the measured value. We conclude that the combination of the LCS and CINDER'90 predicted the resulting dose levels surrounding the target to within a factor of about 2, which is quite remarkable for this type of calculation. Furthermore, our problem had significant activation contributions from both spallation (predominantly in the tungsten) and parasitic neutron absorption (primarily in the steel) and illustrates the ability of LCS/CINDER'90 to accurately account for both mechanisms of radionuclide production. Finally, the material composition of the LANSCE target makes this measurement a strong validation for the use of LCS/CINDER'90 for APT activation calculations. Combining LCS with CINDER'90 results in a very useful package for the analysis of APT radionuclide waste streams and subsequent dose levels generated by the activated material.

Table 6. Decay Dose Values Calculated by LCS/CINDER'90 and Experimental Results

Location	LCS (kR/h)	Measurement (kR/h)	Ratio $\left(\frac{\text{LCC}}{\text{Meas.}}\right)$
Top of Upper Target Assembly	0.07	0.11	0.60
Middle of Upper Target Assembly	0.25	0.39	0.60
Bottom of Upper Target Assembly	0.93	1.30	0.71
Center of Flux Trap	2.21	3.40	0.66
Top of Lower Target Assembly	0.74	1.55	0.47
Middle of Lower Target Assembly	0.65	0.65	0.99
Bottom of Lower Target Assembly	0.46	0.19	2.42

LANSCE Neutron Spectra

Light water. We have measured the neutron flux from the high-intensity H_2O moderator at LANSCE from 0.025 eV to 100 keV [32], and compared the measured values with calculated predictions. The results are shown in Fig. 6 from 0.025 eV to 10 keV. The agreement between calculations and measurements is at the 20% level. This is a very stringent test of the LCS because of the complex geometry and composition of the LANSCE target-moderator-reflector-shield system. (We used the Hughes as-built mockup of the LANSCE target system [29] in our calculations, see Fig. 5.)

Liquid hydrogen. We have also measured the leakage current from the LANSCE liquid para-hydrogen moderator (temperature 20 K) as a function of energy in the range from 0.001 eV to 10 eV. Instead of using gold foil activation analysis, a calibrated low-efficiency neutron beam monitor was used in a time-of-flight experiment to determine the absolute neutron flux. The time distribution (or neutron pulse width) of the leakage current was also measured as a function of energy in range from 0.002 eV to 0.02 eV, but the results are not reported here. The raw data from the beam monitor are shown in Fig. 7.

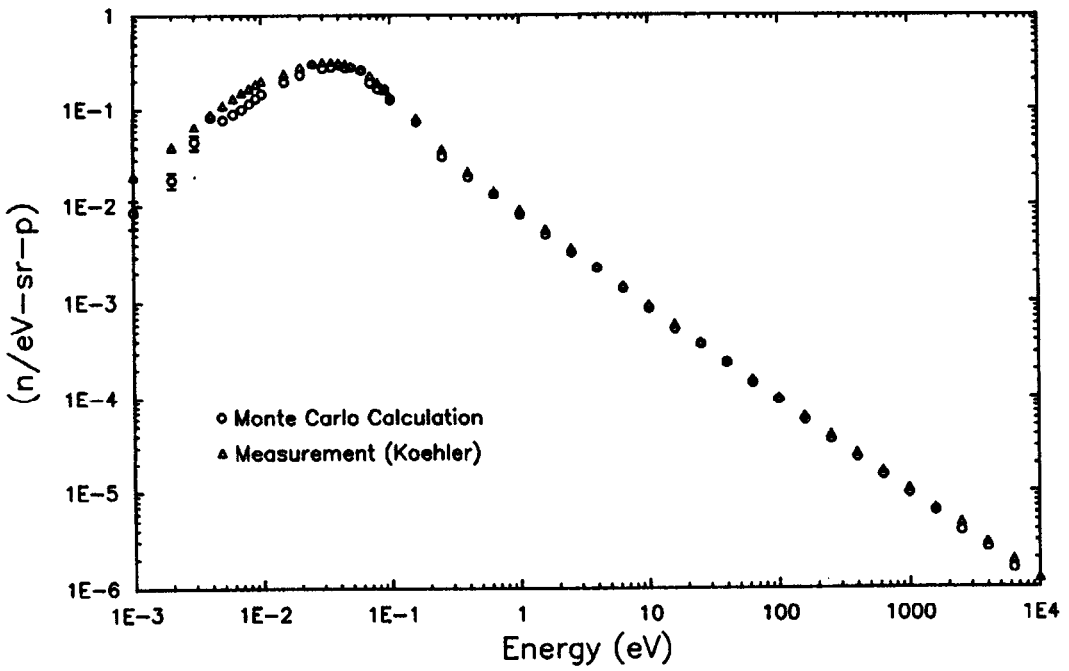

Fig. 6. Calculated and measured neutron energy spectra from the LANSCE high-intensity H_2O moderator.

The neutron counts per channel, N, in the monitor spectrum shown in Fig. 7 can be calculated from the neutron leakage current, $e\Phi(e)$, by

$$N = Conv(t) \times \left(e(t)\Phi(e(t))\right) \tag{1}$$

where e is the energy at time t, and $e\Phi(e)$ is the current in units of neutrons per steradian per proton per lethargy. The function, $Conv(t)$, contains all the experimental parameters (distance, collimation, channel width, efficiency, absorption, number of protons, etc.). In order to obtain an experimental analytical form for $e\Phi(e)$ useful for design, the raw monitor data (dashed line in Fig. 7) were fitted to a parameterized form of the function, $\Phi(e)$, expressed in units of neutrons/sr/p/eV. The current, $\Phi(e)$, is the sum of a thermal contribution and an epithermal contribution and is defined in equation 2.

$$\Phi(e) = \Phi_{th}(e) + \theta_{cut}(e)\Phi_0\Phi_{epi}(e)\exp\left(\frac{abs}{\sqrt{e}}\right) \tag{2}$$

where Φ_0 is an epithermal scale factor. The neutron absorption correction, abs, is included to simulate that the leakage at very low energy will be affected by absorption. The thermal contribution, Φ_{th}(e), is defined as a Maxwellian distribution

$$\Phi_{th}(e) = J\frac{e}{e_{th}^2}\exp\left(-\frac{e}{e_{th}}\right) \tag{3}$$

where J is the Maxwellian integral, and e_{th} is the Maxwellian temperature in eV. This latter

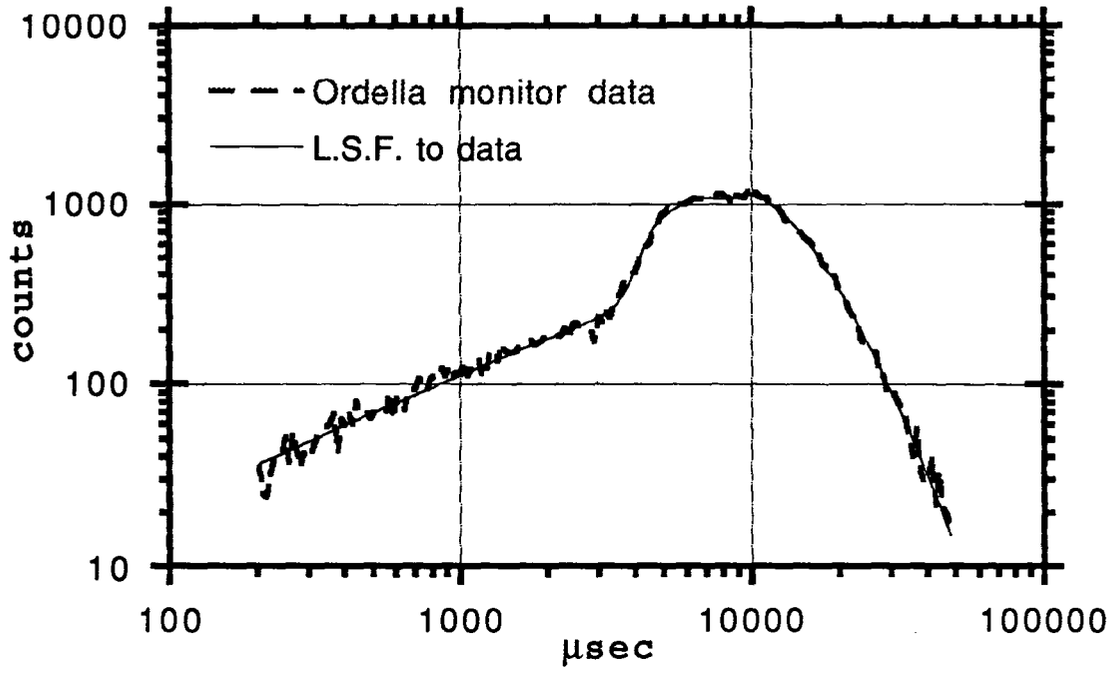

Fig. 7. Monitor spectrum.

parameter can be expected to be somewhat larger than the energy corresponding to 20 K, the temperature of the moderator. The epithermal contribution, $\Phi_{epi}(e)$, joins smoothly on to the thermal part at an energy, e_{cut}, that typically is a few times larger than e_{th}. The joining function, $\Theta_{cut}(e)$, is defined by equation 4. The parameter, β, controls, how rapid Θ_{cut} approaches one.

$$\Theta_{cut}(e) = 1 - \exp(-x)\left(1 + x + 0.5x^2\right)$$

where

$$x = \beta(e - e_{cut}) \qquad e \geq e_{cut} \tag{4}$$

$$x = 0 \qquad e < e_{cut}$$

The Maxwellian maximum for a moderator at 20K should show as a fairly narrow peak at 15000 μsec in the raw monitor data. That peak is clearly not present in Fig. 7. The monitor data show structure in the region between 4000 to 5000 μsec corresponding to neutron energies between 0.015 and 0.020 eV. Since this structure is at much higher energy than expected for both e_{th} and e_{cut}, this structure is associated with the epithermal part, Φ_{epi}, of the neutron leakage. The explanation for the structure is the large change in the neutron scattering cross section for the para-hydrogen molecule at 0.0152 eV (twice the rotational constant for the hydrogen molecule). For neutron energies below 0.0152 eV, only the elastic para-para transition that has a very small neutron cross section is possible. Above 0.0152 eV, the para-ortho transition with a much larger

cross section becomes allowed. The elastic and inelastic contributions to the neutron cross section for para-hydrogen have been calculated in the energy region from 0.0 to 0.04 eV, and the results are shown in Fig. 8. A more complete calculation of the cross section is described by McFarlane [33]. The large decrease in the cross section just below 0.015 eV gives rise to an increase in the leakage. Para-hydrogen becomes almost transparent to neutrons below 0.015 eV. To simulate this change, the traditional functional form for the epithermal part in equation 5 has been multiplied by a switch function, $\rho(e)$.

$$\Phi_{epi}(e) = \rho(e)\Phi_0\left(\frac{e_0}{e}\right)^{1-\alpha} \tag{5}$$

where e_0 is 1 eV. Since the epithermal flux is very nearly inversely proportional to e, the parameter, α, is expected to be small. The switch function, $\rho(e)$, is defined by equation 6.

$$\begin{aligned} &\rho(e) = 1 + \delta_\rho \exp(-x)\left(1 + x + 0.5x^2\right) \\ &\quad \text{where} \\ &\quad x = \gamma\left(e - e_\rho\right) \qquad e \geq e_\rho \\ &\quad x = 0 \qquad\qquad e < e_\rho \end{aligned} \tag{6}$$

where e_ρ is equal to 0.0152 eV, and γ and δ_ρ are parameters. The monitor counts, N, were fitted by a least squares fitting procedure to the neutron leakage current, $\Phi(e)$, defined by equations 2 through 6. The results for the least squares analysis are given in Table 7.

We are repeating the calculations of the neutron spectra for both the light water and liquid hydrogen moderators using: the most recent LCS model parameters; the inclusion of a proton beam

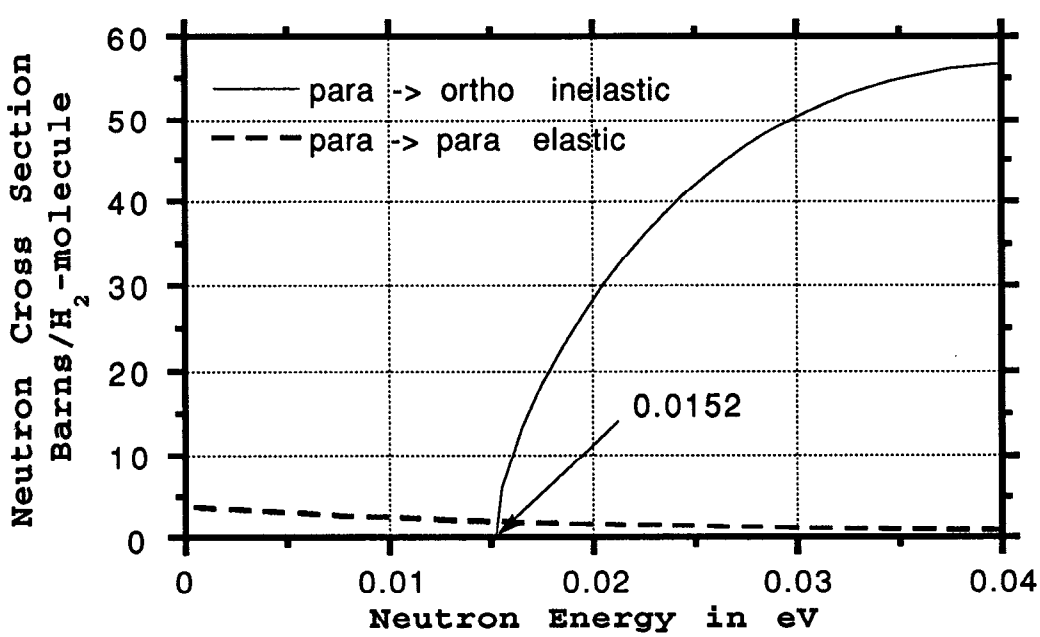

Fig. 8. Calculated hydrogen cross sections.

window in our Monte Carlo simulation; more realistic proton beam profiles; a small addition of ortho-hydrogen; and better statistics. For light water, we use the scattering kernel provided with MCNP, Ref. 11. For liquid hydrogen, we use the scattering kernels for ortho- and para-hydrogen as described by MacFarlane [33].

Figure 9 shows a comparison between the fit to the experimental data and the LCS-calculated neutron beam leakage. The disparity between the calculations and experiment may, in part, be due to the following calculational assumptions and deficiencies:

- the calculation was done for pure para-hydrogen whereas some ortho-hydrogen is present;
- the Monte Carlo computation was not performed with sufficient source particles to yield a small relative error for all energy bins;
- the effects of the proton beam window were not included in the model geometry;
- an "ideal" proton beam profile was used in the calculation, rather than a realistic profile; and
- there may be shortcomings in the scattering kernels with regard to the transition to a $1/E$ spectrum.

The calculations are being redone for both the water and hydrogen moderators with the goal of addressing many of these deficiencies.

Table 7. Parameters for the para-hydrogen moderator leakage current

Maxwellian integral	$J = 0.0101$ n/sr/p
Maxwellian temperature	$e_{th} = 0.00256$ eV
Epithermal scale factor Φ_0 = Leakage current at $E_0 = 1$ eV	$\Phi_0 = 0.00457$ n/sr/p/eV
Epithermal leakage parameter	$\alpha = 0.141$
Parameters for joining function Θ_{cut}	$e_{cut} = 0.00436$ eV $\beta = 645$ eV^{-1}
Parameters for switch function ρ	$\delta_\rho = 1.34$ $\gamma = 358$ eV^{-1} $\varepsilon_\rho = 0.0152$ eV (fixed)
Absorption correction	$abs = 0.0169$
Goodness of fit	$\chi^2 = 237$ Number of points = 186

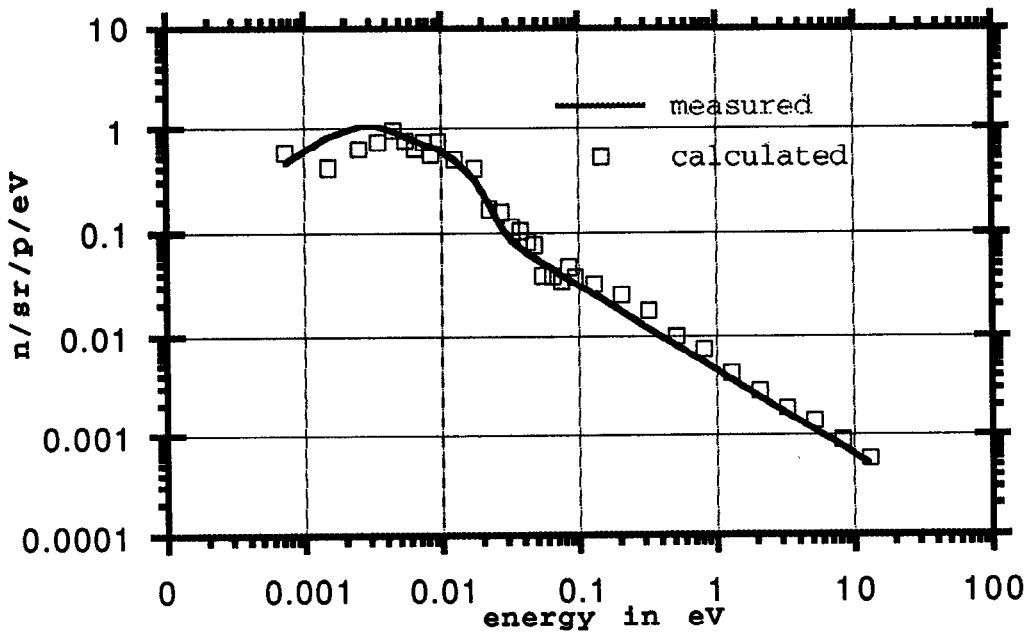

Fig. 9. Comparison of the fit to the measured data and the LCS calculation for the liquid hydrogen moderator.

References

1. Radiation Shielding Information Center, "HETC Monte Carlo High-Energy Nucleon-Meson Transport Code," Oak Ridge National Laboratory report CCC–178 (August 1977).

2. R. E. Prael and H. Lichtenstein, "User Guide to LCS: The LAHET Code System," Los Alamos National Laboratory report LA–UR–89–3014 (September 1989).

3. T. R. England, "CINDER—A One-Point Depletion and Fission Product Program," Bettis Atomic Power Laboratory report WAPD–TM–334 (August 1962, Rev. June 1964).

4. H. W. Bertini, *Phys. Rev.* **188**, 1711 (1969).

5. Y. Yariv and Z. Fraenkel, *Phys. Rev. C* **20**, 2227 (1979).

6. L. Dresner, "EVAP—A Fortran Program for Calculating the Evaporation of Various Particles from Excited Compound Nuclei," Oak Ridge National Laboratory report ORNL–TM–96 (April 1962).

7. K. Chen, et al., *Phys Rev.* **166**, 949 (1968).

8. R. E. Prael and M. Bozoian, "Adaptation of the Multistage Preequilibrium Model for the Monte Carlo Method (I)," Los Alamos National Laboratory report LA–UR–88–3238 (September 1988); R. E. Prael and M. Bozoian, "Adaptation of the Multistage

Preequilibrium Model for the Monte Carlo Method (II),", Los Alamos National Laboratory (to be published).

9. F. Atchison, "Spallation and Fission in Heavy Metal Nuclei under Medium Energy Proton Bombardment," in *Targets for Neutron Beam Spallation Sources*, Jül–Conf–34, Kernforschungsanlage Jülich GmbH (June 1980).

10. J. Barish, T. A. Gabriel, F. S. Alsmiller, and R. G. Alsmiller, Jr., "HET-FIS High-Energy Nucleon-Meson Transport Code with Fission," Oak Ridge National Laboratory report ORNL/TM–7882 (July 1981).

11. J. F. Briesmeister, Ed., "MCNP — A General Monter Carlo Code for Neutron and Photon Transport," Los Alamos National Laboratory report LA–7396–M, Rev. 2 (September 1986).

12. T. R. England, R. Wilczynski, and N. L. Whittemore, "CINDER-7: An Interim Users Report," Los Alamos Scientific Laboratory report LA–5885–MS (April 1975).

13. T. R. England, W. B. Wilson, and M. G. Stamatelatos, "Fission Product Data for Thermal Reactors, Part 1: A Data Set for EPRI–CINDER Using ENDF/B–IV," Los Alamos Scientific Laboratory report LA–6745–MS (December 1976).

14. T. R. England, W. B. Wilson, and M. G. Stamatelatos, "Fission Product Data for Thermal Reactors, Part 2: User Manual for EPRI-CINDER Code and Data," Los Alamos Scientific Laboratory report LA–6746–MS (December 1976).

15. W. B. Wilson, T. R. England, R. J. LaBauve, M. E. Battat, D. E. Wessol, and R. T. Perry, "Status of CINDER and ENDF/B–V Based Libraries for Transmutation Calculations," Proc. Int. Conf. Nuclear Waste Transmutation, Austin, Texas, July 22-24, 1980, p. 673 (March 1981).

16. W. B. Wilson, T. R. England, R. J. LaBauve, and D. C. George, "CINDER-3: Depletion Code for Class VI Computer," Transactions of the American Nuclear Society **46**, 724 (1984).

17. F. M. Mann, "Transmutation of Alloys in MFE Facilities as Calculated by REAC," Hanford Engineering Development Laboratory report HEDL–TME 81–37 (August 1982).

18. F. M. Mann, "REAC-2: A Users Manual and Code Description," Westinghouse Hanford Company report WHC–EP–0282 (December 1989).

19. F. M. Mann, D. E. Lessor, and J. S. Pintler, "REAC Nuclear Data Libraries," Radiation Effects **92**, 207 (1986).

20. F. M. Mann, "Status of Dosimetry and Activation Data," Proceedings of the International Conference on Nuclear Data for Science and Technology, Mito, Japan, May 30-June 3, 1988, p. 1013 (1988).

21. W. B. Wilson and T. R. England, "Nuclear Data Needs for Studies of Accelerator Induced Neutron Transmutation of Nuclear Waste," Proceedings of the Specialists' Meeting on Fission Products and Nuclear Data, May 25–27, 1992, JAERI, Tokai, Japan; organization for Economic Cooperation and Development Nuclear Energy Agency report NEA/NSC/DOC(92)9, pp. 475–481.

22. P. G. Young and W. B. Wilson, "Nuclear Data Requirements for Transmutation," presentation, American Chemical Society, Division of Nuclear Chemistry and Technology Meeting, Denver, Col., March 29, 1993. Los Alamos National Laboratory reports LA–UR–93–994 and –1132.

23. Vassilkov, et al., in Proceeding of the Eleventh Meeting of the International Collaboration on Advanced Neutron Sources, (ICANS–XI), M. Misawa, Ed. (National Laboratory for High-Energy Physics, Tsukuba, 1991), Vol. 1, pp. 340, 612.

24. J. S. Gilmore, G. J. Russell, H. Robinson, and R. E. Prael, "Fertile-to-Fissile and Fission Measurements for Depleted Uranium and Thorium Bombarded by 800-MeV Protons," Nuclear Science and Engineering **99**, 41–52 (1988).

25. V. I. Belyakov-Bodin, et al., "Calorimetric Measurements and Monte Carlo Analyses of Medium-Energy Protons Bombarding Lead and Bismuth Targets," Nuclear Instruments and Methods in Physics Research **A295**, 140–146 (1990).

26. V. I. Belyakov-Bodin, et al., "Calorimetric Measurements and Monte Carlo Analyses of Medium-Energy Protons Bombarding Uranium Targets," Atomic Energy **70**, 339–345 (1991).

27. V. I. Belyakov-Bodin, et al., "Calorimetric Measurements of Medium-Energy Protons Bombarding Beryllium, Carbon, and Aluminum Targets," Nuclear Instruments and Methods in Physics Research **A314**, 508–513 (1992).

28. G. J. Russell, "Predicted LANSCE Target Activity," Los Alamos National Laboratory memorandum LANSCE–92–746, to R. Pynn (October 23, 1992).

29. H. G. Hughes, III, "Monte Carlo Simulation of the LANSCE Target/Moderator/Reflector/Shield Geometry," Advanced Neutron Sources 1988, Proceedings of the 10th Meeting of the International Collaboration of Advanced Neutron Sources (ICANS X) held at Los Alamos, October 3–7, 1988. (IOP Publishing Ltd. Bristol, England 1989).

30. H. G. Hughes and H. L. Lichtenstein, "Enhanced Model of LANSCE Upper Target," Los Alamos National Laboratory memorandum X–6:HGH:HL–92–385, to G. J. Russell (June 11, 1992).

31. *Chart of the Nuclides, Thirteenth Edition*, General Electric Company, Nuclear Energy Operations, San Jose, California (1984).

32. P. E. Koehler, "Measurement of the LANSCE Neutron Flux from 0.025 eV to 100 keV," Los Alamos National Laboratory Report LA–UR–90–290 (1990).

33. R. E. MacFarlane, "Cold Moderator Scattering Kernels," in *Proceedings of the International Workshop on Cold Neutron Sources*, Los Alamos National Laboratory report LA-12146-C (August 1991), pp. 193-216.

INCLUSION OF PREEQUILIBRIUM CALCULATION INTO HIGH ENERGY TRANSPORT CODE

K.ISHIBASHI, H.TAKADA,* Y.YOSHIZAWA,** N.MATSUFUJI, T.NAKAMOTO, Y.WAKUTA and Y.NAKAHARA*
Department of Nuclear Engineering, Kyushu University
Hakozaki, Fukuoka 812, Japan
*Japan Atomic Energy Research Institute
Tokai-mura, Ibaraki 319-11, Japan
**Mitsubishi Research Institute, Inc.
Ote-machi, Chiyoda-ku, Tokyo, 100 Japan

ABSTRACT

The High Energy Transport Code (HETC) has been widely used for engineering purposes. We incorporate the preequilibrium calculation into the HETC with a smooth connection to the cascade process. The preequilibrium process is introduced to retain a clear physical meaning both in the connection method and in the initial number of particles and holes. The calculation results are compared with the experimental preequilibrium spectra which have been decomposed from experimental data by the moving source model. Computation results successfully reproduce the backward neutron spectra particularly for incident proton energies below about 100MeV.

I. INTRODUCTION

A great number of energetic neutrons are produced through the spallation reaction when a target is bombarded by high energy protons of about 1 GeV. The reaction is useful for facilities providing the intense spallation neutron sources or transmuting long-lived radioactive wastes[1]. Some computer codes have been developed for designing these spallation facilities. Nucleon Meson Transport Code (NMTC)[2,3] and High Energy Transport Code (HETC)[4-6] are famous as Monte-Carlo particle-transport codes in analyzing the neutron behavior in thick target systems. The codes consist of two types of calculations, i.e. nuclear reaction and interatomic particle transport. The present paper deals only with the nuclear reaction calculation and accordingly concerns itself with the experimental data taken by the use of thin targets.

For performing the calculation of nuclear reactions, the above transport codes make use of the same program MECC-7, which was originally developed by Bertini[7]. The code MECC-7 utilizes a Monte-Carlo algorithm, and the nuclear calculation is based on the intranuclear-cascade evaporation model, where the computation is divided into two steps of intranuclear-cascade and evaporation processes. This model is called a two-step model in the present study. The program to be used in this study is HETC-KFA2(contained in HERMES[8]) which is the modified version of MECC-7. The major modification was incorporation of the high-energy fission, and the detailed table for level-density parameter.

The two-step model has usually been applied to the reaction for the incident proton energies of 20 to 3000 MeV. This model reproduces the overall characteristics of the nuclear reaction fairly well[9]. Nevertheless, the discrepancy in neutron spectra appears at incident proton energies below or about 113 MeV[10], particularly in the backward direction. The existence of the preequilibrium effects in the neutron spectra has been pointed out by Tsukada and Nakahara[11]. The inclusion of the preequilibrium process is considered to be useful in reproducing the neutron spectra. Nakahara and Nishida[12] were interested in the introduction of the preequilibrium process for describing the spallation reaction, and described the Monte Carlo algorithm for the exciton model calculation. The preequilibrium calculation coupled with HETC was preliminarily attempted at Kyushu University- JAERI[13], and also preformed by Prael at LANL[14].

Experimental spallation neutron data have recently been systematically analyzed[15] by a moving source model, and decomposed into three spectra of the cascade, preequilibrium and evaporation processes. In this paper, we compare the preequilibrium calculation results with the decomposed preequilibrium spectra, and adjust preequilibrium parameters to reproduce the preequilibrium spectra. The present code includes the preequilibrium process into the conventional cascade-evaporation calculation, and constitutes a three-step precedure as follows:

First, the cascade calculation is performed with the standard routines, and is terminated by the use of a simple probability function. Subsequently, the exciton-model calculation is executed by taking into account the exact number of excitons as generated in the preceding cascade process. The evaporation process is then conducted as a last step. The present three-step model is applied to the reaction of incident proton energies down to 25 MeV in this study.

II. THREE STEP MODEL

1. Cascade calculation

The cascade calculation in the present study is made on the basis of the Monte-Carlo program code HETC-KFA2, where the intranuclear-cascade model is the same as that of the code originally developed by Bertini[7]. The model assumes that the high-energy incident particle is scattered by intranuclear nucleons in a binary collision. Additional collisions are induced in series by the scattered or recoiled particles, resulting in formation of a collision cascade in the nucleus. The cross section measured for free particles is assumed to be applicable to each collision during the cascade development. The momentum of the intranuclear nucleons is sampled according to the degenerated Fermi distribution with zero temperature. The Monte-Carlo calculation of each cascade history is terminated on conditions where particles are emitted from the nucleus or their kinetic energy falls below a specified value. This value is defined as the sum of a cut-off energy E_c and the nuclear potential depth at the particle location. In the standard setting, E_c is 0 MeV for neutrons, whereas for protons it is the classical Coulomb barrier height.

The original termination of the cascade calculation is modified in the present study. The experimental neutron emission data were decomposed[11,15] into the processes of cascade, preequilibrium and evaporation components. For emission of neutrons possessing energies below about 30 MeV, neutrons originating from the cascade process contribute to the cross section to a very small extent[11]. To take this result into account, a probability density function $f(E_c)$ is introduced into the cascade calculation to suppress the emission cross section of the low-energy cascade neutrons. This function determines the cut-off energy E_c at terminating the calculation of each cascade history. The function is written by

$$f(E_c) = 2\, E_0^{-1}\, (1-E_c/E_0) \quad , \qquad (1)$$

where E_0 is an adjustable parameter. The value of E_c is then randomly chosen from 0 to E_0 according to Eq. (1). When the particle moving in the nucleus has a kinetic energy below the specified value dependent on the chosen quantity of E_c, the calculation for the particle is terminated. For protons, the cut-off energy E_c is sampled in the same way, but if the sampled value is below the Coulomb barrier height, it is substituted by the barrier energy.

The nuclear phenomenon arising near the end of the cascade process has not so far been elucidated in the proton-induced spallation reaction. As an approach to studying a physical indication of Eq. (1), a particle emission probability is calculated by assuming the applicability of the exciton model[16] to this phenomenon. The description is given in ref. 13. When the two-particle one-hole state is presumed together with the Kalbach constant of K= 500MeV^3, the results of the neutron emission probability are consistent with those deduced by Eq. (1) with E_0=40 MeV. The value of E_0=40 MeV is used in the following calculation. The termination method based on Eq. (1) is supposed to be some correction of the cascade model with regard to the kind of preequilibrium effect.

2. Preequilibrium calculation by a Monte Carlo algorithm

After the above cascade process, the calculation of the preequilibrium process is carried out as the second step. The exciton model is adopted in this process because of its simplicity in computation. The principle of the calculation is basically the same as that described by Gudima et al.[17] In the present study, the master equation is solved by a Monte Carlo algorithm[12]. The flow chart is shown in Fig. 1, where the symbols appearing there are summarized in Table 1. At the beginning of this process, such values of the nucleus as mass number A, atomic number Z, and excitation energy E are brought from the cascade calculation. For nuclear quantum state, neither the angular momentum nor the spin is considered in the preequilibrium and the further evaporation process.

Gudima et al. have assumed the state of two particles and one hole at the start of the preequilibrium process. At high incident energies, however, many particles and holes are already present after the cascade process. The number of these excitons often exceeds ten at an incident proton energy above a few hundred MeV. At the beginning of the preequilibrium calculation, we adopt the exact numbers of particles (p) and holes (h) as generated in the preceding cascade calculation. Computation is made to obtain probabilities for exciton-number increase λ_+, unchange λ_0, decrease λ_-, and particle emission Γj. The event to be encountered is chosen by a random sampling, and subsequently processed by a suited subroutine. For particle emission, both the kinetic energy T and the emission angle θ are random-sampled according to their probability density function. The Gudima formalism contains no adjustable parameter for evaluating the transition rates of λ_+, λ_0 and λ_-. We then multiplied the rates by an adjustable factor F of 2.5. The preequilibrium calculation is terminated when the number of excitons n=p+h exceeds the minimum of a termination value of 15 to 25 and the equilibrium value of $n_{eq}=(2gE)^{1/2}$.

For the angular distribution of neutron emission, Gudima et al. solved the master equation with consideration of the angular dependence. In this study, for simplicity of the calculation, the angular distribution of neutrons is obtained by an empirical method. Kalbach[18] showed the systematics for the angular distribution. We utilized the same function, i.e. combination of hyperbolic- sine and cosine, to reproduce the preequilibrium angular distribution. In our case, however, the angular distribution is almost isotropic and the value a of Kalbach was changed to 0.035a+0.05.

3. Evaporation calculation

After the preequilibrium process, the nuclei are left in a high excitation state. Either nucleons or light nuclei are emitted in the evaporation process as the third step. For choosing the type and energy of the emitted particles, the Weisskopf formula is used in computation. The formula requires the level density parameter for the calculation of the emission probabilities. The detailed compilation values of the level-density parameter[6,19] were used as the automatic choice of HETC-KFA2.

III. CALCULATION RESULTS

Typical calculational results by the present model are compared with those by the conventional two-step model in Fig. 2. The parameters in the calculation are summarized in Table 2. In this figure, the neutron spectra at 60 deg are plotted for incident protons of 113 MeV on lead. The spectra are shown for each process. Emission of the cascade neutrons with energies below 30 MeV is considerably suppressed in the three-step model in contrast to the case of the two-step one. As seen in the results of the three-step model, the preequilibrium process yields neutrons of energies dominantly up to 20 MeV, while the evaporation one produces those of a few to several MeV. The experimental neutron data for thin targets by 113 MeV protons[10] were decomposed into three components by the moving source model[15]. The decomposition is considered to be useful for detailed study of the preequilibrium process. The results for lead are shown in Figs. 3 to 5, and those for iron in Figs. 6 to 8. Marks indicate the decomposed experimental data, and lines stand for calculation results. The decomposed data are reproduced by the three-step calculation, with the exception of some underestimation of the evaporation component.

The experimental neutron spectra[10] are shown by marks in Fig. 9 for lead. The dashed lines represent the calculational results of the two-step model. The differences between the dashed lines and the experimental data are as follows: In the backward direction of 150 deg, the dashed line is appreciably lower than the experimental result in the region above 10 MeV. The experimental spectra at 30 and 60 deg at energies around 10 MeV are overestimated by the two-step calculation.

The computation results by the three-step model are shown by the solid lines in Fig. 9. In the direction of 150 deg, the solid line agrees with the experimental spectrum for the neutrons with energies especially above 10 MeV. This agreement originates from inclusion of the preequilibrium process. The solid lines coincide with the dashed ones at around 10 MeV at angles of 30 and 60 deg: The reduction of cascade neutron emission in this region is reasonably

compensated by the preequilibrium calculation, as deduced by Fig. 2. At a few to several MeV, the solid lines are slightly lower than the dashed ones. In spite of some disagreement of the cross section in the evaporation process, as a whole, it can be said that the solid lines reproduce the experimental data well, especially in the backward direction. The results for iron are shown in Fig. 10. The three-step calculation reproduces the experimental data mostly better than the two-step one.

The results for 25.5 MeV proton incident on lead[20] are shown in Fig. 11. The dashed lines by the two-step calculation appreciably underestimate the experimental cross section in the backward direction. The cascade calculation at such low incident energy tends to produce the forward-peak angular distribution that is not seen in the experimental data. Since the pre-equilibrium process shows more isotropic angular distribution than the cascade process, the backward neutron cross section is greatly improved by adoption of the preequilibrium calculation. For 256[21] and 800 MeV[9] proton incidence on lead, the results are shown in Figs. 12 and 13, respectively. The solid lines by the three-step model in Fig. 13 almost coincide with the dashed ones: The results of the present three-step calculation approaches those of the cascade evaporation model with increasing incident energy.

IV. CONCLUSION

The spallation reaction was calculated by the three-step model composed of the cascade, preequilibrium and evaporation processes. The cascade calculation was performed by counting the number of particles and holes, and was terminated by means of the simple probability function. In the second step of the preequilibrium process, the exciton-model calculation was made with the Monte-Carlo algorithm. The initial number of excitons was brought from the preceding cascade calculation. Parameters for the preequilibrium process were adjusted with reference to the preequilibrium spectra which had been derived from decomposing the experimental 113 MeV proton-incident data. The three-step calculation was made for the reaction induced by protons of 25 to 800 MeV on iron and lead. This model was particularly useful for reproducing the backward neutron spectra at incident proton energies around or below 100 MeV. At higher proton energies, the results of the present model approach those of the standard cascade-evaporation model.

ACKNOWLEDGMENTS

The authors gratefully acknowledge Dr. D. Filges of KFA and F. Atchison of PSI for supplying their versions of the HETC.

REFERENCES

(1) T.Nishida et al.: JAERI-M 90-025 (1990) 343.
(2) W.A.Coleman and T.W.ARMSTRONG: Nucl.Sci.Eng. 43 (1971) 353.
(3) Y.Nakahara and T.Tsutsui: JAERI-M 82-198 (1982).
(4) T.W.Armstrong et al.: Nucl.Sci Eng. 49 (1972) 82.
(5) F.Atchison: RL-81-006 (1981).
(6) D.Filges et al.: Phys. Rev. C36 (1987) 1988.
(7) H.W.Bertini: Phys. Rev. C6 (1973) 631.
(8) P.Cloth et al.: "HERMES (High Energy Radiation Monte Carlo Elaborate System, " KFA-IRE-E AN/12/88 1988".
(9) W.Amian et al.: Nucl.Sci.Eng. 112 (1992) 78.
(10) M.M.Meier et al.: Nucl. Sci. Eng. 102 (1989) 310.
(11) K.Tsukada, Y.Nakahara: Atomkernenerg. • Kerntech. 44 (1984) 186.
(12) Y.Nakahara, T.Nishida: JAERI-M 86-074 (1986).
(13) N.Ishibashi et al.: JAERI-M 90-025 (1990) 362.
(14) R.E.Prael: "Model Cross Section Calculations Using LAHET", presented at Symposium on Nuclear Data Evaluation Methodology, October 1992, BNL.
(15) K.Ishibashi et al.: J.Nucl.Sci.Technol. 29 (1992) 499.
(16) C.C.Kalbach: Nucl. Phys. A210 (1973) 590.
(17) K.K Gudima et al: Nucl.Phys. A401, (1983) 329.
(18) C.Kalbach: Phys. Rev. C37 (1988) 2350.
(19) H.Baba et al: Nucl.Phys. A159, (1970) 625.

(20) K.Harder et al.: Hamburg University HH87-01 (1987)
(21) M.M.Meier et al.: Nucl.Sci.Eng. 104 (1990) 339.

Table 1 Nomenclature of the symbols in Fig. 1 for the exciton model calculation.

A	:	Mass number
Z	:	Atomic number
E	:	Excitation energy (MeV)
p	:	Number of particles
h	:	Number of holes
n	:	Total number of excitons
n_{eq}	:	Equilibrium number of excitons
g	:	Single particle level density (MeV^{-1})
λ_+	:	Interaction rate of increase in the number of excitons (s^{-1})
λ_0	:	Interaction rate of unchange in the number of excitons (s^{-1})
λ_-	:	Interaction rate of decrease in the number of excitons (s^{-1})
Γj	:	Emission rate of particle j integrated over energy (s^{-1})
$\Gamma j(T)$	:	Emission rate of particle j per kinetic energy ($s^{-1}MeV^{-1}$)
r	:	Random number
T	:	Kinetic energy of particle (MeV)
B_j	:	Binding energy of particle (MeV)
θ	:	Emission angle of particle (deg)
$\Theta n(T,\theta)$	:	Probability density function for neutron-emission angular-distribution (deg^{-1})

Table 2 Summary of the major parameters used in the two- and three-step models.

Process	Two-step model	Three-step model
Cascade		
Cut-off energy (E_c)	Neutron: 0 MeV Proton: Half of potential barrier	Eq.(1) Sampling by Eq.(1) with constraint of the left energy as the lowest.
Preequilibrium		
Emission probability	None	According to Gudima et al.[17] with correction of $\lambda_+ / {}_0 / {}_-$
Angular distribution	None	According to Kalbach[18] with correction of a
Evaporation		
Level density	Compiled results in HETC/KFA [6]	

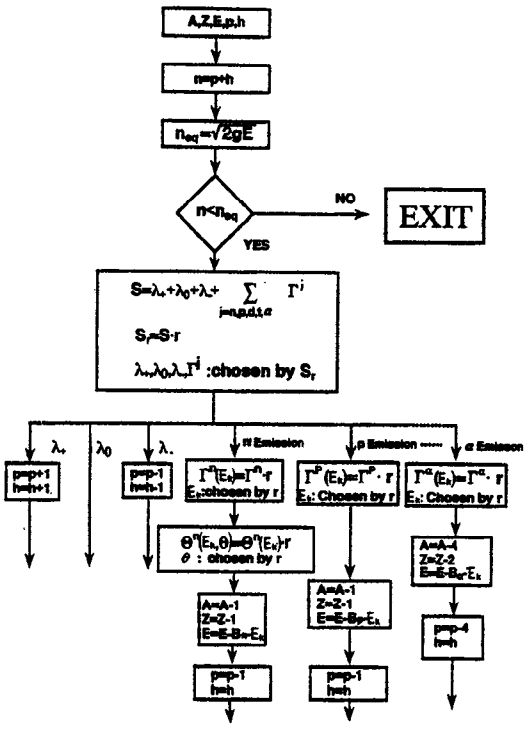

Fig.1 Flow chart for solving the master equation of the exciton model. The symbols are explained in Table 1.

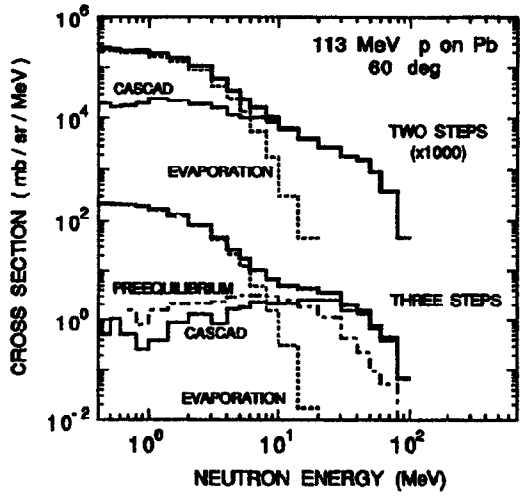

Fig.2 Decomposed neutron spectra obtained in the two- and three-step calculations.

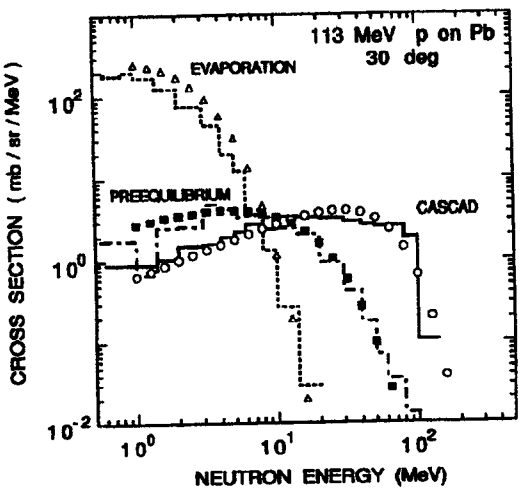

Fig.3 Decomposed neutron spectra for the 113MeV proton incidence on lead at 30deg. The marks stand for the experimental spectra analyzed by the moving source model.

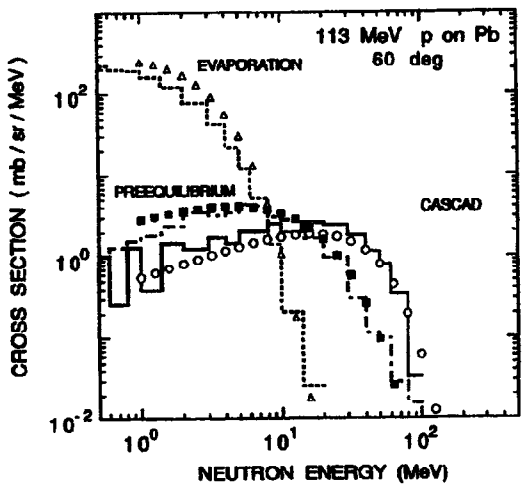

Fig.4 Decomposed neutron spectra for lead at 60deg.

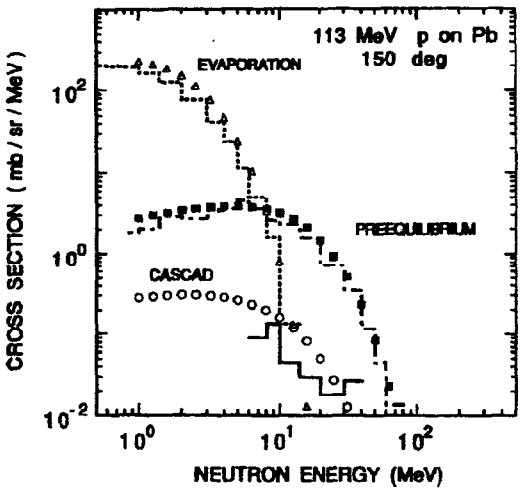

Fig.5 Decomposed neutron spectra for lead at 150deg.

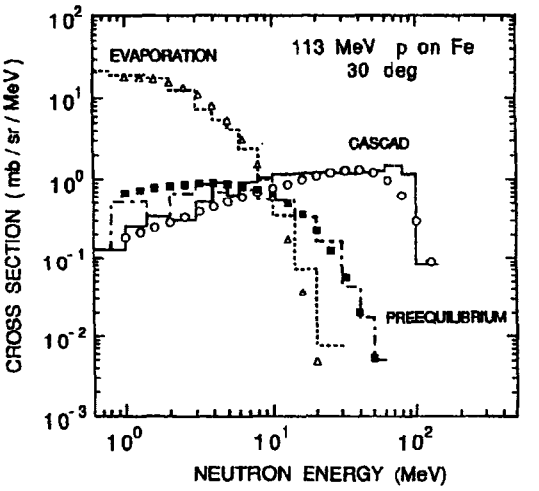

Fig.6 Decomposed neutron spectra for iron at 30deg.

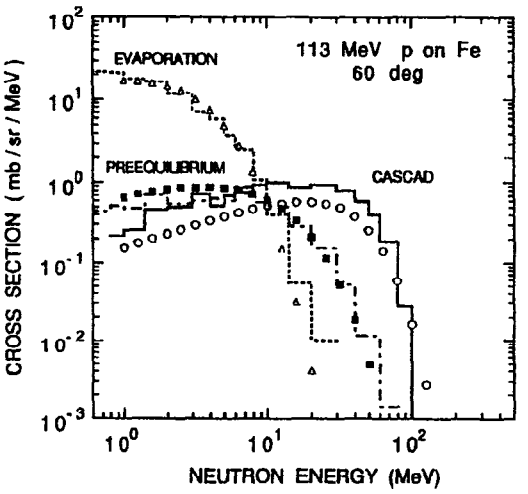

Fig.7 Decomposed neutron spectra for iron at 60deg.

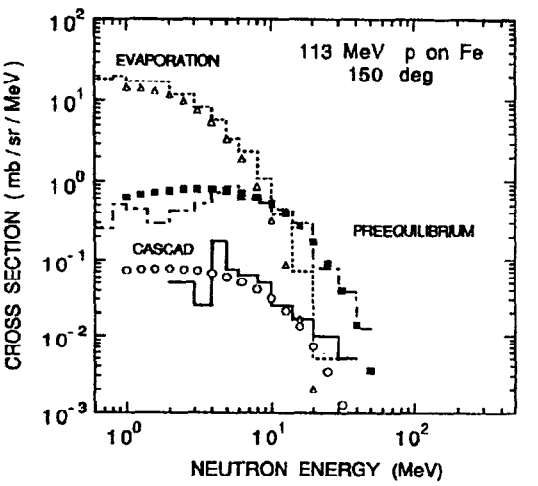

Fig.8 Decomposed neutron spectra for iron at 150deg.

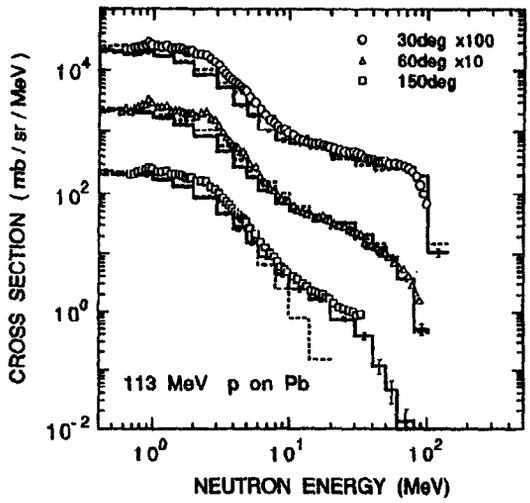

Fig.9 Double differential cross section for the 113MeV proton incidence on lead. Cross marks indicate the experimental data[10]. Dashed and solid lines show the two- and three-step calculations, respectively.

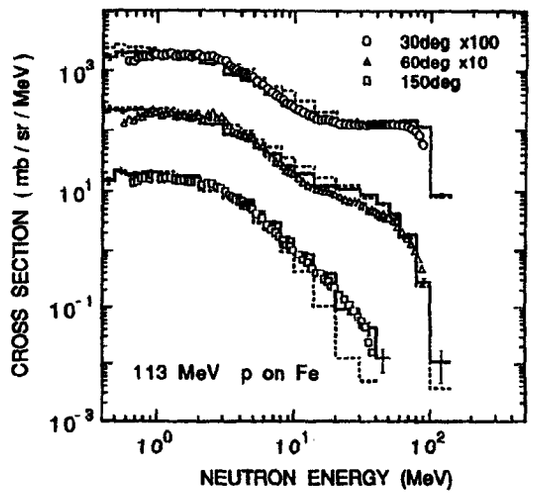

Fig.10 Experimental[10] and calculational double differential cross section for the 113MeV proton incidence on iron.

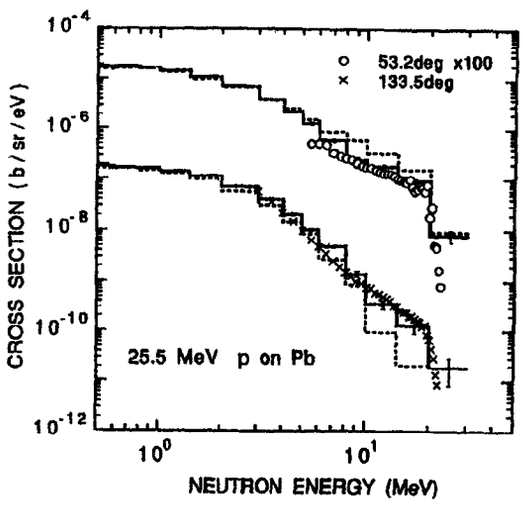

Fig.11 Experimental[20] and calculational double differential cross section for the 25.5MeV proton incidence on lead.

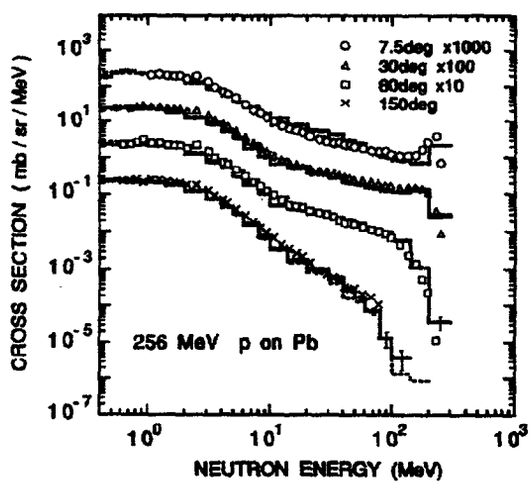

Fig.12 Experimental[21] and calculational double differential cross section for the 256MeV proton incidence on lead.

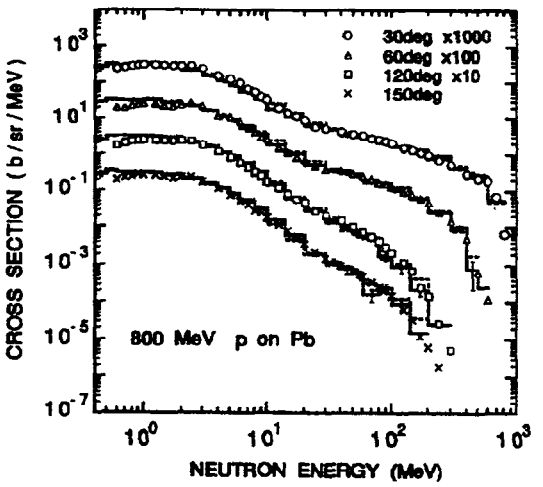

Fig.13 Experimental[9] and calculational double differential cross section for the 800MeV proton incidence on lead.

PULSED NEUTRON SOURCE OF MOSCOW MESON FACTORY

Grachev M I, Kravchuk L V, Kuzin A V, Lebedev S G, Lobashev V M,
Miroshnichenko V G, Matveev V A, Ponomarev O V, Sazanov V N,
Senichev Yu V, Sidorkin S F, Sobolevsky N M
Stavissky Yu Ya.

Institute for Nuclear Research, Russian Academy of Sciences
Moscow

The Pulsed Neutron Source of Moscow Meson Factory is intended for investigations in the field of particle physics, of nucleus structure and mechanism of nuclear reactions, solid state physics in the range of neutron energies from thermal (cold) up to several MeV using the time-of-flight technique.

The neutron emitting occurs on heavy nuclei due to spallation process caused by bombardment of the target with 600 MeV protons from linac. On the primary stage for shaping of the proton pulses, and respectively neutron pulses of needed duration, proton beam chopping after the injector will be used, and later the proton storage ring with the charge-exchange injection will be used in the one-turn extraction mode. The scheme of the neutron source is presented on Fig. 1.

The neutron targets with the reflectors and the system of moderators are placed in two boxes of radiation shield made of iron and heavy concrete.

The shield is supplied with the channels, with shutters for transporting the neutron beams out (Figs 2, 3). The 1st circuit of the water cooling system for targets of heat power up to 2.5 MW (pumps, heat exchangers, ion exchange filters) is placed inside the concrete shield.

The placement of the neutron source in the experimental hall is shown on Fig. 4.

Neutron targets are settled in vessels made of aluminium-magnium alloy that are inserted into vertical channels of the proton beam vacuum system, the wall of the vessel serves as a 'window' of the target that separates accelerator vacuum system from the target coolant. The rubber-based vacuum sealing is placed in the box with the intermediate shield that provides the possibility of maintenance and fast change of the target together with the system of moderators when the proton beam is shut off.

The monitoring of proton beam distribution on the surface of the window is carried out by means of multiwire detector inserted in vertical channel in front of the target window.

The whole target system including the vacuum volume of the target box can be mounted by means of remote-controlled vacuum sealing of the ion tube.

The simultaneous operation of two neutron targets is assumed. The metal tungsten target with titanium coating, water moderators and beryllium reflectors will be used on the 1st stage.

The multiplying targets with the limited gain factor (up to 15-20) are to be used in the second box.

At the first stage the target based on natural uranium in stainless steel cover, which is already designed and manufactured, will be used, creation of targets based on U^{235} and U^{233} is in prospect.

The main parameters of the target systems as the pulsed sources of thermal neutrons are presented in Table 1 for the proton beam from storage ring.

Table 1.

Target parameters		W	U^{238}	U^{235}	U^{233}
Average power	MWt	0.2	0.4	2.12	2.17
Background power	MWt	-	0.004	0.014	0.0063
Thermal neutrons pulse width*	μs	30	30	30	30
Multiplication		0.95	1.15	14.5	20
Lifetime of prompt neutrons	ns	-	-	45	44
Average thermal neutron flux density*	n/cm^2s	$3x10^{12}$	$4x10^{12}$	$1.1x10^{13}$	$1.8x10^{13}$
Peak thermal neutron flux density*	n/cm^2s	$1x10^{15}$	$1.3x10^{15}$	$1.2x10^{16}$	$2.1x10^{16}$
Repetition rate	pps	100	100	30	30

*for 3.5 cm part of water moderator.

Receiving a 100 μs beam pulse from the proton linac, the proton storage ring delivers 330 ns (or smaller) proton pulses to the neutron source. Extraction of the proton beam from PSR is carried out during a pause of the time structure of the linear accelerator. The PSR is built in the beam channelling as a part of the beam layout (Fig 5.).

The beam pulse compression is achieved by one-turn extraction as soon as the filling process is finished. The initial time structure is shaped to provide an azimuthal void to

exclude the beam losses during the rise time of the kicker magnet field. In this case the ring magnet structure is adjusted as an isochronous one ie.

$$\alpha = \gamma^2, \qquad (1)$$

where α is a momentum compaction factor, γ is the energy.

There is no necessity to use the RF system to keep the bunch structure. Similar idea has been proposed and experimentally studied at the CERN. The condition (1) is satisfied in our case only approximately because α-values deviate along the bunch. The magnitude of deviation is $\Delta\alpha = 0.018$ for linear density of the particles $3 \circ 10^{11}$ m^{-1}, which corresponds to the extension of the length of the bunch of 2 m, that is negligible in comparison with the full length of bunch ~75 m.

Table 2.

Orbit circumference (circulation period)	102. m (430ns)
Number of storage turns	240
Maximum intensity per pulse	$3x10^{13}$
Stored beam emittance	3π cm.mrad
Max incoherent tune shift	-0.09
Peak current	11 A
Momentum compaction factor	0.371
Kicker-magnet strength	0.02 T.m
Kicker- magnet rise time	100 ns

The creation of intense neutron sources on the base of proton 7.5 GeV synchrotron (SIN-45) is regarded as second stage of development of the complex of neutron sources of the Moscow Meson Factory. the construction two rings is assumed, the first one - fast-cycling proton synchrotron with the energy 7.5 GeV and mean current 250 μA at 50 pps with charge-exchange injection from linac and one-turn extraction, the second one - the beam stretcher.

The one-turn extraction to two independent neutron targets will allow one to create the next-generation complex of neutron sources with unique characteristics. The first target is assumed to be the Pb-Bi eutectic target with the forced circulation designed for frequency 40 pps (200 μA). The second target is assumed to be the multiplying system based on plutonium or uranium oxide in stainless steel cover with the sodium cooling.

The possibility of extracting part of proton beam from synchrotron to stretcher is foreseen to provide research work in kaon physics.

It's known that the production of secondary neutrons is most efficient at the proton energy 1.5-2 GeV. It can be explained by competition between nuclear interactions and ionisation losses in target. For the energies less than 1 GeV the direct ionisation losses of protons prevail and for the energies above ~1 GeV the ionisation losses due to electron-proton showers initiated by π°-decay begins to work. With the growth of energy the efficiency of secondary neutrons production falls down, but the decrease of specific radiation damages of the target first-wall material becomes very significant that is the main problem of reliability of the system. The decrease of the beam volume charge and collective effects.

The dependence of radiation damage of the first wall by primary protons upon energy of primary protons calculated for a unit of mean density of thermal neutrons on the surface of water moderator is presented on Fig 6.

Comparative characteristics of operating and being designed pulsed neutron sources intended for research mainly in solid state are presented in Table 3.

Table 3.

Facility	Type	Av current on target	$\overline{\Phi}$ n/cm²s	$\hat{\Phi}$ n/cm²s	$K = \frac{\overline{\Phi_T}}{\Theta_T^2}$	Notes
IBR-2	pulsed reactor 4 MW	PuO_2+Na	10^{13}	10^{16} (120μs)	1	design parameters K~1/6
ISIS	PS, 70MeV-0.8 GeV	0.2 mA U^{238}	2.1×10^{12}	1.4×10^{15} (30 μs)	3.4*	oper 0.12 mA
MMF IN-06	storage ring 0.6 GeV K_M=20,2 MW	0.5 mA U^{238}.	4×10^{12}	1.3×10^{15}	6.4*	under constr
		0.15 mA U^{233}.	1.8×10^{13}	2×10^{16} (30 μs)	30*	project
Europ projec	storage rings 1 GeV	6.3 mA Pb-Bi(?)	6.3×10^{13}	4.2×10^{16}	100*	discussion
SIN-45	PS, 0.6GeV-7.5GeV K_M=20,8 MW	0.2 mA Pb-Bi,	1.3×10^{13}	1.1×10^{16}	26*	project
		0.05 mA U^{233}-Na	1.2×10^{14}	4.5×10^{17}	195*	discussions

* IN-06 target-moderator geometry (thin Be reflector)
** thick Ni reflector (factor ~ 4)

In conclusion we would like to express our best acknowledgements to:
A P Alexandrov, M A Markov, Z P Zarapetyan, V N Aseev, S K Esin,
V A Fedchenko, N A Kazarnovsky, N A Khryastov, E A Koptelov, P N Ostroumov,
S V Serezhnikov, Yu P Severgin, I A Shukeylo, N I Trushkin, M T Vorontsov for
useful discussion, support and co-operation.

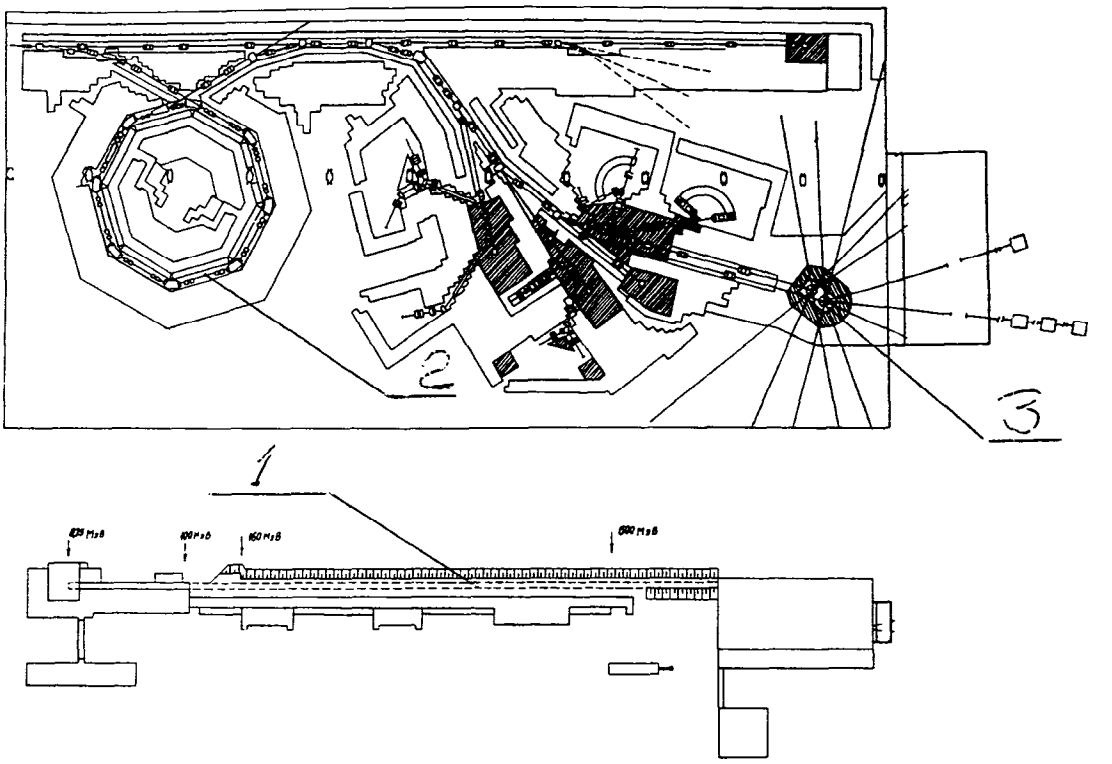

Fig. 1. Scheme of pulsed neutron source IN-06 of Moscow Meson Factory
1 - linear accelerator, 2 - ring compressor, 3 - neutron source

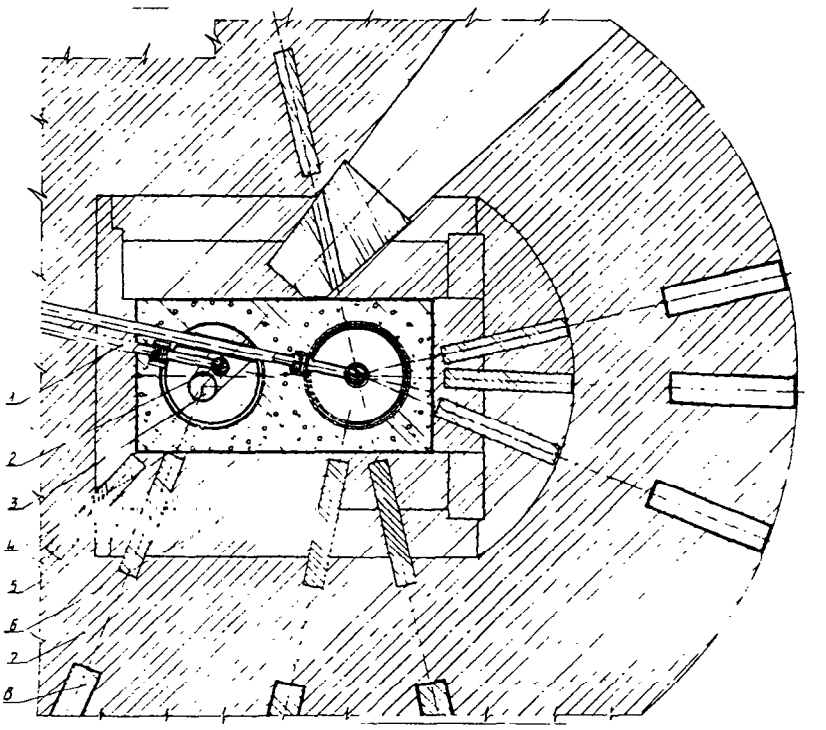

Fig. 2. Neutron source. 1 - proton beam line, 2 - target, 3 - vertical channel,
4 - vacuum tank, 5 - heat shield, 6 - iron shield,
7 - heavy concrete shield, 8 - shutter

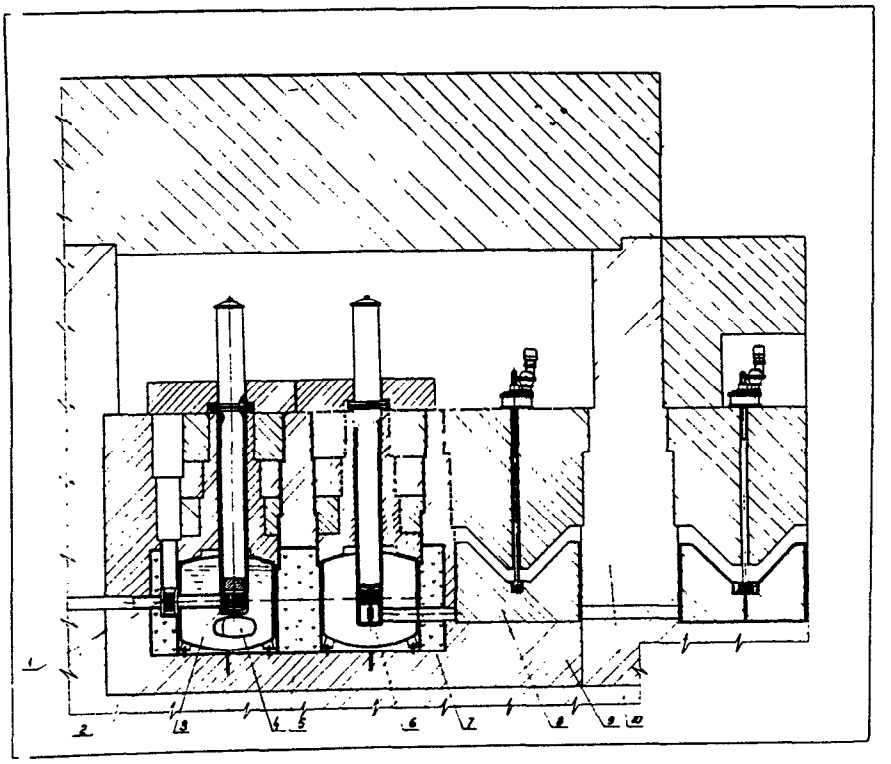

Fig. 3. Neutron source.

1 - remote-controlled vacuum sealing, 2 - neutron target, 3 - vacuum vessel,
4 - neutron channel, 5 - heat shield (iron with water cooling), 6 - water moderator,
7 - neutron channel, 8 - shutter, 9 - iron shield, 10 - heavy concrete shield

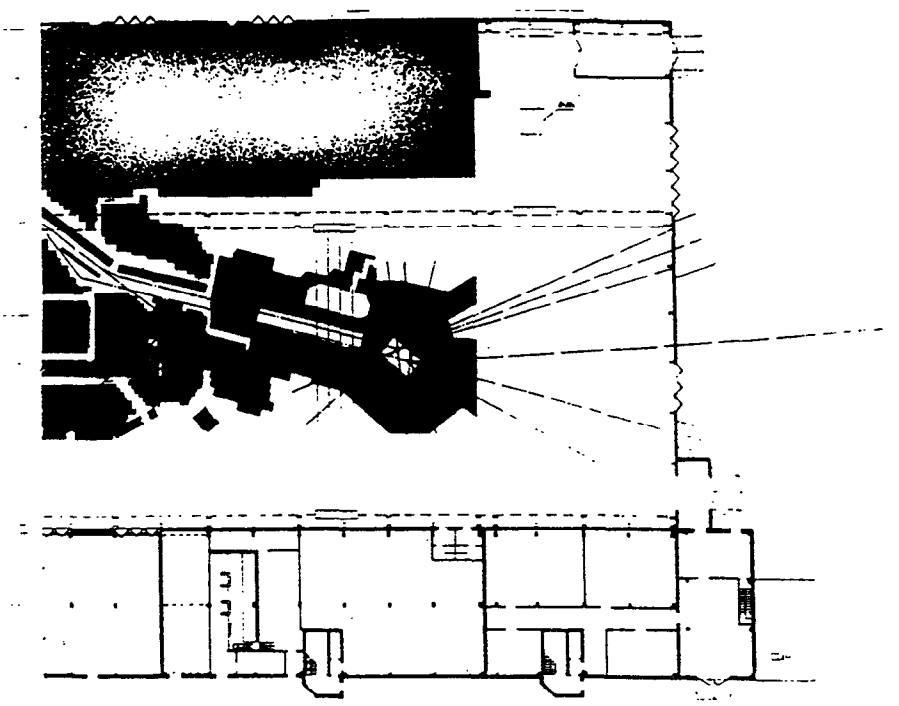

Fig. 4. Placement of the neutron source in the experimental hall

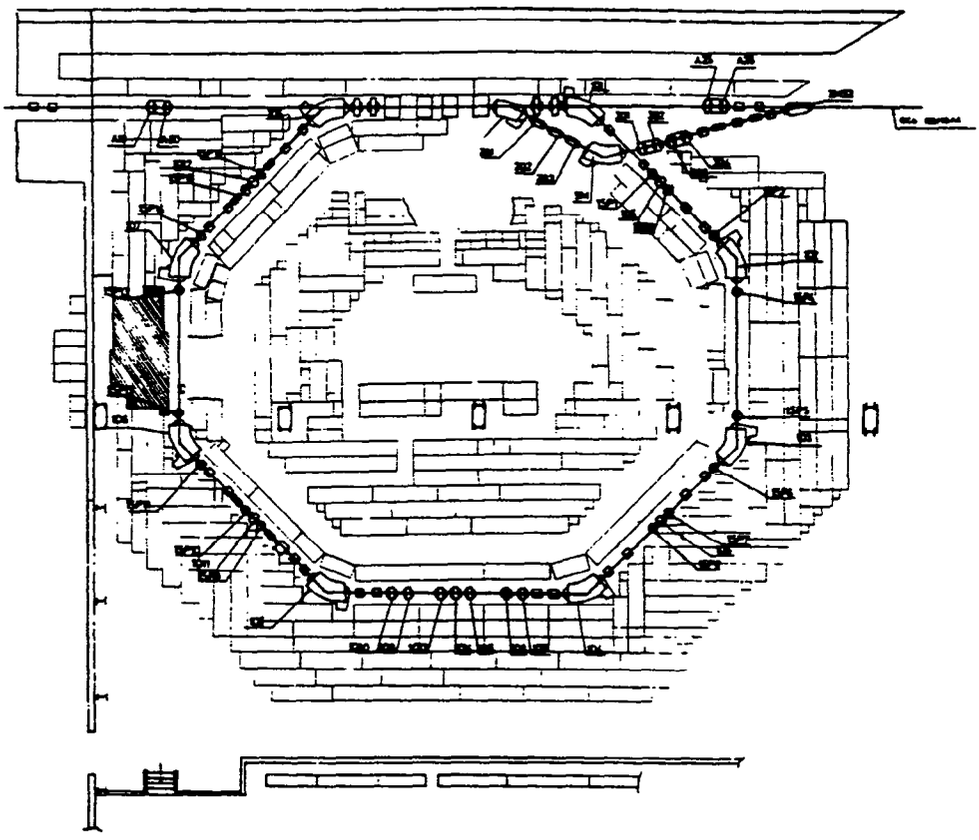

Fig. 5. The proton storage ring.

1D1-1D8 - the mine dipole magnets, B=1.45 T, aperture 20x12 cm², HORxVERT, bending angle=45°: 1Q1-1Q15 - the quadropoles, d=20 cm, length=0.4m, G=4.5 T/m: 1SP - the sextupoles: d=20 cm: 2B1-2B8 - the bump magnets for injection: 3K - kicker magnet for one turn extraction

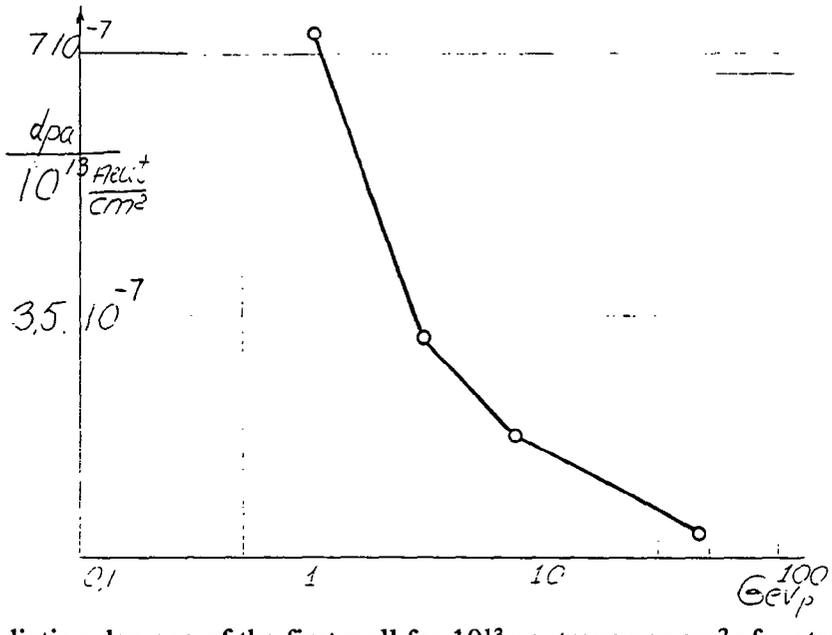

Fig. 6. Radiation damage of the first wall for 10^{13} neutrons per cm² of water moderator surface for protons (beam cross-section 20 cm²)

TARGET–MODERATOR–REFLECTOR ASSEMBLY FOR A HIGH POWER PULSED SPALLATION NEUTRON SOURCE

H. Conrad

Institut für Festkörperforschung
Forschungszentrum Jülich GmbH
Postfach 1913, D–52428 Jülich, GERMANY

A target–moderator configuration is presented, which combines the neutronic advantages of the split target design ("flux trap" geometry) with the strongly relaxed thermohydraulic requirements of a rotating target. Moving only the most highly loaded parts, the target is composed of a twin wheel with vertical rotation axis plus a stationary part downstream of the proton beam. The twin wheel with its rotation axis parallel to the vertical proton beam essentially consists of two water–cooled disks on a common axis and separated by a gap sufficiently wide to contain an adequate number of moderators. The thickness of the two target disks is different in accordance with the optimum flux trap requirements. The annular target zone on the periphery of each disk is hit by the proton beam from the side of the thinner disk. The assembly is completed by a stationary cylindrical target separated from the second wheel by a distance appropriate for the insertion of another two to four moderators in flux trap geometry. One or two so–called back-scattering moderators can be placed in front of the first target wheel.

1. Introduction

It was realized for a long time that stationary, heterogeneously cooled solid targets for proton beam powers beyond 1 MW may either be close to their technical limits or even unfeasible at all. Therefore already the German 5.5 MW SNQ project only considered two options: a liquid metal target and as a reference design a rotating solid target [1]. Even for the 0.9 MW SINQ continuous spallation source under construction at PSI a liquid lead–bismuth eutectic was originally favoured as a target. Only because of possible radiation hazards associated with the use of liquid bismuth in strong thermal neutron fields and corrosion problems, PSI resorted to a cylindrical solid, stationary zircaloy target as the day one solution [2]. (The global concept for SINQ does not allow a solution with a moving target.) The rotating target of the former German SNQ project was planned to be hit horizontally by the protons, the in–plane depth of the target material being such as to completely stop the beam on the wheel periphery. This configuration implied a very heavy mass to be moved as well as very restricted possibilities of placing moderators next to the maximum of the fast neutron leakage. (For the German SNQ as a time–modulated source the latter argument was not stringent.)

Both the neutronically unfavourable but cheaper horizontal proton beam line and prismatic targets with wing type moderators, i.e. tangential neutron extraction, are realized in three of the existing four spallation sources. As one is interested in as many different moderators as possible with one target, the choice of three, four or even more moderators inevitably leads to only two of them placed in the maximum of the fast neutron leakage from the target. The remaining moderators will be located downstream on the tails of the leakage flux. As a remedy a vertical proton beam line enables the grouping of four equivalent wing type moderators around a vertical target. With the introduction of the split target concept [3], placing the moderators in slab orientation adjacent to the target gap, a gain in slow neutron leakage flux by a factor of approx. 1.4 was achieved compared to wing geometry.

2. The concept of a hybrid (moving + stationary) high power target

The heat deposition along the proton beam in a spallation target is very closely described by an exponential, if one neglects the build–up at the target head and the rapid decrease at the protons' range [4]. The decay constant (proton mean free path) is determined by the target material and can be estimated by an empirical expression for the absorption cross section for high energy protons [5], $\sigma_a = \pi \cdot (r_0 A^{0.33})^2$, where $r_0 = 1.26$ fm and A is the atomic mass. Values for the mean free path $\Lambda = (n \cdot \sigma_a)^{-1}$ for selected target materials are given in Table 1. So the highest thermal load is in the foremost part of any target. The maximum power density p_0 can be calculated accordingly by integrating the exponential power deposition over the proton range R, given by the empirical relationship [6] $R = 233\, \rho^{-1} Z^{0.23} (E_{gev} - 0.032)^{1.4}$ and equating the result with the total power per particle P(E) dissipated in the target. One obtains [7]

$$p_0(E) = \frac{(P(E)/\Lambda) \cdot j}{1 - \exp(-R/\Lambda)} \quad (\mathrm{MW/cm^3})$$

where P(E) is given by the empirical expression [8] $P(E) = 0.230 + 0.22\, E_{gev}$ (GeV/p) and j is the average proton current density in units of mA/cm^2. For depleted uranium the maximum power density is higher than calculated with the above formula because of fast fission (see Table 1). In the case of a 5 MW beam on Tantalum, a favourable target material, realized for instance with 800 MeV protons and a current of 6.25 mA, the maximum heat deposition is 12.5 kW/cm^3, assuming a constant current density over a beam cross section of 20 cm^2. (For comparison, this is more than 10 times the power density in the core of the High Flux Reactor in Grenoble.) In Table 1 are listed some relevant parameters for a few candidate target materials.

	Λ(cm)	R(cm)	p_0(kW/cm³)
Pb	17.4	39.3	8.1
W	9.8	22.5	14.4
Ta	11.3	26.0	12.5
^{238}U	10.8	24.0	24.4 *)

Table 1 Proton mean free path Λ, proton range R and maximum power density p_0 for selected target materials for $E_p = 800$ MeV. *) Value for Uranium taken from Atchison [9].

The corresponding current density on a stationary beam window is about 300 $\mu A/cm^2$. This poses an even more serious problem on the technology of a solid target. There is still no reliable prediction possible on the window life under such conditions [10].

Clearly, the technical requirements resulting from these loads can essentially be relaxed by using a moving target. The obvious solution is a rotating solid target, as was already planned for the SNQ project. In contrast to that, the concept presented here combines the advantages of the latter with the exploitation of the split target geometry by letting the proton beam penetrate a target wheel parallel to its axis of rotation. Additionally, a substantial reduction in moving target material is achieved by partitioning the target into a rotating plus a stationary part situated downstream of the wheel. As calculations have shown [11], the optimum depth of the front part of a split target is 7 – 8 cm. On the other hand, the heat deposited in such a depth is lower by about 20 – 30 % only. Therefore it appears reasonable to consider from the very beginning two target wheels separated by the neutronically optimum distance.

The principal target–moderator–reflector assembly is shown in Figure 1, where a solution has been chosen with the proton beam from below.

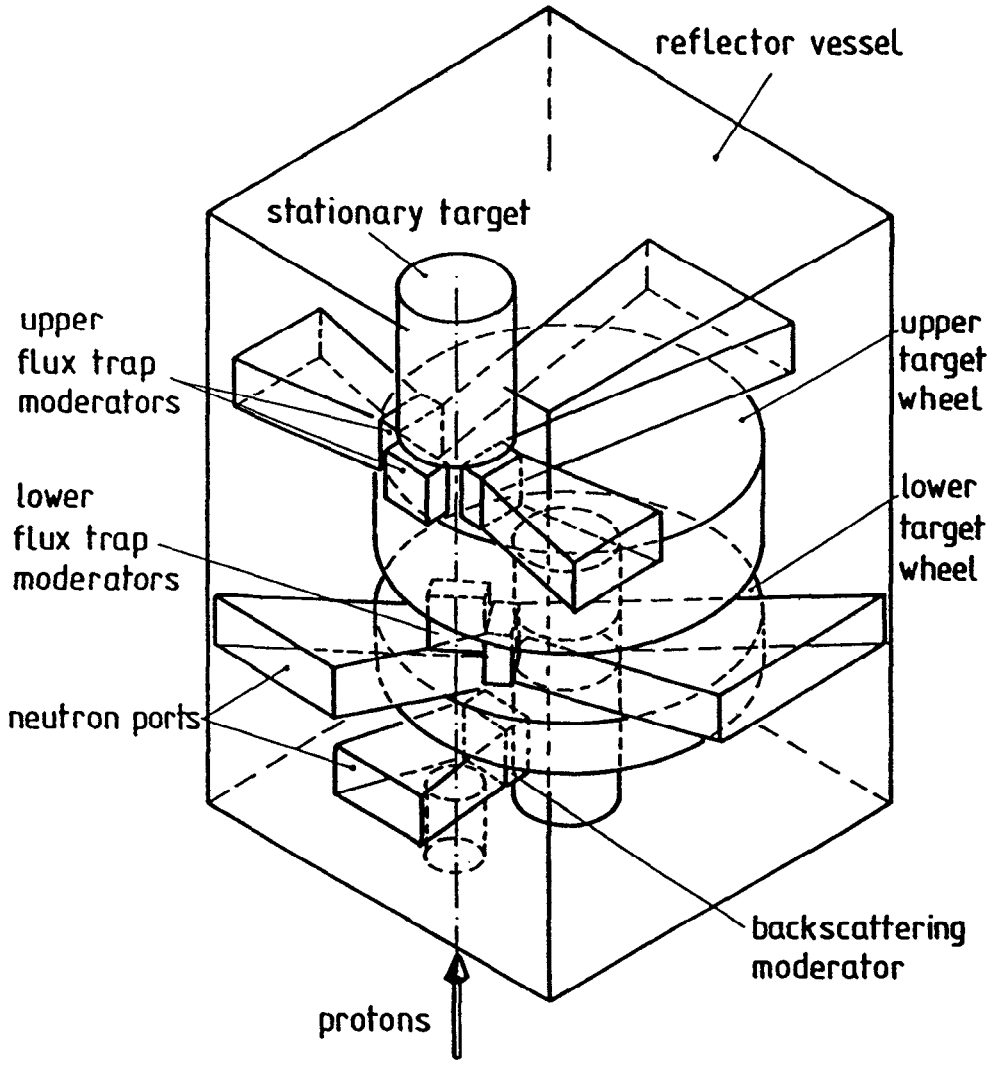

Figure 1: Sketch of the target—moderator—reflector assembly of a high power spallation neutron source. The target consists of a rotating twin wheel followed by a stationary cylindrical part. For the sake of clarity the neutron beam penetrations for one of the inter—wheel moderators are not shown.

Employing such a target assembly, the most highly loaded parts, and only these are moved. By the same token the requirements for as many different moderators as possible as well as maximum neutron beam port number can be fulfilled, i.e. flux trap configuration and vertical proton beam line are realized. The replacement of the second wheel by a corresponding stationary part in the case of medium power spallation source is a straightforward simplification of the present concept.

3. Moderator configuration

Employing a double gap target (a doubly divided, but stationary cylindrical target has been discussed recently [10]) a series of different moderator configurations and combinations can be imagined. One example is discussed in the following. A single "backscattering" moderator is placed next to the proton entrance spot of the first target wheel. Slow neutrons are extracted from the same moderator face (i.e. backscattered) as the fast neutrons are fed in. The corresponding neutron beam hole group is oriented radially away from the wheel axis.

The moderator pair in the gap between the two wheels is positioned such that it can be viewed in both backscattering and "transmission" geometry. Calculations have shown [11] that a somewhat higher flux may be obtained from the backscattering face than from the "transmission" face. So, with only two moderators four beam hole groups will be served. The two moderators are next to each other with their neutron emitting faces forming a right angle. With respect to the single backscattering moderator, however, their faces are rotated through 45 degrees, in order to obtain a symmetrical beam hole distribution. Yet, realizing a moderator pair only is not mandatory. The present concept would also admit four (or even more) "inter–wheel" moderators. But such a configuration would necessarily mean transmission geometry only. It may appear to be reasonable to decouple in that case one or several moderators of such a tight group.

The number of moderators next to the second gap, i.e. between the second target disk and the stationary target part is subject to the same considerations as just described. In the present paper a moderator triplet is assumed. Both backscattering and transmission geometry are realized and the moderator faces oriented such as to complete the 360° utilization of the target block circumference with beam holes. Schematic side and top views of the target environment are depicted in Figure 2. The top view indicates the horizontally uniform neutron beam hole configuration. Shown are the center lines of typically a beam hole triplet, each originating at one of the six moderators discussed above. A total of 24 beam holes is possible in this way.

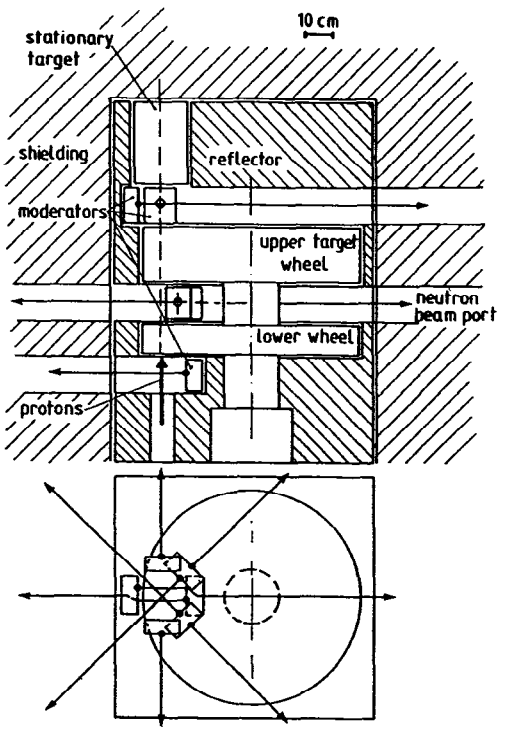

Figure 2:

Schematic side and top views of the proposed target–moderator–reflector assembly. The drawing is approximately to scale. The moderator faces viewed by neutron beam holes are marked by dots.

4. Basic technical target details

4.1 Geometric design

Target geometry and proton beam direction suggest a comparatively simple cooling scheme for the disks. The target material will be divided into flat ring–shaped plates piled on top of each other and separated by sufficiently wide gaps for coolant flow. The coolant water will be fed in through the axis, flowing outwards radially on the upper disk half and flowing back through the lower target plate gaps (see Figures 3 and 4). In this way both beam windows are cooled as well. The structural material of the wheels will be an Aluminum alloy (e.g. AlMgSi1). No engineering details such as the minimization of the number of wheel parts or welding joints will be discussed here.

In the present design the first (thin) target ring has an effective thickness of 7 cm. Including coolant gaps, beam windows and structural materials the overall wheel thickness is about 11 cm. The second (thick) target ring has an effective thickness of 12 cm and an overall wheel thickness of about 16 cm. The effective target thicknesses of the rotating disks will subject to neutronic optimizations. The figures assumed here are taken on the basis of calculations for laterally narrow targets [11]. The inherent reflector action of plate shaped targets may change these values. Both wheels have an overall diameter of 80 cm. Several criteria may be conceived for the selection of the wheel rotation frequency. As an obvious condition it will be required that two consecutive proton pulses just exclude each other spatially. Assuming a circular beam spot of 20 cm^2 as above, penetrating the wheels at a radial distance of 35 cm from the axis and taking a pulse repetition rate of 50 Hz, gives a wheel rotation frequency of about 1 Hz. The wheel drive can be achieved either hydraulically at the hub or mechanically on the circumference. A vertical cross section of the thin target wheel is shown in Figure 3.

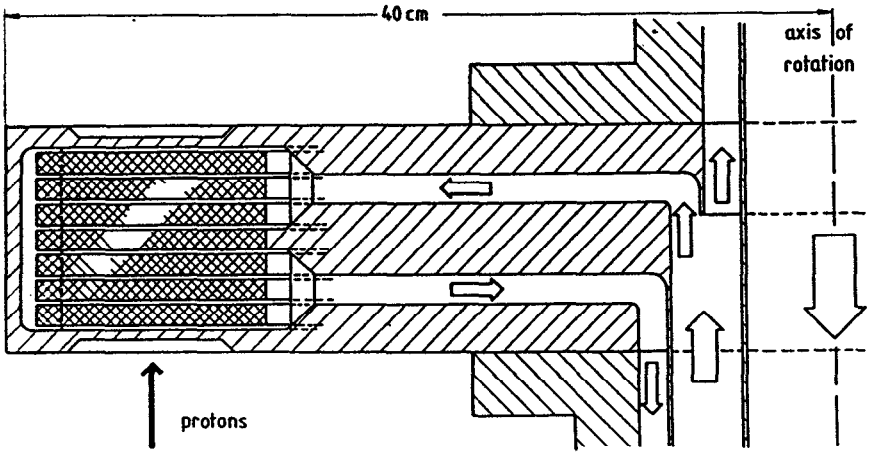

Figure 3: Vertical cut through the first (thin) target wheel (for symmetry reasons only half of the cross section is shown). The coolant flow is indicated by the open arrows.

A top view of one quadrant of a target wheel is presented in Figure 4. The stationary target will typically have an effective length of 30 cm. In order to use this target part also as a final beam stop, its length as well as the ring thicknesses have to be subject to optimizations according to the actual proton energy and target material chosen. The diameter of the stationary target cylinder will be larger than the corresponding lateral ring dimension of the rotating parts in order to intercept most of the wider forward cascade particle cone.

4.2 Thermohydraulic requirements

As the spallation reaction releases quite a number of different high energy neutral and charged particles (neutrons, mesons, protons) leaving the target, only part of the beam power, depending on proton energy, is dissipated in the target itself. At 800 MeV, for instance, this typically amounts to 50 % [8]. For the following discussion we will assume a 5 MW beam at 800 MeV and assume a total deposition of 3 MW in the target in order to obtain an upper limit for the assessment of the necessary thermohydraulic requirements. Furthermore we will take tantalum as the reference case and only consider the most highly loaded, i.e. technically most challenging first thin target wheel. Choosing water as the appropriate coolant (although cooling with Helium would circumvent the complications of radiolysis) we easily calculate the necessary volume flow for removing a total of H = 3 MW from the entire target to be

$$dV/dt = H/(c\,\rho\,\delta T) = 172\ m^3h^{-1}$$

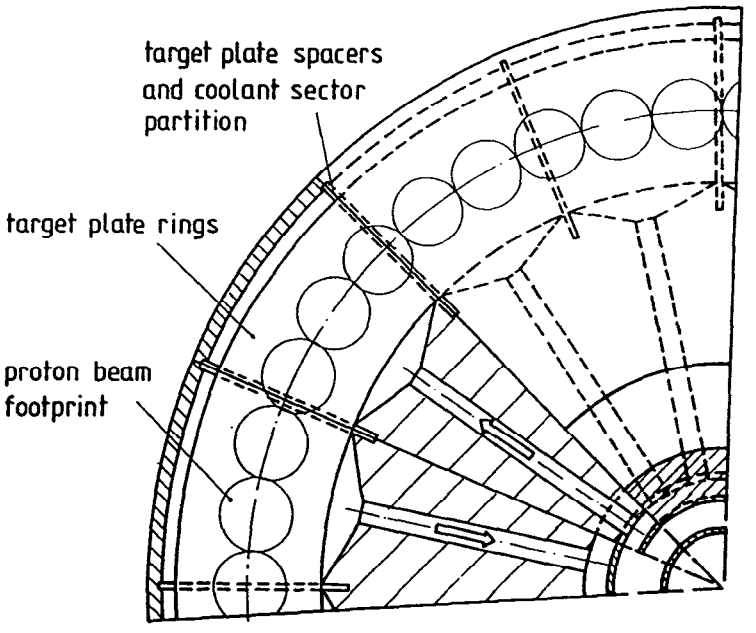

Figure 4

Three–level horizontal cut through one quadrant of the thin target wheel. Sector shown on the bottom is a cut on the level of the coolant outlet boring, adjacent sector is cut through the coolant inlet boring, top is cut halfway between the wheels. The coolant flow is partitioned into 16 independently cooled sectors.

allowing for a temperature rise of $\delta T = 15$ K. According to the exponential behaviour of the power deposition, about 1.5 MW are dissipated in the first, thin wheel, which means 85 m^3/h have to flow through this target part. For the following discussion we have chosen a partitioning of the thin target into 7 plates of equal thickness of 1 cm separated by coolant gaps of $d = 0.2$ cm. With a total cross sectional area $A_{tot} = 0.015\ m^2$ the average flow velocity through the target gaps is

$$<v> = (dV/dt)/A_{tot} = 1.7\ ms^{-1}.$$

The Reynold's number for flow in a channel of narrow rectangular cross section is given by $Re = 2d<v>/\nu$ (the kinematic viscosity ν taken at $T = 50^0C$, $\nu_{50} = 0.56 \cdot 10^{-6}\ m^2s^{-1}$), i.e. $Re \simeq 12100$. This number means turbulent flow, the corresponding pressure drop in one target coolant channel being therefore [12], $\Delta p_t = \ell\zeta\rho<v>^2/(2d_h) \simeq 1090\ Nm^{-2}$, where ℓ is the channel length, $\zeta = 0.316 \cdot Re^{-0.25}$, ρ is the water density and $d_h = 2d$ the hydraulic channel diameter. The pressure drop in a radial feed pipe (see Figures 4 and 5) is $\Delta p_f \simeq 1240\ Nm^{-2}$, i.e. of the same order of magnitude. According to the cooling scheme (compare Fig. 4) the flow resistances in each sector are in series. We therefore obtain a pressure drop in the straight parts $\Delta p_s = 2\ (\Delta p_t + \Delta p_p) = 4660\ N/m^2$, which is a small value. Major contributions to the total pressure drop result from both the flow turns with low bending radii at the wheel axis and at the rear plate edges. These can be estimated by $\Delta p_{turn} = d_h\rho<v>^2/r$, where r is the radius of curvature. With $d_h \simeq r$ we obtain $\Delta p_{turn} = 2890\ N/m^2$. As there are 8 turns, the total loss is $\simeq 23000\ N/m^2$. Adding to this the above value for Δp_s we have as an order of magnitude estimate $\Delta p_{tot} \simeq 28000\ N/m^2$, corresponding to

$$\Delta p_{tot} \simeq 0.28\ bar.$$

Let us now turn to the temperatures and their variations we have to expect in the course of the pulsed proton operation. Let us assume as before a pulse repetition rate of $f_{rep} = 50\ s^{-1}$. The pulse duration t_p will be of the order of a few microseconds only, so we can regard the power deposition as instantaneous. At first we are interested in the corresponding sudden temperature increase of the most highly loaded target part during a single proton pulse. This is given by

$$\Delta T = p_0/(c\ \rho\ f_{rep}), \qquad (1)$$

where p_0 is the time average maximum power density, c is the specific heat capacity and ρ the density of the target material. For tantalum, p_0 is 12.5 kW/cm³ (Table 1), and we obtain for the first few target plates a temperature rise of $\Delta T^{ta} = 96$ K.

As the target rotation frequency is $f_{rot} \simeq 1\ s^{-1}$, the heated volume will cool down by a certain amount during 1 second. Consecutive proton bursts will then result in a sawtooth like behaviour with a rising characteristic until an "equilibrium" temperature is reached, on which oscillations of the above amplitude are superimposed. In order to obtain a quantitative picture of the temperature course after start–up and the time elapsed to reach stationary conditions we calculate the transient heat conduction for plate geometry according to the heat diffusion equation $\partial^2T(x,t)/\partial x^2=(\rho c/\lambda)\partial T(x,t)/\partial t$. The exact solution of this equation is given by the infinite series [13]

$$T(t,x) = T_w + [T(0,x) - T_w] \sum C_i \cdot \exp[-\zeta_i^2 Fo(t)] \cdot \cos(2\zeta_i x/D)$$

where x is the distance from plate center to surface and T_w is the coolant temperature. Fo(t) is the Fourier number, a dimensionless quantity defined as $Fo = (4\lambda/\rho c D^2)t$ (thermal conductivity λ, plate thickness D, time t). C_i and ζ_i are tabulated quantities [13] depending on another dimensionless number, the Biot number $Bi = \alpha D/2\lambda$, where α is the heat transfer coefficient. Only the first term in the above series needs to be retained if $Fo > 0.2$. For tantalum, $Fo = 0.874\ t$, i.e. for $t > 0.23$ s and identifying $T(0,x) - T_w$ with ΔT from equation (1) we obtain the approximate solution

$$T(t,x) = T_w + \Delta T \cdot C_1 \cdot \exp[-\zeta_1^2 Fo(t)] \cdot \cos(2\zeta_1 x/D),$$

a single exponential decay till the next proton burst at $t = t_{rot}$. (For very short times, in fact, more terms of the exact solution were adequate, resulting in slightly blunter sawteeth tips, but not changing the long time features.) With $\alpha = 1.0$ W/cm²K (see below) and 1 cm thick plates we have $Bi = 0.92$, which gives $C_1 = 1.112$ and $\zeta_1 = 0.834$. With $q \equiv C_1 \cdot \exp[-\zeta_1^2 Fo(t_{rot})] = 0.653$, the center temperature ($x = 0$) of a target volume element immediately after it has been hit by the n–th proton pulse is given by

$$T_i^{(n)} = T_w + \Delta T \cdot (1 + q + q^2 + \ldots + q^{n-1})$$

and at the end of the following wheel revolution the temperature in the center plane of that volume element is

$$T_f^{(n)} = T_w + \Delta T \cdot q \cdot (1 + q + q^2 + \ldots + q^{n-1})$$

The maximum and minimum temperatures in the stationary case ($n \to \infty$) are then given by

$$T_{cmax} = T_w + \Delta T/(1 - q) = 327^oC \qquad (2)$$

and $T_{cmin} = T_w + q \cdot \Delta T/(1 - q) = 231^oC$ respectively. The "equilibrium" temperature in the center of the first plate is therefore $T_c^{equ} = (T_{cmax} + T_{cmin})/2 = 279^oC$. In the same manner we calculate the surface temperature ($x = D/2$). We now define $q' \equiv C_1 \cdot \exp[-\zeta_1^2 Fo(t_{rot})] \cdot \cos(\zeta_1)$. For tantalum $q' = 0.438$ and we obtain

$$T_{smax} = T_w + \Delta T/(1 - q') = 221^oC. \qquad (3)$$

Correspondingly $T_{smin} = T_w + q' \cdot \Delta T/(1 - q') = 125^oC$ and $T_s^{equ} = (T_s^{max} + T_s^{min})/2 = 173^oC$. In Table 2 are given some relevant thermodynamic parameters and the operating temperatures for selected target materials and for aluminum as a window material.

	$\overline{p_0}$(W/cm³)	c·ρ(Ws/cm³K)	λ(W/cm K)	T_c(°C)	T_s(°C)	$\Delta\hat{T}$(°C)
Pb	186	1.46	0.346	286	209	110
W	331	2.59	1.674	305	267	111
Ta	288	2.50	0.544	327	221	96
^{238}U	561	2.24	0.251	912	388	218
Al	83	2.42	2.110	(114)*	107	30

Table 2 Thermodynamic parameters and operating temperatures for selected target materials and for aluminum as window material. The items are: specific heat c, density ρ, thermal conductivity λ (at 20°C), maximum plate center temperature T_C (equ. 2), maximum plate surface temperature T_S (equ. 3), (T_C and T_S are for $T_W = 50°C$) and temperature jump ΔT (equ. 1) during a single proton pulse. p_0 is the revolution average power density. Thickness of a single target plate is 1 cm in each case. Aluminum window thickness is 0.5 cm. *) Estimated temperature at the vacuum side.

The temperatures in Table 2 have been calculated assuming equal target geometry and coolant flow (1 cm thick target plates separated by 0.2 cm wide coolant gaps). The temperature course after start–up is shown in Figure 5 for the center plane of the first plate. (Note that the temperature above coolant is plotted.) As can be seen, equilibrium is reached after about 15 wheel revolutions corresponding to about 13 seconds.

The result for the "equilibrium" target temperature can be checked by the following simple consideration. The revolution–average maximum power density $<p_0>$ in the rotating target is given by $<p_0> = (f_{rot}/f_{rep})\cdot p_0$. For tantalum $<p_0>^{ta} = 0.288$ kW/cm³. This means that we have to transport $q_0 = 144$ W/cm² through each of the two water

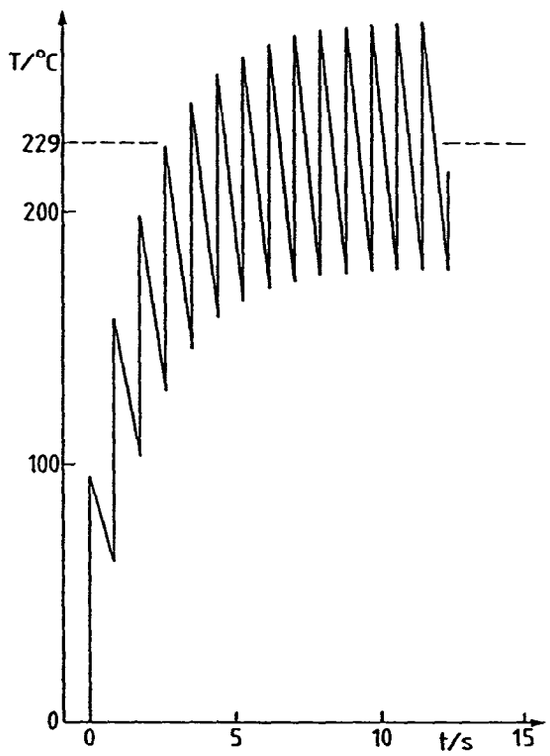

Figure 5

Temperature course in the center plane of the first plate of a Tantalum target after start–up of the proton beam. Note: Plotted temperature is above coolant.

cooled surfaces of the plates. In order to calculate the target surface temperature, we need to know the heat transfer coefficient α of a narrow coolant gap, which is given by $\alpha = \lambda \cdot Nu/d_h$. The Nusselt number for turbulent flow is given by the relation [12] $Nu = 0.037(Re^{0.75}-180)Pr^{0.42}$. With $Re \simeq 12100$ from above and the Prandtl number $Pr = \nu\rho c/\lambda = 3.61$ we obtain $Nu \simeq 61.8$. With $\lambda = 6.48 \times 10^{-3}$ W cm^{-1}K^{-1} for water at $T_w = 50^0$C and $d_h = 2d$ ($d = 0.2$ cm) we finally have $\alpha = 1.0$ Wcm^{-2}K^{-1}. The average target surface temperature T_s is then given by $T_s = T_w + q_0/\alpha A = 50^0C + 144^0C = 194^0C$. The temperature in the target plate center is given by $T_c = T_s + \langle p_0 \rangle D^2/8\lambda$ [12] (λ is the heat conductivity of the target material and D the plate thickness). For tantalum plates with $D = 1$ cm we obtain $\langle p_0 \rangle D^2/8\lambda = 66^0C$ and $T_c^{ta} = 260^0C$. Within the approximations made this is close to the corresponding temperature $T_c^{equ}=279^oC$ from above. For comparison, in a non–moving Ta–target of the same geometry the maximum temperature were $T_{max} \simeq 3190^0C$, which is above the melting temperature.

4.3 Proton beam window

Like the target plates the proton beam windows are subject to similar considerations with respect to their cooling requirements. The maximum power density in an Aluminum window ($R = 108$ cm for 800 MeV, $\Lambda = 37$ cm) is $p_0 = 3.6$ kW/cm^3, yielding a temperature jump of 30°C during a proton pulse. The time average power density is $\langle p_0 \rangle = 0.083$ kW/cm^3. The power deposited in the 5 mm thick window has now to be removed through one surface only (we neglect radiation cooling on the vacuum side), i.e. we have to transport 41.5 W across each square centimeter to the coolant. The corresponding window temperature is about 107°C on its water cooled face and assumes estimated 114°C on the vacuum side. Therefore, temperature is not of particular concern in stress analysis and mechanical design of the beam windows.

5. Concluding remarks

The target concept presented in this paper appears to have a series of advantages as compared to stationary or alternative rotating target designs, i.e.

- flux trap geometry and vertical proton beam line with a rotating disk–shaped target
- specific heat deposition in the target material lower by a factor of about 40
- lower specific radiation damage in the target material
- proton current density on the beam window less than 10 μA/cm^2
- optimum decoupling of the different moderators (no cross talk through target disks)
- inherent reflector action of the laterally extended target disks
- larger proton beam cross section possible, e.g. elongated tangentially to the disk circumference
- only part of the necessary target volume has to be moved
- wheel hub not in the immediate neighborhood of the forward directed high energetic cascade particles (less demanding wheel bearing and coolant inlet conditions)

Clearly, the presented target–moderator concept also holds for a proton beam from above, if the sequence of target parts is reversed as well. In that case the last of the just mentioned advantages is no longer valid.

Some final remarks on user requirements seem to be suitable here. It is generally accepted today [14] that a new spallation source should basically provide four types of moderators, which are characterized according to their spectra and pulse shapes. The present target concept quite naturally accomodates three spatially separated moderator groups. In the example discussed above, even six single moderator locations have been identified. Therefore, a basic set of four differently performing moderators can easliy be realized. According to the user requirements, this set is composed of two pairs of moderators, one pair at ambient and the other one at low (possibly liquid hydrogen)

temperature, respectively. At each temperature there has to be both a high intensity (coupled, unpoisoned) and a high resolution (decoupled and/or poisoned) moderator. Detailed numerical calculations still to come have to guide the assignment of these moderators to their respective locations in the target environment.

A tentative allocation is the following. The high intensity thermal moderator will be the backscattering moderator before the first wheel. The pair of inter–wheel moderators will serve as both the high intensity and high resolution cold moderators. The high resolution moderator may be heterogeneously poisoned and deliver different pulse shapes from its two faces. The triplet on top may either consist of both high intensity and high resolution thermal moderators or a combination of thermal and cold ones, if they are adequately decoupled.

References

[1] G.S.Bauer, Status of the SNQ project at the KFA Jülich. ICANS–VI, p 41, ANL–82–80 (1983)

[2] G.Heidenreich and G.S.Bauer, The PSI–SINQ Target Development Programme. in: Technology of Targets and Moderators for medium to High Power Spallation Neutron Sources, Appendix C. PSI–Proc. 92–03, ISSN 1019–6447 (1992)

[3] G.J.Russell, C.D.Bowman, E.R.Whitaker, H.Robinson and M.M.Meier, LANSCE High Power Target–Moderator–Reflector–Shield. Proc. ICANS–VIII, p 272 (1985)

[4] G.A.Bartholomew and P.R.Tunnicliffe (eds.), The AECL Study for an Intense Neutron Generator. AECL 2600 (1966)

[5] A.Ashmore, G.Cocconi, A.N.Diddens, and A.M.Wetherell, Phys. Rev. Lett. 5, 575 (1960)

[6] J.M.Carpenter, Nucl. Instr. Meth. 145 (1977) 91

[7] G.S.Bauer in: Targets for Neutron Beam Spallation Sources. Jül–Conf–34, p.155 (1980). ISSN 0344–5798

[8] W.A.Coleman, ORNL–TM–220 G (1968)

[9] F. Atchison in: Targets for Neutron Beam Spallation Sources. Jül–Conf–34, p.17 (1980). ISSN 0344–5798

[10] Technology of Targets and Moderators of Medium and High Power Spallation Neutron Sources. PSI–Proceedings 92–03 (1992), ISSN 1019–6447

[11] Y.Kiyanagi and N.Watanabe, Some Neutronic Studies on Flux–Trap Type Moderator. Proc. ICANS–XI, p 408, KEK Report 90–25 (1990)

[12] F.Stelzer, Wärmeübertragung und Strömung, Verlag Thiemig, München (1971)

[13] F.P.Incropera and D.P.de Witt, Fundamentals of Heat and Mass Transfer, John Wiley & Sons, New York (1985)

[14] Instrumentation & Techniques for the European Spallation Source. RAL Report RAL–92–040, (1992)

Acknowledgment

The author would like to thank Prof. Tasso Springer for supporting this work and Dr. Günter Bauer for critical comments and suggestions.

PULSED NEUTRON SOURCE OF THE MOSCOW MESON FACTORY ON THE BASE OF URANIUM TARGETS

A.V. Dementyev, V.G. Miroshnichenko, I.Y. Mosievskaya, S.F. Sidorkin,
N.M. Sobolevsky, Y.Y. Stavissky
Insititute of Nuclear Research, Russian Academy of Science

I.I. Konovalov, A.A. Maslov
All-Union Non-Organic Materials Research Institute

I.T. Tretyakov, V.I. Trushkin
Research Institute of Energotechnics

The pulsed neutron source on the base of the high-current proton linac (average current $\simeq$ 0.5 - 1.0 mA, pulse width 100 to 00 μs and repetition rate up to 100 Hz) and proton storage ring (pulse width $\simeq$ of 0.32 μs, average current up to 0.4 mA, repetition rate 100 Hz) /1/ that is under construction at INR RAS will allow one to develop a wide range of research on condensed matter and nuclear physics.

A set of Ti-coated tungsten plates and close package of natural uranium rods in stainless steel cans placed into the Al-alloy vessel and cooled by light water are supposed to be used as neutron targets. The neutron facility is described in detail in /2-4/. Besides that, even at the initial stage of the experimental complex development, the use of the multiplying target with limited gain factor ($\leq$ 15) is possible. This will allow one:

- to increase significantly the average intensity of the pulsed neutron source at repetition rates 10 to 50 Hz, that is the most suitable range for TOF experiments;

- to decrease the beam current consumption down to 5-50% of the full accelerator intensity, thus making possible more experimental programs to be carried our concurrently;

- to limit the proton beam current in the storage ring (< 0.5 mA), that will make it easier to reach the required operational parameters and will increase its stability;

- to get the high performing neutron source at the initial stage of accelerator operation, before the design parameters will be achieved.

But the multiplying target has the background level much higher than that for non-fissionable targets. So the fissionable isotopes with low delayed neutron ration are preferable.

To create the multiplying target, besides changing natural uranium for highly-enriched fuel, one must decouple the core from moderators to prevent overheating or outer fuel elements by thermal neutrons and provide a short prompt-neutrons generation time /5, 6/.

It is expedient to use the identical design for both natural and enriched uranium targets to provide the full-scope elaboration of all elements of the multiplying target during the natural uranium target operation. It should be noted that existing design of the pulsed neutron source does not allow the transversal dimensions of the target core to be changed without replacing all the central part of the facility, including vacuum and target vessels and shielding plugs. Moreover, the layout of neutron guides inside the biological shield restricts the possibility to vary the core height within the range of 6 to 12 cm (Fig. 1). Therefore, to unify dimensions of the target vessel and reduce expenses, the transversal dimensions of the target could not exceed the adopted earlier diameter of 32.8 cm. Required gain factor could be achieved with changing the height of the target core and upper and lower moderators.

The part of neutron source, shown in Fig. 2, includes core, lower and upper moderators, and Be reflector surrounding the upper moderator /5, 6/.

The target core consists of fuel rods made of sub-stoichiometric U_3Si in stainless steel cans which are 8 mm in diameter and 0.3 mm thick. This fuel composition has the density of 16.1 g/cm^3 and contains 15.8 g/cm^3 of uranium, that is comparable with U-Mo metal alloys (Fig. 3). In case of cladding failure the fuel composition corrosion rate is small enough: less than 0.02 mg/cm^{2}h at 100C and 0.07 mg/cm^{2}h at 200°C. This fuel composition in cylindrical cans promotes good swelling resistance and allows the burn-up of 2 at .% to be achieved, which is very important taking into account the high cost of highly-enriched uranium. The adopted core dsign prevents blocking of coolant channels, which is possible for the scheme with disk fuel elements, and provides the normal target operation for 3 to 5 years. Besides that, U_3Si composition easily changes its state to amorphous and provides good thermal contact between the fuel and can after several tens hours of operation at nominal power. This thermal contact was preserved under conditions of shutdowns and raising the power during reactor tests. The presence of amorphous layer decreases influence of the thermal

impact on the fuel element cladding. In the most stressed case (target on the base of $^{233}U_3Si$ enriched to 98%) the fuel temperature raises up to 15 - 18°C per pulse. To decrease the axial thermal stresses the fuel rod is split into 3 parts. The available technology enables both natural and enriched uranium fuel elements to be manufactured. Prototypes of fuel elements were tested in nuclear reactors for 3.5 years and the burn-up of 3 at .% has been achieved.

The main disadvantage of the cylindrical fuel elements as compared to the slab ones is the decrease in the fuel volume fraction that leads to decrease in a number of spallation neutrons per incident proton - K_n. The computed conversion coefficient K_n and multiplication factor K_m as the functions of the core height are shown in Fig 3. As it can be seen, the use of U_3Si rods instead of tungsten plates of height 6 cm increases th spallation neutron production by a factor of 1.4, while these values for pure uranium and tungsten targets differ by a factor of 1.7÷2.0/10/. This makes us consider the natural uranium target only as an intermediate step toward the highly enriched uranium target with a multiplication factor of 2 to 10. Multiplication factor is limited by the following requirements: low delayed neutrons background nuclear safety requirements for subcritical assemblies without control and safety systems /10/, and, finally, coolant system capacity (2.5 MW). On the other hand, our intent is to construct the thermally stressed target, which provides the total neutron production per proton not less than that for pure uranium and one whose operational lifetime is long enough.

In order to provide the uniform cooling and not to lengthen the fast neutron pulse due to the slowed-down neutrons induced fission, both the coolant inlet and outlet are made as vertical slots in a plate made of material well absorbing epithermal and thermal neutrons. The most suitable materials, compatible with other materials of the target, are hafnium, zirconium-hafnium and titanium-gadolinium alloys with the addition of rare-earth elements. The plate made of the same alloy is placed on top of the core, while the lower side of the target vessel is coated by the thin layer of the absorber.

The use of different metals and allkoys required extensive studies of their compatibility and providing of water conditions. Data on corrosion rate of possible target materials in distilled water at various conditions (including neutron irradiation) are given in Fig. 4. For additional protection against corrosion all aluminium parts of the target are coated by titanium. Reactor tests of A1 and W samples in water have shown that Ti coating is stable and compatible with other core materials. No changs of Ti coating were observed after the priod of time comparable with that of the target operation.

The fuel elements are distantiated by stainless-steel wire of 0.4 mm thickness. To recompense for thermal expansion and to avoid vibrations due to collant flow, the fuel elements assembly is embraced by the spring elements made of Zr-Mo alloy. This alloy preserves its elasticity under irradiation and is compatible with target materials.

The upper moderator is surrounded by the berillium reflector cooled by water flowing to and from the target core. The outer part of the target vessel is coated with Gd, which acts as a decoupler for upper moderator and, at the same time, provides nuclear safety in case of accidental flooding of the vacuum vessel with water. This decision allows one to provide the satisfactory thermal contact of an absorber and construstruction material and to escape the need of additional studies of material compatibility in the water.

The upper moderator has face dimension of 12 x 12 cm^2 and thickness of 5.5 cm. To shorten the thermal neutron pulse width the moderator is split with Ti-Gd plate into two parts - say, 2 and 3.5 cm. This allows the moderator to be customised for particular experiments. The lower moderator has dimensions of 20 x 20 x 3 cm^3 and is optimised for experiments with intermediate and epithermal neutrons.

Parameters of pulsed neutron sources based on the W, U^{238}, U^{235} and U^{233}, with the storage ring are compared in Table 1. It can be seen that the multiplying target has the thermal neutron flux density 6 times higher than the natural uranium one.

At present, natural uranium fuel elements, Be reflector, Al target vessel, and shielding plug are manufactured. Tests on compatibility and corrosion rates of target materials are completed. Now we are finishing manufacturing the parts made of Ti-Gd and Zr-Mo alloys and coating target core parts with Ti. In the next year we plan to complete assembly, certification and coating the target with Gd.

References

1. S K Esin et al. INR linear accelerator and compressor ring project for the spallation neutron source. Proc. ICANS-11, v.1, p. 194, KEK, Japan, 1990.

2. Y M Bulkin et al. Neutron source complex on the base of proton beams of the Moscow Meson Factory. Proc. Conf. on neutron scattering in the 'nineties, Julich, IAEA, 1985.

3. Y Y Stavissky. Neutron facilities of Moscow meson and kaon factories. Proc. ICANS-11, v.1, p. 87.

4. M I Grachev et al. Pulsed and quasi steady-state neutron sources based on proton beams of Moscow meson facility. Iid., v.1, p. 454.

5. V G Miroshnichenko, S F Sidorkin, U U Stavissky. Multiplying neutron targets on the base of the proton beam of Moscow meson factory. Procs. of INES-89, pp.119-124.

6. M Holding, T A Broome. The status of ISIS targets. Proc. ICANS-11, v.1, p. 478.

7. A S Il'inov et al. INR RAS Preprint, P-0299, 1983.

8. G F Liman et al. Questions of atomic science and technology. Ser. Physics and technology of nuclear reactors, v.7, pp.27-31, 1985.

9. N Watanabe et al. Depleted uranium target system. KENS Report-6, p.11, 1985-86.

10. Rules of nuclear safety for subcritical systems. ПВR-01-75.

11. I I Konovalov, A A Maslov. Choice of materials and radiation-resistant coating technology. Interim report, 1990.

TABLE 1.

Target parameters	W	U^{238}	U^{235}	U^{233}
Average power, MW	0.2	0.4	2.12	2.17
Background power, MW	-	0.004	0.014	0.0063
Thermal neutrons pulse width, mks*	30	30	30	30
Multiplication	0.95	1.15	14.5	20
Lifetime of prompt neutrons, ns	-	-	45	44
Average thermal neutron flux density, n/cm^2s*	$3.0 \cdot 10^{12}$	$4.0 \cdot 10^{12}$	$10.6 \cdot 10^{12}$	$18.1 \cdot 10^{12}$
Peak thermal neutron flux density, n/cm^2s*	$1.0 \cdot 10^{15}$	$1.3 \cdot 10^{15}$	$11.8 \cdot 10^{15}$	$20.1 \cdot 10^{15}$
Repetition rate, pps	100	100	30	30

*For 3.5 cm part of water moderator.

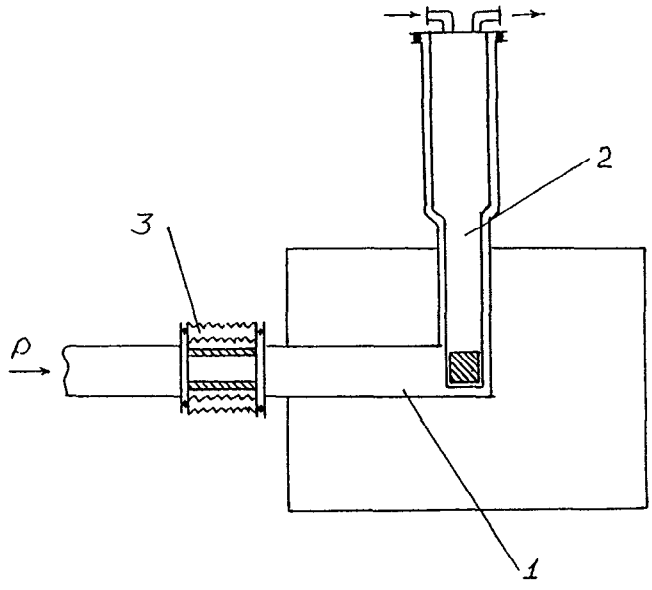

Fig. 1 Design of neutron source.

1 - Tank with vacuum system; 2. - Ampoule of source,

3 - Remote-controlled vacuum seal.

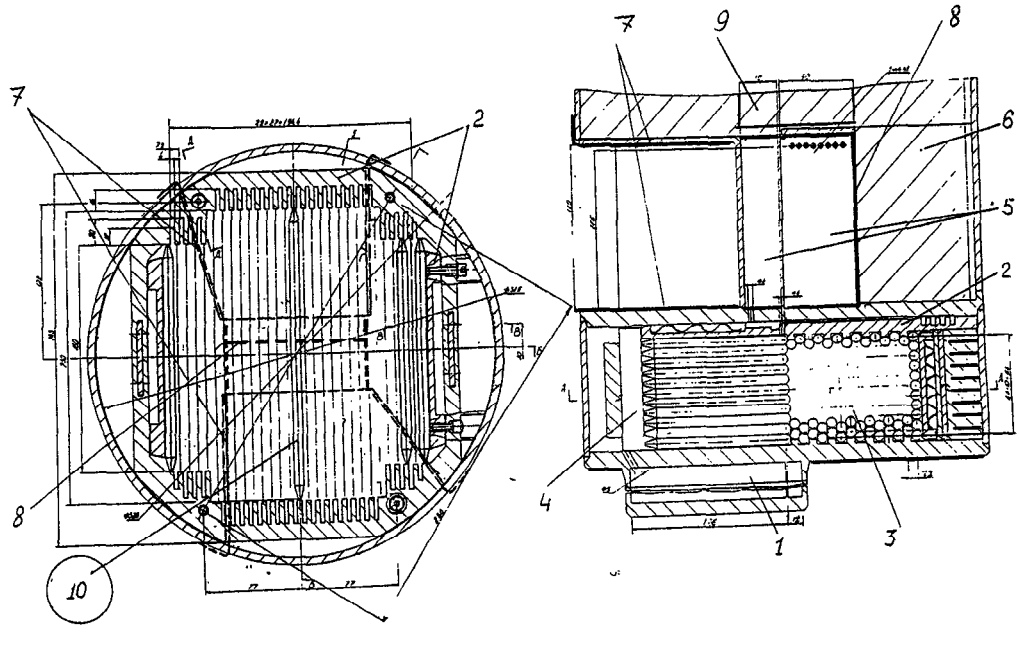

Fig. 2a. Central part of the multiplying neutron source.

1 - lower moderator; 2 - Ti-Gd decoupler; 3 - core; 4 - coolant inlet and outlet;

5 - upper moderator; 6 - reflector; 7 - Gd decoupler; 8 - Ti-Gd insertion;

9 - Be plug; 10 - fuel element.

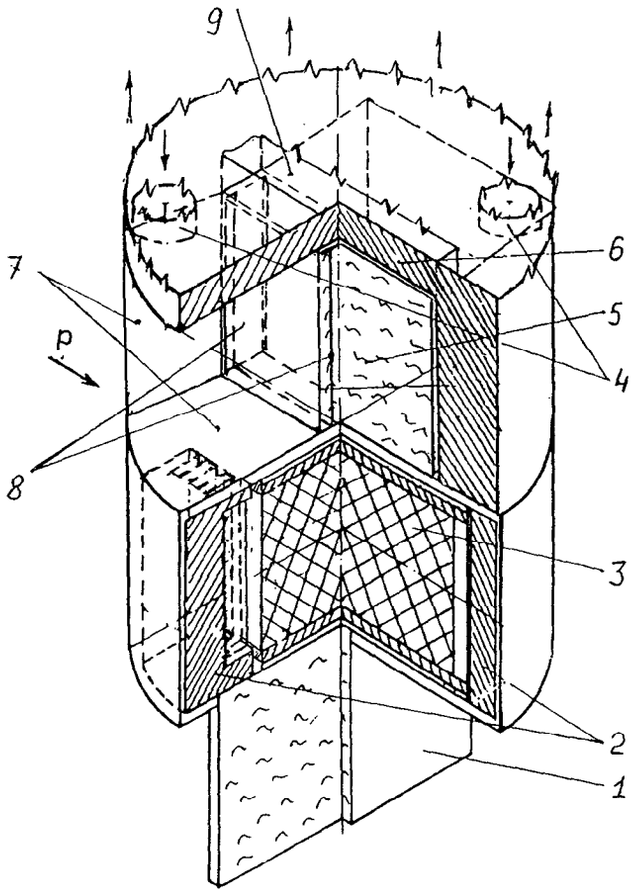

Fig. 2b. Central part of the multiplying neutron source.

1 - lower moderator; 2 - Ti-Gd decoupler; 3 - core; 4 - coolant inlet and outlet;

5 - upper moderator; 6 - reflector; 7 - Gd decoupler; 8 - Ti-Gd insertion;

9 - Be plug; 10 - fuel element.

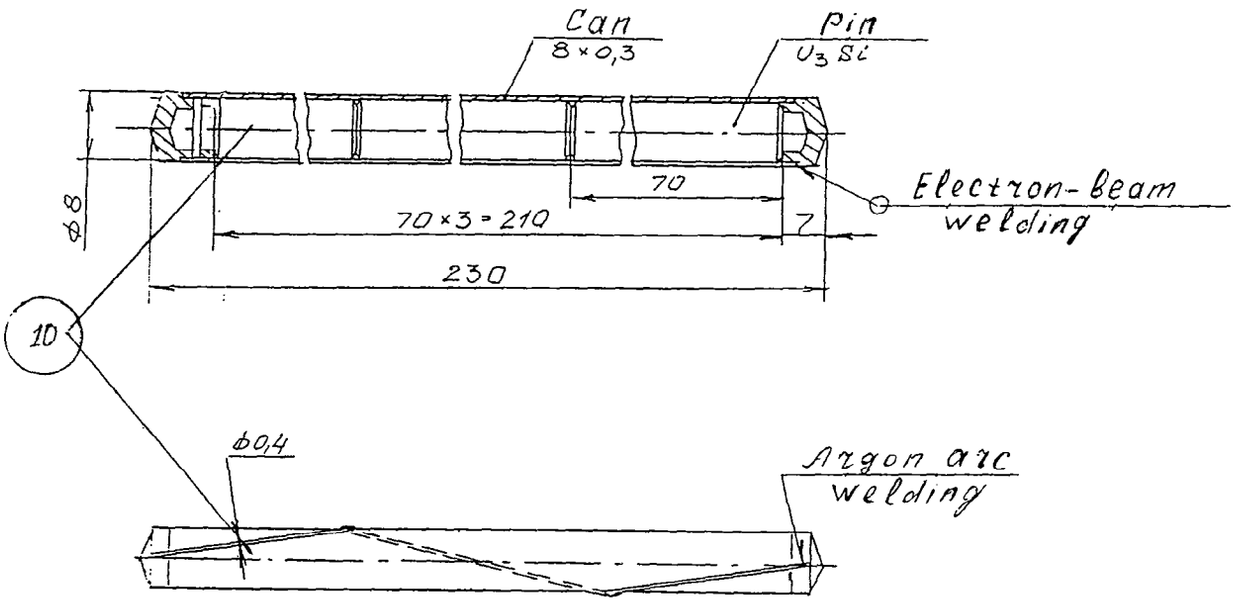

Fig. 2c. Fuel element

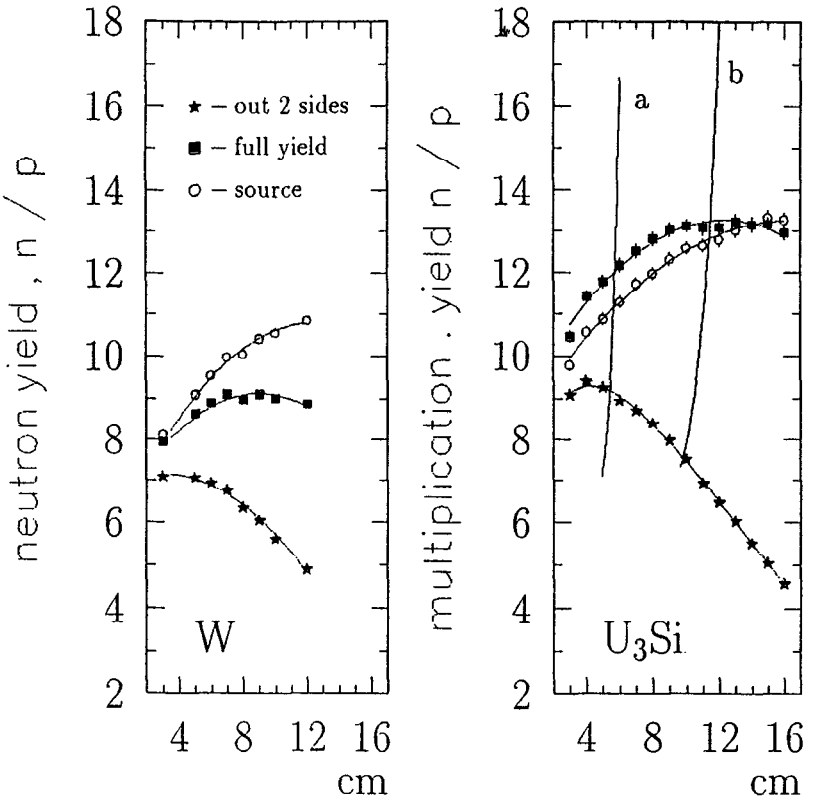

Fig. 3. Computed spallation neutron yield per 600 MeV incident proton for tungsten (1) and natural U3Si (2) targets and multiplication factor for U235 (b) and U233 (a) targets as the functions of the core height.

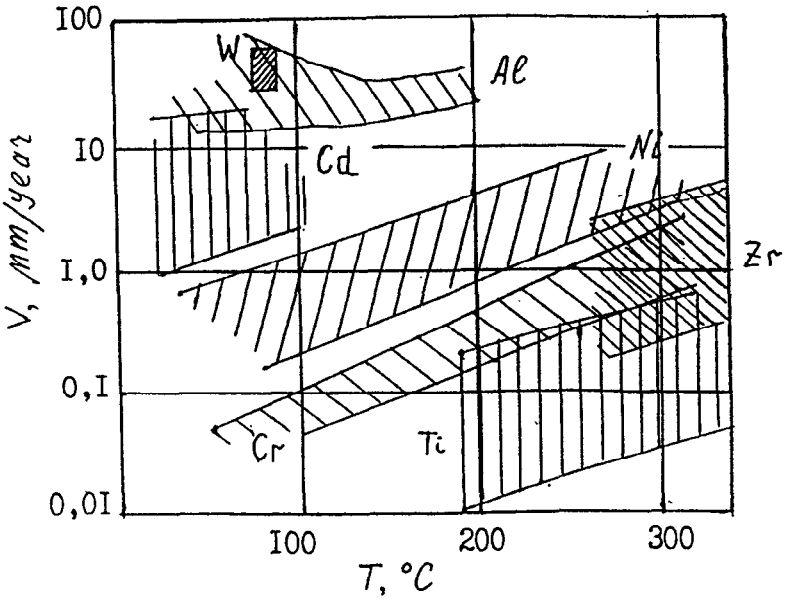

Fig. 4. Corrosion rates of possible target materials in distilled water at various conditions.

SPALLATION NEUTRON MEASUREMENT AT INCIDENT PROTON ENERGIES OF 0.8 TO 3 GEV

T.NAKAMOTO, K.ISHIBASHI, N.MATSUFUJI, K.MAEHATA, Y.WAKUTA,
Department of Nuclear Engineering, Kyushu University
Hakozaki, Fukuoka 812, Japan
M. NUMAJIRI
National Laboratory for High Energy Physics (KEK)
Oho, Tsukuba 305, Japan
H. TAKADA, S. MEIGO and S. CHIBA
Japan Atomic Energy Research Institute (JAERI)
Tokai-mura, Ibaraki 319-11, Japan
Y. WATANABE
Energy Conversion Engineering, Kyushu University
Kasuga-koen, Kasuga 816, Japan
T. NAKAMURA
Cyclotron and Radioisotope Center, Tohoku University
Aoba, Sendai 980, Japan
M. ARAI
Department of Physics, Kobe University
Rokkoudai, Kobe 657, Japan

ABSTRACT

It has been experimentally confirmed that the high-energy nucleon(proton or neutron) spectra from the nuclear spallation reaction are in good agreement with the results of the cascade calculation. However, low-energy nucleon spectra below several 10 MeV have not been measured for the spallation reaction for incident protons of GeV range. The experiment on the neutron-emission double-differential cross section was carried out at proton energies of 0.8, 1.5 and 3 GeV at KEK. The neutrons were measured by the time-of-flight method with a typical flight path of 1 m. The experiment for C and Pb targets was completed last November. Neutrons having energies of 1 to 300 MeV were successfully measured with acceptable uncertainty. Measurements will be continued this year to cover a few targets between C and Pb.

I. INTRODUCTION

It is of interest to investigate the neutron-emission cross section for the reaction (p,xn) by incident protons in the medium energy region. The data are useful for studying such facilities as the spallation neutron sources and the accelerator-driven transmutation systems. The experimental data were obtained by the time-of-flight (TOF) method at IUCF[1] with incident proton energies of 120 and 160 MeV, at PSI (SIN)[2] with that of 585 MeV, and at LANL[3-6] with those of 113 to 800 MeV. At higher energies than these, a test measurement[7] was made at National Laboratory for High Energy Physics (KEK). However, systematic data covering many targets have not been taken in the energy region above 800 MeV so far.

With increasing proton energy from 113 to 800 MeV, the experimental neutron cross section showed a systematic difference[5] from the calculated results in the evaporation and/or preequilibrium region. In the GeV region of incident proton energy, it is well known that the high-energy nucleon (proton or neutron) spectra from the nuclear reaction are in good agreement with the results of the cascade model calculation. A special interest attaches to the spallation neutrons with energies of 1 to 100 MeV. We have planned to measure the double differential cross section (DDX) of the spallation neutrons by the TOF method. The incident proton energies were chosen to be 0.8, 1.5 and 3 GeV. Protons were supplied by $\pi 2$ beam line at KEK. The protons are obtained as secondary particles generated by an internal target, which is placed in the accelerator ring of the 12 GeV proton synchrotron. Before performing the experiment for the cross sections, we made a preliminary measurement to check the experimental methods.

II. PRELIMINARY MEASUREMENT

Some test measurements were made at the $\pi 2$ beam line with protons of 1.5 GeV. The scintillator NE213 was chosen for the neutron detection. An early question was whether or not to shield neutron detectors from background neutrons and gamma rays. The results at 90° are plotted in Fig. 1. Open triangular marks show the data taken by a bare neutron detector, while solid square ones indicate those by the detector surrounded with iron blocks of 0.5 to 1 m thick. A large disagreement is seen at a few MeV. The heavy shielding was not appropriate in the experimental circumstances. Neutron detectors were, therefore, determined to be used on the bare condition.

At first, we followed the zero-cross method[8] for the pulse-shape discrimination between neutron and gamma ray. The results by this method ware shown in Fig. 2. The discrimination was worse for high-energy events. This is because the saturation effect was induced on the zero-cross time in a pulse-shaping preamplifier, due to the very large energy-range of the incident particles. To eliminate such saturation, a two-gate integration method[9] was tested at a later test run. The photomultiplier signal was branched into two pulses, and they were input into charge ADCs worked by different gate pulses. The fast gate on one ADC covered the initial peak of the photomultiplier signal, whereas the tail gate made another ADC to accept the slow-tail portion thereof. The fast gate had a duration of 30 ns, and the tail gate owned that of 500 ns after a delay of 130 ns. The results are shown in Fig. 3. The discrimination is excellent and the above saturation effect is not seen. The two-gate integration method was adopted in the measurement thereafter.

The simplest method for background correction is to make two kinds of experiments of target-in and -out measurements: The cross section is obtained by subtracting the latter data from the former ones. However, in this case, the influence from such effects as the floor-scattered (or -generated) neutrons may not be removed. We were afraid that the floor-scattering effect might arise because of the rather short height (1.7 m) between the floor and the beam line. The experimental check was made by inserting a shadow bar of 1 m length between target and detector. The detector was placed at the beam -line level with a TOF flight path of 1.5 m. The results at 60 deg are shown in Fig. 4, together with the cross section measured. One can see the effect like the floor scattering is negligible in the energy region at the flight path.

III. EXPERIMENTAL ARRANGEMENTS

The experimental specification is listed in Table 1. The NE213 detectors have two kinds of sizes (Φ5"×5" and Φ2"×2"). The larger detectors were used for making the neutron-detection efficiency as high as possible, although they produce a rather poor time resolution in the TOF measurement. The smaller ones exhibit good neutron-gamma pulse-shape discrimination even in the neutron energy region around 1 MeV.

The experimental arrangement is illustrated in Fig. 5. The beam intensity of the $\pi 2$ beam was very weak and in a level of 10^5 particles/2.5s because of its generation as a secondary beam. Incident particles were counted one by one by plastic scintillators. The protons were identified from pions by a pair of TOF scintillators (Pilot U) located at a separation distance of 20 m. Each Pilot U scintillator was connected on opposite sides with two photomultipliers (Hamamatsu H2431). The particle identification is shown in Fig. 6, for instance, at a beam momentum of 3.83 GeV/c, i.e. proton kinetic energy of 3.0 GeV. The time signals of the two sides were averaged by software. The time resolution was 0.35 ns, and protons are well discerned from pions having a separation time of 1.7 ns.

For the neutron TOF measurement, the time standard was taken by the Pilot U scintillator adjacent to the target. The beam-incident target area was defined by a pair of scintillators. Because of the low beam intensity, the flight path of the neutron TOF was limited to short distances: It was 1 to 1.5 m for the Φ5"×5" detectors, and 0.6 to 0.9 m for Φ2"×2" ones. The values of flight path were shorter than the beam-line height 1.7 m from the floor. Veto plastic scintillators were used for finding charged-particle events in the neutron detectors. They were installed in front of all neutron detectors as illustrated in Fig. 5. The picture of the detector system is presented in Fig. 7. The whole frame was made of aluminum alloy. The 5" detectors were arranged over the beam line, for the redundant safety for the floor-scattering effect. The beam damp was formed by carbon of 0.5×0.5 m^2 in area and 1 m thick. The carbon

was surrounded by sufficiently thick iron blocks except at the beam-incident surface. The distance between the target and the beam dump was 8.5 m.

The block diagram of the measurement circuit is shown in Fig. 8 with simplified drawing. When the incident-beam coincidence took place at all the beam scintillators, the pulse with a typical width of 150 ns was sent to the next coincidence module. Then, the signal of neutron detectors was accepted by this module for 150 ns. The events arising from incident pions were eliminated by tuning a hardware timing in the beam coincidence. The example of the TOF spectrum is shown in Fig. 9. The prompt gamma rays are seen as a sharp peak in the right hand side. The time resolution of the neutron TOF measurement was 0.96 ns for 5" detectors and 0.55 ns for 2" ones.

The detection efficiency of the neutron detectors was calculated by the use of the Cecil code[10] of the Kent State University version. The experimental check on the detection efficiency has recently performed at JAERI for neutrons with energies below 30 MeV. Although detailed analysis for the experiment was not made completely, we considered that the experimental efficiency was close to or slightly (~10%) below the calculated values. In this paper, the detection efficiency as calculated is utilized for converting the measured TOF events into the cross sections.

IV. EXPERIMENTAL RESULTS

The measurement has already been carried out for targets of Pb and C at proton energies of 0.8, 1.5 and 3.0 GeV. The preliminary DDX data are shown in Figs. 10-12 for Pb and Figs. 13-15 for C. The relatively worse time resolution for the short flight path lead to considerable ambiguity in neutron energies above 200 MeV as listed in Table 2; we are not concerned about it because our interest is mainly in the evaporation (and preequilibrium) neutrons. Calculation results by the cascade-evaporation model (HETC)[11] was shown by lines. The experimental data at 0.8 GeV are compared with those[5,6] of LANL in Fig. 16. The present preliminary DDX agrees with the LANL data typically within a discrepancy of 10%. Further checks and corrections will be made on such items as the detection efficiency and multiple scattering effects in the target itself. The measurements for other targets i.e. Al, Fe, and In are to be performed in 1993.

The measurement data are converted into a linear scale on the vertical axis: The cross section are plotted with normalization by $\ln(E_{n+1})-\ln(E_n)$ instead of conventional method of $E_{n+1}-E_n$. The linearized data are shown in Figs. 17 and 18 for proton energies of 0.8 and 3.0 GeV, respectively. The calculated values of the evaporation component are clearly higher than the experimental data in Fig.18 for 3.0 GeV protons, but such difference is not seen in Fig.17 for 0.8 GeV. The overestimation in the evaporation region in Fig.18 may be attributed to the lack of theoretical consideration on the fragmentation phenomenon, which appears at high incident energies around 3 GeV.

V. CONCLUSION

The measurement of (p,xn) reaction at incident proton energies of 0.8, 1.5 and 3.0 GeV was started. The experimental difficulties were overcome through the test measurement. The measurement on the heaviest element of Pb and the lightest C had already been carried out. The DDX for Pb at 0.8 GeV was compared preliminarily with the LANL data, and was confirmed to agree with them in an acceptable manner. Further experiment on the rest of the targets is planned to be completed in 1993.

The authors express their gratitude to Prof. K. Nakai and the beam channel staffs of KEK for his continuous encouragement and their generous support of this experiment, and tender their acknowledgements to Prof. H. Hirabayashi and Prof. N. Watanabe of KEK, and Prof. M. Arai of Kobe University for their useful discussion.

REFERENCES

1) W.Scobel et al.: Phys. Rev. C 41 (1990) 2010.
2) S.Cierjacks et al.: Phys. Rev. C 36 (1987) 1976.

3) M.Meier et al.: Radiation Effects 196 (1987) 1415.
4) M.Meier et al.: Nucl.Sci.Eng. 104 (1990) 339.
5) W.Amian et al.: Proc. Nucl. Data for Sci. and Technol. (1991) p.696
6) W.Amian et al.: Nucl.Sci.Eng. 112 (1992) 78.
7) R.Chiba: Genshikaku-kenkyu 21 (1985) 41 in Japanese.
8) P.Plischke et al.: Nucl. Instrum. Meth. 139 (1976) 579.
9) Z.W.Bell et. al.: Nucl. Instrum. Meth. 188 (1981) 105.
10) R.A.Cecil et al.: Nucl. Instrum. Meth. 161 (1979) 439.
11) F.Atchison : JUL-CONF-34 (1980)

Table 1 Experimental specification

Proton energy (GeV)	0.8, 1.5, 3.0
Targets (thickness)	C(10cm), Pb(1.2cm) Al, Fe, In (planned)
Method	Time of Flight
Neutron detector	NE213, Φ2"×2" and Φ5"×5"
Flight path (m)	0.6~0.9 for Φ2"×2" 1~1.5 for Φ5"×5"
Photomuliplier	H1250 for Φ5"×5" H1161 for Φ2"×2" H2431 for Pilot-U
Angle (deg)	15, 30, 60, 90, 120, 150

Table 2 Neutron energy resolution*

Neutron energy(MeV)	Flight time(ns)	Energy resolu.(%)
3	46	5.5
10	25	5.8
30	15	7.5
100	8.6	12
200	6.5	18
300	5.6	23
400	5.1	28

*TOF with a mean flight path of 1.1m and a time resolution of 0.96 ns.

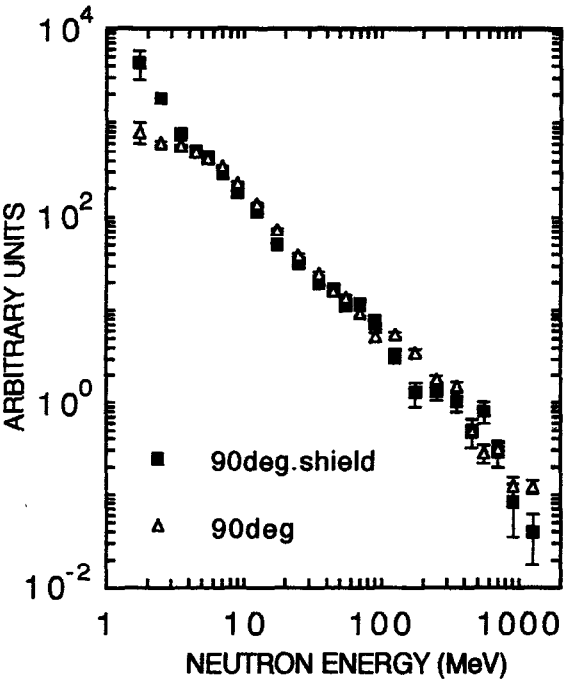

Fig. 1 Neutron spectra at 90° by 1.5 GeV protons with and without iron shielding around a neutron detector. The vertical axis is in a relative scale.

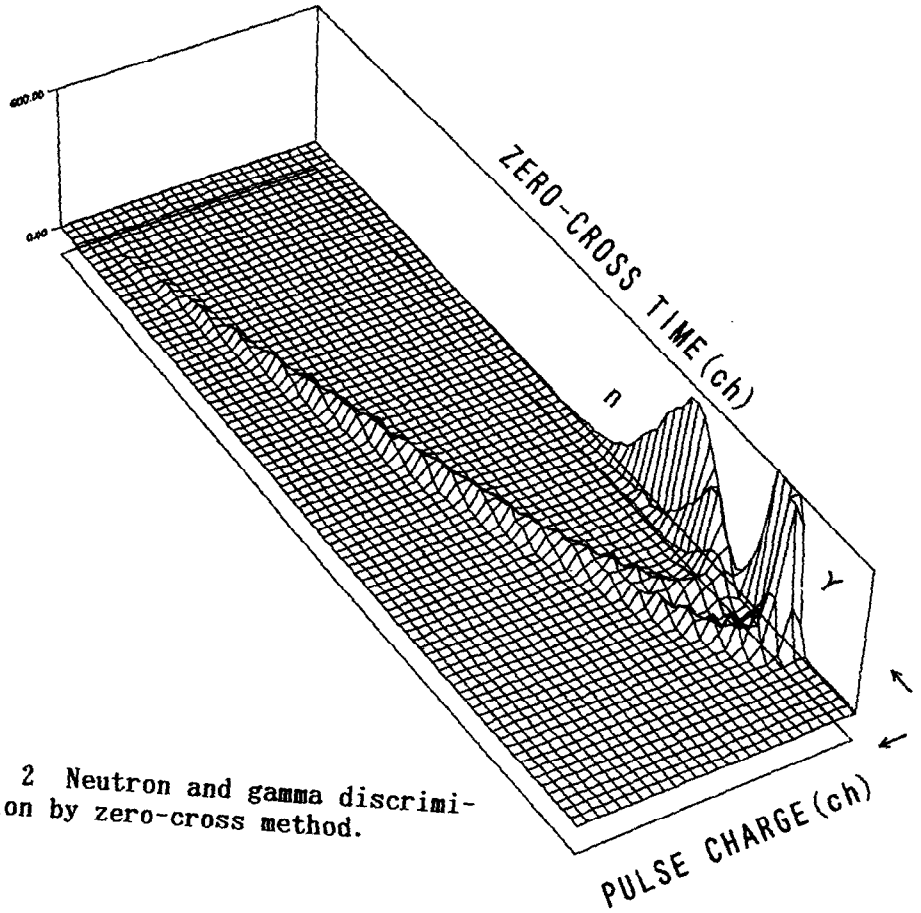

Fig. 2 Neutron and gamma discrimination by zero-cross method.

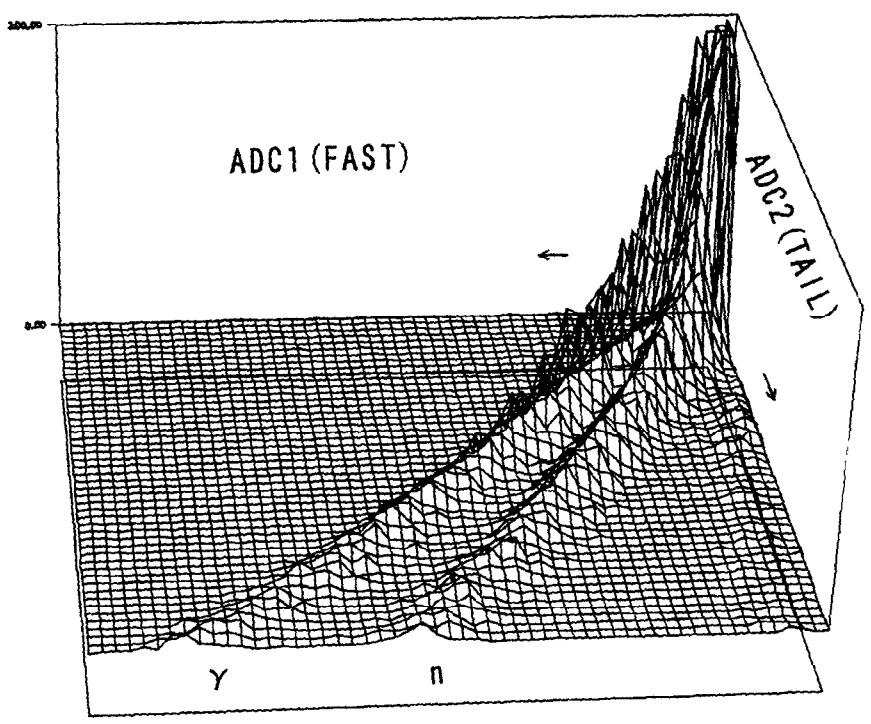

Fig. 3 Neutron and gamma discrimination by two-gate integration method.

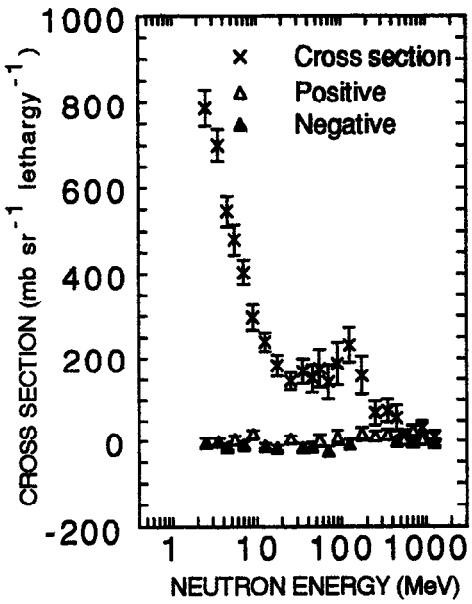

Fig. 4 Results of the shadow bar test. The shadow bar size was $\phi 15 \times 100 cm^2$ and the flight path 1.5 m. The vertical axis is linearized by the use of lethargy $\ln(E_{n+1})-\ln(E_n)$.

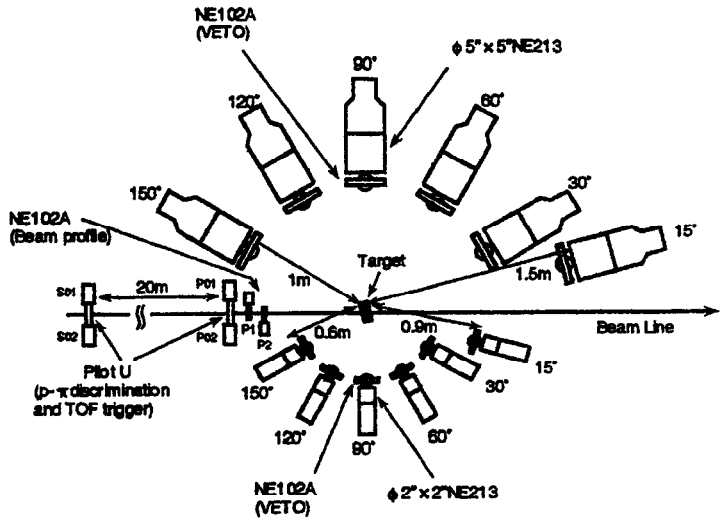

Fig. 5 Illustration of the experimental arrangement.

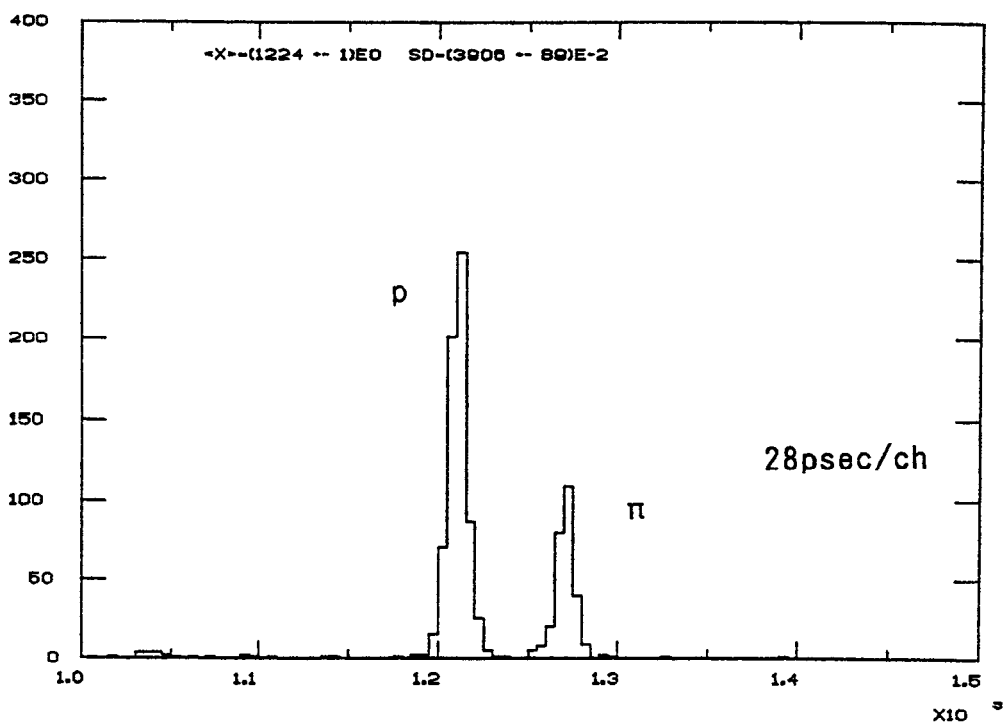

Fig. 6 Proton-pion separation in TOF spectrum for beam of 3.83 GeV/c.

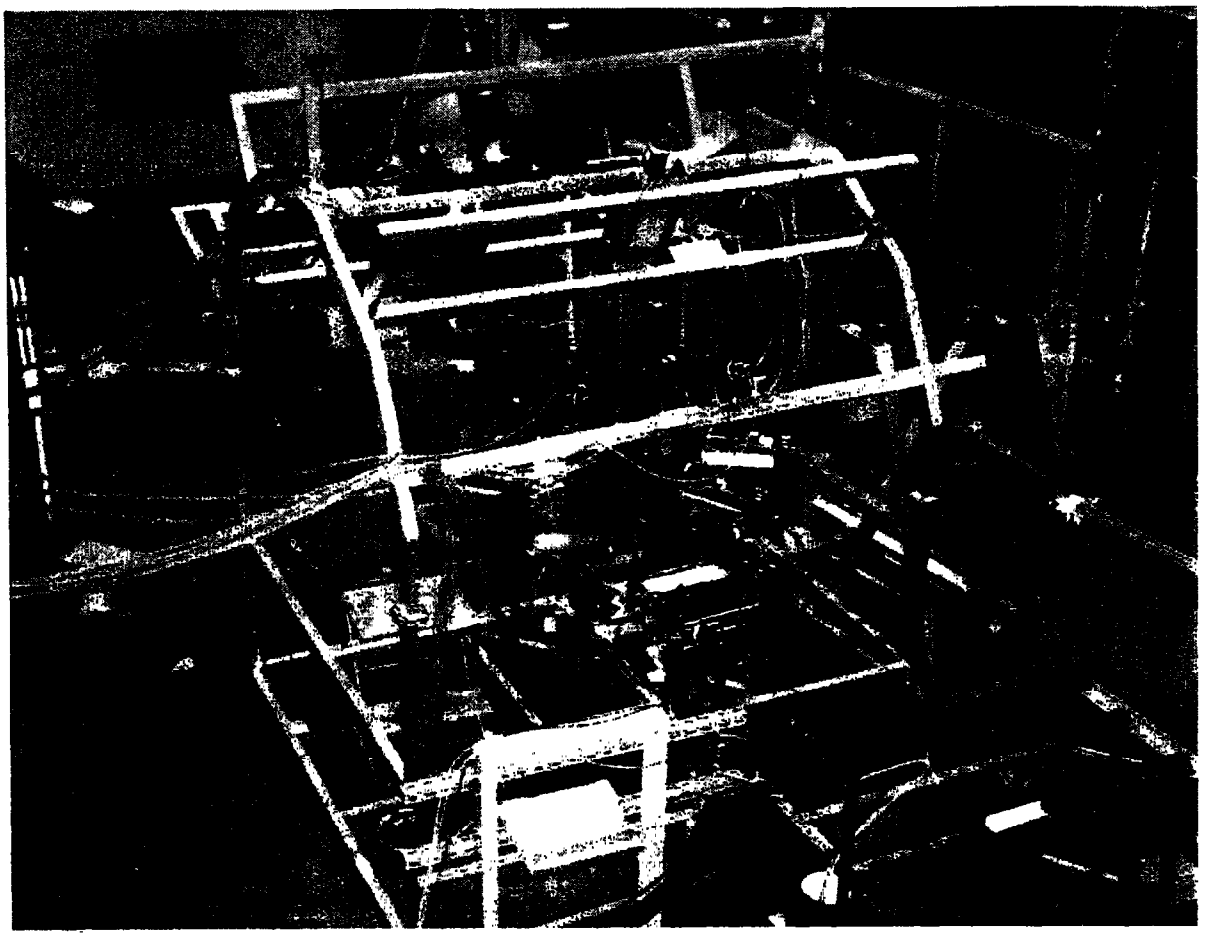

Fig. 7 Picture of the detector system. Incident particles come from the right side.

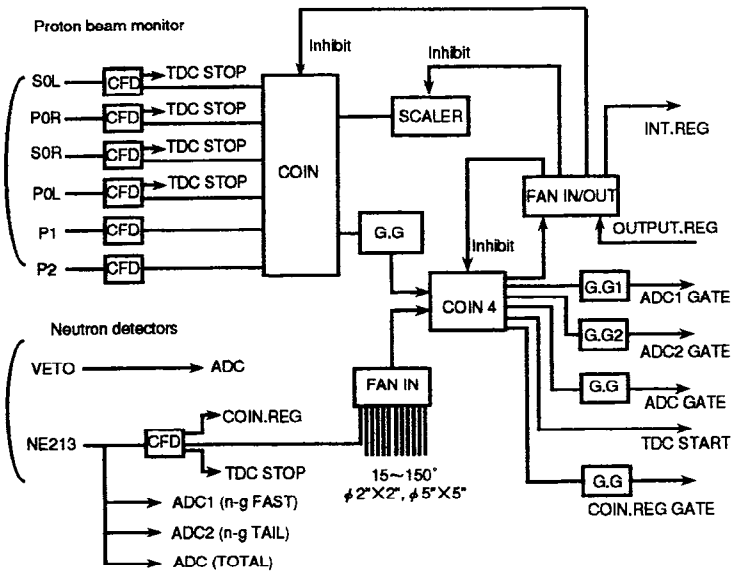

Fig. 8 Block diagram of the electronic system with simplification.

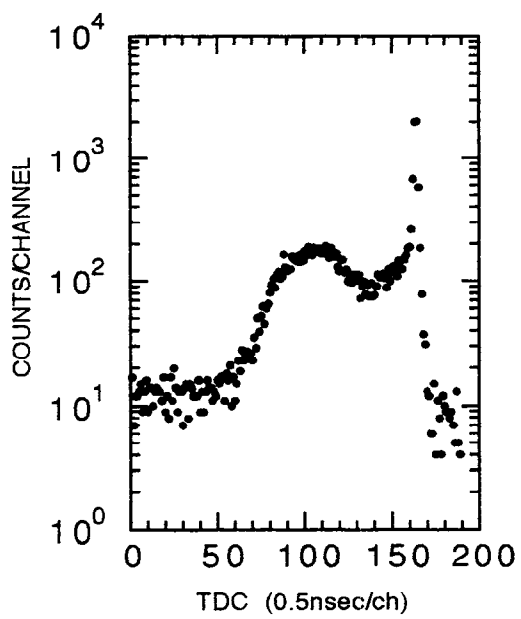

Fig. 9 TOF spectrum at 15° for an incident proton energy of 1.5 GeV.

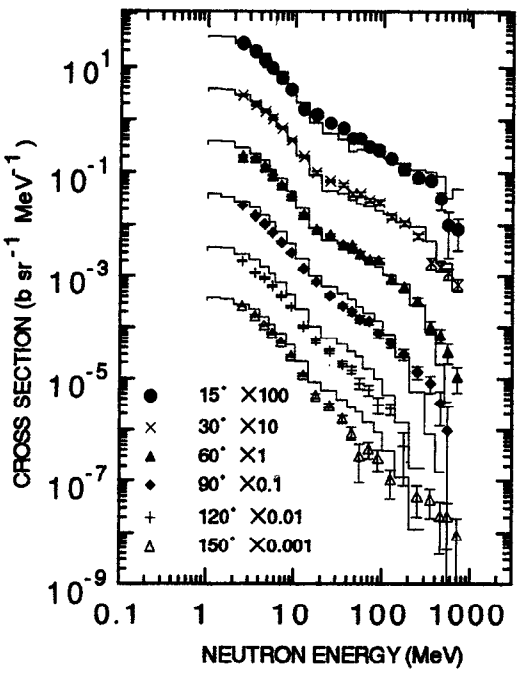

Fig.10 Double differential cross section at 0.8 GeV for Pb. Lines show calculation results by HETC.

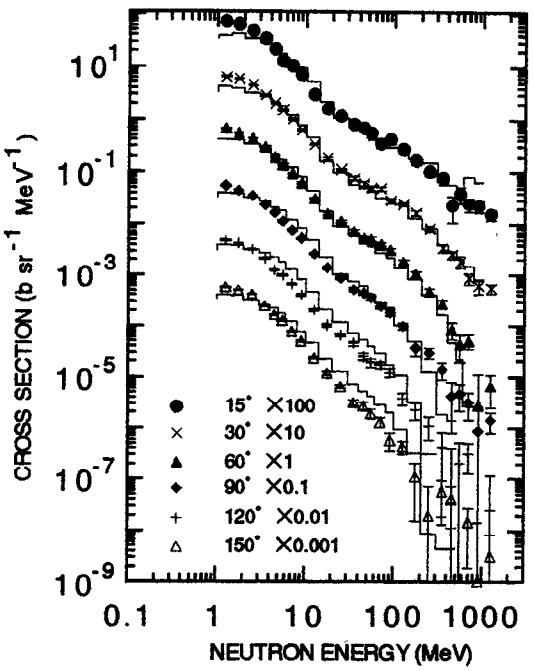

Fig.11 Double differential cross section at 1.5 GeV for Pb. Lines show calculation results by HETC.

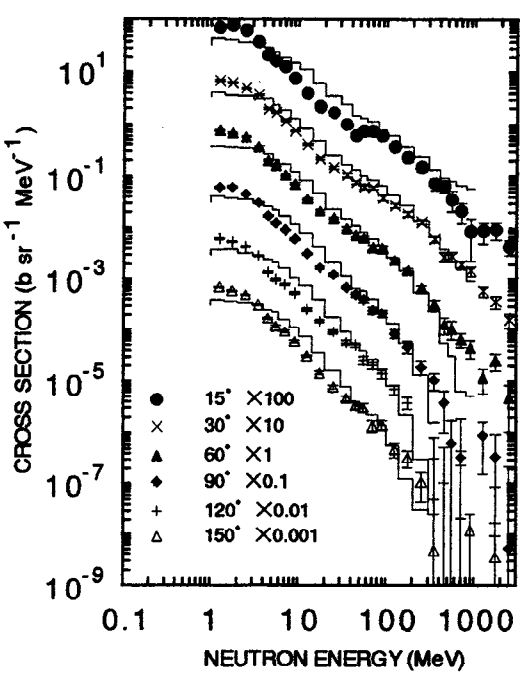

Fig.12 Double differential cross section at 3.0 GeV for Pb. Lines show calculation results by HETC.

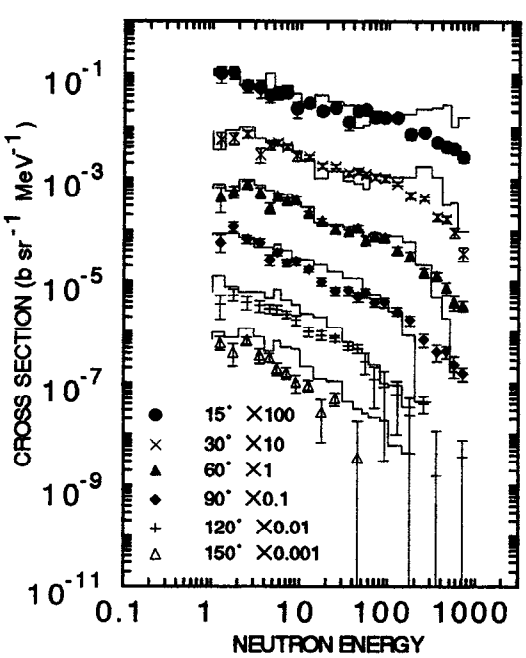

Fig.13 Double differential cross section at 0.8 GeV for C. Lines show calculation results by HETC.

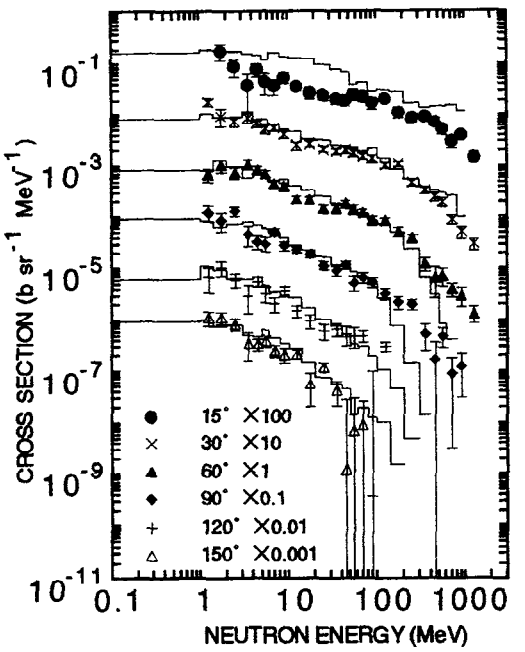

Fig.14 Double differential cross section at 1.5 GeV for C. Lines show calculation results by HETC.

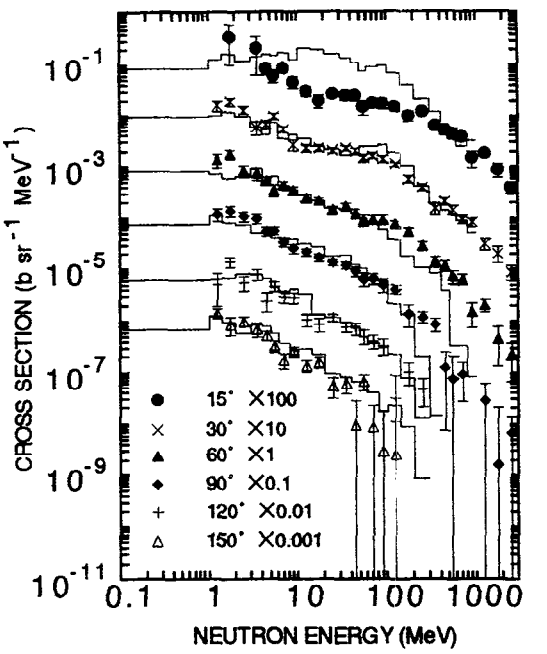

Fig.15 Double differential cross section at 3.0 GeV for C. Lines show calculation results by HETC.

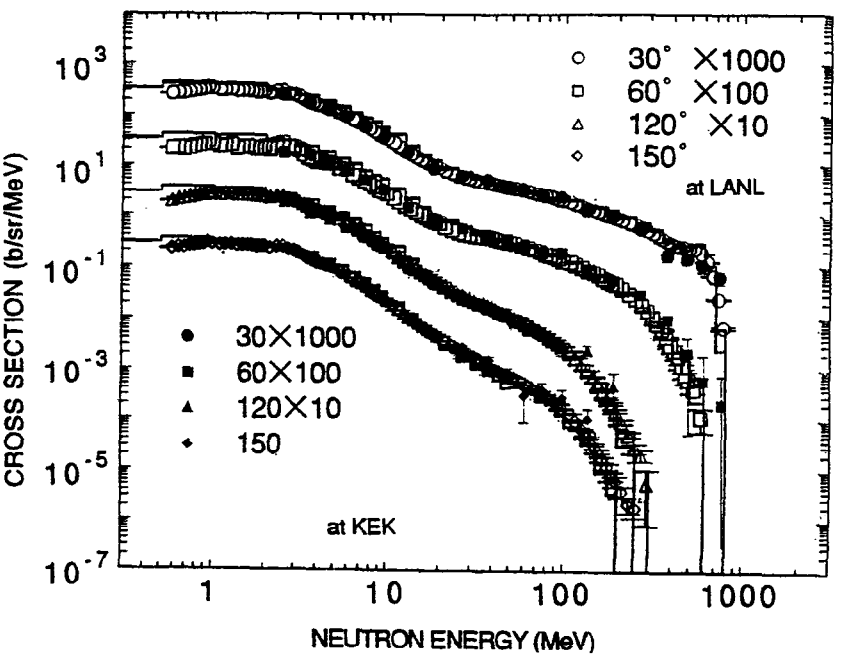

Fig.16 Double differential cross section at 0.8 GeV for Pb, presented together with the results of LANL.

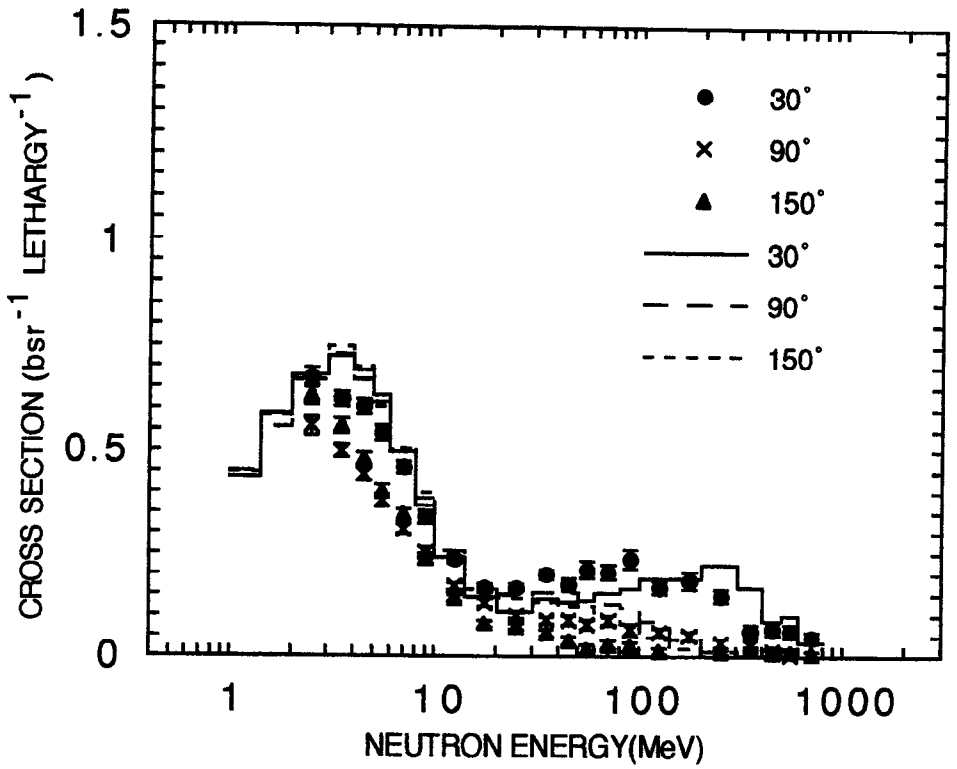

Fig.17 Linearized cross sections at 0.8 GeV for Pb. Lines show the results of HETC calculation. The lethargy of $\ln(E_{n+1})-\ln(E_n)$ is used for the vertical axis.

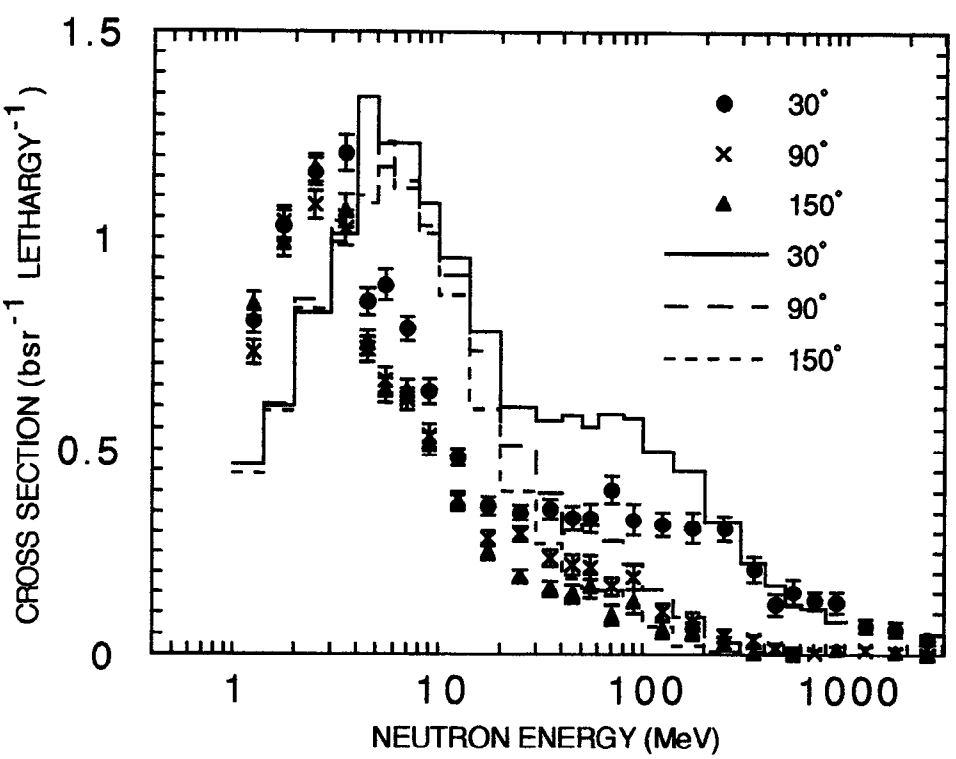

Fig.18 Linearized cross sections at 3.0 GeV for Pb. Lines show the results of HETC calculation. The lethargy of $\ln(E_{n+1})-\ln(E_n)$ is used for the vertical axis.

Comparison of the Slow-Neutron Intensity -0.8 GeV vs 3 GeV Protons-

Y. Kiyanagi, N. Watanabe* and M. Arai**

Department of Nuclear Engineering, Faculty of Engineering, Hokkaido Univ., Sapporo 060
*National Laboratory for High Energy Physics, 1-1 Oho, Tsukuba-shi, Ibaraki 305
**Department of Physics, Faculty of Science, Kobe University, Kobe 657

Abstract

The choice of the proton energy for an intense pulsed spallation neutron source is one of the most important topics in recent years. A high proton energy, but with a modest beam current, is more acceptable from an accelerator point of view. We calculated the slow-neutron intensities from a reference target-moderator-reflector assembly for various proton energies over the range 0.8 - 3 GeV. The result shows that the slow-neutron intensity per unit proton beam powder with 3-GeV protons is about 80% of the 0.8-GeV case. A higher proton energy is also well acceptable from a neutronic point of view.

1. Introduction

When we consider an intense "pulsed" spallation neutron source, a high-intensity proton ring accelerator, such as a compressor ring, a synchrotron or an FFAG is generally indispensable, combined with a high-current proton linac of full energy or an appropriate injection energy. A higher energy, but having a modest beam current, is more feasible from an accelerator point of view (space charge limit). The merits and demerits for using higher energies ($E_p > 0.8$ GeV) are being extensively discussed at various laboratories (e.g. for ESS :European Spallation-neutron Source, IPNS upgrade, etc.). We had a similar problem in choosing the proton energy for the Japanese Hadron Project (JHP) where KENS-II, a next-generation pulsed spallation neutron source, is to be involved. The neutron society stressed the adoption of a lower energy, say 1 GeV, while the nuclear physics society suggested a higher energy, at least 2 GeV (hopefully 3 GeV). We performed some neutronic calculations (1) in order to understand the proton-energy dependence of the neutron intensity using a hadron transport code NMTC/JAERI (2) combined with some low-energy neutron transport codes. Our results were very much unfavorable for higher proton energies. Based on these results we chose 1 GeV in the first-phase JHP.

We recently found our earlier calculation (1) to be some misleading. NMTC/JAERI gave smaller neutron yields at higher proton energies (above 1 GeV). After that, the code was revised and confirmed to give consistent results with those using an HETC code in some benchmark calculations, and with some measured results. (3) We performed re-calculations using the revised NMTC/JAERI on a target-moderator-reflector system which was the same as in the previous calculations, since the results are so important for the strategy of a new source. We briefly report on the new results, while mainly focussing on the slow-neutron intensity with 3 GeV protons compared with the 0.8 GeV case.

2. Fast Neutrons from Target

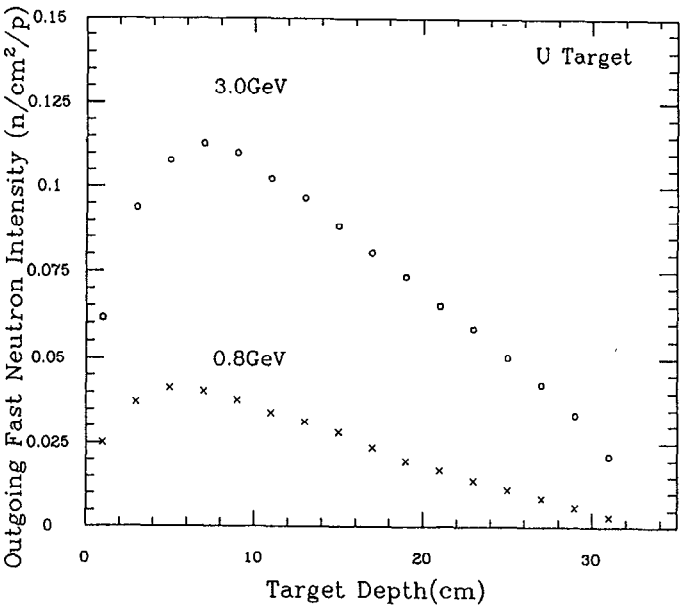

Fig. 3 Axial distributions of outgoing fast neutrons from a cylindrical surface.

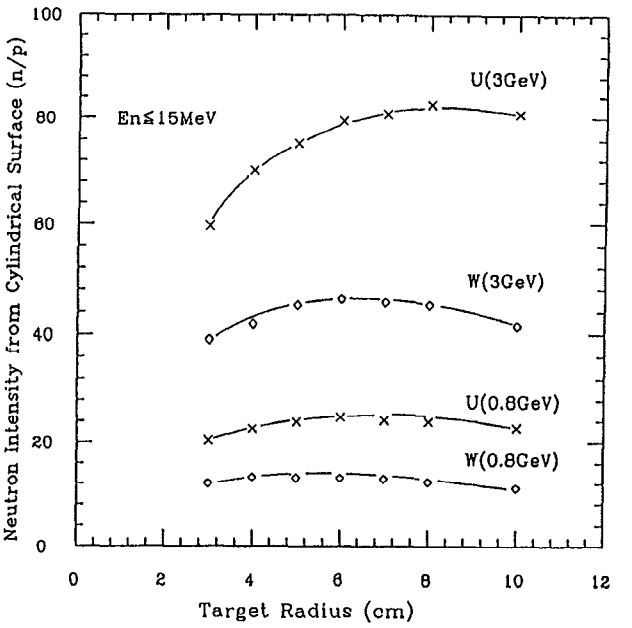

Fig. 4 Escape fast-neutron intensities from a cylindrical surface of targets as a function of the target radius.

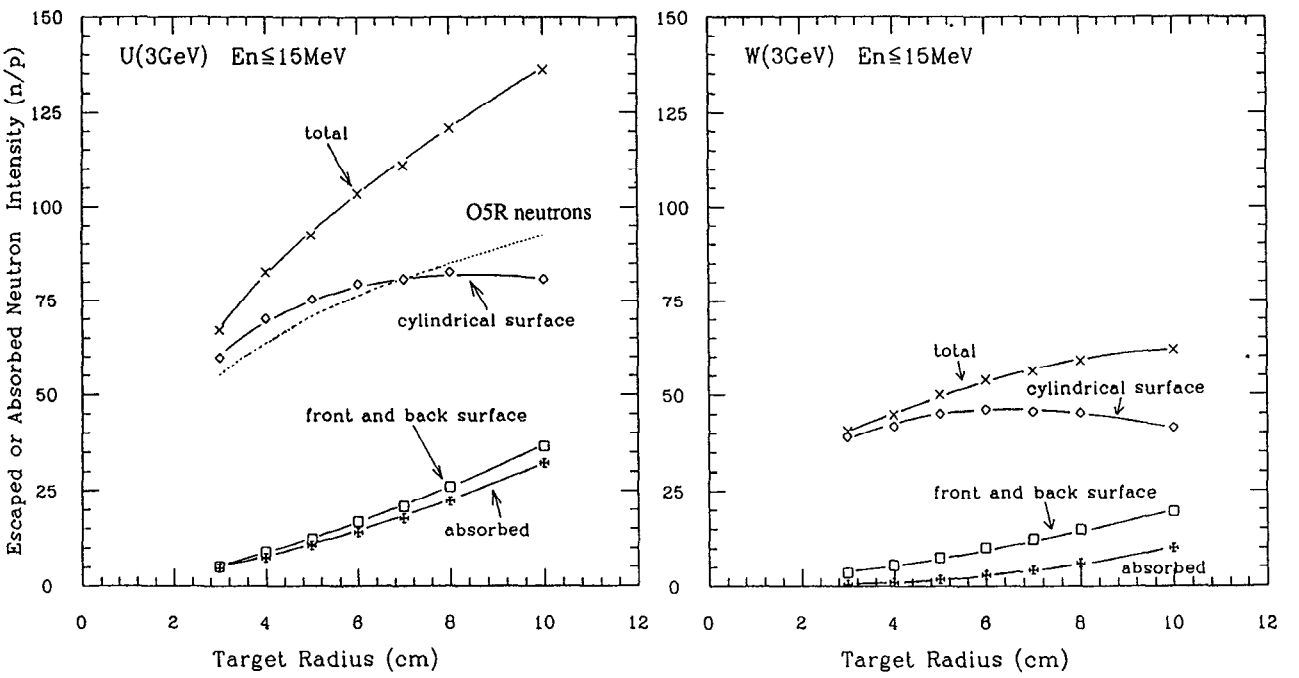

Fig. 5 Contribution of each process (escape and absorption) as a function of the target radius.

and adsorption) for U and W targets. The absorption in the U target is considerable compared to that in the W case, since the cross sections of (n, f) and (n, xn) are significant.

Figure 1 shows the calculated results of the O5R neutron intensities as a function of the proton energy for various target materials with dimensions of 32 cm long and 10 cm in diameter. Although this size is not sufficient for higher proton energies, it will be more realistic. We assumed a cylindrical proton beam profile of 4.7 cm in diameter. O5R neutrons mean those below 15 MeV directly obtained from a hadron transport calculation, which does not include neutron generation below 15 MeV. However, the O5R neutron will be a simple, but good, measure of the neutronic performance of a target (full calculations are given later). In the present results the intensities increase more linearly with the proton energy than in the previous results. The lower intensities in the lead target are due to its lower number density; i.e. the diameter of 10 cm and the length of 32 cm are not sufficient for lead.

The axial distributions of O5R neutrons (s (z)) in a uranium (depleted U) target are shown in Fig. 2 for various proton energies. In the present results, by increasing the proton energy the peak intensities increase monotonically with the peak position shifting a bit downstream, in contrast with the previous results, in which the peak intensities were almost saturated at higher energies (say above 1.5 GeV) and the shifts of the peak position were not small.

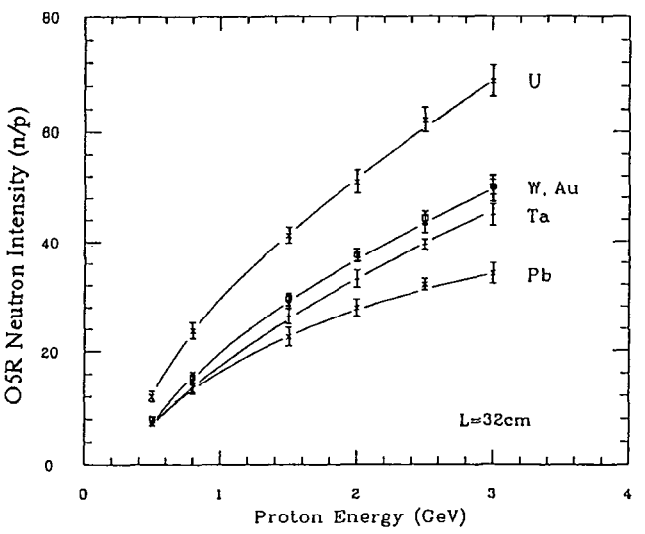

Fig. 1 O5R neutron intensities for various target materials as a function of the proton energy.

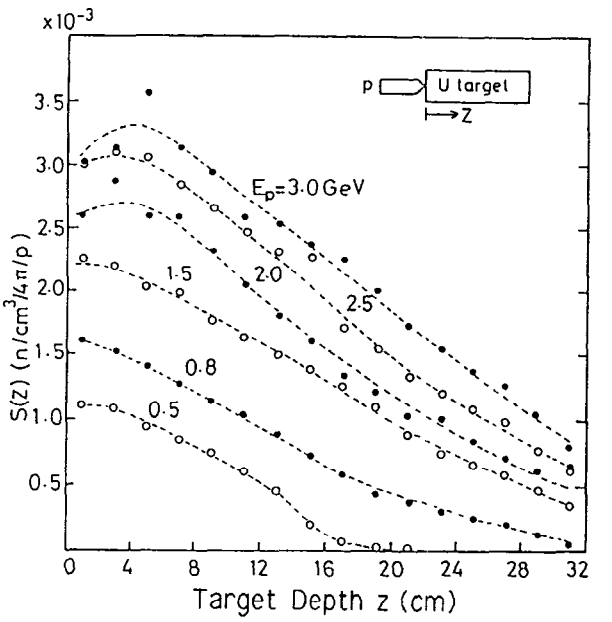

Fig. 2 Axial distributions of O5R neutrons in a U target at various proton energies.

We then calculated the intensities of escaping fast neutrons from the cylindrical surface of the targets, since the slow-neutron intensity from the moderators is directly related to those neutrons. Figure 3 shows the outgoing fast-neutron intensities from U target as a function of the axial depth of the targets for 0.8 and 3 GeV protons. In this calculation and the following neutron production below 15 MeV during neutron transport in the target was included.

Figure 4 shows the escape fast-neutron intensities as a function of the target radius. Although the total number of neutrons produced in the target increases with the target radius, the intensity of escaping neutrons from a cylindrical surface does not increase monotonically, due to escaping from both ends and absorption in the target. Figure 5 shows the contributions of each process (escape

3. Slow-Neutron Intensity

We calculated the slow-neutron intensities ($E_n < 0.9$ eV) from the moderators in the model target-moderator-reflector system shown in Fig. 6. In this model two reference light-water moderators were put on the target in a wing geometry, although in a real system it would be typical to put at least four moderators with different neutronic characteristics (2 above, other 2 below the target). This model would be sufficient to examine the slow-neutron intensities from the moderators. The intensities as a function of the target radius are shown in Fig. 7 for proton energies of 0.8 and 3 GeV. The neutron intensity increases with the target radius and then decreases. This is partly due to the fact shown in Fig. 4. However, the peak appears at a smaller radius than in Fig. 4. This is due to the fact that the coupling between the target and moderator becomes loose with increasing target radius. The proton energy dependence is rather modest. The optimal target radius is 4 - 5 cm. We chose a radius of 5 cm in the following calculations.

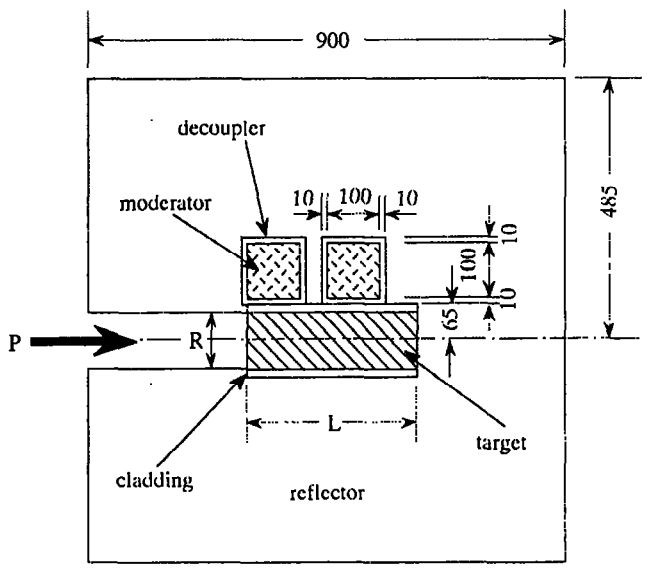

Fig. 6 Target-moderator-reflector system used for a calculation of the slow-neutron intensity.

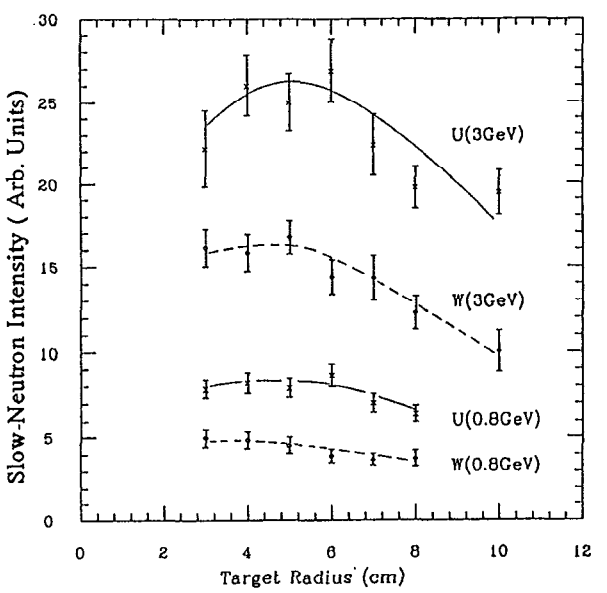

Fig. 7 Sum of the slow-neutron intensities from reference moderators as a function of the target radius.

In Fig. 8 the sum of the slow-neutron intensities from the two moderators set at the optimal positions are plotted as a function of the proton energy. The intensity increases almost linearly with proton energy. Vassil'kov [3] showed that the total neutron yield from a target $Y(E_p)$ can be expressed as

$$Y(E_p) = A + BE_p^y,$$

where A and B are constants. The value of y determined by a measurement for a lead target (20 cm in diam.) was $y = 0.75 \sim 0.85$, depending on the measuring methods. The solid curves in Fig.8 are the calculated values using the above equation with the given constants. The curves were normalized to the present data at 2 GeV. The agreement is fairly good. This means that the slow-neutron intensity is almost proportional to the total neutron yield in the proton energy range $0.8 \sim 3$ GeV. In other words, the slight deviation in the slow neutron intensity from a linear line at higher energies is mainly due to the energy dependence of the total neutron yield, rather than a broadening in the axial distribution of out-going neutrons.

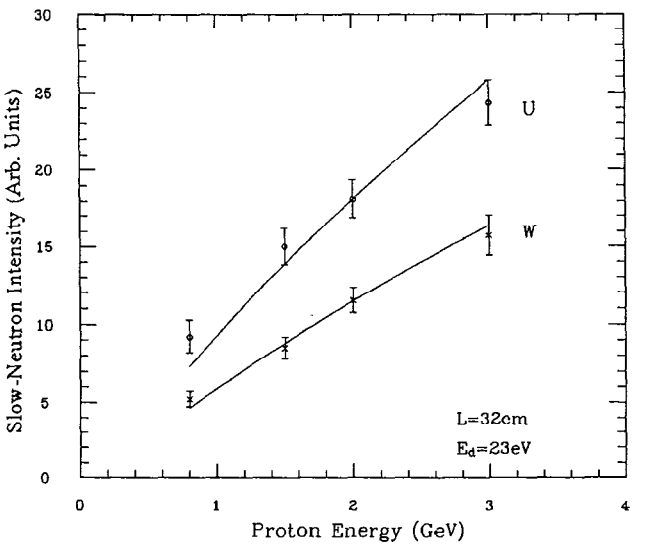

Fig. 8 Sum of the slow-neutron intensities from reference moderators optimally placed as a function of the proton energy. The solid curves are the calculated values of the total neutron yields normalized at 2 GeV.

4. Conclusion

In summarizing the results, the slow-neutron intensities per proton can be increased by about a factor of 3 when the proton energy is increased from 0.8 to 3 GeV. This number should be compared to the increase in the proton beam power (3.75 times). The slow-neutron intensity per proton beam power with 3-GeV protons is about 80% of the 0.8-GeV case. This value is quite acceptable.

References

(1) Y. Kiyanagi, M. Arai and N. Watanabe, "Advanced Neutron Source 1988," Institute of Physics Conference Series Number 97, Institute of Physics, Bristl and New York, pp.753 (1988).
(2) Y. Nakahara and T. Tsutsui, JAERI-M 82-198 (1982).
(3) R. G. Vassil'kov and V. I. Yurevich, Proc. Int. Collaboration on Advanced Neutron Sources (Tsukuba, October 22-26, 1990) pp.340.

CONCEPTUAL DESIGN OF THE TARGET STATIONS OF THE IPNS UPGRADE

J. M. Carpenter , R. K. Crawford, R. Kleb and A. E. Knox
Argonne National Laboratory

Abstract

The IPNS Upgrade is a new Pulsed Spallation Neutron Source based on a nominal 1 MW proton beam. The accelerator system delivers 0.5 mA of 2.2 GeV protons in 0.3 μsec pulses at 30 Hz. Two target stations receive the pulses, one at 10 Hz, the other at 30 Hz with every third pulse missing. Protons impinge horizontally on the targets. The targets in each target station are identical for the purposes of this reference design, and consist of Tantalum-Tungsten alloy plates in a split target (flux trap) arrangement, each section separately cooled by normal water. The high frequency target and associated moderators can accept the full 1 MW beam power. Each target supports six moderators, two at the front, two at the back and two vertically extended moderators in the flux traps. Three beams are led from one surface of each moderator, providing eighteen beams lines in each target station, diverging 13 ° from each other. The moderators are separately optimized to fit the needs of the scattering instruments, and are of circulating water, liquid methane and liquid Hydrogen, reflected by Beryllium and/or heavy material, decoupled or coupled as meets the instrument requirements. Extensive use of premoderators and composite moderators maintains low levels of heating and radiation damage in the moderators. Both target stations are equipped with hot cells for servicing the target-moderator-reflector systems, and both contain irradiation tubes for use in neutron activation and radiation damage applications.

The target stations are located in existing large experiment halls, which will require little modification. Columns extending to bedrock support the massive shields. Space is available to accommodate secondary applications such as pulsed muon facilities.

This paper describes the design of the new facilities and some of the pertinent engineering analysis.

Introduction: Considerations Underlying the Design

Discussions held during its meetings in September, 1992, led the DOE Basic Energy Sciences Advisory Committee's Panel on Neutron Sources(1), chaired by W. Kohn, to recommend "development of competitive proposals for the cost effective design and construction of a 1 MW pulsed spallation [neutron] source." The recommendation was based on the understanding that such a source would be feasible to construct with present day technology, and would represent a highly effective complement to the Advanced Neutron Source, which the Panel recommended as its first priority to "complete ... according to the schedule proposed by the project." The IPNS Upgrade is Argonne's response to the pulsed source recommendation. Our feasibility study has taken place over about the last six months, funded by Argonne National Laboratory, and reached the stage of preliminary documentation.

The IPNS Upgrade is to be installed in existing buildings in the former ZGS accelerator complex at Argonne. Preliminary calculations indicate that total neutron yields are nearly proportional to the proton energy, while power and neutron production densities are only mild functions of the proton energy. Figure 1 shows the total neutron yield calculated for 10 cm diameter Tantalum targets. Figure 2 shows the power density, emerging fast neutron current and total power in the target. These observations essentially freed accelerator designers to choose their own proton energy. The paper of Jerng elsewhere in these proceedings describes further calculations.

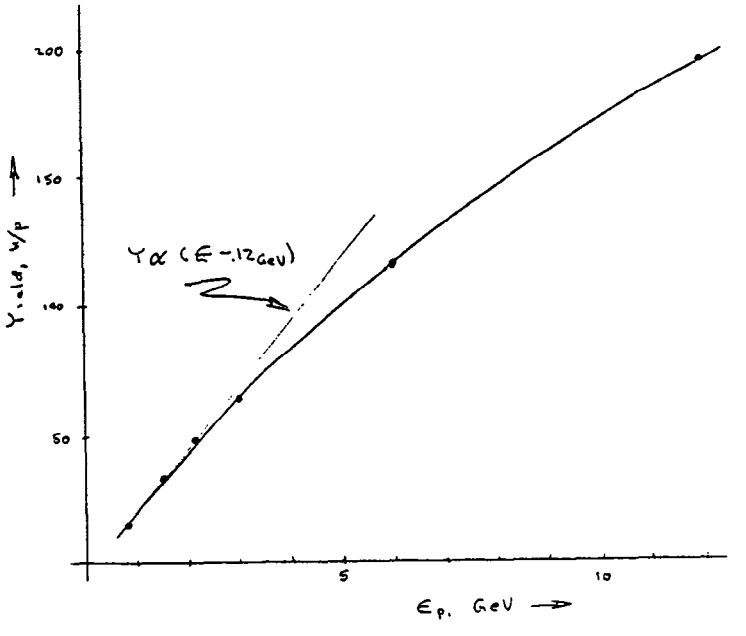

Figure 1 Neutron yield for 10-cm diameter Tantalum targets 100 cm (200 for higher energies) long, as a function of proton energy.

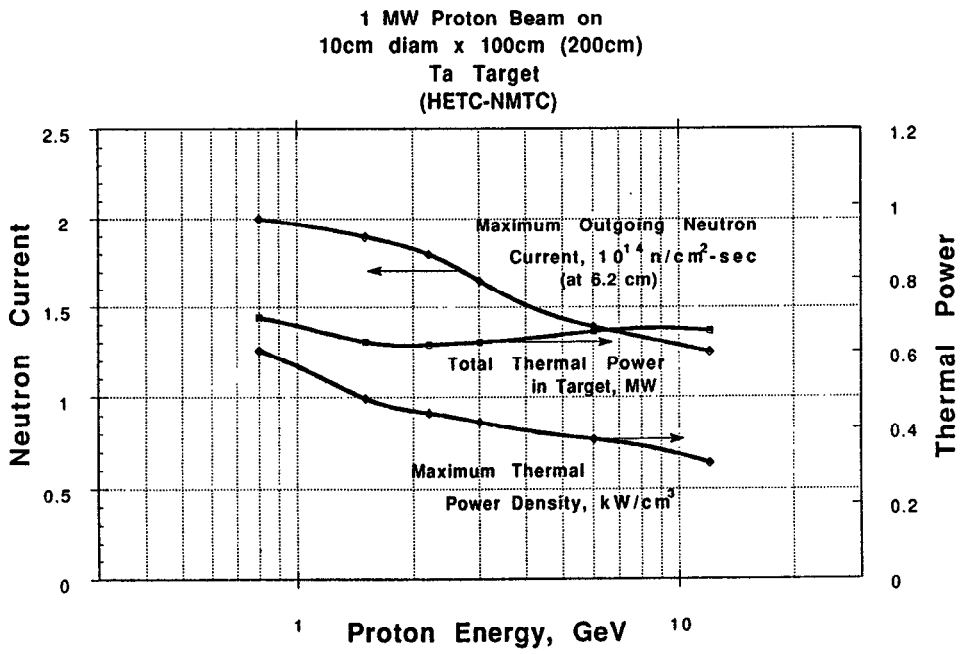

Figure 2 Maximum outgoing fast neutron current, total thermal power and maximum power density in Tantalum targets.

A survey, compiled for reference, of neutron scattering instruments appropriate for a 1 MW source provided important guidance. There must be provision for about forty instruments. There are two roughly-equally-populated classes of instruments, ones for which 30 Hz pulsing is appropriate, and those for which 10 Hz is required. These considerations led to the conclusion that two target stations are needed, one operating at 10 Hz, the other normally receiving the remainder of a 30 Hz pulse train. Each target station must provide about twenty beams. The paper of Crawford, elsewhere in these proceedings further describes the reference instrument complement. The study also indicated moderator and flight path requirements.

Preliminary considerations of vertical proton beam geometry led us to adopt horizontal proton beam geometry in view of the greater expense and difficulty of providing the large 90° bends implied by the vertical arrangement, and because the required number of beams can be provided by targets with horizontal proton beams.

The realization that targets, moderators and other components near the targets will have finite lifetimes and require convenient replacement and alteration, led us to incorporate a fully-equipped hot cell with each target station.

Opportunity to use the existing ring building and shield of the former 12 GeV Zero Gradient Synchrotron led us to choose 2.2 GeV proton energy, the highest energy

machine for which the space is adequate in view of the needs for straight section space dictated by the 1 MW power requirement. The paper of Cho elsewhere in these proceedings further describes the accelerator system. Figure 3 shows the layout of the IPNS Upgrade. The design proceeded on the basis of these established fundamental parameters.

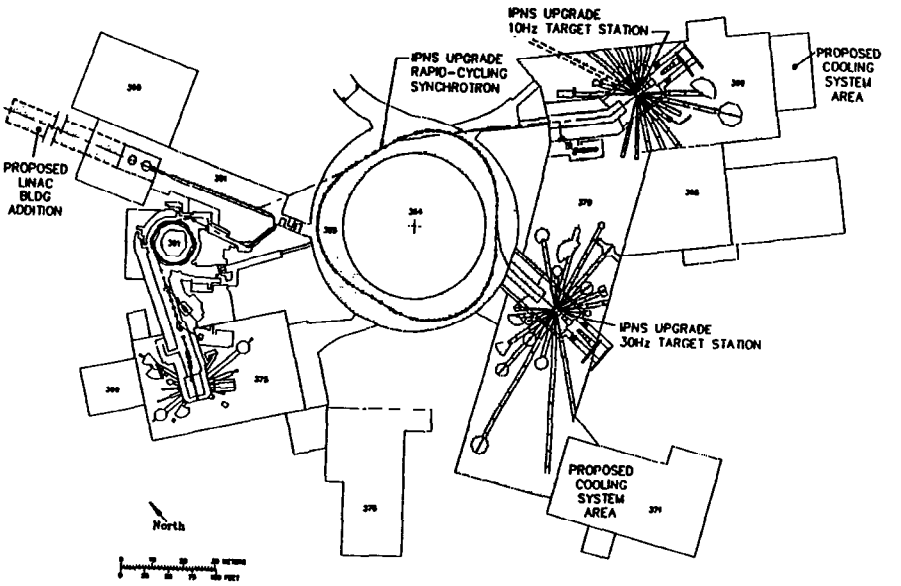

Figure 3 Layout of the IPNS Upgrade. The existing IPNS is in the lower corner of the drawing.

Details of the Target Station Design

We adopted the split target design for our targets, with six independently-optimizable moderators. At this level of description, the two target stations are identical. Figure 4 shows the target and moderator arrangement. Each moderator has one viewed surface that provides three beams. Nine beams emerge from each side; neighboring beams diverge 13°.

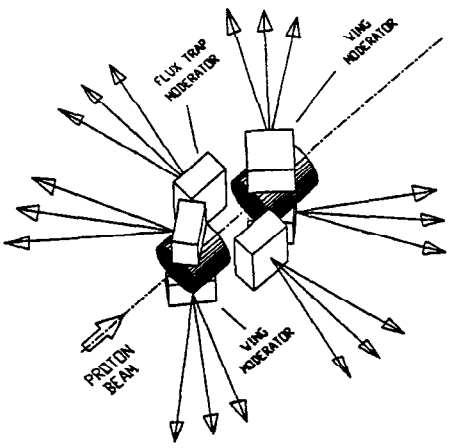

Figure 4 Split target with six moderators; flux trap moderators are 20 cm tall.

Designs of targets and moderators provide for simple servicing. Figure 5 shows the target and moderator assembly.

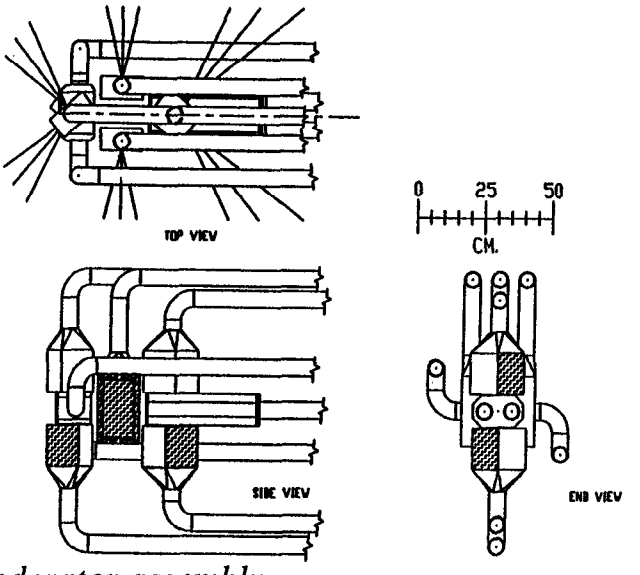

Figure 5 Target and moderator assembly

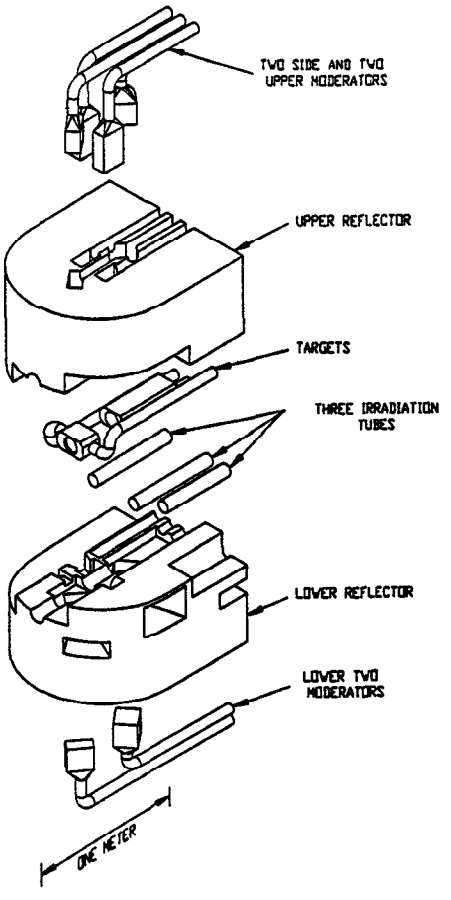

Figure 6 Exploded view of the target-moderator-reflector assembly

Figure 6 shows an exploded view of the target-moderator-reflector assembly. These, with an outer iron shield block, form a "train", which moves as a unit. Three irradiation tubes provide access for neutron activation and neutron radiation effects experiments. Samples can be inserted and withdrawn from remote locations within and outside the remote handling facility. Components fit together in such a way that when the target train is retracted into the servicing cell, each part in order can be lifted free with minimal interference.

All components nearby the target require active cooling, which is provided by separate water streams. During operation, the target train rests inside a sealed, Helium-filled volume defined by a stationary liner inside the shield. Neutron beams pass through thin window sections in the Aluminum target tank. The target is triply

enclosed. The outer end of the target train carries a seal sheet which can be disengaged to enable the many plumbing connections to be made and unmade and allows the train to be moved into the servicing cell. The main biological shield consists of an inner iron core and an outer layer of concrete a total of 6.5 m thick in the shortest (90°) direction. The 15,000 ton shield rests on a reinforced concrete pad supported by columns extending about 90 ft down to bedrock. Figure 7 shows the target station and hot cell with the target train in the servicing position.

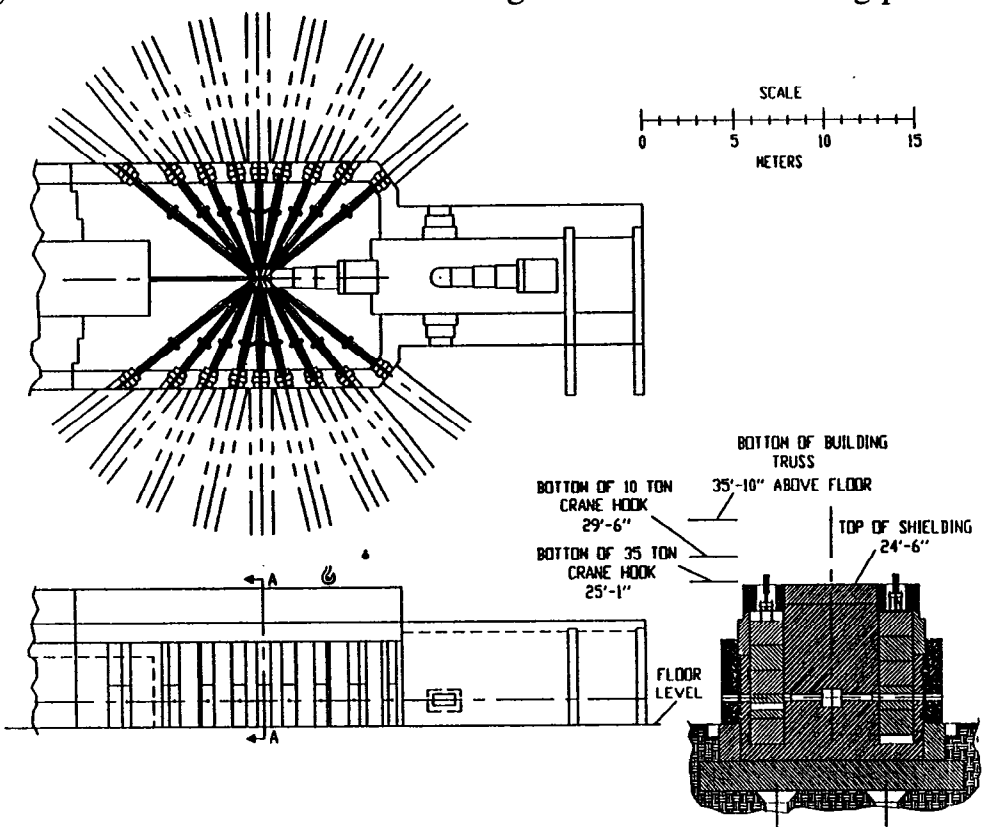

Figure 7 Target station and servicing cell

Neutron beams pass through ports which contain collimating or neutron guide elements. Gates, Figure 8, of steel and other material of high shielding effectiveness, 2 m thick, provide for hands-on changing of samples during operation. Gates have fine adjustment mechanisms to enable close alignment of collimating and guide sections as required.

Figure 9 shows the two target stations as they will be located in existing experiment halls adjacent to the accelerator.

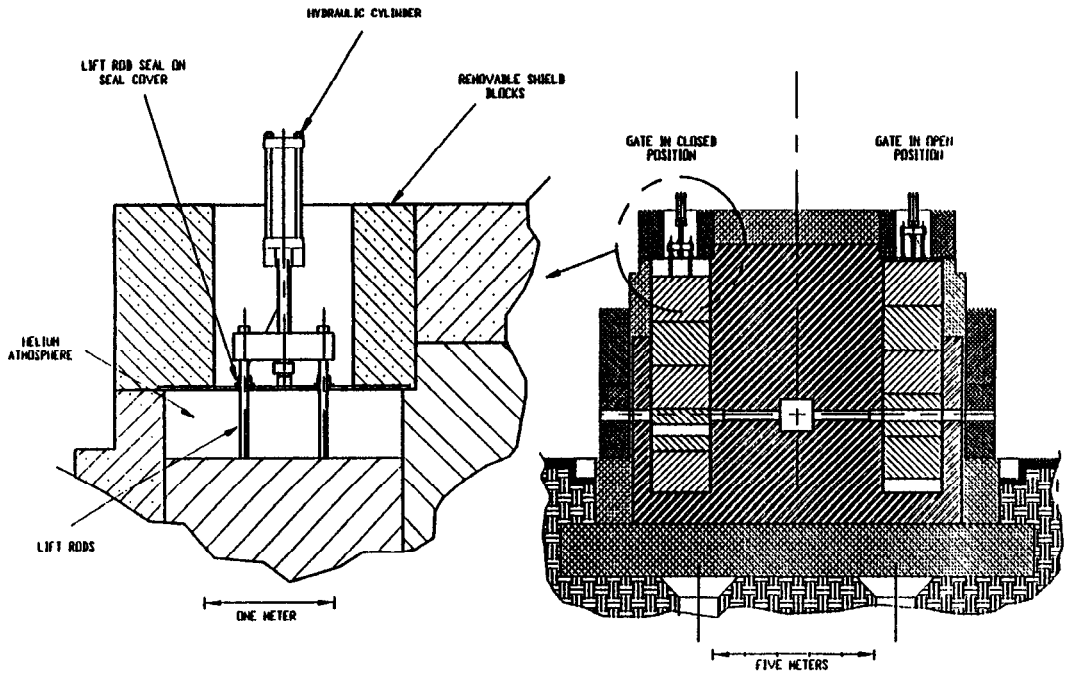

Figure 8 Beam gate and drive mechanism

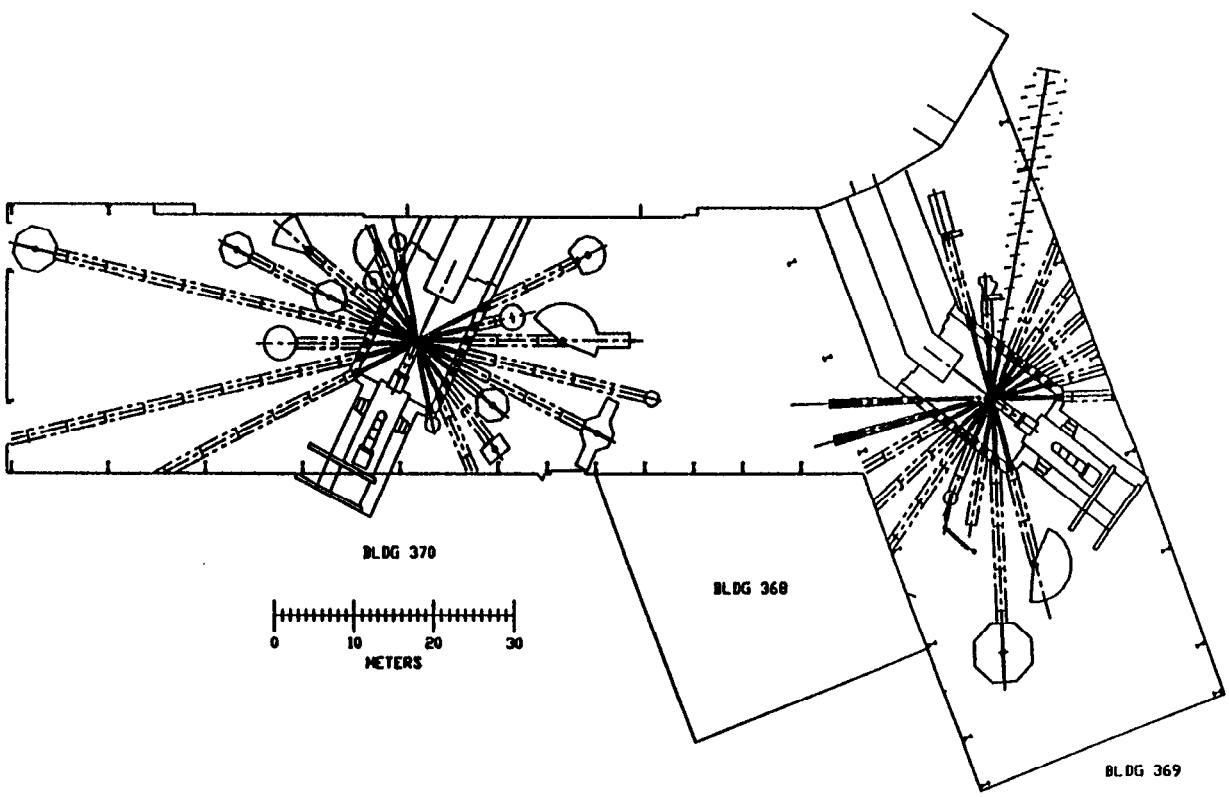

Figure 9 The high frequency and low frequency target stations

Targets

Preliminary considerations of neutron yield, density, structural properties and corrosion resistance led us to choose a Tantalum metal, water cooled target. Figure 10 shows three views of the split target arrangement. The target plates are roughly elliptical in shape.

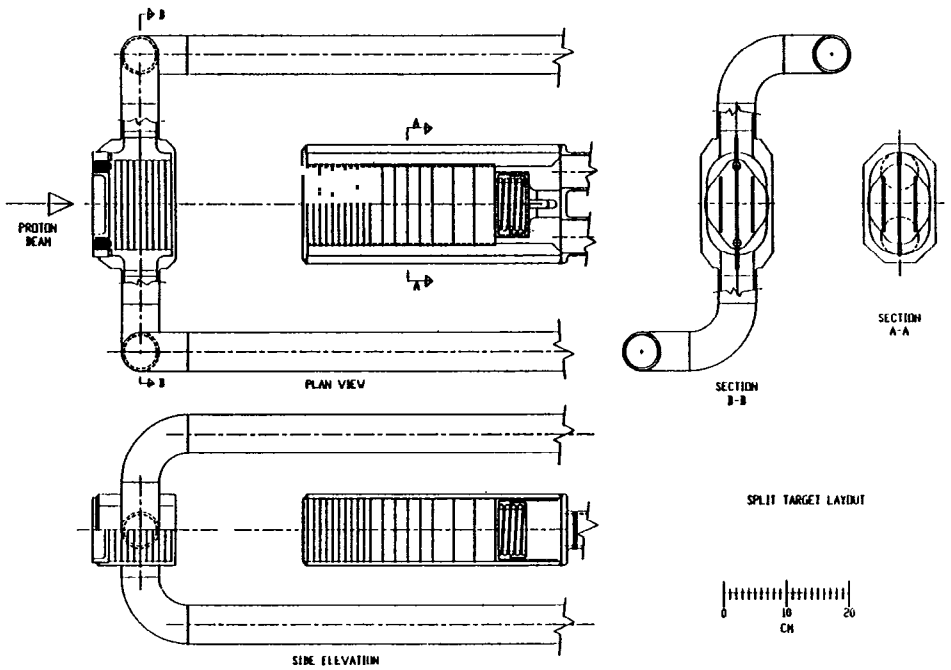

Figure 10 Three views of the front and back sections of the target

Each target half is cooled by a separate system with all the usual components. HETC-NMTC power density calculations for a 2.5 cm-radius at half-maximum, Gaussian, 2.2 GeV proton current distribution, truncated at 5 cm radius, formed the basis for thermal hydraulic analysis. The design provides that the target can accept the full 1-MW, 30 Hz beam. Water flow velocity is about 5 m/sec; coolant channel gaps are 1.6 mm. In the front target, the surface heat flux determines the disk thickness on the basis of avoiding local boiling. In the back target, disk thicknesses are determined by a criterion on maximum center temperature. Figure 11 shows the disk center surface temperatures and interior disk center temperatures as functions of the distance into the target.

Thermal stress calculations indicate that for the conditions of this analysis, Tantalum metal has inadequate yield strength. However, Tantalum-10%Tungsten, a commercial alloy, has much higher strength and comparable properties otherwise, and is our choice for this reference target design.

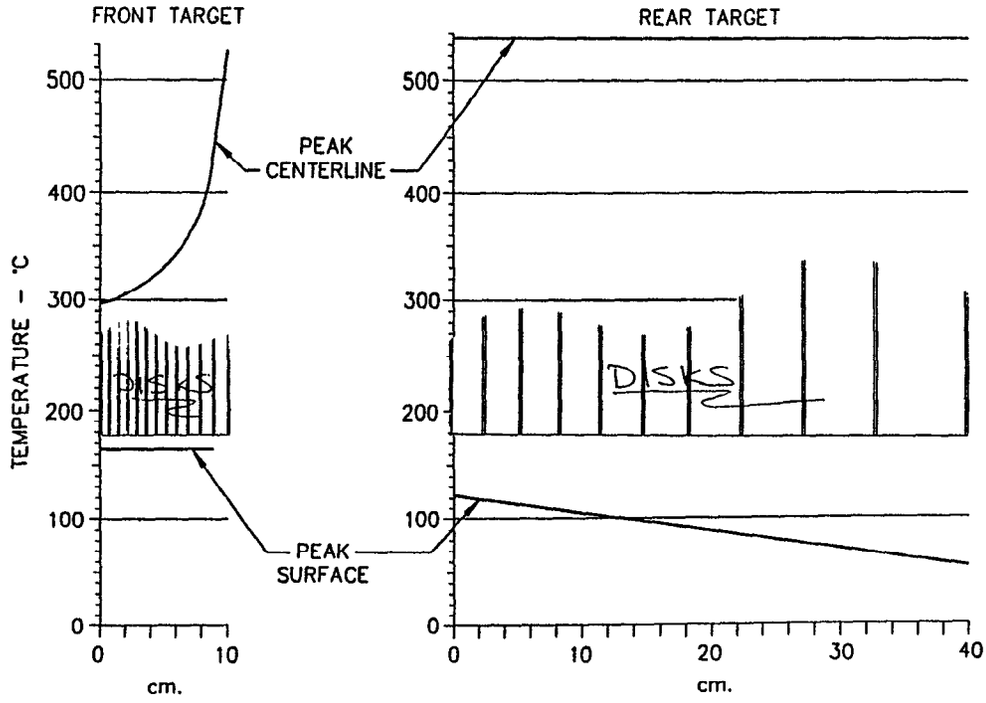

Figure 11 Disk surface center and disk interior center temperatures

A survey of metallurgical data relevant to candidate target materials uncovered information on hydride embrittlement of various Tantalum and Tungsten alloys, Figure 12. In the corrosion tests cited, samples were exposed to concentrated

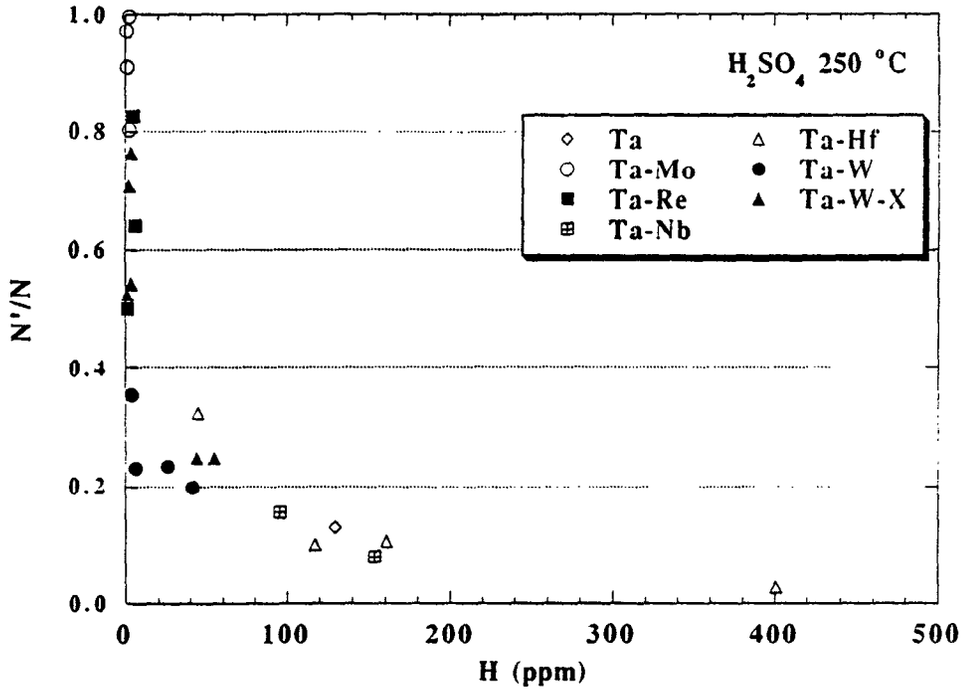

Figure 12 Ratio of the number of stress cycles to failure of hydrided Tantalum alloys

sulfuric acid, then subjected to cyclic mechanical stress. The figure shows the ratio of the number of cycles to failure of the corroded specimens to the number of cycles for uncorroded materials, and relates the reduction in cyclic stress tolerance to the measured concentration of Hydrogen introduced due to corrosion. Hydrogen concentrations at the level of 100 ppm appear to produce very significant reductions in cyclic stress tolerance, moreover such concentrations can readily be imagined to develop in rather short times in targets irradiated by proton beams of the contemplated current density. Two issues arise from these observations, namely, the significance of the indicated reduction in stress tolerance and the actual rate of Hydrogen buildup. The latter question requires calculation and perhaps measurement, since, on the one hand, most of the incoming protons react in nuclear reactions and disappear, while on the other, secondary protons are produced in spallation reactions. This is one of the more significant R&D questions uncovered in the course of our feasibility study.

Conclusion

We have produced a feasible design for a neutron source with two target station, subject to favorable answers to only a few R&D questions. Exclusive of the cost of supporting research, the Total Estimated Cost for the two stations is approximately $60 M. Cost and schedule estimates, and the list and cost of needed Research and Development efforts are being refined.

References

1. W. Kohn, "Neutron Sources for America's Future", Report of the Basic Energy Sciences Advisory Committee Panel on Neutron Sources, January, 1993.

Heat Generation and Neutron Beam Characteristics in A High Power Pulsed Neutron Source*

Dong W. Jerng and John M. Carpenter
Intense Pulsed Neutron Source
Argonne National Laboratory
Argonne, Illinois 60439, U.S. A.

Abstract

As an effort for the conceptual design of a high power pulsed spallation source, a Monte Carlo model was developed for heat generation and neutronics studies. In this paper, we present two sets of our calculation results. The first set of calculation was performed with a simple target model to investigate general characteristics of power distribution and neutron production with various proton energies ranging from 0.8 to 12 GeV. The second set of calculation was performed with a more realistic target model including major components of the target system to provide basic parameters for engineering design of the high power pulsed spallation source. Calculation results generally confirms that higher proton energy provides an advantage in target cooling system requirements and yet lower neutron beam intensity as a counter effect.

1. Introduction

The pulsed spallation neutron source under the present study consists of two targets split by a vaccume region in-between called flux trap and six moderators. The proton beam is at 1 MW time-averaged power with the proposed proton energy of 2.2 GeV. It is intended to deliver five times higher neutron flux than any currently operating facility in the world. The power distributions and the neutron beam characteristics in such a high power pulsed neutron source are main results of this paper. Although 2.2 GeV is the proposed energy of protons for the high power spallation source currently under consideration, a calculation with 9 GeV protons was also performed for the investigation of the effects of extremely high proton energies on the heat load and neutron utilization. Also, a series of calculation was performed to provide an insight to the relationship between impinging proton energy and the distribution of power and neutrons using an idealized target system. This calculation also served as a benchmark for the validation of the code system and physical models used in the Monte Carlo method.

As a computing tool for the Monte Carlo calculations, the LAHET code system was used. The LAHET code system has been developed in Los Alamos National Laboratory (LANL) and mainly consists of an LANL version of the high energy transport code (LAHET) and the general Monte Carlo code for neutron and photon transport (MCNP) with several associated codes [1]. LAHET calculates high energy particle cascades and transports including neutrons above 20 MeV. For the intranuclear cascade calculation in LAHET, the Bertini model has been used which is generally recognized as acceptable up to the particle energy of 3.5 GeV. For the transport calculation of neutrons below 20 MeV and photons, MCNP has been used.

A validation of the LAHET code system and physical model was performed for two parameters which were of most interests for our objectives: the energy deposition in the target and the neutron production rate. For the validation, the target was modeled as 20 disks of 5 cm thickness and 10 cm diameter with 2 mm gaps between disks for water coolant. The target was housed by stainless steel structure imbedded in the beryllium reflector. The proton beam was assumed of a gaussian distribution truncated at 4 cm in radius with the full-width-at-half-maximum (FWHM) radius of 2 cm. The target length was enough to encompass the stopping

* Work sponsored by the U.S. Department of Energy

length of energetic protons and tantalum was assumed for the target material. Fig. 1 shows the calculated ratio of energy deposition in the target to the proton beam energy. Considering the small difference in mass and nuclear composition between lead and tantalum, it is concluded that Fig. 1 confirms the validity of the LAHET code system and physical models used in the calculation. Fig. 2 shows the neutron production rate in the tantalum target compared with that in the lead target. It is seen that the neutron production rate is a little higher with tantalum than with lead. However, it is again concluded that the computer code and physical models set up for this study are sound enough for the next stage calculation.

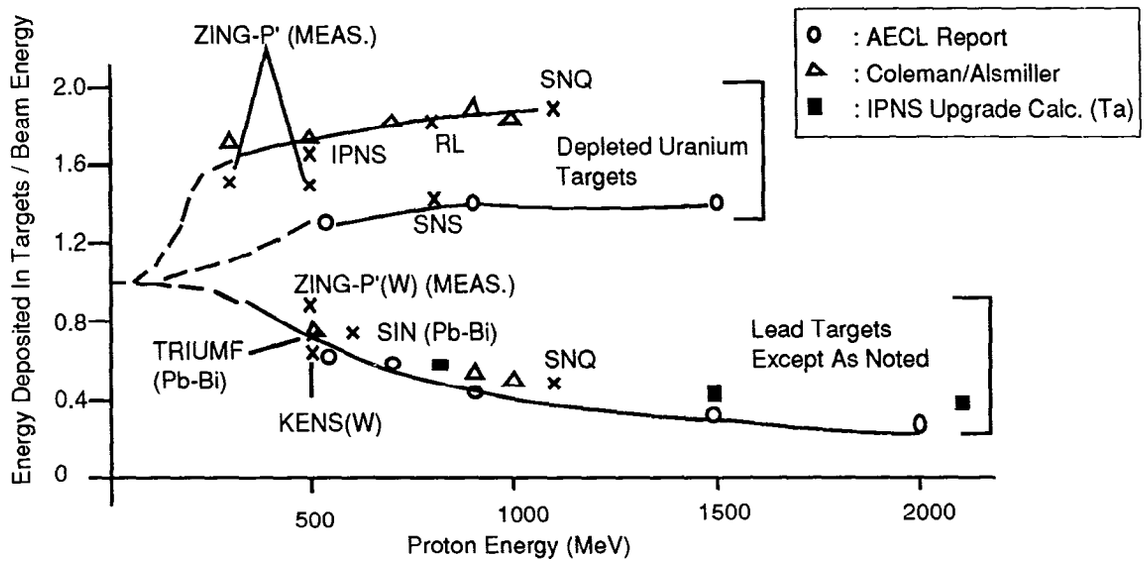

Fig.1 A validation of IPNS Upgrade calculation model - heat deposition in targets (Source for other than IPNS upgrade calculation : Reference 2)

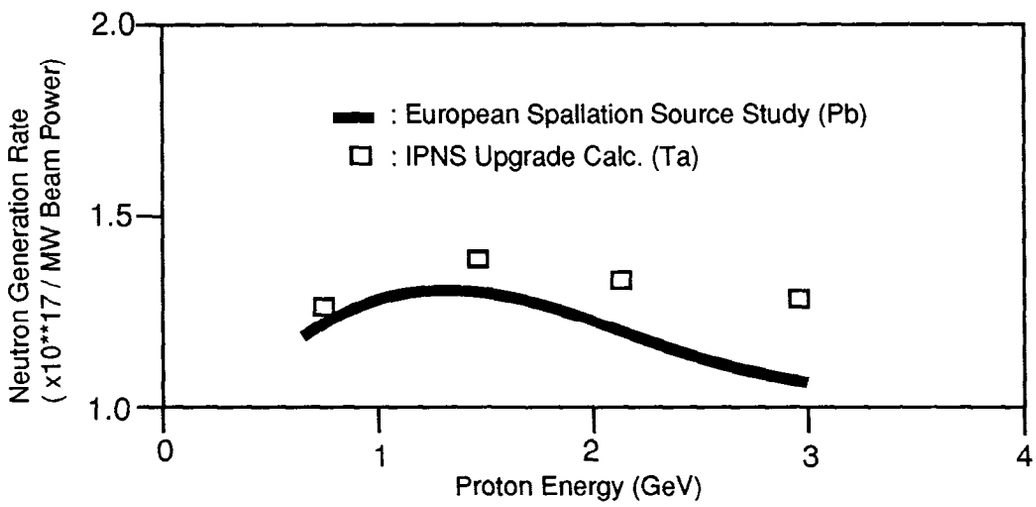

Fig.2 A validation of IPNS Upgrade calculation model - neutron generation rate (Source for European Spallation Source Study : Reference 3)

2. Heat Deposition and Neutron Production with Various Proton Energies

Although the hardron cascade model incorporated in LAHET is recommended for the proton energy up to 3.5 GeV, we calculated power density and neutron current distributions with several proton energies up to 12 GeV. The target model and proton beam conditions used in this series of calculation was the same as used for the code validation except that the target length was prolonged to 2 m for the calculations with 6 and 12 GeV protons. The calculation results are summarized in Table 1 and Figs. 3 and 4 show the spatial distributions of power density and neutron currents. As expected, higher proton energy yields higher neutron production per proton but the neutron production rate normalized to 1 MW proton beam is found to be peaked at 1.5 GeV and slowly decrease as proton energy increases. The maximum current and power density are observed to be proportional to each other although the location of the maximum power density occurs at the first disk and that of the maximum current occurs at the second disk as seen in Figs.3 and 4 respectively. The total power deposited in the target is found to be almost constant, i.e. between 60 to 70 % of beam power as long as the target dimension is sufficiently large enough to accommodate the slow-down of cascade particles. The fluctuation of the power density and neutron current near the end of target shown in Figs.3 and 4 are due to the statistical uncertainty of the Monte Carlo calculation, since the fewer particles remain at the deeper location in the target.

Table 1. Calculation summary (based on 1-MW Beam except neutron yields)

Proton energy	Neutron yield per proton	Neutron production rate ($\times 10^{17}$ n/sec)	Maximum current [a] ($\times 10^{14}$ n/cm^2 /sec)	Maximum power density [b] (kW/cm^3)	Total power deposition in the target (MW)
0.8 GeV	16.3	1.28	2.0	0.604	0.692
1.5 GeV	33.6	1.41	1.90	0.477	0.627
2.2 GeV	48.8	1.39	1.80	0.439	0.619
3.0 GeV	64.4	1.34	1.65	0.415	0.626
6.0 GeV	115.6	1.20	1.39	0.371	0.654
12.0 GeV	194.8	1.01	1.25	0.307	0.656

[a] neutron current at the cylindrical surface (radius: 6.2 cm) of the target housing
[b] power density over a disk (radius: 5 cm and thickness :5 cm) of the target

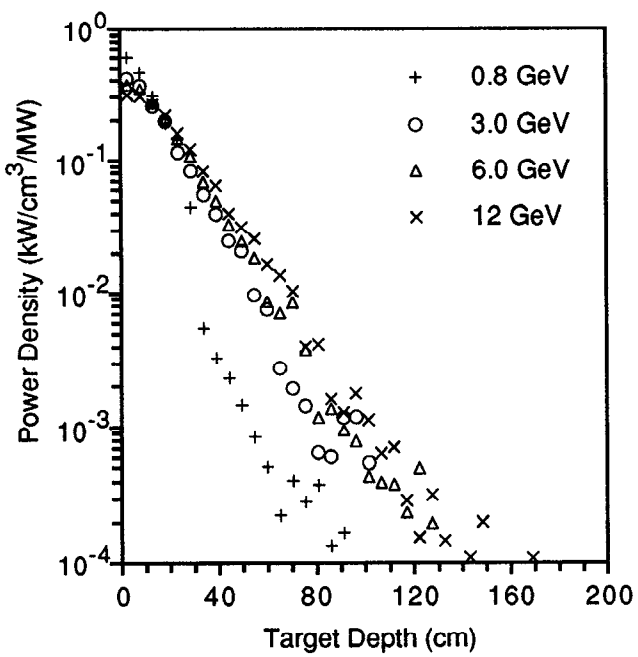

Fig 3. Power density along the target depth

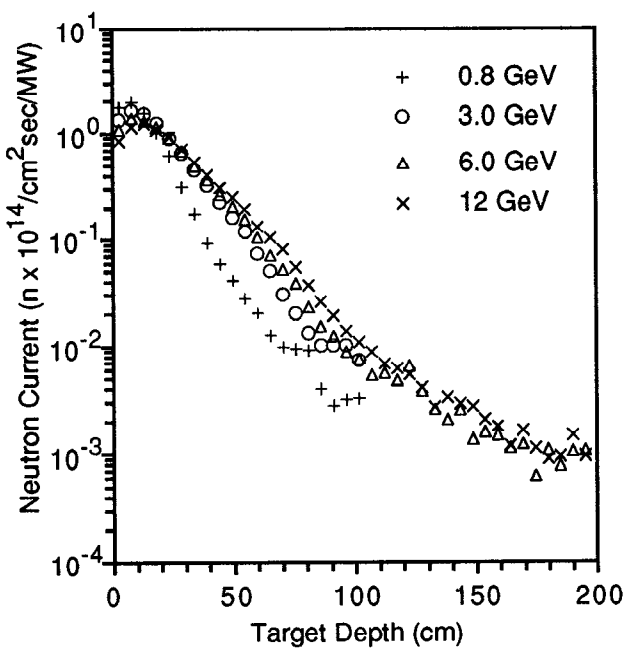

Fig 4. Neutron current along the target depth

3. High Power Target Station Model

The target station including targets, moderators, and neutron beam lines were modeled with a reflector and shield surrounding these components. Geometrical and material features of key components modeled for Monte Carlo simulation are listed in Table 2. An isometric view of the target and moderators is shown in Fig. 5 and the labels for six moderators are indicated also in Fig.5. Fig.6 shows a plan view of the target station from the top for the illustration of neutron beam lines. The moderators and neutron beam lines are covered by the boron decoupler to cut off the thermal neutron scattered into the beam lines from the reflector. There are three neutron beam lines from each moderator totaling 18 beam lines in the target station. The beam lines are separated by an angle of 15°. Fig.7 shows the arrangements of the reflector, shield and removable assemblies for remote handling systems. All calculations are based on proton beam with a gaussian distribution of 2.5 cm FWHM radius and 5 cm radius truncated conditions. The calculation results in subsequent sections are normalized results based on 1 MW proton beam in time average.

Table 2. Geometrical and material features of the key target station components

Component	Geometry and Dimension	Material
Target	split targets : four elliptic disks [a] in the1st target nine elliptic disks [a] in the 2nd target	tantalum
Housing	rectangle with rounded side surfaces 18 cm wide, 12 cm high, and 12 cm long (1st target housing) and 40 cm long (2nd target housing) with a spring at the back	0.5 cm thick stainless steel
Flux Trap	18 cm long section between the housings	vacuum
Coolant	coolant channel gap between target disks : 0.2 cm	water
Moderator	1st target moderators: 5 cm x10 cm x 10 cm flux trap moderators: 5 cm x10 cm x 20 cm 2nd target moderators: 10 cm x 10 cm x 10 cm	water
Boron Decoupler	2 cm thick clad surrounding moderators and neutron beam lines except the beam line face	natural boron with 3.3 % of normal density [b]
Reflector	cylinder of r = 54 cm, h = 100 cm	beryllium
Shield	annulus of r_i = 54 cm, r_o = 100 cm, h = 100 cm	iron

[a] minor radius = 5.5 cm, major radius = 7.5 cm, thickness = 2.5 cm (1st target), 3.5 cm (2nd target)
[b] boron density for the decoupling energy of 1.0 eV and 1/e reduction of neutron flux cross the decoupler.

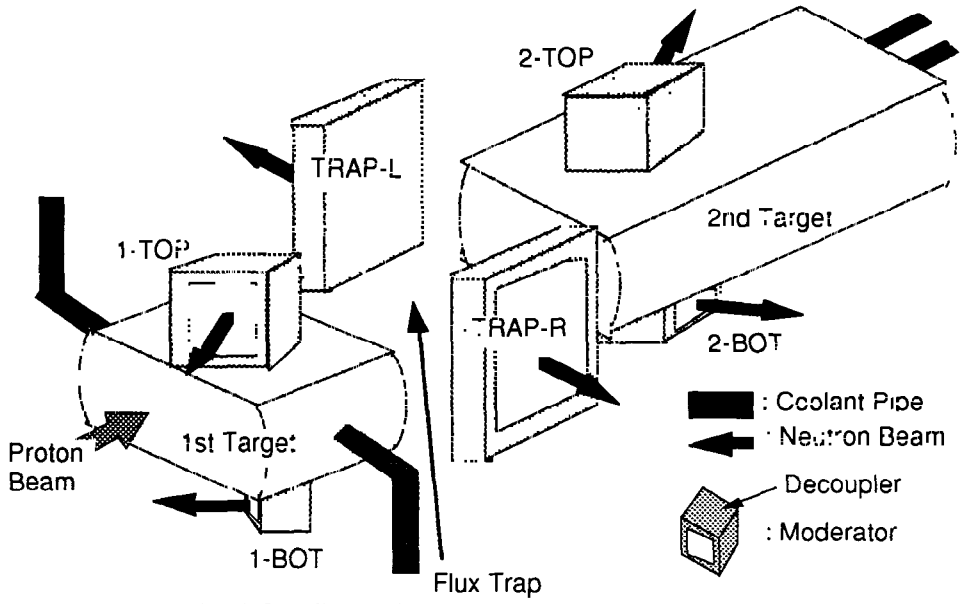

Fig.5 Configurations of targets and moderators

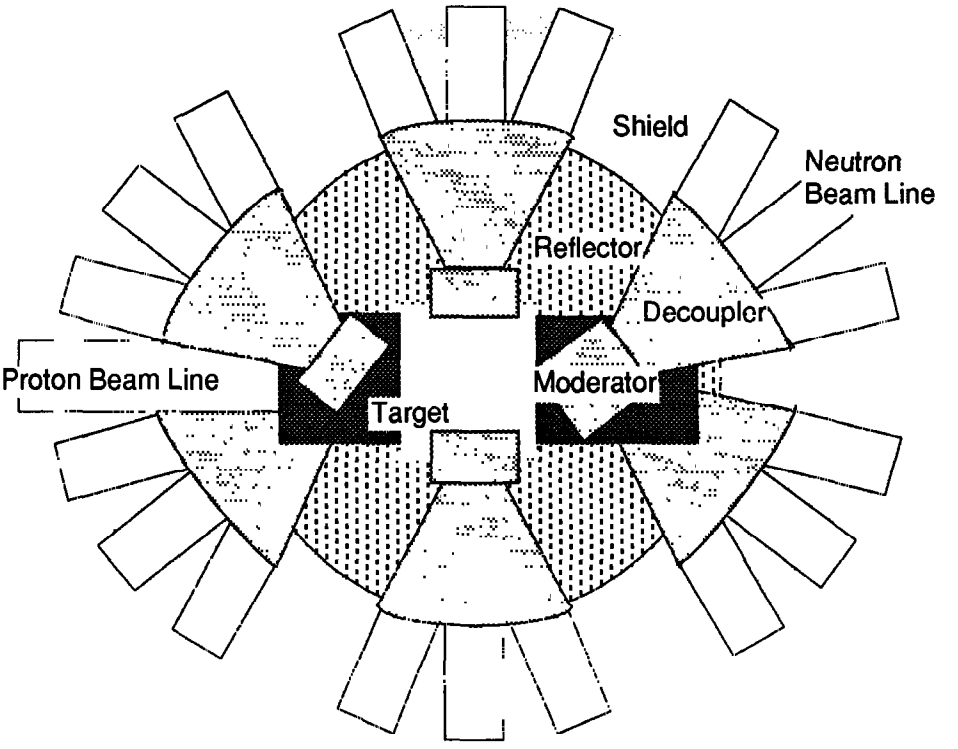

Fig.6 Arrangement of neutron beam lines

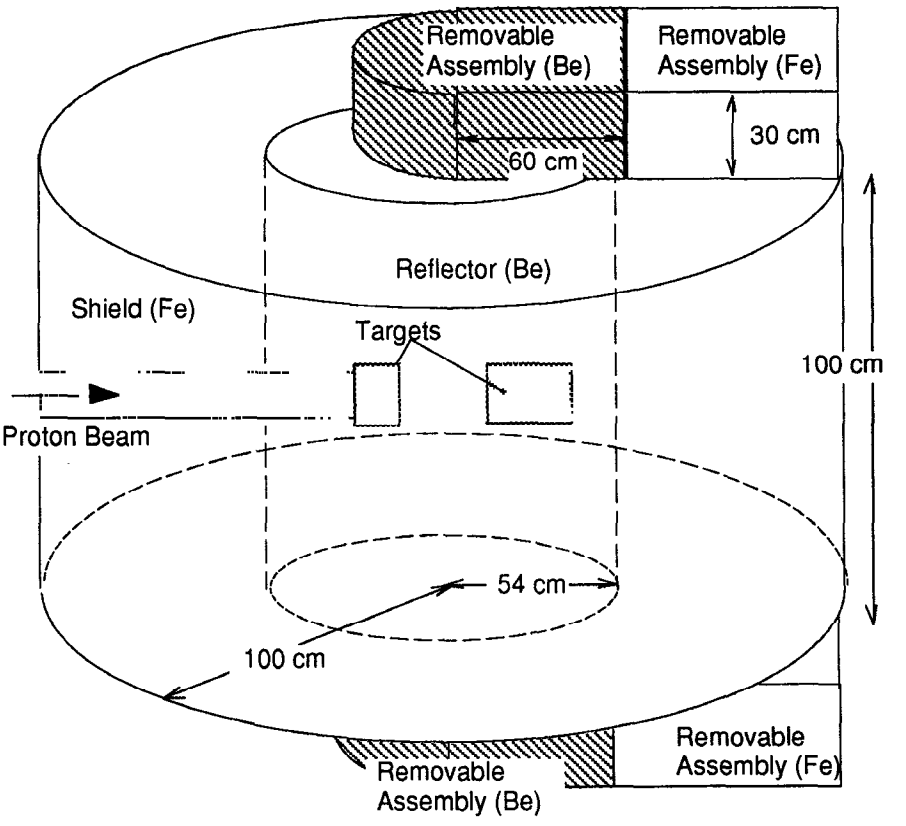

Fig.7 Schematic of the systems surrounding the targets

4. Power Distribution in the Target Station

The power distribution in the target station is summarized in Table 3. With 2.2 GeV protons, about 90 % of the beam power is deposited in the target station and the 10 % is thought either to be absorbed in the form of binding energy resulting from the change of isotope compositions during the cascade process or to escape through neutron and photon leak. For instance, the neutrons escaping from the system in the model is about 9.7 neutrons/proton. Assuming 8 MeV for the neutron binding energy, this leak constitutes about 35 kW/MW-beam. Thus, the overall energy balance is thought to be satisfied in the calculation. The overall energy balance was also confirmed in the case of 9 GeV protons. In this case, about 95 % of the beam power was deposited in the target station and 5 % is thought to be absorbed as binding energy or escape the system. For both proton energies, the total power deposited in the target was found to be about 55 % of the proton beam power.

A considerable difference in heat deposition between 2.2 and 9.0 GeV protons is noticed in the moderators and shield. Since the volume of the first target moderators are a half of the flux trap or second target moderators, the power density of the moderators are approximately same for 2.2 GeV protons. For 9.0 GeV protons, however, the power density of the first target moderators is about 53 % of the second target moderators. This is because the neutron distribution around the target is more anisotropic and skewed toward the back of the target with higher proton energy. The spatial distribution of the power in moderators has been also investigated because the power density of around 1.5 W/cm^3 for crygenic moderators is significantly high. We have found that about 30 % of heat deposited in water moderators occurs in the 17 % of the moderator volume near the target and at leat 50 % of heat in the moderator can be removed by attaching a premoderator region of 4 cm thickness between the moderator and target.

Table 4 shows a comparison of the results from 2.2 GeV and 9.0 GeV protons. The neutron yield per proton is much higher for 9.0 GeV protons. However, the neutron production rate per MW-beam is higher for 2.2 GeV protons because the target dimension is not adequate to utilize all the energy of 9.0 GeV protons. The neutron leak from the station is higher for 9.0 GeV protons as expected because neutron spectrum is thought to be harder. The maximum power density is lower for 9.0 GeV protons because of longer stopping length of higher energy protons. Thus, higher energy protons penetrates deeper in the target and deposits more energy in the back of the target than lower energy protons. Fig.8 shows a comparison of the axial power distribution in the target between 2.2 and 9.0 GeV protons. It is noticed in Fig.8 that the peak power occurs in the first disk for 2.2 GeV protons but it occurs in the second disk for 9.0 protons. Also, it is observed that the powers in the first target disks are higher for 2.2 GeV protons but the powers in the second target disks are higher for 9.0 GeV protons.

We have further analyzed the power distribution in the reflector and shield as illustrated in Figs. 9 and 10. The volumes of the front and back segments of the reflector are approximately the same while the middle segment is much smaller. Also, the segmentation of the shield are the same as that of the reflector. Hence, it is noticed in Figs.9 and 10 that the heat deposited in the back of both reflectors and shield is much greater than in the front. This is because protons are still energetic even at the end of the target in addition to the anisotropic distribution of neutrons as discussed earlier. The anisotropic power distribution in the reflector and shield is more significant with 9.0 GeV protons, for instance, the power in the back half of the shield is seven times larger than the power in the front half of the shield. This spatial distribution of heat load in the surroundings of the target is though to bring a special attention not only to the cooling system design but also to the radiation protection consideration because higher heat load indicates higher radiation dose also. For the heat load in the back of the shield, the heat deposited by high energy particles (i.e., heat load calculated by LAHET) was 1.5 time higher than that deposited by low energy neutrons (i.e., heat load calculated by MCNP) for 2.2 GeV protons. The ratio of the two heat depositions was 2.07 for 9.0 GeV protons. The statistical uncertainty of the calculation is less than 3 % for the target power and maximum 10 % for the individual moderator powers.

Table 3 Heat deposition in the target station per MW proton beam

Component	Heat Deposition (kW) by 2.2 GeV protons	Heat Deposition (kW) by 9 GeV protons
Target	550.8 (total)	553.6 (total)
1st target	306.5	251.0
2nd target	244.3	302.6
Coolant	21.0	14.5
Housing	34.2	40.0
Moderator Total	7.6 (total)	6.4 (total)
1st top moderator	0.775	0.413
1st bottom moderator	0.773	0.417
flux trap moderator - right	1.516	1.30
flux trap moderator - left	1.498	1.27
2nd top moderator	1.582	1.54
2nd bottom moderator	1.477	1.50
Boron Decoupler	26.7	20.1
Reflector	126.6	120.4
Shield	128.0	187.0
Removable Assembly	7.0	6.6
Target Station Total	901.9	948.6

Table 4 A comparison of key results between 2.2 and 9.0 GeV protons

Proton energy	Neutron yield per proton	Neutron production rate per MW-beam	Maximum power density [a] (kW/cm^3)per MW-beam	Neutron leak per proton
2.2 GeV	49.3	1.40×10^{17}n/sec	1.650 at 1st disk	9.67
9.0 GeV	151.5	1.05×10^{17}n/sec	1.216 at 2nd disk	38.83

[a] the power density at the center with r = 1 cm

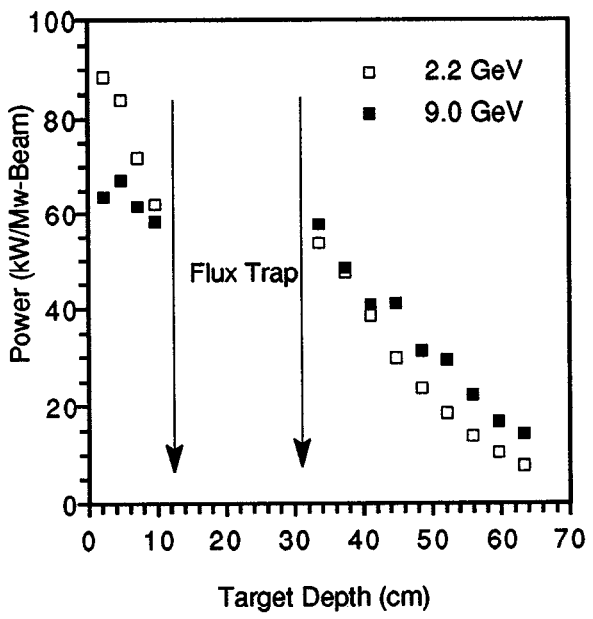

Fig.8 Axial power distribution along the target

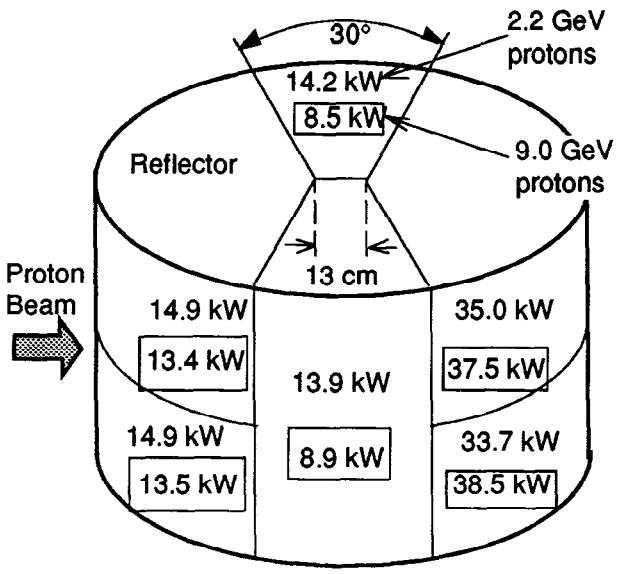

Fig.9 Power distribution in the reflector

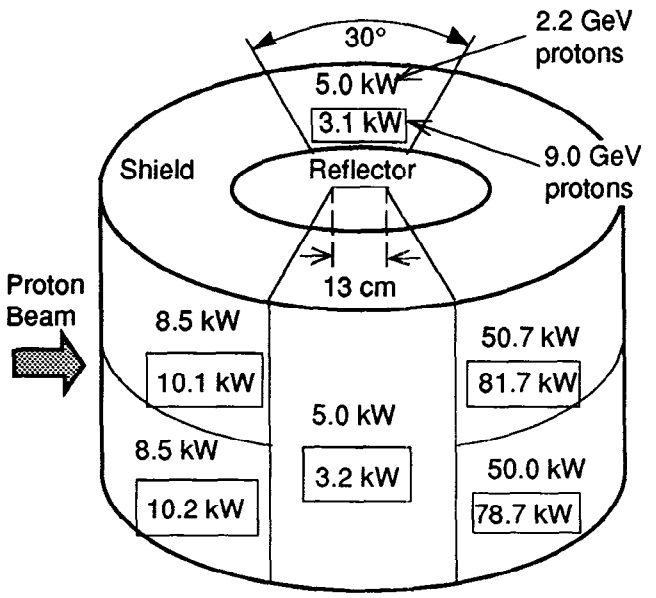

Fig.10 Power distribution in the shield

4. Neuron Beam Characteristics

In Fig.11 the neutron current spectra outgoing from the surface of the moderators are compared for the case of 2.2 GeV protons. It is seen in Fig.11 that the shape of neutron spectrum is almost same for all six moderators and that the 1st moderators result in the highest neutron current in all energy bins. Fig. 12 shows the neutron spectra at the end of the center beam lines from the 1st target, flux-trap, and 2nd target moderators. At the end of beam lines, the neutron beam from the flux-trap moderator is slightly higher than those from the other two moderators especially for the thermal energy region. The change of the neutron beam spectrum along the beam line from the moderator surface to the end of beam line is shown in Fig.13 The neutron beam intensity becomes smaller as it approaches the end of beam line over the entire range of neutron energy as expected. However, the ratio of thermal to fast neutrons decreases most significantly in the decoupling region which is between the moderator to the end of decoupler. The decoupler cuts off the thermal neutrons coming into the beam line from the reflector while it is transparent to fast neutrons. The total number of neutrons produced in the target is 49 neutrons per proton with 2.2 GeV protons. The total number of neutrons available at the end of beam lines which are about 85 ~ 90 cm away from the moderator surface is found to be 0.62 per proton.

The comparisons of neutron beam characteristics between 2.2 and 9.0 GeV protons are shown in Figs.14 through 16. A noticeable effect of higher proton energy is that the neutron distribution around the target is more skewed toward the back of the target, i.e., the tangential angle of the neutron velocity to the proton beam direction is smaller in addition to the increase of the neutron generation in the back of the target with higher energy protons. Thus, more neutrons are concentrated in the back region of the target. As seen in Figs. 14 and 15, the neutron spectra from the first target and flux trap moderators are smaller for 9.0 GeV protons than 2.2 GeV protons while those from the second target moderators are almost the same. The shape of neutron spectra from all moderators are almost identical regardless of impinging proton energies. This is thought to indicate that the volume of moderators used in the calculation is adequate to attain an equilibrium spectrum regardless of the source neutron spectrum generated in the target.

The statistical errors of the Monte Carlo calculations are less than 7 % for the neutron beams at moderators for all energy bins. Because of small population of neutrons at the end of beam lines, the statistical uncertainty at the end of beam lines is relatively large. Thus, the error ranges are indicated in Fig.11.

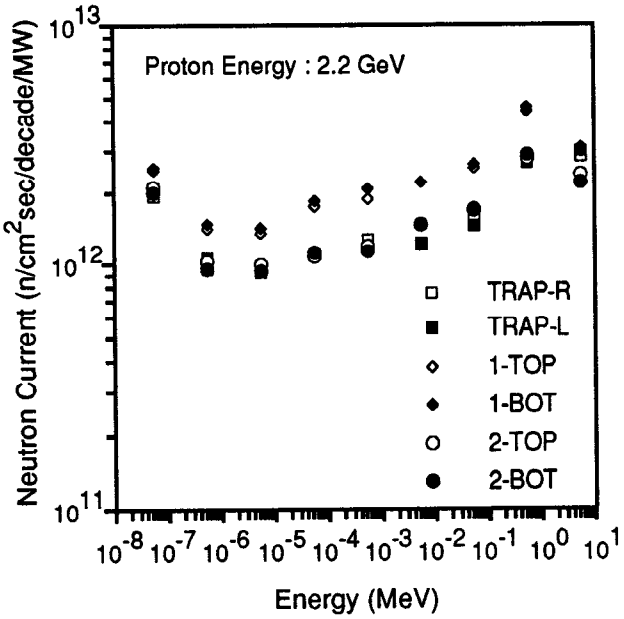

Fig.11 Neutron beam spectra at the moderator surfaces

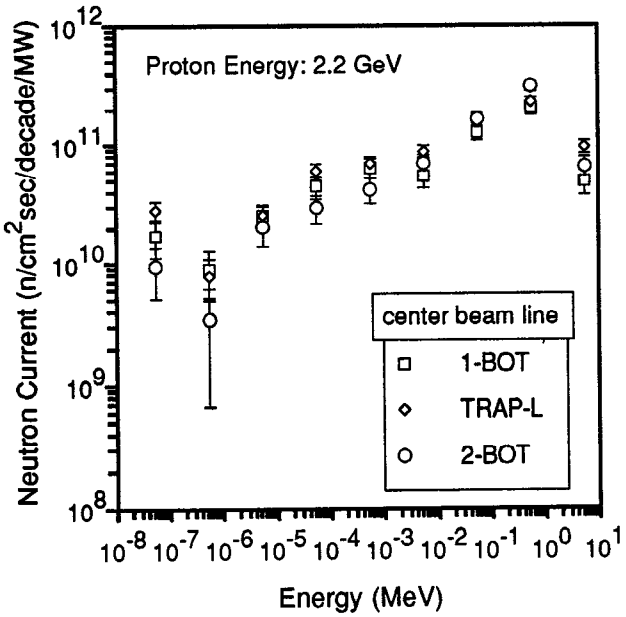

Fig.12 Neutron beam spectra at the end of beam lines

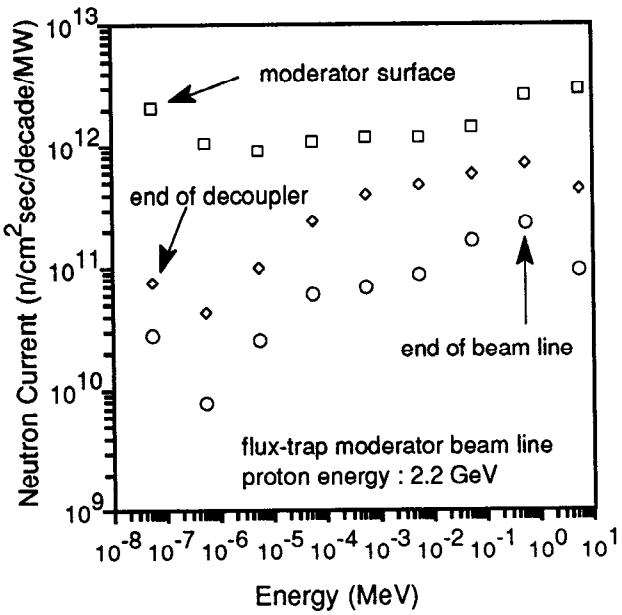

Fig.13 Change of neutron beam spectrum along the beam line

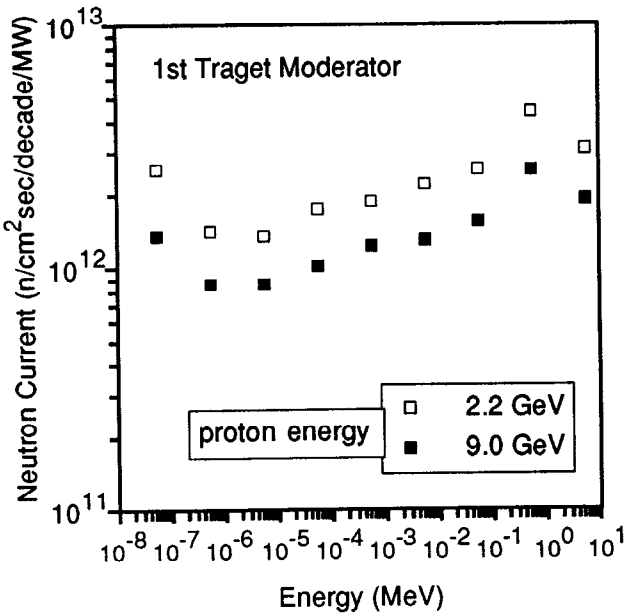

Fig.14 Effect of proton energy on neutron beam from the 1st target moderator

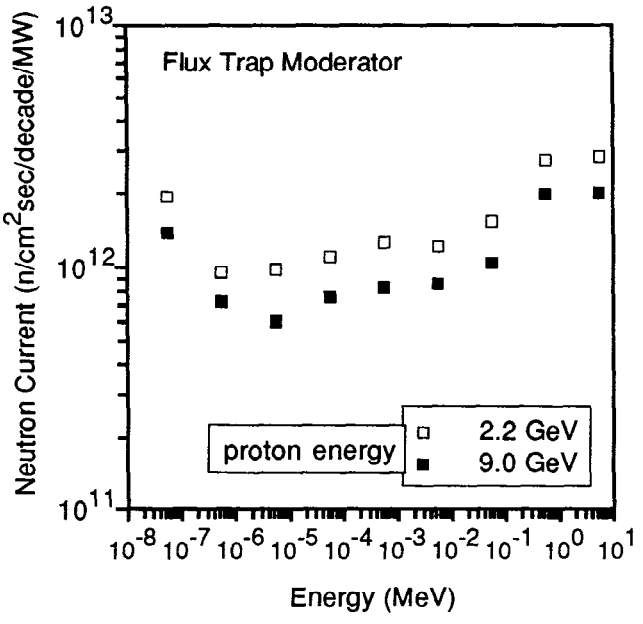

Fig.15 Effect of proton energy on neutron beam from the flux trap moderator

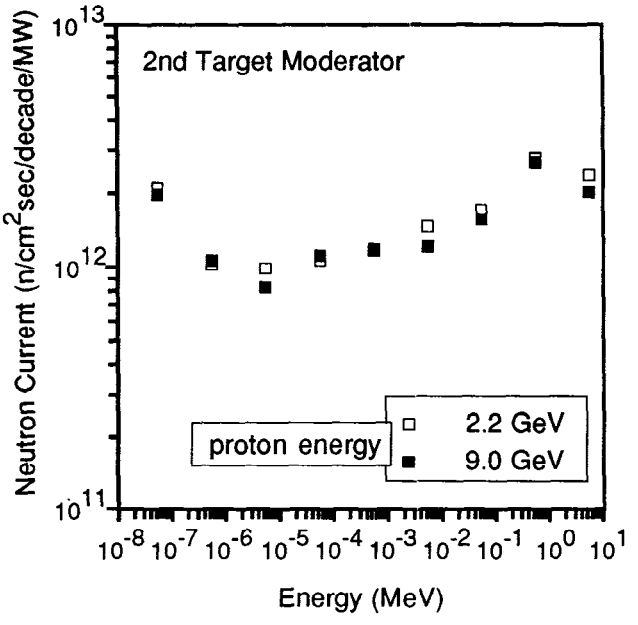

Fig.16 Effect of proton energy on neutron beam from the 2nd target moderator

5. Conclusions

We have investigated the effect of proton energy on the heat load and neutron yield in the target. The results have shown that the higher proton energy offers an advantage in target cooling because the peak power density is lower. However, the neutron production rate and maximum neutron current at a given proton beam power was observed to be reduced if proton energy is higher than 1.5 GeV. The total power deposited in the target was found to be insensitive to proton energy. The ratio of the target heat load to proton beam power was approximately 0.6 to 0.7 if the target dimension is sufficiently large to accomodate proton beam and cascade process. With a realistic target model under the current study, this conclusion of the target heat load was observed as well. However, for the power distribution in the surrounding system, i.e., reflector and shield, a large difference of heat load in space was found. The heat load was much higher in the back of the target station than in the front. Thus, the cooling of the surroundings needs to take account of the spatial variation of heat load. The neutron beam spectrum from moderators in the realistic target model did not change significantly with different proton energies. However, the spatial distribution of neutron beam was found to vary significantly according to the proton energy, i.e., higher proton energy resulted in lower neutron beam intensity from the moderators installed at the front of the target.

REFERENCES

1. Richard E. Prael and Henry Lichtenstein, " User Guide to LCS: the LAHET Code System", LA-UR-89-3014, Los Alamos National Laboratory, Sept. 1989.
2. T. W. Armstrong et al, "Theoretical Target Physics Studies for the SNQ Spallation Neutron Source", Jul-Spez-120, KfK Karlsruhe, Germany, July 1981.
3. N. Watanabe et al, "Report of the Moderator Working Group", International Workshop on the Technology of Targets and Moderators for Medium to High Power Spallation Neutron Sources, Paul Scherrer Institute, Switzerland, Feb. 1992.

Twelfth Meeting of the International Collaboration on Advanced Neutron Sources (ICANS XII),
24-28 May 1993, The Cosener's House, Abingdon, Oxfordshire, UK.

Target Station Design for a 1 MW Pulsed Spallation Neutron Source

G.J. Russell, G.D. Baker, R.J. Brewton, A. Bridge, T.O. Brun, M. Cappiello, C.E. Cummings, L.L. Daemen, D. Davis, D. Grisham, R.P. Hjelm, J.S. Elson, A. Kernodle, M.A. Merrigan, E.J. Pitcher, H. Robinson, L. Walker, R. Woods
Los Alamos National Laboratory,
Los Alamos, New Mexico, USA

Target stations are vital components of the 1 MW, next generation spallation neutron source proposed for LANSCE (colloquially referred to as LANSCE-II in this report). By and large, target stations design determines the overall performance of the facility. Many traditional concepts will probably have to be rethought, and many new concepts will have to be put forward to meet the 1 MW challenge. This article gives a brief overview of the proposed neutron spallation source from the target station viewpoint, as well as the general philosophy adopted for the design of the LANSCE-II target stations. Some of the saliant concepts and features envisioned for LANSCE-II are briefly described.

Target stations overview

The present concept calls for two target stations sharing one large building. The first target station is pulsed at 40 Hz, whereas the second station is pulsed at 20 Hz. These specifications are driven by user requirements. The average proton beam current is 1.25 mA at 800 MeV, i.e., 1 MW of proton beam power. The target stations are separated in the middle of the experimental hall by a large service area for remote-handling of the target system, storage of target components, and laboratory space for activities such as sample preparation.

The basic target configuration has not been chosen yet, and we are still exploring the advantages and disadvantages of horizontal vs. vertical proton beam insertion (from below in the case of vertical insertion). However, we have selected a reference case for further study, namely proton beam insertion from below into two target stations. These issues are addressed for the reference case in more detail below and involve far more than the neutronic performance of these different schemes.

The LANSCE-II target stations, although dedicated primarily to the production of thermal neutron beams for materials science and engineering, biology, chemistry, and condensed matter physics, will also include facilities for radiation damage studies and μSR. These issues have not been examined in detail yet.

Basic specifications

We review briefly the general requirements for LANSCE-II, and, more specifically, those requirements that impact significantly the design of the target systems.

Perhaps the most stringent specification is the proton beam power, namely 1 MW at 800

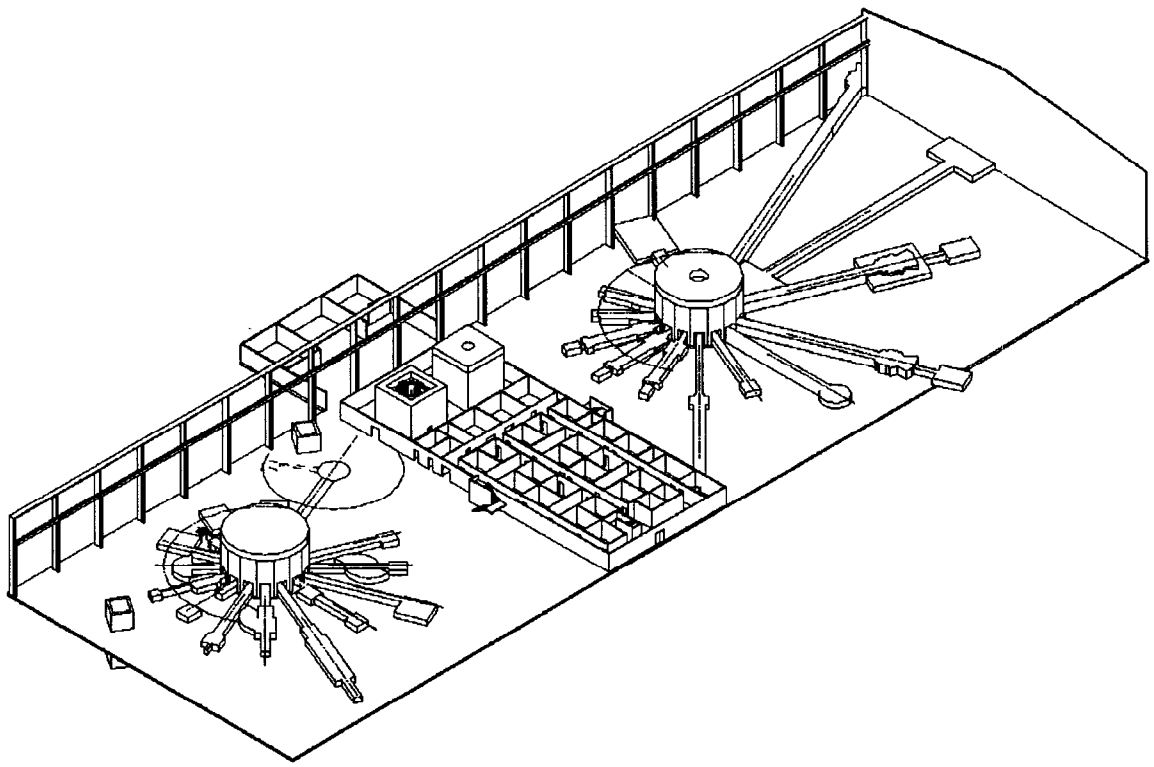

Figure 1: LANSCE-II: View of the experimental hall and the target stations.

MeV, with a possible upgrade to 5 MW in the not-too-distant future. These specifications are driven by the need to use as much of the present LAMPF facility hardware as practical to keep costs and performance as favorable as possible. The average current is 1.25 mA and the beam is to be divided between two target stations operating at 20 Hz and 40 Hz, Fig.1. The average proton beam power to the target stations is thus 333.3 kW and 666.7 kW, respectively. The large powers involved (compared, say, to ISIS at the Rutherford-Appleton Laboratory (England) where the average proton beam power is 160 kW, and presently the most powerful pulsed neutron source in the world) complicates greatly target design and the target cooling system. Ideally, the target stations should be designed so that an upgrade to 5 MW can be achieved at minimum cost. Although at this point we do not consider this to be a driving force behind the design of LANSCE-II, the possibility of a 5 MW upgrade has often been kept in mind in the design of many of the components of the target stations.

Other aspects of target design are very strongly affected by the power requirement. Problems associated with radiation damage, corrosion, and activation in the targets, to cite but a few, are likely to be much more severe than in present facilities. Similarly, the shielding requirements increase in size and complexity with proton beam power. To summarize, many problems that do not exist or are secondary problems at lower beam powers become more accute, and sometimes even dominate the design, at 1 MW.

A second important requirement is the *quality* of the neutron beams produced. A com-

promise must be reached between the number of viewed surfaces and the intensity of the neutron beam current leaking from the moderators. Opening more holes in the reflector to accomodate more flight paths has, generally speaking, a detrimental effect on the neutron beam current. The problem of finding a target configuration that has as many high-intensity beams as possible without sacrificing too many flight paths, or vice-versa, is not trivial.

The intensity of the neutron beam current (in the appropriate energy range for materials studies, typically $E < 100$ meV, but some applications require higher energy neutrons, in the 1-2 eV range) is only one criterion to determine the quality of the beam. Attention must be paid to the higher energy background ($E > 1$ eV), as well as to the shape of the neutron pulses. The former becomes a rather significant problem at 1 MW, and is essentially a function of target-moderator arrangement. The latter is determined mostly by the nature and geometry of the moderators.

A third requirement concerns the reliability and availability of the proposed neutron source. Obviously, this problem is linked directly to the reliability of the accelerator. However, there are many aspects of target station design that are crucial to ensure the regular and continued delivery of high-quality neutron beams to the users. The present goal is to provide beam time nine months per year with an availability of 85 % or more to about 2000 users.

First, and perhaps foremost, is maintenance. This includes routine maintenance operations, or more complex operations such as target or moderators replacement. How quickly, efficiently, and safely these operations can be carried out will depend largely on the remote-handling facilities to be designed and implemented in parallel with the target stations themselves.

Factors that determine the target lifetime such as radiation damage, thermal stress, and other requirements discussed above also influence directly the reliability of the target stations and must be carefully considered and optimized.

Monitoring the vital signs of the target stations, such as proton beam current, profile and location, coolant flow and pressure, and target temperature among others is even more crucial at 1 MW than in the present LANSCE target station. Extensive, state-of-the-art, and redundant instrumentation will allow us to react quickly and efficiently and eliminate potential problems before they become major problems forcing the target station to shut down. Target station instrumentation is thus a most crucial tool to increase reliability and therefore availability.

The above, sometimes contradictory, requirements ultimately impact the mechanical design and physical layout of the target-moderator-reflector-shield (TMRS) assembly: Increasing the number of flight paths per target station (compared to existing designs) adds to the complexity of the mechanical design of the TMRS assembly. This difficulty is compounded with the increased complexity of the cooling system required to operate at 1 MW and the reliability requirement that would ideally demand quick and easy access to the target and moderators if a problem develops.

All these problems and challenges are being addressed and resolved. The next section is devoted to the neutronics of the target station while the following section deals in detail with some of the engineering aspects of the design. Because there is no difference between the 40 Hz or the 20 Hz station, except for the average power deposited in the target, the design

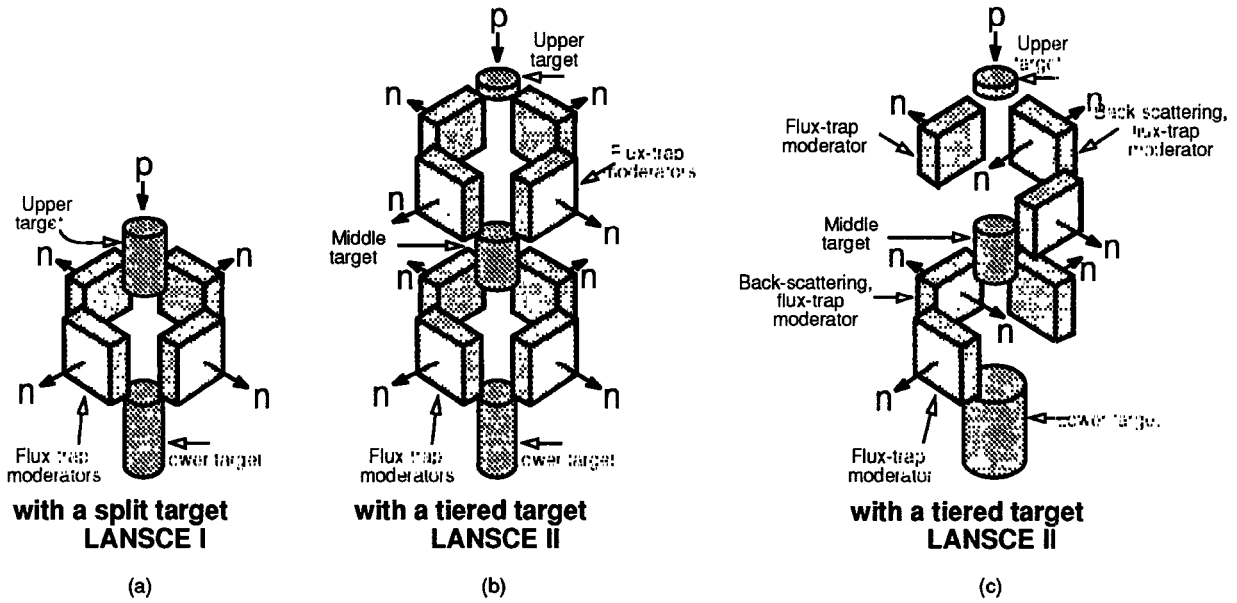

Figure 2: TMRS concepts. (a) Present LANSCE design; (b) Tiered target geometry with 8 moderators in flux-trap geometry; (c) Tiered target geometry with backscattering moderators.

procedures are the same for the two stations, and in what follows we will discuss a "generic" target station unless the distinction is explicitely required.

Neutronics - Target/moderator/reflector/shield assembly

The present LANSCE pulsed neutron source is based on the split target concept, [1,2] and provides the highest peak neutron flux of any spallation neutron source. Instead of the traditional solid, cylindrical target with four moderators in wing geometry [3-5], the present LANSCE target is split into two distinct target cylinders with four moderators facing the gap between the target cylinders, Fig.2(a). This geometry has several advantages; among them is the fact that the four moderators now have equal intensity. (In the traditional wing moderator design, the downstream moderators have lower intensity compared to the upstream moderators.) Furthermore, the split-target/flux-trap moderators geometry in combination with a vertical proton beam insertion scheme allows 360° access to the target station. The more common horizontal insertion scheme sacrifices up to ~120° for proton beam insertion and the remote-handling cell.

In an extensive study at Los Alamos, we are probing the vast parameter space associated with the design of a pulsed spallation neutron source, including:

- proton beam energy, pulse width, and repetition rate;
- horizontal versus vertical proton beam insertion;
- choice of target geometry and material;

- target thermal hydraulics;
- moderator geometry (wing, flux-trap, backscattering, coupled, composite, etc ...), material, and neutronic performance;
- number of moderators, viewed surfaces, flight-paths characteristics, etc ... ;
- composite reflector-shield, and bulk shield design;
- neutron beamline, chopper, and beam stop shielding requirements;
- target system engineering, including remote-handling and servicing;
- target instrumentation.

The results of some of these studies are described elsewhere in these proceedings.

We have settled on a reference concept which seems to perform well at 1 MW, and incorporates many desirable features of a future high-power target station. The concept will evolve as larger portions of the target station parameter space are explored. Table 1 summarizes some of the issues that affect target station design. A promising target concept on which our efforts are currently being focussed has two (possibly three) target cylinders with two flux-traps and four moderators per flux-trap, see Fig.2(b). This implies a total of eight moderators (and eight viewed surfaces) per target station. At three flight paths per viewed surface, the new facility could provide as many as 48 neutron beams. We also considered the use of backscattering moderators, as shown in Fig.2(c), in a two flux-trap geometry. A global view showing the location of the TMRS inside the shield, and part of the magnet optics is shown in Fig.3. A more detailed, preliminary engineering layout of the TMRS is shown in Fig.4.

Moderators represent another important aspect of target station optimization where much can be done to increase the neutron beam intensity. With a total of 16 moderators, one can consider a great variety of moderators, and thus a great variety of spectra and neutron pulse shape characteristics to suit the users needs. For example, a new, innovative concept being considered at LANSCE is that of a composite moderator where the neutron spectra of different materials (e.g., water and liquid hydrogen) could be mixed in different proportions to yield an intense, "broad-band" spectrum [6,7], or other desirable characteristics from the user's viewpoint. In addition, we have investigated coupled and backscattering moderators, Fig.2(c).

We also use the concept of a composite-reflector shield for the new spallation source. This concept was proposed and has been implemented at the present LANSCE facility [1,2]. We propose to replace the traditional Be reflector surrounding the target-moderators assembly by a composite assembly of Be and Ni. The inner Be core extends some 20 cm or so from the proton beam axis, while the outer part of the reflector is pure Ni. The Ni outer layer is a fast neutron reflector while the inner Be core acts as both a reflector and a moderator. This has several advantages. First, computer studies show a 10% increase in neutron beam intensity. Second, Ni is a better radiation shield than Be, which reduces the total amount of shielding

Target System Configuration		Neutronics	Total Angular Access	Angular Sep. of Instrum.		Shielding	Maintenance
				2 FP/ viewed surface	3 FP/ viewed surface		
Vertical Beam Insertion Upward	Hot cell on top	Allows for more moderator viewed surfaces than does horizontal insertion	360°	8 viewed surfaces		Hot cell displaces downstream shield	Access to 90° bending magnets and target complicated
				22.5°	15°		
	Hot cell on side		300° (60° for hot cell)	6 viewed surfaces		Hot cell shielding displaces intrument floor space	Access to 90° bending magnets complicated; Target maintenance similar to ISIS
				25°	16.7°		
	Segregated detached hot cell		360°	8 viewed surfaces		Shield geometry relatively simple	Access to 90° bending magnets and target complicated; Requires transportation of target to hot cell
				22.5°	15°		
	Integrated detached hot cell		360°	8 viewed surfaces		Shield geometry relatively simple	Access to 90° bending magnets and target complicated; Target maintenance may limit access to experimental hall; Similar to SINQ
				22.5°	15°		
Vertical Beam Insertion Downward	Hot cell below	Allows for more moderator viewed surfaces than does horizontal insertion	360°	8 viewed surfaces		Hot cell displaces downstream shield	Access to target complicated
				22.5°	15°		
	Hot cell on side		300° (60° for hot cell)	6 viewed surfaces		Hot cell shielding displaces intrument floor space	Target maintenance similar to ISIS
				25°	16.7°		
	Segregated detached hot cell		360°	8 viewed surfaces		Simple bulk shielding; Complex beamline shielding	Access to target complicated; Requires transportation of target to hot cell
				22.5°	15°		
	Integrated detached hot cell		360°	8 viewed surfaces		Simple bulk shielding; Complex beamline shielding	Access to target complicated; Target maintenance may limit access to experimental hall
				22.5°	15°		
Horizontal Beam Insertion	Hot cell on top	Good performance obtained from wing + flux trap geometry	300° (60° for beam insertion)	7 viewed surfaces		Hot cell need not displace shield	Relatively difficult access to target
				21.4°	14.2°		
	Hot cell on downstream side		240° (120° for hot cell & beam)	6 viewed surfaces		Hot cell displaces downstream shield	Proven design (ISIS)
				20°	13.3°		
	Hot cell below		300° (60° for beam insertion)	7 viewed surfaces		Hot cell need not displace shield	Conceptually designed (SNQ)
				21.4°	14.2°		

Table 1: Issues to be considered in the selection of a target station design for LANSCE-II.

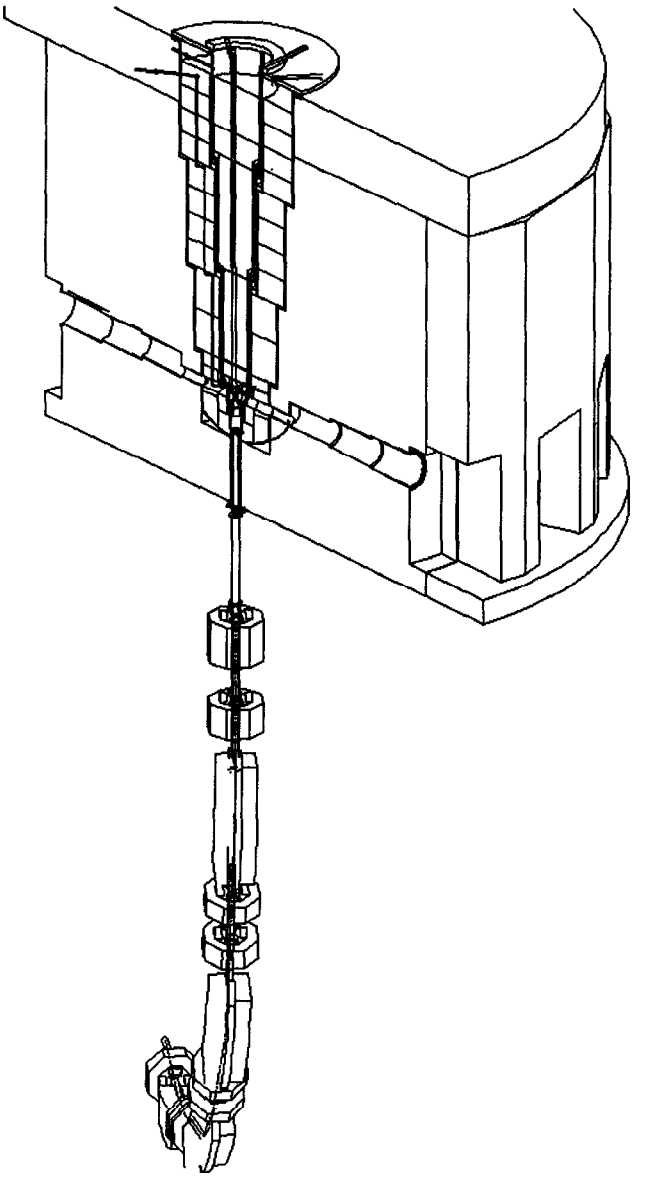

Figure 3: Cross-sectional view of the reference LANSCE-II target station. Access to the TMRS module is obtained by removal of a number of shielding segments shown explicitely in the diagram. Also shown is the magnet optics under the target station, including the 90° bending magnet. The bulk shield is approximately 12 m in diameter and 9 m high.

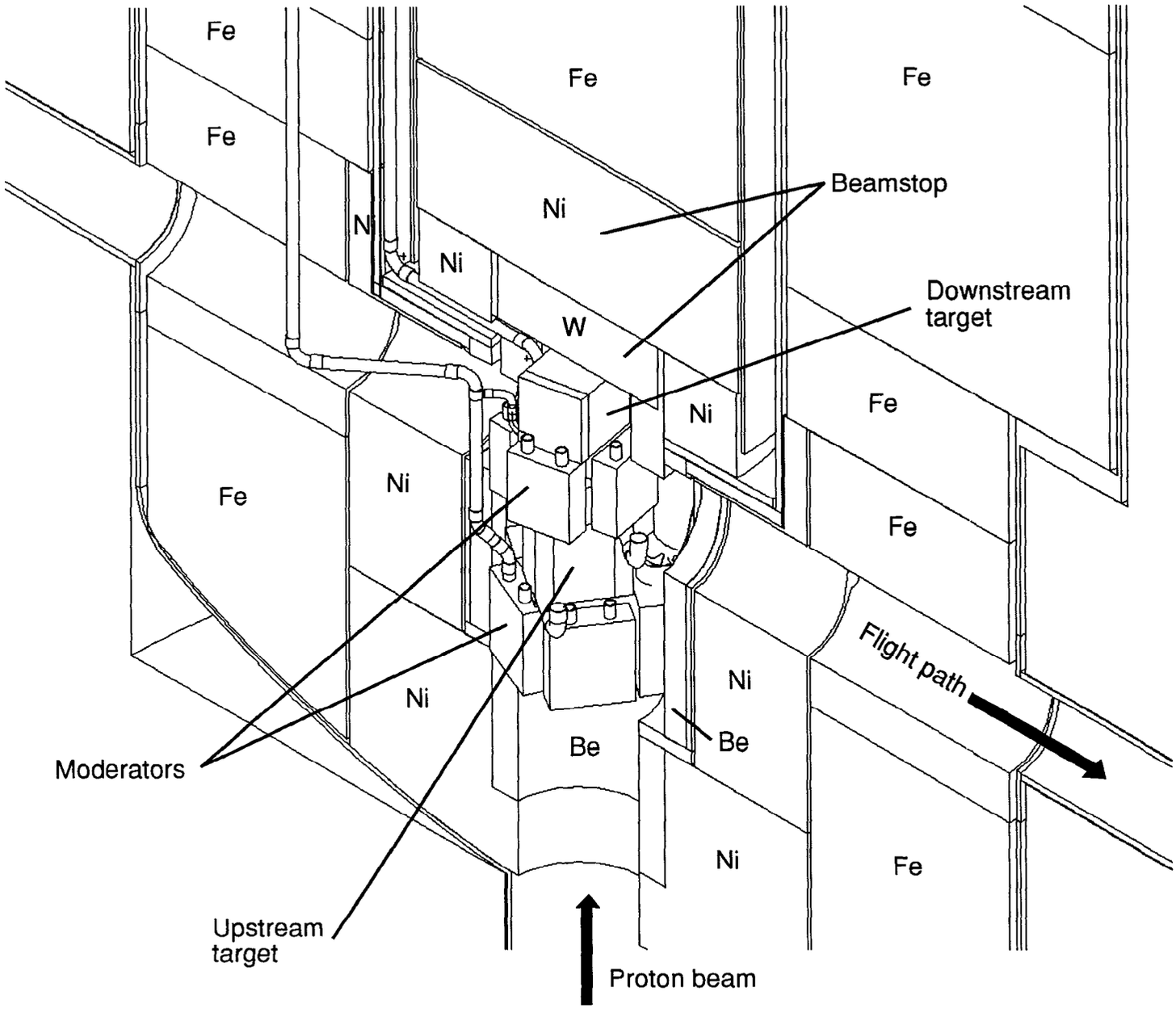

Figure 4: LANSCE-II preliminary TMRS layout.

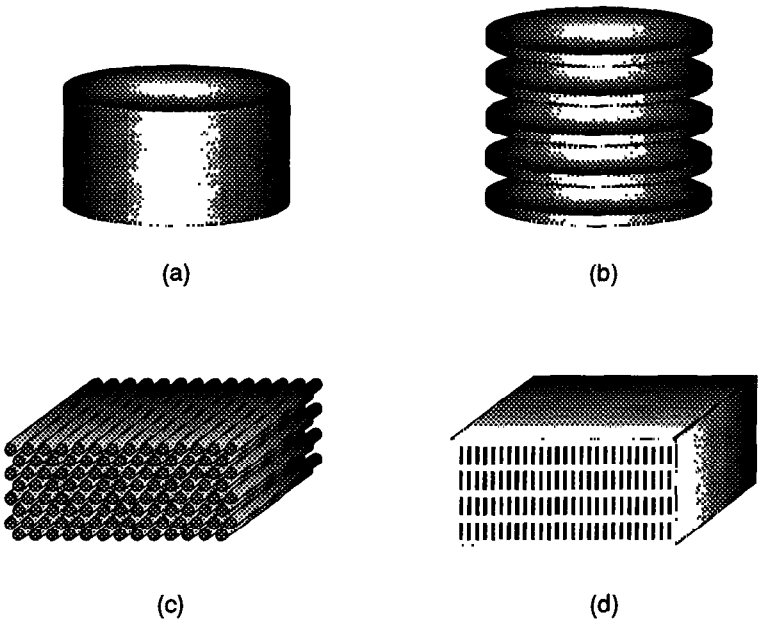

Figure 5: Target concepts for LANSCE-II. (a) Monolithic target, (b) Plates, (c) Rod bundles, (d) Microchannel target.

material required for the bulk shield. Third, less Be is needed – a distinct advantage in view of the materials cost, cost of machining, and toxicity of Be metal.

This summarizes very briefly an extensive set of studies aimed at neutronics optimization. The new concepts proposed to meet the 1 MW challenge call for the resolution of many engineering problems, such as target thermal hydraulics.

Target thermal hydraulics

We evaluated a variety of target design concepts, including monolithic targets, plates, concentric annuli, packed meshes, microchannels, and a variety of rod bundle configurations. In selecting concepts for further studies, we focused on neutronic performance, thermal-hydraulics, stress, and fabrication issues. We also kept in mind the possibility of increasing the proton beam power to 5 MW. Two of these concepts, the microchannel and rod bundle targets, were selected for further study, Fig.5.

Microchannel Target Design: The microchannel target is an extremely compact heat exchanger design composed of multiple, thin tungsten layers with channels etched on each layer surface using photolithography, Fig.5(d). The layers are furnace-brazed together using an alloy as the braze material. The brazing allows for a large heat transfer area and minimizes temperature differences within the target. The design provides a total temperature difference from the beam hot spot to the fluid exit on the order of 10-20°C. Because of the small dimensions of the individual flow passages, the resulting assembly behaves as a monolithic unit under thermal and mechanical loads. The fluid distribution headers can be made an integral part of the target, and the low flow requirement allows the inlet and exit piping to be kept small. The target structure is insensitive to internal pressure loads because of the small fluid

passage dimensions, and it has minimal thermal loads because of the low temperature differentials. Microchannel cooling technology has been used in a variety of high power density applications including laser mirrors, hypersonic infrared windows, semiconductor chips, and compact heat exchangers.

Our main objective in the design of the microchannel target is to cool an average power density of at least 1 MW/l so that the target may accomodate full beam power in a manner that minimally impacts the neutronic performance of the target. From a neutronics standpoint, desirable characteristics are: use of heavy water (instead of light water) as coolant; and minimize the volume of coolant in the proton beam path. We can achieve this thermal power density by ensuring low thermal stress using a low temperature differential between the inlet and outlet streams as well as low temperature differences in the solid metal sections of the target. Structural integrity of the target under induced thermal and mechanical stress is another important objective as well as low coolant fraction and flow rates, allowing a compact, mechanically simple design. The target concept should be scalable to an average power density of 5 MW/l in order to handle potential beam power increases. Further studies are required, however, to assess target performance at this power level.

The microchannel target design provides a very high thermal capacity with low fluid fraction. Because the metal cross-sections are small and the individual flow passages distributed throughout the target, the maximum temperatures resulting from the beam are low. As a result, the temperature-induced stresses in the target are also low. In addition, because of the distributed nature of flow passage voids in the target material, the moment of inertia of the target is high. The microchannel target is similar to a monolithic target in its structural behavior but without the large temperature differences and high resulting stresses seen in the monolithic target. Commercial suppliers have demonstrated fabrication of microchannel structures in tungsten and tungsten/rhenium alloys, and the fabrication of the proposed target configuration does not present any new process development problems.

Rod-Target Design: The rod-target concept is based on an array of short, tightly packed tungsten rods oriented perpendicular to the incident beam, Fig.5(c). The rod bundles, comprised of approximately 800 tungsten rods, are arranged into two target tiers and provide a total effective tungsten thickness of 22.5 cm (stopping length for 800 MeV protons on W). Coolant plena are provided at both ends of the rod bundles, and forced flow along the bundle length provides cooling for the target. Within each target tier, the tungsten rods and associated coolant (water) are contained inside an Inconel-718 target canister.

One of our main goals in the design of a target for LANSCE-II is to minimize the coolant fraction interior to the target tiers, thereby minimizing neutron moderation and parasitic absorption within the target. We used parameter studies to characterize the influence of rod diameter and pitch-to-diameter ratio on the coolant volume fraction; pressure drop across the rod bundle; and temperature gradient across the rods. To support 1 MW total beam power, we chose tungsten rods 0.6 cm in-diameter arranged on a triangular pitch with a rod pitch-to-diameter ratio of 1.05. The 10-cm-long rods are arranged in 27 and 24 rows for the first and second target tiers, respectively, and the maximum number of rods per pin row is 16. This configuration yields 10 cm^2 target tiers with effective tungsten thicknesses of approximately 12 cm and 10.5 cm. Each row is mechanically supported at both ends by a slot and hanger arrangement, and the Inconel-718 structure provides the mechanical and pressure boundaries

around each target tier. To minimize unnecessary coolant volume and bypass flow at the edge of the bundles the interior Inconel surfaces would be designed with a scalloped shape corresponding to the adjacent rod rows.

The results of extensive studies are that: (1) the rod target design concept can achieve relatively small coolant volume fractions with a high-surface-to-volume ratio; (2) the rod target concept can also be readily scaled with energy deposition while still preserving the small coolant volume fractions; and (3) the target cooling system operates at low pressure, which greatly simplifies mechanical and safety aspects of the design.

Further analysis effort should be devoted to system level performance of the target cooling system for the microchannel and rod-target design. This should include evaluation of off-normal transient scenarios such as loss of heat sink, loss of flow, loss of power, and loss of pressure/coolant.

Remote-handling

The remote-handling systems initially considered for the LANSCE-II reference case make use of the monitor/servo-manipulator system developed at LAMPF [8,9]. This system of remote-handling utilizes servo-manipulators mounted on hydraulic booms, cranes, and remotely operated vehicles. Because the reference LANSCE-II design calls for beam delivery from below with the target stations located in two large experimental halls, the large remote-handling area is located between the two experimental halls, Fig.1. This concept permits a central, single facility to service both target areas. Remote-handling, removal, and reinstallation of the target system is done from the top of the target monolith. The ventilation system over the target monolith would be designed to give a forced flow of air across the top into High Efficiency Particulate Air (HEPA) filter intake ducts. If any airborne particulate radiation is expected or found, ventilation containment enclosures could be placed over the top of the monolith.

The targets, moderators, and part of the reflector form a modular assembly inside the target crypt. This module is removed from the crypt into a shielded cask, which is transported by crane to the remote-handling area. The module is then placed into storage wells in the floor or in shielded assembly/disassembly caves if immediate replacement or repair of the target-moderator-reflector module components is required.

The assembly cells will be designed to permit the precise locating and alignment of all system components. Remote-handling procedures will be developed and carefully tested prior to implementation. Major components will be designed in a modular fashion so they can easily be removed, repaired, or replaced. Rack-mounted tools and positioning devices will be designed for the system. The most advanced equipment will be placed in this facility to give the largest possible ability for performing delicate tasks on complicated hardware. The disassembly cell will be designed to accommodate the remote-handling tasks and constructed from stackable shielding. A water-tight liner connected to the facility contaminated waste system will be used to contain any liquid spills. A HEPA-filtered ventilation system will be installed to control the air emissions. Facilities must be provided to decontaminate remote handling equipment, tools, and experimental hardware.

This approach corresponds to the vertical beam insertion (upward)/detached hot-cell concept presented in Table 1 and is our reference case. However, we are revisiting the remote-

handling issue as we probe more of the parameter space of target station design.

Other aspects of target station design

It is not possible to give here an exhaustive overview of all those aspects that affect target station design. Beside the crucially important issues discussed above, many other, equally important, problems have to be addressed.

Among those problems is the poorly understood issue of target and target coolant radiochemistry. The intense radiation field to which the target is subjected modifies drastically its physical and chemical properties. This, in turn, complicates the thermal hydraulics of the target and its resistance to thermal stress for instance, but also contributes to a decrease in the target lifetime. Indeed, the formation of spallation products and their subsequent chemical interaction with the coolant and the target material, coupled with the radiation damage and the likely modification of the materials microstructure under thermal stress and radiation could ultimately lead to the early demise of the target if no precautions are taken to alleviate these problems. Unfortunately little information is available regarding these difficulties. However, present operational experience with various types of targets at spallation sources indicates that these problems already exist at the power levels currently used. At proton beam powers of 1 MW or more, these problems could very well become a vital aspect of target design.

Another important problem that was deliberately ignored here is that of target station instrumentation and control. Proper instrumentation is necessary to ensure that the various target station components are operating as expected within the operational safety limits. The consequences of an undetected failure, particularly at 1 MW, in any one of these systems can result in costly repairs and loss of valuable experiment time for the users. In addition to satisfying basic safety requirements, target instrumentation should be sufficiently varied and flexible to be useful in collecting data for target station development. Of particular importance is proton beam monitoring. The exact beam profile, intensity, and location on target are most crucial pieces of information, and should be monitored at all times. With high-power targets such as those proposed for LANSCE-II, cooling requirements (target, moderators, reflector, shield, beamstop) are likely to be complex. Monitoring (temperature, flow, pressure) of the cooling circuitry is thus essential.

Other problems include: target decay heat, radionuclides production, mechanical design and layout, activation of ancillary equipment, radiation protection, vacuum enclosures, interfacing with the accelerator and the scientific instruments, etc. Clearly these are out of the scope of this review.

References

[1] G.J. Russell, C.D. Bowman, E.R. Whitaker, H. Robinson, and M.M. Meier, "LANSCE high-power (200 μA) target-moderator-reflector-shield", Proceedings of the Eighth Meeting of the International Collaboration on Advanced Neutron Sources, Rutherford-Appleton Laboratory report RAL-85-110 (November 1985), p.272.

[2] G.J. Russell, H. Robinson, G.L. Legate, R. Woods, E.R. Whitaker, A. Bridge, K.J. Hughes,

and R.D. Neef, "The LANSCE target system", Proceedings of the Ninth Meeting of the International Collaboration on Advanced Neutron Sources, F. Atchison and W. Fischer, Eds., Swiss Institute for Nuclear Research Report ISBN 3-907998-01-4 (April 1987), p.177.

[3] A. Carne, "Review of the SNS target station", Proceedings of the Fourth Meeting of the International Collaboration on Advanced Neutron Sources, (ICANS-IV), Y. Ishikawa, N. Watanabe, Y. Endoh, N. Niimura, and J. Newsam, Eds., National Laboratory for High-Energy Physics report, KENS-II (March 1981), p.136.

[4] J.M. Carpenter, C.W. Potts, and G.H. Lander, "Intense Pulsed Neutron Source (IPNS) at Argonne National Laboratory: A status report as of June 1982", Proceedings of the Fourth Meeting of the International Collaboration on Advanced Neutron Sources, (ICANS-VI), Argonne National Laboratory report ANL-82-80 (January 1983), p.77.

[5] N. Watanabe, S. Ikeda, and Y. Ishikawa, "KENS target station", Procceedings of the Fourth Meeting of the International Collaboration on Advanced Neutron Sources, (ICANS-IV), Y. Ishikawa, N. Watanabe, Y. Endoh, N. Niimura, and J. Newsam, Eds., National Laboratory for High-Energy Physics report, KENS-II (March 1981), p.181.

[6] L.L. Daemen, E.J. Pitcher, G.J. Russell, "Moderator materials and neutronic performance comparisons.", this meeting.

[7] G.J. Russell and H. Robinson, "LANSCE Upgrade Cold-Sources", in Proceedings of the International Workshop on Cold Neutron Sources, Los Alamos National Laboratory report LA-12146-C (August 1991), pp.471-489.

[8] G.L. Grisham and J.E. Lambert, "History of remote Handling at LAMPF", ANS 30, Volume I, 1982.

[9] D.L. Grisham and J.E. Lambert, "Monitor 1983", IEEE Trans.Nucl.Sci., 1983

THE CHOICE OF OPTIMUM PROTON ENERGY FOR A HIGH POWER SPALLATION SOURCE - ISSUES FOR THE TARGET STATION.

T A Broome
Rutherford Appleton Laboratory

1. INTRODUCTION.

A debate central to the design of a new spallation source with proton beam power in excess of 1 MW is the choice of the energy of the proton beam. This paper presents a brief review of some of the effects of the proton beam energy on the design of a Target Station.

The main issue is to achieve maximum performance in terms of neutron beam characteristics within the constraint of practical engineering and material limits.

In the following discussion a constant proton beam power is assumed. Thus higher energies imply lower proton beam currents. The dimensions of the biological shield are dependant on proton beam power and are essentially independent of proton energy. The nuclear particle cascade which characterises the basic neutron production increases in physical extent as the proton energy increases which is the crucial feature as far as the Target Station is concerned.

2. NEUTRONIC PERFORMANCE.

The yield of fast neutrons from a spallation target varies essentially linearly with proton energy. Experimental data indicate a small fall off at energies above about 2 to 2.5 GeV but for practical purposes the basic fast neutron yield for a given proton beam power can be taken as independent of energy below 3 GeV. New data [1] confirming this have been presented at this meeting as well as new calculations [2].

Rather than considering fast neutron production the performance of the source must be judged by the neutron beam fluxes and time pulse characteristics at the experiments. These have to be matched to the requirements of the neutron scattering instruments. This implies that several moderators with different temperatures, materials and pulse shaping will be required.

At the workshop on High Power Targets at PSI [3] there was a concern that the useful neutron fluxes would be lower for the higher energy beams. This was based on calculations indicating that the fast neutron flux from the target surface, the 'brightness', is reduced for higher energy due the increased longitudinal extend of the nuclear cascade.

Studies have been reported at this meeting [4] of calculated and measured moderator fluxes for realistic configurations. With limited optimisation these show that the useful neutron fluxes per MW of beam power are essentially independent of the proton energy. This is new and important data. The work has covered both of the standard target/moderator configurations, wing and flux trap.

There is one caveat to this which concerns neutron backgrounds in the experiments. There is considerable experience to show that at, or below, 800 MeV backgrounds are acceptable. There is very little experimental evidence for energies above this. The magnitude of the background problem remains an area to be studied.

However, a general conclusion is clear. The neutron beam characteristics required by experiments can be achieved for a wide range of proton beam energies. The experimental aspects of the source specification will have only a marginal role in the consideration of the choice of proton energy for a high power source.

3. CALCULATIONAL METHODS

The main body of data available to validate theoretical calculations and phenomenological models is restricted to energies around 1 GeV. However, extrapolation to higher energies has been successful in several areas. In particular the work done on the design of calorimeters for high energy physics experiments give some confidence that reliable calculations of nuclear cascades can be performed up to several GeV.

4. ENGINEERING.

The target stations required for a high power spallation source present a formidable engineering challenge.

4.1 Cooling Systems

A crucial concern is cooling systems. The peak power deposition of up to 8 MW per litre for a stationary solid target is very clearly at the limit of the capabilities of pressurised water cooling. There are ways to reduce the peak power deposition.

- Decrease the longitudinal interaction density by increasing the proton energy.

The peak power deposition at 800 MeV is 8 MW/l and at 3 GeV this drops to about half this value.

- Decrease the lateral density either by moving the target or increasing the proton beam size.

Studies on neutron production have shown that increasing the beam diameter in a 'wing' geometry results in reduced neutron flux from the moderators. Calculations of the effect of increasing proton beam diameter for a 'flux trap' configuration have not yet been performed and this data will be crucial in the consideration of the optimum proton energy.

Rotating solid targets were extensively studied during the SNQ and practical solutions found to the engineering problems. A new design for a solid rotating target giving a flux trap configuration was presented at this meeting.

Detailed work is now needed to establish the practical limit for pressurised water cooling given the geometric constraints of achieving the required neutron fluxes.

A general conclusion is that cooling the target whilst maintaining neutron beam fluxes becomes progressively easier as the proton energy increases. However, while the lower energies present greater difficulties, further work is required to establish whether or not practical engineering solutions exist.

4.2 Thermal Shock

The effect of the short duration proton pulses (<3 μs) is to deposit power beyond the rate that normal thermal conduction processes can transport the heat. This results in shock wave propagation with its associated high transient stresses. This could present a serious materials problem. As the power deposited per unit volume reduces as the energy increases the effects of thermal shock will also reduce with increasing proton energy. Thermal shock is a phenomenon which will require investigation.

4. RADIATION DAMAGE.

A spallation source based on a 5 MW proton beam will produce irradiation of structural materials comparable to that of a high flux research reactor such as that at the Institute Laue Langevin. Experience with such reactors does not suggest that there are any insuperable problems. However, spallation sources presents some special problems. As with peak power deposition the 'density' of radiation damage will decrease as the proton beam energy increases.

4.1 Assessment.

The crucial difficulty is the reliability of the assessment of component lifetimes. There is little data available for the irradiation conditions in a spallation source although the experience at existing sources such as ISIS will be valuable. Accurate prediction of lifetimes is important as this will determine the strategy for component replacement which in turn will dominate the detailed design of theses components and the handling philosophy.

4.1 The Proton Beam Window.

Most target station designs requires a window separating the proton beam vacuum from the target. This component which requires special consideration. Experience at existing accelerators is limited to proton beam current densities below 100 $\mu A.cm^{-2}$. For a typical parabolic proton beam profile a limit of 100 $\mu A\ cm^{-2}$ would require a beam diameter of 250 mm at 800 MeV and 70 mm at 3 GeV for 5 MW beam power. Proton beam diameter has a significant effect on the possible neutron fluxes as mentioned above in the considerations of the effects of peak power deposition in the target.

Design of a window for beam current densities well above 100 $\mu A\ cm^{-2}$ with a minimum lifetime of one or two years may well be impossible. However, a window

with relatively short lifetime for example three months could still be acceptable if replacement is a short operation of say one or two days. This would be a practical solution within the normal constraints of an accelerator complex.

4.3 The Target and Moderators.

For the reasons discussed above there may well be a proton energy below which a solid stationary target is impractical. Radiation damage will result in changes in material properties such as embrittlement is likely to make the design problem more rather than less difficult. However, as with the window a solution which gives relatively short lifetime with fast replacement could still be practical.

5. CONCLUSIONS.

In principle it would appear that, by careful optimisation, target/reflector/moderator configurations can be designed to give about the same neutron beam fluxes independent of the proton energy. Solutions to the engineering difficulties, in general, get easier as the proton energy increases.

However, the implied lower energy limit for a practical target station is not known at present. This is the main issue for the Target Station design.

References.

[1] Spallation Neutron Measurements at Proton Energies of 0.8 to 3 GeV
T. Nakamoto et. al.
Proceedings of this meeting

[2] LAHET Code System/CINDER'90 Validation Calculations and Comparison With Experimental Data.
T. O. Brun et. al.
Proceedings of this meeting

[3] International Workshop on the Technology of Targets and Moderators for High Power Spallation Sources. PSI Villigen, Switzerland, February 1992
Editor Yasushi Takeda

PSI- Proceedings 92-03

[4] Comparison of the slow neutron intensity - 0.8 GeV vs 3 GeV Protons
Y. Kiyanagi et. al.
Proceedings of this meeting

[5] Target-Moderator-Reflector Assembly for a High Power Spallation Source
H. Conrad
Proceedings of this meeting

D_2-cold moderator system at SINQ

- pressure tests of the moderator vessel -

H. Spitzer, K. Geissmann, W. Wagner and G.S. Bauer

Paul Scherrer Institut
5232 Villigen PSI
Switzerland

Abstract:

The design concept of the liquid D_2-cold moderator system of SINQ is based on the principle of isothermal convection of liquid D_2 between a He/D_2-heat exchanger and phase separator in the vertical leg, and a 22 l liquid D_2-moderator vessel at the tip of a horizontal insert. The moderator vessel is made of pure (99.5 %) aluminium in order to avoid radiation embrittlement. Pressure test with He-gas at 78 K up to 4 bar abs. and with water at room tempearture up to the forced rupture at about 30 bar abs. proved that the presssure resistance of the moderator vessel is sufficient for the safe operation under normal conditions as well as in the case of possible malfunctioning, such as the sudden breakdown of the insulating vacuum. The tests show that the onset of plastic deformation occurs at about 6 bar, sufficiently above the operating pressure (2.8 bar) and the design internal pressure (4.4 bar). The forced rupture of a prototype vessel occured between 30 and 31 bar.

Technical concept and status

At the previous ICANS meeting [1], the technical concept of the liquid D_2-cold moderator for the Swiss spallation source SINQ was presented. Meanwhile, the realization of this project made substantial progress: several man years of engineering work have been invested since then to transform the basic concept into a detailed technical layout suitable for manufacturing and purchase of components. Most of the major plant components have now been ordered and will be delivered successively during the current year. Our goal is to have the entire plant assembled and ready for testing and pre-commissioning at a separate testing emplacement in July 1994, about six months before its planned integration into the target shielding block. Thus we count on having it ready for reliable operation with the first proton beam on target.

Horizontal insert and moderator vessel

The heart of the system is the horizontal insert shown in Figure 1. At its tip it carries the D_2-moderator vessel with a volume capacity of approximately 22 l of liquid D_2. The distance from its front surface to the target surface is approximately 10 cm. The moderator vessel is enclosed by a double walled vacuum jacket consisting of an outer 2 mm thick AlMg3-tube and an inner zircaloy tube, 3 to 4 mm thick, which being the pressure safety tube, is designed to withstand an internal pressure of 30 bar.

Behind the D_2-moderator vessel, the horizontal insert carries a D_2O reflector vessel to minimize neutron losses. The D_2/He-heat exchanger ist not inside the horizontal insert but is mounted in a separate, vertical leg in order to minimize the radiation load and to realize the necessary vertical separation for the natural convection system. This system is driven by the liquid-gas mixture flowing back from the moderator vessel and up to a phase separator below the heat exchanger.

Pressure load of the moderator vessel

Fig. 2 shows a vertical cut through the D_2-moderator vessel and its concentric D_2-flow tubes. Some relevant data are given in Table 1. The vessel will be made of 99.5 % pure aluminium, semi-hard with one welding seam around its cylindrical surface at the far end with respect to the target. Material softening around the weld requires the wall thickness of the vessel to be increased from 3 to 5 mm in this region to obtain the strength necessary to resist an internal pressure of 4.4 bar.

Material	Al 99.5	
Outer diameter	296/300	mm
Length	354	mm
Wall thickness	3 resp. 5	mm
Total volume	22.3	l
Volume filled with liquid D_2	~ 20	l
Total mass of Al	4.375	kg
Total weight of filled vessel	~ 7.6	kg
Design internal pressure	4.4	bar
Max. operating pressure	2.8	bar

Table 1: Some relevant data for the D_2-vessel of the SINQ cold moderator

The choice of pure aluminium for the wall material of the moderator vessel was governed by concerns about radiation embrittlement during long-term source operation. Its disadvantage is a relatively low material strength, and in particular a possible uncontrolled softening by the necessary welding. The **real** strength and pressure resistance of the final vessel or an equivalent prototype is therefore a crucial property to guarantee safe operation and to rate the chances of the system to survive conceivable malfunctioning without fatal damage. It was therefore decided to undertake relevant tests with 1:1 prototype vessels by measuring the real strength at different positions of the vessel after fabrication and by investigating the deformation of the vessels when exposed to excessive internal pressure.

One of the most severe failures one can imagine and should design for is the sudden complete breakdown of the insulating cryo-vacuum when the system - vessel and transfer tubes - are filled with liquid D_2. The vacuum breakdown leads to boiling and evaporation of the liquid D_2 with the consequence of a sudden pressure increase in the system. Fig. 3 shows the calculated pressure rise in the moderator vessel for the relevant time period after this event for three different assumptions for the heat input into the system [2]. The figure shows that for all three cases the pressures rises quite fast, i.e. within the first two-tenths of a second, and then relaxes due to the onset of backflow into the buffer tank. The highest pressure predicted is at about 3.3 bar, occuring as expected for the shortest time constant of 3 ms. Although this is unrealistically fast, this value together with an appropriate safety factor was used as a basis for the design pressure of 4.4 bar as given in Table 1.

Pressure test with He-gas at 78 K

In order to monitor the deformations during the pressure tests, the prototype vessel was equipped with 18 strain gauges at representative positions, as illustrated in Fig. 4. For safety the vessel was water-loaded at room temperature up to 5 bar abs. prior to the He-gas test at liquid nitrogen temperature. After cooling to liquid nitrogen temperature the vessel was filled with He-gas, increasing the pressure in steps of 0.5 bar to a maximum of 4 bar abs. The results from the strain gauges, read after each pressure run and subsequent relaxation to normal pressure, are shown in Fig. 5. Within the sensitivity of the sensors (± 2 μm/m) no indication for a permanent deformation was found. This indicates that all deformations up to a load of 4 bar at 78 K are in the fully elastic range.

Rupture tests with water at room temperature

A second sequence of pressure tests was carried out at room temperature, using water as pressurizing medium, with the aim to exceed the elastic range and to induce plastic deformations up to the forced rupture of the vessel. The deformations remaining after relaxation to normal pressure are plotted in Fig. 6 for the pressure range up to 15 bar. According to these results, at all positions monitored the deformation is in the elastic range up to a pressure of about 6 bar. Between 6 and about 11 bar, considerable plastic deformation occurs but only in the vicinity of the weld. As expected, the material softening due to the welding is the limiting factor for the resistance to plastic deformation of the moderator vessel. Yet, the threshold pressure for the outset of plastic deformations is not less than 6 bar in this region, i.e. well above the required design pressure of 4.4 bar (cf. table 1). Pressure increase above 15 bar led to further considerable plastic defomation and to visible expansion. It finally led to the rupture of the vessel at a pressure between 30 and 31 bar. A photograph of the ruptured vessel is given as Fig. 7. It shows that the rupture occured by a crack of about 10 cm length along the cylinder surface, extending parallel to the cylinder axis. The material around the weld is deformed but unruptured, which is attributed to the higher wall thickness in this region combined with work hardening during the testing and the more favourable position at the edge of the cylinder around the bottom. Generally, the observed rupture behaviour followed the predictions of classical rupture mechanics for the given vessel geometry and the assumption of (almost) equally strengthened material all around.

All tests reported here were repeated with a second prototype vessel. This second test sequence yielded almost identical results as the reported one.

Conclusions

The tests performed on two prototypes of the liquid D_2 moderator vessel at the temperature of liquid nitrogen confirmed that the vessel can withstand any pressure level that might be expected to arise as a consequence of a sudden heat influx into the liquid while the transfer pipes to the expansion tank are open. Room temperature testing revealed that the moderator vessel can withstand a pressure up to 6 bar without any plastic deformation and can withhold a pressure of more than 25 bar when plastic deformation is allowed. Rupture as a consequence of excessively high pressure occurs in the form of a gap opening on the cylindrical circumference and not in a catastrophic way. Operationg of the SINQ D_2 cold moderator is therefore considered to be safe under all circumstances.

References

[1] H. Spitzer, A. Höchli, G.S. Bauer and W. Wagner: Proc. of ICANS-XI, KEK, Tsukuba, Japan (1990), 430

[2] K. Skala, H. Spitzer, G.S. Bauer, ibid. p.416

Figure 1: Vertical section through the horizontal insert of the SINQ cold D_2-source.

Figure 2: The D_2-moderator vessel and its concentric flow tubes (vertical section).

Figure 3: Pressure rise in the moderator vessel for the three different assumptions on heat input
a) heat input along the whole D_2-system with 3.6 W/cm^2 of surface, heat flux
b) Heat input concentrated on moderator and phase separator volumes but matching the total heat input of curve a)
c) as b) but time constant of power rise reduced from 300 ms to 3 ms.

Figure 5: Remaining deformation at various positions of the moderator vessel after pressurizing to different levels and returning to normal pressure at 78 K. The precision of the calibration is ± 0.2 μm/m.

Figure 6: Deformations measured in the room temperature pressure tests. Clearly the limit of elastic deformation (zero after return to normal pressure) is given by the softening around the weld.

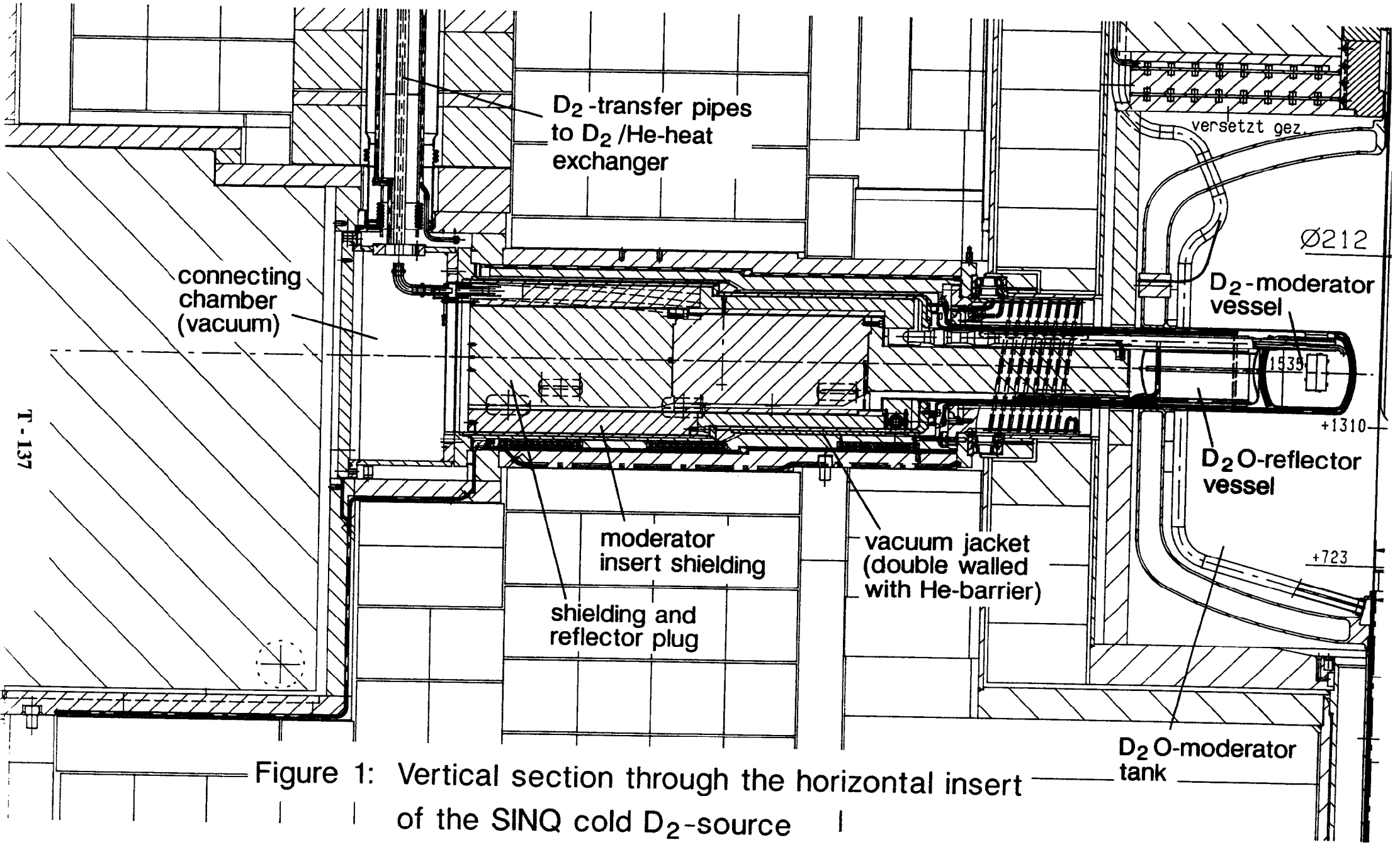

Figure 1: Vertical section through the horizontal insert of the SINQ cold D_2-source

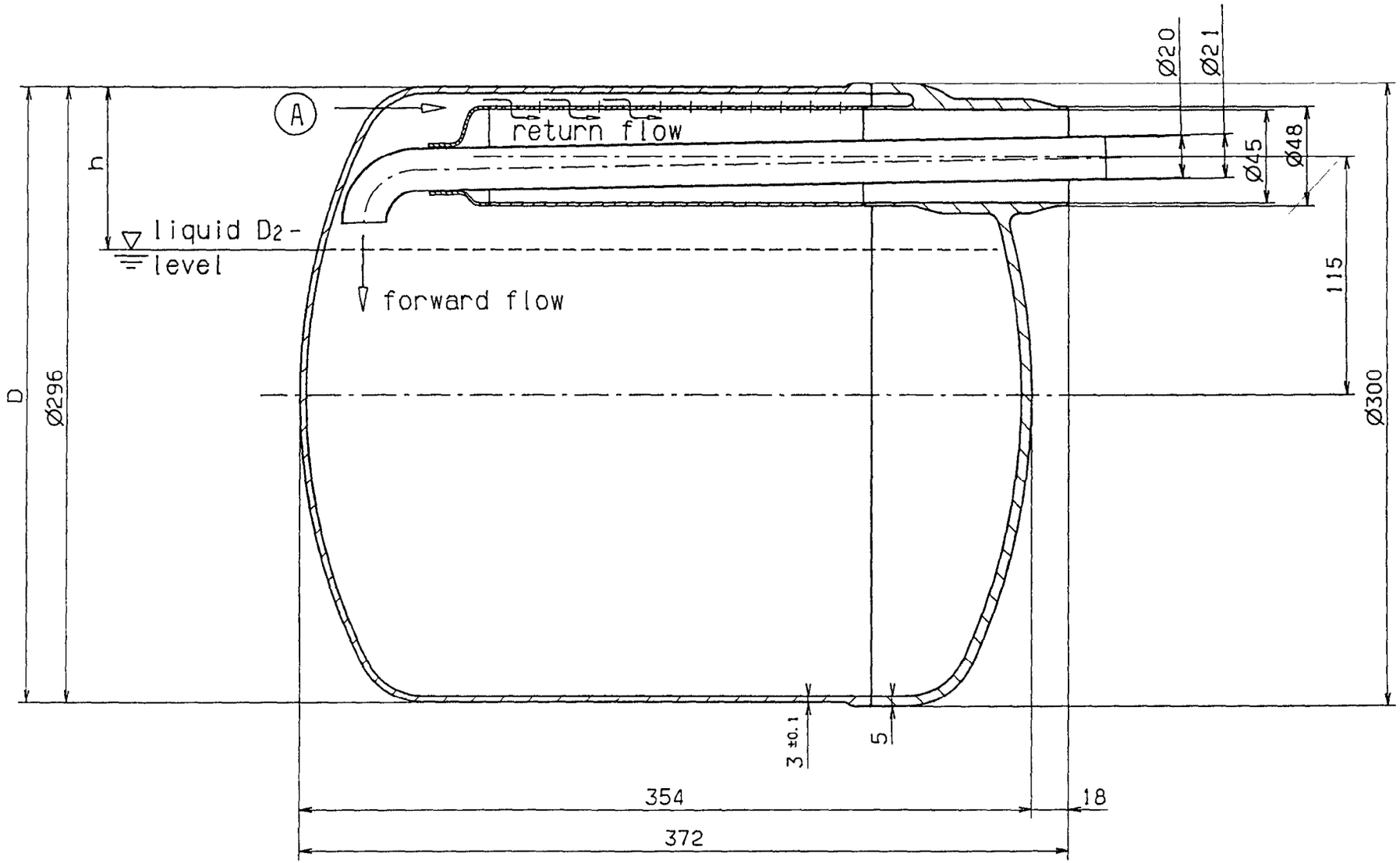

Figure 2: The D_2-moderator vessel and its concentric flow tubes (vertical section)

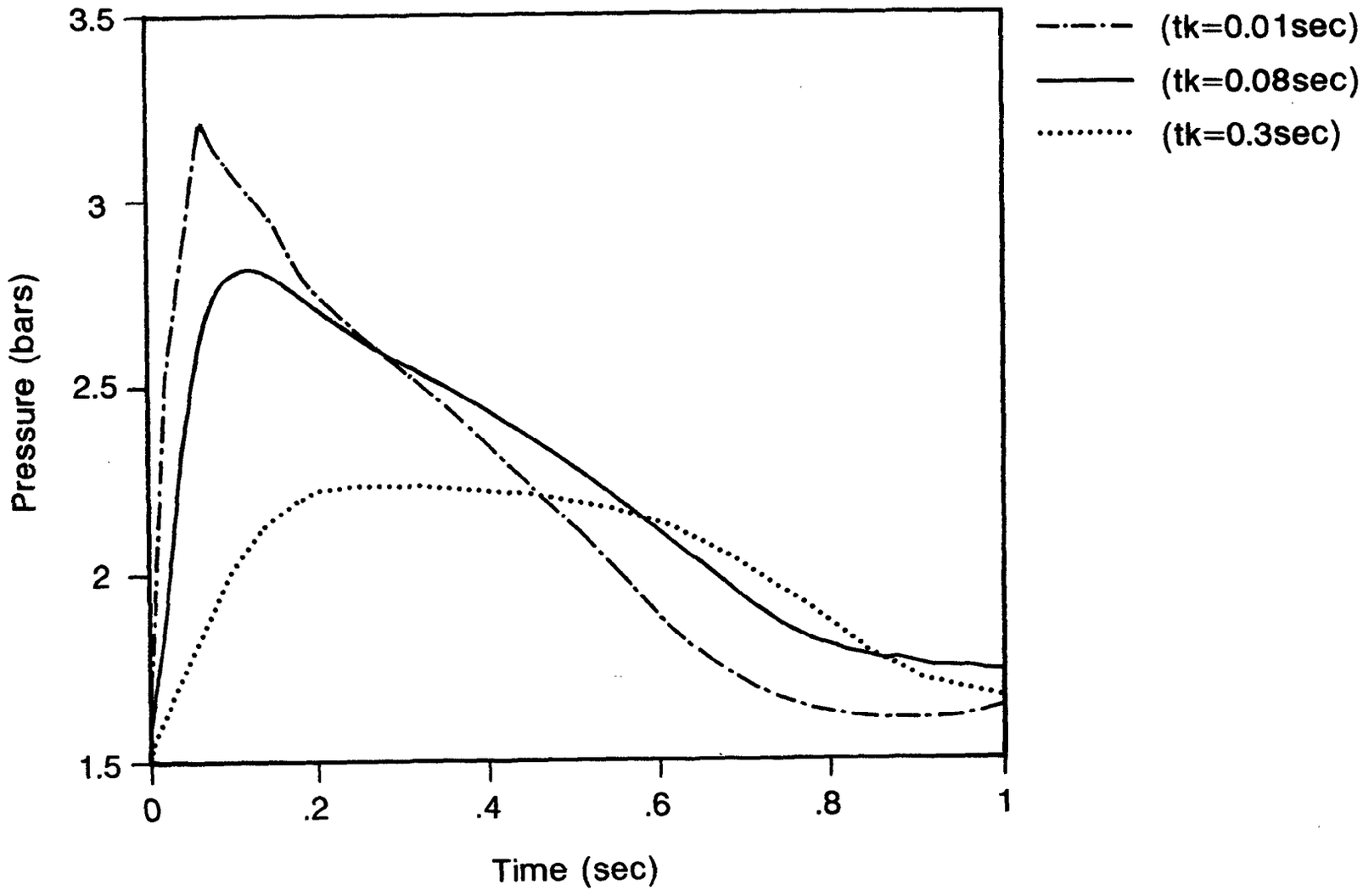

Figure 3: Pressure rise in the moderator vessel for three different assumptions on heat input

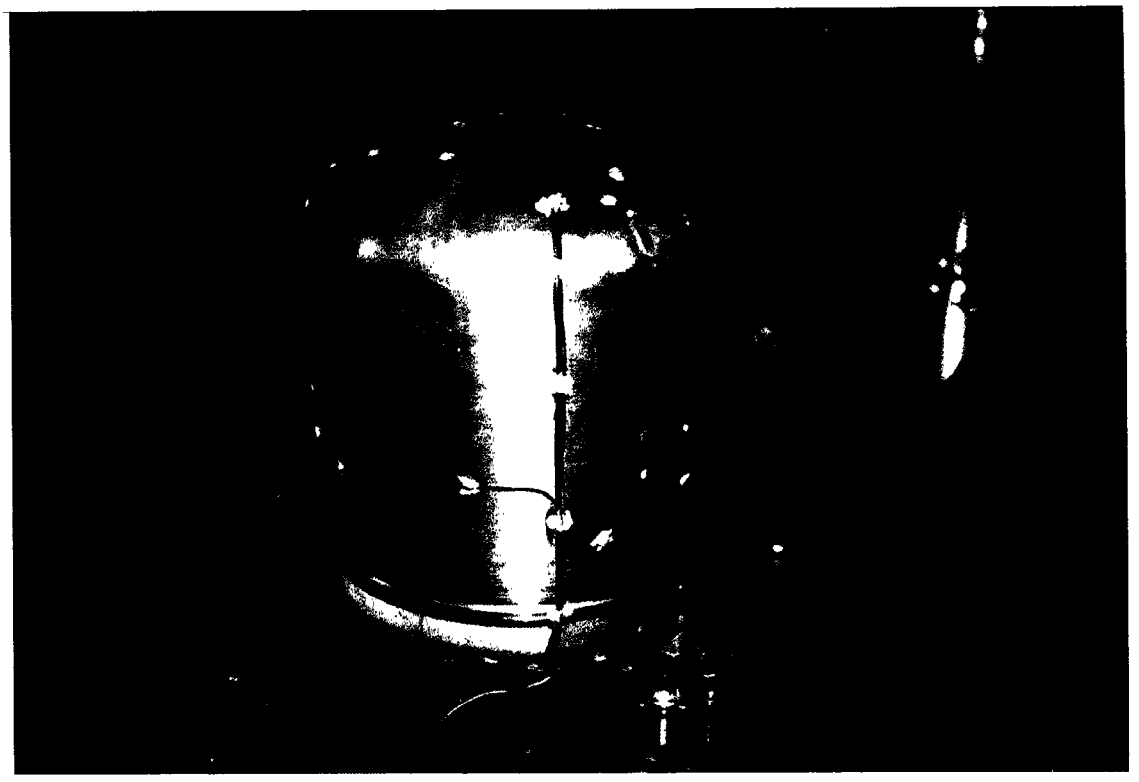

Figure 4: Moderator vessel equipment with strain gauges. Temperature compensation was accomplished by two monitoring positions visible at the lower right.

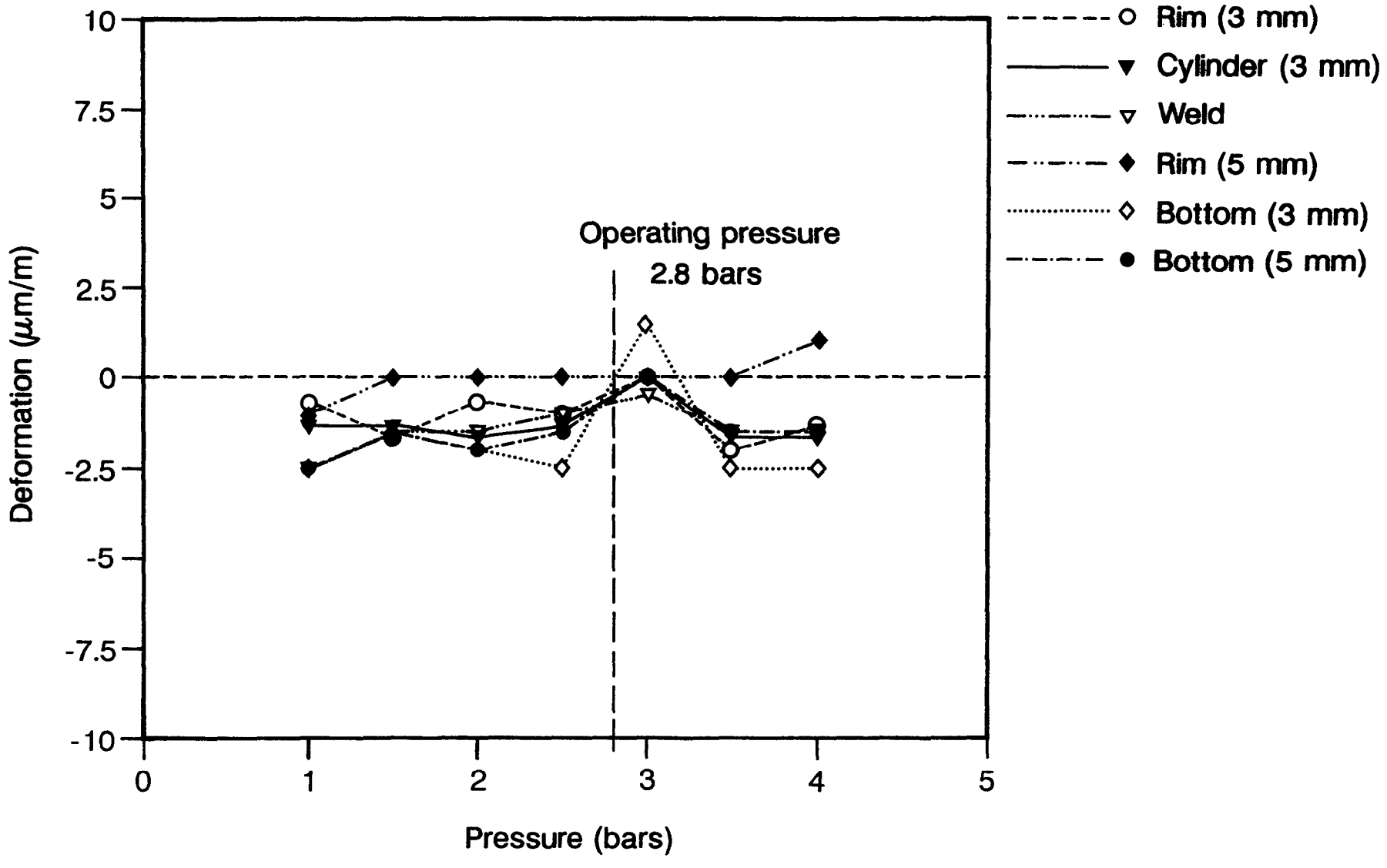

Figure 5: Remaining deformation at various positions of the moderator vessel after pressurizing to different levels and returning to normal pressure at 78K. The precision of the calibration is ±0.2 μm/m

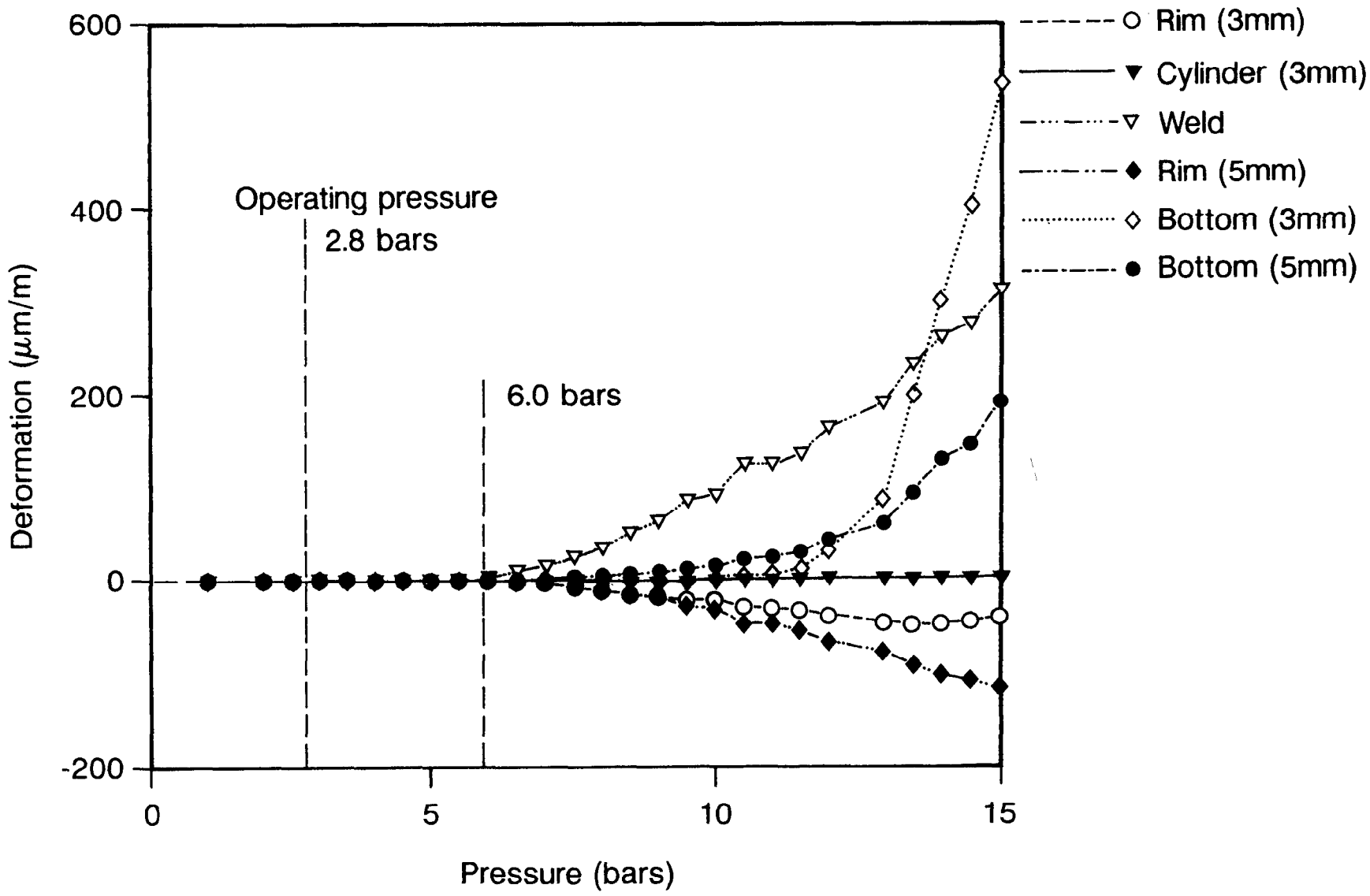

Figure 6: Deformations measured in the room temperature pressure tests. Clearly the limit of elastic deformation is given at around 6 bar by the softening around the weld.

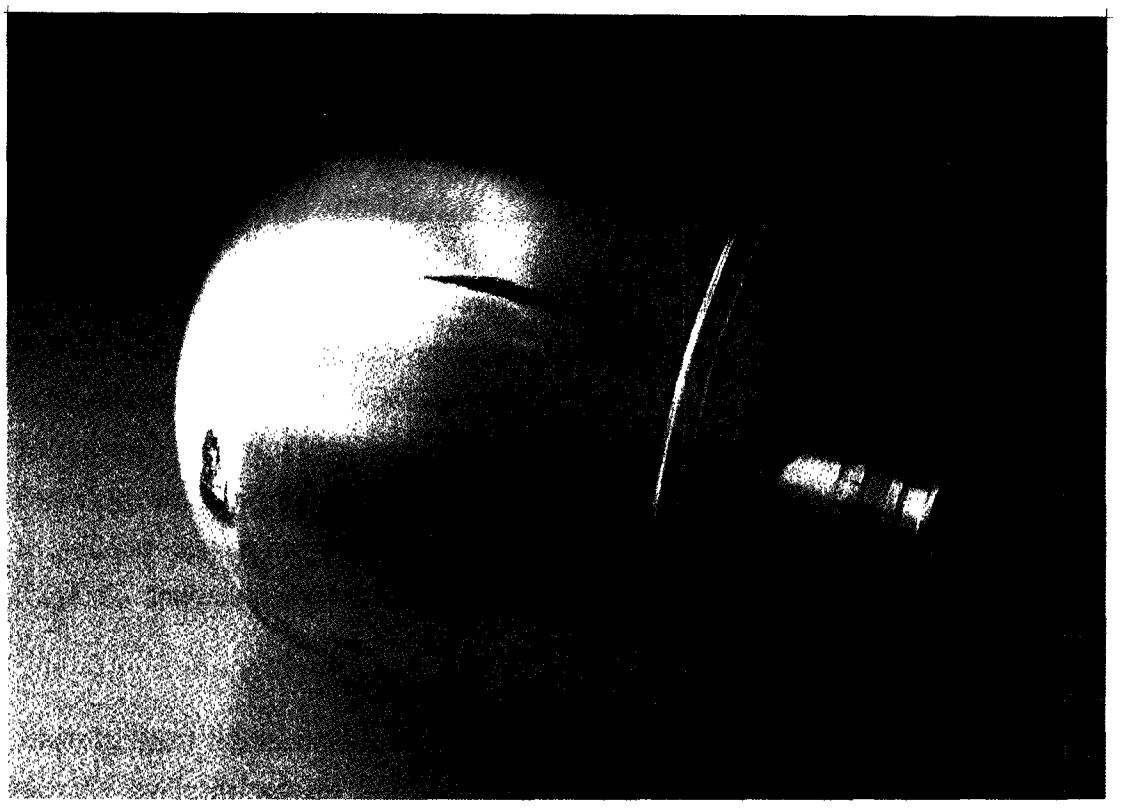

Figure 7: Moderator vessel after rupturing at its cylindrical surface at a pressure around 30 bar. The whole vessel is seen to be plastically deformed (Cylindrical surface as well as the caps).

FIRST EXPERIENCE OF COLD MODERATOR OPERATION AND SOLID METHANE IRRIATION AT THE IBR-2 PULSED REACTOR

A A BELJAKOV, V G ERMILOV, V L LOMIDZE, V V MELICHOV
E P SHABALIN
(Joint Institute of Nuclear Research, Dubna, Russia)

ABSTRACT

A device comprising three solid methane-containing chambers cooled by 15-60K helium was installed near the reactor core of the IBR-2 reactor. Heat deposition due to irradiation was about 0.12 W/gram. That is a few times higher than earlier experienced at ANL and KENS SNS. A number of effects, such as hydrogen production rate, temperature and pressure dependence of hydrogen release, swelling of methane, thermally induced chemical reactions of radicals recombinations ("burps") were carefully investigated.

The main result was that solid methane can be used as a cold moderator material under the strong neutron irradiation conditions that the IBR-2 reactor displays. It can withstand 4-5 days of continuous operation without recharging, if hydrogen is released periodically. The only limitation is decrease of cold neutron intensity.

Additionally, the cold moderator itself was installed at the IBR-2 reactor to test its neutronic performances. The cold neutron intensity gain, compared to the light water grooved type moderator appeared to be a factor of 20-30. That is in agreement with predictions. The solid methane moderator will begin routine operation as soon as it is commissioned.

INTRODUCTION

It is a fact that the solid methane moderator being installed at a pulsed neutron source offers the highest cold neutron flux /1-3/. For SNS the gain factor is considered to be 5-6 if compared with a liquid hydrogen moderator. For the IBR-2, the gain factor is estimated to be as much as 3. But, developing the CH_4-moderator for IBR-2 was a very difficult task due to the high value of fast neutron irradiation that is on the order of 10^{13}n/cm^{2}sec. We could not have overcome the problems of radiolytic hydrogen generation and thermal explosion of radicals if we had not learned from the experience of American and Japanese scientists with sCH_4-moderators.

The IBR-2 CH_4-moderator (abbreviation is CM) was fabricated in 1991-1992; the construction features and predicted performances have been explained at the last ICANS-XI in Tsukuba /4/. Neutron performance of the CM was measured during a short-term testing run in November 1992. In December 1992 - January 1993 the complex programme of investigation of CH_4 resistance of radiation was pursued ("URAM experiments"). Irradiation conditions were consistent with those for the standard operation of the CM.

This paper deals with both the CH_4 irradiation investigations and the short-term test operation of the CM.

TEST RUN OF THE IBR-2 COLD MODERATOR

The CM was installed behind a 75 mm thick, light water premoderator. Methane was condensed and cooled with a cryogenic machine HGU-500 with 500 W of cooling power, before the reactor was started up. Power of the reactor was raised step by step to 1 MW, 50% of nominal power. At each step, the cold neutron flux was measured by four experimental groups. The CM was operated for 5 MW-hours. The gain factors of the CM to the customary light water, grooved - type moderator are in Fig 1. Measured neutron fluxes match the predicted values (see Table 1).

Temperatures inside methane were 16 - 20 K (at 0.5 and 1 MW, respectively). At 2 MW it was expected to be 27K. Radiation heat production in the methane chamber at 1 MW was 180 W, about 50W was due to neutron moderation. The lag time free thermometer, based on neutron spectrum measurement during one period of reactor pulsation, appeared to be the perfect instrument. Neutron spectrum does not fit the Maxwell shape well, but the closest approximation gives 31k.

After the analysis of reliability of the CM operation based on the URAM-experiments results is completed, the CM will be put into permanent operation, presumably, in the Fall of the current year.

Table 1. NEUTRON FLUX FOR CH_4-MODERATOR, IBR-2, 2 MW.

	Predicted, minimum	Experiment
Gain factor, $\lambda \geq 4A$, CH_4H_20 grooved	5	4.7 ± 0.5
Vector flux of the source $\lambda > 4A$, S=300 cm^2	$0.5\ 10^{14}$ n/s/sr	0.34 ± 0.1
Scalar flux on a sample, L=18m	-	$1.8\ 10^6$ n/cm^2/s

URAM-EXPERIMENTS: INSTALLATION & IRRADIATION CONDITIONS

The basic element of the URAM installation is an Al framework (1) cooled with gaseous helium to 25-20K, Fig 2. Two cylindrical cavities (2) are cut inside it, 70mm in diameter and 10 mm thick, to condense methane. A membrane (3) forms the side of each cavity, and is welded into the framework. Its displacement is detected with induction gauges (4). Helium passes through many small channels (5) that are cut to enhance the heat transfer area. The framework is placed inside a vacuum jacket (6). The gaseous methane supply, and extraction of radiolytic hydrogen too, pass through a single access tube connected to a vacuum pump (7) and a pressure bottle (8). When the latter is valved off, gas space in the tube amounts to 2.3 ltr. Temperature of the methane can be controlled with the helium flow rate within a range of 22-60K (as measured in the centre of the solid methane bulk) and detected by two themocouples. All parameters (pressure, position of membranes, temperatures) are recorded in computer files for off-line processing.

Heat production in URAM methane due to fast neutron slowing-down was estimated to be 0.055 W/cm^3. This is based on the spectral density distribution of neutrons measured by using the threshold detectors method. Together with heat production due to γ and β radiation, this adds up to 0.06 W/cm^3 (+10%) and corresponds to the heat

production in the real CM. The calculated temperature difference in the bulk of methane is 10-12K which also corresponds to the gradient in the CM.

Seven runs of CH_4 condensation followed by irradiation were accomplished, with irradiation times ranging from 15 to 95 hours. Irradiation temperatures varied from 22 to 60K (in the centre of methane bulk); minimal temperature was 15K (in the outer area of a sample). During some runs, radiolytic hydrogen release was forced daily by heating methane up to 65-70K.

URAM-EXPERIMENTS: RESULTS & ANALYSIS

Swelling of Methane.

It was planned that a primary task of the URAM-experiments was to observe the swelling of methane due to radiation decomposition, by means of measuring the position of membranes at constant pressure and temperature conditions. However, no significant displacement of membranes that could be attributed to swelling was detected, even after 40% of the methane had been disintegrated as a result of 4-days irradiation. This is not surprising if one considers that the products of CH_4 decomposition are H-saturated hydrocarbons. Therefore, the number of molecules stays almost constant during irradiation. Moreover, it is easy to estimate that the end products occupy space of a lesser volume than the volume of source CH_4 molecules (if radiolytic hydrogen does not form bubbles!). Approximately, the ratio of volumes is (5n+1)/6n, where n is a number of carbon atoms in a daughter hydrocarbon.

Radiolytic Hydrogen: Radiation Yield.

Radiation induced formation of H_2 molecules was estimated by two methods - analysing the rate of pressure increase in the tube at equilibrium at 55K (when production of hydrogen equals to its release from a sample) and by measuring the pressure in a tank during the heating of the methane, at just the moment when hydrogen has already left the methane bulk, but methane has not yet started to vaporise.

Output of radiolytic hydrogen on the first day of each run of irradiation appeared to be about twice as much as afterwards: $(4.8 \pm 0.3)\ 10^{-3}$ mol/mol/ hour against (2.4 ± 0.2). These values are G=6 and 3., respectively, expressed in the conventional unit of "radiation yield", molecules per 100eV. The first value corresponds to the referenced

H_2 output for both gaseous and liquid phases of methane [5]. The second is 20% greater than the H_2 output of solid methane at the LINAC machine moderator in Japan [1] and about twice as much as Dr J Carpenter's value for CH_4 irradiated at 10-15K [3]. Taking into account these two referenced values and the fact that the irradiation temperature oat URAM was higher than 20K (about 25K space-averaged), we should make a conclusion regarding the tendency to H_2 output to decrease at lower temperatures. Probably, this has to do with the two phase transitions in methane at 20K and 12-14K.

Radiolytic Hydrogen: Diffusion in Methane.

One reason that could cause swelling of methane might be a formation of hydrogen bubbles but it became evident from the analysis of H_2 release that the radiolytic hydrogen exists in methane mainly in a solution. Really, a long-term monitoring of gas pressure in the access tube at 55K, 45K, 35K, 25K has showed us that hydrogen continuously releases from the matrix during irradiation; the higher the temperature the faster it passes to the access tube, see fig. 3. Diffusion is rather slow: to reach equilibrium at 55K, it takes about 2.5h. At T<30K the rate of H_2 leakage is too small to be detected. Behaviour of H_2 in the methane matrix at T<60K is consistent with a diffusion mechanism ruled by Arrhenius expression $D=Do\ \exp(T_{act}/T)$ with effective parameters $Do \simeq 0.005$ cm²/sec and $T_{act} \simeq 300K$.

During transients, when methane is heated fast enough, hydrogen, stored in matrix at lower temperatures, releases much faster at T>55-60K - by about two orders of magnitude more than it should if diffusion is ruled by the parameters above. This process takes some minutes, see Fig. 4. During burps, H_2 leaves the methane in seconds. Such a fast diffusion is consistent with penetration of solid methane as in a gas phase, or through cracks. Calculation for a gaseous model gives $D \simeq 0.02$ cm²/sec - just the value needed to explain the hydrogen diffusion at 65-70K. It is interesting to note, that dependence of the diffusion rate on temperature at high temperatures appears to be nearly the same as at low temperature. This was concluded after analysing the dependence on irradiation time of the H_2 fraction released due to a burp, see Fig. 5 (analysis is too difficult to be displayed in the paper). One possible explanation of such behaviour of H_2 is that hydrogen gas travels through cracks, but that the temperature dependence of diffusion is defined by H_2 molecules diffusing inside crystallines.

Radicals: Observation of "Burps" & Analysis.

As it was observed and interpreted by Dr J Carpenter [3, 6], radiation induced radicals, mainly CH_3, can be stored in methane and recombine violently in a spontaneous way or owing to a slight change in the cooling conditions. He called the occurrence "a burp", because an ejection of radiolytic H_2 usually accompanies it. In chemical kinetics, such a phenomenon is called a "thermal explosion". The critical conditions, a relationship between radical concentration, N, temperature, size of a methane slug and cooling rate, have to be fulfilled for a fast reaction of radicals recombination (RRR) can occur. A lot of expressions for the critical condition are known; one is Dr Carpenter's derived for a slug of methane of any shape, cooled from outside and heated inside, but neglecting temperature Laplacian in the heat balance equation:

$$Q_R \cdot T_{act} \cdot K(T) \cdot N^2/(\alpha \cdot T^2) = 1, \qquad (1)$$

where Q_R is an energy of recombination, T_{act} is an activation temperature, K(T) is an Arrhenius factor, $\alpha = q/(T-T_0)$, q is the heat density due to irradiation and T_0 is a coolant temperature.

Another is D A Frank-Kamenetsky's, the classic of chemical kinetics theory [7], derived for a slab slug of thickness "a", with no heat sources, except RRR, at a given periphery temperature, but with Laplacian in the heat balance equation:

$$Q_R \cdot T_{act} \cdot a \cdot K(T) \cdot N^2/(\lambda \cdot T^2) = 0.88, \qquad (2)$$

where λ is a thermal conductivity of methane. Eq. (1) can be transformed into (2), except the right term, when thermal conductivity is poor, and $1/\alpha \simeq a^2/\lambda$.

Unfortunately, none of these could be applied to our case, because the space distribution of temperature, due to the high density of energy release, was too steep to neglect. It causes the T value needed for Eq. (1) or (2) to remain unknown. Therefore, nothing could be derived except a single conclusion that "at a constant irradiation temperature T>20K the critical conditions for spontaneous development of a burp are not satisfied, however long the irradiation proceeds". This was confirmed in the URAM experiments. But, it appeared that fast RRR can be ignited by increasing helium temperature after methane had been irradiated for more than 4 hours at T<28-29K. The temperature rise needed to ignate a burp was 3-5K. Some pictures of burps are in Fig 6 and 7.

Sixteen pairs (in both chambers) of burps were detected. For two them, the maximum methane temperature reached about 90K at outlying parts of a bulk. The burp data gave us an opportunity to estimate a rate of radical recombination energy accumulation - (140 ± 20) J/mol CH_4 per hour, or (2 ± 0.4)% of an absorbed dose rate. This value is consistent with Carpenter's value. Considering that CH_3 radicals are relevant to a RRR process, the rate of their production is $R \simeq (0.84 \pm 0.12)\ 10^{-3}$m/m per hour, or (1.3 ± 0.2) 10^{-7} mol/J - one-third as much as the H_2 production rate.

Another value that can be estimated from the burp data is an activation energy (we will use it in terms of temperature), the parameter in the Arrhenius law for RRR. By a theory, $N \alpha \exp(-T_{act}/nT)$ at saturation, where n is the power law of the reaction. Then, an energy yield in a burp, Q, and irradiation temperature T should satisfy an expression:

$$\ln Q = T_{act}/nT) + \text{const.}$$

Actually we have used an expression:

$$\ln Q_1/Q_2 = T_{act}/nT_1 \cdot T_2 \cdot (T_2 - T_1) + \text{const}, \qquad (3)$$

for pairs of burps occurred simultaneously in both methane cavities - 1 and 2, because variation of irradiation temperature in time vigorously affects the saturation concentration of radicals. It allowed us to avoid the effect of temperature variation.

Expression (3) was confirmed, see fig 8, for the burps with irradiation time more than 7h. The activation temperature value appeared to be (290 ±30)K, if one takes n=2. This value is twice J. Carpenter's T=155K estimated from two burps observed. This discrepancy is not surprising. But we derived a surprise conclusion from the analysis of the temperature behaviour at the leading edges of burps: the drastic temperature rise, up to 15K/sec could not be understood if T_{act} = 300K or 150K. Calculations based on the classical model of thermal explosion give T_{act}>700K for n=2 or even more, if n>2. There are two ways to explain this clumsy situation.

1. Different chemical reactions are responsible for fast RRR during a burp ("hot reaction") and for recombination of radicals at lower temperatures during storing ("cold reaction"). So, Arrhenius factors K_{cold} and K_{hot}, that

are consistent to these mechanisms of RRR, should satisfy the conditions: $K_{cold} > K_{hot}$ at 25K but $K_{cold} << K_{hot}$ at T>30K

2. Fast RRR has a nature other than thermal explosion, maybe, of a chain reaction.

This conclusion is, in fact, rather of a theoretical than practical interest. On the contrary, the dependence on irradiation time of H_2 fraction, released after a burp, (see in fig 5), is of importance for practice. It allowed us to decide how fast annealing of radicals should be repeated to prevent damage of the CM moderator in a casual H_2 release. Now we estimate that it has to be done 3 times a day.

Finally, some information about the rates of "cold" RRR, if it obeys a 2-power reaction:

the rate of RRR at 26K $K_{cold} = Ko \exp(-300/T) \simeq (37 \pm 8)$ mol/mol per hour;
the same at 20K $K_{cold} \simeq (1.3 \pm 0.4.)$ mol/mol per hour;

$Ko \simeq 10^6 - 10^7$ m/m/hour. For comparison, Ko for gaseous phase of CH_3 is equal to $1.7.10^3$ m/m/h.

The time constant for relaxation of the density of radicals to its equilibrium value $\tau = 5.7$ hours for 26K and 30 hours for 20K.

REFERENCES:

1. Inoue K. Nucl. Instr. & Meth., 1983, v.216, N3, p. 537-540.

2. Carpenter J M et al. Proc. of the 8th Meeting of ICANS Oct 8-12 1985. RAL-85-110, v.I, p. 311-318.

3. Carpenter J M Proc. of Int. Conf. on Cold Neutron Sources, LANSCE, Los-Alamos, 1990, March 5-8. LA-12146-C, P. 131-156.

4. Shabalin E P Proc. of the 11th Meeting of ICANS, KEK, Tsukuba, Oct 22-26, 1990. KEK-90-25 v.I, p. 109-118.

5. S Ya Pshezhetsky. Mechanisms & Kinetics of Radiation Induced Chemical Reactions (in Russian). Moscow, "Chimiya", 1968.

6. Carpenter J M. Nature, v.330, p 358, 1987.

7. F Bowden, A Yoffe. Fast Reactions in Solids. London, 1958.

Fig. 1. Neutron flux of the CH4 cold moderator at IBR-2 compared with that of the light water, room temperature moderator (measured at four neutron beams.

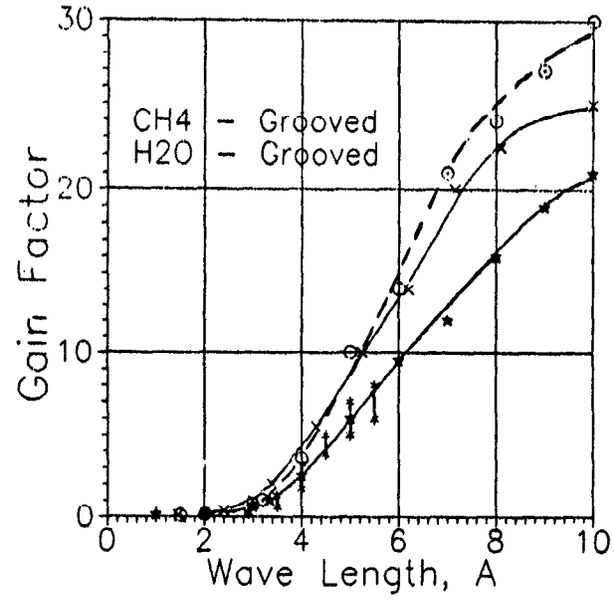

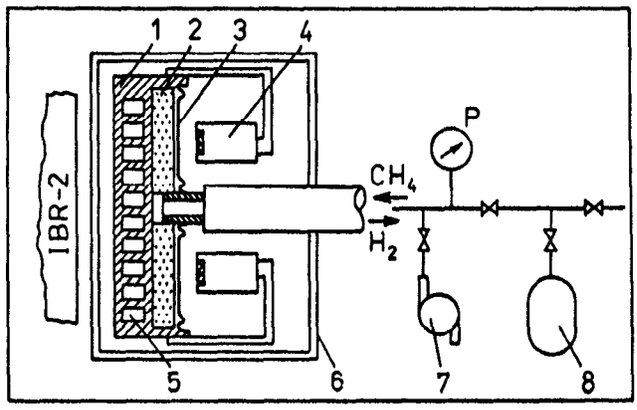

Fig. 2. The sketch of the URAM facility (for comments see the text)

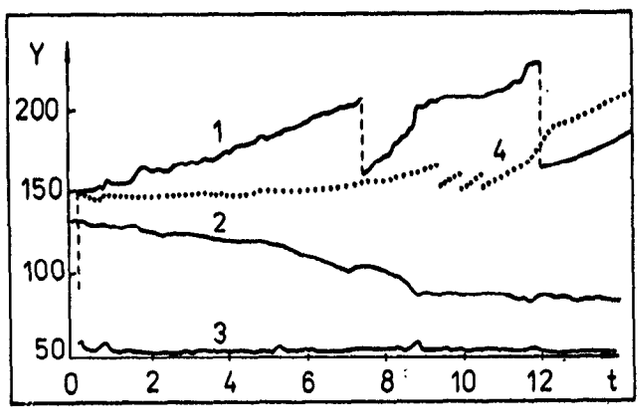

Fig. 3. The diagram of hydrogen release during irradiation.
1- pressure in the tube at t=55k; 2- displacement of the membrane; 3- methane temperature,K; 4- pressure in the tube at T=45K. Time scale: hours

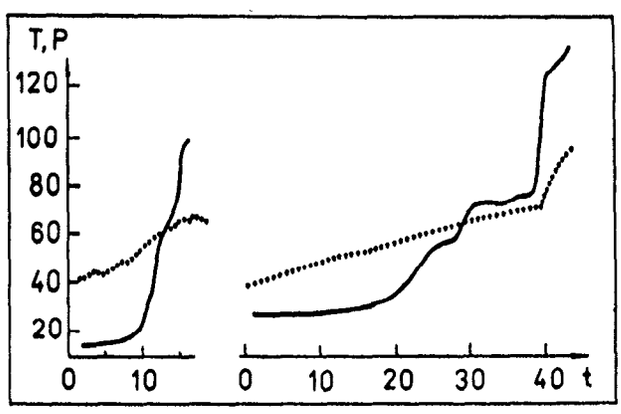

Fig. 4. The diagrams of hydrogen release during heating the methane.
Solid lines are pressure in the tube; dotted - temperature of methane.
Time scale: minutes

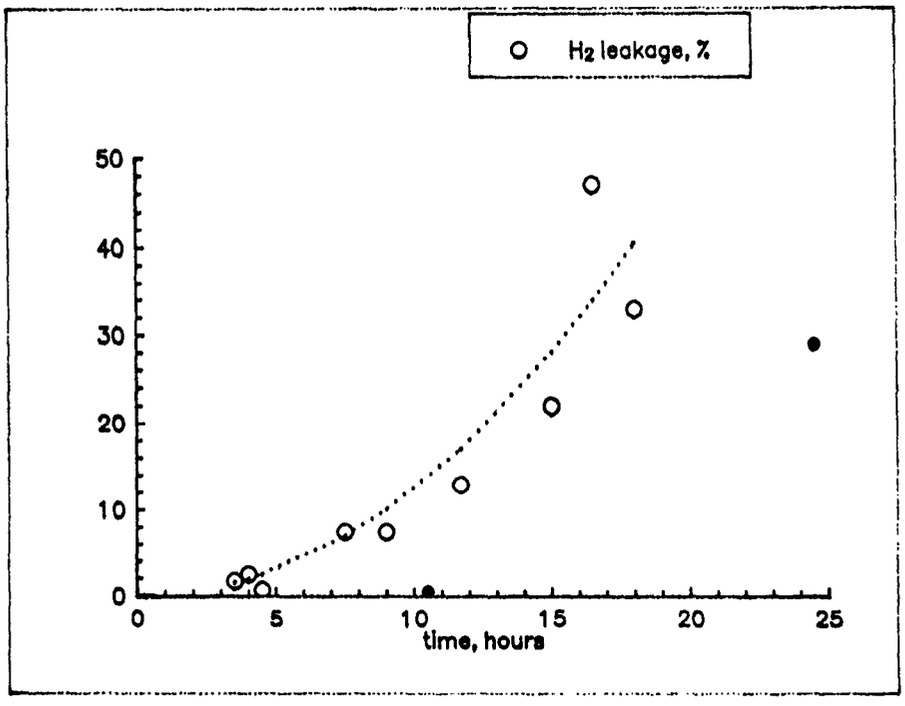

Fig. 5. Hydrogen fraction released after burps.

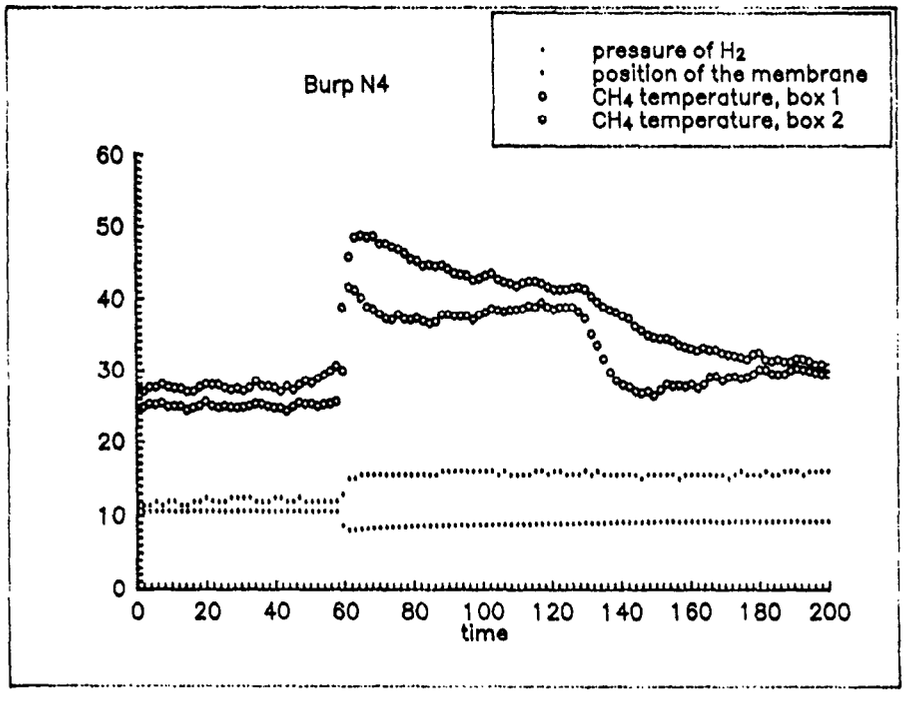

Fig. 6. Time diagram of methane parameters during the burp. Time scale is in seconds, temerature - K degress, pressure - mbars.

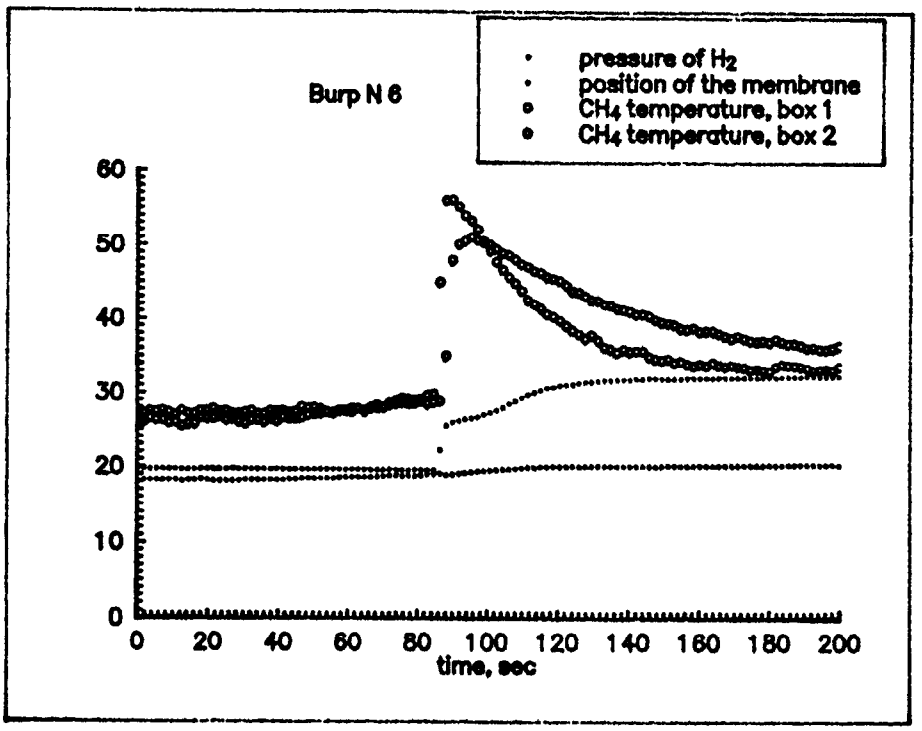

Fig.7. Time diagram of methane parameters during the burp.
Time scale is in seconds, temperature - K degrees, pressure - mbars.

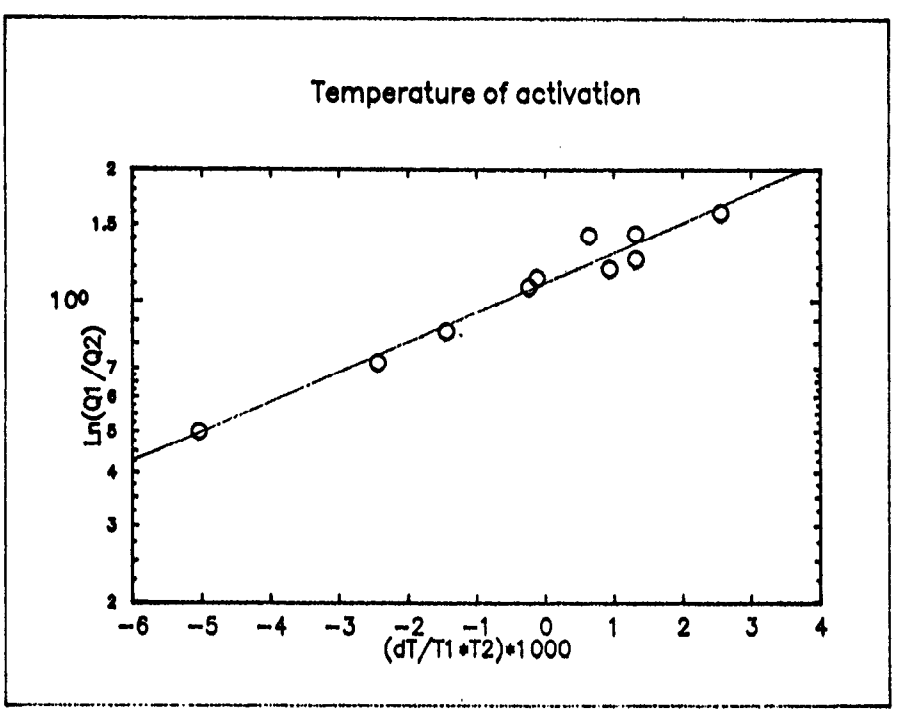

Fig. 8. The diagram for activation temperature estimation from the dependence of a burp energy on irradiation temperature (see text for more comments.

THE ISIS METHANE MODERATOR

T A Broome, J R Hogston M Holding and W S Howells
Rutherford Appleton Laboratory

1. INTRODUCTION.

A liquid Methane moderator has been in use on ISIS since start-up. This paper reviews the operation of the three moderators which have been used and describes the steps which have been taken to deal with the radiation damage to the Methane. The results of the post irradiation examination of the first moderator are described.

The Methane moderator is one of the prime moderators on ISIS. Its location on the target moderator and reflector assembly is shown in figure 1. The moderator consists of an aluminium alloy can with a volume of about 0.5 litres. The first two moderators had a Gadolinium poison foil 0.05 mm thick positioned centrally through the vessel shown in figure 2. This gives pulse widths in the slowing down region of, typically, 35 μs.

2. EXAMINATION OF MODERATOR NUMBER 1

In December 1991 after 4 years of operation at steadily increasing operating current the first moderator blocked.

From outset of ISIS operations there was clear evidence, as expected, of radiation damage to the Methane. When components of the circuit such as filters and circulators were removed for servicing they were found to be wet with 'oil'. Analysis of the oil showed it to be a mixture of hydrocarbons. The viscosity of the oil recovered from the circuit steadily increased with increasing irradiation. In the original design the cryogenic system was emptied by removing the pressure and allowing the Methane to boil off. It was recognised that this would result in the non volatile hydrocarbons remaining in the circuit. However, there was insufficient data available on their production rates to make a reliable estimate of the quantities of hydrocarbon which would be produced.

The neutronic performance of the moderator had shown a steady deterioration from mid 1989 as shown in figure 3. In December 1990 the pressure drop across the moderator became sufficiently large the flow rate of liquid Methane was insufficient to maintain cooling. The system was flushed with Methyl Ethyl Ketone. While a substantial amount of oil was removed the blockage was not cleared and the decision was taken to replace the moderator.

By the time of failure the moderator had been operated for 5 years during which time the integrated number of protons on target was 978 mAh. This had been at two proton energies and both Uranium and Tantalum targets had been used. The irradiation data is summarised in Table 1.

Proton energy	Uranium target	Tantalum Target
550 MeV	22.6	0
750 MeV	628.1	327.5

Table 1. The Irradiation History of Methane Moderator Number 1

The measured neutron flux from the moderator when operating with a Uranium target is two times that with a Tantalum target. Scaling also for effect of proton energy the effective dose to the moderator is calculated to be equivalent to 747 mAh of 800 MeV protons with a Uranium target.

The moderator was dismantled in the remote handling facilities of the Harwell Laboratory of AEA Technology. Figure 4 shows the cuts made through the moderator assembly. The condition of the moderator is shown in figure 5. The can was almost completely full of a solid black substance with some patches of brown discoloration. This deposit was restricted to the moderator can itself. The transfer lines and pipework feeding the moderator was found to be clean. The flushing with Methyl Ethyl Ketone had clearly been successful in cleaning all but the moderator can.

The composition of the deposit was examined by mounting a sample in the LAD spectrometer at ISIS. The structure factor S(Q) shows amorphous features with no Bragg peaks (Figure 6). The pattern is very similar to that of amorphous carbon hydrogen alloys produced by decomposition of hydrocarbon gases which had been a programme of study on LAD. From the shape and variation of S(Q) with scattering angle it can be deduced that there is still considerable hydrogen content.

3. THE LIQUID REPLACEMENT SYSTEM.

It was clear during 1989 that the lifetime of the Methane moderator could well be limited by the effects of radiation damage. Several options to deal with this problem were considered. These included improved filtering to remove the hydrocarbons which are solid at the normal operating temperature and various kinds of phase separators. Finally the decision was taken to redesign the cryogenic system to allow on line replacement of the irradiated methane with fresh liquid.

The assumption made was that the formation of high mass hydrocarbons was a many stage process and could be limited by removal of the damage products at an early stage. For the scheme to work required that the damage products were carried in the liquid flow.

Figure 7 shows a schematic of the new system. A condenser was added to the original circuit, cooled by the main liquid flow, to provide the fresh liquid Methane. Valves were added to make it possible to interrupt the main cooling loop and introduce the fresh liquid Methane which displaces the irradiated Methane into a dump tank. The main cooling loop is then reinstated. The irradiated liquid is then allowed to boil off and any residue can be collected from the dump tank.

The design and installation of this system were in progress when the first moderator blocked. Regular liquid replacement did not start until November 1991.

The system has worked as designed and considerable quantities of 'oil' have been collected from the dump tank. Between 100 ml and 200 ml is not uncommon after a 30 day run of ISIS.

4. THE SECOND MODERATOR.

The second moderator became operational in May 1991. Figure 8 shows the pressure drop across the moderator for the subsequent operational periods. As can be seen the pressure drop had risen significantly by the time routine liquid replacement started.

The moderator blocked early in 1993 after 814 mAh of 800 MeV protons. As with the first moderator the running was split between Uranium targets (335 mAh) and Tantalum (479 mAh) targets. This was equivalent to 575 mAh of 800 MeV protons on a Uranium target which was somewhat less than the integrated beam current on the first moderator when it blocked.

The lifetime of the second moderator was disappointing. There are several comments which can be made.

- The build-up of solid hydrocarbons in the moderator during the first year of operation may have been sufficiently well advanced that the use of the liquid replacement system was ineffective.

- Hydrocarbons form and stick to the surfaces of the moderator and a layer builds up, progressively, unaffected by the liquid flow and gradually blocking the moderator.

- The formation of insoluble, solid deposits is a direct process again building up to form a blockage.

At present there is insufficient evidence to provide a clear understanding of the phenomena involved.

5. PROSPECTS FOR THE FUTURE.

A third moderator was fitted in 1993. This has two poison foils designed to produce pulse widths of about 25 μs. In operation the pulse width turned out to be 18 μs but the resulting penalty in neutron flux has proved to be unacceptable. This moderator will be replaced late in 1993 by a single poison foil moderator with the same design as the first two.

The double poison foil moderator will be dismantled after it has been removed and should provide valuable information. The liquid replacement system will have been used from the outset. The intention is to replace the liquid at least once per week. The

condition of the moderator will then indicate the effectiveness of this technique in inhibiting the blockage of the moderator.

If there has been a significant build-up of deposits in the moderator and from this point of view liquid replacement is ineffective there seem to be only two options. The first is to perform some tests to determine whether regular flushing with a solvent will clean the moderator before the deposits are converted to insoluble compounds. The second is simply to replace the moderator regularly. On the basis of the lifetime of the first two moderators this would require annual replacement which, while undesirable from the point of view of scheduling and cost, is not impractical. Investigations are continuing into chemical methods to limit the production of the higher mass hydrocarbons but the initial advice received is not encouraging.

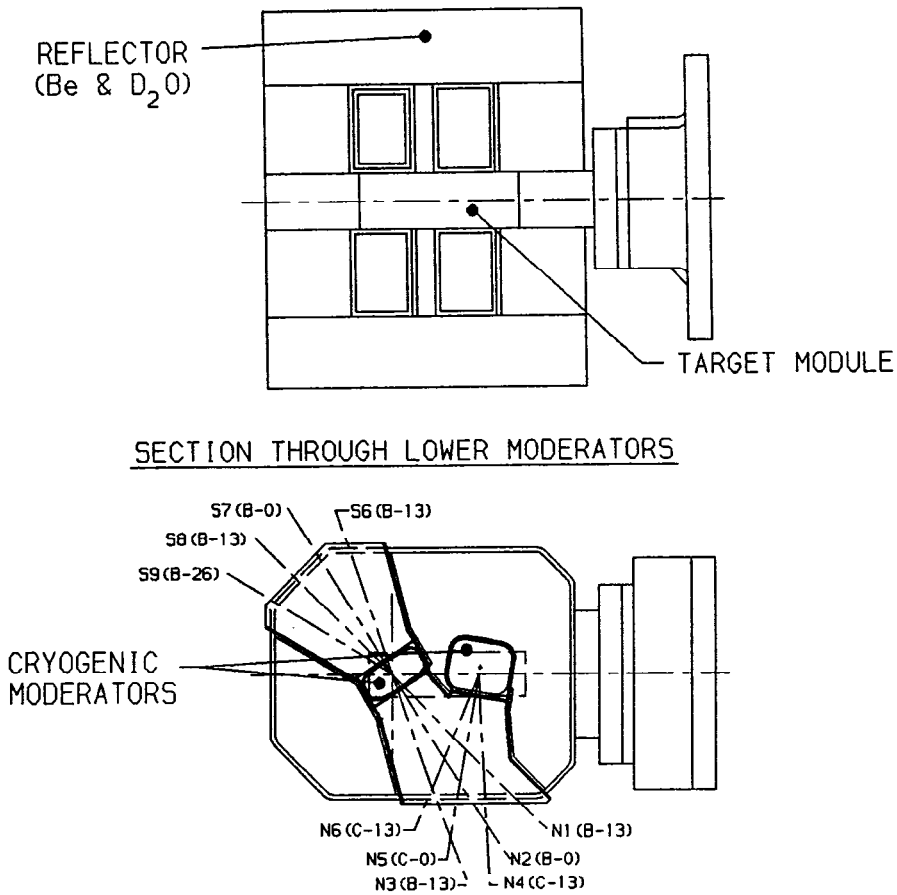

Figure 1. The ISIS Target Moderator Reflector Assembly

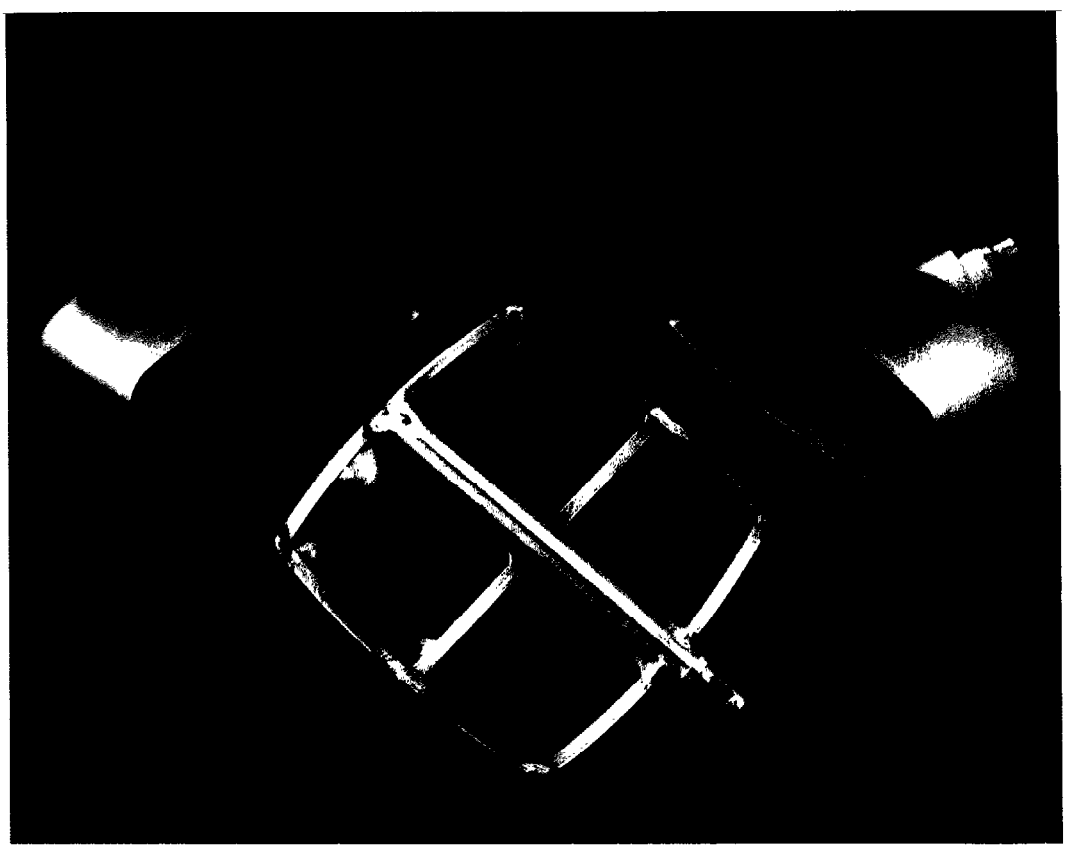

Figure 2. The Construction of the First Methane Moderator

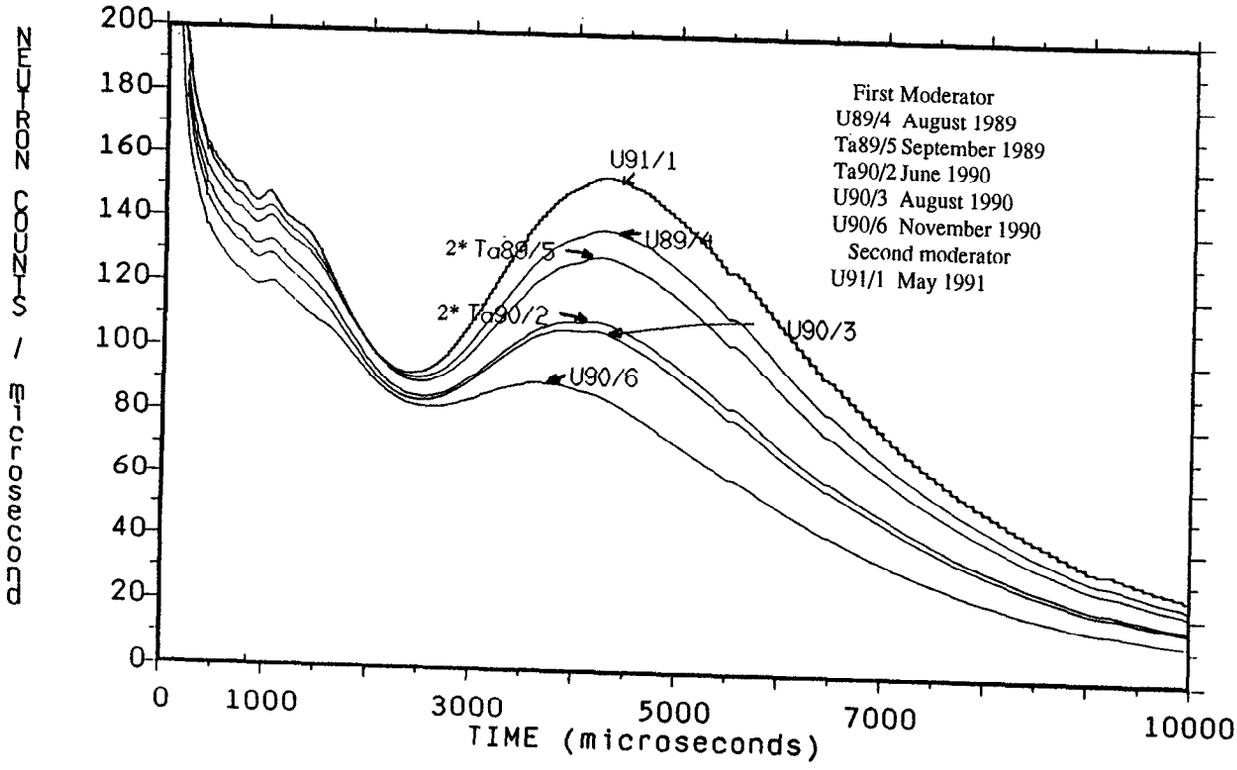

Figure 3. The Deterioration of the Moderator Performance with Time.

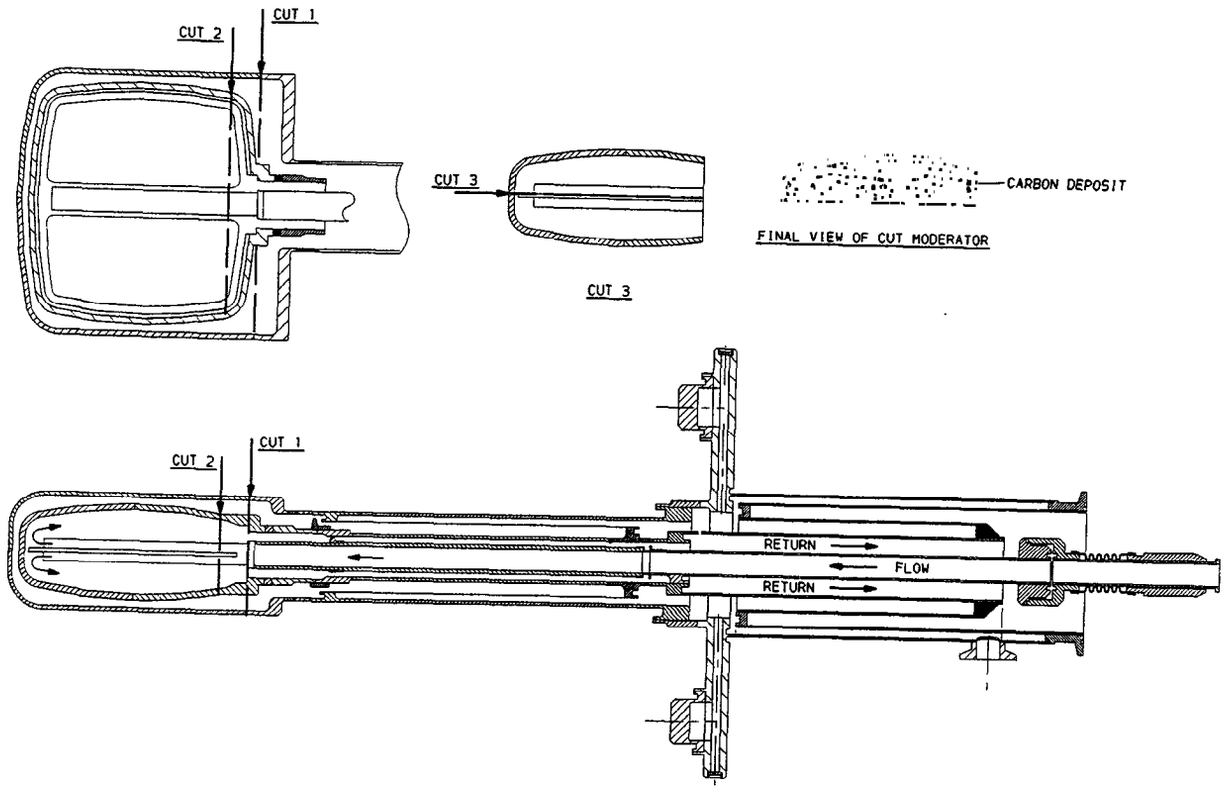

Figure 4. The First Moderator Showing the Position of the Cuts Made to Dismantle it.

Figure 5. The Build Up of Solid Deposits in the First Moderator.

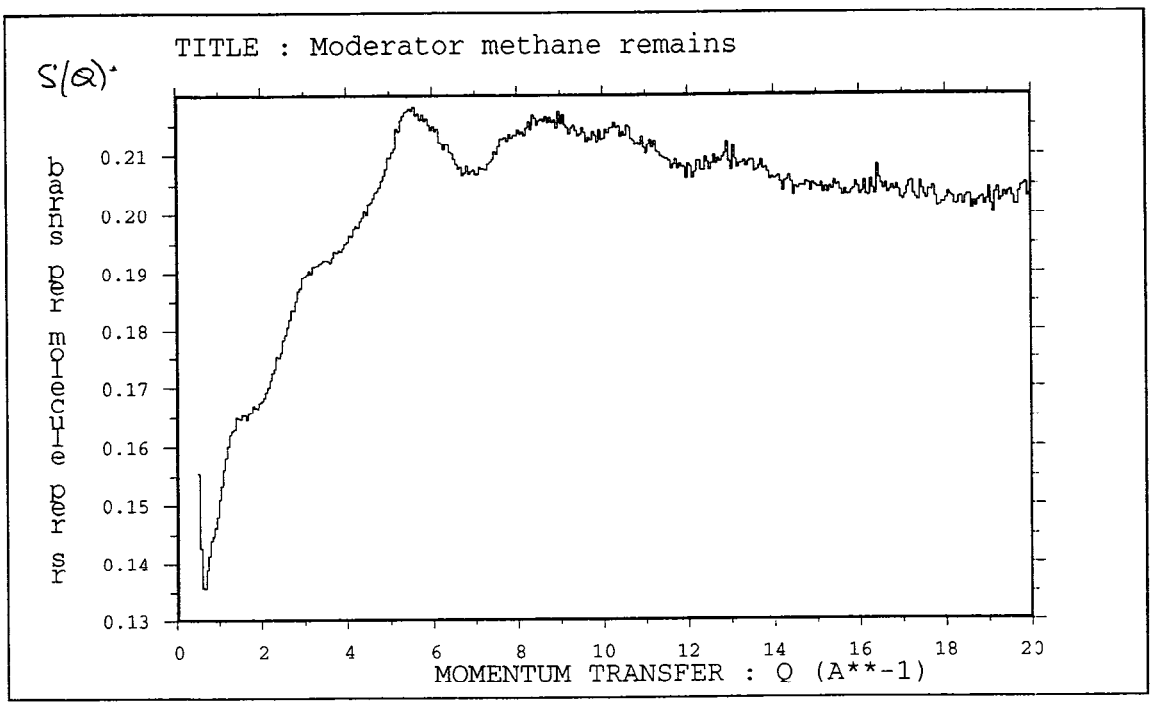

Figure 6. The S(Q) measured on the LAD Spectrometer for a Sample of the Solid Deposit from the First Moderator.

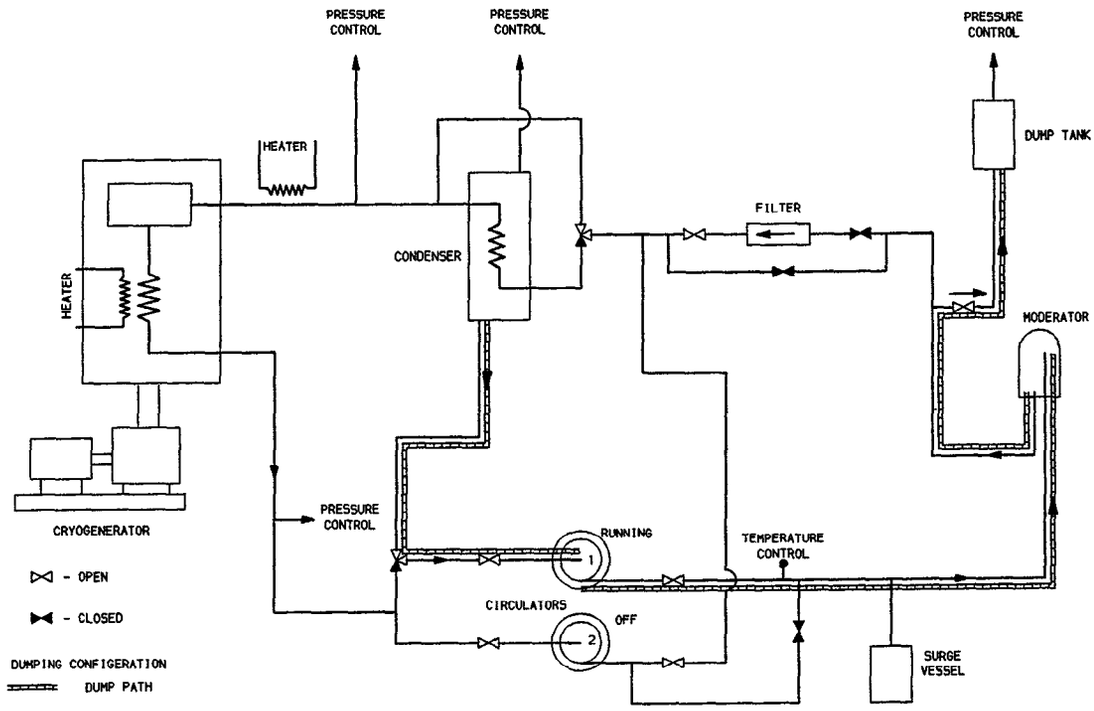

Figure 7. The Cryogenic Circuit for Liquid Replacement

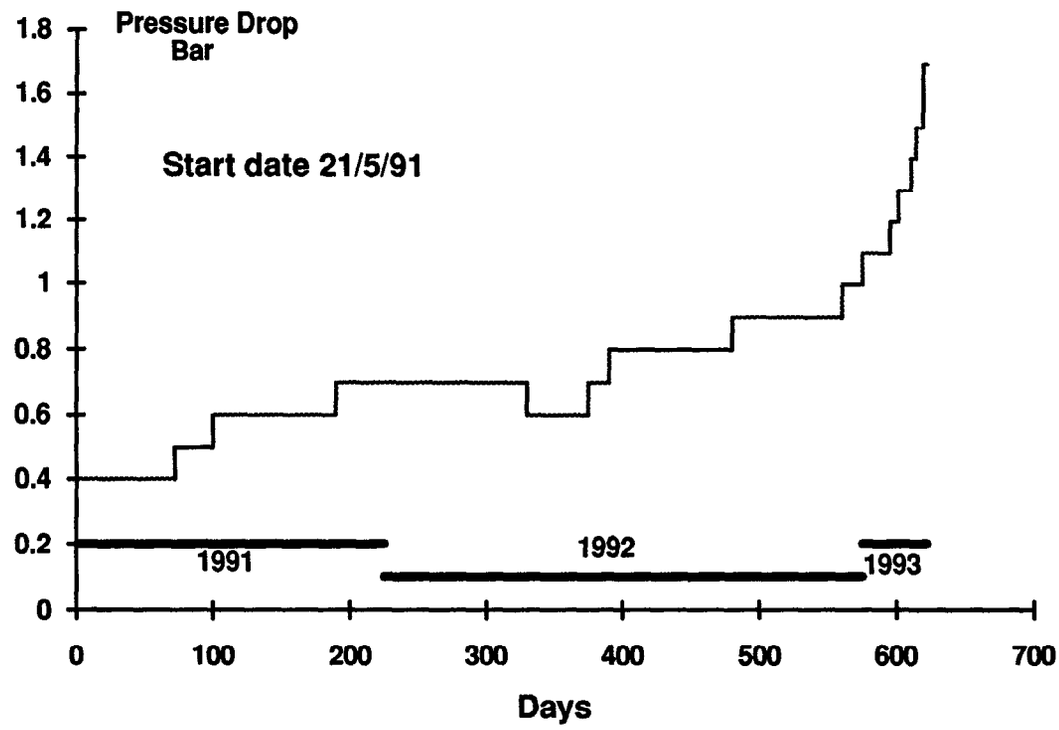

Figure 8. The Pressure drop Accross the Second Moderator as a Function of Time.

Tailoring Intensities and Pulse Shapes in Coupled Moderator-Reflector Systems

J. M. Carpenter[a], Y. Kiyanagi[b], N. Watanabe[c], H. Iwasa[b] and M. Nakajima[b]

[a] Argonne National Laboratory, Argonne, Illinois and Visiting Scientist, National Laboratory for High Energy Physics, Tsukuba, Japan.
[b]Department of Nuclear Engineering, Hokkaido University, Sapporo, Japan.
[c]National Laboratory for High Energy Physics, Tsukuba, Japan.

Abstract

In this paper we introduce an idea for controlling the trading off of intensity and pulse width in coupled moderator-reflector systems by heterogeneously poisoning the reflector, with particular application for cold moderators. We describe measurements which illustrate the effect, performed at the Hokkaido Linac neutron source. The principle may be useful for varying on-line the performance of coupled moderator-reflector systems.

Introduction

Coupled moderator-reflector systems, in which neutrons pass freely back and forth between the hydrogenous principal moderator and the surrounding reflector provide higher time-average neutron beam intensities but have longer pulse widths than decoupled moderators in pulsed neutron sources. The concept has been recognized for some time (Bauer, et al[1)], Kiyanagi, et al[2)]) but has not yet been applied in an operating facility. In general, such systems would be useful for purposes that need cold neutrons but do not require precise time resolution, such as small angle scattering, or for instruments requiring "quasi-steady" beams. In these systems, the cold moderator may be of liquid Hydrogen, which is suitable for use in high intensity facilities. Neutrons from the reflector entering the moderator at long times are thermal neutrons equilibrated in the ambient-temperature reflector, rethermalize in the cold moderator and contribute to the neutron flux emerging from the viewed surface of the moderator. The lifetime of the thermal neutrons in the reflector is typically quite long, several hundreds of microseconds up to milliseconds, which is the reason for decoupling in the more conventional cases where it is desired to maintain short pulses. The central idea here is to vary the lifetime (and the spatial distribution) of the neutron distribution in the reflector, thus to vary the duration and consequently the time-integrated intensity of the neutron pulse emerging from the cold moderator.

Our study is by no means complete and has been constrained by practical requirements to contain certain features recognizably undesirable and unnecessary in potential practical applications, but successfully demonstrates the principle. Here, we describe our measurements and report the resulting time-average neutron spectra and the pulse widths and decay times of the beam from a liquid Hydrogen moderator. We conjecture how the principle might be applied to provide pulsed beams whose width and intensity could be varied from time to time without requiring disassembly and reassembly of the moderator-reflector system, and make some general observations.

Experimental Arrangements

The Hokkaido University electron linac provided a pulsed fast neutron source for the measurements, operating at approximately 50 Hz, with .3 μA time average current and 20 nsec pulse width for energy spectrum measurements and at 30 μA current and 3 μsec pulse width for pulse shape measurements. The target was a water-cooled lead block. Figure 1 shows the moderator-reflector assembly, which consisted of a graphite reflector approximately $1 \times 1 \times 1$ m^3 in volume, a $2 \times 12 \times 12$ cm^3 18 K liquid Hydrogen moderator with a 2 cm thick polyethylene premoderator (the setup remained from another series of measurements performed in the same interval, not a necessary feature of the principle under study here). Cadmium apertures defined the 10x10 cm^2 viewed area of the moderator. No absorbing liner was present in the beam path void. The electron beam struck the target in the direction perpendicular to the plane of the figure.

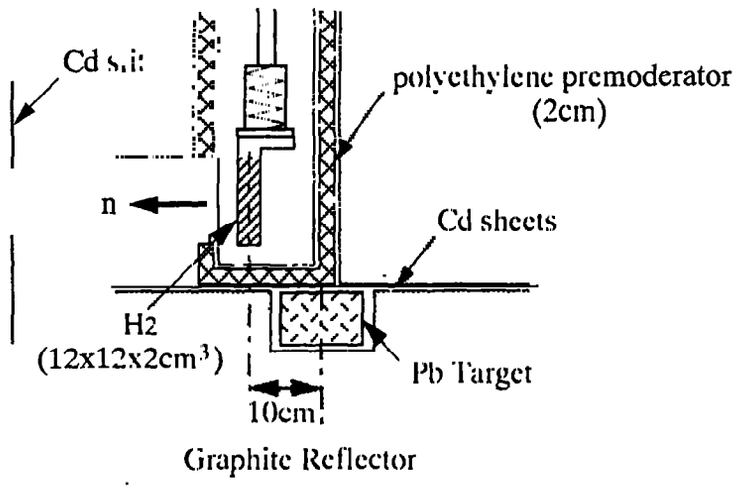

Figure 1 Coupled Liquid Hydrogen moderator with 2 cm ambient-temperature polyethylene premoderator. The present experiment was performed with and without the Cadmium sheets.

Figure 2 shows the flight path and detector systems. The flight path length between the moderator and the detector for spectrum measurements was 5.6 meters. The detector was a 1-inch diameter, 10 atmosphere ^3He counter with 6 inch active length. Cadmium apertures at the ends of the evacuated flight tube defined the neutron beam. Time channels were 40 μsec long.

For pulse shape measurements, the analyzer system consisted of a 5 mm thick mica crystal stack oriented at a Bragg angle of 85°. A Soller collimator of 30' divergence defined the beam incident on the crystal. A 1.6 mm wide aperture defined the opening in front of the detector, which was the same ^3He counter. The total flight path length for the pulse shape measurements was 6.6 meters. The time resolution of the analyzer system was approximately 0.1 %. Time channels were 5 μsec long for the pulse shape measurements.

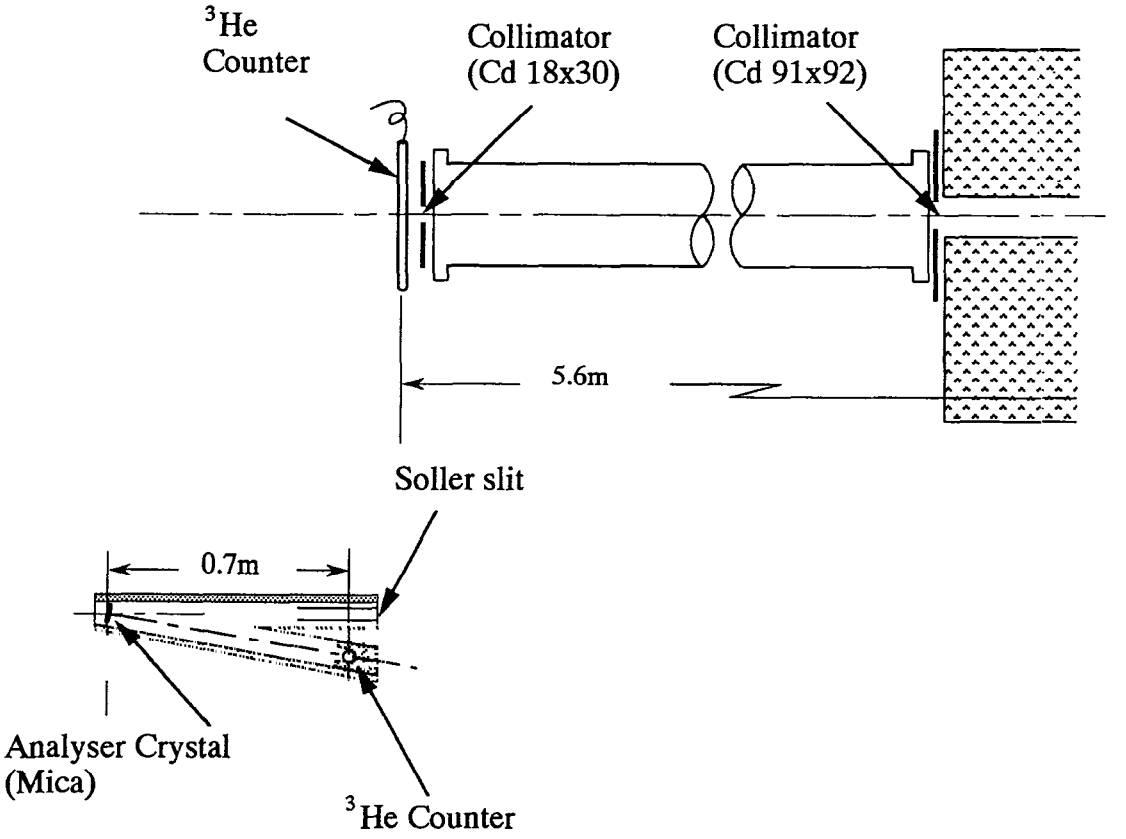

Figure 2. Detector arrangements for the spectrum measurements (upper figure) and for the pulse shape measurements (lower figure).

Spectra

Figure 3 shows the similarly-normalized time-of-flight counting rate distributions measured with and without Cadmium poisoning sheets in the reflector, and the ratio of the counting rate without to the rate with the Cadmium. Notable features are the epithermal components, which approach each other at short times, where their ratio is close to unity. The peaks at about 1.5 Å wavelength represent thermal neutrons from the ambient temperature premoderator. The peaks around 3 Å are due to the discontinuity in the H_2 scattering cross section. The hump at about 6 Å wavelength (difficult to discern) represents the rollover of the cold neutron spectrum from liquid Hydrogen, which is not a good Maxwellian as is well known. We conclude from these spectra as well as from the pulse shape measurements described below, that a significant number of neutrons from the premoderator behind the liquid Hydrogen, either penetrate the Hydrogen or are transmitted with only a few elastic scattering collisions, to emerge from the viewed surface. The ratio of intensities is about a factor of 1.4 for longer wavelength neutrons.

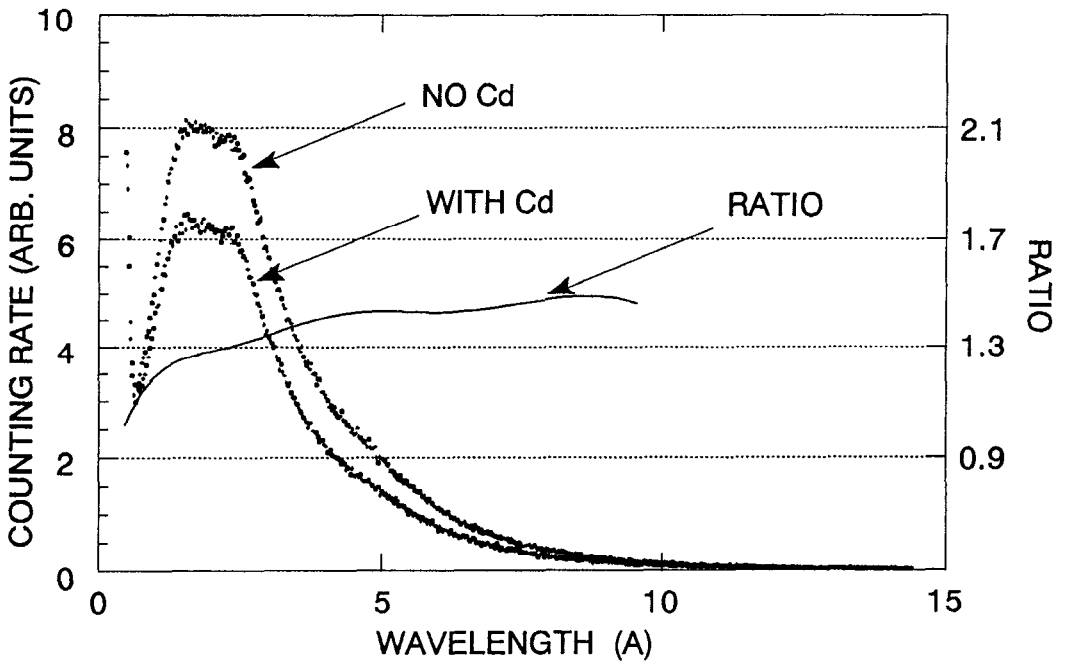

Figure 3. Counting rate per unit time-of-flight (arbitrary scale, same normalization) as a function of neutron wavelength for poisoned (lower curve) and unpoisoned (upper curve) reflector, and the ratio.

For the pulse shape measurements, the analyzer crystal reflects into the detector just those neutrons that satisfy the Bragg condition, $\lambda = 2d_{(00n)} \sin \vartheta_B$, which have separated in time as they have traveled the flight path. The time resolution of the analyzer system is sufficiently good that the shape of the emission time distribution is preserved when the neutrons arrive at the detector. We recorded the counting rate as a function of time over a interval which included the peaks due to neutrons reflected in all orders down to (004) of mica (d ~10.0 Å.) The highest order observed was (0038), above which the reflected intensity becomes small because of the rapidly-decreasing Debye-Waller factor. Vestiges of the (002) reflection can be seen in the data between the (004) and (006) peaks, where it overlaps from the previous frame.

First, we discuss the double peaks that we observed, although this is not the main point of our paper. Figure 4 shows the peaks (0018) to (0036) (λ = 1.11 ~ 2.22 Å) for the case without Cadmium in the reflector, and for reference, for another case with the same experimental arrangement, but decoupled and without premoderator, which provides short pulses from the Hydrogen only. Arrows (located by eye) indicate the peak locations.

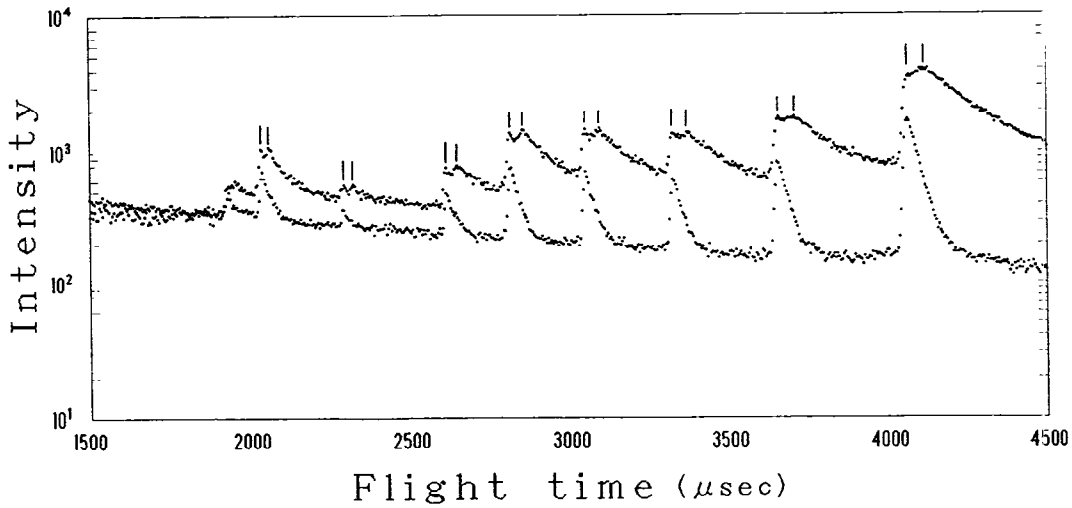

Figure 4. Observed double peaks for neutrons of wavelengths λ = 1.11 ~ 2.22 Å, for the case without Cadmium in the reflector (upper), and for the same moderator, decoupled and without premoderator (lower). Arrows indicate the locations of the peak doublets.

The double peaks arise from neutrons differently delayed by traveling different distances to the detector, but emerging simultaneously from their respective sources. Figure 5 shows the interval between the double peak pairs, for both cases with and without Cadmium in the reflector, plotted vs wavelength.

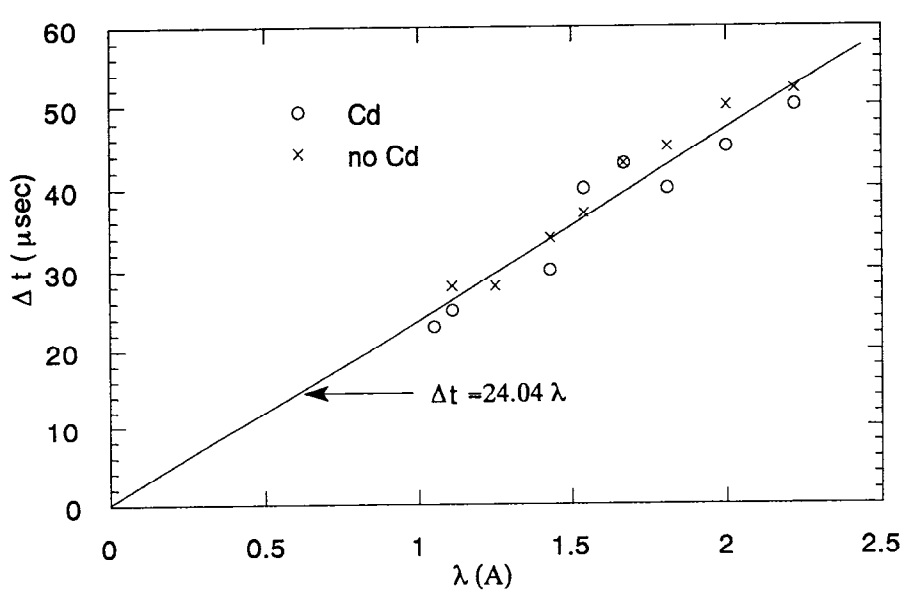

Figure 5. The interval between double peak pairs as a function of wavelength, for the cases with and without Cadmium in the reflector.

The fitted line represents the relationship $\Delta t = \Delta L/v = (m/h)\Delta L\lambda$; the slope of the line gives $\Delta L = 9.5$ cm, which is almost identical to the actual distance between the viewed surface of the liquid Hydrogen moderator and the polyethylene premoderator behind it ($\Delta L = 9.6$ cm.) The sharper pulses from the decoupled liquid Hydrogen moderator, shown for comparison in Figure 4, coincide

exactly with the leading pulses of the double pulse pairs. These observations lend credence to the interpretation that the leading pulse is from the liquid Hydrogen and the following pulse is from the warm polyethylene premoderator, 9.6 cm farther away. Pulses of longer wavelengths than about 2.2 Å do not exhibit double peaks, as is reasonable because the intensity from the Hydrogen becomes dominant and the attenuation by the Hydrogen of the neutrons from behind diminishes their intensity.

Figures 6 a-d show the observed pulse shapes for wavelengths 3.94, 4.93, 6.57 and 9.86 Å respectively, after subtraction of a rationally-determined background, for the cases without and with Cadmium reflector poisoning, and normalized so that the areas correspond to the measured spectra. The time scales have been adjusted to correspond to the emission time, that is, the time that neutrons

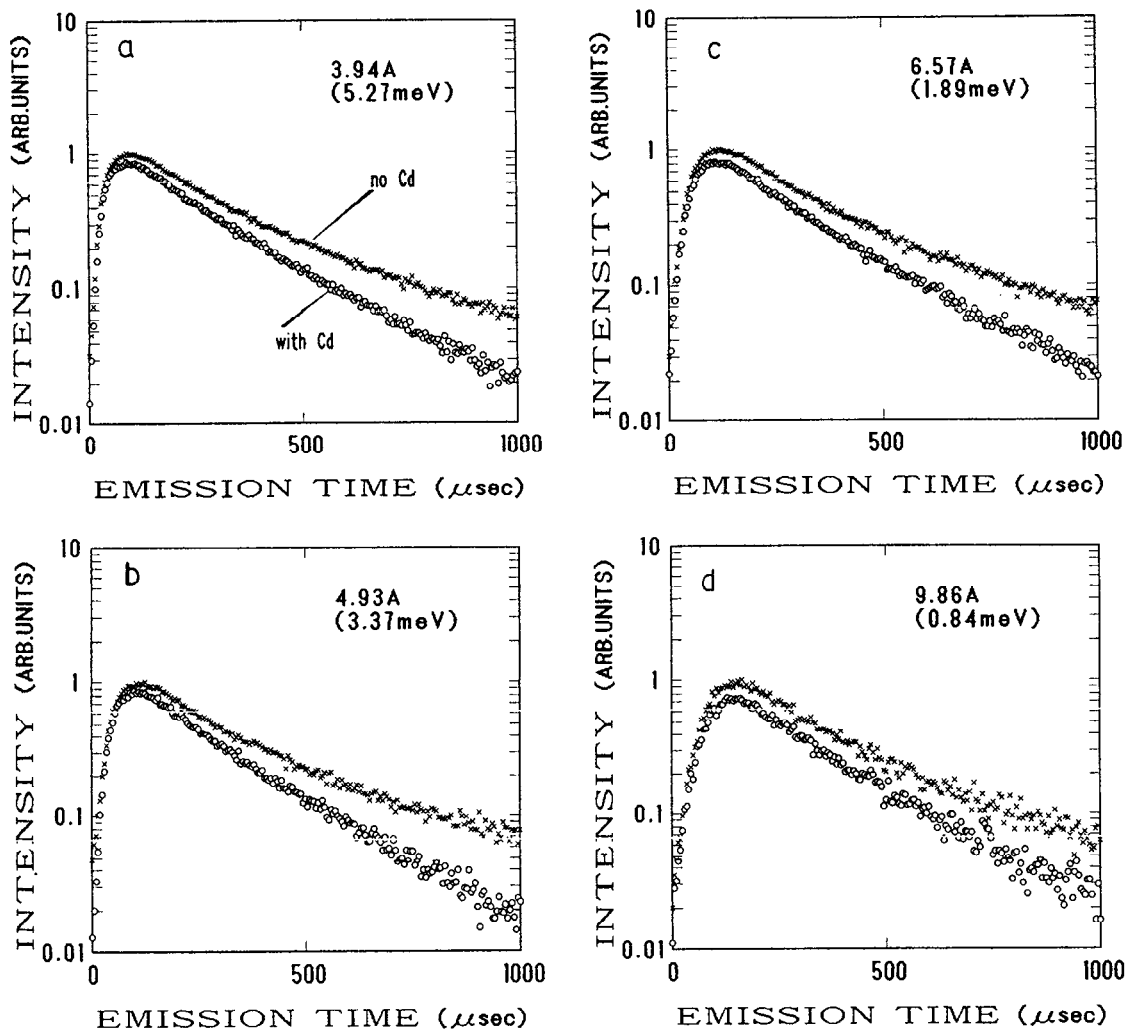

Figure 6. Intensity (log scale) as a function of emission time of neutrons from the liquid Hydrogen moderator in unpoisoned and poisoned reflectors. a. λ = 3.943Å; b. λ = 4.93Å; c. λ = 6.757Å, d. λ = 9.86Å.

crossed the viewed surface of the liquid Hydrogen. Notable features are that the shapes of the leading edges and the early decays are nearly indistinguishable, and that the trailing edges are shorter in the poisoned case than in the unpoisoned case. The peak values are about 20 % smaller in the poisoned case than in the unpoisoned case, and the remainder of the gain for the unpoisoned case over the poisoned case is due to the increased area in the longer tail.

Figure 7 shows the decay times determined as the slope of the logarithmic plot of intensity vs time on the trailing edges of the pulse shapes displayed in Figure 6. The decay in trailing edges exhibits two components. The decay time for the earlier decay was determined by fitting an exponential function to the decay after subtracting the longer-time exponential function determined from the long-time data. The decay times are independent of the wavelength in this range of wavelengths, as is to be expected if the decay is dominated by distinct eigenmodes of neutrons in the system. The long term decay time for the unpoisoned reflector is greater than that for the poisoned reflector, also as expected. The early decay time is independent of the reflector poisoning. The actual values are specific to the present geometry, not only of the reflector but also of the moderator and its immediate surroundings, since the total system represents a coupled entity.

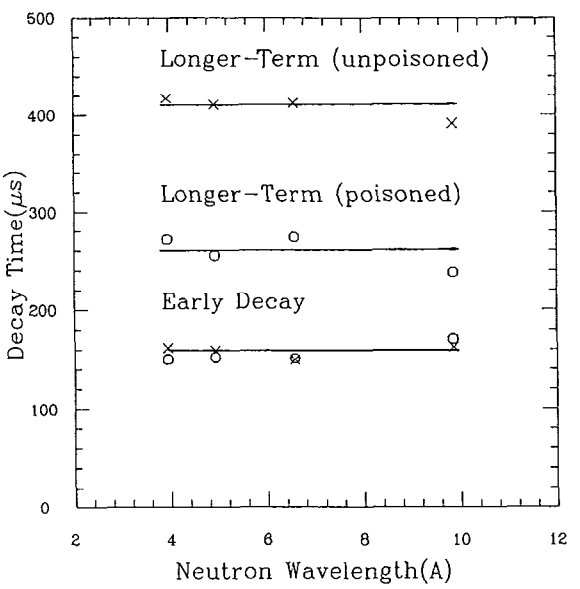

Figure 7. Decay times of the trailing edges of pulses from the liquid Hydrogen moderator in poisoned and unpoisoned reflectors.

The values of the decay times observed here are considerably shorter than would be expected in a uniform block of graphite the same size as the overall system. This is understandable, since the moderator and its surroundings themselves represent sinks for neutrons and are located in the center of the block, the position of greatest importance, analogous to the importance of control rods in a reactor.

Discussion and Conclusions

We have demonstrated that it is possible to control the decay times of coupled, reflected cold moderators, by introducing heterogeneous poisons in the reflector. This may make possible the

trading off of intensity for resolution in a way that can be adjusted remotely without disassembling and reassembling a moderator-reflector system, say by moving absorber rods in the reflector or changing the density of neutron absorber in circulating channels in the reflector. The adjustments need not affect the performance of other, decoupled moderators within the same reflector. The fundamental design of such a system, however, would be greatly affected by the requirements imposed by the presence of other moderators, decouplers and void liners. Not only would attention need to be given to the desired range of pulse lengths, which could be adjusted in a large number of ways, but also to the requirement to provide the highest intensity, which implies tailoring the spatial distribution of neutrons in the reflector.

We are aware of the shortcomings of our analysis and discussion, that is, at least in the language we have used to describe the observations, we have implied the existence of discrete decay eigenvalues, which may not actually exist, particularly in systems with large voids, even though our exponential fitting seems to have provided a satisfactory result.

The double peaks that we saw prompts us to make a cautionary observation concerning cross talk and pulse broadening in coupled systems containing significant voids; the intuitive conclusion that the viewed moderator shields the viewed surface from what is behind is questionable. In any case, premoderators should be placed as close as possible to the viewed moderator, to avoid pulse distortion.

References

1. G.S.Bauer, et al., Proc. ICANS-IIIV(Didcot, July 8-12,1985) p.344.
2. Y.Kiyanagi, N.Watanabe and H.Iwasa, Nucl. Instrum. Methods, A312(1992)561.

Some Optimization Studies on Flux-Trap Moderators for Increasing The Slow-Neutron Beam Intensity

Y. Kiyanagi, N. Watanabe* and M. Nakajima

Department of Nuclear Engineering, Faculty of Engineering, Hokkaido Univ., Sapporo 060
*National Laboratory for High Energy Physics, 1-1 Oho, Tsukuba-shi, Ibaraki, 305

Abstract

A flux trap geometry has various possibilities to increase the slow-neutron intensity, compared with the traditional wing geometry. We compared the slow-neutron intensities from various flux-trap moderators (extended, overlap and back-scattering) by computer simulations and mock-up experiments. The results show that those moderators are useful for enhancing the intensity. A gain factor of more than 1.5 is obtainable. It was found that back scattering moderators give a higher intensity with a narrower pulse width, compared to normal extraction.

1. Introduction

Flux-trap moderators have been discussed extensively.(1)-(4) We have shown that a flux-trap moderator can provide a comparable slow-neutron intensity to that of a wing type.(4) In the flux-trap geometry, however the combination of target and moderator is more flexible than in the traditional wing geometry, which suggests the possibility to increase the slow-neutron intensities more than the latter. Among the various possible combinations in the target and moderator, we examined extended, overlap and back-scattering moderators by computer simulation as well as by mock-up experiments.

Since the pulse characteristics are sensitive to the ralative position of the primary neutron source, we can expect a different pulse shape with a back-scattering moderator compared to that from normal extraction. To confirm this we performed some pulse-shape measurements for both moderators.

It will also be important to compare the slow-neutron intensity from the flux-trap moderator with those from other types of target-moderator couplings (wing and slab). For this purpose it is necessary to define a reference case which is reasonable for each type coupling. Nevertheless, we tried to perform a direct comparison for a very simple system by computer simulation in order to obtain a crude scope concerning its problem.

2. Calculation

2. 1. Calculational Model and Codes

The calculations were performed for a proton energy of 1 GeV, since this energy has been proposed for the KENS-II, the next-generation pulsed-spallation neutron source in Japan. For simplicity, a cylindrical beam profile of a radius 2.35 cm was assumed (typical in existing facilities). The

calculational model of the target-moderator-reflector system is shown in Fig. 1. The target is split into two parts: the first target onto which protons are injected, and the second target after the void space. The length of the first target was kept at 7.5 cm (the optimal length) and the target radius at 5 cm.[3] For simplicity, the targets were assumed to be made of pure tungsten metal, and not diluted by the coolant and cladding materials, as in the case of LANSCE, Los Alamos National Laboratory. The total target length is fixed at 34.5 cm, which is sufficient for 1-GeV protons. As a reference system, four decoupled light-water moderators ($10 \times 10 \times 5$ cm^3) are placed around the void space between the two target halves with a center line distance between the target and moderator of d = 9.5 cm. A beryllium reflector (at least 30 cm thick) is used as shown in the figure. The beam holes in the reflector are lined with B_4C decouplers. The decoupling energy was adjusted to 20 eV. The moderators are also covered by the same decouplers, except for the viewed surfaces. The height and the opening angle of the beam-extraction holes in the reflector are 10 cm and ±25 degrees, respectively. For low-energy neutron transport calculations a Monte-Carlo code, MORSE-DD,[5][6] was used in combination with a high-energy hadron transport code, NMTC/JAERI. An S_N neutron transport code, TWOTRAN-II,[7] was used to calculate the spatial distributions of the low-energy neutrons. For both calculations the cross-section library ENDF-B/IV[8] was used.

2. 2. Extended Moderator

What will happen if we increase the height (h) of the moderator with a larger separation (l) of the target halves? Figure 2 shows the calculated results. The beam intensities are normalized to that for the reference case (l = 14 cm, d = 9.5 cm, $10 \times 10 \times 5$ cm^3 moderators at the center of the void height). Although the beam intensity decreases with a larger separation of the target halves, it increases almost linearly with the moderator height (up to 2.3 at h = 26 cm with l = 30 cm). One

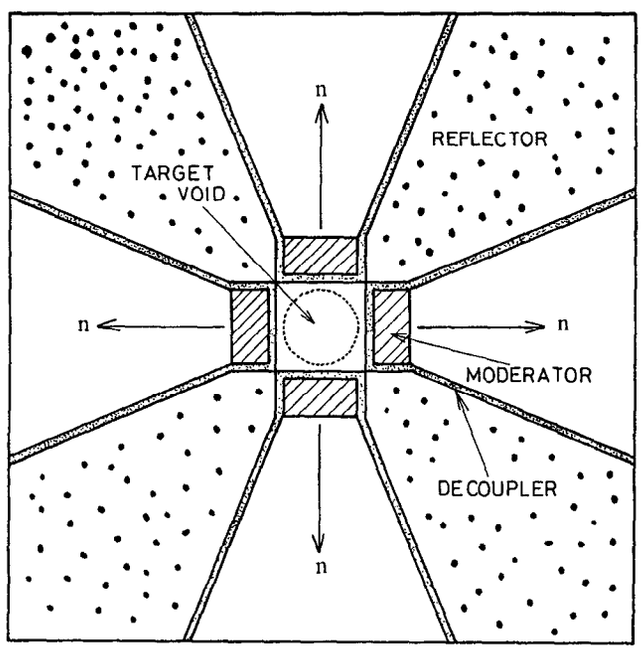

Fig. 1 Calculational model of the flux-trap type target-moderator-reflector system.

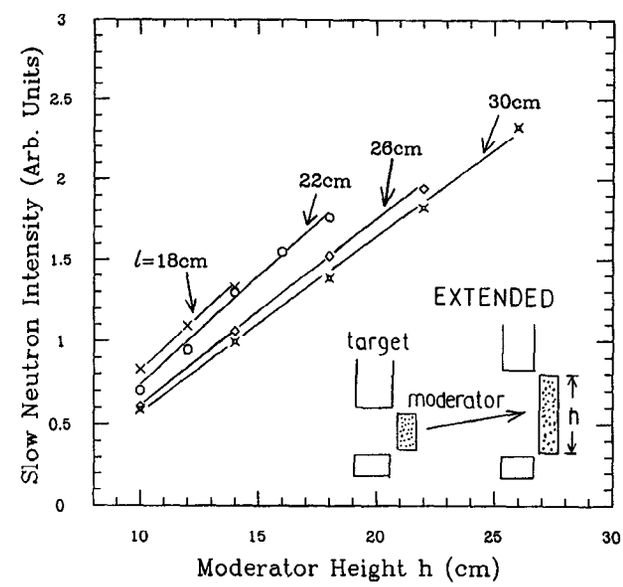

Fig. 2 Slow-neutron intensities from extended moderators.

can take full advantage of a higher beam intensity obtained with such an extended moderator in some classes of experiments in which the vertical beam collimation is not so important. In order to understand the above results, we calculated the spatial distribution of the neutron intensities on the viewed surface along the proton beam direction. Since a three-dimensional Monte-Carlo calculation is very time consuming to obtain the required statistics, we performed a two-dimensional calculation using TWOTRAN-II for a two-dimensional model (Fig. 3); the moderator is an annulus with a thickness of 5 cm at d = 9.5 cm and l = h + 4 cm. Figure 4 shows the results of the distributions of slow-neutron beam intensities along the proton beam direction(Z). The distributions are rather more flat and symmetric than those for a wing-geometry moderator in which the asymmetry (peaking towards the target) is more enchanced. This is the reason why the intensities increase linearly with the moderator height (h). For a reference, the calculated results of the spatial distributions on the viewed surface of the moderator of h = 10 cm during the slowing-down process are shown in Fig. 5. The distribution in the fast-neutron region (E_n = 0.821 ~ 1.35 MeV) strongly reflects the distribution of the first collision density of neutrons in the moderator. With decreasing energies the distribution becomes more flat.

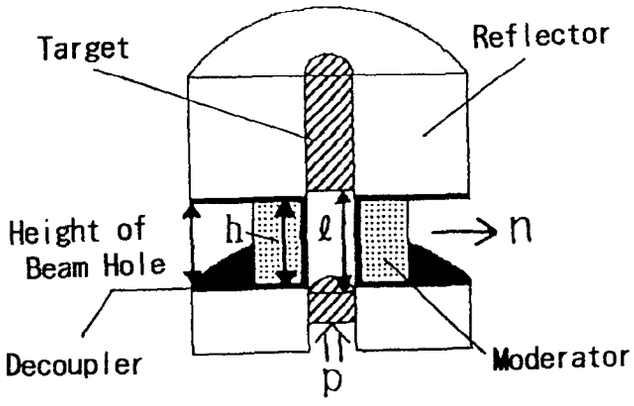

Fig. 3 Calculational model for a two-dimensional calculation.

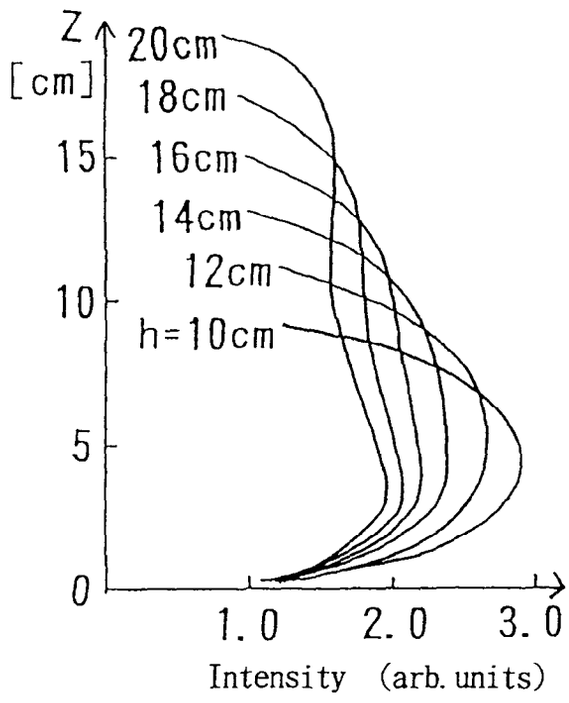

Fig. 4 Vertical spatial distributions of the slow-neutron intensities on extended moderators.

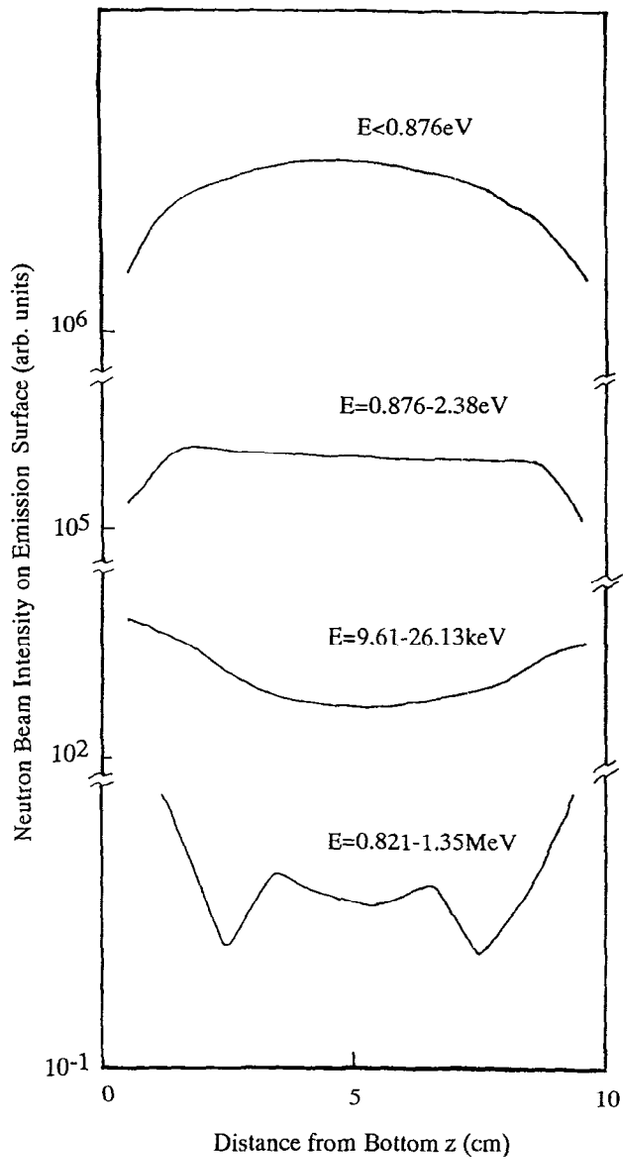

Fig. 5 Spatial distributions of neutrons during the slowing-down process.

2. 3. Overlap Moderator

Even in the case that neutrons from such extended moderators cannot be utilized, due to the required vertical collimation of the neutron beams, those moderators with a limited viewed surface of 10×10 cm^2 will give a higher slow-neutron intensity than the reference moderator of $10 \times 10 \times 5$ cm^3, by overlapping the moderator with the target, as shown in the inset of Fig. 6, keeping the separation of the target halves at 14 cm. We examined such moderators and obtained the results shown in Fig. 6. A moderator with a larger height gives a higher intensity by about 10%. When the width of the moderator (w) is also increased to 12 cm, a gain about 1.3 results in total for the case of a 10×10 cm^2 viewed surface and about 1.5 for a larger viewed surface of 10 cm high by 12 cm wide. The vertical spatial distributions were also calculated for this moderator system. The results are shown in Fig. 7. The increase in the intensity is mainly due to the flatter distributions with an unchanged peak height.

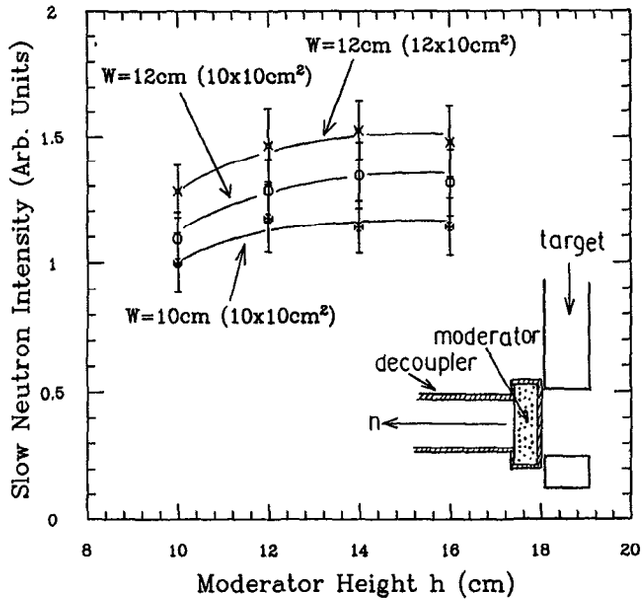

Fig. 6 Slow-neutron intensities from overlap moderators. The moderator size is h cm × w cm × 5 cm thick. w is moderator width. Areas of viewed surfaces are indicated in parentheses (y cm wide × 10 cm high).

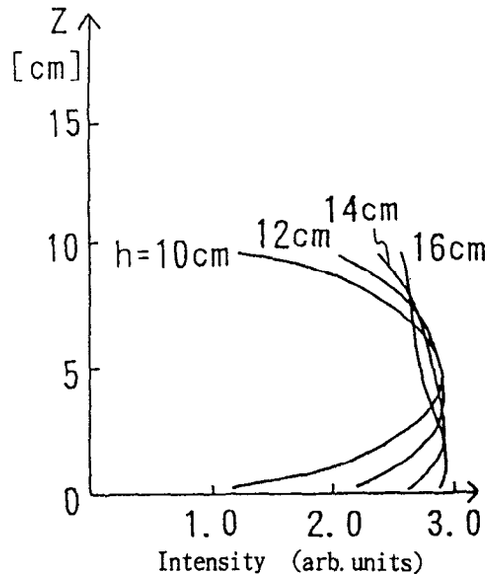

Fig. 7 Vertical spatial distributions of the slow-neutron intensity on the viewed surfaces of the overlap moderators.

3. Mock-up Experiments

3. 1. Simulation by an Electron Linac Neutron Source

We aimed at performing mock-up experiments of those moderator systems mentioned above, since the statistics of the calculated results were rather poor and information concerning the time distribution of the neutron pulse was not given. More reliable data can be obtained by measurements. However, such experiments using the proton beam are very difficult; there are almost no opportunities to use proton accelerators in this energy range. We, therefore, tried to utilize an electron linac pulsed-neutron source for this purpose. It seems to be almost impossible to

simulate a split-target geometry by an electron-based neutron source, due to the completely different spatial distribution of neutrons produced in the target. However, if we consider only the contribution of fast neutrons from the first target, a simulation by an electron linac would be reasonable, since the geometry between the neutron source and the moderator is not so much different. The contribution from the second target would be close to a reflected image of that from the first target with a proper coefficient, determined by the ratio of both contributions. Therefore, the variation of the neutron-beam intensity from different moderators can be estimated by a simple mock-up with one target. Figure 8 shows the layout of this mock-up, where a lead block was placed downstream of the void space in order to simulate the second target material. The moderator is a polyethylene block ($10 \times 10 \times 5$ cm^3 at room temperature for the reference case). Cd sheets were lined inside the beam-extraction holes in the graphite reflector.

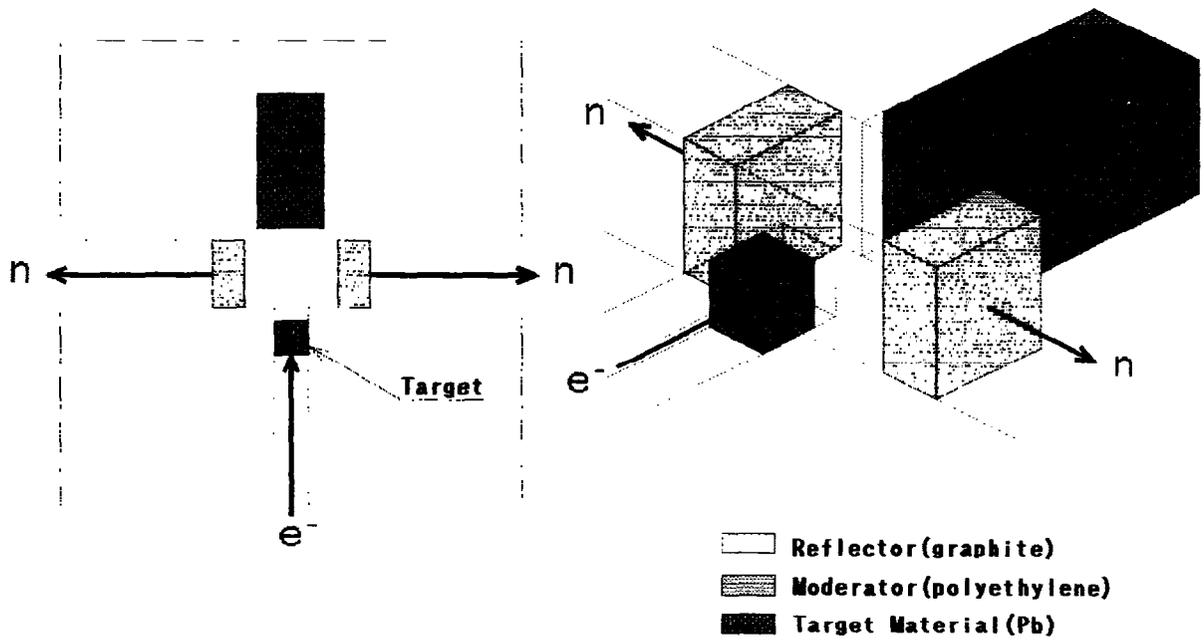

Fig. 8 Mock-up of the flux-trap moderator system.

To compare the present measured results with calculations for 1-GeV protons, we performed independent calculations for a system that was almost the same as that shown in Fig.1, except for the different beam-extraction hole (a rectangular shape in this case).

3. 2. Measured Results

A. Moderator Thickness

The moderator thickness-dependent slow neutron intensity is a good measure for characterizing the coupling nature between the target and the moderator. Figure 9 shows the measured thermal-neutron intensities for various moderator thicknesses. The lateral dimensions of the moderators were 10 cm $\times$ 10 cm. The solid curve is the calculated results after smoothing. The agreement between the measurement and the calculation is fairly good. The thickness dependence of the slow-

neutron intensities is rather closer to that in a slab geometry than in a wing type: the coupling nature of this system is closer to that of the slab geometry.

B. Extended Moderator

Figure 10 shows the measured thermal-neutron intensities from extended moderators of different dimensions along the target axis. The agreement between the measurement and the calculation (solid curve) is satisfactory. The difference in the gain factor from those in Fig. 2 is due to the different opening angles of the beam-extraction hole in the reflector (this mock-up has only one rectangular straight beam-extraction hole).

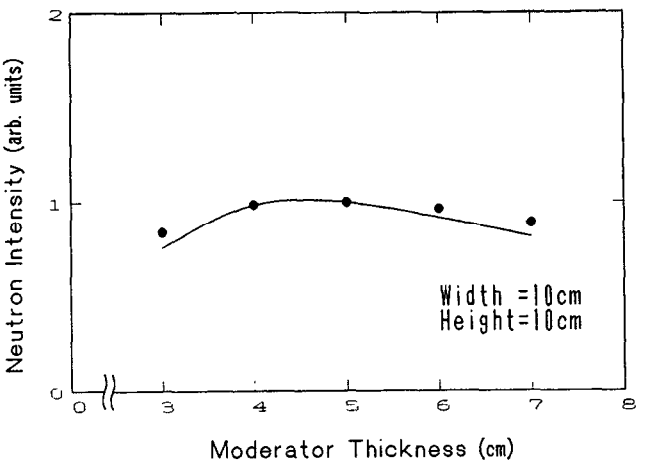

Fig. 9 Measured moderator thickness-dependent thermal-neutron intensity. The solid curve is the calculated one after smoothing.

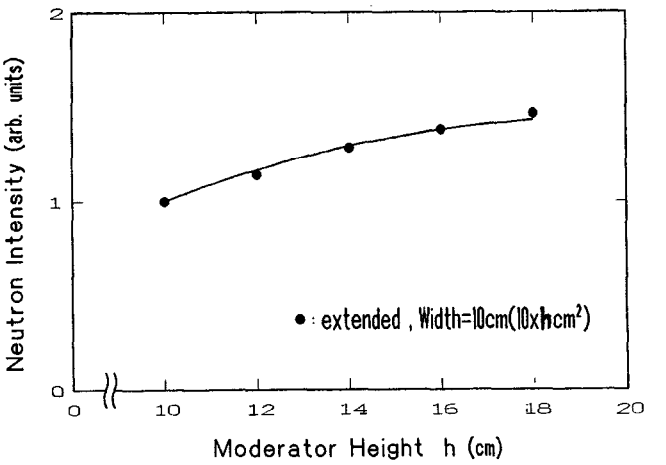

Fig. 10 Measured thermal neutron intensities from extended moderators. The solid curve is the calculated one after smoothing.

C. Overlap Moderator

Figure 11 shows the measured thermal-neutron intensities from the overlap moderators, as shown in Fig. 6. The agreement between the measurements and the calculation (solid curves) is again very good. The gain factors in Fig. 11 are almost the same as in Fig. 6, since in the overlap moderator system the missing reflector is not as large as that in the extended moderator system.

D. Optimal Moderator Position and Back-scattering Moderator

The slow-neutron intensity is sensitive to the location of the moderator relative to the target. We can expect an additional gain factor by positioning the moderator optimally. Furthermore, beam extraction from the other side can provide a higher intensity than under normal extraction. This moderator is called a "back-scattering moderator". We experimentally confirmed the performance of a back-scattering moderator. Fig. 12 shows the measured results. The moderator size is $10 \times 10 \times 5$ cm^3. In normal extraction if one can put the moderator on the center line of the target, a gain factor of about 1.5 relative to the reference position (d = 9.5 cm) can be obtained. Technical efforts to put the moderator as close as possible to the target center line should be pursued.

In back-scattering extraction, a higher gain factor than normal was confirmed: about 1.22 at the reference position (d = 9.5 cm). The maximum value is the same as that of normal extraction. However, the maximum value is almost conserved up to about d = 3.5 cm. This relaxes various engineering difficulties. We also confirmed experimentally that a further gain factor of about 1.2 is obtainable by putting a plug reflector in the beam hole at the opposite side.

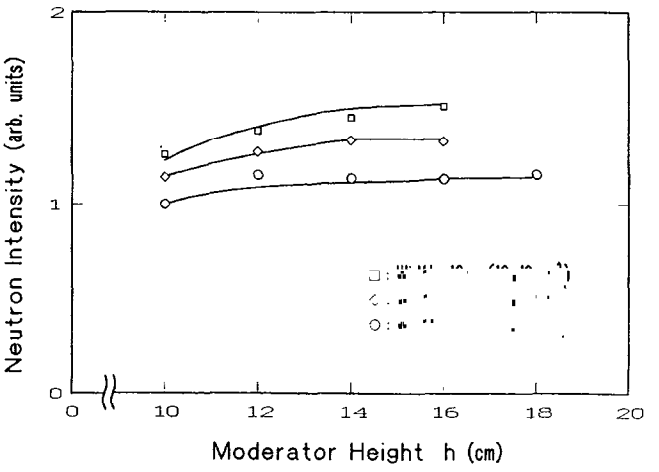

Fig. 11 Measured thermal neutron intensities from overlap moderators. The solid curves is the calculated ones after smoothing.

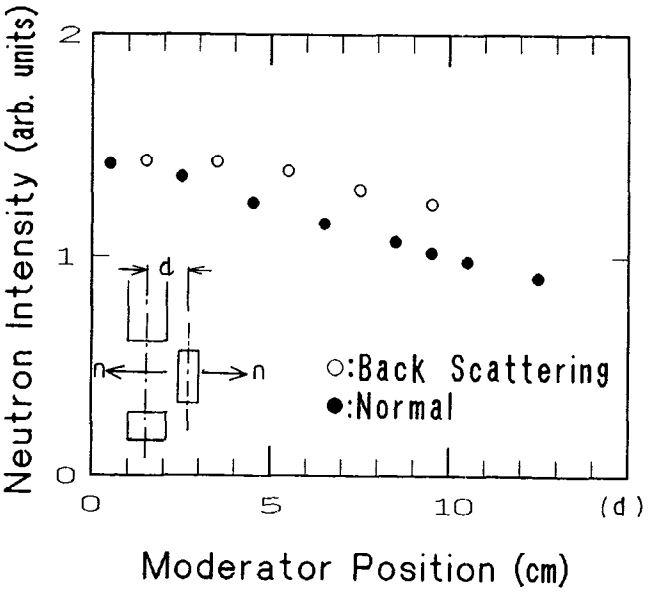

Fig. 12 Measured thermal-neutron intensities from the reference moderator (10 × 10 × 5 cm^3) as a function of the moderator position.

3. 3. Pulse Shape

We performed measurements of the pulse shapes of thermal neutrons using the device described in a reference.(9) Figure 13 shows a typical result measured at the reference moderator position (d = 9.5 cm). The superiority of the back-scattering moderator is clearly demonstrated: a higher peak intensity with a narrower pulse width (FWHM). Fig. 14 shows plots of the pulse widths for both extractions as a function of the neutron energy.

4. Discussions

We have shown various possibilities for increasing the slow-neutron beam intensities from flux-trap moderators. With an overlap moderator and a back-scattering moderator a gain factor of about 1.5 has already been achieved. This value is considerable. We now compare the present results with a typical performance of a slab-type moderator which is well known for providing the highest intensity among the three configurations of target-moderator coupling. However, the slab configuration has not been adopted in any pulsed spallation neutron sources, since in this configuration a huge amount of fast and high-energy neutron background cannot be avoided. A combination of the slab moderator with a burst-suppression chopper and/or a curved guide tube is sometimes discussed as a possibility for realizing a higher intensity. Our calculation confirmed that the relative intensity of a reference slab moderator to the reference flux-trap type is about 1.5; this

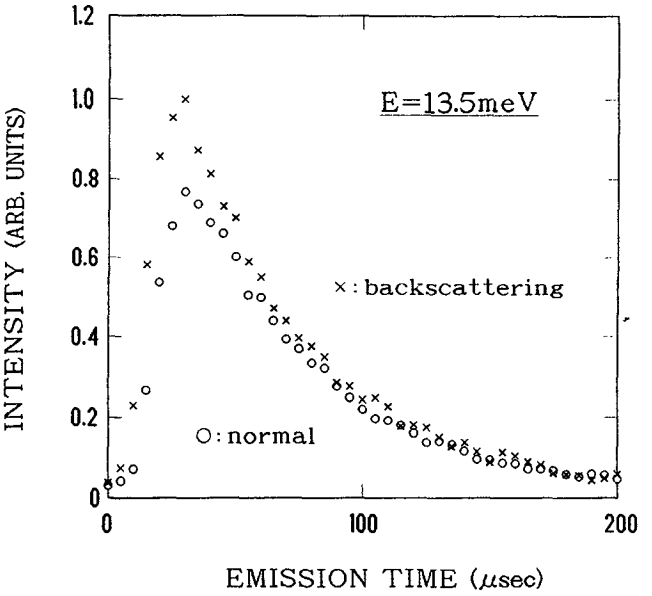

Fig. 13 Measured thermal-neutron pulse shapes for both extractions from the reference moderator at the reference position (9.5 cm).

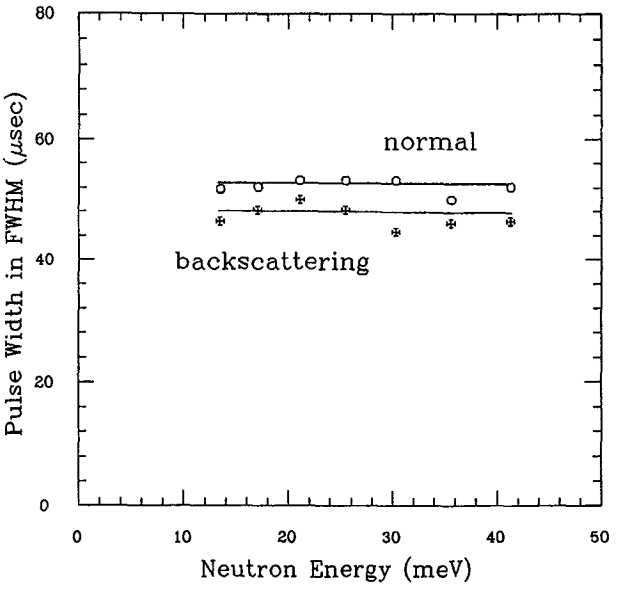

Fig. 14 Measured pulse widths of thermal neutrons for both extractions as a function of the neuron energy.

is the same as the above gain factor. The present geometry is therefore much better than the slab one: much less fast and high-energy neutron backgrounds.

For a direct comparison of the flux-trap moderator to the wing type, we calculated the intensity for both reference moderators. The relative value of the flux-trap to that of the wing was about 0.94, almost comparable. However, by adopting the extended (l = 30 cm, h = 26 cm), the overlap (h = 14 cm, w = 12 cm, l = 14 cm; viewed surface 10 × 12 cm^2) or the backscattering (d ~ 3.5), we obtain a gain factor of about 2.3 × 0.94 = 2.2, 1.5 × 0.94 = 1.4 or 1.5 × 0.94 = 1.4, respectively, relative to the reference wing moderator.

We performed mock-up experiments using an electron linac neutron source to simulate the flux - trap moderator, and obtained consistent results with the calculated ones. The present results show that this method, using an electron linac, is reasonable for estimating the performance of the flux - trap moderator system.

We reported that a coupled liquid-hydrogen moderator with a hydrogenous premoderator at ambient temperature in a wing geometry can provide a much higher cold-neutron beam intensity: about 6-times higher than a typical decoupled one.(9) Such moderators at a flux-trap geometry are expected to have a similar advantage to the ambient-temperature moderator in this geometry. This possibility is to be studied experimentally.

Reference

(1) G. J. Russell, H. Robinson, G. L. Legate, R. Woods, E. R. Whitaker, A. Bridge and K. J. Hughes : Proc. 9th Meeting of International Collaboration on Advanced Neutron Sources, ICANS-IX (Villigen, Sept. 22-26, 1986) pp.177.

(2) G. J. Russell: Proc. ICANS-XI (Tsukuba, Oct. 22-26 1990) pp.335.
(3) Y. Kiyanagi and N. Watanabe: Proc. ICANS-XI (Tsukuba, Oct. 22-26 1990) pp.408.
(4) N. Watanabe and Y. Kiyanagi: Physica B. 180 & 181, 893 (1992).
(5) E. A. Straker et. al.: ORNL-4585 (1970).
(6) M. Nakagawa and T. Mori: JAERI-M 84-126 (1984).
(7) K. D. Lathlop and F. W. Brinkley: LA-4848-MS (1973).
(8) ENDF/B Summary Documentation, BNL-NCS-17541 (ENDF-201), 2nd Edition, compiled by D. Garber, available from the National Nuclear Data Center, BNL, Upton N.Y. (1975).
(9) Y. Kiyanagi, N. Watanabe and H. Iwasa: Nucl. Instrum. Meth., A312, 561 (1992).

Twelfth Meeting of the International Collaboration on Advanced Neutron Sources (ICANS XII),
24-28 May 1993, The Cosener's House, Abingdon, Oxfordshire, UK.

Moderator Materials and Neutronic Performance

L.L. Daemen, G.J. Russell, and E.J. Pitcher,
Manuel Lujan Jr. Neutron Scattering Center (LANSCE),
Los Alamos National Laboratory,
Los Alamos, New Mexico, USA

The great variety of instruments proposed for LANSCE-II entails an equally varied set of requirements for the target stations moderators. Besides the obvious features such as intensity and pulse width of the neutron pulse, a number of more pragmatic questions have to be addressed such as fast neutron background and energy deposition in the moderators, especially at large proton beam powers such as the 1 MW proton beam power proposed for LANSCE-II.

Introduction

The moderator is the interface between the neutron production target and the instruments. It affects directly the performance of the instrument connected to it, and its optimization (materials, size, position, coupling/decoupling, poisoning, temperature, etc...) is therefore a most crucial aspect of target station design.

We review briefly the performance of light water, liquid methane, and liquid hydrogen moderators in flux-trap geometry. Various figures of merit such as peak intensity, integrated intensity, pulse width, pulse decay times, etc ... are tabulated systematically. These results were meant to serve as references for future studies.

The instruments proposed for the 1 MW sources at LANSCE and IPNS, and for the 5 MW source at the ESS will place further demands on moderators and moderators design that in some cases will require to go beyond the capabilities of the three traditional moderators mentioned above. To meet this challenge, we propose a new type of moderator, namely the composite moderator. The basic motivation behind the particular type of composite moderator presented below is spectrum mixing to produce neutron spectral characteristics that are well- or better-adpated to a given instrument. The results of computer simulations show that this particular concept seems to be very promising.

Another particularly important aspect of moderator research at pulsed spallation neutron sources is the moderator longevity. The intense radiation field to which a moderator is subjected, as well as the large amounts of energy deposited in the moderator conspire to compromise the mechanical integrity of the moderator assembly. This is the main reason that, so far, only liquid moderators have been used in practice at pulsed spallation neutron sources. The liquids used traditionally, namely light water, liquid methane, or liquid hydrogen, represent a good compromise between excellent resistance to radiation damage (with the

exception of liquid methane) and ease of cooling, and a reasonable hydrogen density. Solid metal hydrides typically have significantly higher hydrogen densities, and so could potentially increase dramatically the performance of moderators for the next generation of pulsed spallation neutron sources. On the other hand, simple hydrides such as ZrH_2, for instance, suffer from the problem that the density of low energy vibrational modes that matter most for neutron thermalization is low compared to liquids. Although this is somewhat of a disadvantage for moderation to thermal energies, the material could still act as a very efficient premoderator. Altogether, little work has been done on the possibility of using solid metal hydrides for neutron thermalization, with the exception perhaps of ZrH_2 and TiH_2. The latter was investigated as a premoderator in the early days of the WNR facility at LANL. In particular, calculation of neutron scattering kernels in metal hydrides are inexsistent, not to mention a lack of knowledge of resistance to radiation damage, or basic mechanical properties in all but a few metal hydrides. Because of the potential advantages shown by solid metal hydrides moderator, we plan to investigate solid moderators in great detail in the near future.

Although we do not address directly the radiation damage aspects of moderator design, we describe the results of a number of computer studies regarding energy deposition in the moderators at LANSCE. The results of these studies should prove useful in estimating the cooling capacity required for typical moderators, and should help in estimating the lifetime and failure modes of moderators at a pulsed spallation neutron source.

Reference moderators

Traditionally, three types of moderators have been used at spallation sources. Light water moderators produce a neutron spectrum peaking at about 40 to 50 meV; liquid methane moderators peak at about 10 to 20 meV and liquid hydrogen moderators spectra show a maximum around 2-3 meV. By suitably poisoning and decoupling these moderators, the pulse shape can be varied to meet different resolution or intensity criteria imposed by the instruments. We have examined in detail how these reference moderators would perform at a typical LANSCE-II spallation target, and paid attention not only to major features such as neutron beam intensity and time distributions, but also to arguably less crucial characteristics such as fast neutron background.

The first step in the moderators selection process is to assess the users' needs. In order to help the users in making this choice, we studied a number of reference moderators, and characterized them in detail:

- high-resolution H_2O; Gd poison
- high-intensity H_2O; Gd poison
- liquid H_2 (decoupled), no poison
- liquid H_2 (coupled), no poison
- H_2O/liquid H_2 (decoupled), no poison
- H_2O/liquid H_2 (coupled), no poison
- H_2O/Gd/liquid H_2 (decoupled), poisoned
- H_2O/Gd/liquid H_2 (coupled), poisoned

Moderator	Peak intensity (n/p/sr/μs)	FWHM (μs)	Rise time (10%-90%) (μs)	Decay time (μs)
H_2O high-intensity	0.00075	28	5	24.7
H_2O high-resolution	0.00071	16	4	11.7
Liquid CH_4, high-intensity	0.00088	20	4	34.0
Liquid CH_4, high-resolution	0.00087	13	4	20.2
H_2, decoupled	0.00083	22	6	83.7
H_2, coupled	0.00082	33	6	169.4
H_2O/H_2, decoupled	0.00076	23	6	113.0
H_2O/H_2, coupled	0.00076	33	6	217.1
$H_2O/Gd/H_2$, decoupled	0.00063	18	6	73.7
$H_2O/Gd/H_2$, coupled	0.00063	26	6	132.4
H_2 high resolution (boral)	0.00029	13	4	70.0

Table 1: Neutron pulse characteristics

- H_2 high resolution (decoupled with boral), no poison

The study was performed for these moderators in flux-trap geometry. The computer model for the target/moderator/reflector/shield assembly used in the simulations is shown in Fig.1.

In each case, we considered four identical moderators. The moderators were all 13 x 13 cm^2 moderators. The geometry was always kept fixed; we changed only the moderator material. For a LANSCE-II configuration with 2 flux traps, a reasonable rule of thumb is to decrease the flux by 20 % (relative to the one-flux trap geometry used in the present study) if the moderator belongs to the downstream flux trap, and 35% if the moderator belongs to the upstream flux trap. The moderator thickness is 4 cm for the H_2O moderators with the poison layer 2.5 cm from the viewed surface for high-intensity moderator, and 1.5 cm from the viewed surface for the high-resolution moderator. The liquid CH_4 moderators are 4 cm thick. The liquid H_2 moderators all have a 5 cm H_2 moderator. When the moderators are decoupled, the decoupler is usually Cd, 32 mils thick. The H_2O and liquid CH_4 moderators are always decoupled. The high-resolution liquid H_2 moderator is decoupled with boral. The calculated values for the liquid methane moderator are in very good agreement with the values measured by J. Carpenter et al. [1].

The studies illustrate the effects of coupling and poisoning moderators, and the effect of premoderators. The results cover a fairly broad range of neutron pulse characteristics, that are to be regarded as typical for LANSCE-II instruments design. Features such as pulse width in a given energy range, decay times in the time distributions, and peak intensity, for instance, were tabulated from Monte-Carlo simulation. In Table 1, the peak intensity, full width at half maximum, rise time (from 10% to 90% of the peak intensity), and decay times are given for all of the above moderators. All neutrons with energy less than 100 meV were included.

In the case of the water moderators, we also studied systematically the effect of varying the thickness of the premoderator while keeping the moderator thickness constant at 2.5 cm. The moderator was poisoned with 2 mils of Gd between the premoderator and the moderator. From the results shown in Fig.2, it can be seen that, up to a point, the useful

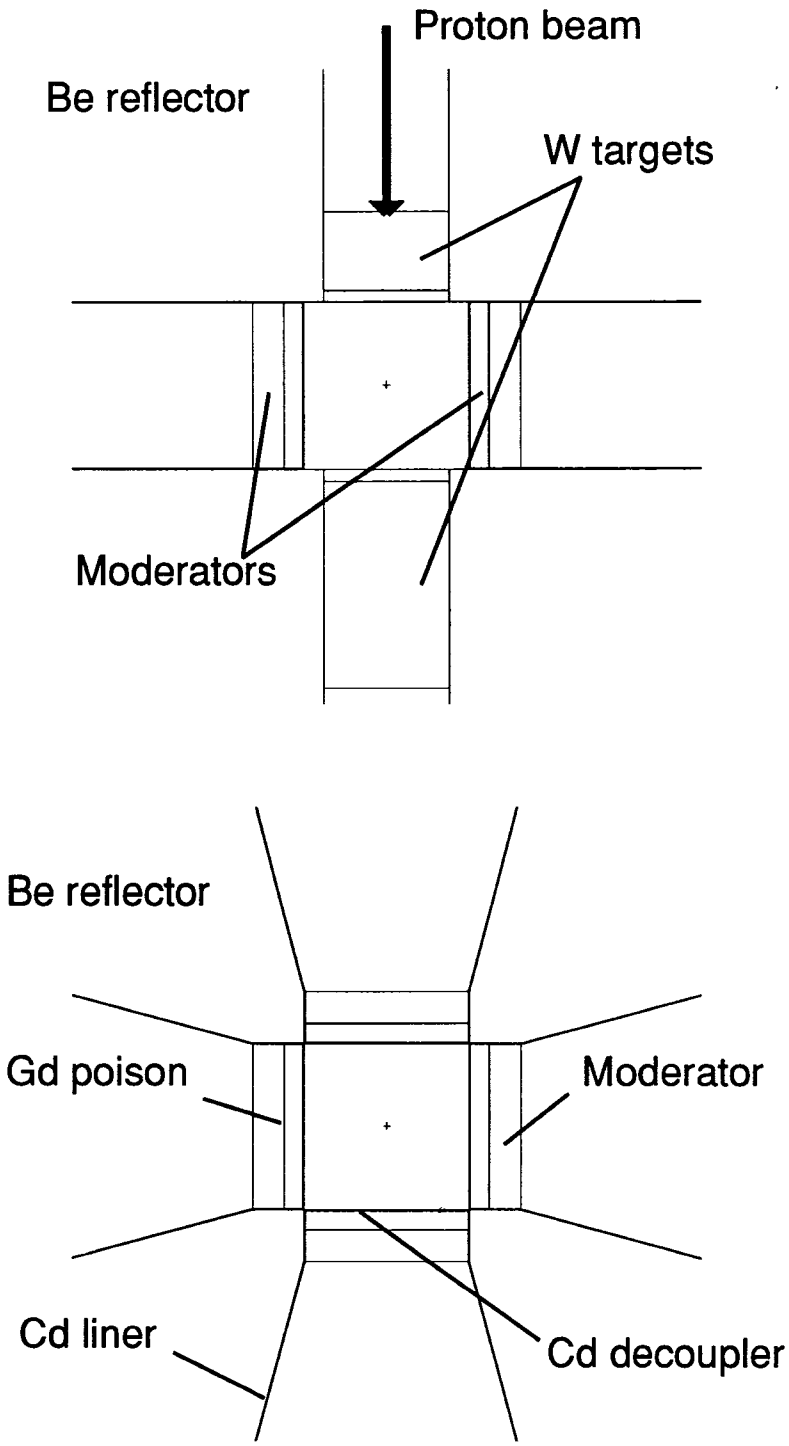

Figure 1: The simplified flux trap geometry used in the calculation of the reference moderators. The top figure is a vertical cross-section of the model; the bottom figure is a horizontal cross-section at the flux trap level.

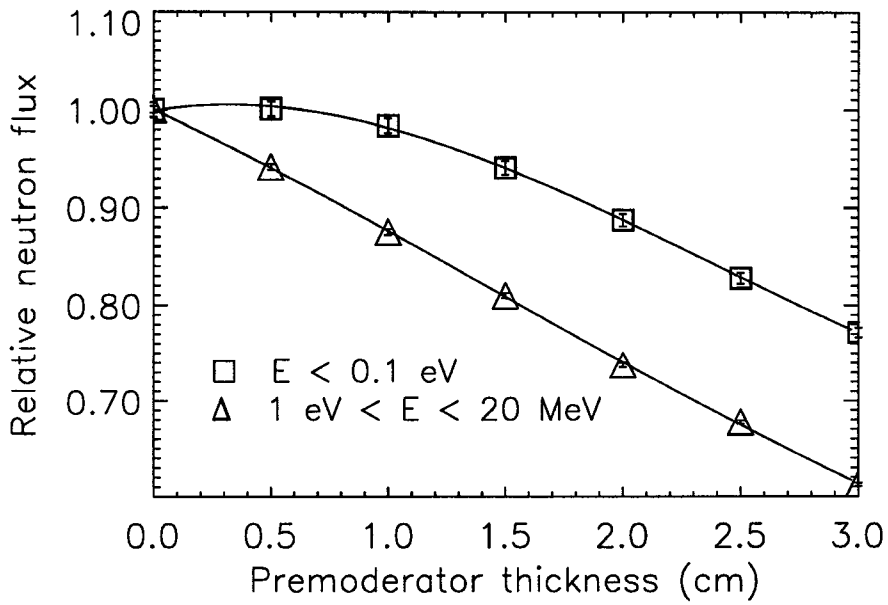

Figure 2: Effect of the premoderator thickness on the performance of a light water moderator in flux trap geometry

signal is unaffected, but the fast neutron background can be substantially reduced if the adequate premoderator thickness is selected. Although maybe not an issue at lower powers, this could become important at 1 MW. Notice that if the premoderator thickness is too large, the neutrons moderate exclusively in the premoderator and never get a chance to leak in the moderator through the Gd poison. This explains the decrease in useful signal intensity as the premoderator thickness is increased.

Composite moderators

In order to go beyond this traditional set of moderators, we propose a new moderator concept. For lack of a better term, these moderators will be refered to in what follows as composite moderators. A composite moderator is made of two (or perhaps more) layers of distinct materials. This by itself is not a new idea, and the concept of a premoderator/moderator assembly has been proposed previously: The premoderator material with a larger scattering cross section at higher energies scatters the neutrons down to a lower energy, and feeds them to the moderator layer where they are more rapidly and easily moderated to thermal energies [2-5]. The composite moderator (or what we call here a composite moderator) serves a different purpose. The idea is to mix the neutron spectra of two different materials to obtain an intense "broadband" neutron spectrum [5].

A good example consists in trying to emulate a methane spectrum by mixing a water spectrum with a liquid hydrogen spectrum. This is realized in practice by having a thick layer, say, a few cm, of water followed by a thin layer, say less than 1 cm, of liquid hydrogen. The viewed surface is the liquid hydrogen layer. In this way, it is possible to see through the

hydrogen layer into the water moderator. For this reason, a more appropriate name for what we call a composite moderator would be a moderator/moderator assembly, as opposed to the premoderator/moderator assembly already mentioned. Fig.3 shows how the spectrum varies with the relative thicknesses of the water and hydrogen layers. In this particular study, the total thickness of the moderator is kept constant at 5 cm. A 1 cm layer of liquid hydrogen may not appear to be much moderator material, but it should be recalled that the neutrons fed to the hydrogen layer have already been heavily thermalized in the water moderator so that it does not take much hydrogen to lower their energy further. The time distribution of the pulse from a composite moderator is reasonably good, e.g., the full width at half-maximum of the neutron pulse (E $<$ 100 meV) is $\sim$ 25 μs. Although the pulse width and decay time are slightly larger than for a methane moderator, the difference is probably not significant for most applications.

This kind of moderating assembly (the composite moderator) works very differently from the traditional premoderator/thick-moderator assembly where the spectrum seen is that of the moderator, and the spectral characteristics of the premoderator are essentially invisible.

Another interesting aspect of composite moderators is the fact that the thin liquid hydrogen layer might be easily removable, leaving one with a thick, conventional water moderator. So, an experiment could be repeated at the same instrument with a pure water spectrum, then a composite moderator spectrum. One could even envisage having the hydrogen layer divided into two or more sub-layers e.g., by having a number of thin canisters, and fill these canisters progressively with liquid hydrogen to produce more and more colder neutrons and therefore change the spectral characteristics of the neutron beam.

Energy deposition in moderators

The work described here gives quantitative estimates of the impact of proton beam shape and location on energy deposition in the existing liquid hydrogen moderator at LANSCE. More precisely, we describe below the results of two sets of studies:

- Influence of the proton beam shape on moderator and target heating.
- Energy deposition in the cryogenic (liquid hydrogen) moderator and in the targets for various beam configurations.

In each case, energy deposition in the moderators was calculated for the moderating medium as well as for the aluminum canisters containing the moderator itself.

The results were obtained with the LAHET Code System (LCS) [6]. We used a detailed computer model of the as-built LANSCE target station created by X-6, and further developed at LANSCE. Fig.4 shows the exact geometry used in our calculations; more details can be found in Ref.[7].

First set of studies : Proton beam shape

Previous studies seem to indicate that at the 5% (or less) level, the exact beam shape does not matter much as far as neutron production is concerned (at least not as long as most of the beam reaches the target) [8]. Energy deposition in the moderators and targets, however, is rather sensitive to the exact location and shape of the proton beam.

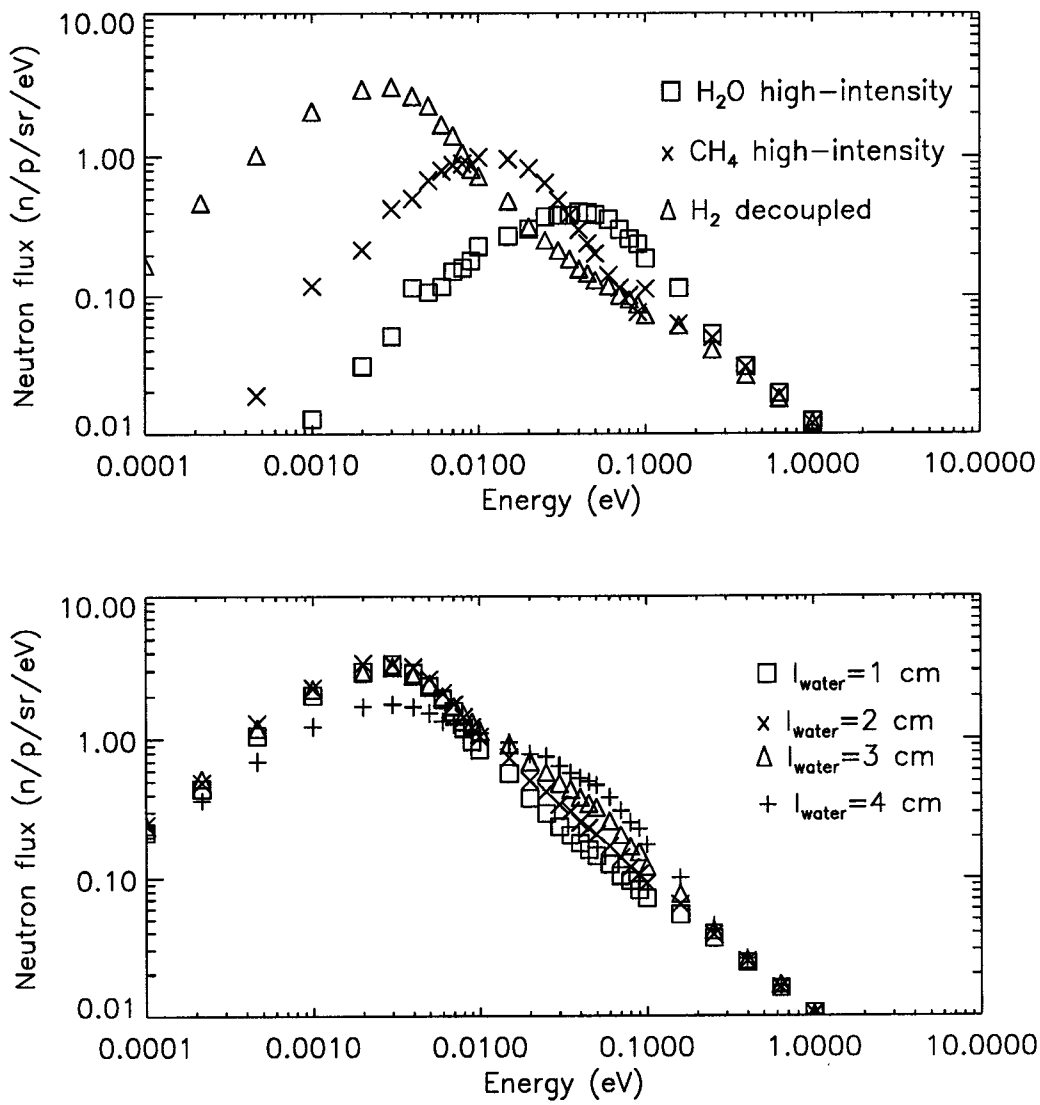

Figure 3: The top figure shows typical moderator spectra for liquid hydrogen, liquid methane, and light water moderators. The spectra were obtained for the moderators in flux trap geometry as described in the preceding section. The bottom figure shows composite moderator spectra for the light water/liquid hydrogen composite moderator described in the text. The total thickness of the moderator (water + liquid hydrogen) is fixed at 5 cm. Notice how the water spectrum emerges as the thickness of the liquid hydrogen layer is reduced. Compare the spectrum corresponding to $l_{water} = 4$ cm to the liquid methane spectrum in the top figure.

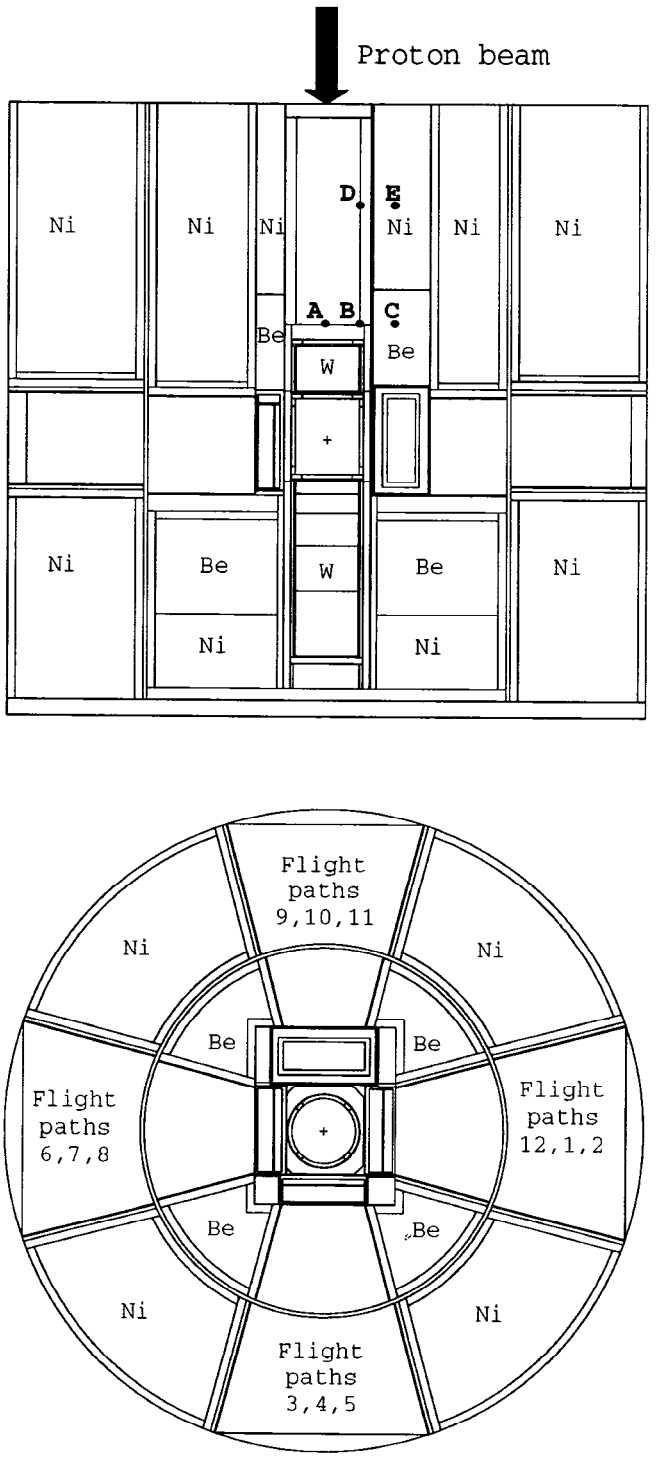

Figure 4: Computer model of the as-built LANSCE target station.

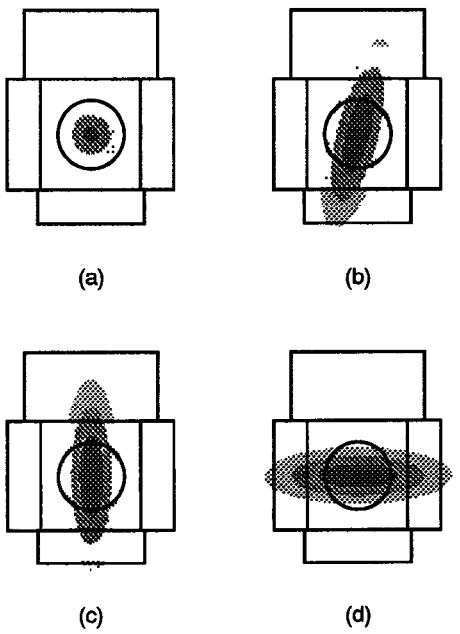

Figure 5: Beam spot shapes

In what follows, we assume that the beam is centered on target, and we vary its shape. Ideally, a circular beam spot on target would probably be the best situation one could imagine, Fig.5(a). Except for beam profile effects, target heating would be uniform azimuthally with no temperature gradients other than radial and axial gradients. Past experience at LANSCE has shown that if the proton beam is focussed to create a circular beam spot on target, the centerline thermocouples in the upper target register rather large temperatures, but energy deposition in the cryogenic moderator decreases. The beam was therefore defocussed to reduce centerline temperatures to acceptable levels. So far, we have not been able to reconcile in a fully satisfactory manner theoretical calculations of target temperatures with the measured temperatures. An effort is underway to explore systematically beam spot shapes effects. The results described below originate from studies performed in support of this effort.

The current production beam spot at LANSCE is assumed to be elliptical [9]. The beam profile is approximately Gaussian. The standard deviation along the semi-major axis and semi-minor axis of the ellipse are $\sigma_x = 3.8$ cm and $\sigma_y = 1$ cm, respectively, as measured by the thermocouples array above the target window. The semi-major axis is rotated (clockwise) 15° with respect to the normal to the viewed surface of the cryogenic moderator, Fig.5(b).

In our computer studies, we simulated these two situations, as well as the situation shown in Fig.5(c). In all cases, the beam was centered on target. The beam profile was cut off at three standard deviations, i.e., the beam spot is an ellipse with semi-major axis and semi-minor axis equal to 11.4 cm and 3 cm, respectively. The beam was started at the top of the LANSCE reflector/shield. Notice that the beam is somewhat too wide to fit inside the beam hole, and is therefore truncated by the reflector/shield. Most protons reach the target nonetheless because 86.47 % of the protons are contained within 2 standard deviations (and this fits easily in the beam hole). Some high-energy protons hit the reflector as may be the

(a) Cell	Energy deposition High-energy particles (MeV/p)	Energy deposition Low-energy n (MeV/p)	Energy deposition γ rays (MeV/p)	Total (MeV/p)	Power Density (W/l/μA)
Moderators					
(12,1,2)	0.573	0.665	0.217	1.454	2.177
(3,4,5)	0.562	0.632	0.187	1.381	2.202
(6,7,8)	0.721	0.717	0.222	1.659	2.397
(9,10,11)	0.0597	0.368	0.0201	0.448	0.596
Al canisters					
(12,1,2)	0.567	0.0502	0.248	0.865	2.688
(3,4,5)	0.570	0.0467	0.199	0.816	2.587
(6,7,8)	0.710	0.0519	0.218	0.980	3.017
Inner (9,10,11)	0.553	0.0561	0.293	0.902	1.801
Outer (9,10,11)	0.411	0.0394	0.239	0.690	2.048
Targets					
Upper	246.203	0.484	14.839	261.5	475.6
Lower	204.263	0.375	15.667	219.3	103.4

Table 2: Energy deposition for the beam profile shown in Fig.5(a)

case in practice.

Tables 2-4 summarize the results of our computer study. In particular, the study confirms that the heat load in the cryogenic moderator decreases when going from the production beam to a circular beam; energy deposition in the target increases. The energy deposited in each cell is the sum of three contributions: The high-energy contribution includes heating from inelastic scattering of high-energy (> 20 MeV) primary and secondary particles; The low-energy (< 20 MeV) contributions include inelastic scattering of low-energy neutrons, and gamma-ray heating.

The variations in energy deposition either in the targets or in the moderators are rather modest, of the order of 10 to 20 %. Although not dramatic, these changes could affect a cooling system that is running close to its capacity. Finally, it is probably useful to emphasize that the energy deposition from high- or low-energy particles is virtually instantaneous compared to the time scale involved for a refrigeration or cooling system to react to a rapidly changing heat load.

Second set of studies : Beam location

The purpose of this study was to investigate the impact of beam location on target on the heat load in targets and moderators. More specifically, we considered extreme conditions where, for instance, the proton beam is directed directly to the cryogenic moderator, or hits the walls of the proton beam hole halfway down the hole, above the cryogenic moderator. These proton beam steering scenarios are somewhat extreme, but they set an upper bound on the heating conditions that may exist in the targets and moderators at LANSCE.

In order to simulate a worst case situation for the hydrogen moderator when the proton beam is directed above it, we used the beam spot shown in Fig.5(d) rather than the production beam spot. The preceding set of studies has shown that there is little difference between the beam spots shown in Figs.5(b), (c), or (d) anyway. Furthermore, in order to make the situation

(b) Cell	Energy deposition High-energy particles (MeV/p)	Energy deposition Low-energy n (MeV/p)	Energy deposition γ rays (MeV/p)	Total (MeV/p)	Power Density (W/l/μA)
Moderators					
(12,1,2)	0.536	0.630	0.208	1.374	2.058
(3,4,5)	0.640	0.617	0.204	1.440	2.296
(6,7,8)	0.679	0.674	0.218	1.571	2.270
(9,10,11)	0.0915	0.369	0.0756	0.481	0.640
Al canisters					
(12,1,2)	0.525	0.0467	0.238	0.810	2.517
(3,4,5)	0.762	0.0490	0.198	1.009	3.199
(6,7,8)	0.641	0.0495	0.206	0.897	2.761
Inner (9,10,11)	0.765	0.0550	0.294	1.114	2.224
Outer (9,10,11)	0.557	0.0405	0.236	0.834	2.476
Targets					
Upper	237.882	0.442	13.589	251.9	458.2
Lower	189.622	0.345	14.646	211.3	99.6

Table 3: Energy deposition for the beam profile shown in Fig.5(b)

(c) Cell	Energy deposition High-energy particles (MeV/p)	Energy deposition Low-energy n (MeV/p)	Energy deposition γ rays (MeV/p)	Total (MeV/p)	Power Density (W/l/μA)
Moderators					
(12,1,2)	0.566	0.622	0.208	1.396	2.091
(3,4,5)	0.668	0.613	0.189	1.471	2.345
(6,7,8)	0.673	0.664	0.215	1.553	2.244
(9,10,11)	0.0976	0.378	0.020	0.496	0.660
Al canisters					
(12,1,2)	0.546	0.0453	0.238	0.829	2.576
(3,4,5)	0.758	0.0471	0.204	1.009	3.199
(6,7,8)	0.687	0.0485	0.211	0.947	2.915
nner (9,10,11)	0.844	0.0568	0.285	1.186	2.368
Outer (9,10,11)	0.534	0.0405	0.236	0.811	2.407
Targets					
Upper	237.834	0.441	13.663	251.9	458.2
Lower	189.656	0.343	14.619	204.6	96.5

Table 4: Energy deposition for the beam profile shown in Fig.5(c)

A Cell	Energy deposition High-energy particles (MeV/p)	Energy deposition Low-energy n (MeV/p)	Energy deposition γ rays (MeV/p)	Total (MeV/p)	Power Density (W/l/μA)
Moderator (9,10,11)	0.0796	0.311	0.0168	0.407	0.541
Al canisters					
Inner (9,10,11)	0.500	0.0311	0.206	0.737	1.471
Outer (9,10,11)	0.586	0.0458	0.252	0.884	2.624
Targets					
Upper	192.783	0.349	11.075	204.2	371.4
Lower	160.927	0.301	13.137	174.4	82.2

Table 5: Energy deposition in the liquid H_2 moderator for proton beam at A, Fig.4

even worse, we started the beam right above the target, at different locations indicated by the letters A to E in Fig.4. So the beam is not truncated as it comes down the beam hole. Finally, we tried to spray as many high-energy protons as possible in the immediate vicinity of the targets and moderators by defocussing the beam further: The beam profile was cut off at 3.7 standard deviations (instead of 3 standard deviations).

The results are shown in Tables 5-9. Even when the beam is started right above the cryogenic moderator, although the energy deposited in the moderator is significantly larger, but not by several orders of magnitude – a factor of about 30 at most compared to a beam at location A. Notice that the situation corresponding to a beam at location C is not so far-fetched in practice. Indeed, the the cryogenic moderator is fed by a large pipe located directly above it, and running vertically parallel to the proton beam hole. This large pipe filled with liquid hydrogen provides a streaming path to the hydrogen moderator for any proton that hits the reflector in the vicinity of the pipe. We have made the requisite changes to our target computer model, and are in the process of testing this scenario. This situation is not limited to the hydrogen moderators: the other light-water moderators suffer from the same problem. The situation where the beam is started at location D is also a distinct possibility, should the beam drift towards the wall of the beam hole at some angle. Notice however that the effect is not particularly dramatic (if we ignore, for the sake of argument, the presence of the liquid hydrogen pipe just mentioned). The moderators are protected by the Ni and Be reflector/shield. The total length of Ni/Be above the moderators provides more than a stopping length for 800 MeV protons, thereby protecting the moderators against accidental excursions of the beam towards the moderators. The results for a beam started at location E confirm this.

Another interesting remark concerns the heat deposited in the moderating medium. From Tables 5-9, it is clear that the total energy deposited in the liquid hydrogen itself is a small fraction of the energy deposited in the entire moderator (Al canisters + liquid hydrogen). By far the largest amount of energy deposited in the moderator is deposited in the Al canisters. Of course, in practice, this energy is immediatly removed by the flow of liquid hydrogen in the inner canister, and it is the energy deposited in the liquid hydrogen plus the energy deposited in the inner canister that is considered in sizing the thermal capacity of the hydrogen circuit. The energy deposited in the outer canister is not so readily dissipated. It can only be dissipated by conduction through the sides of the canister that are directly in contact with the Be

B Cell	Energy deposition High-energy particles (MeV/p)	Energy deposition Low-energy n (MeV/p)	Energy deposition γ rays (MeV/p)	Total (MeV/p)	Power Density (W/l/μA)
Moderator (9,10,11)	0.240	0.241	0.0102	0.491	0.653
Al canisters					
Inner (9,10,11)	2.352	0.0400	0.151	2.543	5.077
Outer (9,10,11)	2.417	0.0293	0.128	2.574	7.641
Targets					
Upper	58.972	0.0944	5.150	64.216	116.8
Lower	63.605	0.114	8.074	71.793	33.9

Table 6: Energy deposition in the liquid H_2 moderator for proton beam at B, Fig.4

C Cell	Energy deposition High-energy particles (MeV/p)	Energy deposition Low-energy n (MeV/p)	Energy deposition γ rays (MeV/p)	Total (MeV/p)	Power Density (W/l/μA)
Moderator (9,10,11)	3.289	0.200	0.0066	3.496	4.650
Al canisters					
Inner (9,10,11)	31.839	0.0500	0.101	31.990	63.9
Outer (9,10,11)	7.507	0.0282	0.0830	7.618	22.6
Targets					
Upper	0.983	0.0530	2.945	3.933	7.154
Lower	11.678	0.0592	5.519	17.256	8.137

Table 7: Energy deposition in the liquid H_2 moderator for proton beam at C, Fig.4

D Cell	Energy deposition High-energy particles (MeV/p)	Energy deposition Low-energy n (MeV/p)	Energy deposition γ rays (MeV/p)	Total (MeV/p)	Power Density (W/l/μA)
Moderator (9,10,11)	0.289	0.208	0.0109	0.508	0.676
Al canisters					
Inner (9,10,11)	2.518	0.0366	0.163	2.718	5.426
Outer (9,10,11)	1.942	0.026	0.130	2.098	6.228
Targets					
Upper	65.818	0.106	3.844	69.8	127.0
Lower	55.967	0.101	5.760	61.8	29.1

Table 8: Energy deposition in the liquid H_2 moderator for proton beam at D, Fig.4

E Cell	Energy deposition High-energy particles (MeV/p)	Energy deposition Low-energy n (MeV/p)	Energy deposition γ rays (MeV/p)	Total (MeV/p)	Power Density (W/l/μA)
Moderator (9,10,11)	0.0362	0.0616	0.0062	0.104	0.138
Al canisters					
Inner (9,10,11)	0.337	0.0105	0.0904	0.438	0.874
Outer (9,10,11)	0.243	0.0075	0.0649	0.315	0.935
Targets					
Upper	0.0929	0.0017	1.183	1.278	2.235
Lower	0.396	0.0051	1.195	1.596	0.753

Table 9: Energy deposition in the liquid H_2 moderator for proton beam at E, Fig.4

reflector. If anything, this outer canister is the likely candidate for damage following a proton beam excursion. However, even in the worst case described above (location C), there seems to be enough heat conduction to keep the outer Al canister at a temperature well below the temperature range where structural damage to the material would compromise its mechanical integrity.

References

[1] J.M. Carpenter, R.A. Robinson, A.D. Taylor, and D.J. Picton, "Measurement and fitting of spectrum and pulse shapes of a liquid methane moderator at IPNS", Nucl.Instr.Meth., A**234**, 542 (1985).

[2] G.J. Russell, "Neutronics of the WNR target/moderator relevant to beam plug design", Procceedings of the Third Meeting of the International Collaboration on Advanced Neutron Sources, (ICANS-III), G.J. Russell, Ed., Los Alamos Scientific Laboratory report (March 1979), p.92.

[3] G.J. Russell, M.M. Meier, J.S. Gilmore, and A.D. Taylor, "Measurements of spallation target-moderator-reflector neutronics at the Weapons Neutron Research facility", Procceedings of the Fourth Meeting of the International Collaboration on Advanced Neutron Sources, (ICANS-IV), Y. Ishikawa, N. Watanabe, Y. Endoh, N. Niimura, and J. Newsam, Eds., National Laboratory for High-Energy Physics report, KENS-II (March 1981), p.210.

[4] G.J. Russell, M.M. Meier, H. Robinson, and A.D. Taylor, "Preliminary neutronics of a reflected T-shape premoderator/moderator for the Weapons Neutron Research facility", Procceedings of the Fifth Meeting of the International Collaboration on Advanced Neutron Sources, (ICANS-V), G. Bauer, D. Filges, Eds., KFA Jülich report Jul-Conf-45 ISSN 0344-5789 (October 1981), p.389.

[5] G.J. Russell, "LANSCE upgrade cold sources", Proceedings of the International Workshop on Cold Neutron Sources, Los Alamos National Laboratory report LA-12146-C (August 1991), p.471.

[6] R.E. Prael and H. Lichtenstein, "User guide to LCS: The LAHET Code System", Los Alamos National Laboratory report LA-UR-89-3014 (September 1989).

[7] H.G. Hughes, "Monte-Carlo simulation of the LANSCE target/moderator/reflector/shield geometry", Proceedings of the 10-th international collaboration on advanced neutron sources, (ICANS X), Los Alamos 3-7 October 1988 (American Institute of Physics, Bristol, 1989), p.455

[8] G.J. Russell, unpublished.

[9] R. Hutson, "An estimation of beamsize at the LANSCE target from vacuum thermocouple array data", Technical Note, July 24, 1991 - R. Hutson, "1L quad settings for adjusting

the beam size at the LANSCE target", Technical Note, July 26, 1991 - R. Hutson, "Some data/calculations about beam spot at LANSCE target", Technical Note, August 6, 1991.

Premoderator Studies for a Coupled Liquid-Hydrogen Moderator

Y. Kiyanagi, N. Watanabe*, H. Iwasa and Y. Nakayama

Department of Nuclear Engineering, Faculty of Engineering, Hokkaido Univ., Sapporo 060
*National Laboratory for High Energy Physics, 1-1 Oho, Tsukuba-shi, Ibaraki, 305

Abstract

A coupled liquid-hydrogen moderator with a premoderator is one of the most promising candidates for a cold neuron source at an intense pulsed spallation neutron source. The choice of the premoderator material is especially important since the neutronic performance strongly depends on the material. Premoderators of polyethylene, water and zirconium hydride have been studied experimentally. The cold neutron intensity from a moderator system with a ZrH_2 premoderator is unexpectedly low: about 75 % of that from a reference coupled liquid-hydrogen moderator with a polyethylene premoderator. However, the pulse widths (FWHM) are narrower than those from the reference modeartor, and the peak intensities are almost unchanged. We also discuss the function of the premoderator.

1. Introduction

We have developed a high-efficiency pulsed cold-neutron source: a coupled liquid-hydrogen moderator (5 cm thick) with premoderator at ambient temperature. (1) A gain factor of about 6 has already been achieved with a 2-cm thick polyethylene premoderator. What material is the best for the premoderator? In order to obtain a better understanding of this moderator system and to seek the best material we performed some experiments with three different premoderators of H_2O, ZrH_2 and, as a reference, polyethylene. At an intense pulsed spallation neutron source polyethylene cannot be used due to serious radiation damage; H_2O would be only one hydrogenous liquid material which could work under such conditions. ZrH_2 has often been proposed as one of the best candidates, probably because it has a high hydrogen density and a large cross section of the hydrogen local mode at about 130 meV, which may play an important role for supplying rich epithermal-neutrons to liquid hydrogen.

2. Experimental

The experimental set up used in the present experiments is shown in Fig. 1; it is the same as that used in previous measurements (1) The size of the liquid-hydrogen moderator is 12 cm wide, 12 cm high and 5 cm thick. The temperature of the liquid hydrogen was about 18 K. The liquid-hydrogen moderator with the premoderator was coupled to a graphite reflector having a size of about 1 m^3.

H_2O and ZrH_2 powders were contained in alminium boxes to form the necessary shape for a premoderator having a given thickness. The hydrogen content of the ZrH_x powder was confirmed to be x = 2.0 from a measurement of the lattice constant by x-ray diffraction as well as a chemical analysis. The number density of protons in the ZrH_2 powder filled in the container was 0.64×10^{24} /cm^3. As a pulsed-neutron source, the electron linac at Hokkaido University was used. The energy

spectra and time-distribution of neutrons at various energies were measured by the usual time-of-flight method and a crystal analyzer system used in the previous measurements.(1)

3. Neutrnonic Performance of a Coupled Moderator System with Various Premoderators

Figure 2 shows the premoderator gain factors as a function of the premoderator thickness. The maximum gain factor is obtained at about 3 cm thick for ZrH_2 and 2 ~ 3 cm for H_2O, which should be compared with 2 cm thick for polyethylene. Figure 3 shows the energy spectra from those

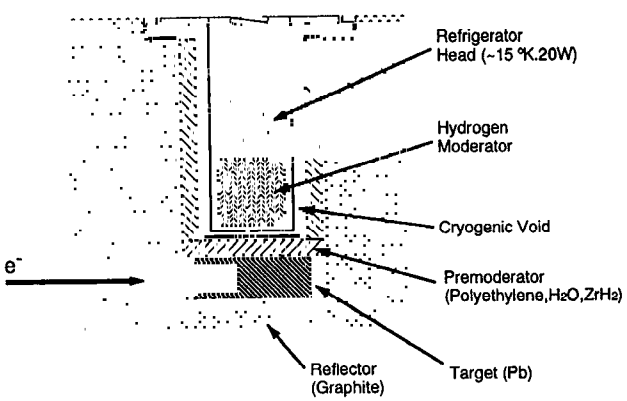

Fig. 1 Target-moderator-reflector assembly for a coupled liquid-hydrogen moderator with a premoderator.

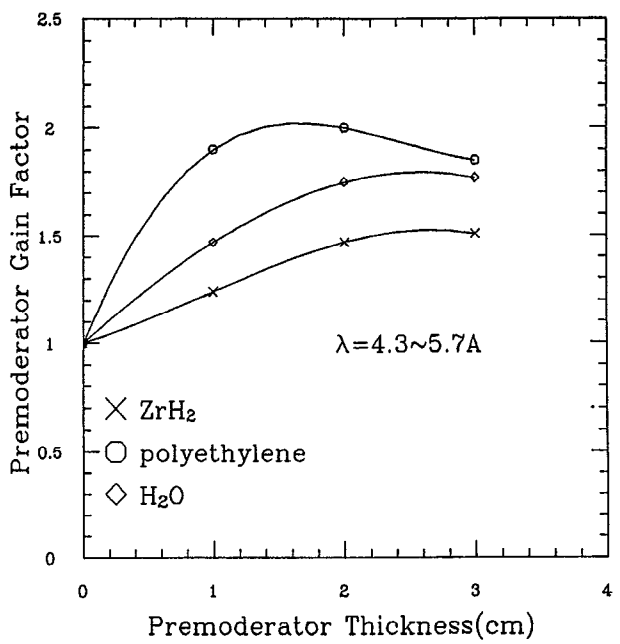

Fig. 2 Premoderator gain factors for a coupled liquid-hydrogen moderator with three different premoderators as a function of the premoderator thickness.

moderators with three different premoderators at the optimal thicknesses. The spectra are almost unchanged. Figure 4 shows the relative values of the premoderator gain factor for ZrH_2 (3 cm thick) and H_2O (3 cm thick) to polyethylene (2 cm thick) as a function of the neutron wavelength. The gain factor for H_2O is slightly less than unity: almost the same as in the polyethylene case. The gain factor for ZrH_2 is about 75% of that for polyethylene. This is due to the fact that ZrH_2 has no appreciable energy-exchange cross-section below 130 meV. From this result it can be concluded that the most important neutrons supplied to liquid hydrogen from premoderator are not epithermal neutrons, but thermal.

Figure 5 shows the time distributions of cold neutrons emitted from the coupled liquid-hydrogen moderator with a 3 cm thick ZrH_2 premoderator, compared with the 2 cm thick polyethylene premoderator case at two different wavelengths (left side is linear plots and the right semi-logarithmic plots). From the semi-logarithmic plots the decay seems to comprise at least two components: early decay and a long tail. The decay time for the former depends on the premoderator, while that of long tail is almost unchanged with the premoderator. This may be due to the fact that the reflector plays an important role for the decay of the latter component. Tailoring

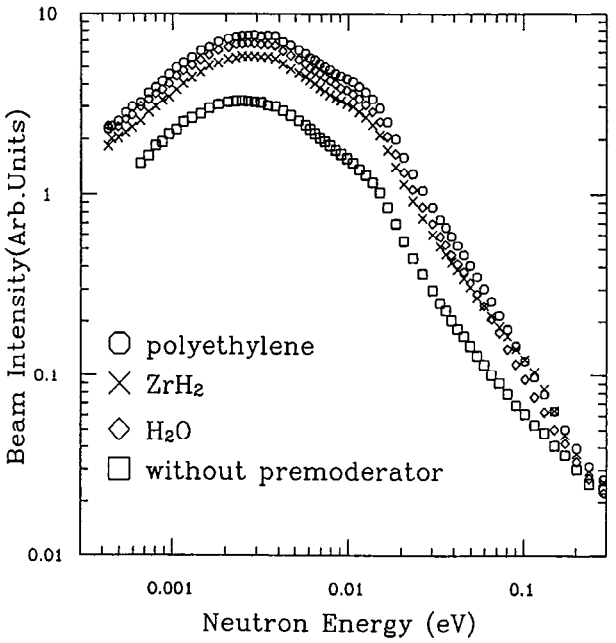

Fig. 3 Neutron energy spectra from a coupled liquid-hydrogen moderator with three different premoderators at the optimal thickness.

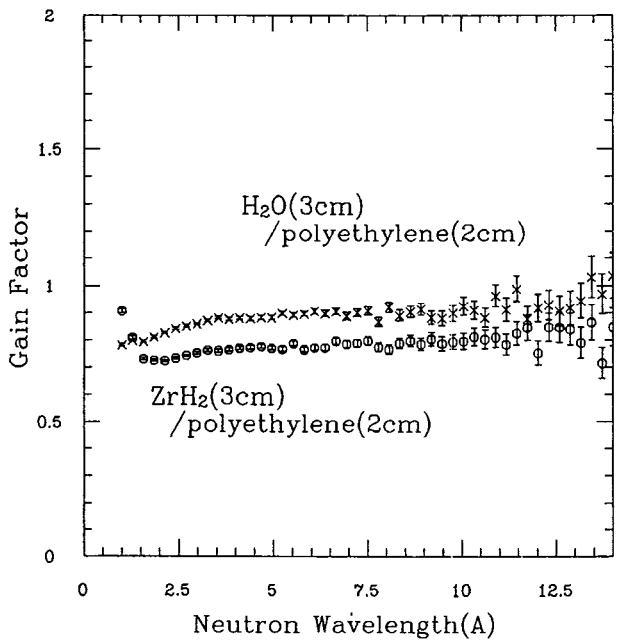

Fig. 4 Relative gain factors for ZrH_2 and H_2O systems to polyethylene as a function of the neutron wavelength.

of the long tail will be reported elsewhere in these proceedings (J. M. Carpenter et al.). The full-width-at-half-maximum (FWHM) pulse widths are plotted in Fig. 6 as a function of the neutron wavelength. The values of FWHM for the ZrH_2 system is about 75-80% of the polyethylene system. This means that the peak intensity is not so much decreased, as shown in Fig. 7. For high resolution neutron-scattering experiments, we proved that the figure-of-merit of the neutron source is proportional only to the pulse peak height, provided that a neutron guide tube of the required length can be used.(2) However, since a guide tube beyond 200 m long is unrealistic, narrower pulses are more acceptable as long as the peak intensity is conserved.

4. Function of Premoderator

In order to understand the neutronic characteristics obtained above we performed some elementary experiments. As the first stage we measured bare rectangular parallelepiped moderators of each premoderator material. The energy spectrum from each moderator was measured in a slab geometry at three different thickness. Figure 8 shows the results for ZrH_2 and polyethylene moderators. In the case of polyethylene, the thermal equilibrium (Maxwellian) spectrum is already recognized at 2 cm thick, while for ZrH_2 the spectrum is far before equilibrium. The result for H_2O is close to that of polyethylene. The result gives a qualitative explanation for the measured thickness dependence of the premoderator gain factors shown in Fig. 2. Figure 9 compares the spectrum from each bare moderator of the optimal thickness for the premoderator. The neutron intensity from the 3 cm thick ZrH_2 is much smaller than those from 3 cm thick H_2O and 2 cm thick polyethylene.

We then measured the neutron intensities from each premoderator (hydrogen moderator is removed from the system shown in Fig. 1). Figure 10 shows the result where the energy spectrum from the

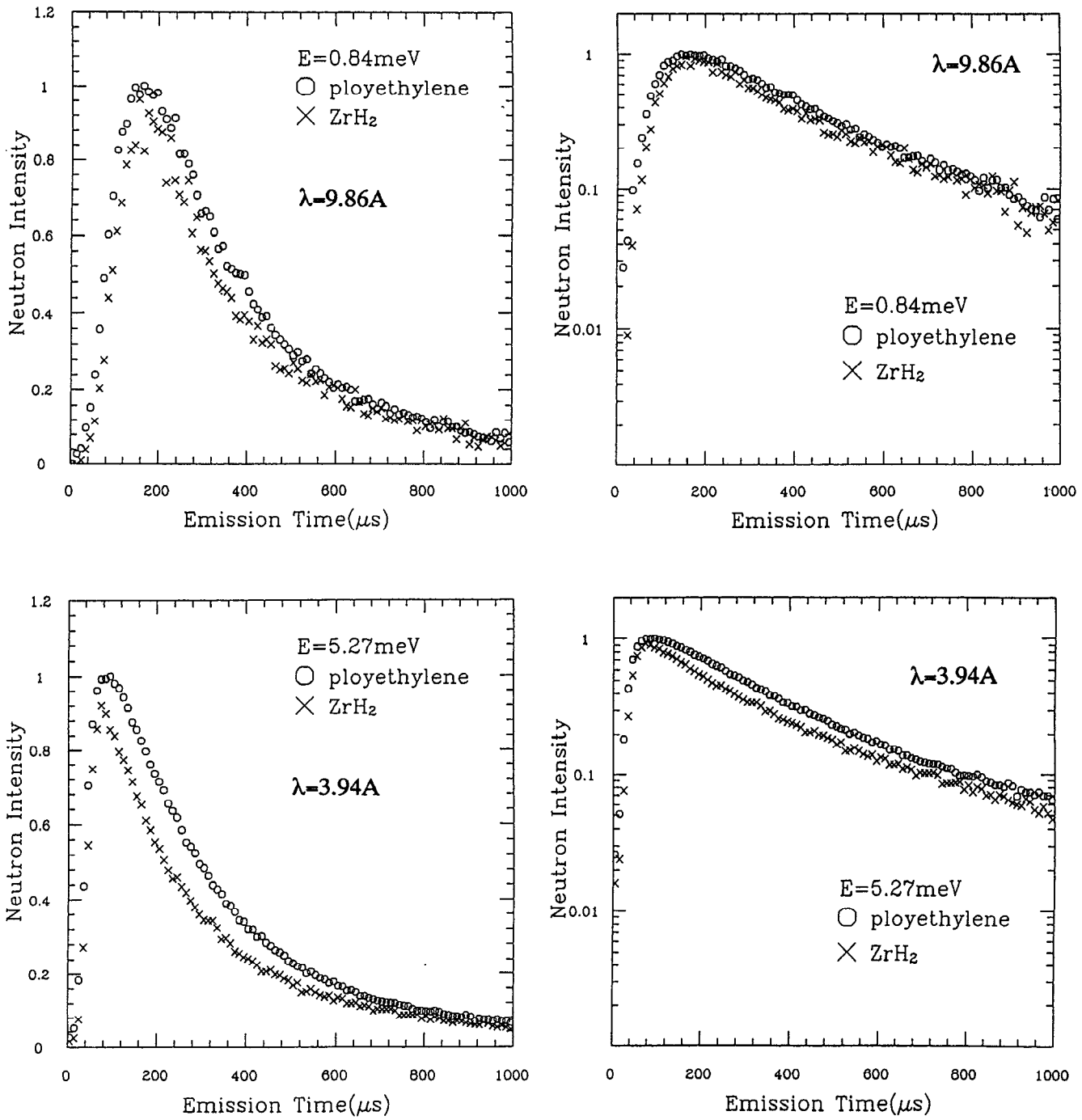

Fig. 5 Time distributions of cold neutrons at two different wavelengths from ZrH_2 and polyethylene systems.

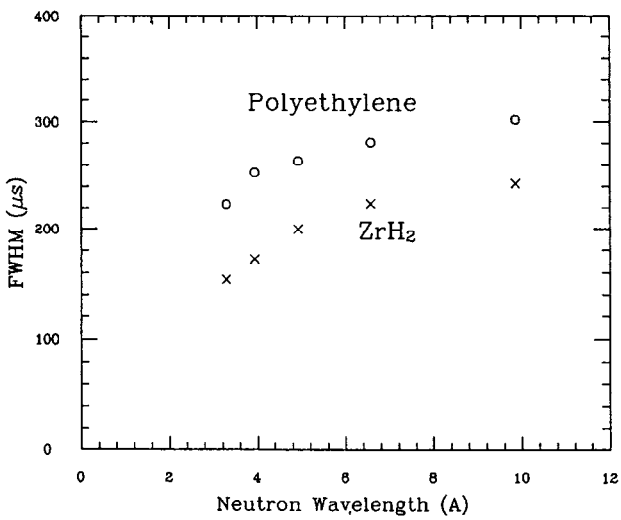

Fig. 6 Pulse widths (FWHM) for ZrH_2 and polyethylene systems as a function of the neutron wavelength.

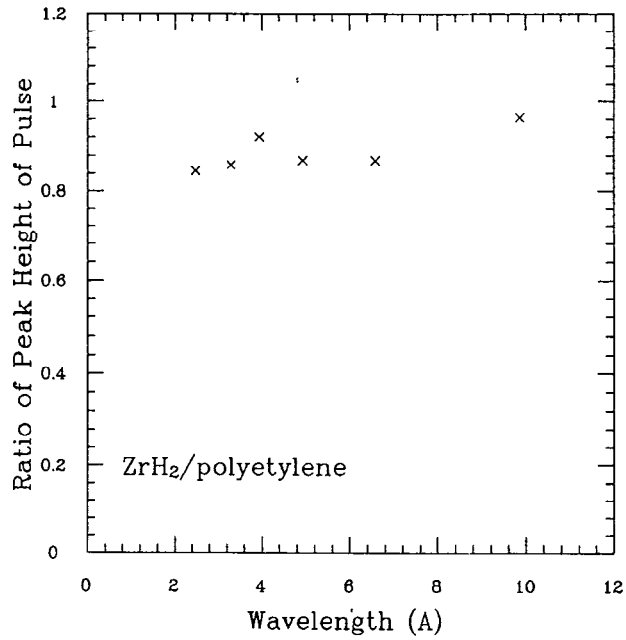

Fig. 7 Peak heights of the neutron pulses from the ZrH_2 system relative to polyethylene as a function of the neutron wavelength.

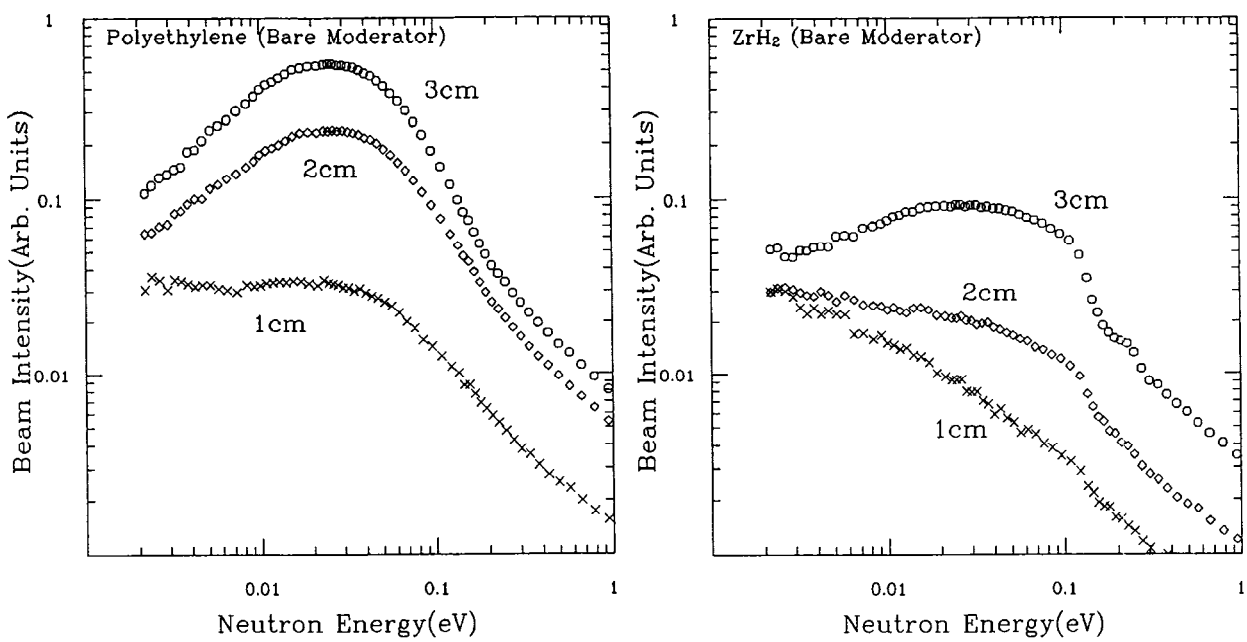

Fig. 8 Neutron energy spectra from bare ZrH_2 and polyethylene moderators of three different thicknesses.

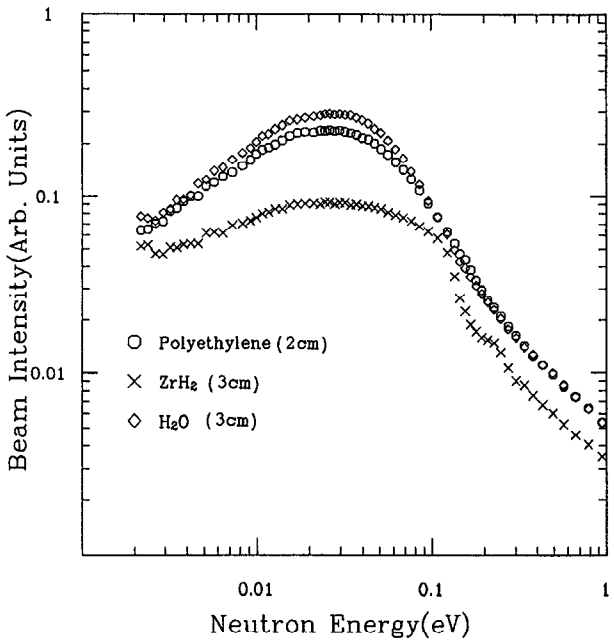

Fig. 9 Comparison of the neutron-energy spectra from each bare moderator of the optimal thickness for the premoderator.

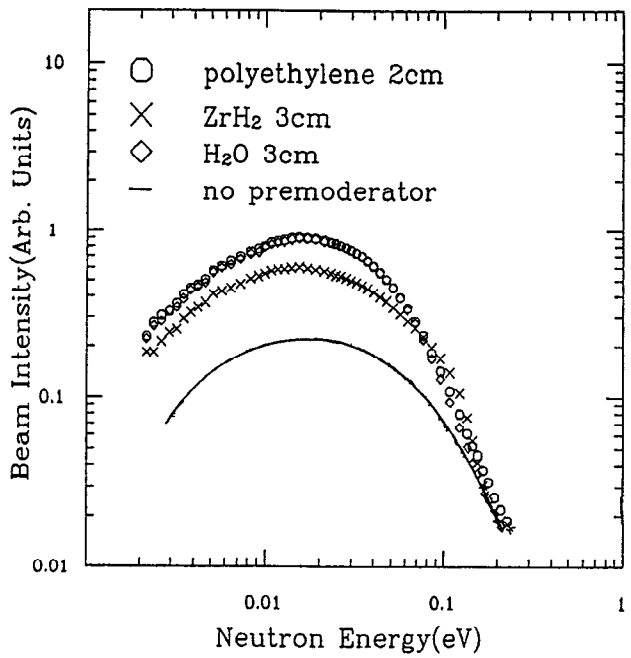

Fig. 10 Comparison of the neutron energy spectra from each premoderator box coupled to the reflector.

ZrH_2 box becomes more Maxwellian like and the intensity difference from the other two becomes much smaller than that of the simple bare moderator. This is because we measured the neutrons from a sort of re-entrant hole in a large hydrogenous moderator coupled to the reflector. The measured premoderator gain factors shown in Fig. 4 are almost governed by the thermal-neutron intensity ratios. This result again proved that the source neutrons to the liquid-hydrogen moderator are not epithermal neutrons, but thermal.

5. Conclusions

Although the ZrH_2 premoderator gives lower cold-neutron intensity than do polyethylene and H_2O premoderators in a coupled liquid-hydrogen system, the pulse widths are narrower than in the polyethylene case. This result indicates that the pulse shape can be controled by the choice of the premoderator material as well as by adjusting the premoderator thickness. Further studies towards this direction are in progress.

It is also concluded that in intense spallation neutron sources, H_2O is the best realistic premoderator material to obtain the highest gain factor.

References

(1) Y. Kiyanagi, N. Watanabe and H. Iwasa: Nucl. Instrum. Methods, A312, 561 (1992).
(2) N. Watanabe and Y. Kiyanagi: Physica B 180&181 (1992) 893.

Twelfth Meeting of the International Collaboration on Advanced Neutron Sources (ICANS XII),
24-28 May 1993, The Cosener's House, Abingdon, Oxfordshire, UK.

A Hybrid Be/D_2O Reflector for ISIS

L.L. Daemen, E.J. Pitcher, and G.J. Russell,
Manuel Lujan Jr. Neutron Scattering Center (LANSCE),
Los Alamos National Laboratory,
Los Alamos, New Mexico, USA

T.A. Broome and M. Holding,
ISIS facility,
Rutherford-Appleton Laboratory
Chilton, DIDCOT, Oxon

We examine how the replacement of the inner portion of the beryllium reflector near the cryogenic moderators at ISIS by heavy water affects the performance of the neutron source.

In order to give a new reflectometer at ISIS a full view of the hydrogen moderator, it became apparent that the portion of the beryllium reflector surrounding the liquid hydrogen moderator would have to be reshaped. Unfortunately, because of the very high radiation field, it is virtually impossible to retrieve the reflector to have it machined. The fabrication of a new Be reflector is an equally unattractive solution in view of the rather high costs of Be and Be machining. A possible alternative is to abandon the idea of using Be around the cryogenic moderators, and replace Be with some other reflecting medium. Although heavy water is not as good a material for neutron reflection as beryllium, the calculations presented below show that it is a very acceptable substitute. In practice, one would build a stainless steel container shaped like the piece of Be reflector to be replaced, and fill it with heavy water. Computer simulations based on the LAHET Code System show that the neutronic penalties associated with this operation are acceptable.

The model used for the Monte-Carlo simulations does not have many of the engineering realities of the actual target system. Some of the most drastic simplifying assumptions are

- The target is a solid cylinder; the plates and their cladding were not mocked-up,
- A D_2O jacket surrounding the target cylinder to take into account the presence of coolant,
- Details of the steel pressure vessel surrounding the target were ignored,
- Details of the moderators and the canisters surrounding them were left out,
- The moderators have not been rotated,
- The openings cut in the reflector in front of the moderators have zero angular opening.

(The model is not unlike the computer models used in the initial design of ISIS [..], with perhaps a slightly greater degree of details.) Of course, some (if not most) of the details that

	All Be refl.	Be/D_2O refl.	All D_2O refl.
H_2O (fore)	1	1	0.71
H_2O (aft)	1	1.1	1.2
CH_4	1	0.93	0.81
H_2	1	0.86	0.70

Table 1: Calculated (relative) intensities for a Be/D_2O and a pure D_2O reflector at ISIS. Neutrons with energy E < 100 meV define the "useful" signal.

	All Be refl.	Be/D_2O refl.	All D_2O refl.
H_2O (fore)	14 ± 0.7	13 ± 0.7	10 ± 1
H_2O (aft)	32 ± 2	26 ± 2	24 ± 2
CH_4	35 ± 2	33 ± 2	30 ± 2
H_2	52 ± 3	58 ± 3	58 ± 2

Table 2: Second moment of the time distribution ($\sim$ pulse width) for a Be/D_2O and a pure D_2O reflector at ISIS. Neutrons with energy E < 100 meV define the "useful" signal.

were omitted are important for an absolute determination of the neutron source performance. However, this need not concern us here, and the model is probably adequate for our purpose. The results will thus be quoted in terms of performance *relative* to, say, a pure Be reflector. We studied not only the effect of a partial replacement of the Be reflector by D_2O (as described above), but also the effect of replacing the entire reflector by D_2O. This latter situation, besides its intrinsic interest, might become relevant one day if more moderator replacements are required or requested by the users.

Our reference case is an all Be reflector - a situation similar to the present ISIS target station. We then replaced the inner part of the reflector surrounding the cryogenic moderators by a heavy water tank (Fig.1), and determined the penalty paid in terms of neutron current at each moderator (relative to what the current was for an all-Be reflector). In the next computer simulation, we turned the entire reflector into heavy water. In both cases, we also calculated the second moment of the time distribution averaged over all neutrons with energy E < 100 meV:

$$\sigma = \frac{1}{100\mathrm{meV}} \int_0^{100\mathrm{meV}} (\overline{t^2} - \bar{t}^2)^{1/2} dE,$$

where $\bar{t}$ is the mean-emission time for neutrons leaking from the moderator for a neutron with energy E. In all cases it was assumed that the proton pulse is a delta function at $t = 0$. The quantity σ is a measure of the pulse width. The results are summarized in Tables 1 and 2.

The replacement of the central portion of the Be reflector by D_2O does not affect adversely the performance of the water moderators in a significant manner. The effect is more pronounced for the cryogenic moderators. Interestingly, the intensity from the aft light water

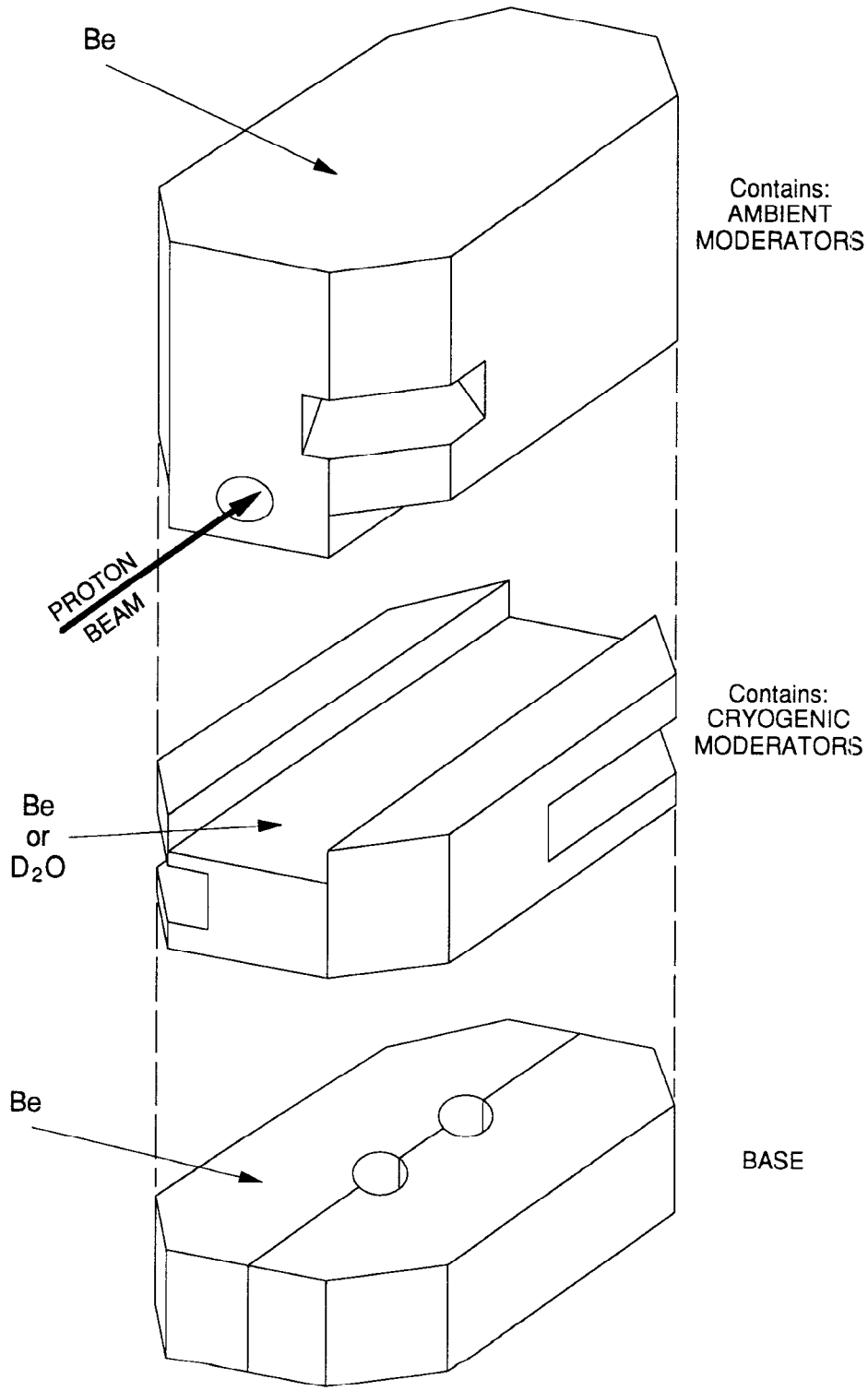

Figure 1: Geometry of the neutron reflector at ISIS

moderator *increases.* A possible explanation is that the average mean free path in D_2O of the (fast) neutrons produced in the target is larger than in Be. This seems to suggest that more neutrons are now able to leak through the D_2O reflector and find their way to the aft light water moderator than before (when the all-Be reflector was in place). Notice that the light water moderator is still surrounded by Be in its immediate vicinity. The situation is somewhat different for the hydrogen moderator which, following the same reasoning, should also see more neutrons, but is incapable of making efficient use of these extra neutrons because it is now entirely surrounded by D_2O, a much less efficient reflector than Be. An all-D_2O reflector leads to more drastic reductions in intensity - between 20% to 30% - except at the aft water moderator whose intensity *increases* further. In both cases (Be/D_2O or all D_2O) the pulse width is not significantly affected. The neutron pulses from the water moderators are somewhat sharper; the pulse width of neutron pulses from the liquid hydrogen moderator are somewhat broader, but altogether the resolution of the various moderators should not be dramatically affected.

References

[1] F. Atchison, "A theoretical study of a target reflector and moderator assembly for SNS", Rutherford-Appleton Laboratories Internal Report, RL-81-006, (1981).

Studies of Decoupled Composite Moderators of Liquid Hydrogen and Zirconium Hydride

Y. Kiyanagi[a], J. M. Carpenter[b], N. Watanabe[c], H. Iwasa[a] and M. Nakajima[a]

[a]Department of Nuclear Engineering, Hokkaido University, Sapporo, Japan.
[b]Argonne National Laboratory, Argonne, Illinois and Visiting Scientist, National Laboratory for High Energy Physics, Tsukuba, Japan.
[c]National Laboratory for High Energy Physics, Tsukuba, Japan.

Abstract

We report the results of a series of measurements of the intensities and pulse shapes of decoupled composite 2 cm-thick liquid Hydrogen moderators, with various thickness of cold Zirconium hydride backing.

Introduction

The purpose of these studies is to explore the possible alternatives to liquid methane as a moderator to provide short pulses of thermal and cold neutrons in high power pulsed spallation neutron sources. The attractive properties of liquid methane in this application are well known, which follow from its reasonably low temperature in the liquid state ($T_{melt} \sim 90°K$), its high proton density and its excellent thermalizing power extending to small energy transfers ($\Delta E_{rot} \sim 1.$ meV). However, radiation damage in liquid methane leads to the release of Hydrogen gas and to the accumulation of solids which obstruct flow and diminish heat transfer. These problems are observable but manageable in present-day facilities, but especially the latter gravitates against the use of liquid methane in the high power facilities that are now being designed.

Liquid Hydrogen has the advantage that it is insensitive to radiation damage, in that the products of radiolysis rapidly recombine into the parent material (although the low-temperature para form tends to revert to the high-temperature normal ortho-para mixture under intense irradiation). Additionally, Hydrogen remains liquid to lower temperatures ($T_{melt} \sim 15°K$) than methane and exists at near liquid density as supercritical vapor at reasonable pressure ($p_{crit} \sim 15$ atm) still at low temperature ($T_{crit} \sim 35°K$), which are engineering advantages. The disadvantages of liquid Hydrogen are also well known, namely its relatively low proton density and its relatively poor thermalizing power ($\Delta E_{rot} \sim 15.$ meV), which inhibits thermalization to the low temperature of the liquid.

Zirconium hydride, ZrH_2, on the other hand, has a high proton density and is also stable at high levels of irradiation and at reasonably high temperatures; engineering data exist in relation to its use in TRIGA reactor fuel. However, ZrH_2 lacks thermalizing power at low energies because the proton is so tightly bound in the metal lattice ($\Delta E_{vib} \sim 130.$ meV). Composite moderators in which the viewed layer is of liquid Hydrogen and the backing is of Zirconium hydride have the prospect of providing the high efficiency and short epithermal pulse structure that follow from the high proton density of the backing material, and the reasonably low spectral temperature and efficient thermalization that characterize liquid Hydrogen. Furthermore, the cryogenic material in a composite moderator will be of smaller volume than in a monolithic moderator, so that the

cryogenic cooling requirements are reduced in proportion to the volume, since the backing material can assumedly be cooled separately and less aggressively. Still further, depending on the relative positions of primary neutron source, moderator and backing, the backing may function as premoderator, further reducing the cryogenic heat load. The present work extends the earlier investigations of composite 5 cm thick liquid Hydrogen moderator systems with ambient temperature ZrH_2, H_2O and polyethylene premoderators.

We have investigated systems consisting of liquid Hydrogen 2 cm thick with 0 to 3 cm thick Zirconium hydride backings, reflected with graphite and decoupled with Cadmium. We have measured spectral intensities for wavelengths between 0.3 and 13. Å, and determined the pulse shapes for neutrons of wavelength from 1. to 10 Å. We present pulse widths and comparably-normalized spectra as functions of wavelength for the studied systems, and provide detailed pulse shapes for selected wavelengths.

Experimental Arrangements

The Hokkaido University 45 MeV electron linac provided a pulsed fast neutron source for the measurements, operating at approximately 50 Hz, with 0.3 μA time average current and 20 nsec pulse width for energy spectrum measurements and at 30 μA current and 3 μsec pulse width for pulse shape measurements. The target was a water-cooled lead block. Figure 1 shows the moderator-reflector assembly, which consisted of a graphite reflector approximately $1 \times 1 \times 1$ m^3 in volume, a $2 \times 12 \times 12$ cm^3 18 K liquid Hydrogen moderator. Packed Zirconium hydride powder, at a hydrogen number density of 0.64×10^{24} gm/cm^3, was contained in Aluminum cans. A thermocouple in the backing moderator registered the temperature, which was the same as that of the Hydrogen in these studies. Cadmium apertures defined the 10×10 cm^2 viewed area of the moderator, and the beam path void was lined with Cadmium. The electron beam struck the target in the direction perpendicular to the plane of the figure.

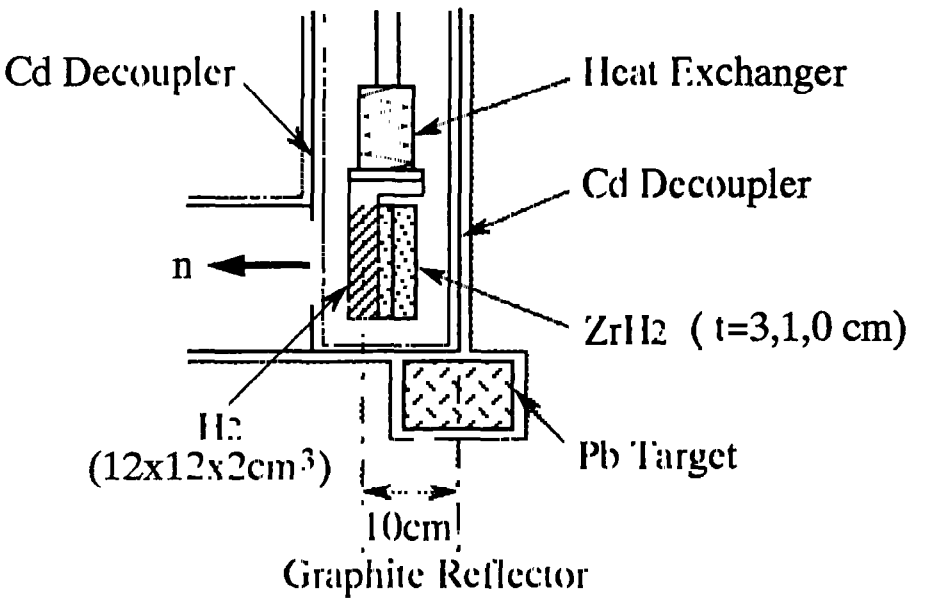

Fig. 1 Decoupled composite Liquid Hydrogen -Zirconium hydride moderator system

The measuring system for the spectra and pulse widths was the same for these measurements as is described elsewhere[1]. The time resolution of the analyzer system was approximately 0.1 %. Time channels were 5 μsec long for the pulse shape measurements.

Energy Spectra

Figure 2 shows the flux per unit energy normalized to the same electron beam current and for fixed target and liquid Hydrogen positions. Also shown is the spectrum measured earlier for a 5-cm-thick liquid Hydrogen moderator, approximately normalized for the same conditions. At low energies the shapes of the spectra are almost identical. The intensities increase with increasing thickness of ZrH_2; for 3 cm thickness, the intensity is almost the same as for 5 cm thick liquid Hydrogen with no premoderator.

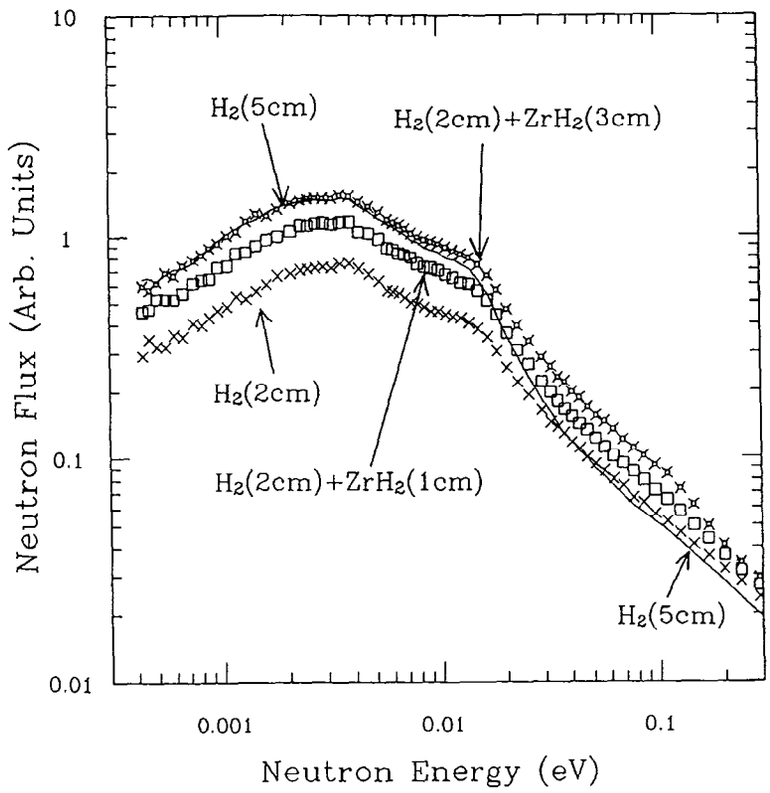

Fig. 2 Flux per unit energy for 2 cm thick liquid Hydrogen moderators with 0, 1 and 3 cm thick Zirconium hydride premoderators, and for a 5 cm thick liquid Hydrogen moderator with no premoderator.

Figure 3 shows the ratios of the spectral intensities for the cases with ZrH_2 to the intensity for the case for 2 cm L-H_2 only. The intensity gain factor at low energy is a factor of 2 for the 3 cm thick ZrH_2 case.

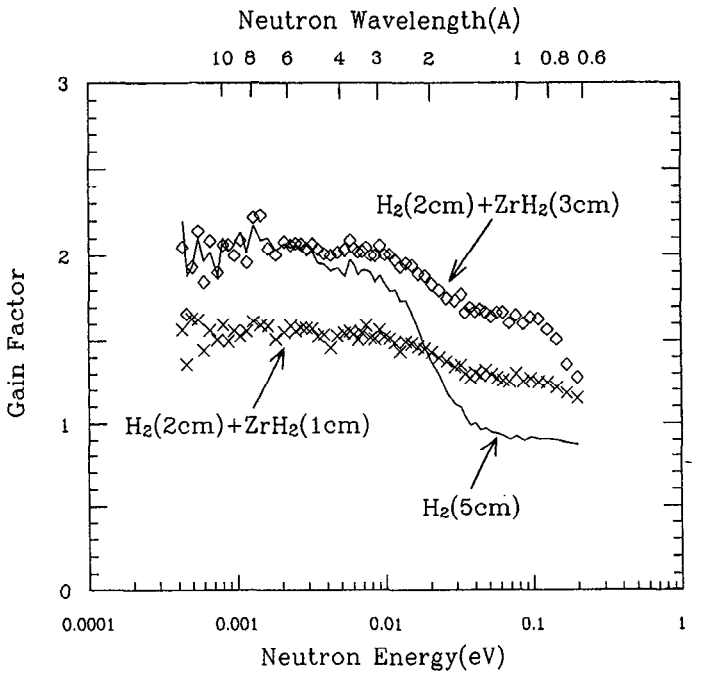

Fig. 3 Ratios of fluxes of liquid Hydrogen moderators with Zirconium hydride premoderators of various thickness and of a 5 cm thick liquid Hydrogen moderator with no premoderator, to the flux for the 2 cm thick moderator with no premoderator.

Pulse Shapes

Figure 4 shows the pulse shapes for three representative wavelengths, in linear and similogarithmic form, from the three different moderator systems and for the 5 cm thick liquid Hydrogen moderator. The time scales have been adjusted to correspond to the emission time, that is, the time that neutrons crossed the viewed surface of the liquid Hydrogen, by subtracting the known time of flight across the path from the moderator to the detector. The intensities for the three studied moderators are consistently normalized.

For each wavelength, the widths of the pulses and the peak intensities increase slightly as the thickness of the ZrH_2 layer increases. The changing width is almost entirely due to the change in the length of the decay time. The shapes of the leading edges are almost identical; we believe that this represents the real situation, because the rise times are longer than the resolution time of the analyzer system.

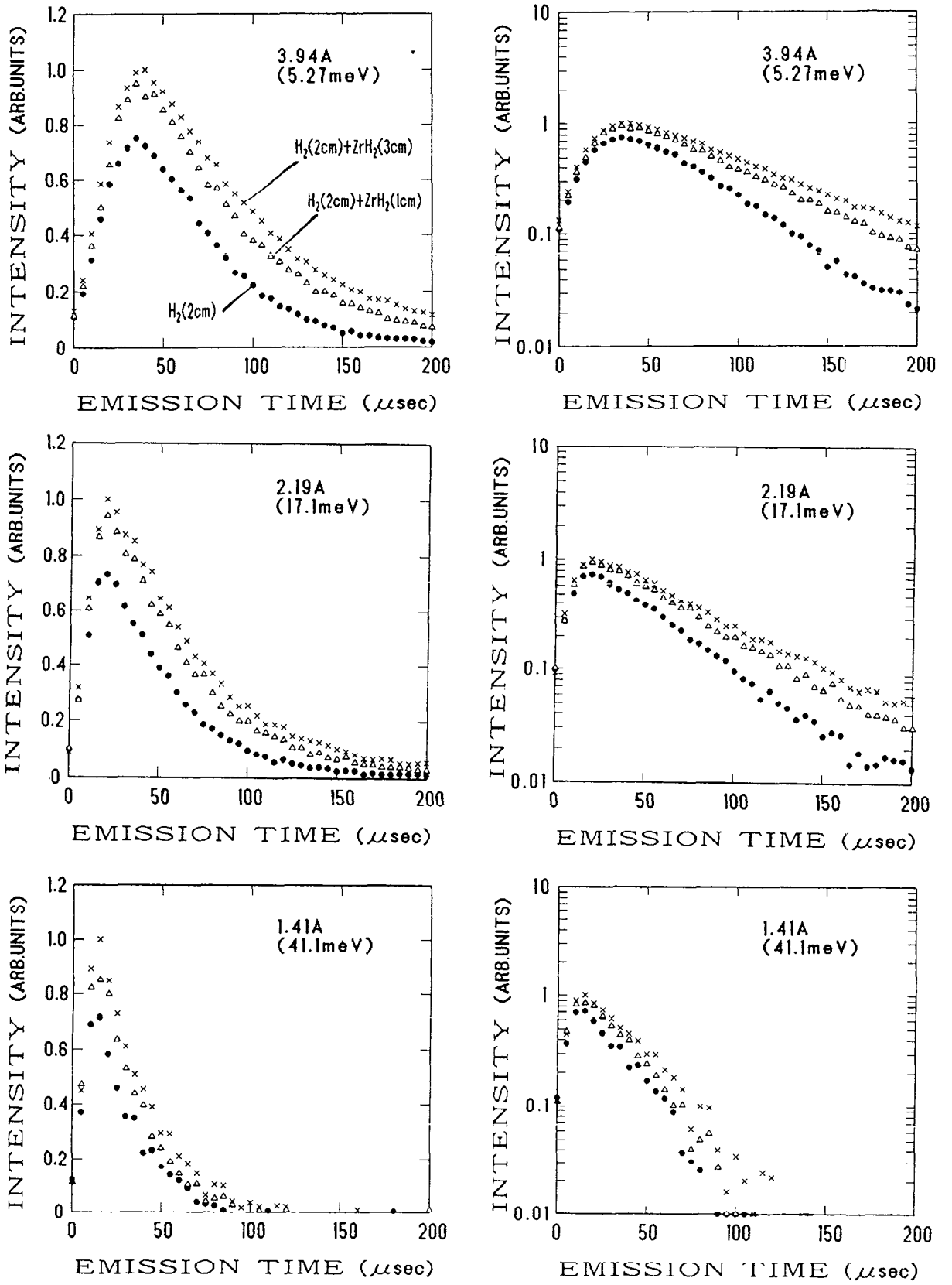

Fig. 4 Pulse shapes for neutron of 3.94, 2.19 and 1.41 Å wavelength, for 2 cm thick liquid Hydrogen moderators with 0, 1 and 3 cm thick Zirconium hydride premoderators.

Figure 5 shows the pulse FWHM as a function of wavelength, determined from data on all the wavelengths measured. For comparison, the figure also shows FWHM for the 5 cm L-H_2 and for 5 cm thick L-CH_4[2] and poisoned L-CH_4[3][4]moderators. The widths of the pulses of composite moderators studied are less than the widths for the 5 cm L-H_2 case at longer wavelengths.

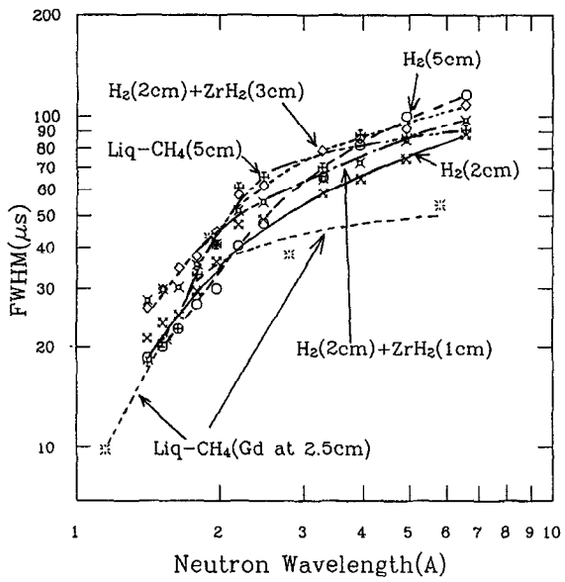

Fig. 5 Pulse FWHM as a function of wavelength for neutrons from 2 cm thick liquid Hydrogen moderators with 0, 1 and 3 cm thick Zirconium hydride premoderators, and from a 5 cm thick liquid Hydrogen moderator with no premoderator. For comparison, the figure also shows the width of pulses from a 12 × 12 × 5 cm liquid methane moderator and a 10 × 10 × 5 cm liquid methane moderator, poisoned with Gd 2.5 cm below the surface.

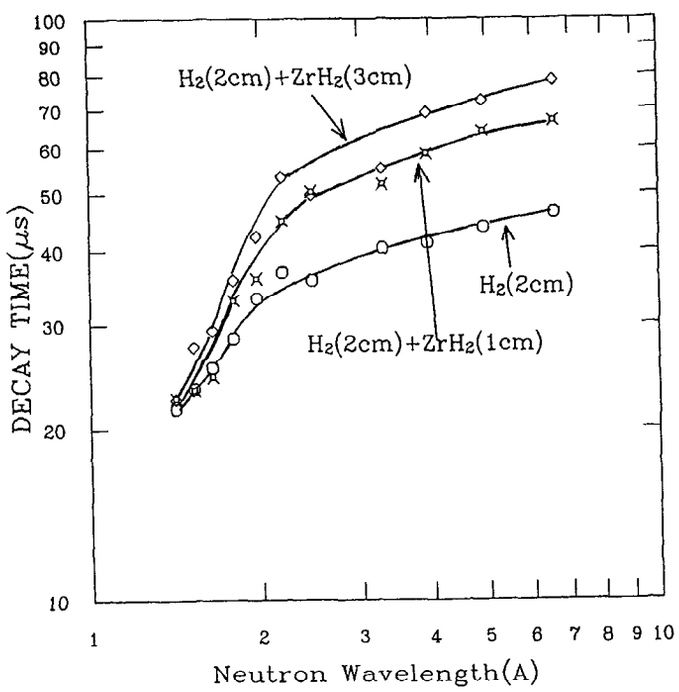

Fig. 6 Decay times of neutron pulses.

Figure 6 shows the decay times of the exponential functions fitted to the decay as a function of wavelength.

Discussion and Conclusions

We have found that composite moderators of liquid Hydrogen offer good prospects for providing high intensities and short pulses in high power pulsed spallation neutron sources. These are the first results on composite cold moderators. The measurements reported here probably do not represent a system that would actually be employed in practice, however, optimization within the framework of this idea will certainly lead to systems with better performance. Further work along this line is certainly justified. Meanwhile, the present results are a valuable benchmark against which to test calculations and to compare with other alternative moderator systems.

Intensities and to a lesser extent the spectra and pulse shapes of moderator systems depend sensitively on the relative arrangement of moderators, primary source(s) and reflectors. As systems become more complex, the problem of providing consistent normalization for different systems in different geometries becomes more difficult. We cannot resolve the question of how to present data so that results are precisely transferable from one geometry to another, but believe that the present results are reasonably representative of the performance of composite moderators in other source arrangements.

References

(1) Y. Kiyanagi, N. Watanabe and H. Iwasa, Nucl. Instrum. Methods, A312, 561 (1992).
(2) Y. Nakayama, Master's Degree thesis, Hokkaido Univ, Sapporo, 1992.
(3) R. L. Bywater, jr., R. E. Williams ad J. M. Carpenter, "Progress report on measurement and fitting of pulse shapes of moderators at IPNS,", Advanced Neutron Sources, 1988, Institute of Physics Conference Series Number 97, Institute of Physics, Bristol and New York, p. 655, (1989).
(4) R. L. Bywater, "Neutron emission-time distributions of mthane moderators at the Argonne National Laboratory Intense Pulsed Neutron source", Master's Degree Thesis, Iowa State University, Ames, Iowa, 1989.

List of Contributors

Volume 1
Instrument Workshop

Adams M A I - 73, I - 106
Aeppli G I - 60
Aksenov V L I - 124
Allen D I - 216
Allison J E I - 224
Anderson I S I - 347
Antson O I - 124
Arai M I - 260, I - 283
Asahi K I - 338
Balagurov A M I - 124
Besson J M I - 268
Böni P I - 347
Bokui T I - 260
Boothroyd A T I - 60
Boram A J I - 185
Bourke M A I - 224
Bragin S I I - 89
Brankowski J I - 89
Buffat P I - 347
Bulkin A P I - 124
Carlile C J I - 73, I - 106, I - 118
Carpenter J M I - 320
Chen J I - 208
Crawford R K I - 24, I - 144, I - 208
Crennell K I - 301, I - 308
Davis D I - 224
Doi M I - 338
Donley L I I - 36
Duppich J I - 368
Eckold G I - 232
Edwards L I - 158
Ellison A J G I - 144
Elsenhans O I - 347
Finney J L I - 1
Fitzsimmons M R I - 355
Forsyth J B I - 73
Friedli H P I - 347
Fujikawa I I - 166
Fujita M I - 260
Furusaka M I - 166
Geick R I - 97, I - 292
Goldstone J A I - 224, I - 273
Grimmer H I - 347
Hagen M I - 232, I - 314
Hamel G I - 268
Hammonds J P I - 36
Hannon A C I - 152, I - 283
Hauert R I - 347
Heenan R K I - 241
Hiismaki P I - 124
Hjelm R P I - 172
Howells W S I - 152
Hull S I - 268
Ikeda S I - 320
Jansen E I - 200
Jericha E I - 118
Jian Z Z I - 338
Johnson M W I - 32, I - 158, I - 185
Kleb R I - 36
Klotz S I - 268
Korneev D A I - 363
Krishna P S R I - 73, I - 106
Kudrjashev V A I - 124
Larson A C I - 273
Larson E I - 44
Lawson A C I - 224, I - 273
Leifer K I - 347
Loong C-K I - 36, I - 320
Loveday J S I - 268
Lysaght P I - 44, I - 52
Duppich J I - 368
Masuda Y I - 338
Mayer J I - 89
Mayers J I - 248
Mezei F I - 377
Mino M I - 260
Motokawa M I - 260
Mott E M I - 185
Müller K D I - 200
Muratov V G I - 124
Nastasi M A I - 355
Natkaniec I I - 89
Nelmes R J I - 268
Newport R J I - 152
Norris J I - 216
Nutter M I - 44, I - 52
Olivier B J I - 44, I - 52
Osawa M I - 166
Osborn R I - 60
Ostrowski G E I - 36
Otomo T I - 283
Paul D McK I - 60
Penfold J I - 347
Perring T G I - 60, I - 328
Prager M I - 106
Price D L I - 144

Priesmeyer H G I - 158
Pynn R I - 355
Quinton S I - 216
Rauch H I - 118
Reinartz R I - 200
Rennie A R I - 241
Rhodes N J I - 185
Ricketts R L I - 44
Robinson R A I - 44, I - 52, I - 273
Rustichelli F I - 158
Sakai K I - 338
Sandoval J P I - 44, I - 52
Sato H I - 338
Satoh S I - 166
Schäfer W I - 200
Schmidt W I - 97, I - 292
Schuster M I - 118
Seeger P A I - 172
Shi N I - 224
Shibata K I - 106
Simkin V G I - 124
Sivia D S I - 291
Skowronek R I - 200
Smith G S I - 355
Soderholm L I - 36
Söchtig J I - 347
Soper A K I - 152
Steigenberger U I - 232, I - 314
Suzuya K I - 166
Szepesvary A I - 200
Takahashi S I - 36
Taran Yu V I - 124
Taylor A D I - 60
Thiyagarajan P I - 208
Tietze-Jaensch H I - 97, I - 292
Tiitta A I - 124
Trounov V A I - 124
Ubukata K I - 260
Volin K J I - 144
von Dreele R B I - 273
Wagner W I - 368
Wardle A G I - 185
Watanabe N I - 166
Westerhuijs P I - 106
Will G I - 200
Wilson C C I - 132
Withers P J I - 158
Wright J S I - 158
Wilson R M I - 268

Volume 2

Proposals for new Spallation Neutron Sources

Aiginger H P - 26
Breunlich H P - 26
Brown B S P - 13
Bryant P J P - 26
Carpenter J P - 13
Cho Y P - 13
Crawford R K P - 13
Hübner K P - 26
Knox A E P - 13
Lengeler H P - 1
Pirkl W P - 26
Pynn R P - 7
Regler M P - 26
Rees G P - 26
Senichev Yu V P - 36
Schindl K P - 26
Schönauer H P - 26
Stavissky Yu Ya P - 36
Watanabe N P - 21
Wrulich A P - 26

Accelerator Workshop

Bailey J A - 57
Barratt P J S A - 109
Blumberg L N A -20
Bongardt K A - 115
Brown B A - 57
Brumwell F A - 57
Carpenter J A - 57
Cho Y A - 57
Craddock M K A - 1
Crawford K A - 57
Fathizadeh M A - 80
Gardner I S K A - 176
Heinrichs H A- 144
Horan D A - 57, A - 64
Irie Y A - 131
Jason A J A - 38, A - 49
Jerng D A - 57
Johnson K F A - 49
Kleb R A - 57
Knox A A - 57
Kustom R A - 57, A - 64, A - 159
Lessner E A - 57
Macek R J A - 25
McGhee D A - 57, A - 73, A - 80
Mannix R P A - 93
Martin S A A -153

Meads P F A - 153
Mills F A - 57
Moe H A - 57
Nath S A - 49
Nielsen R A - 57
Ninomiya S A - 137
Planner C W A - 4
Prior C R A - 11
Potts C A - 57
Rauchas A A - 57
Rees G H A - 168
Thompson K A - 57
Warsop C M A - 101
West N D A - 85
Wustefeld G A - 153
Yamane I A - 124
Zaplatin E A - 153
Ziegler K A - 153

Target Station Workshop

Allen G M T - 12
Arai M T - 80, T - 90
Baker G D T - 115
Bauer G S T - 132
Beard C A T - 26
Beljakov A A T - 144
Brewton R J T - 115
Bridge A T - 115
Broome T A T - 12, T - 20, T - 128, T - 156, T - 202
Brun T O T - 26, T - 115
Cappiello M T - 115
Carpenter J M T - 1, T - 95, T - 105, T - 164, T - 206
Chiba S T - 80
Clarke-Gayther M A T - 12
Conrad H T - 61
Crawford R K T - 95
Cummings C E T - 115
Daemen L L T - 26, T - 115, T - 181, T - 202
Davis D T - 115
Dementyev A D T - 71
Elson J S T - 115
Ermilov V G T - 144
Geissmann K T - 132
Grachev M I T - 53
Grisham D T - 115
Hins A G T - 1
Hjelm R P T - 115
Hogston J R T - 156
Holding M T - 156, T - 202
Howells W S T - 156
Ishibashi K T - 44, T - 80
Iwasa H T - 164, T - 196, T - 206
Jerng D W T - 105
Kernodle A T - 115
Kiyanagi Y T - 90, T - 164, T - 172, T - 196, T - 206
Kleb R T - 95
Knox A E T - 95
Konovalov I I T - 71
Kravchuk L V T - 53
Kuzin A V T - 53
Lebedev S G T - 53
Lobashev V M T - 53
Lomidze V L T - 144
Maehata K T - 80
Maslov A A T - 71
Mateev V A T - 53
Matsufuji N T - 44, T - 80
Meigo S T - 80
Melichov V V T - 144
Merrigan M A T - 115
Miroshnichenko V G T - 53, T - 71
Mosievskaya I Y T - 71
Nakahara Y T - 44
Nakajima M T - 164, T - 172, T - 206
Nakamoto T T - 44, T - 80
Nakamura T T - 80
Nakayama Y T - 196
Numajiri N T - 80
Pitcher E J T26, T - 115, T - 181, T - 202
Planner C W T - 12
Ponomarev O V T - 53
Robinson H T - 115
Russell G J T - 26, T - 115, T - 181, T - 202
Sazanov V N T - 53
Senichev Yu V T - 53
Shabalin E P T - 144
Sidorkin S F T - 53, T - 71
Sobolevsky N M T - 53, T - 71
Spitzer H T - 132
Stavissky Yu Ya T - 53, T - 71
Takeda H T - 44, T - 80
Tretyakov I T T - 71
Trushkin V I T - 71
Wagner W T - 132
Wakuta Y T - 44, T - 80
Walker L T - 115
Watanabe N T - 90, T - 164, T - 172, T - 196, T - 206
Watanabe Y T - 80
Wilson W B T - 26
Woods R T - 115
Yoshizawa Y T - 44

Subject Index

Volume 1

Instrument Workshop

Calibration	I - 144, I - 208
Chopper spectrometers	I - 24, I - 36, I - 44, I - 52, I - 60, I - 320, I - 328
Choppers	I - 36, I - 44, I - 124, I - 377
Cold neutrons	I - 1, I - 24, I - 73, I - 118
Crystal analyser spectrometers	I - 24, I - 73, I - 89, I - 97, I - 106, I - 232, I - 292, I - 314
Data acquisition electronics	I - 216
Data analysis	I - 241, I - 283, I - 291, I - 301, I - 308
Database	I - 308
Data visualisation	I - 32, I - 60, I - 292, I - 301
Detectors	I - 32, I - 44, I - 52, I - 144, I - 185, I - 200, I - 208
Diffractometers	I - 24, I - 73, I - 124, I - 132, I - 144, I - 152, I - 166, I - 172, I - 200, I - 377
Diffuse scattering	I - 132
ENGIN	I - 158
eVS	I - 248
Fixed scattering geometry	I - 1
GLAD	I - 144
^{3}He filter	I - 338
HET	I - 328
High energy excitations	I - 1, I - 60
High pressure	I - 268
High resolution diffraction	I - 1, I - 24, I - 73, I - 124
HIPD	I - 273
HRFD	I - 124
HRMECS	I - 36, I - 320
Intermultiplet transitions	I - 1
IRIS	I - 73, I - 106, I - 301
JULIOS	I - 200
Laue technique	I - 132
LOQ	I - 241
LRMECS	I - 36, I - 320
Magnetic diffraction	I - 1, I - 73, I - 260, I - 273
MARI	I - 283
MAPS	I - 60
Monte Carlo calculations	I - 172
NERA-PR	I - 89
Neutrino physics	I - 1
Neutron Compton scattering	I - 248
Neutron guides	I - 368
Neutron storage	I - 118
NPD	I - 273
PHAROS	I - 44, I - 52
Phase transition	I - 132, I - 232
Polarisation	I - 32, I - 338, I - 347, I - 355, I - 363
Powder diffraction	I - 268, I - 273
PRISMA	I - 232, I - 314
Pulsed magnetic fields	I - 260
Reflectometers	I - 24, I - 355
Resolution	I - 36, I - 89, I - 124, I - 144, I - 314, I - 320, I - 328

ROTAX I - 97, I - 292
SANDALS I - 308
SANS I - 166, I - 172, I - 241, I - 301, I - 377
Signal processing I - 200
Simultaneous diffraction and spectroscopy I - 73, I - 89
Single crystal measurements I - 24, I - 60, I - 132
SPEAR I - 355
SPIDA I - 152
Stress measurements I - 158, I - 224
Supermirrors I - 347, I - 368
SXD I - 132
Time resolved studies I - 1, I - 232
VESTA I - 118
WINK I - 166

Volume 2

Accelerator Workshop

Acceleration A - 11
Accumulator A - 25, A - 35
Amplifier A - 65
Availability A - 80
Beam-Losses A - 89, A - 125, A - 174
Buncher A - 52
Cathode-Follower A - 131
Chopper A - 104
Compressor A - 2, A - 115, A - 168
Control-System A - 93
Costs A - 148, A - 179
Database A - 93
Deflector A - 52
Diagnostics A - 105
Dual Harmonic A - 11, A - 60, A - 74
Emittance A - 43
e-p-Instability A - 30
Feed-Forward A - 112
Ferrite A - 64
FFAG A - 1, A - 153, A - 159
Funnelling A - 49
H-minus A - 35, A - 41, A - 169
H-zero A - 25
Ion-Source A - 131, A - 137
Linac A - 4, A - 20, A - 35, A - 49, A - 85, A - 115, A - 144
Magnet A - 160
Matching A - 115
NCNR A - 33
Neutron-Source A - 3, A - 20, A - 57, A - 73, A - 80, A - 115, A - 153, A - 168, A - 176
Plasma-Source A - 41
Power Supply A - 60, A - 73, A -80
PSR A - 25
Q-Values A - 105
Radio-frequency A - 64, A - 109, A - 131, A - 137, A - 154, A -160

Reliability	A - 80, A - 90, A - 141, A - 180
Resonant	A - 60, A - 73
Room Temperature	A - 144
Space Charge	A - 125
Shielding	A - 179
Simulation	A - 14
Stability	A - 131
Superconducting	A - 144, A - 154
Synchrotron	A - 2, A - 5, A - 20, A - 124, A - 137
Target	A - 7, A - 22
Tuning	A - 111
Two-Stage	A - 95

Target Station Workshop

Calculational Methods	T - 26, T - 44
Codes	T - 26, T - 44
Cooling Systems	T - 20
HETC	T - 26, T - 44
High Power	T - 61, T - 95, T - 105, T - 115, T - 128
Hydrogen Moderators	T - 132, T - 196, T - 206
Induced Activity	T - 20
IPNS	T - 1, T - 95, T - 105
ISIS	T - 12, T - 156, T - 202
LANSCE	T - 26, T - 115
Metal Hydrides	T - 206
Methane Moderators	T - 144, T - 156
MMF	T - 53, T - 71
Moderator	T - 61, T - 132, T - 144, T - 156, T - 164, T - 172, T - 181, T - 196, T - 206
Neutron Yields	T - 80,T - 90
New Sources	T - 95, T - 105, T - 115,T - 128
Proton Energy	T - 61, T - 164, T - 202
Remote Handling	T - 20
Tantalum	T - 12
Targets	T - 1, T - 12, T61
Tritium	T - 20
Uranium	T - 1, T - 71

ICANS - XII

List of Participants

M. ADAMS
ISIS Facility
Rutherford Appleton Laboratory
Chilton
Oxon
OX11 0QX
UK

Tel: + 44 235 446157
Fax: + 44 235 445720

V. AKSENOV
Frank Laboratory of
Neutron Physics
JINR
141980 Dubna
Moscow Region
RUSSIA

Tel:
Fax: + 7 096 2165085

M. ARAI
Physics Department
Kobe University
1-1 Rokkodai
Nada
Kobe 657
JAPAN

Tel: + 81 78 881 1212
Fax: + 81 78 881 7593

F. ATCHISON
Paul Scherrer Institute
CH-5232 Villigen
PSI
SWITZERLAND

Tel: + 41 56 993256
Fax: + 41 56 992327

I. F. BAILEY
ISIS Facility
Rutherford Appleton Laboratory
Chilton
Oxon
OX11 0QX
UK

Tel: + 44 235 44 5881
Fax: + 44 235 44 5720

A. BALAGUROV
Frank Laboratory of
Neutron Physics
JINR
141980 Dubna
Moscow Region
RUSSIA

Tel:
Fax: + 7 096 21 65085

P. J. S. B. BARRATT
ISIS Facility
Rutherford Appleton Laboratory
Chilton
Oxon
OX11 0QX
UK

Tel: + 44 235 44 6715
Fax: + 44 235 445632

G. BAUER
Paul Scherrer Institute
CH-5232 Villigen,
PSI
SWITZERLAND

Tel: + 41 5699 2524
Fax: + 41 5699 3294

S. BENNINGTON
ISIS Facility
Rutherford Appleton Laboratory
Chilton
Oxon
OX11 0QX
UK

Tel: + 44 235 44 5193
Fax: + 44 235 44 5720

J. R. J. BENNETT
ISIS Facility
Rutherford Appleton Laboratory
Chilton
Oxon
OX11 0QX
UK

Tel: + 44 235 44 6379
Fax: + 44 235 44 5383

T. D. BEYNON
School of Physics and
Space Research
Birmingham University
Birmingham
B15 2TT
UK

Tel: + 44 21 414 4694
Fax: + 44 21 414 4725

L. N. BLUMBERG
National Synchrotron Light
Source
Building 725
Brookhaven National Laboratory
Upton
NY 11973
USA

Tel: + 1 516 282 4600
Fax: + 1 516 282 4745

D. BÖHNE
Gesellschaft für
Schwerionenforschung mbH
Planckstrasse 1
D-6100 Darmstadt
GERMANY

Tel: + 49 6151 359 411
Fax: + 49 6151 359 985

B. BOLAND
ISIS Facility
Rutherford Appleton Laboratory
Chilton
Oxon
OX11 0QX
UK

Tel: + 44 235 44 5679
Fax: + 44 235 44 5383

K. BONGARDT
KFA
D-52425 Jülich
GERMANY

Tel: + 49 2461 61 5468
Fax: + 49 2461 61 2670

P. BÖNI
Labor für Neutronenstreuung
ETH & PSI
CH-5232 Villigen PSI
SWITZERLAND

Tel: + 41 56 99 2518
Fax: + 41 56 98 2635

Z. BOWDEN
ISIS Facility
Rutherford Appleton Laboratory
Chilton
Oxon
OX11 0QX
UK

Tel: + 44 235 44 5683
Fax: + 44 235 44 5383

B. S. BROWN
IPNS Division Building 360
Argonne National Laboratory
9700 South Cass Avenue
Argonne
IL 60439
USA

Tel: + 1 708 252 4999
Fax: + 1 708 252 4163

T. A. BROOME
ISIS Facility
Rutherford Appleton Laboratory
Chilton
Oxon
OX11 0QX
UK

Tel: + 44 235 44 6255
Fax: + 44 235 44 5632

T. O. BRUN
Manuel Lujan Jr
Neutron Scattering Centre
LANSCE ms h805
Los Alamos
New Mexico 87545
USA

Tel: + 1 505 667 8841
Fax: + 1 505 665 2676

D. G. BUCKNALL
ISIS Facility
Rutherford Appleton Laboratory
Chilton
Oxon
OX11 0QX
UK

Tel: + 44 235 44 5871
Fax: + 44 235 44 5383

C. J. CARLILE
ISIS Facility
Rutherford Appleton Laboratory
Chilton
Oxon
OX11 0QX
UK

Tel: + 44 235 44 5684
Fax: + 44 235 44 5383

J. M. CARPENTER
IPNS
Argonne National Laboratory
9700 South Cass Avenue
Argonne
Illinois 60439
USA

Tel: + 1 708 972 5519
Fax: + 1 708 972 4163

Y. CHO
Advanced Photon Source
Argonne National Laboratory
9700 South Cass Avenue
Argonne
Illinois 60439
USA

Tel: + 1 708 252 6616
Fax: + 1708 252 4599

M. A. CLARKE-GAYTHER
ISIS Facility
Rutherford Appleton Laboratory
Chilton
Oxon
OX11 0QX
UK

Tel: + 44 235 44 6133
Fax: + 44 235 44 5642

K. N. CLAUSEN
Solid State Physics Department
Risø National Laboratory
DK 4000 Roskilde
DENMARK

Tel: + 45 4677 4704
Fax: + 45 42 370115

R. L. S. COLEMAN
ISIS Facility
Rutherford Appleton Laboratory
Chilton
Oxon
OX11 0QX
UK

Tel: + 44 235 44 6339
Fax: + 44 235 44 5642

H. CONRAD
Institut für Festkörperforschung
Forschungszentrum Jülich
Postfach 1913
D-52425 Jülich
GERMANY

Tel: + 49 2461 612610
Fax: + 49 2461 615327

M. K. CRADDOCK
Triumf
4004 Westbrook Mall
Vancouver BC
V6T 2A3
CANADA

Tel: + 1 604 222 1047
Fax: + 1 604 222 1074

R. K. CRAWFORD
IPNS
Argonne National Laboratory
9700 South Cass Avenue
Argonne
Illinois 60439
USA

Tel: + 1 708 972 5519
Fax: + 1 708 972 4163

K. CRENNELL
ISIS Facility
Rutherford Appleton Laboratory
Chilton
Oxon
OX11 0QX
UK

L. De GRAAF
IRI
Mekelweg 15
2629 JM Delft
The NETHERLANDS

Tel: + 31 15 78 55 45
Fax: + 31 15 78 64 22

C. J. DENSHAM
ISIS Facility
Rutherford Appleton Laboratory
Chilton
Oxon
OX11 0QX
UK

Tel: + 44 235 44 6273
Fax: + 44 235 44 5642

J. DUPPICH
Paul Scherrer Institute
CH-5232 Villigen,
PSI
SWITZERLAND

Tel: + 41 5699 3320
Fax: + 41 5699 3294

R. S. ECCLESTON
ISIS Facility
Rutherford Appleton Laboratory
Chilton
Oxon
OX11 0QX
UK

Tel: + 44 235 44 6437
Fax: + 44 235 44 5383

Y. ENDOH
Faculty of Science
Tohoko University
Aoba, Aramaki
Aoba-ku
Sendai-shi 980
JAPAN

Tel: + 81 22 222 1800 ext 3306
Fax: + 81 22 225 1891

D. FILGES
Forschungszentrum Jülich GmbH
Institut für Kernphysik
Postfach 19 13
D-52425 Jülich
GERMANY

Tel: + 49 2451 61 5232
Fax: + 49 2461 61 3930

J. L. FINNEY
Department of Physics and
Astronomy
University College London
Gower Street
London
WC1E 6BT
UK

Tel: + 44 71 380 7850
Fax: + 44 71 380 7145

T. FLEMMING
Reuter Stokes Inc.
Edison Park
8499 Darrow Road
Twinsburg
OH 44087
USA

Tel: + 1 216 425 3755
Fax: + 1 216 425 4045

M. FUJITA
Physics Faculty of Science
Kobe University
Rokkodai
Nada
Kobe 657
JAPAN

Tel: + 81 78 881 1212 ext 4376
Fax: + 81 78 881 7593

T. FUKUNAGA
School of Engineering
Nagoya University
Furo-cho, Chikusa-ku
Nagoya-shi 464
JAPAN

Tel: + 81 52 781 5111
Fax: + 81 52 782 2129

M. FURUSAKA
BSF
National Laboratory for High
Energy Physics
1-1, Oho
Tsukuba-shi 305
JAPAN

Tel: + 81 298 64 1171
Fax: + 81 298 64 3202

I. S. K. GARDNER
ISIS Facility
Rutherford Appleton Laboratory
Chilton
Oxon
OX11 0QX
UK

Tel: + 44 235 44 6109
Fax: + 44 235 44 5383

R. GEICK
Physikalisches Institut
Am Hubland
D-8700 Würzburg
GERMANY

Tel: + 49 931 8885898
Fax: + 49 931 8885142

J. A. GOLDSTONE
Lansce MS H805
Los Alamos National Laboratory
Los Alamos
NM 87545
USA

Tel: + 1 505 667 3629
Fax: + 1 505 655 2676

M. E. HAGEN
ISIS Facility
Rutherford Appleton Laboratory
Chilton
Oxon
OX11 0QX
UK

Tel: + 44 235 44 5805
Fax: + 44 235 44 5383

A. C. HANNON
ISIS Facility
Rutherford Appleton Laboratory
Chilton
Oxon
OX11 0QX
UK

Tel: + 44 235 44 5358
Fax: + 44 235 44 5383

M. R. HAROLD
ISIS Facility
Rutherford Appleton Laboratory
Chilton
Oxon
OX11 0QX
UK

Tel: + 44 235 44 5371
Fax: + 44 235 44 5632

R. K. HEENAN
ISIS Facility
Rutherford Appleton Laboratory
Chilton
Oxon
OX11 0QX
UK

Tel: + 44 235 44 6744
Fax: + 44 235 44 5720

H. HEINRICHS
University of Wuppertal
Gausstr 20
D-5600 Wuppertal 1
GERMANY

Tel: + 49 202 4392753
Fax: + 49 202 4392811

M. HOLDING
ISIS Facility
Rutherford Appleton Laboratory
Chilton
Oxon
OX11 0QX
UK

Tel: + 44 235 44 6692
Fax: + 44 235 44 5720

W. S. HOWELLS
ISIS Facility
Rutherford Appleton Laboratory
Chilton
Oxon
OX11 0QX
UK

Tel: + 44 235 44 5680
Fax: + 44 235 44 5383

H. IKEDA
BSF National Laboratory for
High Energy Physics
(KEK)
Oho 1-1
Tsukuba 305
JAPAN

Tel: + 81 298 64 5613
Fax: + 81 298 64 3202

Y. IRIE
BSF National Laboratory for
High Energy Physics
(KEK)
Oho 1-1
Tsukuba 305
JAPAN

Tel: + 81 298 64 5607
Fax: + 81 298 64 3202

K. ISHIBASHI
Dept. for Nuclear Engineering
Kyushu University
6-10-1 Hakozaki
Higashi-ku
Fukuoka 812
JAPAN

Tel: + 81 92 641 1101 ext 5822
Fax: + 81 92 641 7098

A. JASON
Los Alamos National Laboratory
Los Alamos
NM 87544
USA

Tel: + 1 505 667 2842
Fax: + 1 505 665 2904

E. JERICHA
Atom Institut
Schuttelstrasse 115
A-10020 Wien
AUSTRIA

Tel: + 43 1 21701 271
Fax: + 43 1 2189220

M. W. JOHNSON
ISIS Facility
Rutherford Appleton Laboratory
Chilton
Oxon
OX11 0QX
UK

Tel: + 44 235 44 5418
Fax: + 44 235 44 5383

H. J. JONES
ISIS Facility
Rutherford Appleton Laboratory
Chilton
Oxon
OX11 0QX
UK

Tel: + 44 235 44 5182
Fax: + 44 235 44 5720

Y. KIYANAGI
Hokkaido University
Kita 13
Nishi 8
Sapporo 060
JAPAN

Tel: + 81 11 716 2111 ext 6651
Fax: + 81 11 717 4745

S. KLOTZ
Physique des Milieux Condensés
CNRS, URA 782
Paris

K. J. KNOWLES
ISIS Facility
Rutherford Appleton Laboratory
Chilton
Oxon
OX11 0QX
UK

Tel: + 44 235 44 5305
Fax: + 44 235 44 5383

R. L. KUSTOM
Argonne National Laboratory
9700 South Cass Avenue
Building 371T
Argonne
IL 60439
USA

Tel: + 1 708 252 6533
Fax: + 1 708 252 5291

H. LENGELER
CERN
CH-1211
Geneva 23
SWITZERLAND

Tel: + 41 22 767 5862
Fax: + 41 22 767 8666

C. LOONG
IPNS/360
Argonne National Laboratory
9700 South Cass Avenue
Argonne
IL 60439
USA

Tel: + 1 708 252 5596
Fax: + 1 708 252 4163

R. J. MACEK
MP Division
Los Alamos Laboratory
Mail Stop H848
Los Alamos
NM 87545
USA

Tel: + 1 505 667 5670
Fax: + 1 505 665 1712

D. MARTIN
ISIS Facility
Rutherford Appleton Laboratory
Chilton
Oxon
OX11 0QX
UK

Tel: + 44 235 44 5718
Fax: + 44 235 44 5720

Y. MASUDA
c/o Dr J D Bowman
MP-9 LANL
Los Alamos
NM 87545
USA

Tel: + 1 505 667 5670
Fax: + 1 505 665 1712

J. MAYERS
ISIS Facility
Rutherford Appleton Laboratory
Chilton
Oxon
OX11 0QX
UK

Tel: + 44 235 44 5882
Fax: + 44 235 44 5383

D. McGEE
Accelerator Systems Division
Argonne National Laboratory
9700 South Cass Avenue
Argonne
IL 60439-4814
USA

Tel: + 1 708 262 2000
Fax: + 1 708 252 9480

F. MEZEI
HMI/BENSC
D-14109
Berlin 39
Glienicker Str. 100
GERMANY

Tel: + 49 30 80622322
Fax: + 49 30 80622523

S. P. MØLLER
Institute for Synchrotron
Radiation (ISA)
Aarhus University
DK-8000
Aarthus C
DENMARK

Tel: + 45 86 12 8899
Fax: + 45 86 12 0440

M. MOTOKAWA
Faculty of Science
Kobe University
Rokkodai
Nada
Koba 657
JAPAN

Tel: + 81 78 881 1212 ext 4379
Fax: + 81 78 881 7593

E. M. MOTT
ISIS Facility
Rutherford Appleton Laboratory
Chilton
Oxon
OX11 0QX
UK

Tel: + 44 235 44 5708
Fax: + 44 235 44 5720

I. NATKANIEC
Frank Laboratory of
Neutron Physics
JINR
141980 Dubna
Moscow Region
RUSSIA

Fax: + 7 096 21 65085

R.D. NEEF
Forschungszentrum Jülich GmbH
Institut für Kernphysik
Postfach 19 13
D-52425 Jülich
GERMANY

Tel: + 49 2461 61 5232
Fax: + 49 2461 61 3930

S. NINOMIYA
PS Div. Accelerator Department
KEK National Laboratory for
High Energy Physics
1-1 Oho Tsukuba-city
Ibaraki 3205
JAPAN

Tel: + 81 298 64 1171
Fax: + 81 298 64 3182

J. NORRIS
ISIS Facility
Rutherford Appleton Laboratory
Chilton
Oxon
OX11 0QX
UK

Tel: + 44 235 44 5807
Fax: + 44 235 44 5720

J. PENFOLD
ISIS Facility
Rutherford Appleton Laboratory
Chilton
Oxon
OX11 0QX
UK

Tel: + 44 235 44 5681
Fax: + 44 235 44 5383

T. G.PERRING
ISIS Facility
Rutherford Appleton Laboratory
Chilton
Oxon
OX11 0QX
UK

Tel: + 44 235 44 5428
Fax: + 44 235 44 5383

C. W. PLANNER
ISIS Facility
Rutherford Appleton Laboratory
Chilton
Oxon
OX11 0QX
UK

Tel: + 44 235 44 5434
Fax: + 44 235 44 5632

C. R. PRIOR
ISIS Facility
Rutherford Appleton Laboratory
Chilton
Oxon
OX11 0QX
UK

Tel: + 44 235 44 5262
Fax: + 44 235 44 5632

R. PYNN
Los Alamos National Laboratory
P O Box 1663
MS H805
Los Alamos
NM 87545
USA

Tel: + 1 505 665 1583
Fax: + 1 505 665 2676

S. P. H. QUINTON
ISIS Facility
Rutherford Appleton Laboratory
Chilton
Oxon
OX11 0QX
UK

Tel: + 44 235 44 5534
Fax: + 44 235 44 5383

G. H. REES
ISIS Facility
Rutherford Appleton Laboratory
Chilton
Oxon
OX11 0QX
UK

Tel: + 44 235 44 5595
Fax: + 44 235 44 5632

M. REGLER
c/o Institut für
Hochenergiephysik der
Österreichischen Akademie
der Wissenschaften
Nikolsdorfer Gasse 18
A 1050 Wien
AUSTRIA

Tel: + 43 222 55 73 28
Fax: + 43 222 55 75 89

N. J. RHODES
ISIS Facility
Rutherford Appleton Laboratory
Chilton
Oxon
OX11 0QX
UK

Tel: + 44 235 44 5491
Fax: + 44 235 44 5720

R. ROBINSON
LANSCE MS-H805
Los Alamos National Laboratory
Los Alamos
NM 87545
USA

Tel: + 1 505 667 3626
Fax: + 1 505 665 2676

G. J. RUSSELL
LANSCE MS-H505
Los Alamos National Laboratory
Los Alamos
NM 87545
USA

Fax: + 1 505 665 2676

H. L. RUTKOWSKI
Lawrence Berkely Laboratory
50-149
1 Cyclotron Road
Berkeley
CA 94720
USA

Tel: + 1 510 486 7209
Fax: + 1 510 486 6003

W. SCHÄFER
Forschungszentrum Jülich
Postfach 1913
D-52425 Jülich
GERMANY

Tel: + 49 2461 616024
Fax: + 49 2461 613841

H. SCHÖNAUER
PS Division
CERN
CH 1211
Geneve 23
SWITZERLAND

Tel: + 41 22 767 40 78
Fax: + 41 22 767 8200

S. SCHRIBER
Los Alamos National Laboratory
P O Box 1663
M S H811
Los Alamos
NM 87545
USA

W. SCHMIDT
ISIS Facility
Rutherford Appleton Laboratory
Chilton
Oxon
OX11 0QX
UK

Tel: + 44 235 44 5352
Fax: + 44 235 44 5383

M. SCHUSTER
Atominstitut der
Österreichischen Universitäten
Schottelstr 115
A-1020 Wien
AUSTRIA

Tel: + 43 1 557328 36
Fax: + 43 1 2189220

P. A. SEEGER
MS/HB05
Los Alamos National Laboratory
P O Box 1663
M S H811
Los Alamos
NM 87545
USA

Tel: + 1 505 662 7163
Fax: + 1 505 665 2676

E. SHABALIN
Frank Laboratory of
Neutron Physics
JINR
141980 Dubna
Moscow Region
RUSSIA

Fax: + 7 096 21 65085

R. SIDLOW
ISIS Facility
Rutherford Appleton Laboratory
Chilton
Oxon
OX11 0QX
UK

Tel: + 44 235 44 5219
Fax: + 44 235 44 5632

D. S. SIVIA
ISIS Facility
Rutherford Appleton Laboratory
Chilton
Oxon
OX11 0QX
UK

Tel: + 44 235 44 5685
Fax: + 44 235 44 5383

A. K. SOPER
ISIS Facility
Rutherford Appleton Laboratory
Chilton
Oxon
OX11 0QX
UK

Tel: + 44 235 44 5543
Fax: + 44 235 44 5383

T. SPRINGER
Institut für Festkörperforschung
Forschungszentrum Jülich GmbH
Postfach 1913
D-52425 Jülich
GERMANY

Tel: + 49 2461 61 4693
Fax: + 49 2461 61 2610

Y. STAVISSKY
Institute for Nuclear Research
60th October Anniversary
Prospect 7a
117312 Moscow
RUSSIA

Tel: + 7 95 334 0191
Fax: + 7 95 135 2268

H. STECHEMESSER
Zentralabteilung Technologie
Forschungszentrum Jülich
Postfach 1913
D - 52425 Jülich
GERMANY

Tel: + 49 2461 616740
Fax: + 49 2461 616816

U. STEIGENBERGER
ISIS Facility
Rutherford Appleton Laboratory
Chilton
Oxon
OX11 0QX
UK

Tel: + 44 235 44 5145
Fax: + 44 235 44 5383

A. D. TAYLOR
ISIS Facility
Rutherford Appleton Laboratory
Chilton
Oxon
OX11 0QX
UK

Tel: + 44 235 44 6681
Fax: + 44 235 44 5383

H. TIETZE-JAENSCH
ISIS Facility
Rutherford Appleton Laboratory
Chilton
Oxon
OX11 0QX
UK

Tel: + 44 235 44 5685
Fax: + 44 235 44 5383

J. TOMKINSON
ISIS Facility
Rutherford Appleton Laboratory
Chilton
Oxon
OX11 0QX
UK

Tel: + 44 235 44 6686
Fax: + 44 235 44 5383

W. WAGNER
Paul Scherrer Institute
CH-5232 Villigen
PSI
SWITZERLAND

Tel: + 41 56 992517
Fax: + 41 56 98 2635

C. M. WORSOP
ISIS Facility
Rutherford Appleton Laboratory
Chilton
Oxon
OX11 0QX
UK

Tel: + 44 235 44 6374
Fax: + 44 235 44 5632

N. WATANABE
National Laboratory for
High Energy Physics
1-1 Oho
Tsukuba
Ibaraki 305
JAPAN

Tel: + 81 298 64 5601
Fax + 81 298 64 3202

J. R. P. WEBSTER
ISIS Facility
Rutherford Appleton Laboratory
Chilton
Oxon
OX11 0QX
UK

Tel: + 44 235 44 5193
Fax: + 44 235 44 5383

N. D. WEST
ISIS Facility
Rutherford Appleton Laboratory
Chilton
Oxon
OX11 0QX
UK

Tel: + 44 235 44 6122
Fax: + 44 235 44 5632

P. R. WILLIAMS
Director
Rutherford Appleton Laboratory
Chilton
Oxon
OX11 0QX
UK

Tel: + 44 235 44 5533
Fax: + 44 235 44 5632

C. C. WILSON
ISIS Facility
Rutherford Appleton Laboratory
Chilton
Oxon
OX11 0QX
UK

Tel: + 44 235 44 5137
Fax: + 44 235 44 5383

I. YAMANE
PS Division
National Laboratory for
High Energy Physics
1-1 Oho
Tsukuba
Ibaraki 305
JAPAN

Tel: + 81 298 64 5268
Fax: + 81 298 64 3182

V. YOUNG
Reuter Stokes Inc.
Edison Park
8499 Darrow Road
Twinsburg
OH 44087
USA

Tel: + 1 216 425 3755
Fax: + 1 216 425 4045

E. ZAPLATINE
Hahn-Meitner Institut
Glienicker Str. 100
D-14109 Berlin 33
GERMANY

Tel: + 49 30 8062 2293
Fax: + 49 30 8062 2293

K. ZIEGLER
Hahn-Meitner Institut
Berlin GmBH
Glienicker Str. 100
D-14109 Berlin 39
Germany

Tel: + 49 30 8062 2498
Fax: + 49 30 8062 2293